The game show where science wins big *p. 493*

Precision medicine for psychiatry *p. 499*

Climate change threatens one in six species *pp. 501 & 571*

Science

$10
1 MAY 2015
sciencemag.org

AAAS

SPECIAL ISSUE

FRONTIERS IN LIGHT AND OPTICS

CONTENTS

501 & 571
Biodiversity loss in a changing climate

1 MAY 2015 • VOLUME 348 • ISSUE 6234

NEWS

IN BRIEF

480 Roundup of the week's news

IN DEPTH

484 NEPAL DISASTER PRESAGES A COMING MEGAQUAKE
Rupture in quiet region of crust suggests Himalayan threat was underestimated *By E. Hand and P. Pulla*

485 IN GUINEA, A LONG, DIFFICULT ROAD TO ZERO EBOLA CASES
The country could soon be the epidemic's last holdout *By M. Enserink*

486 EMBRYO ENGINEERING STUDY SPLITS SCIENTIFIC COMMUNITY
First test of gene-editing technique on human embryos illustrates clinical risks *By J. Kaiser and D. Normile*

488 HAVE A SWEET TOOTH? NEW BLOOD TEST COULD TELL
Isotope ratios could aid research by tracking added sugars *By V. Callier*

489 GREECE RAIDS RESEARCH FUNDS TO PAY SALARIES
Beleaguered scientists are spending reserves to protect them from confiscation *By E. Cartlidge*

FEATURES

490 BEYOND GRAPHENE
The ultrathin form of carbon has inspired other atoms-thick materials that promise even bigger technological payoffs *By R. F. Service*

493 WHAT IS *JEOPARDY!*?
This popular TV game show has a thing for science *By J. Cohen*

INSIGHTS

PERSPECTIVES

496 1000 DAMS DOWN AND COUNTING
Dam removals are reconnecting rivers in the United States *By J. E. O'Connor* et al.

498 THE QUANTUM HALO STATE OF THE HELIUM TRIMER
Femtosecond laser pulses help to take a snapshot of the huge elusive Efimov state *By O. Kornilov*
▸ REPORT P. 551

499 BRAIN DISORDERS? PRECISELY
Precision medicine comes to psychiatry *By T. R. Insel and B. N. Cuthbert*

501 EXTINCTION RISKS FROM CLIMATE CHANGE
How will climate change affect global biodiversity? *By J. Hille Ris Lambers*
▸ REPORT P. 571

502 HUMAN-WILDLIFE CONFLICTS IN A CROWDED AIRSPACE
How can the ecological consequences of the increasing use of airspace by humans be minimized?
By S. A. Lambertucci et al.

504 SECURE SUSTAINABLE SEAFOOD FROM DEVELOPING COUNTRIES
Require improvements as conditions for market access *By G. S. Sampson* et al.
▸ PODCAST

506 EARLY LIFE AIRE
The development of particular T cells at a specific time prevents autoimmunity *By A. Tanaka and S. Sakaguchi*
▸ REPORT P. 589

BOOKS *ET AL.*

508 FORAGERS, FARMERS, AND FOSSIL FUELS
By I. Morris, reviewed by P. Turchin

509 FROM SIGHT TO LIGHT
By A. M. Smith, reviewed by C. Dainty
▸ LIGHT AND OPTICS SECTION P. 514

509 WILD IDEAS
By E. Kelsey

LETTERS

511 AMERICA'S CRISIS OF FAITH IN SCIENCE
By T. L. Pittinsky

511 OUTSIDE THE TOWER: BRINGING SCIENCE INSIDE PRISON WALLS
By C. J. LeRoy

512 BEWARE STUDY DESIGN MEASUREMENT ERRORS
By D. B. Khatry

Published by AAAS

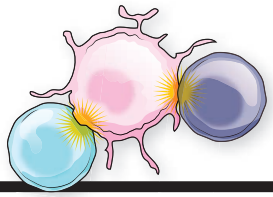

506 & 589
Suppressing autoimmunity

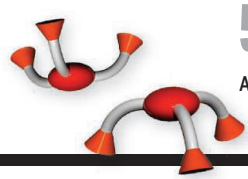

555
A tool to probe salt bridges

RESEARCH

IN BRIEF

536 From *Science* and other journals

RESEARCH ARTICLE

539 **DNA REPAIR**
Proteomics reveals dynamic assembly of repair complexes during bypass of DNA cross-links *M. Räschle* et al.
RESEARCH ARTICLE SUMMARY; FOR FULL TEXT: dx.doi.org/10.1126/science.1253671

REPORTS

540 **QUANTUM SIMULATION**
Two-dimensional superexchange-mediated magnetization dynamics in an optical lattice *R. C. Brown* et al.

544 **QUANTUM GASES**
Observation of isolated monopoles in a quantum field *M. W. Ray* et al.

547 **FERROELECTRICS**
Observation of a periodic array of flux-closure quadrants in strained ferroelectric $PbTiO_3$ films
Y. L. Tang et al.

551 **THREE-BODY PHYSICS**
Observation of the Efimov state of the helium trimer *M. Kunitski* et al.
▸ PERSPECTIVE P. 498

555 **IONIC INTERACTIONS**
Subnanoscale hydrophobic modulation of salt bridges in aqueous media
S. Chen et al.

560 **BRAIN COMPUTATION**
Selective information routing by ventral hippocampal CA1 projection neurons
S. Ciocchi et al.

563 **BIOMECHANICS**
Mechanistic origins of bombardier beetle (Brachinini) explosion-induced defensive spray pulsation *E. M. Arndt* et al.

567 **EXTINCTIONS**
Paleontological baselines for evaluating extinction risk in the modern oceans *S. Finnegan* et al.

571 **CLIMATE CHANGE**
Accelerating extinction risk from climate change *M. C. Urban*
▸ PERSPECTIVE P. 501

574 **BACTERIAL DIVISION**
Mechanical crack propagation drives millisecond daughter cell separation in *Staphylococcus aureus*
X. Zhou et al.

578 **PROTEIN DYNAMICS**
Direct observation of hierarchical protein dynamics
J. R. Lewandowski et al.

581 **STRUCTURAL BIOLOGY**
Structures of the CRISPR-Cmr complex reveal mode of RNA target positioning
D. W. Taylor et al.

585 **RETROTRANSPOSONS**
An RNA polymerase III subunit determines sites of retrotransposon integration *A. Bridier-Nahmias* et al.

589 **IMMUNE TOLERANCE**
Regulatory T cells generated early in life play a distinct role in maintaining self-tolerance
S. Yang et al.
▸ PERSPECTIVE P. 506

DEPARTMENTS

479 **EDITORIAL**
Transparency versus harassment
By Michael Halpern and Michael Mann

602 **WORKING LIFE**
From war to science paradise
By Rachel Bernstein

SPECIAL SECTION

Light and Optics

INTRODUCTION

514 Frontiers in light and optics

REVIEWS

516 Nanophotonics: Shrinking light-based technology
A. F. Koenderink et al.

521 Transforming the optical landscape *J. B. Pendry* et al.

525 Quantum optics: Science and technology in a new light
I. A. Walmsley

530 Beyond crystallography: Diffractive imaging using coherent x-ray light sources *J. Miao* et al.

SEE ALSO
▸ BOOKS *ET AL*. P. 509

ON THE COVER

Sculpting coherent x-ray light with visible lasers. When an atom is hit by a strong rosette-shaped laser field (purple) (a superposition of red and blue circularly polarized lasers with opposite helicity), an electron (green) is ripped from, and recollides with, the parent ion. The result is the emission of bright, circularly polarized light at extreme ultraviolet wavelengths (blue). For more on cutting-edge advances in light and optics, see page 514. *Image: The Kapteyn/Murnane Group and Steve Burrows, JILA; and the Cohen Group, Technion*

Science Staff 478
New Products 595
Science Careers 596

SCIENCE (ISSN 0036-8075) is published weekly on Friday, except the last week in December, by the American Association for the Advancement of Science, 1200 New York Avenue, NW, Washington, DC 20005. Periodicals mail postage (publication No. 484460) paid at Washington, DC, and additional mailing offices. Copyright © 2015 by the American Association for the Advancement of Science. The title SCIENCE is a registered trademark of the AAAS. Domestic individual membership and subscription (51 issues): $153 ($74 allocated to subscription). Domestic institutional subscription (51 issues): $1282; Foreign postage extra: Mexico, Caribbean (surface mail) $55; other countries (air assist delivery) $85. First class, airmail, student, and emeritus rates on request. Canadian rates with GST available upon request, GST #1254 88122. Publications Mail Agreement Number 1069624. **Printed in the U.S.A.**
Change of address: Allow 4 weeks, giving old and new addresses and 8-digit account number. **Postmaster:** Send change of address to AAAS, P.O. Box 96178, Washington, DC 20090–6178. **Single-copy sales:** $10.00 current issue, $15.00 back issue prepaid includes surface postage; bulk rates on request. **Authorization to photocopy** material for internal or personal use under circumstances not falling within the fair use provisions of the Copyright Act is granted by AAAS to libraries and other users registered with the Copyright Clearance Center (CCC) Transactional Reporting Service, provided that $30.00 per article is paid directly to CCC, 222 Rosewood Drive, Danvers, MA 01923. The identification code for *Science* is 0036-8075. *Science* is indexed in the *Reader's Guide to Periodical Literature* and in several specialized indexes.

Published by AAAS

Science
AAAS
1200 New York Avenue, NW, Washington, DC 20005
Bateman House, 82-88 Hills Road, Cambridge, UK CB2 1LQ

Editor-in-Chief Marcia McNutt
Executive Editor Monica M. Bradford **News Editor** Tim Appenzeller
Managing Editor, Research Journals Katrina L. Kelner
Deputy Editors Barbara R. Jasny, Andrew M. Sugden(UK), Valda J. Vinson, Jake S. Yeston

Research and Insights

SR. EDITORS Caroline Ash(UK), Gilbert J. Chin, Lisa D. Chong, Julia Fahrenkamp-Uppenbrink(UK), Pamela J. Hines, Stella M. Hurtley(UK), Paula A. Kiberstis, Marc S. Lavine(Canada), Kristen L. Mueller, Ian S. Osborne(UK), Beverly A. Purnell, L. Bryan Ray, Guy Riddihough, H. Jesse Smith, Jelena Stajic, Peter Stern(UK), Phillip D. Szuromi, Brad Wible, Nicholas S. Wigginton, Laura M. Zahn **ASSOCIATE EDITORS** Brent Grocholski, Sacha Vignieri **ASSOCIATE BOOK REVIEW EDITOR** Valerie B. Thompson **ASSOCIATE LETTERS EDITOR** Jennifer Sills **CHIEF CONTENT PRODUCTION EDITOR** Cara Tate **SR. CONTENT PRODUCTION EDITORS** Harry Jach **CONTENT PRODUCTION EDITORS** Jeffrey E. Cook, Chris Filiatreau, Cynthia Howe, Lauren Kmec, Barbara P. Ordway **SR. EDITORIAL COORDINATORS** Carolyn Kyle, Beverly Shields **EDITORIAL COORDINATORS** Ramatoulaye Diop, Joi S. Granger, Lisa Johnson, Anita Wynn **PUBLICATIONS ASSISTANTS** Aneera Dobbins, Jeffrey Hearn, Dona Mathieu, Le-Toya Mayne Flood, Shannon McMahon, Scott Miller, Jerry Richardson, Rachel Roberts(UK), Alice Whaley(UK), Brian White **EXECUTIVE ASSISTANT** Anna Bashkirova **ADMINISTRATIVE SUPPORT** Janet Clements(UK), Monika Magon(UK, Intern), Lizanne Newton(UK), Maryrose Madrid, John Wood(UK)

News

NEWS MANAGING EDITOR John Travis **INTERNATIONAL EDITOR** Richard Stone **DEPUTY NEWS EDITORS** Daniel Clery(UK), Robert Coontz, Elizabeth Culotta, David Grimm, David Malakoff, Leslie Roberts **CONTRIBUING EDITORS** Martin Enserink(Europe), Mara Hvistendahl **SR. CORRESPONDENTS** Jeffrey Mervis, Elizabeth Pennisi **NEWS WRITERS** Adrian Cho, Jon Cohen, Jennifer Couzin-Frankel, Carolyn Gramling, Eric Hand, Jocelyn Kaiser, Kelly Servick, Robert F. Service, Erik Stokstad(Cambridge, UK), Emily Underwood **INTERNS** Emily Conover, David Shultz, Jia You **CONTRIBUTING CORRESPONDENTS** Pallava Bagla(South Asia), Michael Balter(Paris), John Bohannon, Ann Gibbons, Sam Kean, Richard A. Kerr, Eli Kintisch, Kai Kupferschmidt(Berlin), Andrew Lawler, Christina Larson(Beijing), Mitch Leslie, Charles C. Mann, Eliot Marshall, Virginia Morell, Dennis Normile(Tokyo), Heather Pringle, Tania Rabesandratana(Brussels), Gretchen Vogel(Berlin), Lizzie Wade(Mexico City) **CAREERS** Jim Austin(Editor), Donisha Adams, Rachel Bernstein **COPY EDITORS** Kara Estelle, Nora Kelly, Jennifer Levin **ADMINISTRATIVE SUPPORT** Scherraine Mack

Executive Publisher Rush D. Holt
Publisher Kent R. Anderson **Chief Digital Media Officer** Rob Covey

BUSINESS OPERATIONS AND ADMINISTRATION DIRECTOR Deborah Rivera-Wienhold **BUSINESS SYSTEMS AND FINANCIAL ANALYSIS DIRECTOR** Randy Yi **MANAGER OF FULFILLMENT SYSTEMS** Neal Hawkins **SYSTEMS ANALYST** Nicole Mehmedovich **ASSISTANT DIRECTOR, BUSINESS OPERATIONS** Eric Knott **MANAGER, BUSINESS OPERATIONS** Jessica Tierney **BUSINESS ANALYSTS** Cory Lipman, Cooper Tilton, Celeste Troxler **FINANCIAL ANALYST** Jeremy Clay **RIGHTS AND PERMISSIONS ASSISTANT DIRECTOR** Emilie David **PERMISSIONS ASSOCIATE** Elizabeth Sandler **RIGHTS, CONTRACTS, AND LICENSING ASSOCIATE** Lili Kiser

MARKETING DIRECTOR Ian King **MARKETING MANAGER** Julianne Wielga **MARKETING ASSOCIATE** Elizabeth Sattler **SR. MARKETING EXECUTIVE** Jennifer Reeves **SR. ART ASSOCIATE, PROJECT MANAGER** Tzeitel Sorrosa **ART ASSOCIATE** Seil Lee **ASSISTANT COMMERCIAL EDITOR** Selby Frame **MARKETING PROJECT MANAGER** Angelissa McArthur **SR. WRITER** Bill Zimmer **PROGRAM DIRECTOR, AAAS MEMBER CENTRAL** Peggy Mihelich **FULFILLMENT SYSTEMS AND OPERATIONS** membership@aaas.org **MANAGER, MEMBER SERVICES** Pat Butler **SPECIALISTS** LaToya Casteel, Javia Flemmings, Latasha Russell **MANAGER, DATA ENTRY** Mickie Napoleoni **DATA ENTRY SPECIALISTS** JJ Regan, Jaimee Wise, Fiona Giblin

DIRECTOR, SITE LICENSING Tom Ryan **DIRECTOR, CORPORATE RELATIONS** Eileen Bernadette Moran **SR. PUBLISHER RELATIONS SPECIALIST** Kiki Forsythe **PUBLISHER RELATIONS MANAGER** Catherine Holland **PUBLISHER RELATIONS, EASTERN REGION** Keith Layson **PUBLISHER RELATIONS, WESTERN REGION** Ryan Rexroth **MANAGER, SITE LICENSE OPERATIONS** Iquo Edim **FULFILLMENT ANALYST** Lana Guz **ASSOCIATE DIRECTOR, MARKETING** Christina Schlecht **MARKETING ASSOCIATES** Thomas Landreth, Minah Kim

DIRECTOR OF WEB TECHNOLOGIES Ahmed Khadr **SR. DEVELOPER** Chris Coleman **DEVELOPERS** Dan Berger, Jimmy Marks **SR. PROJECT MANAGER** Trista Smith **SYSTEMS ENGINEER** Luke Johnson **PRODUCT MANAGER** Walter Jones

CREATIVE DIRECTOR, MULTIMEDIA Martyn Green **DIRECTOR OF ANALYTICS** Enrique Gonzales **SR. WEB PRODUCER** Sarah Crespi **WEB PRODUCER** Alison Crawford **VIDEO PRODUCER** Nguyen Nguyen **SOCIAL MEDIA PRODUCER** Meghna Sachdev

DIRECTOR OF OPERATIONS PRINT AND ONLINE Lizabeth Harman **DIGITAL/PRINT STRATEGY MANAGER** Jason Hillman **QUALITY TECHNICAL MANAGER** Marcus Spiegler **DIGITAL PRODUCTION MANAGER** Lisa Stanford **ASSISTANT MANAGER DIGITAL/PRINT** Rebecca Doshi **DIGITAL MEDIA SPECIALIST** Tara Kelly **SENIOR CONTENT SPECIALISTS** Steve Forrester, Antoinette Hodal, Lori Murphy, Anthony Rosen **CONTENT SPECIALISTS** Jacob Hedrick, Kimberley Oster

DESIGN DIRECTOR Beth Rakouskas **DESIGN EDITOR** Marcy Atarod **SENIOR SCIENTIFIC ILLUSTRATORS** Chris Bickel, Katharine Sutliff **SCIENTIFIC ILLUSTRATOR** Valerie Altounian **SENIOR ART ASSOCIATES** Holly Bishop, Preston Huey **SENIOR DESIGNER** Garvin Grullón **DESIGNER** Chrystal Smith **SENIOR PHOTO EDITOR** William Douthitt **PHOTO EDITOR** Leslie Blizard

DIRECTOR, GLOBAL COLLABORATION, CUSTOM PUBLICATIONS, ADVERTISING Bill Moran **EDITOR, CUSTOM PUBLISHING** Sean Sanders: 202-326-6430 **ASSISTANT EDITOR, CUSTOM PUBLISHING** Tianna Hicklin: 202-326-6463 **ADVERTISING MARKETING MANAGER** Justin Sawyers: 202-326-7061 science_advertising@aaas.org **ADVERTISING MARKETING ASSOCIATE** Javia Flemmings **ADVERTISING SUPPORT MANAGER** Karen Foote: 202-326-6740 **ADVERTISING PRODUCTION OPERATIONS MANAGER** Deborah Tompkins **SR. PRODUCTION SPECIALIST/GRAPHIC DESIGNER** Amy Hardcastle **PRODUCTION SPECIALIST** Yuse Lajiminmuhip **SR. TRAFFIC ASSOCIATE** Christine Hall **SALES COORDINATOR** Shirley Young **ASSOCIATE DIRECTOR, COLLABORATION, CUSTOM PUBLICATIONS/CHINA/TAIWAN/KOREA/SINGAPORE** Ruolei Wu: +86-186 0822 9345, rwu@aaas.org **COLLABORATION/CUSTOM PUBLICATIONS/JAPAN** Adarsh Sandhu + 81532-81-5142 asandhu@aaas.org **EAST COAST/E. CANADA** Laurie Faraday: 508-747-9395, FAX 617-507-8189 **WEST COAST/W. CANADA** Lynne Stickrod: 415-931-9782, FAX 415-520-6940 **MIDWEST** Jeffrey Dembksi: 847-498-4520 x3005, Steven Loerch: 847-498-4520 x3006 **UK EUROPE/ASIA** Roger Goncalves: TEL/FAX +41 43 243 1358 **JAPAN** Katsuyoshi Fukamizu(Tokyo): +81-3-3219-5777 kfukamizu@aaas.org **CHINA/TAIWAN** Ruolei Wu: +186-0082-9345

WORLDWIDE ASSOCIATE DIRECTOR OF SCIENCE CAREERS Tracy Holmes: +44 (0) 1223 326525, FAX +44 (0) 1223 326532 tholmes@science-int.co.uk **CLASSIFIED** advertise@sciencecareers.org **U.S. SALES** Tina Burks: 202-326-6577, Nancy Toema: 202-326-6578 **SALES ADMINISTRATOR** Marci Gallun **EUROPE/ROW SALES** Axel Gesatzki, Sarah Lelarge **SALES ASSISTANT** Kelly Grace **JAPAN** Hiroyuki Mashiki(Kyoto): +81-75-823-1109 hmashiki@aaas.org **CHINA/TAIWAN** Ruolei Wu: +86-186 0082 9345 rwu@aaas.org **MARKETING MANAGER** Allison Pritchard **MARKETING ASSOCIATE** Aimee Aponte

AAAS BOARD OF DIRECTORS RETIRING PRESIDENT, CHAIR Gerald R. Fink **PRESIDENT** Geraldine (Geri) Richmond **PRESIDENT-ELECT** Barbara A. Schaal **TREASURER** David Evans Shaw **CHIEF EXECUTIVE OFFICER** Rush D. Holt **BOARD** Bonnie L. Bassler, May R. Berenbaum, Carlos J. Bustamante, Stephen P.A. Fodor, Claire M. Fraser, Michael S. Gazzaniga, Laura H. Greene, Elizabeth Loftus, Mercedes Pascual

SUBSCRIPTION SERVICES For change of address, missing issues, new orders and renewals, and payment questions: 866-434-AAAS (2227) or 202-326-6417, FAX 202-842-1065. Mailing addresses: AAAS, P.O. Box 96178, Washington, DC 20090-6178 or AAAS Member Services, 1200 New York Avenue, NW, Washington, DC 20005

INSTITUTIONAL SITE LICENSES 202-326-6755 **REPRINTS:** Author Inquiries 800-635-7181 **COMMERCIAL INQUIRIES** 803-359-4578 **PERMISSIONS** 202-326-6765, permissions@aaas.org **AAAS Member Services** 202-326-6417 or http://membercentral.aaas.org/discounts

Science serves as a forum for discussion of important issues related to the advancement of science by publishing material on which a consensus has been reached as well as including the presentation of minority of conflicting points of view. Accordingly, all articles published in *Science*—including editorials, news and comment, and books reviews—are signed and reflect the individual views of the authors and not official points of view adopted by AAAS or the institutions with which the authors are affiliated.

INFORMATION FOR AUTHORS See pages 678 and 679 of the 6 February 2015 issue or access www.sciencemag.org/about/authors

SENIOR EDITORIAL BOARD

Gary King, *Harvard University*
Susan M. Rosenberg, *Baylor College of Medicine,* **Ali Shilatifard,** *Northwestern University*
Feinberg School of Medicine, **Michael S. Turner**, *U. of Chicago*

BOARD OF REVIEWING EDITORS (Statistics board members indicated with **(S)**)

Adriano Aguzzi, *U. Hospital Zürich*
Takuzo Aida, *U. of Tokyo*
Leslie Aiello, *Wenner-Gren Foundation*
Judith Allen, *U. of Edinburgh*
Sonia Altizer, *U. of Georgia*
Sebastian Amigorena, *Institut Curie*
Kathryn Anderson, *Memorial Sloan-Kettering Cancer Center*
Meinrat O. Andreae, *Max-Planck Inst. Mainz*
Paola Arlotta, *Harvard U.*
Johan Auwerx, *EPFL*
David Awschalom, *U. of Chicago*
Jordi Bascompte, *Estación Biológica de Doñana CSIC*
Facundo Batista, *London Research Inst.*
Ray H. Baughman, *U. of Texas, Dallas*
David Baum, *U. of Wisconsin*
Carlo Beenakker, *Leiden U.*
Kamran Behnia, *ESPCI-ParisTech*
Yasmine Belkaid, *NIAID, NIH*
Philip Benfey, *Duke U.*
Stephen J. Benkovic, *Penn State U.*
May Berenbaum, *U. of Illinois*
Gabriele Bergers, *U. of California, San Francisco*
Bradley Bernstein, *Massachusettes General Hospital*
Peer Bork, *EMBL*
Bernard Bourdon, *Ecole Normale Supérieure de Lyon*
Chris Bowler, *École Normale Supérieure*
Ian Boyd, *U. of St. Andrews*
Emily Brodsky, *U. of California, Santa Cruz*
Ron Brookmeyer, *U. of California Los Angeles* **(S)**
Christian Büchel, *U. Hamburg-Eppendorf*
Joseph A. Burns, *Cornell U.*
Gyorgy Buzsaki, *New York U. School of Medicine*
Blanche Capel, *Duke U.*
Mats Carlsson, *U. of Oslo*
David Clapham, *Children's Hospital Boston*
David Clary, *U. of Oxford*
Joel Cohen, *Rockefeller U., Columbia U.*
Jonathan D. Cohen, *Princeton U.*
James Collins, *Boston U.*
Robert Cook-Deegan, *Duke U.*
Alan Cowman, *Walter & Eliza Hall Inst.*
Robert H. Crabtree, *Yale U.*
Roberta Croce, *Vrije Universiteit*
Janet Currie, *Princeton U.*
Jeff L. Dangl, *U. of North Carolina*
Tom Daniel, *U. of Washington*
Frans de Waal, *Emory U.*
Stanislas Dehaene, *Collège de France*
Robert Desimone, *MIT*
Claude Desplan, *New York U.*
Ap Dijksterhuis, *Radboud U. of Nijmegen*
Dennis Discher, *U. of Pennsylvania*
Gerald W. Dorn II, *Washington U. School of Medicine*
Jennifer A. Doudna, *U. of California, Berkeley*
Bruce Dunn, *U. of California, Los Angeles*
Christopher Dye, *WHO*
Todd Ehlers, *U. of Tuebingen*
David Ehrhardt, *Carnegie Inst. of Washington*
Tim Elston, *U. of North Carolina at Chapel Hill*
Gerhard Ertl, *Fritz-Haber-Institut, Berlin*
Barry Everitt, *U. of Cambridge*
Ernst Fehr, *U. of Zurich*
Anne C. Ferguson-Smith, *U. of Cambridge*
Michael Feuer, *The George Washington U.*
Kate Fitzgerald, *U. of Massachusetts*
Peter Fratzl, *Max-Planck Inst.*
Elaine Fuchs, *Rockefeller U.*
Daniel Geschwind, *UCLA*
Andrew Gewirth, *U. of Illinois*
Karl-Heinz Glassmeier, *TU Braunschweig*
Ramon Gonzalez, *Rice U.*
Julia R. Greer, *Caltech*
Elizabeth Grove, *U. of Chicago*
Nicolas Gruber, *ETH Zurich*
Kip Guy, *St. Jude's Children's Research Hospital*
Taekjip Ha, *U. of Illinois at Urbana-Champaign*
Christian Haass, *Ludwig Maximilians U.*
Steven Hahn, *Fred Hutchinson Cancer Research Center*
Michael Hasselmo, *Boston U.*
Martin Heimann, *Max-Planck Inst. Jena*
Yka Helariutta, *U. of Cambridge*
James A. Hendler, *Rensselaer Polytechnic Inst.*
Janet G. Hering, *Swiss Fed. Inst. of Aquatic Science & Technology*
Kai-Uwe Hinrichs, *U. of Bremen*
Kei Hirose, *Tokyo Inst. of Technology*
David Hodell, *U. of Cambridge*
David Holden, *Imperial College*
Lora Hooper, *UT Southwestern Medical Ctr. at Dallas*
Raymond Huey, *U. of Washington*
Steven Jacobsen, *U. of California, Los Angeles*
Kai Johnsson, *EPFL Lausanne*
Peter Jonas, *Inst. of Science & Technology (IST) Austria*
Matt Kaeberlein, *U. of Washington*
William Kaelin Jr., *Dana-Farber Cancer Inst.*
Daniel Kahne, *Harvard U.*
Daniel Kammen, *U. of California, Berkeley*
Masashi Kawasaki, *U. of Tokyo*
Joel Kingsolver, *U. of North Carolina at Chapel Hill*
Robert Kingston, *Harvard Medical School*
Etienne Koechlin, *Ecole Normale Supérieure*
Alexander Kolodkin, *Johns Hopkins U.*
Alberto R. Kornblihtt, *U. of Buenos Aires*
Leonid Kruglyak, *UCLA*
Thomas Langer, *U. of Cologne*
Mitchell A. Lazar, *U. of Pennsylvania*
David Lazer, *Harvard U.*
Thomas Lecuit, *IBDM*
Virginia Lee, *U. of Pennsylvania*
Stanley Lemon, *U. of North Carolina at Chapel Hill*
Ottoline Leyser, *Cambridge U.*
Marcia C. Linn, *U. of California, Berkeley*
Jianguo Liu, *Michigan State U.*
Luis Liz-Marzan, *CIC biomaGUNE*
Jonathan Losos, *Harvard U.*
Ke Lu, *Chinese Acad. of Sciences*
Christian Lüscher, *U. of Geneva*
Laura Machesky, *CRUK Beatson Inst. for Cancer Research*
Anne Magurran, *U. of St. Andrews*
Oscar Marin, *CSIC & U. Miguel Hernández*
Charles Marshall, *U. of California, Berkeley*
C. Robertson McClung, *Dartmouth College*
Graham Medley, *U. of Warwick*
Yasushi Miyashita, *U. of Tokyo*
Mary Ann Moran, *U. of Georgia*
Richard Morris, *U. of Edinburgh*
Alison Motsinger-Reif, *NC State U.* **(S)**
Sean Munro, *MRC Lab. of Molecular Biology*
Thomas Murray, *The Hastings Center*
James Nelson, *Stanford U. School of Med.*
Daniel Neumark, *U. of California, Berkeley*
Timothy W. Nilsen, *Case Western Reserve U.*
Pär Nordlund, *Karolinska Inst.*
Helga Nowotny, *European Research Advisory Board*
Ben Olken, *MIT*
Joe Orenstein, *U. of California Berkeley & Lawrence Berkeley National Lab*
Harry Orr, *U. of Minnesota*
Andrew Oswald, *U. of Warwick*
Steve Palumbi, *Stanford U.*
Jane Parker, *Max-Planck Inst. of Plant Breeding Research*
Giovanni Parmigiani, *Dana-Farber Cancer Inst.* **(S)**
Donald R. Paul, *U. of Texas, Austin*
John H. J. Petrini, *Memorial Sloan-Kettering Cancer Center*
Joshua Plotkin, *U. of Pennsylvania*
Albert Polman, *FOM Institute AMOLF*
Philippe Poulin, *CNRS*
Jonathan Pritchard, *Stanford U.*
David Randall, *Colorado State U.*
Colin Renfrew, *U. of Cambridge*
Felix Rey, *Institut Pasteur*
Trevor Robbins, *U. of Cambridge*
Jim Roberts, *Fred Hutchinson Cancer Research Ctr.*
Barbara A. Romanowicz, *U. of California, Berkeley*
Jens Rostrup-Nielsen, *Haldor Topsoe*
Mike Ryan, *U. of Texas, Austin*
Mitinori Saitou, *Kyoto U.*
Shimon Sakaguchi, *Kyoto U.*
Miquel Salmeron, *Lawrence Berkeley National Lab*
Jürgen Sandkühler, *Medical U. of Vienna*
Alexander Schier, *Harvard U.*
Randy Seeley, *U. of Cincinnati*
Vladimir Shalaev, *Purdue U.*
Robert Siliciano, *Johns Hopkins School of Medicine*
Joseph Silk, *Institut d'Astrophysique de Paris*
Denis Simon, *Arizona State U.*
Alison Smith, *John Innes Centre*
Richard Smith, *U. of North Carolina* **(S)**
John Speakman, *U. of Aberdeen*
Allan C. Spradling, *Carnegie Institution of Washington*
Jonathan Sprent, *Garvan Inst. of Medical Research*
Eric Steig, *U. of Washington*
Paula Stephan, *Georgia State U. and National Bureau of Economic Research*
Molly Stevens, *Imperial College London*
V. S. Subrahmanian, *U. of Maryland*
Ira Tabas, *Columbia U.*
Sarah Teichmann, *Cambridge U.*
John Thomas, *North Carolina State U.*
Shubha Tole, *Tata Institute of Fundamental Research*
Christopher Tyler-Smith, *The Wellcome Trust Sanger Inst.*
Herbert Virgin, *Washington U.*
Bert Vogelstein, *Johns Hopkins U.*
Cynthia Volkert, *U. of Göttingen*
Douglas Wallace, *Dalhousie U.*
David Wallach, *Weizmann Inst. of Science*
Ian Walmsley, *U. of Oxford*
David A. Wardle, *Swedish U. of Agric. Sciences*
David Waxman, *Fudan U.*
Jonathan Weissman, *U. of California, San Francisco*
Chris Wikle, *U. of Missouri* **(S)**
Ian A. Wilson, *The Scripps Res. Inst.* **(S)**
Timothy D. Wilson, *U. of Virginia*
Rosemary Wyse, *Johns Hopkins U.*
Jan Zaanen, *Leiden U.*
Kenneth Zaret, *U. of Pennsylvania School of Medicine*
Jonathan Zehr, *U. of California, Santa Cruz*
Len Zon, *Children's Hospital Boston*
Maria Zuber, *MIT*

BOOK REVIEW BOARD

David Bloom, *Harvard U.,* **Samuel Bowring,** *MIT,* **Angela Creager,** *Princeton U.,*
Richard Shweder, *U. of Chicago,* **Ed Wasserman,** *DuPont*

Published by AAAS

EDITORIAL

Transparency versus harassment

Open records laws worldwide are critical to holding public institutions, including universities, accountable. Such laws protect against inappropriate influence on the scientific enterprise and promote public trust in the integrity of science and scientists. But the growing use of electronic communications by researchers makes these laws vulnerable to misuse. Conversations that used to occur in person and by other less-recordable means are now electronically written. Increasingly, activists across the political spectrum in several countries are requesting not only records of discussions about the strengths and weaknesses of work, but also preliminary paper drafts and private constructive criticisms from colleagues. These requests can attack and intimidate academics, threatening their reputations, chilling their speech, disrupting their research, discouraging them from tackling contentious topics, and ultimately confusing the public.* So what level of disclosure is appropriate? How can public accountability be balanced with the privacy essential for scientific inquiry?

"Open records laws...are... vulnerable to misuse."

As AAAS President Rush Holt noted, "…excessively intrusive demands for personal or irrelevant information that go beyond appropriate levels of oversight" can negatively affect scientific discovery.† As recent examples, four U.S. universities received open records requests for years of correspondence between biologists and several private companies from activists who oppose genetically modified organisms. In 2012, a mining company asked West Virginia University for draft documents and peer-review comments about occupational health research. The burden from these requests can be considerable even if documents are ultimately kept confidential. In 2009, British tobacco marketing researchers reported stress and weeks of lost time after a tobacco manufacturer requested not only correspondence but also primary data, questionnaires, and record descriptions. In 2015, University of Arizona climate researchers reported spending weeks culling through e-mails in response to a request for their correspondence documents.

Court battles are even more time- and resource-intensive. One of us (M.M.) was subjected to a request for all records created as a University of Virginia professor. The request followed congressional inquests, none of which unearthed any impropriety, but manufactured doubt in public understanding of climate change science.‡ The Virginia Supreme Court ruled in 2014 that excessive disclosure could put the university at a "competitive disadvantage," and cause "harm to university-wide research efforts, damage to faculty recruitment and retention, undermining of faculty expectations of privacy and confidentiality, and impairment of free thought and expression."§ Elsewhere, academics have not been as fortunate. The patchwork of state and national open records laws means that disclosure varies among universities, putting researchers at more-transparent institutions at a disadvantage and giving private university scientists (who are generally exempt from open records laws, even if they receive public funding) an edge over those at public institutions.

Universities should articulate how to respond to requests in accordance with the law and ensure that faculty know their rights and responsibilities. They should better understand requesters' motivations—not to determine the appropriate response, but to help employees understand how access to correspondence could be misused. Legislatures should ensure that laws protect faculty correspondence when disclosure would compromise the conduct of science. The scientific community should develop common disclosure standards for all researchers and creative mechanisms for enforcement. Implementation could become a requirement for university accreditation. The standards could also be adopted by government grant-making bodies, increasing the likelihood that state laws will be modernized, or by legislatures and executive agencies for academics who choose to provide testimony.

Ultimately, more uniform disclosure standards will create more public trust in science.

– Michael Halpern and Michael Mann

Michael Halpern is the manager of strategy and innovation at the Center for Science and Democracy, Union of Concerned Scientists, Cambridge, MA. E-mail: mhalpern@ucsusa.org

Michael Mann is Distinguished Professor of Meteorology (with joint appointments in the Department of Geosciences and Earth and Environmental Systems Institute) at the Pennsylvania State University, State College, PA. E-mail: mann@psu.edu

*www.ucsusa.org/openrecordsabuse. †www.aaas.org/news/aaas-balance-scientific-freedom-and-accountability.
‡http://cup.columbia.edu/book/the-hockey-stick-and-the-climate-wars/9780231152549.
§www.courts.state.va.us/opinions/opnscvwp/1130934.pdf

10.1126/science.aac4245

PHOTOS: (TOP RIGHT) UNION OF CONCERNED SCIENTISTS; (BOTTOM RIGHT) GREG RICO; (INSET) © ERHUI1979/ISTOCKPHOTO.COM

Downloaded from www.sciencemag.org on April 30, 2015

Published by AAAS

NEWS

> “We clearly need a fundamental change of course, to protect the earth and its people. … This moral obligation extends to all.”
>
> **Cardinal Peter Turkson**, urging action on 28 April at a Vatican summit on climate change and poverty. Pope Francis is expected to release an encyclical on the environment in June.

IN BRIEF

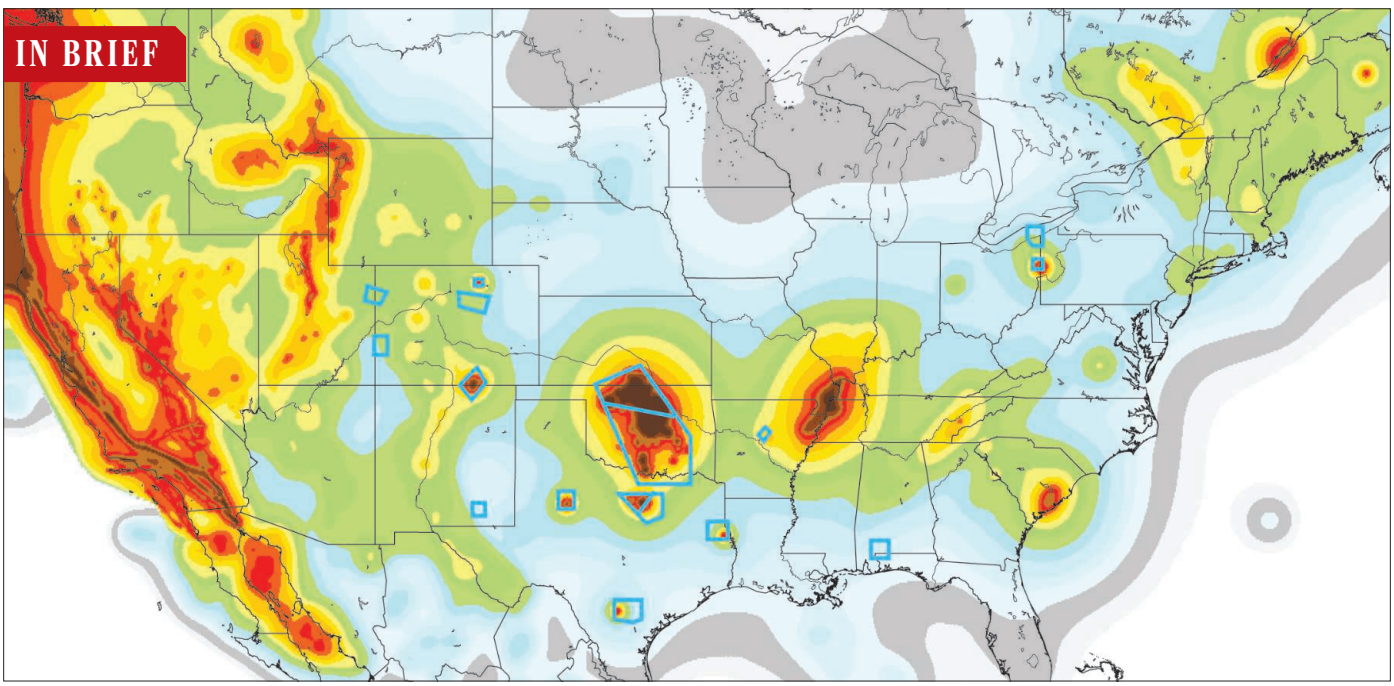

New earthquake danger zones in U.S. heartland

Scientists say that the injection of wastewater from oil and gas operations is triggering a surge in small earthquakes in the U.S. heartland, pushing critically stressed faults past the snapping point. On 23 April, the U.S. Geological Survey (USGS) released a report that identifies 17 areas in eight states with frequent induced earthquakes (boxed areas on map); in some areas, such as Oklahoma, the threat of earthquake shaking rivals that in California. Previous USGS hazard maps were built on decades if not centuries of data, but for the induced earthquake regions, the researchers modeled future hazards based on tremors only in the past year. USGS also offered hazard predictions for just 1 year into the future, rather than the usual 50 years, noting that uncertain factors such as the price of oil and actions of regulators could influence earthquake rates. Although most induced earthquakes so far have been small, some have been big enough to damage buildings—and USGS says it can't rule out the possibility of a magnitude-7 temblor. http://scim.ag/usgseqhaz

AROUND THE WORLD

Replica of a cave of wonders

VALLON-PONT-D'ARC, FRANCE | When spelunkers discovered the 36,000-year-old Chauvet Cave in southern France's Ardèche region in 1994, they beheld exquisite paintings of horses, lions, bison, and other animals. These ancient masterpieces—the oldest cave drawings then known—rewrote the prehistory of art. At the urging of archaeologists, the French government, worried about damage to the works from exhaled CO_2, locked the cave behind a steel door and allowed in only cave art experts and occasional VIPs. But now tourists can get an idea of the wonders experienced by early humans and researchers: Last week, a $59 million replica of Chauvet opened just down the road in the village of Vallon-Pont-d'Arc. On walls fashioned from mortar and resin, skilled painters, supervised by Chauvet archaeologists, recreated some 400 artworks using natural pigments and working directly from digital photographs taken during the last 20 years of research.

CREDITS: (MAP) USGS; (PHOTO) © CLAUDE PARIS/AP/CORBIS

Downloaded from www.sciencemag.org on April 30, 2015

Published by AAAS

Invasive lionfish found off Brazil

ARRAIAL DO CABO, BRAZIL | The spread of the lionfish continues. The venomous coral reef dwellers, native to tropical Indian and western Pacific waters, have spread rapidly in less than 30 years across the eastern U.S. coast, the Gulf of Mexico, and the Caribbean (possibly introduced by aquarium dumping in the mid-1990s). Now, scientists say, the voracious lionfish—which have a strong appetite for native reef fish—have reached the southeastern coast of Brazil, crossing what was once thought to be a substantial barrier to its dispersal, the freshwater and sediment plume emerging from the mouth of the Amazon and Orinoco rivers. In 2014, recreational divers speared a lionfish of the species *Pterois volitans* in the reefs off Brazil's southeastern coast. A new genetic analysis of the fish, published last week in *PLOS ONE*, links it to the Caribbean invaders. This could spell significant trouble for native Brazilian reef fish, already suffering from overfishing and habitat degradation.

Chilly climate for COMPETES bill

WASHINGTON, D.C. | The chair of the science committee in the U.S. House of Representatives and his Republican colleagues acknowledge that global climate is changing—but not that humans are the driving force. Last week, the committee approved a controversial bill to reshape U.S. science policy by a straight party-line vote (*Science*, 24 April, p. 380). Attempts by Democrats to revise portions of the COMPETES bill that they believe are hampering the National Science Foundation and research at the Department of Energy were voted down. An amendment by Representative Eric Swalwell (D–CA) offering "the sense of Congress that climate change is real and human activity significantly contributes to climate change" did pass—but only after the panel's chair, Representative Lamar Smith (R–TX), lopped off the second clause. And even that toothless statement was too bold for two Republicans, who voted no.

MESSENGER goes out with a bang

LAUREL, MARYLAND | MESSENGER has delivered its final missive. NASA's mission to the planet Mercury, launched in 2004, flew past Venus twice and Mercury three times before settling into orbit around Mercury in 2011. In those 4 years, the MErcury Surface, Space ENvironment, GEochemistry, and Ranging (MESSENGER) spacecraft provided new evidence that the planet has water ice and other volatiles in its permanently shadowed polar craters, probably delivered by comets and asteroids. The spacecraft also discovered a dark, probably carbon-rich layer overlying most of the polar deposits, also most likely from comets—an intriguing possible analog to the early delivery of water and organic compounds to Earth. Now, more than 3 years past its expected mission end date, the spacecraft has finally run out of propellant, and gravity has taken over. At press time, the spacecraft was expected to crash into Mercury's surface on 30 April at a speed of more than 3.91 kilometers per second.

ILLUSTRATION: DINOSTAR CO., LTD.

Holy batwings! Dino had webbed forelimbs

Test your dinosaur knowledge: The creature depicted here a) is the only known flying dino with wings like those of a bat or a flying squirrel, rather than a bird; b) had wings made of skin rather than feathers; or c) has the shortest name ever given to a dinosaur. Answer: All of the above. The 160-million-year-old dinosaur, dubbed *Yi qi* ("strange wing" in Mandarin Chinese, and pronounced "ee chee"), was discovered in northeastern China and is reported this week in *Nature*. It weighed just under 400 grams and was closely related to the earliest birds (like the 150-million-year-old *Archaeopteryx*). But unlike any other bird or dino, *Yi qi* had stiff rods projecting from each wrist that apparently supported wings made of skin, as suggested by the remains of membranous material found between the rods. Researchers are pretty sure that it could fly, but whether it was a glider or was capable of powered flight is not yet clear.

FINDINGS

Malaria vaccine's mixed results

The final results from a clinical trial of the first malaria vaccine are as lackluster as preliminary results suggested they would be. More than 15,000 children and infants in seven African countries received either three shots of the malaria vaccine known as RTS,S, three shots of RTS,S plus a booster, or a control vaccine. The vaccine worked best with the booster: Older children who received all four shots had a third fewer cases of malaria, and severe complications of the disease were also reduced by

Published by AAAS

The eruption of Chile's Calbuco volcano, seen from Puerto Montt on 22 April.

A fiery reawakening

The Calbuco volcano broke its 43-year dormant streak when it erupted twice last week, in the late afternoon of 22 April and the early morning of 23 April. The eruptions sent ash plumes billowing as high as 17 kilometers into the atmosphere, and thousands were evacuated from the surrounding areas. Over the course of 3 days, Calbuco belched out 210 million cubic meters of ash, Chile's National Geology and Mining Service (SERNAGEOMIN) reported. There were no injuries or deaths, but many buildings in the rural region have collapsed under the weight of the falling ash, according to BBC. SERNAGEOMIN warns that another round of destruction could be on its way: Heavy rains forecasted in the coming weeks could set off lahars, or landslides of volcanic material.

BY THE NUMBERS

75%

Human-induced global warming accounts for this fraction of heat extremes worldwide, and 18% of heavy precipitation events, finds a study in *Nature Climate Change*.

47.4%

Fraction of people in an Indiana community study who tested positive for HIV after sharing syringes or having sex with HIV-infected injection drug users.

200

Levels, in parts per million, of flame retardant chemical polybrominated diphenyl ether found in a Cooper's hawk near Vancouver, Canada, called the most polluted wild bird in the world.

a third. Older children who didn't receive the booster also had a third fewer cases of malaria, but there was no effect on severe complications, scientists reported this week in *The Lancet*. Meanwhile, malaria may be on the rise following the Ebola outbreak in Guinea, Sierra Leone, and Liberia, a separate team of scientists reported in *The Lancet Infectious Diseases*. The disease already kills half a million children a year, mostly in Africa; in the new study, modelers from Imperial College London estimated that the disruption of health care services may have led to up to 3.5 million extra untreated malaria cases and 11,000 deaths in 2014 in those countries. They say emergency interventions like mass drug administration are urgently needed while health systems recover.

Women's cancer drug helps men

A new type of cancer drug originally aimed at women with rare, inherited forms of breast and ovarian cancer may also help many men with deadly prostate cancer, according to a study presented last week in Philadelphia, Pennsylvania, at the annual meeting of the American Association for Cancer Research. The drug is AstraZeneca's olaparib, which blocks an enzyme called PARP that helps cancer cells survive chemotherapy and radiation by repairing DNA damage. Oncologists are often testing PARP inhibitors in ovarian and breast cancer patients born with mutations in *BRCA1* or *BRCA2*, two genes also involved in DNA repair. But a team led by Johann de Bono of the Institute of Cancer Research and the Royal Marsden NHS Foundation Trust in London found that 16 of 49 men with metastatic castration-resistant prostate cancer also responded to olaparib, usually for at least 6 months. Nearly all of them had inherited mutations in *BRCA* or other DNA repair genes or had acquired mutations to these genes in their tumors.
http://scim.ag/_cancerdrug

A new breast cancer drug may also help men with prostate cancer (*shown*).

PHOTOS: (TOP TO BOTTOM) © ALEX VIDAL BRECAS/EPA/CORBIS; SPL/SCIENCE SOURCE

Published by AAAS

IN DEPTH

SEISMOLOGY

Nepal disaster presages a coming megaquake

Rupture in quiet region of crust suggests Himalayan threat was underestimated

By **Eric Hand** *and* **Priyanka Pulla**

As rescuers searched for survivors of a devastating earthquake in Nepal on 25 April, geophysicists made a disturbing discovery. An initial assessment suggests that the underground rupture responsible for the magnitude-7.8 quake extended deep below the Himalayas, into a region that many scientists had deemed impervious to tearing. The unexpected extent of the rupture suggests that, as awful as the present disaster is, future earthquakes in the Himalayas could end up being mightier—and more calamitous—than modelers assumed.

The discovery "is going to radically change how we predict and interpret future and historic earthquakes," says Roger Bilham, a geologist at the University of Colorado, Boulder. And it adds a new level of foreboding to seismologists' conclusion that last Saturday's event released only some of the strain that has been building in the crust beneath Nepal, raising the odds of another great earthquake in the coming decades.

The ultimate driver of Himalayan earthquakes is the slow-motion collision of the Indian subcontinent with mainland Asia, which is also pushing the mountains skyward. Some 15 kilometers below the surface, a nearly horizontal thrust fault marks the plane where the Indian plate is plunging beneath southern Tibet at a rate of about 18 millimeters per year. Microearthquakes—most of them too small to feel at the surface—cluster along a line that trends east to west across this plane. Most of the region's substantial earthquakes have occurred south of the line, where the plates are locked together and strain builds up. North of this "lock line," however, the Indian plate dives downward and the character of the rock slab changes. Under higher temperatures and rising pressures, the brittle rocks become more plastic, and they creep past the Tibetan crust without rupturing. Or so researchers had thought.

The 25 April earthquake followed an ominous new rupture path. Analyzing seismometer recordings in the immediate aftermath of the earthquake, Gavin Hayes, a geophysicist at the U.S. Geological Survey in Golden, Colorado, found that the temblor ruptured crust well north of the lock line, suggesting the potential for future quakes with a far larger rupture area than seismologists had thought possible. "We therefore have the potential for bigger earthquakes than we might have otherwise expected," he says. The calculation will become more certain in the coming weeks, Hayes says, as he and colleagues fold in measurements of surface movements taken by satellites and GPS stations.

It will be "a big deal" if the discovery holds up, says Michael Taylor, a geologist at the University of Kansas, Lawrence. "A lot of people will be very interested in this," he says. The find raises the specter of earthquakes as large as magnitude 9, he says—larger than any quake ever recorded in the region.

Last week's earthquake was long overdue. The segment that ruptured hadn't seen a quake since 1344 C.E., says Laurent Bollinger, a geologist from the French Alternative Energies and Atomic Energy Commission who has studied historical earthquakes in the region. In 1934, however, a magnitude-8.4 quake struck 150 kilometers east of Kathmandu. Bollinger notes a precedent: The 1344 quake, too, was preceded by one farther to the east, in 1255 C.E., suggesting

An alarming slip

Crust ruptured north of a "lock line" marked by microearthquakes, where rock was expected to move plastically—and quietly.

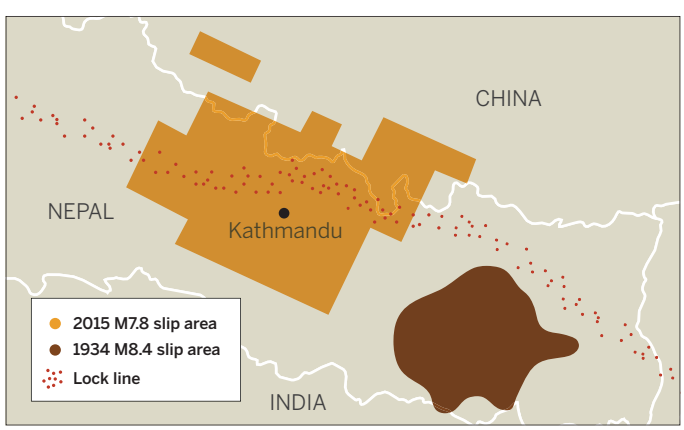

CREDITS: (PHOTO) AP PHOTO/NIRANJAN SHRESTHA; (DATA) GAVIN HAYES, USGS

Downloaded from www.sciencemag.org on April 30, 2015

Published by AAAS

Last Saturday's earthquake buckled roads in Kathmandu.

PHOTO: IDRISSA SOUMARÉ

that the latest quakes were not the first time that central Nepal has been visited by a one-two punch within a century.

A still more brutal blow could be coming. Although the Nepal quake released some of the seismic energy in the locked plates, more strain west of the 25 April epicenter must be released, Bollinger says. The timing, however, is impossible to predict, says Vinod Gaur, a geophysicist at the CSIR Fourth Paradigm Institute in Bangalore, India. "It may rupture tomorrow, or it can rupture 75 years from now," he says. Bilham says the westward quake could end up as powerful as a magnitude 8.4. "The region to the west is definitely overdue because we haven't seen one for quite some time," he says.

Even though the Nepal earthquake's epicenter was 80 kilometers northwest of Kathmandu, some of the worst shaking occurred in the densely populated capital. Situated on an ancient lakebed, the Kathmandu Valley's soil is soft and liquefies easily. "The ground motion gets amplified," says Vineet Kumar Gahalaut, a geologist at the National Geophysical Research Institute in Hyderabad, India.

Bad weather, landslides, and aftershocks are compounding the suffering caused by the original shock. Another concern is that landslides in the mountainous region may have blocked rivers, damming them to form earthquake lakes. When the dams fail, the lakes can cause catastrophic flooding downstream, says Marin Clark, a geologist at the University of Michigan, Ann Arbor. By correlating maps of ground shaking and topography, Clark has identified six areas that are at high risk for landslide dams and flooding. She is searching satellite images for signs of newborn lakes, but clouds have obscured the sites. "We're waiting for a clear view," she says.

As *Science* went to press, the earthquake's death toll had surpassed 4300. In the midst of the devastation, it was clear that the losses could have been even more horrific. Many modern buildings remained standing while historical ones tumbled into rubble, suggesting that tighter building codes and recent efforts to reinforce hospitals and schools had made a difference. The Nepal disaster "could have been much worse had engineers not sprung into action to retrofit critical facilities in Kathmandu," says Bilham, who has long sounded an alarm over the Himalayan earthquake hazard. But with an even greater threat looming, Nepal and its neighbors will have to take a hard look at their earthquake preparedness. ■

INFECTIOUS DISEASES

In Guinea, a long, difficult road to zero Ebola cases

The country could soon be the epidemic's last holdout

By **Martin Enserink**, *in Conakry*

The most striking thing about the Ebola treatment unit in the center of this West African capital is how quiet it is. When *Science* visited on 24 April, the center was home to just a single confirmed Ebola case—the only known patient in this teeming city of almost 2 million. (Four other patients at the unit were suspected cases awaiting test results.) Tents designated for family visits were empty, washing machines stood idle, and staff seemed relaxed. That's a huge shift from late December, when 55 confirmed patients crowded the small tent village, set up by Doctors Without Borders at a former parking lot of the Donka Hospital.

Guinea is where some of the last embers of West Africa's Ebola epidemic are smoldering. It had only 21 new Ebola cases in the past week, 16 of them in the city of Forécariah, a 3-hour drive from the capital. Guards at many official buildings still routinely point the Thermoflash, a contactless, revolver-shaped thermometer, at visitors' temples, and vats full of bleach are still omnipresent. But Ebola rarely makes headlines anymore, and antigovernment protests that paralyzed Conakry last week were about upcoming elections, not the virus.

Still, Guinea's Ebola czar, Sakoba Keita, notes that there have been lulls before, the last one in January, that were invariably followed by flare-ups. From a six-story office building overlooking Conakry's rusty seaport, Keita is collaborating with multiple international partners to plot a path to zero cases.

Liberia, another country hit hard by the epidemic, appears to have accomplished that feat already; its last case—a woman assumed to have become infected through the semen of her partner, an Ebola survivor—was reported more than a month ago. The third country stricken, Sierra Leone, had only 12 cases last week.

Although the epidemic started in Guinea in late 2013, it has had far fewer cases than the other two countries: just over 3500, compared with more than 10,000 in Liberia and 12,000 in Sierra Leone. The 66% mortality rate, however, is far higher. And while the other two countries saw a rapid explosion followed by a steady drop in new cases, Guinea's case count has swung up and down.

Pratima Raghunathan, an epidemiologist with the U.S. Centers for Disease Control and Prevention in Atlanta who's currently supporting the Ebola effort in Guinea, notes that the virus never got out of control in Conakry the way it did in the other two capitals, Monrovia and Freetown. One reason may be that treatment centers in the Conakry region had enough beds early on, so that

An experimental Ebola vaccine produced by Merck and NewLink Genetics is currently being tested in Guinea.

Published by AAAS

patients weren't turned away, she says.

On the other hand, distrust of the government, resentment against teams raising awareness, and rumors have hampered the response more in Guinea than elsewhere. The worst setback happened in September, when eight Ebola workers and journalists were killed with machetes and clubs in a remote village called Womey. (Eleven people were sentenced to life in prison for the murders last week.) In April, two people were seriously wounded when an Ebola team was attacked in Boffa prefecture; the only functioning ambulance there was badly damaged. In Forécariah, now the virus's main holdout, resistance to the anti-Ebola efforts has been fierce as well.

As part of the endgame, hundreds of local workers have gone house to house in the remaining Ebola pockets the past few weeks, to explain how Ebola spreads, encourage people to report suspected cases, and try to find any hidden Ebola patients or corpses. So far, the campaigns have been well received, Sakoba says. In Forécariah, the teams reached 91% of the population and identified 12 new Ebola cases, seven of whom were already dead.

William Perea, who has coordinated the World Health Organization's (WHO's) Ebola response in Guinea since last September, says he'd rather see those resources go to a focused, in-depth investigation of every new case to better understand the remaining routes of transmission—the kind of serious sleuthing that wasn't possible when the country had more patients. Even after the mass drive in Forécariah, some Ebola patients died at home, Perea says; that means that despite all the efforts, some people still don't understand the importance of reporting suspected cases. "We are missing things, and we need to understand exactly what they are," he says. "I think that's what will get us to zero."

Guinea's stubborn epidemic means that it may soon be the last place where researchers can do real-world tests of Ebola treatments and vaccines. Three treatment studies and two vaccine trials are already under way, and just last week, a delegation from the U.S. National Institutes of Health, already active in Liberia, was in town to gauge whether it can set up research partnerships in Guinea as well. An end to the epidemic—which Keita now tentatively predicts will come in June—may mean that most of the studies will not yield clear answers, says Mandy Kader Kondé, a former WHO epidemiologist who recently started his own research and training institute in Conakry and is involved in several of the studies. But, he says, that's a price that the country is more than happy to pay. ■

BIOETHICS

Embryo engineering study splits scientific community

First test of gene-editing technique on human embryos illustrates clinical risks

By **Jocelyn Kaiser** *and* **Dennis Normile**

A Chinese team's recent report that they have genetically altered human embryos for the first time has ignited a firestorm of controversy worldwide and renewed recent calls for a moratorium on such work. Scientists appear united in opposing any clinical use of such genome editing at the moment, whether to treat genetic diseases or create "designer babies." But some biologists are equally adamant that basic research on genome editing in human embryos is scientifically and ethically justifiable.

In China, where the precedent-setting research is big news and some in the public have expressed concern about it on the Internet, "most scientists are more positive," says Guo-Qiang Chen, a microbiologist at Tsinghua University in Beijing. "My personal opinion is that as long as they can control the consequences they should continue this work." That view is echoed by many outside of China. "I personally would defend the fundamental scientific value of [such] research," in part to explore the risks of any potential clinical use, says George Daley, a stem cell biologist at Harvard Medical School in Boston.

> ***"I personally would defend the fundamental scientific value of [such] research."***
>
> **George Daley**, Harvard Medical School

The paper at the heart of the debate appeared online on 18 April in *Protein & Cell*, a little-known journal co-published by Springer and an affiliate of China's Ministry of Education, but drew widespread attention only after *Nature* News reported it on 22 April. An editorial posted online on 28 April says the journal's objective in publishing the study was "the sounding of an alarm to draw immediate attention to the urgent need to rein in applications of gene-editing technologies, especially in the human germ cells or embryos."

The paper makes sobering reading for anyone optimistic about genetically altering human embryos. In it, Junjiu Huang and colleagues at Sun Yat-sen University in Guangzhou described how they attempted to use the CRISPR-Cas9 system, a new technology that makes it easy to modify genes in cells, to edit the human β-globin (*HBB*) gene in 86 human embryos donated for research by couples at an in vitro fertilization (IVF) clinic. In theory, such editing could be a way to prevent IVF-produced newborns from having beta thalassemia, a blood disorder resulting from a mutation in the *HBB* gene.

Two days after the single-celled embryos, or zygotes, had been injected with gene-editing molecules, 71 had survived and grown. But only four of 54 tested carried the desired genetic changes, and they were genetic mosaics, meaning only some of their cells had the intended changes to *HBB*. The edited embryos also had a large number of off-target effects, or mutations in genes other than *HBB*, which could be potentially harmful. The performance of the technique proved so poor that the researchers emphasized that any clinical use of CRISPR-Cas9 for embryo editing is "premature at this stage."

The project was reviewed by a medical ethics board at Huang's university and complied with international and national ethical standards, according to the paper. The researchers used abnormal zygotes that were not viable because they had an extra set of chromosomes as a result of being fertilized by two sperm and would have otherwise been discarded. "They did the research ethically," says Tetsuya Ishii of Hokkaido University in Sapporo, Japan, who studies ethical issues surrounding genome editing.

Still, the paper set off alarms. The Center for Genetics and Society in Berkeley, California, a watchdog group, called for a halt to such experiments. The Society for Developmental Biology in Bethesda, Maryland, called for a voluntary moratorium as well. Huang told *Nature* News that the paper was rejected by *Science* and *Nature* in part because of ethical concerns. (In an e-mail, Huang initially welcomed an inquiry from *Science* and asked for questions by e-mail, but then did not reply.)

Published by AAAS

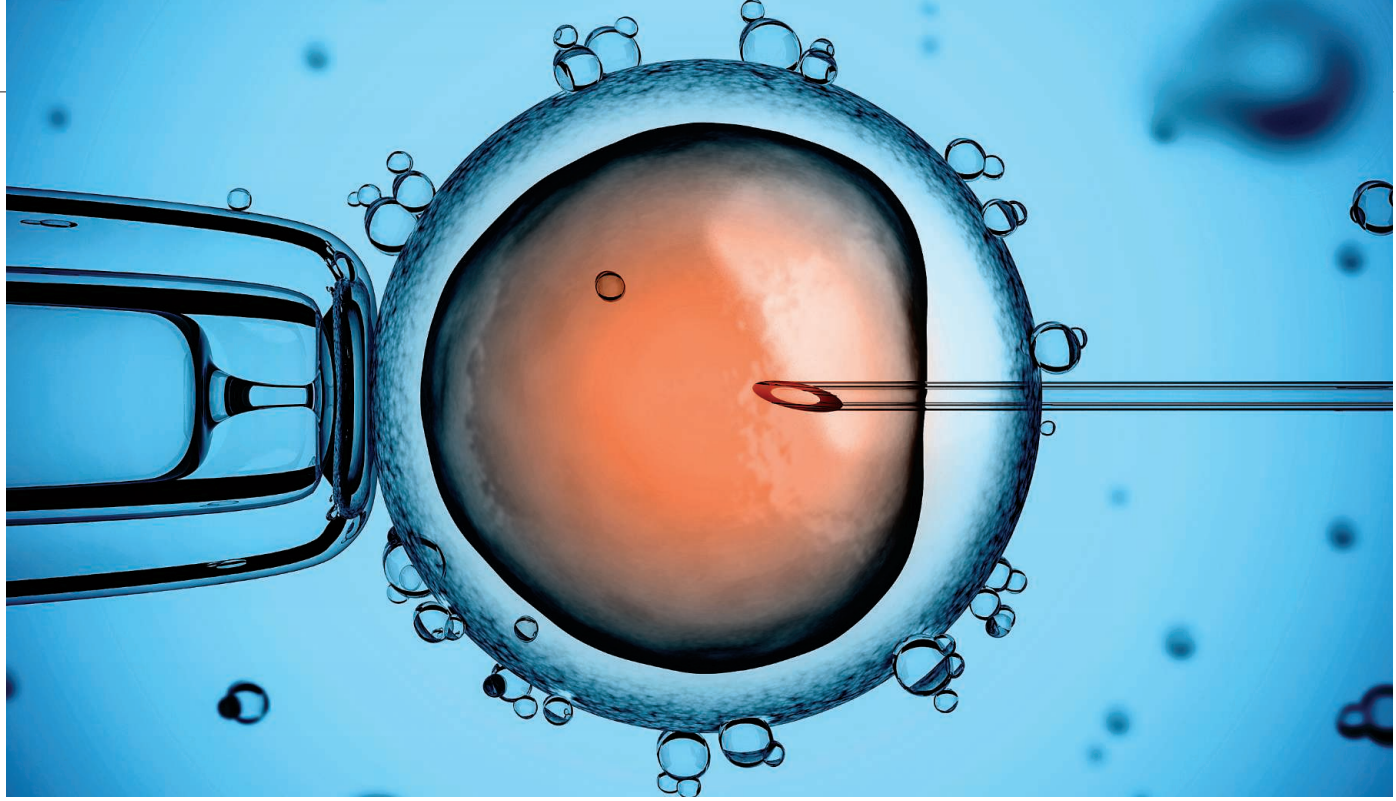

A team has published the first report of using a new gene-editing method on human embryos created by in vitro fertilization (illustration).

Rumors that such a paper was in the works sparked two published commentaries about a month ago. In *Nature*, Edward Lanphier, CEO of Sangamo BioSciences in Richmond, California, and several others from industry and elsewhere called for a voluntary moratorium on all research involving gene modification of human embryos, eggs, or sperm. "We said 'Let's not perfect these technologies ahead of a conversation about whether we should allow this technology' " to be used in the clinic, or even need it, Lanphier explains. In a *Science* commentary, however, Nobel Prize–winning molecular biologist David Baltimore, president emeritus of the California Institute of Technology in Pasadena, and 17 co-authors limited their call for restraint to clinical applications (*Science*, 3 April, p. 36).

Some of the authors of the *Science* article say that they are comfortable with basic research like the Huang experiment. Daley points out that international guidelines developed by stem cell researchers allow for experiments with human embryos as long as the cells are not allowed to grow for more than 14 days. "To further inform any debate on whether this technology could be useful for eradicating disease, one has to understand the range of efficacy and off-target mutagenesis," Daley says. Harvard molecular geneticist George Church, another author, agrees that the research does not appear to violate ethical guidelines.

Yet Church and several others are unimpressed with the Chinese group's results. One reason the researchers got so many off-target effects, Church suggests, is that they did not use the latest version of the gene-editing technology. University of California, Berkeley, molecular biologist Jennifer Doudna, who organized a workshop that led to the *Science* commentary, adds that the Huang experiment was premature because scientists are still a long way from perfecting the CRISPR-Cas9 gene-editing method. "I don't see the value in working with human embryos right now. There's a lot to be learned by working in other systems," she says.

Doudna is also troubled that, according to the dates noted in the paper, *Protein & Cell* apparently accepted the study 2 days after it was submitted. "I have to conclude this was not peer reviewed," she says.

> ***"I don't see the value in working with human embryos right now."***
>
> **Jennifer Doudna**, University of California, Berkeley

On the contrary, says *Protein & Cell* Editor-in-Chief Zihe Rao, a structural biologist at Nankai University in Tianjin. "Due to the scientific value and ethical dispute of this study, we not only conducted scientific peer-review, but also consulted related publishing and ethical experts," he says. "The authors also revised the manuscript based on our suggestions." Rao explains that the journal typically reviews submitted papers within 2 weeks, but for significant work they expedite the process.

Neither *Science* nor *Nature* would confirm that the journals reviewed the paper and rejected it in part because of ethical concerns. Asked whether it has a policy that would preclude considering such a paper, a *Nature* representative said the journal sometimes has papers reviewed by a bioethicist. *Science* issued a statement saying it supports recommendations in its earlier commentary and that while a consensus about germline genome editing is being developed, the journal "will carefully scrutinize all submissions for both technical and societal concerns and consult broadly."

Scientists in China defend the country's ethical oversight of research. The reviews in the United States and in China are very similar and based on the same principles, says Kehkooi Kee, a stem cell scientist also at Tsinghua, who earned his advanced degrees in the United States. Chen adds that in light of the current controversy, review boards "will probably be more strict," but he's adamant that the newly published research was worth doing. Determining if these embryo engineering techniques can be useful in curing disease can be achieved "only by doing this kind of research," Chen says.

Doudna is now helping organize an international meeting later this year that she says aims to "identify a broader consensus about the appropriate way to proceed with these experiments." Now that the first human embryo gene-editing paper has been published, Doudna adds, "we feel some urgency." ■

ILLUSTRATION: © KOYA79/ISTOCKPHOTO.COM

Published by AAAS

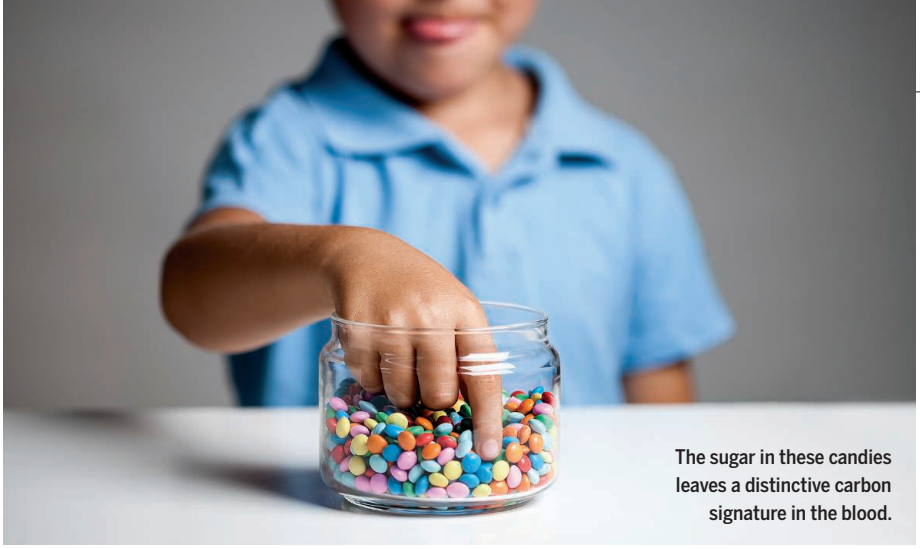

The sugar in these candies leaves a distinctive carbon signature in the blood.

NUTRITION

Have a sweet tooth? New blood test could tell

Isotope ratios could aid research by tracking added sugars

By **Viviane Callier**

Monitoring—and modifying—diet isn't easy, as people struggling with obesity or diabetes are well aware. Keeping track of the added sugars that lurk in foods from soft drinks to cereals is especially hard. Researchers have now come up with a blood test that could help both dieters and nutrition researchers—and they've shown that it is as good at monitoring added sugars as the complex diet reporting usually used in medicine and research.

The test, based on the ratio of common carbon isotopes in blood serum, "could be transformative for combating the ongoing obesity epidemic," declares Hope Jahren, a plant biologist at the University of Hawaii, Manoa, and a co-author of the study, which appeared online last week in *Public Health Nutrition*. Obesity experts see potential, too. The test "provides a simple, objective measure of added sugar in a person's diet that can be used by clinicians and by patients," says Nicholas Christakis, a social scientist and physician at Yale University. "People are often motivated by feedback."

Jahren and collaborators at the Johns Hopkins Bloomberg School of Public Health began developing the test in 2006, exploiting the fact that carbon isotope ratios differ between crops. Carbon-12, by far the commonest isotope, is present in all plants. But a scarcer isotope, carbon-13, is enriched in one group of plants, the so-called C4 plants. Adapted to dry conditions, they have a photosynthetic enzyme that enables them to grab more of the heavier carbons from the air than their cousins, the C3 plants. Corn and sugar cane—the major sources of added sugar in processed food—are both C4 plants.

The result is distinctive carbon signatures in common foods (see table, below), Jahren and her colleagues found. Added cane and corn sugars—major contributors to the obesity and diabetes epidemics—lend a higher carbon-13 ratio to processed foods like candy and soda. Foods from C3 plants—bananas, beets, and wheat, for example—have much lower ratios of carbon-13. Foods containing both C3 and C4 plants—cereal, cookies, and even dark chocolate—fall somewhere in between.

Jahren and her team set out to see whether such isotopes could be measured in people. In 2010, they developed their blood test, which measured the carbon isotopes using mass spectrometry. In a pilot study of 186 men, the test showed that those who consumed more soda had a measurably higher ratio of carbon-13 in their blood. Indeed, just one sugar-sweetened beverage was enough to produce a detectable change.

The latest study, led by dietitian Valisa Hedrick of the Virginia Polytechnic Institute and State University (Virginia Tech) in Blacksburg, probed whether the test—since refined—is a good substitute for the standardized diet recalls used to estimate added sugar consumption. The team recruited 216 adults from rural Virginia who consumed at least 200 calories of sugar-sweetened beverages, about 1.25 cans of soda, per day. They then asked subjects to recall every single item they had eaten over three 24-hour periods and compared the inventories with the test results. They discovered that subjects' carbon-13 ratios rose in lockstep with the amount of added sugar they consumed.

Added sugars now account for 15% of the calories Americans take in, three times as many as the American Heart Association recommends. "Most people simply are not aware of how much added sugar they are consuming," says dietitian Jamie Zoellner of Virginia Tech, a co-author of the study; she thinks the test could help. Researchers need such a test as well, says Mark Friedman of the Nutrition Science Initiative in San Diego, California, a private research foundation. "The lack of an objective measure of what people are eating is the single biggest obstacle in nutrition research."

The test has drawbacks, however. It relies on expensive analytical equipment, and it measures all C4 products in the blood, which can come from corn products like tortillas and popcorn or corn-fed livestock as well as from corn syrup sweetener. A follow-up study in the *Journal of Nutrition* showed that the confounding effects of these foods are small. But other added sugars can slip past the test if they come from C3 plants, such as honey, maple syrup, fruit juices, and beet sugar. The trials also relied on self-reported diets, which are notoriously unreliable. Friedman calls for an experiment in which researchers strictly control and monitor subjects' diets before measuring the blood biomarker.

The team is now planning controlled feeding trials. They are also studying how well the test can track changes in sugar intake through time, and adapting it to run on cheaper technology. If all goes well, they hope to commercialize the test and make it widely available in clinics and hospitals, perhaps as part of a standard blood panel. ■

Viviane Callier is a freelance science writer in Washington, D.C.

Telltale carbons

Foods carry distinctive ratios of carbon isotopes depending on whether they come from C3 or C4 plants.

C4 SIGNATURE	C3 SIGNATURE
Cane sugar	Beet sugar
High-fructose corn syrup	Maple sugar
Coca-Cola	Apple juice
SweeTarts	Dark chocolate
Popcorn	Bananas
Cornstarch	Wheat flour

Downloaded from www.sciencemag.org on April 30, 2015

CREDITS: (PHOTO) © MARSBARS; (DATA) A. H. JAHREN *ET AL.*, *THE AMERICAN JOURNAL OF CLINICAL NUTRITION* **84**, 6 (DECEMBER 2006) © 2006 AMERICAN SOCIETY FOR NUTRITION

Published by AAAS

FUNDING

Greece raids research funds to pay salaries

Beleaguered scientists are spending reserves to protect them from confiscation

By **Edwin Cartlidge**

Greece's ongoing economic crisis and political shifts are taking a new toll on the country's scientists, already reeling from cuts in salaries and research spending. Now, the government plans to confiscate research funding to plug a hole in the country's ever worsening finances. And the left-wing government in power since January is pushing through a reform of higher education that scientists say will make universities more politicized and less meritocratic.

The cash seizure was authorized by Greece's Parliament in a heated and emotional session last week. The emergency decree forces local government and other state bodies, including universities and research centers, to transfer their cash reserves to the Bank of Greece in order to pay salaries and pensions of public-sector employees. As *Science* went to press, it remained unclear exactly how much money would be targeted and when it would be taken, but researchers expect the government to grab funds set aside to pay for research overheads. These amount to as much as 20% of the value of grants and are hived off to pay for expenses such as utility bills and temporary staff.

Costas Fotakis, research vice minister in the government coalition led by the Syriza Party, describes the move as an "interim measure" that will see the money placed in accounts earning interest rates of 2.5% and then returned later, providing Greece wins favorable terms in its negotiations with the European Union over its national debt. "We do hope that a fair agreement in the ongoing negotiations for the Greek debt will be reached soon, by the end of June," he said in an e-mail. "Then this measure will be waived."

Greek scientists are particularly resentful of the raid because their salaries have fallen about 30% in the past 3 years and because Greece spends just 0.6% of its gross domestic product on R&D, forcing them to rely more heavily on the European Union for support. To reduce the level of confiscations, many researchers are frantically shifting or spending as much of their overhead reserves as they can, in some cases by stocking up on consumables and paying Ph.D. students' salaries for several months in advance. "I have little doubt that a massive exercise in hiding research money from the government is probably under way," says Costas Synolakis, a marine scientist at the University of Southern California in Los Angeles.

Researchers are also fighting an education reform that the government announced on 17 April without public consultation. The measure—expected to be approved by Parliament within the next few weeks—would scrap universities' governing boards, remove existing rectors, and give students a large share of the votes to appoint new rectors. As such, it reverses many changes brought in by a 2011 law that sought to limit the powers of students and administrative staff.

That earlier law proved highly controversial and triggered huge student protests. But academics saw it as a positive step in reducing the power of political parties over university appointments. "Since the 1980s, university administrations [had] been voted, not on merit or administrative prowess, but on party credentials," Synolakis says. In effect, he maintains, the latest reform would "move Greek higher education back about 30 years." Mathematician Thanasis Fokas of the University of Cambridge in the United Kingdom agrees that the reform would weaken academic standards. He notes that, among other things, it lifts a cap on the length of time a student can take to complete his or her studies. It also scraps electronic voting in university elections, which, he says, may allow students to steal ballot boxes and intimidate voters, as they have done in the past.

The new law also seeks to change the composition and functions of the National Council for Research and Technology, an 11-member panel that advises the government on the organization and funding of research. The council had clashed with Fotakis earlier this year. Its members resigned en masse on 4 March because, they claimed, Fotakis had told the press a week earlier that the council was "illegal."

Fotakis denies making that assertion. He says instead that changes to the council instituted last year by the previous government created a "legal vacuum" that may have affected the smooth running of the country's research centers. But the chair of the now disbanded council, Joseph Sifakis, a computer scientist at the Swiss Federal Institute of Technology in Lausanne, claims that the government disliked a number of reforms that the council had proposed to build ties between universities and research centers, increase collaboration between universities and industry, and reduce corruption in the distribution of European funds.

The new law, Fotakis says, which will see most members elected by peers rather than being appointed, will allow researchers easier access to E.U. "structural funds," designed to boost economic growth in poorer regions. He adds that more comprehensive legislation will follow to "fully reflect our ideas and policies for research." Greek's embattled scientists will be waiting apprehensively. ■

The Bank of Greece needs cash to pay salaries of public employees.

PHOTO: AP PHOTO/THANASSIS STAVRAKIS

Edwin Cartlidge is a science writer in Rome.

Published by AAAS

FEATURES

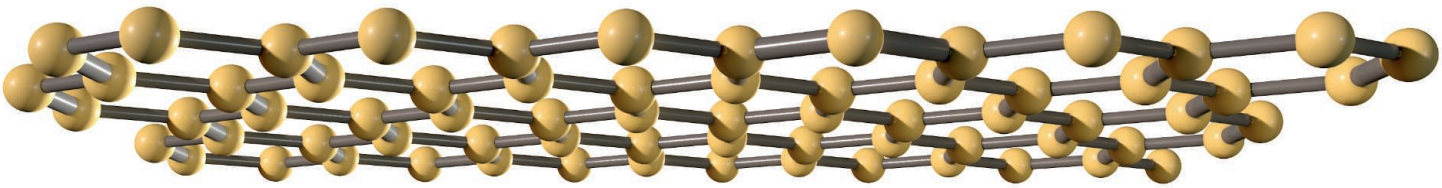

BEYOND GRAPHENE

The ultrathin form of carbon has inspired other atoms-thick materials that promise even bigger technological payoffs

By **Robert F. Service**, *in San Antonio, Texas*

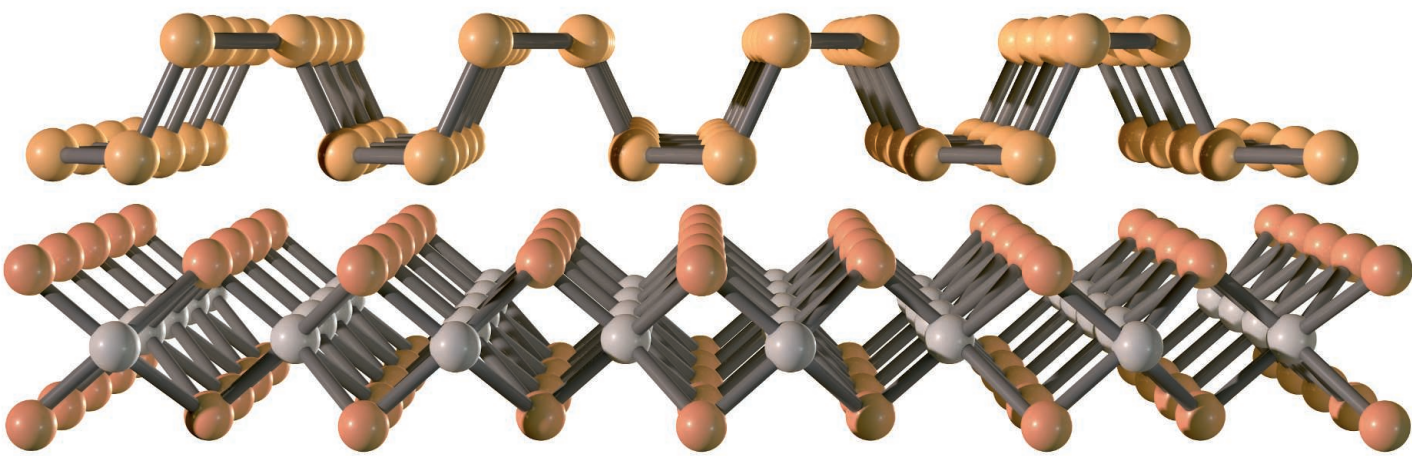

Graphene (*top*) has spurred scientists to explore flat semiconductors such as phosphorene (*middle*) and molybdenum disulfide (*above*).

ILLUSTRATIONS: C. BICKEL (3)

Sticky tape isn't normally thought of as the stuff of scientific breakthroughs. But when physicists Andre Geim and Konstantin Novoselov of the University of Manchester in the United Kingdom and colleagues reported in *Science* in 2004 that they had used clear tape to peel off single atomically thin sheets of carbon atoms from a chunk of graphite, it set off a revolution in materials science that is still unfolding.

Last year, researchers around the globe published more than 15,000 papers on single-layer graphite, called graphene, a number that has grown exponentially since the Manchester team's sticky innovation 11 years ago. And for good reason. Graphene is the thinnest material ever made. It's 100 times stronger than steel, a better electrical and heat conductor than copper, flexible, and largely transparent. Investigators envision a future for it in everything from the next generation of computer chips and flexible displays to batteries and fuel cells.

Yet graphene may have its biggest impact not as a wonder material in its own right, but through its offspring. For all its dazzling promise, graphene has drawbacks, especially its inability to act as a semiconductor, the keystone of microelectronics. Now, chemists and materials scientists are striving to move beyond graphene. They're synthesizing other two-dimensional sheetlike materials that promise to combine flexibility and transparency with electronic properties graphene can't match. And they are already turning some of them into thin, flexible, speedy electronic and optical devices that they hope will form the backbone of industries of the future. "The field is wide open," says David Tomanek, a condensed matter physicist at Michigan State University in East Lansing. Keji Lai, a physicist at the University of Texas (UT), Austin, agrees, calling 2D materials "one of the hottest topics in physics."

IN ONE SENSE, 2D materials aren't new at all. Researchers have been growing atomically thin sheets of materials since the 1960s using tools called molecular beam epitaxy (MBE) machines. But MBE machines are typically used to deposit thin layers of materials like silicon and gallium arsenide: crystalline materials whose component atoms normally prefer to bond in three dimensions.

Downloaded from www.sciencemag.org on April 30, 2015

Published by AAAS

In that respect, the layers made by MBE are like a slice of cheese, a 2D version of a 3D substance.

Graphene is different. It's more like the pages in a book, says Yi-Hsien Lee, a materials scientist at the National Tsing Hua University in Hsinchu, Taiwan. Its carbon atoms form strong, covalent links with other carbons in a single 2D plane, creating a hexagonal lattice that looks like miniature chicken wire. But separate planes of atoms are only loosely paired with weak bonds known as van der Waals interactions. As a result, the layers can slip past one another, which is why graphite is used to make the gray flaky "lead" in pencils.

The big surprise was that when researchers began to study graphene closely, they discovered it had electronic and optical properties not found in bulk graphite. "The biggest lesson is that less is different," says Yuanbo Zhang, a condensed matter physicist at Fudan University in Shanghai, China. And with that lesson, Tomanek says, "graphene brought 2D materials into the limelight."

Yet when it comes to making high-tech devices, graphene's promise dims a bit. While the most prized materials of the electronics age are semiconductors, whose conductivity can be switched on and off to generate the digital currency of 1s and 0s, graphene is more like a conducting metal. "Graphene is an absolutely wonderful material," Tomanek says. "But it's irrelevant for electronics."

Researchers have spent years trying to convert graphene into a semiconductor by bonding oxygen to the graphene sheets or by cutting the sheets into ribbons just a few nanometers wide. Both changes do alter graphene's electronic structure, turning it into a semiconductor. But these "solutions" brought other problems. Graphene oxide's electronic properties are strongly affected by molecules that interact with it, a foible that undermines its reliability. And the nanoribbons' electronic properties depend so critically on a ribbon's precise structure that they are hard to control.

Yet graphene opened researchers' eyes to a new world of flatland electronics. They saw that similar materials might have novel optical and electrical properties. And because 2D sheets are so thin and mostly transparent, they offered the prospect of creating flexible and transparent electronics that could produce see-through displays of the sort dreamed up years ago by Hollywood. Since then, researchers have been surveying that landscape for richer treasures.

By looking for materials that naturally form 2D sheets and finding ways of stabilizing sheets of atoms that normally want to form a 3D architecture, materials scientists have already come up with dozens of new 2D materials, and many more are likely to follow. They've engineered single-layer silicon (known as silicene), single-layer germanium (germanene), and single-layer tin (stanene). They've created an insulator made from boron nitride, which has the same chicken-wire lattice structure as graphene. They've made single-layer metal oxides that may serve as highly active catalysts for controlling particular chemical reactions. And they've even trapped water molecules in thin sheets, although what this will be useful for isn't yet clear.

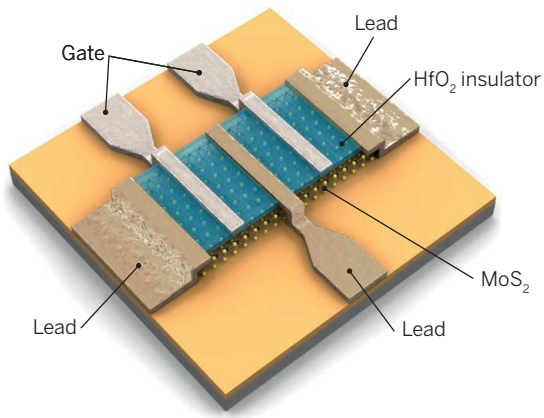

Researchers have made quick progress in turning 2D materials into devices, such as this simple circuit in which two transistors use MoS_2 to ferry charges between electrode leads.

But for now, most of the buzz among flatlanders surrounds just two materials: a compound called molybdenum disulfide (MoS_2) and a double layer of phosphorus atoms called phosphorene. Both have tantalizing electronic properties, and the competition between their acolytes is fierce.

OF THE TWO MATERIALS, MoS_2 had the head start. Originally synthesized in 2008, MoS_2 is a member of a broader family of materials called transition metal dichalcogenides (TMDs). The name is just a fancy term for their makeup: one transition metal atom (in this case molybdenum) and a pair of atoms from column 16 of the periodic table (a family known as the chalcogens), which contains sulfur and selenium, among others. Much to the delight of electronics makers, all TMDs are semiconductors. They aren't quite as thin as graphene (in MoS_2, twin sheets of sulfur atoms sandwich a middle layer of molybdenum atoms), but they offer other advantages. In the case of MoS_2, one is the speed at which electrons travel through the flat sheets—a property called electron mobility. MoS_2's mobility is a decent 100 or so centimeters squared per volt second (cm^2/vs). That's well below the 1400 cm^2/vs mobility of crystalline silicon, but it's better than the number for amorphous silicon and many other ultrathin semiconductors being tested for use in futuristic applications such as roll-up displays and other flexible, stretchable electronics.

MoS_2 also turns out to be fairly easy to make, even in large sheets. And that has helped engineers move quickly to testing it in devices. In 2011, for example, researchers led by Andras Kis of the Swiss Federal Institute of Technology in Lausanne reported in *Nature Nanotechnology* that they had made the first transistors using a single layer of MoS_2 just 0.65 nanometers thick. Those devices and their successors turned out to have other exceptional properties that rival those of far more developed silicon-based technology. They can switch on and off billions of times per second. They also boast a large on/off ratio, which makes it easy to differentiate between digital 1s and 0s—a property prized by circuit designers. Since 2011, Kis's group and others have engineered a host of MoS_2-based electronic devices including logic circuits and always-on flash memory devices, both of which are widely used in today's computers.

Beyond that, MoS_2 has another desirable property known as a direct bandgap, which enables the material to convert electrons into photons of light—and vice versa. That makes MoS_2 a good candidate for use in optical devices, such as light emitters, lasers, photodetectors, and even solar cells. Lee, an expert in growing large-area MoS_2 films, notes the material is also abundant, cheap, and nontoxic. "It has a bright future," he says.

Tomanek, however, is among MoS_2's detractors, saying "it has been oversold." In particular, Tomanek says he isn't convinced that MoS_2's electron mobility will ever be high enough to compete in the crowded electronics marketplace. The reason, he says, lies in the material's very makeup. Electrons traveling through it ricochet off large metal atoms in its structure and slow down.

That stumbling block will prove temporary, Lee says. Researchers are already learning to navigate around it by growing slightly thicker multilayers of MoS_2 that offer zipping electrons alternative routes to bypass roadblocks. "The mobility issue of MoS_2 will be solved," Lee says.

ITS RIVAL, phosphorene, has sparked even more excitement. Also known as black phosphorus, phosphorene is one of three

ILLUSTRATION: ANDRAS KIS (EPFL)

Published by AAAS

The rise of the flattest materials

The number of papers on graphene has grown exponentially since the material was isolated in 2004. Publications about molybdenum disulfide (MoS_2) and phosphorene are now repeating the pattern.

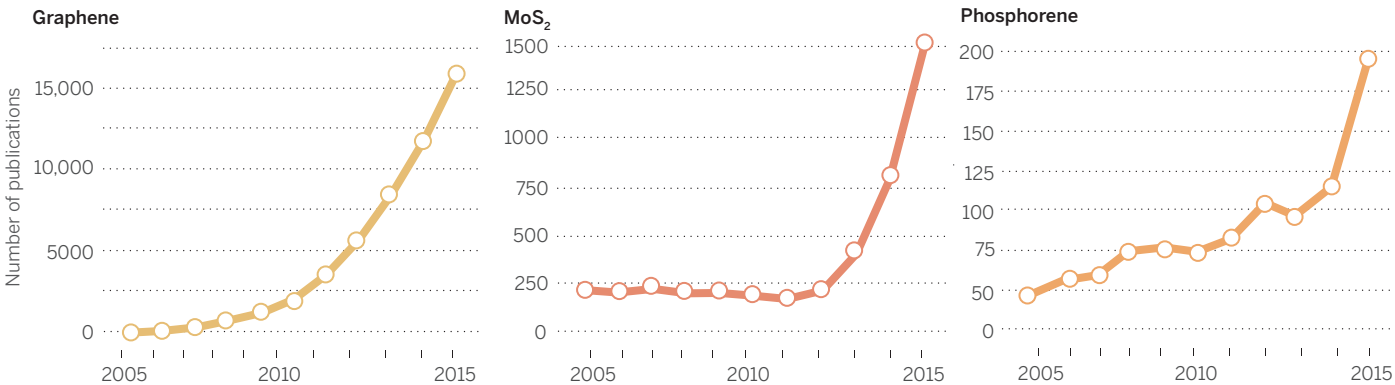

different crystal structures—or allotropes—that pure phosphorus can adopt. The others are white phosphorus, which is used in making fireworks, and red phosphorus, used to make the heads of matches. Phosphorene, which consists of a corrugated pattern of phosphorus atoms that lie in two different planes, was first synthesized only last year. But its properties have already made it a materials-science darling. It has an electron mobility of 600, which some researchers hope to increase even further, and its bandgap—the voltage needed to drive a current through it—is tunable. Electrical engineers can adjust the bandgap simply by varying the number of phosphorene layers they stack one atop another, making it easier to engineer devices with the exact behavior desired. "All this makes black phosphorus a superior material," Tomanek says.

Researchers have made rapid progress toward incorporating it into devices. On 2 March 2014, Zhang and his colleagues at Fudan University reported online in *Nature Nanotechnology* that they had made phosphorene-based field effect transistors, devices that serve as the heart of computer logic circuitry. Two weeks later, Tomanek and colleagues at Michigan State, together with researchers led by Peter Ye, an electrical engineer at Purdue University in West Lafayette, Indiana, reported online in *ACS Nano* that they, too, had made phosphorene-based transistors, along with simple circuits.

Unfortunately, phosphorene is unstable in air. "We see bubbles cover the surface after 24 hours and total device failure in days," says Joon-Seok Kim, a phosphorene device maker at UT Austin. The culprit, Lee says, is water vapor, which reacts with the phosphorus, eroding it by converting it to phosphoric acid. Even so, Kim's group at Texas and others are making progress in protecting it. Kim reported at the March meeting of the American Physical Society (APS) in San Antonio, Texas, for example, that he and his colleagues were able to stabilize phosphorene-based transistors for 3 months and counting by encapsulating them in a protective layer of aluminum oxide and Teflon. At the same meeting, researchers from Northwestern University in Evanston, Illinois, reported that a similar strategy gave them stable devices out to 5 months and counting.

But Lee, for one, is not convinced the fixes will lead to long-term stability. "You can put a capping layer on top, but it just reduces the degradation rate," Lee says. Phosphorene, he argues, is gaining attention because it's easy for researchers to get their hands on: It can simply be peeled off a chunk of black phosphorus with sticky tape, like graphene. "It's a kind of fashion," Lee says. "But that doesn't mean it will have a future."

IN THE END, there may be plenty of room for both materials. "We're still just at the beginning," says Luis Balicas, a physicist at Florida State University and the National High Magnetic Field Laboratory in Tallahassee. He suggests that over time engineers may wind up favoring MoS_2's strong interactions with light to make solar cells, light emitters, and other optical devices, while harnessing phosphorene's higher electron mobility for making electronic devices.

Two-dimensional materials also offer another tantalizing option: They can be stacked like cards in a deck to create the different electronic layers needed in functional electronic devices.

In devices made using conventional 3D materials, neighboring crystalline layers usually bind tightly to one another. But if the atomic lattice of adjacent layers differs by more than 15% or so, the strain at the interface causes one or both layers to crack, a potential device killer. That means electrical engineers must either severely limit their selection of neighboring materials so that the layers can join without strain, or resort to complex workarounds, such as adding "buffer" layers at each interface. With stacked 2D materials, "we don't need to worry about this," Lee says, because they don't form tight bonds with the layers above and below.

That advantage has prompted scientists to build such devices, called van der Waals heterostructures after the weak bonds between adjacent layers. The first ones are already emerging. Last year, Ye's group at Purdue reported that they had used both MoS_2 and phosphorene to make ultrathin photovoltaics (PVs). At the APS meeting, Balicas's group reported similar PVs made by combining layers of TMDs, boron nitride, and graphene. And in February, Geim and colleagues reported online in *Nature Materials* that they had assembled multiple 2D materials to make efficient, thin light-emitting diodes.

Such progress has the community of device makers salivating over what may soon be possible. "In principal, we can build an electronic system fully based on 2D materials," says Xiaomu Wang, an electrical engineer at Yale University. Such devices would be flexible, transparent, temperature stable, and cheap to manufacture, Wang says. Contemplating prospects like that, Tomanek thinks the latest revolution in electronics and optics is just getting started: "2D materials are here to stay." ■

DATA SOURCE: WEB OF SCIENCE

Published by AAAS

Jeopardy! host Alex Trebek

PHOTO: JEOPARDY PRODUCTIONS INC.

This popular TV game show has a thing for science

WHAT IS *JEOPARDY!*?

By **Jon Cohen**, *in Culver City, California*

On 10 March, at a massive sound stage here in the heart of Los Angeles, Alex Trebek stared down three contestants on the game show *Jeopardy!*. The legendary host has presided over the TV show for 31 years, and that day he read off the following clue, which also appeared on a blue screen behind him:

THIS CONDITION HAS DOUBLED IN THE LAST 30 YEARS IN U.S. KIDS & IS LINKED TO INCREASED RISK FOR DIABETES

Jeopardy! famously phrases its clues as answers. Contestants win money if they are first to press their buzzer and can then come up with the matching question—or lose money if they fail. After one contestant buzzed in and offered **What is autism?**, Trebek swiftly rejected the response and turned to the next one to buzz in. That person earned Trebek's approval with: **What is obesity?**

But this was a matter of science, which is both a mainstay of the show and among the trickiest territory it covers. Billy Wisse, head writer for *Jeopardy!* and one of the judges who sits on the set to evaluate nuances in responses, immediately got on the phone to his team of 15 writers and researchers, who sit about a city block from the sound stage. They watch the taping live and Google madly when a "wrong" response is plausible. Wisse soon asked a producer on the set to stop taping while his team figured out if autism was also linked to diabetes. (To find out the resolution, you'll have to watch the show on 2 June, when the taped episode will air.)

For those who have never seen an episode of *Jeopardy!*—it debuted in 1964 and ranked number 45 on *TV Guide*'s list of the 60 greatest American television programs of all time—this "smart person's game show" presents contestants with six categories, each of which has five clues of increasing difficulty and value. The game has two initial rounds, with more money at stake in the second one—Double Jeopardy!. A final round has a single clue that allows contestants to wager up to their total earnings from that game.

THIS BIOINFORMATICS SPECIALIST IN 2010 WON $77,000 ON A SINGLE SHOW, A JEOPARDY! RECORD
Who is Roger Craig?

When it comes to succeeding on *Jeopardy!*, science knowledge appears to pay off handsomely. In an analysis provided by *Jeopardy!*, winning contestants over the last seven seasons pocketed an average of $40,517, but a breakdown by professions showed that people in the catchall category data scientists/mathematicians/analysts had the highest

Published by AAAS

In one "Battle of the Decades" round that aired in September 2014, three contestants with scientific backgrounds squared off: (from left) aerospace engineer Tom Nosek, psychology grad student Pam Mueller, and meteorologist Russ Schumacher, who won the round.

winnings—$139,743 per person. Scientists/technicians/computer scientists also fared better than average at $54,963. On "Battle of the Decades," a contest in 2014 that pitted the show's biggest winners over the past 30 years against each other, roughly half of the contestants had scientific backgrounds.

To get on *Jeopardy!*, about 100,000 people each year take a test that the show posts on its website. The game requires a vast range of knowledge of everything from academic topics such as science and literature to pop culture, plays on words, and lifestyle questions. Some 3000 people who pass the test are invited for an interview, and from that pool, the show annually selects 400 contestants.

A FORMER U.S. CONGRESSMAN WHO HAS A PH.D. IN PHYSICS, THIS MAN WON FIVE JEOPARDY! GAMES WHILE IN GRADUATE SCHOOL AND ALSO LATER APPEARED IN A CLUE

Who is Rush Holt, the new CEO of AAAS, which publishes *Science*?

"People who are interested in science are quite often interested in a lot of different things and have a voracious need for sources," says another five-time *Jeopardy!* winner, Leszek Pawlowicz, who earned a Ph.D. in materials science and engineering from the Massachusetts Institute of Technology. Scientists may also have an edge because most have solid backgrounds in math, he says, and many *Jeopardy!* winners have deliberate wagering strategies. Pawlowicz says he has done well on *Jeopardy!* because he can retrieve information quickly. But more important, he believes, he can relate facts to each other. "That's almost certainly a good trait for scientists to have," says Pawlowicz, who now works as an archaeologist in Flagstaff, Arizona.

A science-related category presented a make-or-break moment for Pawlowicz in a Double Jeopardy! round of Battle of the Decades. The category was RUN EMC, and Pawlowicz and his two opponents initially avoided it. "We all thought it was a rap category," he says.

But when the first clue came up—**E = MC2 WAS CONCEIVED BY THIS MAN**—Pawlowicz thought, This is my category, and responded correctly. Then Pawlowicz, who also has a B.A. in physics, decided to gamble big and jump to the fourth level, or $1600, question. Pawlowicz knew that Daily Doubles—clues that allow contestants to wager as much of their winnings as they like—most often appear in that slot. His choice paid off, and he wagered $10,000 on this clue: **THE EQUATION WOULD NEVER HAVE MADE IT BIG IN ITS ORIGINAL VERSION, WHICH WAS CONCEIVED AS THE EQUIVALENT M = THIS.**

It was an easy response for a physics major: **What is E over c squared?** Pawlowicz ended up handily winning the game.

Those who don't reach such heights are sometimes sore losers. "They can work up very fearsome sounding expertise and 10 pages of citations to show us why they were right and we were wrong," Wisse says. "It's not very often that they really have a case." One of the biggest disasters the show had did involve a scientific clue. "There was a nightmarish episode over tensile strength, and I'm not even going to go any further into it," he says.

Billy Wisse (*left*) leads a team that writes some 20,000 clues per season.

THIS WORD DESCRIBES HOW JEOPARDY! WRITERS AND RESEARCHERS TRY TO REDUCE THE ODDS THAT A CLUE WILL HAVE MORE THAN ONE CORRECT RESPONSE

What is "pinned"?

None of the current *Jeopardy!* writers or researchers have scientific backgrounds, which Wisse says usually works to their advantage. "There are subjects we tend to know a lot about and those you have to guard against becoming too esoteric," explains Wisse, who has a master's degree in English. "In that sense, it's almost

PHOTOS: (TOP TO BOTTOM) JEOPARDY PRODUCTIONS INC.; J. COHEN/*SCIENCE*

Published by AAAS

easier to write science categories than something I'm more familiar with." But the flip side is that when the writers do not intimately know a subject, what they deem the "natural" response may have an equally valid alternative that slips under their pregame radar.

UNIMAGINABLY DENSE MATERIAL IS FOUND IN THESE "STARS" NAMED FOR SUBATOMIC PARTICLES
What are neutron stars?

Neutron stars was the "right" response, but when this clue aired as a Daily Double in 1999, one of the three contestants, who had wagered $1900, offered a response—**What are quark stars?**—that Trebek rejected. After some quick checking by Wisse and his team, however, the host had to offer a rare mea culpa. "Although there is very little known about quark stars, they do exist, and that is a correct response, given the way we phrased that clue," Trebek conceded. The contestant received a $3800 boost and moved into the lead (but ultimately lost).

Wisse and his crew must produce nearly 20,000 carefully sourced clues to fill the 230 shows that air each season. In *Jeopardy!* speak, the writers rank clues as 1, 2, 3, 4, or 5; they dismiss ideas that are too easy as a 1/2 and too hard as a 14. "If there's something people know, we will do it to death," Wisse says. "We've given them Watson and gone for Crick and given them Crick and gone for Watson." In the Battle of the Decades, they asked the name of the lab where Watson and Crick worked, which turned out to be a "triple stumper"—a veritable 14—as no one even guessed Cavendish Lab.

JANE GOODALL, NOBELIST DAVID BALTIMORE, AND THE LARGE HADRON COLLIDER AT CERN HAVE SHARED THIS MOST UNUSUAL TV EXPERIENCE
What is appearing in a *Jeopardy!* video clue?

In one of its most popular scientific gambits, *Jeopardy!* in 2011 pitted champions against an IBM supercomputer system, dubbed Watson, that was programmed to play the game. Along with a vast database of information, Watson had the advantage of speed, says *Jeopardy!* champion Russ Schumacher, a meteorologist at Colorado State University, Fort Collins. "Watson's buzzer timing was not human," Schumacher says. The supercomputer won that contest. But a few weeks later, Holt was one of five members of Congress who competed against Watson in an untelevised Capitol Hill showdown. Holt beat the computer. "I think Watson was having a low voltage night," he said at the time.

JEOPARDY! CONTESTANTS USE THIS INTONATION PATTERN FAR MORE FREQUENTLY WHEN THEY HAVE AN INCORRECT RESPONSE, AND WOMEN USE IT MORE THAN MEN OVERALL
What is uptalk?

Researchers have published several studies of *Jeopardy!* over the years (see http://scim.ag/jeopaRdy), including one by a sociologist who analyzed vocal intonations in 5473 responses from 300 contestants. As he reported 2 years ago in *Gender & Society*, 48% of women and 27% of men used uptalk when they had the correct response to a clue, but 76% of females and 57% of males uptalked when they were wrong. Another *Jeopardy!* study focused on smart wagering strategies in the final round and ran in *Mathematics Magazine* in 1994.

But more science goes into *Jeopardy!* than emerges from it. Take bioinformaticist Roger Craig and his big win. Before he made it onto the show, Craig downloaded J! Archive (http://j-archive.com/), an online site made by *Jeopardy!* fans that to date has cataloged more than 280,000 clues and responses and analyzed the relationship between high dollar amount questions and topics. This allowed Craig to see trends—for example, questions about astronomy most often appear in Double Jeopardy!, when the clues are worth more money—and focus on increasing his knowledge in high value areas. (A video where he describes his analysis is at http://scim.ag/jeopaRdy.) "It wasn't like I sat down one day and said I want to reverse engineer the game and crush it," Craig says. "I just did a little experiment here and it led to another. That's how science works."

In his first game, a category called ELEMENTAL CLUES beckoned him, because his extensive preparation had shown chemistry was his strongest subject. "I had told my friends if I ever get a Daily Double on the periodic table, I'm going to bet it all," he says. Craig hit a Daily Double and wagered the entire $12,000 he had amassed.

PD: A GREAT PLACE FOR LIVE MUSIC
What is palladium?

Craig would go on to win the game—and four others taped that same day. But he says this four-letter, nonscientific factor also helped him, as it has all big winners.

What is luck? ■

Put yourself in *Jeopardy!*

Time to cue the *Jeopardy!* theme. We've compiled 10 clues from past episodes of the game show for your entertainment. You can also take the quiz online and see more detailed answers at **http://scim.ag/jeopaRdy** and you will find Roger Craig explaining his winning secrets and a list of research papers about *Jeopardy!*.

1. WEIRD SCIENCE: Researchers at NC State are equipping these household insect pests with mini-transmitters for eventual use in disaster zones

2. GENERAL SCIENCE: George Beadle & E.L. Tatum's studies of the Neurospora crassa mold on this food helped launch molecular genetics in 1941

3. SCIENTISTS: His "The Galvanic Circuit Investigated Mathematically" received so much "resistance," he resigned his post at Cologne

4. ALL SCIENCE: Adrenaline is another name for this hormone secreted in response to stress or fear

5. "C" IN SCIENCE: The earliest period of the Paleozoic Era, it extends from about 542 to 488 million years ago

6. LIFE SCIENCES: Organic chemistry focuses specifically on this element's compounds & their reactions

7. YOU DO THE MATH: It's the square root of a gross

8. LIFE SCIENCES: Alimentary, my dear! Waves of contractions moving swallowed food through the esophagus are called this

9. MEDICINE: The word for this disease comes from the same Latin root as "rage"

10. SCIENTIFIC FIRSTS: The first object in our solar system discovered by telescope was not a planet but one of these

ANSWERS: **1.** cockroaches **2.** bread **3.** Georg Ohm **4.** epinephrine **5.** Cambrian **6.** carbon **7.** 12 **8.** peristalsis **9.** rabies **10.** moon

Published by AAAS

INSIGHTS

Precision medicine comes to psychiatry *p. 499*

Secure sustainable seafood from developing countries *p. 504*

PERSPECTIVES

ECOLOGY

1000 dams down and counting

Dam removals are reconnecting rivers in the United States

By **J. E. O'Connor,[1] J. J. Duda,[2] G. E. Grant[3]**

Forty years ago, the demolition of large dams was mostly fiction, notably plotted in Edward Abbey's novel *The Monkey Wrench Gang*. Its 1975 publication roughly coincided with the end of large-dam construction in the United States. Since then, dams have been taken down in increasing numbers as they have filled with sediment, become unsafe or inefficient, or otherwise outlived their usefulness (*1*) (see the figure, panel A). Last year's removals of the 64-m-high Glines Canyon Dam and the 32-m-high Elwha Dam in northwestern Washington State were among the largest yet, releasing over 10 million cubic meters of stored sediment. Published studies conducted in conjunction with about 100 U.S. dam removals and at least 26 removals outside the United States are now providing detailed insights into how rivers respond (*2, 3*).

A major finding is that rivers are resilient, with many responding quickly to dam removal. Most river channels stabilize within months or years, not decades (*4*), particularly when dams are removed rapidly; phased or incremental removals typically have longer response times. The rapid physical response is driven by the strong upstream/downstream coupling intrinsic to river systems. Reservoir erosion commonly begins at knickpoints, or short steep

Goodbye to a large dam. Elwha River passing through the remains of Glines Canyon Dam on 21 February 2015. The former Lake Mills can be seen in the background.

PHOTO: JOHN GUSSMAN/JGUSSMAN@DCPRODUCTIONS.COM

Downloaded from www.sciencemag.org on April 30, 2015

Published by AAAS

reaches of channel, that migrate upstream while cutting through reservoir sediment. Substantial fractions of stored reservoir sediment—50% or more—can be eroded within weeks or months of breaching (*4*) (see the figure, panel B). Sediment eroded from reservoirs rapidly moves downstream (*5*, *6*). Some sediment is deposited downstream, but is often redistributed within months. Many rivers soon trend toward their pre-dam states (*5, 7*).

Migratory fish have also responded quickly to restored river connectivity. Removal of a dam on Virginia's Rappahannock River increased American eel populations in Shenandoah National Park, 150 km upstream (*8*). Similarly, following a small dam removal in Maine, sea lamprey recolonized newly accessible habitat, increasing abundance and nesting sites by a factor of 4 (*9*). Within days of the blast removing the last of Glines Canyon Dam, Elwha River Chinook salmon swam upstream past its rocky abutments. Responses have been mixed for less mobile bottom-dwelling plants and animals in former reservoirs and downstream channels (*10, 11*).

Dam size, river size, reservoir size and shape, and sediment volume and grain size all exert first-order controls on physical and ecological responses to dam removal. Larger dam removals have had longer-lasting and more widespread downstream effects than the much more common small-dam removals (*4*). Local environmental and habitat conditions and the dam's position in the watershed also affect physical and ecologic consequences. In the case of the Elwha River, both dams were near the river mouth, minimizing the extent of downstream effects while reconnecting large areas of high-quality fish habitat upstream in Olympic National Park.

Removals can also have additional consequences, some of them unintended. For example, changes to a headwater fish assemblage occurred when a removal allowed upstream colonization by reservoir species present behind a dam farther downstream (*12*). Watershed contaminants, organic accumulations, nutrients, once-inundated structures, and landforms from past land uses may be uncovered and sometimes mobilized by dam removal.

Numerical and physical models have guided removal and monitoring strategies, forecast broad-scale trends, and helped avoid negative outcomes (*13*), but cannot yet predict fine-scale changes driving many ecological processes. Quantitative models of species and ecosystem responses to dam removal lag even further behind.

Most dam-removal studies so far have been short-duration and opportunistic. Most dam-removal analyses are from the northern United States. Few removals have markedly altered flow and/or released large volumes of fine sediment. Furthermore, studies truly integrating biological and physical responses are rare. Common protocols, more coordination among disciplines, and longer, more systematic monitoring and research would benefit future syntheses (*13*).

Dam removals in the United States

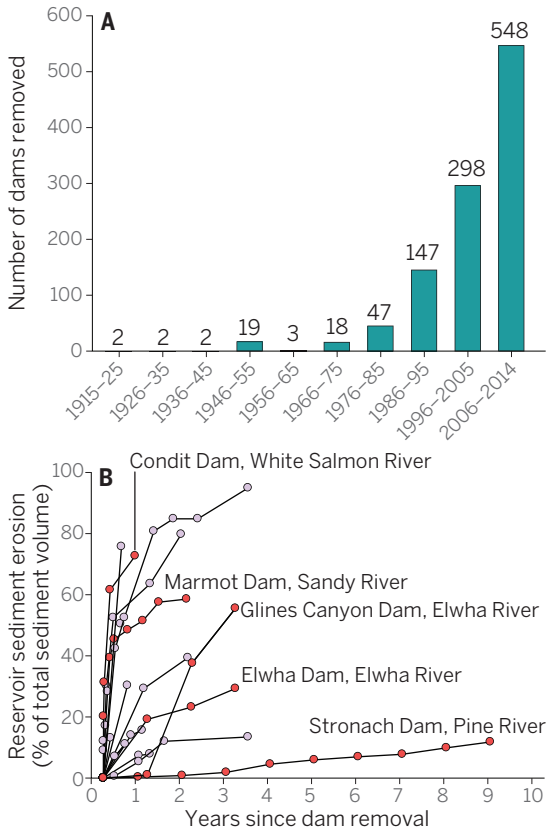

Coming down. (**A**) U.S. dam removals by decade. Data from (*1*). (**B**) Rates of reservoir sediment erosion for 16 recent U.S. dam removals. Condit, Marmot, Glines Canyon, and Elwha dams impounded sand-rich sediment accumulations and were removed over short periods ranging from hours to 3 years, leading to rapid reservoir sediment erosion. Stronach Dam was removed in several phases over 7 years, slowing reservoir erosion (*15*). Data from (*4*).

In the United States, many dam removals have improved ecosystem function while avoiding catastrophic consequences to either ecosystems or human uses. The high pace of dam removal will likely continue. But the future is murky. As mostly small dams continue to come down, dam-removal advocates will gaze up at the many large and ecologically disruptive dams across the country that are decaying and filling with sediment. Decisions regarding these dams will require balancing risks, continued economic function, and the potential for ecologic restoration. Also clouding the future is climate change, which is likely to increase the demand for fresh-water storage, both as a low-carbon energy source and for consumptive use.

Dams are also being removed internationally; the 26 removals with published studies are just a sample from a total probably numbering in the hundreds. Like most of those in the United States, many are small structures at the end of their useful lives. And many removals, such as the ongoing one of Japan's Arase Dam, are motivated by economic and ecological considerations similar to those spurring U.S. dam removal.

The total number of U.S. and international removals are, however, more than offset by a renewed global boom in dam construction, chiefly for hydropower and in regions with emerging economies, such as Southeast Asia, South America, and Africa (*14*). But the dams of this ongoing boom will also age, just like those of the U.S. dam-building heyday. Dam removal looks like an activity with a long future ahead. ■

REFERENCES AND NOTES

1. www.americanrivers.org/initiatives/dams/dam-removals-map
2. A. G. Lejon, B. M. Renöfält, C. Nilsson, *Ecol. Soc.* **14**, 4 (2009).
3. J. R. Bellmore *et al.*, USGS Dam Removal Science Database (2015); http://doi.org/.10.5066/F7K935KT.
4. G. E. Grant, S. L. Lewis, in *Engineering Geology for Society and Territory*, vol. 3, G. Lollino *et al.*, Eds. (Springer, Switzerland, 2015), pp. 31–35.
5. J. J. Major *et al.*, *Geomorphic response of the Sandy River, Oregon, to removal of Marmot Dam: U.S. Geological Survey Professional Paper 1792* (2012).
6. A. J. Pearson, N. P. Snyder, M. J. Collins, *Water Resourc. Res.* **47**, W08504 (2009).
7. A. E. East *et al.*, *Geomorphology* **228**, 765 (2015).
8. N. P. Hitt *et al.*, *Trans. Am. Fish. Soc.* **141**, 1171 (2012).
9. R. Hogg, S. Coghlan Jr., J. Zydlewski, *Trans. Am. Fish. Soc.* **142**, 1381 (2013).
10. D. D. Tullos *et al.*, *PLOS ONE* **9**, e108091 (2014).
11. C. H. Orr *et al.*, *River Res. Appl.* **24**, 804 (2008).
12. M. S. Kornis *et al.*, *Aquat. Sci.* 10.1007/s00027-014-0391-2 (2014).
13. P. W. Downs *et al.*, *Int. J. River Basin Manag.* **7**, 433 (2009).
14. C. Zarfl, A. E. Lumsdon, J. Berlekamp, L. Tydecks, K. Tockner, *Aquat. Sci.* **77**, 161 (2015).
15. B. A. Burroughs *et al.*, *Geomorphology* **110**, 96 (2009).

ACKNOWLEDGMENTS

This Perspective is derived from discussions and analysis efforts conducted by the working group on *Dam removal: Synthesis of ecological and physical responses* of the U.S. Geological Survey John Wesley Powell Center for Analysis and Synthesis.

10.1126/science.aaa9204

[1]U.S. Geological Survey, Portland, OR, USA. [2]U.S. Geological Survey, Seattle, WA, USA. [3]USDA Forest Service, Corvallis, OR, USA. E-mail: oconnor@usgs.gov

Published by AAAS

CHEMICAL PHYSICS

The quantum halo state of the helium trimer

Femtosecond laser pulses help to take a snapshot of the huge elusive Efimov state

By **Oleg Kornilov**

The systems of two interacting particles are often simple enough to appear in textbooks. The situation is drastically different when three interacting particles are involved. General solutions for "the three-body problem" do not yet exist in classical or in quantum domains. A step forward was made in 1970 by Vitaly Efimov, who established that when two identical bosons are either very weakly bound or just unbound, an infinite series of three-body bound states emerges (*1*). The forces are sufficient to bind the trimer even when they are too weak to hold the particles in pairs, very much like Borromean rings. Efimov's original proposal concerned nuclear physics, but the helium trimer $^4He_3$ was soon suggested as the most likely candidate for experiments (*2*). Now, after 38 years, Kunitski *et al.* (*3*) report on page 551 of this issue the detection of these very fragile clusters and image their structure.

The three-body states discovered by Efimov belong to the class of quantum halos (*4*), in which particles are mostly found in classically forbidden regions of space, i.e., outside the range of the interaction potential. Their properties are universal—they are independent of the exact laws of interaction (*5*). The search for Efimov states in nuclear systems and in the $^4He_3$ trimer had long been unsuccessful. Another opportunity emerged in 1999, when it was suggested that Efimov states can lead to atomic loss features in ultracold clouds of alkali atoms, when the magnetic field in the cloud is scanned over the Feshbach resonances that correspond to binding thresholds for two-body states (*6*). This experiment was successfully performed by Kraemer *et al.* with a cloud of cesium atoms (*7*), demonstrating the existence of Efimov states.

Since then, the Efimov effect has been found for several other alkali metals. The experimental detection of helium trimers turned out to be more complicated than the theory because of the extreme fragility of these clusters. The development of the matter-wave nanograting diffraction technique allowed the separation of helium trimers in molecular beam expansions and measurement of their spatial extent (*8*). However, the diffraction is sensitive to the de Broglie wavelength of the clusters, and thus the ground and excited (Efimov) states of $^4He_3$ could not be told apart. The measurement of the trimer size, which was obtained by recording the envelope of the diffraction pattern, yielded a helium atom–pair distance of 1.1 nm, in agreement with the theoretical expectations for the ground state, but much less than the Efimov state that extends to almost 8 nm far into the classically forbidden region (*9*). The authors, therefore, concluded that no excited trimers were detected.

Kunitski *et al.* adopted the diffraction technique but used a far more advanced detection method. They applied an intense femtosecond laser pulse to instantaneously ionize all three atoms of the trimer. The three helium ions experience a strong repulsion via the Coulomb force and fly apart, much like the debris after an explosion (hence the term "Coulomb explosion"). The momenta of all three ions, recorded using the sophisticated COLTRIMS technique (cold target recoil ion momentum spectroscopy), were converted to the relative positions of the three atoms and provided the trimer spatial structure (see the figure).

These results revealed two distinct structures of the $^4He_3$ trimer with the sizes match-

Max Born Institute, 12489 Berlin, Germany.
E-mail: kornilov@mbi-berlin.de

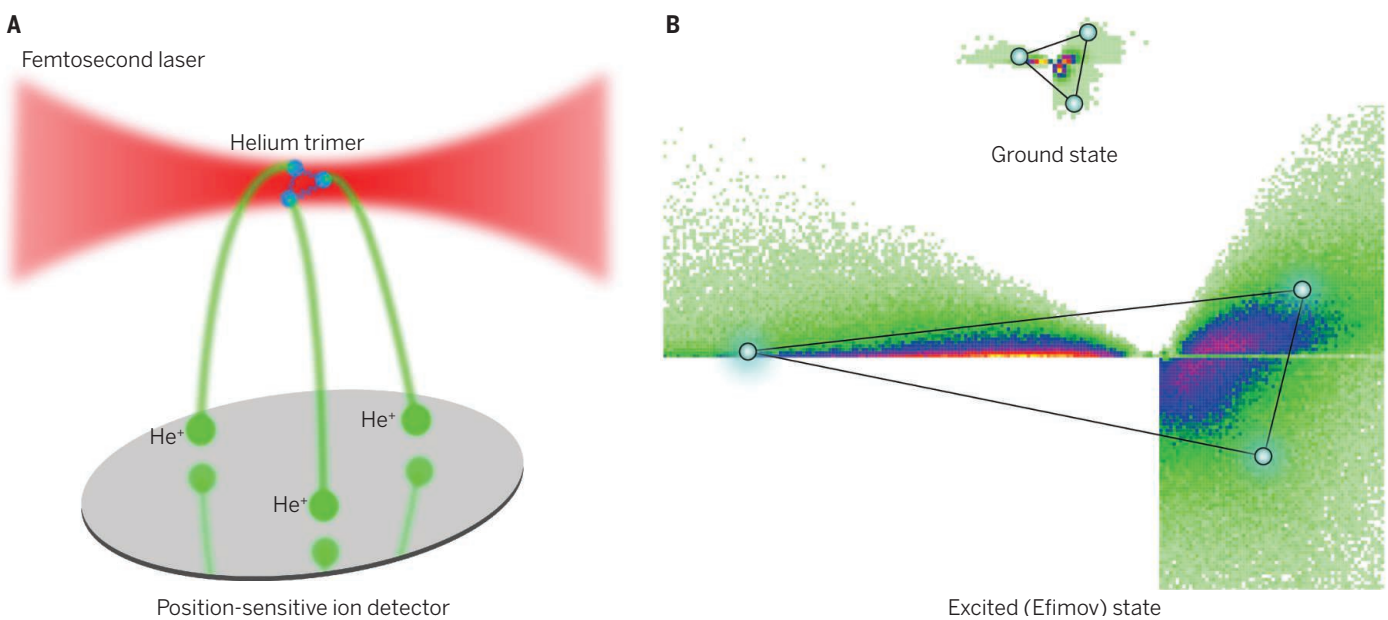

Bound and determined. In the experiment of Kunitski *et al.*, a femtosecond laser ionizes helium trimers selected by a nanoscale diffraction grating. (**A**) The three helium ions fly apart and reach the time- and position-sensitive detector. (**B**) The experiment reveals trimers with two distinct structures: a small and compact one corresponding to the trimers in the well-known ground state, and a large and floppy structure, which is now assigned to the long-sought Efimov state of the helium trimer.

Published by AAAS

Downloaded from www.sciencemag.org on April 30, 2015

ing the ground- and excited-state predictions. The authors proved the existence of the $^4He_3$ Efimov state and confirmed its enormous size, largest of all known triatomic molecules. Not only do the experiments of Kunitski *et al.* give access to a new class of quantum halo systems, but also their method provides direct information on the structure of these peculiar objects. The predominant structure of the Efimov trimer turns out to be a triangle with a relatively small acute angle. Because of the universality of the Efimov phenomenon, other suitable systems of identical bosons probably should adopt similar structures.

The use of femtosecond laser pulses in the detection opens new perspectives in the field of Efimov physics. The electric fields in a femtosecond pulse can reach very high values of several volts per angstrom. In 1999, Nielsen *et al.* (*10*) proposed that such electric fields could be sufficient to modify interaction potentials of helium atoms and tune creation or destruction of Efimov states. With the advent of the experiment of Kunitski *et al.*, one can now imagine using a long-wavelength laser pulse to manipulate the interaction potentials between helium atoms, while the second pulse could induce the Coulomb explosion. Furthermore, the very short durations of the femtosecond pulses provide opportunities to study a new class of transient Efimov states with ultrashort lifetimes. Quantum halos involving electrons as one of the particles seem promising in this context (*4*).

Although the general treatment of three-body systems is still out of reach, the experimental technique of Kunitski *et al.* opens insights into new molecular systems exhibiting the Efimov effect. This approach not only provides information on their structure, but may in the future allow manipulation of the states and access to a completely new class of short-lived quantum halo systems. Prospective experimental achievements in the case of molecular Efimov states will be directly applicable to similar problems in other physical situations. ■

REFERENCES AND NOTES

1. V. Efimov, *Phys. Lett.* **33**, 563 (1970).
2. T. K. Lim, S. K. Duffy, W. C. Damer, *Phys. Rev. Lett.* **38**, 341 (1977).
3. M. Kunitski *et al.*, *Science* **348**, 551 (2015).
4. A. S. Jensen, K. Riisager, D. V. Fedorov, E. Garrido, *Rev. Mod. Phys.* **76**, 215 (2004).
5. E. Braaten, H.-W. Hammer, *Phys. Rep.* **428**, 259 (2006).
6. B. D. Esry, C. H. Greene, J. P. Burke Jr., *Phys. Rev. Lett.* **83**, 1751 (1999).
7. T. Kraemer *et al.*, *Nature* **440**, 315 (2006).
8. W. Schöllkopf, J. P. Toennies, *Science* **266**, 1345 (1994).
9. R. Brühl *et al.*, *Phys. Rev. Lett.* **95**, 063002 (2005).
10. E. Nielsen, D. V. Fedorov, A. S. Jensen, *Phys. Rev. Lett.* **82**, 2844 (1999).

ACKNOWLEDGMENTS

I thank J. Peter Toennies for valuable comments on the manuscript.

10.1126/science.aaa9102

MEDICINE

Brain disorders? Precisely

Precision medicine comes to psychiatry

By **Thomas R. Insel** *and* **Bruce N. Cuthbert**

Mental disorders represent a public health challenge of staggering proportions. In the most recent Global Burden of Disease study, mental and substance abuse disorders constitute the leading source of years lost to disability from all medical causes (*1*). The World Health Organization estimates over 800,000 suicides each year globally, nearly all of which are a consequence of a mental disorder (*2*). These high morbidity and mortality figures speak to the potential for overall health gains if mental disorders can be more effectively diagnosed and treated. Could a "precision medicine" approach find traction here?

Precision medicine—a more targeted approach to disease—is already becoming a reality in cancer, where molecular diagnosis is leading to better defined, individualized treatments with improved outcomes (*3*). Precision medicine is also the basis for planning large-cohort studies, using genomics and phenotyping (physiological and behavioral characteristics) to improve diagnostics and therapeutics across medicine. The idea is to integrate clinical data with other patient information to uncover disease subtypes and improve the accuracy with which patients are categorized and treated.

Diagnosis in psychiatry, in contrast to most of medicine, remains restricted to subjective symptoms and observable signs. Clinicians rightly pride themselves on their empathic listening and well-honed observational skills. But recently psychiatry has undergone a tectonic shift as the intellectual foundation of the discipline begins to incorporate the concepts of modern biology, especially contemporary cognitive, affective, and social neuroscience. As these rapidly evolving sciences yield new insights into the neural basis of normal and abnormal behavior, syndromes once considered exclusively as "mental" are being reconsidered as "brain" disorders—or, to be more precise, as syndromes of disrupted neural, cognitive, and behavioral systems.

But before research on the convergence of biology and behavior can deliver on the promise of precision medicine for mental disorders, the field must address the imprecise concepts that constrain both research and practice. Labels like "behavioral health disorders" or "mental disorders" or the awkwardly euphemistic "mental health conditions," when juxtaposed against brain science, invite continual recapitulation of the fruitless "mind-body" and "nature-nurture" debates that have impeded a deep understanding of psychopathology. The brain continually rewires itself and changes gene expression as a function of learning and life events. And the brain is organized around tightly regulated circuits that subserve perception, motivation, cognition, emotion, and social behavior. Thus, it is imperative to include measures of both brain and behavior to understand the various aspects of dysfunction associated with disorders. Shifting from the language of "mental disorders" to "brain disorders" or "neural circuit disorders" may seem premature, but recognizing the need to incorporate more than subjective reports or observable behavior in our diagnosis of these illnesses is long overdue.

> ***"...syndromes once considered exclusively as 'mental' are being reconsidered ... as syndromes of disrupted neural, cognitive, and behavioral systems."***

About 5 years ago, the U.S. National Institute of Mental Health launched a "precision medicine for psychiatry" project (*4*). This Research Domain Criteria (RDoC) initiative was seen by some as a radical attempt to immediately change the framework for how clinicians would diagnose and care for patients they were currently treating. But, the concept was actually to rethink research on psychopathology by building a framework beyond symptoms. Symptoms would be an important starting point, but the framework would include a focus on systems or dimensions that had both cognitive and biological validity. Genomic variants and brain circuit–level differences are evident in studies of people with psychopathology, but the findings cross current diagnostic boundaries rather than validating them (*5*, *6*). Similarly,

National Institute of Mental Health, National Institutes of Health, Bethesda, MD, USA. E-mail: tinsel@mail.nih.gov

Downloaded from www.sciencemag.org on April 30, 2015

Published by AAAS

Deconstructed, parsed, and diagnosed.

A hypothetical example illustrates how precision medicine might deconstruct traditional symptom-based categories. Patients with a range of mood disorders are studied across several analytical platforms to parse current heterogeneous syndromes into homogeneous clusters.

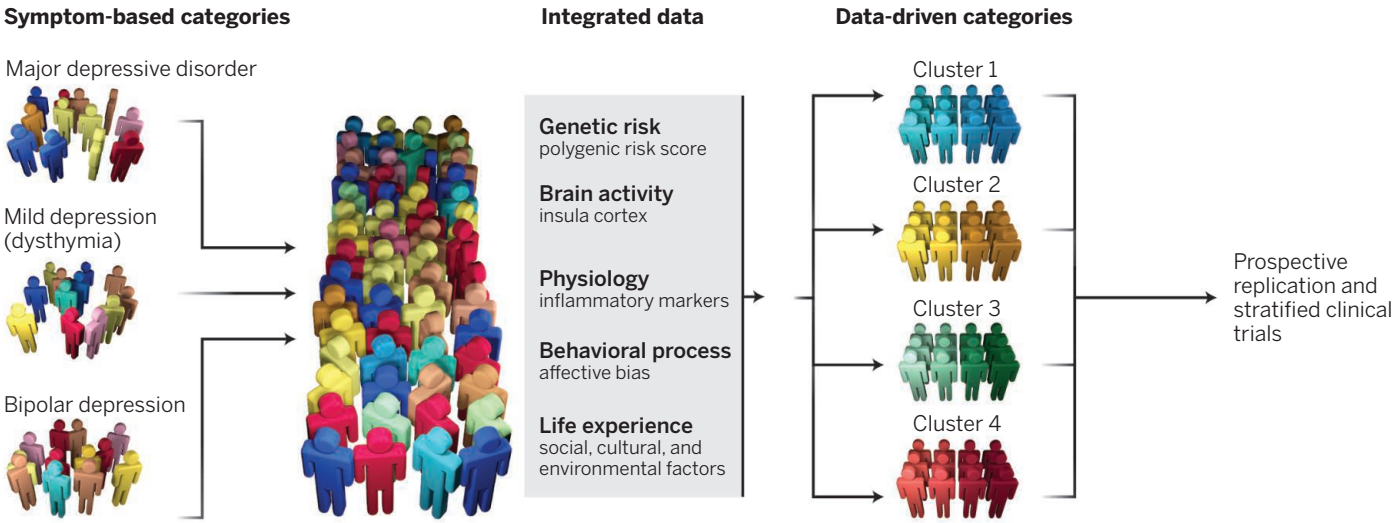

constructs such as anhedonia (inability to experience pleasure) and executive function cut across many current diagnostic categories (*7*, *8*). RDoC asks researchers to shift from designing research projects narrowly built around current diagnostic categories to dimensions or systems, such as social processes or negative valence (responding to aversive objects or situations), which are supported by a deep cognitive and neural science and can be the basis for objective measures of psychopathology (see the figure).

An early promising result from this project has emerged from studies that deconstruct current diagnostic groups to identify subgroups that have biological validity, and predict treatment response. For instance, imaging and neurophysiology have demonstrated three subtypes of attention deficit hyperactivity disorder with quite different responses to stimulant medication (*9*). Preliminary reports from studies using cognitive testing, imaging, and/or genomic panels are finding biologically meaningful subgroups of psychotic or mood disorders (*10*, *11*). Notably, these biologically defined subgroups do not map neatly onto clusters of symptoms. Although these results will need replication and, most important, will need to be shown to be predictive of prognosis or treatment response, they illustrate the potential for empirically defined, convergent methods of stratifying patients. Indeed, results using information retrieval and natural language processing methods to extract RDoC dimensions from electronic health records suggest that RDoC domains, but not symptom-based diagnosis, predicted length of hospital stay or hospital readmission (*12*).

Already the scientific community has embraced the opportunity to think beyond current classifiers, with nearly 1000 papers addressing various aspects of RDoC over the past year. RDoC has also served as a catalyst for new efforts outside the United States to transform diagnosis, including the European Commission–funded Roadmap for Mental Health Research (*13*) and a new call from the European Union Innovative Medicines Initiative to link clinical neuropsychiatry and quantitative neurobiology. There is an emerging consensus that such new approaches are necessary to move the field forward, coupled with the realization that many challenges must be faced—such as the pressing need for new measurement instruments in the laboratory and the clinic, and for determining the degree of precision with which functions and neural systems must be assessed for optimal diagnosis and treatment.

As new diagnostics will likely be redefining "mental disorders" as "brain circuit disorders," new therapeutics will likely focus on tuning these circuits. What is the best way to tune a negative valence or social processing circuit? Medications might be useful, but recent attention has focused on devices that invasively (deep brain stimulation) or noninvasively (transcranial magnetic stimulation) alter brain circuit activity (*14*). Paradoxically, one of the most powerful and precise interventions to alter such activity may be targeted psychotherapy, such as cognitive behavioral therapy, which uses the brain's intrinsic plasticity to alter neural circuits and as a consequence, deleterious thoughts and behavior (*15*).

Just as the precision medicine approach for cancer can alter our approach to diagnosing mental disorders, psychiatry can leverage important therapeutic insights from cancer and other studies of chronic diseases. For complex, chronic disorders, from diabetes to hypertension, the search for a magic bullet is giving way to combinatorial or convergent solutions. Medications, devices, mobile health apps, social support, education, and team care are all part of the package needed for improving outcomes. Part of transforming treatments and improving outcomes for people with brain circuit disorders will include these kinds of packages built around patient choice, and individualized based on each person's needs and specific neural pathology. This will ultimately be the precision medicine that can bend the morbidity and mortality curves for people with disorders previously known as "mental disorders." ■

REFERENCES

1. H. A. Whiteford *et al.*, *Lancet* **382**, 1575 (2013).
2. World Health Organization, Preventing suicide: A global imperative (2014). www.who.int/mental_health/suicide-prevention/world_report_2014/en/.
3. F. S. Collins, H. Varmus, *N. Engl. J. Med.* **372**, 793 (2015).
4. T. Insel *et al.*, *Am. J. Psychiatry* **167**, 748 (2010).
5. S. H. Lee *et al.*, *Nat. Genet.* **45**, 984 (2013).
6. M. Goodkind *et al.*, *J. Am. Med. Assoc. Psychiatry* 10.1001/jamapsychiatry.2014.2206 (2015).
7. G. S. Dichter, et al., *J. Neurodev. Disord.* **4**, 19 (2012).
8. M. W. Cole et al., *Neuroscientist* **20**, 652 (2014).
9. S. L. Karalunas *et al.*, *J. Am. Med. Assoc. Psychiatry* **71**, 1015 (2014).
10. C. A. Tamminga *et al.*, *Schizophr. Bull.* **40** (suppl. 2), S131 (2014).
11. B. S. Hall et al., *Neurobiol. Stress* **1**, 174 (2015).
12. T. H. McCoy *et al.*, *Am. J. Psychiatry* **172**, 316 (2015).
13. G. Schumann *et al.*, *Eur. Neuropsychopharmacol.* **24**, 5 (2014).
14. M. A. Rosa, S. H. Lisanby, *Neuropsychopharmacol.* **37**, 102 (2012).
15. L. D. Crocker *et al.*, *Front. Hum. Neurosci.* **7**, 261 (2013).

10.1126/science.aab2358

ILLUSTRATION: V. ALTOUNIAN AND C. SMITH/*SCIENCE*

Published by AAAS

ECOLOGY

Extinction risks from climate change

How will climate change affect global biodiversity?

By **Janneke Hille Ris Lambers**

Complex threats. In addition to climate change, habitat transformation, invasive species, and pathogens also threaten amphibians like the Cascades frog, *Rana cascadae* (*8*, *11*).

Biologists worry that the rapid rates of warming projected for the planet (*1*) will doom many species to extinction. Species could face extinction with climate change if climatically suitable habitat disappears or is made inaccessible by geographic barriers or species' inability to disperse (see the figure, panels A to E). Previous studies have provided region- or taxon-specific estimates of biodiversity loss with climate change that range from 0% to 54%, making it difficult to assess the seriousness of this problem. On page 571 of this issue, Urban (*2*) provides a synthetic and sobering estimate of climate change–induced biodiversity loss by applying a model-averaging approach to 131 of these studies. The result is a projection that up to one-sixth of all species may go extinct if we follow "business as usual" trajectories of carbon emissions.

By quantitatively assessing how extinction risk depends on model assumptions, Urban's study provides insight into factors that increase biodiversity loss with climate change. Surprisingly, the modeling approaches used in the studies that Urban surveyed did not have the largest effect on estimates of extinction risk, despite substantial methodological differences. Instead, the magnitude of future climate change was the most important predictor of extinction risk, with increased warming resulting in greater biodiversity loss.

What is worrying, given the current anthropogenic carbon emissions trajectory, is that biodiversity loss is predicted to accelerate with greater climate change. Geography also plays a role, with higher extinction risks projected for Australia, New Zealand, and South America—regions with high numbers of endemic species (that is, species with narrow distribution ranges) that face disappearing habitats or geographic barriers to migration (see the figure, panels C and D). Urban also found higher biodiversity loss for studies focusing on endemic species, but few differences among taxonomic groups (such as birds and amphibians). Projections of geographic and trait-based variation in extinction risk such as these are essential for targeted conservation efforts (*3*).

The study also highlights critical uncertainties in our understanding of how climate change drives extinction. For example, if suitable habitat disappears entirely with climate change, extinction seems inevitable. However, what if climatically suitable habitats still exist but shrink in size or quality (see the figure, panel C) (*4*)? Biologists believe extinction will occur before suitable habitats disappear, but they lack information on species-specific threshold habitat sizes for extinction. Similarly, what happens if species cannot reach a newly suitable habitat (see the figure, panels D and E) (*5*)? Biologists assume that slow-moving organisms will have trouble "keeping up"

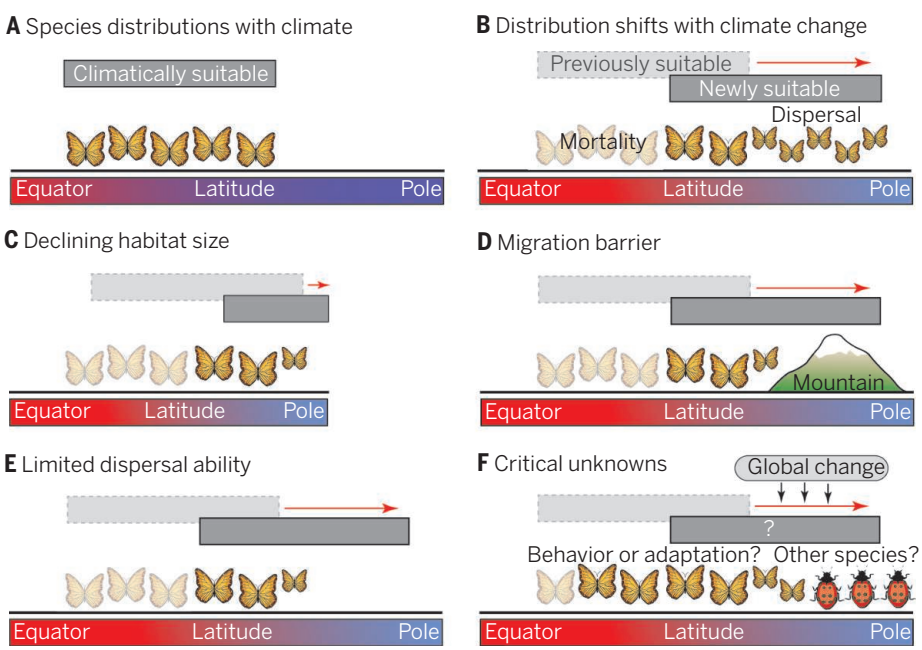

Move, adapt, or perish. Species distributions are generally determined by climate (**A**). They track climate change (red arrows) if populations can disperse and establish in newly suitable habitats, and disappear where climate has become unsuitable (**B**). Species may face extinction if habitat sizes shrink (for example, at the poles or at mountaintops) (**C**), or if migration barriers (**D**) or limited dispersal ability (**E**) prevent them from reaching newly suitable habitat. The ability of species to adapt (or modify their behavior), species interactions, and other global change stressors represent key uncertainties (**F**) that affect our ability to predict biodiversity loss with climate change.

Department of Biology, University of Washington, Seattle, WA 98195, USA. E-mail: jhrl@uw.edu

PHOTO: BRAD MITCHELL/ALAMY

Published by AAAS

with climate change, but there is sparse information on just how rapidly most species can migrate. Urban's study illustrates that our uncertainty about these processes matters greatly, with assumptions about dispersal and threshold habitat sizes for extinction strongly influencing projected biodiversity loss.

The biggest unknowns about biodiversity loss with climate change arise from processes that are never (or only rarely) included in the predictive models that Urban surveyed. For example, can adaptation or behavior buffer species from the negative impacts of climate change? Given that extinction is not instantaneous, how rapidly will biodiversity be lost (*6*)? Will other global change factors, such as invasive species, exacerbate climate change impacts (see the photo) (*7*, *8*)? Will species interactions magnify biodiversity loss from climate change (*9*) or, alternatively, buffer species from negative impacts of climate change (*10*)? These are challenging questions that biologists are only just beginning to address when considering climate change impacts on biodiversity (*7*).

Midway through what could well turn out to be the warmest decade in the past 170 years (*1*), Urban's study joins many others suggesting that climate change will have enormous impacts on the organisms with which we share our planet. Many uncertainties remain, and biologists will continue to improve forecasts of biodiversity loss with climate change by gathering additional data and incorporating additional complexities into models. However, we should not wait for these forecasts before taking action, preferentially by curbing emissions (*1*) but also by devising strategies to mitigate the negative impacts of climate change on biodiversity (*3*, *7*). If we do not, it is clear that we will soon be able to directly observe the impacts of climate change on biodiversity. ■

REFERENCES

1. Summary for Policymakers, in *Climate Change 2013: The Physical Science Basis. Contribution of the Working Group I to the Fifth Assessment Report of the Intergovernmental Panel on Climate Change*, T. F. Stocker *et al.*, Eds. (Cambridge Univ. Press, Cambridge, 2013).
2. M. C. Urban, *Science* **348**, 571 (2015).
3. O. Hoegh-Guldberg *et al.*, *Science* **321**, 345 (2008).
4. S. C. Amstrup *et al.*, *Nature* **468**, 955 (2010).
5. C. A. Schloss, T. A. Nuñez, J. J. Lawler, *Proc. Natl. Acad. Sci. U.S.A.* **109**, 8606 (2012).
6. S. T. Jackson, D. F. Sax, *Trends Ecol. Evol.* **25**, 153 (2010).
7. J. J. Lawler, A. S. Ruesch, J. D. Olden, B. H. McRae, *Ecol. Lett.* **16**, 1014 (2013).
8. C. Hof, M. B. Araújo, W. Jetz, C. Rahbek, *Nature* **480**, 516 (2011).
9. R. K. Colwell, R. R. Dunn, N. C. Harris, *Annu. Rev. Ecol. Evol. Syst.* **43**, 183 (2012).
10. R. M. Pateman, J. K. Hill, D. B. Roy, R. Fox, C. D. Thomas, *Science* **336**, 1028 (2012).
11. M. E. Ryan, W. J. Palen, M. J. Adams, R. M. Rochefort, *Front. Ecol. Environ.* **12**, 232 (2014).

10.1126/science.aab2057

ECOLOGY

Human-wildlife conflicts in a crowded airspace

How can the ecological consequences of the increasing use of airspace by humans be minimized?

By **Sergio A. Lambertucci**,[1] **Emily L. C. Shepard**,[2] **Rory P. Wilson**[2]

Over the past century, humans have increasingly used the airspace for purposes such as transportation, energy generation, and surveillance. Conflict with wildlife may arise from buildings, turbines, power lines, and antennae that project into space and from flying objects such as aircrafts, helicopters, and unmanned aerial vehicles (UAVs, or drones) (see the figure) (*1*–*3*). The resulting collision and disturbance risks profoundly affect species ecology and conservation (*1*, *4*, *5*). Yet, aerial interactions between humans and wildlife are often neglected when considering the ecological consequences of human activities.

Airspace is needed for key ecological processes and ecosystem services. For instance, billions of individuals from different taxa migrate every year, modulating patterns of biodiversity via the transport of nutrients, energy, toxicants, propagules, and parasites (*6*). Therefore maintaining the diversity, abundance and movement of aerial organisms is vital for a range of ecosystem-level processes.

Most flying animals operate within a hundred meters from the ground, with abundance decreasing with height (*7*). Animals thus move at heights relevant to most human-made structures and moving objects (see the figure). Buildings, power lines, antennae, and wind farms cause millions of animal deaths via collisions annually, both over land and water, and have increased the extinction risk of several vertebrate species (*1*, *5*). Collisions with flying aircraft mostly occur at altitudes of 60 to 120 m during takeoff and landing, although occasional collisions occur at cruising altitudes (*8*). To date, more than two hundred people have been killed globally and thousands of aircraft damaged as a result of bird collisions (*2*). In the United States, the cost of bird strikes exceeds $900 million a year, with strikes increasing six-fold over the past two decades (11,315 recorded strikes in 2013) (*2*).

There are also less obvious effects. For example, buildings and wind farms influence

A seagull sweeps at a Sky TV drone.

PHOTO: MARTY MELVILLE/AFP/GETTY IMAGES

Published by AAAS

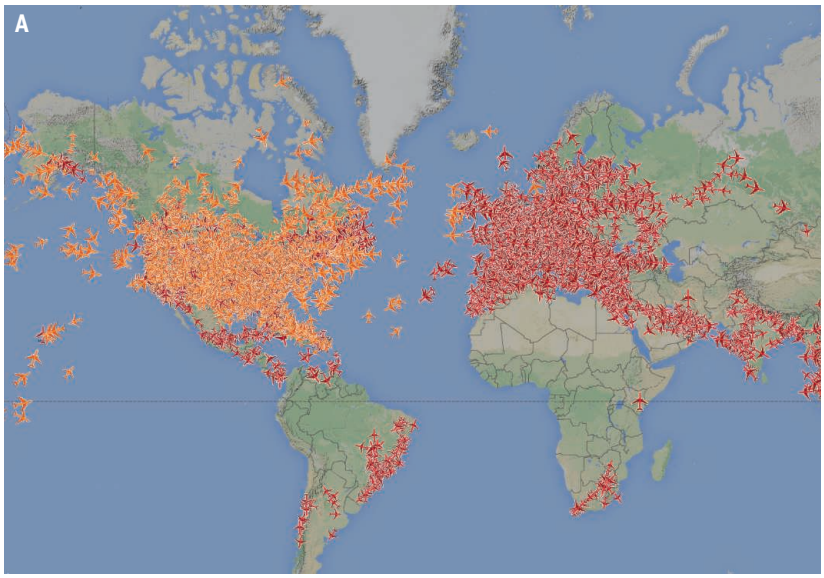

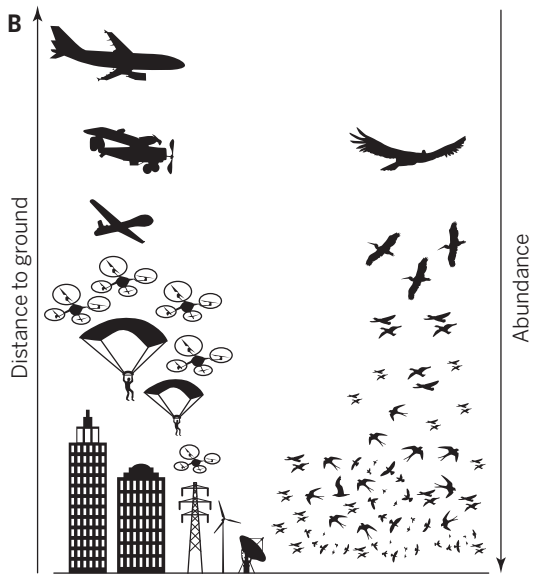

Crowded sky. (**A**) Global distribution of the ~8000 commercial and private aircraft in flight at 10:17 GMT on 25 March 2015. This figure only includes aircrafts that are covered by http://planefinder.net, and the regions of the world with the highest traffic.

(**B**) Schematic distribution of human-made artifacts and relative abundance of flying vertebrates using the same airspace. Artifacts and animals are not to scale.

local airflow regimes, with likely secondary effects on the distribution and habitat use of different species. The airspace is also used by aerial microbiota: organisms from bacteria to algae that are transported in aerosols and may act as cloud and ice condensation nuclei, influencing cloud chemistry and climate (*9*, *10*). The increasing production of industrial gases and pollutants affects aerial microbiota. The resulting changes in precipitation regimes and weather conditions have cascading effects on human and wildlife communities (*9, 10*).

Problems may also arise from UAVs, which are increasingly used in conflict, research, and control tasks and by the media (*11*, *12*). Serious debate on the use of UAVs is lacking in most countries, and almost no concerns have been raised on the influence of UAVs on wildlife (*12*). In some countries (such as Canada and the United States), UAVs are only allowed to fly within 120 m of the ground, where most flying animals are found (see the figure). UAVs can be invaluable for monitoring the physical and biological environment (*12*), and some aquatic birds do not visibly modify their behavior when UAVs approach them vertically (*3*). But other species, such as seagulls or territorial raptors, can be disturbed by UAVs flying close to their nests (see the photo). UAVs might also produce physiological reactions such as stress, but these effects remain to be investigated (*3*).

Effective environmental management of the airspace will require a detailed understanding of the movement of aerial animals at the scales of land development and management. This is a considerable challenge. Currently, more is known about the routes taken by migrating animals that cross continents (*6*) than those taken by animals in parks or towns. The aerial environment is also highly dynamic, and animals respond to airflows in complex ways. Detailed data on how animals use space in both horizontal and vertical dimensions are needed at scales from meters to kilometers. These data should be coupled with information on the sensory capacities [e.g., of birds (*1*)] and physiological mechanisms [e.g., in bats (*4*)] that may allow animals to detect and respond to individual human-made structures.

This knowledge can then guide artifact design, local planning decisions, and mitigation measures. Current measures to avoid harming wildlife include modifying windows using visual markers and removing carcasses from wind farms to reduce the collision risk for scavengers. More recently developed mitigation measures include bird-deterrent technologies using ultraviolet light that birds can easily see for avoiding collisions with windows. More experimental is the use of radar detection of flying animals to allow near-instantaneous mitigation (e.g., through modification of turbine speeds). However, they are still partial solutions that are only applied in a few places, mainly in developed countries. It is important to extend measures to national and regional levels, because many aerial animals routinely travel thousands of kilometers during migration or dispersion.

Management of airspace will also require conservation-focused use of the ground beneath—for instance, avoiding building infrastructure that could be dangerous to passing animals, distracting flying animals (particularly vulnerable species) from risky areas (*1*), and reducing light pollution, which can disrupt animal movement patterns and threaten biodiversity (*13*). Many migratory movements follow well-defined transnational flyways, and restrictions for flying or for operating wind farms in those areas would help to reduce animal deaths. Daily wildlife movements between breeding and foraging areas (*14*) must also be considered when building or using new artifacts that intrude into the airspace.

Although appropriate mitigation measures are important, the focus should be on reducing the need for post hoc management measures. For example, considering the abundance and patterns of habitat use of the flying animals living nearby before building an airport will strongly reduce future conflicts.

There are also strong arguments for the establishment of airspace reserves (*15*), both temporal and permanent, in aerial wildlife hot spots where human-made structures may cause disproportionate damage. In some areas, temporal restrictions for using the airspace may be introduced—for example, to protect migratory birds. The conservation of migratory birds has historically been focused on the ground (breeding, wintering, and stopover areas), but threats found in the airspace have rarely been considered. Permanent reserves, with partial or complete restriction on human use of the

[1]*Laboratorio Ecotono, INIBIOMA (CONICET–Universidad Nacional del Comahue), Bariloche, 8400, Argentina.* [2]*Swansea Lab for Animal Movement, Biosciences, Swansea University, UK. E-mail: slambertucci@comahue-conicet.gob.ar*

ILLUSTRATION: (PANEL B) ADAPTED FROM PLANEFINDER.NET

Published by AAAS

airspace, could protect daily animal movements such as for foraging. However, many air users cover large distances, taking them beyond their reserves (*14*). This complicates efforts to protect them and must be taken into account when designing reserves.

Conservation measures must also consider the sociocultural aspects of human-wildlife conflict. For example, the spring bird hunt in Malta has negative demographic effects on bird species that are migrating to breed. However, it is considered a traditional practice and in a recent referendum, the Maltese population narrowly voted to continue with the practice. This case shows how difficult it is to translate some traditions into current conservation practices. Similarly, military practices may also have negative impacts in areas sensitive for wildlife (e.g., flying through rocky canyons where vultures and many other species fly). These sociocultural conflicts with flying species occur throughout the world and require integrative conservation approaches that go beyond reserves.

There are thus three main levels at which to deal with airspace conflict: identification of pristine airspaces with high aerial wildlife densities where valuable air reserves can be created; identification of airspaces where humans and wildlife are already in severe conflict and where more dramatic measures must be taken to reduce collisions; and a suite of standard measures, such as anti–bird collision light systems, that should be implemented in places when bird strike probabilities are appreciable. Such a combination of strategies will provide a better perspective for airspace conservation. ■

REFERENCES AND NOTES

1. G. R. Martin, *Ibis* **153**, 239 (2011).
2. R. A. Dolbeer, S. E. Wright, J. R. Weller, M. J. Begier, Wildlife strikes to civil aircraft in the United States 1990–2013 (Federal Aviation Administration, Washington, DC, 2014); see www.faa.gov/airports/airport_safety/wildlife/resources/media/bash90-11.pdf.
3. E. Vas, A. Lescroël, O. Duriez, G. Boguszewski, D. Grémillet, *Biol. Lett.* **11**, 20140754 (2015).
4. T. H. Kunz *et al.*, *Integr. Comp. Biol.* **48**, 1 (2008).
5. K. Dai, A. Bergot, C. Liang, W.-N. Xiang, Z. Huang, *Renew. Energy* **75**, 911 (2015).
6. S. Bauer, B. J. Hoye, *Science* **344**, 1242552 (2014).
7. R. A. Dolbeer, *J. Wildl. Manage.* **70**, 1345 (2006).
8. S. M. Satheesan, M. Satheesan, *Serious vulture-hits to aircraft over the world* (International Bird Strike Committee IBSC25/WP-SA3, Amsterdam, 2000).
9. J. M. Creamean *et al.*, *Science* **339**, 1572 (2013).
10. P. N. Polymenakou, *Atmosphere (Toronto)* **3**, 87 (2012).
11. K. Anderson, K. J. Gaston, *Front. Ecol. Environ* **11**, 138 (2013).
12. B. Hayes *et al.*, *Eurodrones Inc.* (Transnational Institute, Amsterdam, Netherlands, 2014).
13. K. J. Gaston et al., *Biol. Rev.* **88**, 912 (2013).
14. S. A. Lambertucci *et al.*, *Biol. Conserv.* **170**, 145 (2014).
15. R. H. Diehl, *Trends Ecol. Evol.* **28**, 377 (2013).

ACKNOWLEDGMENTS

The authors thank PICT1156/2010, PIP 0095, CONICET, and Swansea University for funding; reviewers for comments; and F. Ballejo for help with the figure.

10.1126/science.aaa6743

SUSTAINABILITY

Secure sustainable seafood from developing countries

Require improvements as conditions for market access

By **Gabriel S. Sampson,[1] James N. Sanchirico,[1,2]* Cathy A. Roheim,[3] Simon R. Bush,[4] J. Edward Taylor,[1] Edward H. Allison,[5] James L. Anderson,[6] Natalie C. Ban,[7] Rod Fujita,[8] Stacy Jupiter,[9] Jono R. Wilson[10]**

POLICY

Demand for sustainably certified wild-caught fish and crustaceans is increasingly shaping global seafood markets. Retailers such as Walmart in the United States, Sainsbury's in the United Kingdom, and Carrefour in France, and processors such as Canadian-based High Liner Foods, have promised to source all fresh, frozen, farmed, and wild seafood from sustainable sources by 2015 (*1*, *2*). Credible arbiters of certifications, such as the Marine Stewardship Council (MSC), require detailed environmental and traceability standards. Although these standards have been met in many commercial fisheries throughout the developed world (*3*), developing country fisheries (DCFs) represent only 7% of ~220 total MSC-certified fisheries (*4*, *5*). With the United Nations Food and Agriculture Organization reporting that developing countries account for ~50% of seafood entering international trade, this presents a fundamental challenge for marketers of sustainable seafood (see the photo).

Progress toward sustainability means overcoming difficulties DCFs face in complying with MSC-like standards (*6*–*8*). With a limited amount of certified wild-caught seafood available, some firms include seafood sourced from fishery improvement projects (FIPs) (*9*), in which fishers are rewarded with market access conditional on the fishery making progress toward sustainability. Rapid spread of FIPs, which often operate without transparent and independent assessment, raises questions about their effectiveness as a tool to foster environmental, economic, and social improvement.

ACCESS, THEN IMPROVEMENTS. FIPs are varied in their scale and scope, developed and funded by nongovernmental organizations (NGOs) and the private sector. At their core, they are partnerships with the supply chain seeking to source seafood for developed country markets to supplement the stock of MSC-certified products (*6*) (fig. S1). Although FIPs are not formally part of the MSC or any other certification process, they provide fisheries, especially those that might perform poorly during pre-assessment stages of formal certification, an opportunity to be rewarded with access to markets (and potentially higher ex-vessel prices) (*10*). The costs of engaging a fishery in a FIP or MSC process appear similar (*11*, *12*) and depend on the size and complexity of the fishery, but the distribution over time can vary because of the larger upfront costs associated with MSC certification.

According to the FishSource data library

The municipal port in Bitung, North Sulawesi. Indonesia.

PHOTO: SIMON R. BUSH/WAGENINGEN UNIVERSITY

Published by AAAS

(see supplementary materials), there are >130 fisheries in FIPs worldwide, with DCFs accounting for nearly half (fig. S1). In the next 2 years, hundreds more FIPs are expected (*13*). The National Fish and Wildlife Foundation's Fishery Improvement Partnership Fund estimates that "more than 400 FIPs are needed to meet buyer demand for sustainable seafood worldwide" (*14*).

The Sustainable Fisheries Partnership (SFP) (*15*) process for a FIP includes five stages (fig. S2). After an initial scoping stage, stage 2 involves stakeholder meetings to develop work plans. At this stage, participating fishers and processors gain access to major markets. In stage 3, work plans are made publicly available and suppliers engage with fishery regulators to reform practices. Stage 4 is when changes in fisheries policies, practices, or both happen (e.g., regular vessel inspections or port data collection). The fifth stage involves demonstrating improvements in the water on measurable indicators like biomass or fishing mortality. An optional sixth stage is entry to the MSC certification process.

We find that nearly two-thirds of DCFs in FIPs (table S1) have obtained market access but are not yet delivering fisheries improvements (see the graph, top). On average, DCFs have spent more time (50 months, SEM = 3.1) than fisheries in developed countries (41 months, SEM = 4.9) in the first 3 FIP stages (see the graph, bottom). There seems to be a set of DCFs that are not moving past stages 1 and 2, given that their median cumulative time in a FIP is ~20 months longer than for those DCFs that move on to stage 3 (table S2). In addition, the median time spent by DCFs that are in stages 1 and 2 is ~10 months longer than the median time for developed country fisheries in stage 3. Although not all FIPs may be driven by a desire for greater access to export markets (*16*), for those that are, it is unclear whether retail partners' conditions—progressive improvements in exchange for continued market access—are effective. For both developed and developing countries, fewer than one-fourth of fisheries in FIPs have reached stage 4 or beyond, at which they are delivering policy or conservation gains.

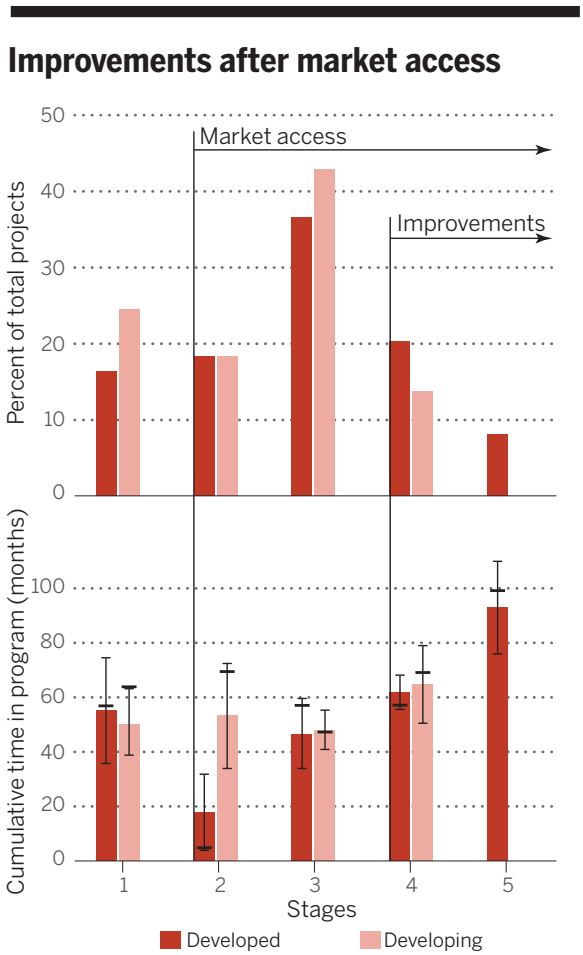

Fisheries stagnate in early stages of FIPs. (**Top**) Developed and developing country fisheries according to FIP stage (n = 111). Market access occurs in stage 2 and regulatory and ecological improvements after stage 3. (**Bottom**) Cumulative time since the fishery was established as a FIP and current stage for developed and developing countries. The vertical bars represent mean time, the horizontal lines are medians, and error bars represent ±2 SEM. Data are from (*15*).

RACE TO THE BOTTOM. What factors and practices enable improved fishery management and ecosystem conservation in developing countries? MSC certification is an obvious yardstick to measure FIP success and is the basis for the SFP's FishSource scoring metric. In response to demands from major seafood buyers, MSC has reinforced its position in the "FIP market" by developing a benchmarking and tracking tool that FIPs can voluntarily use to report progress against the MSC framework (*2*). Legitimized by these metrics as fisheries on a path to sustainability, FIPs are creating de facto sustainability claims recognized by retailers and others in the supply chain, effectively competing with MSC and other third-party certifications. This competition could lead to a race to the bottom in standards for sustainability unless FIPs' conditional access to markets is closely adhered to by retailers.

DCFs present particular challenges for FIPs. These fisheries are important components of local economies and culture, upon which fisher and nonfisher livelihoods depend (*17*). FIPs can have uncertain effects on fishing communities when they result in increased pressure on local and regional marine stocks (*18*) and push fisheries toward export rather than local markets. Although developing countries as a whole derive improvements in food security from seafood trade (*19*), the distribution of benefits and costs of increased seafood trade and effects on local food security for individual developing countries remain unclear.

Characteristics of fishing communities also affect the ability to change fishery governance and management systems, both of which determine outcomes of a FIP. Most DCFs in the FishSource database are characterized by weak fisheries management and use input restrictions (e.g., time or area closures and/or gear restrictions) that only indirectly affect total catch and often do not control fishing effort (table S3). Only 5 of the 66 DCFs in FIPs specify a cap on total catch. Even with reforms, a FIP may not lead to control of total output in this environment. Market access may create economic returns for fishers, leading to expanded fishing effort and larger harvests (or greater incentives to land catches outside the FIP) to meet growing demand.

Most FIPs in DCFs are focused on single species (table S3). If FIPs create incentives to target single stocks, they could lead to a concentration of fishing capacity by those fishers with access to capital and high-value markets rather than support communities built on multispecies fisheries (*5*, *17*). FIPs may not address the issues of spillover to other fisheries and natural resources (e.g., bycatch and effort creep) [see, e.g., (*9*)].

More positively, FIPs can provide a means to protect marine life in weak institutional environments where local and national governments have not taken ac-

[1]University of California, Davis, Davis, CA 95616, USA. [2]Resources for the Future, Washington, DC 20036, USA. [3]University of Idaho, Moscow, ID 83844, USA. [4]Wageningen University, Wageningen 6708 LX, Netherlands. [5]University of Washington, Seattle, WA 98105, USA. [6]University of Florida, Gainesville, FL 32611, USA. [7]University of Victoria, Victoria, British Columbia V8W 2Y2, Canada. [8]Environmental Defense Fund, San Francisco, CA 94105, USA. [9]Wildlife Conservation Society, Suva, Fiji. [10]The Nature Conservancy, Santa Barbara, CA 93106, USA.
*Corresponding author. jsanchirico@ucdavis.edu

Published by AAAS

tion. For example, FIPs can improve data collection and monitoring to address illegal, unreported, and unregulated (IUU) fishing. The blue swimming crab FIPs in Vietnam, Indonesia, and the Philippines have accomplished various forms of catch data collection that did not exist before FIP formation (*15*). Traceability along the supply chain, as being developed by the Brazilian Lobster FIP (*15*), can play an important role discouraging IUU fishing (*20*, *21*). FIPs in the Ecuador mahi mahi fishery resulted in policies that reduced sea turtle bycatch (*22*).

Finally, retailers and NGOs involved in a FIP must maintain their partnerships and support for an extended period of time. Yet success of FIPs may be challenged if financial support is vulnerable to market pressures (e.g., changing demand for seafood and donations to NGOs).

"Strict adherence by retailers to conditionality of market access on continued improvements ... is needed ..."

ADHERE TO CONDITIONAL ACCESS. Advocates of fishery management reform and ocean conservation should view FIPs as an opportunity to capitalize on ongoing stakeholder engagement to enact durable reforms, but in ways that take into account characteristics of the social-ecological system. Achieving successful and durable outcomes, however, is not assured.

Consideration of basic exclusionary rights for fish stocks (e.g., individual quotas, territorial user rights, fishing cooperatives) may be necessary to ensure that fishing activity is effectively measured and disclosed in the interest of substantiating fishery improvements. Exclusion is a particularly sensitive subject in poor fishing communities that rely on fishery resources for their livelihood. Yet, without controlled access, the race to secure sustainable wild-caught seafood could stimulate a race to fish.

Strict adherence by retailers to conditionality of market access on continued improvements, transparently monitored by independent third parties, is needed, albeit at additional cost. FIPs might encourage better and more durable protection by withholding market access until after fishery management systems are in place or by withdrawing market access if targets are not met in a timely manner. This could also provide assurances to the consumer that "sustainable" seafood is accurately described in the marketplace.

Retailers will continue to seek and develop sources of sustainable seafood to make good on their declarations. But FIPs may do little for environmental, economic, and social sustainability without investments in understanding the social-ecological systems in which they operate. For example, how effective are market-based incentives for motivating and maintaining engagement of fishing communities? How are costs and benefits of FIPs—in the short and long run—distributed through supply chains and fishing communities? How do fishery and community characteristics affect the durability of value chain-driven improvements? How can greater regulation and surveillance of FIPs in DCFs be balanced with the higher cost they would entail? Are there local community characteristics that correlate with beneficial impacts of current FIPs that can help guide where and how new FIPs should be created? ■

REFERENCES AND NOTES

1. Wal-Mart Stores, Inc. (Walmart, Bentonville, AK, 2014); http://corporate.walmart.com/global-responsibility/environmental-sustainability/sustainable-food.
2. MSC, "Annual report 2013–2014" (MSC, London, 2014).
3. M. Pérez-Ramírez *et al.*, *Mar. Policy* **36**, 297 (2012).
4. MSC, "Global impacts report 2013: Monitoring and evaluation" (MSC, London, 2013).
5. J. Jacquet *et al.*, *Nature* **467**, 28 (2010).
6. S. R. Bush *et al.*, *Mar. Policy* **37**, 288 (2013).
7. M. Mills *et al.*, *Conserv. Lett.* **6**, 418 (2013).
8. F. Micheli *et al.*, *Front. Ecol. Environ* **12**, 297 (2014).
9. S. Bush, P. Oosterveer, *Sustainability* **7**, 1861 (2015).
10. L. K. Deighan, L. D. Jenkins, *Mar. Policy* **51**, 476 (2015).
11. C. Christian *et al.*, *Biol. Conserv.* **161**, 10 (2013).
12. W. Goyert *et al.*, *Mar. Policy* **34**, 1103 (2010).
13. Communicating Fishery Improvement Projects—Guidance from Sustainable Fisheries Partnership (SFP, Honolulu, 2013); www.sustainablefish.org.
14. National Fish and Wildlife Foundation, Fishery Improvement Partnership Fund, www.nfwf.org/fipfund/Pages/home.aspx#.VSvyjfBLOh0.
15. SFP, Fisheries Improvement; www.sustainablefish.org/fisheries-improvement.
16. M. Pérez-Ramírez, G. Ponce-Díaz, S. Lluch-Cota, *Ocean Coast. Manage.* **63**, 24 (2012).
17. K. Ruddle, F. Hickey, *Environ. Dev. Sustain.* **10**, 565–589 (2008).
18. B. Crona *et al.*, *Mar. Policy* **34**, 761 (2010).
19. F. Asche *et al.*, *World Dev.* **67**, 151 (2015).
20. M. Borit, P. Olsen, *Mar. Policy* **36**, 96 (2012).
21. S. J. Helyar *et al.*, *PLOS ONE* **9**, e98691 (2014).
22. R. J. Trumble, "A review of the Ecuador mahi mahi Fishery Improvement Project," Ecuador Mahi Mahi FIP Review Meeting, Manta, Ecuador, 27 and 28 March 2013 (MRAG Americas, Inc., St. Petersburg, FL, 2013).

ACKNOWLEDGMENTS

This research is an output of a workshop hosted by the University of California Davis Coastal and Marine Science Institute (J.N.S.) and funded by the David and Lucile Packard Foundation in June of 2014 (grant no. 9072). We thank K. Lee, W. Reid, R. Cudney, J. Claussen, S. Hogan, H. Ludemann, M. Weber, and M. Levine for comments.

SUPPLEMENTARY MATERIALS

www.sciencemag.org/content/348/6234/504/suppl/DC1

10.1126/science.aaa4639

IMMUNOLOGY

Early life Aire

The development of particular T cells at a specific time prevents autoimmunity

By **Atsushi Tanaka** *and* **Shimon Sakaguchi**

The immune system protects us from invading microbes but does not react with the constituents of our body. When this immunological unresponsiveness to self is broken, autoimmune diseases such as type I diabetes and rheumatoid arthritis may develop. To establish and maintain this self-tolerance, lymphocytes—in particular, T cells—are subjected to two essential processes during their development in the thymus: the elimination (negative selection) of self-reactive T cells, and the generation of regulatory T (T_{reg}) cells. The latter are specialized for suppressing peripheral activation and expansion of those self-reactive T cells that have escaped elimination in the thymus. On page 589 of this issue, Yang *et al.* (*1*) show that a specific population of T_{reg} cells produced particularly early in life are highly efficient in preventing autoimmune disease and sustaining stable self-tolerance.

Genetic anomalies of T_{reg} cell development cause severe autoimmune diseases including type 1 diabetes in humans, indicating that they are indispensable for immune self-tolerance and homeostasis (*2*). As another genetic anomaly, mutations of the *autoimmune regulator* (*Aire*) gene, which is expressed in medullary thymic epithelial cells, produce autoimmune diseases collectively called autoimmune polyendocrinopathy–candidiasis–ectodermal dystrophy (or autoimmune polyglandular syndrome 1), although it is a matter of debate whether *Aire* mutations cause autoimmunity through effects on negative selection, T_{reg} cell generation, or both (*3*). Yang *et al.* show a new link between T_{reg} cell development and the function of Aire during perinatal life.

Medullary thymic epithelial cells present peripheral tissue antigens to developing T cells. These antigens include those that are targeted in autoimmune disease, such as insulin (*4*). Aire, which is a nuclear factor that controls transcription, is involved in the expression of a variety of peripheral tissue antigens by medullary thymic epithelial cells. Several studies have suggested that these Aire-expressing cells are engaged

Published by AAAS

in both negative selection and T_{reg} cell generation, altering the T cell repertoire to some extent and producing some tissue-specific or organ-specific T_{reg} cells (*5*–*8*) (see the first figure). In mice engineered to lack *Aire*, it was shown that the presence of Aire during the first few weeks after birth is necessary and sufficient to prevent multiorgan autoimmune diseases caused by Aire deficiency (*9*). This finding prompted the search for processes that are affected by the presence or absence of Aire in the perinatal window of time that endows lifelong protection from autoimmunity.

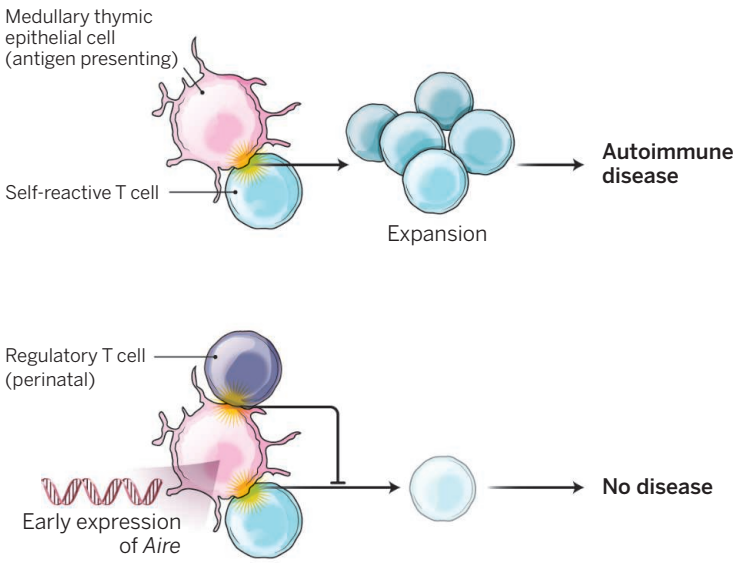

Aire-dependent T_{reg} cells produced early in life prevent autoimmunity. (**Top**) In the mouse thymus, some self-reactive T cells are deleted (negative selection; not shown), whereas others expand and can lead to autoimmune disease. (**Bottom**) Production of T_{reg} cells (Aire dependent) in early development can suppress self-reactive T cells.

Yang *et al.* show that T_{reg} cells generated during this perinatal window during mouse development (from the day of birth to about 10 days later) bear a distinct phenotype and stably persist in adult mice to protect them from autoimmunity. More precisely, the efficiency of thymic negative selection of self-reactive T cells in perinatal mice was as efficient as in adult mice, yet the number of T_{reg} cells in Aire-deficient mice was substantially reduced until day 10 relative to wild-type mice (see the second figure). In NOD mice (an animal model that spontaneously develops type 1 diabetes), T_{reg} cell depletion specifically during the perinatal window led to multiorgan autoimmunity similar to that of mice lacking Aire. By contrast, no substantial effects were observed when T_{reg} cells were depleted in adult NOD mice. In addition, transfer of T_{reg} cells from either young (20-day-old) mice lacking Aire or wild-type mice into the mice lacking Aire or into T_{reg} cell–depleted mice during the perinatal window revealed that only T_{reg} cells from wild-type mice had an autoimmune-protective effect. These perinatally produced T_{reg} cells were functionally stable and persisted in adults, showing a more potent suppressive activity and a distinct profile of transcribed genes relative to adult-produced T_{reg} cells. The authors further show that relative to those in the adult, perinatal medullary thymic epithelial cells likely present a different repertoire of peptides to developing T cells. This is in part because of low expression of the molecules involved in processing and presenting self peptides in medullary thymic epithelial cells. This may generate a distinct antigen-recognizing repertoire of Aire-dependent perinatal T_{reg} cells potent enough to suppress autoimmune T cells.

These results by Yang *et al.* and others indicate that the perinatal period in mice, which corresponds to the 13th or 14th week of gestation in humans (*10*), is special in establishing self-tolerance. Indeed, it is well known that in wild-type mice, removal of the thymus around day 3 after birth produces autoimmune diseases immunologically similar to those seen in mice lacking Aire, and that transfer of T_{reg} cells from normal mice can prevent disease development in thymectomized mice (*11*). In the thymus, where developing thymocytes are selected by a self-ligand to differentiate into T_{reg} cells or conventional T cells, the former appear to stay longer than the latter and differentiate into mature suppression-competent T_{reg} cells before emigrating to the thymus (*12*). Therefore, in a critical neonatal period when some self-reactive T cells have already migrated to the periphery while T_{reg} cells have not, thymectomy produces an immunological condition in which T_{reg} cells are scarce but self-reactive T cells are "out and about." Neonatal thymectomy produces this dominance of self-reactive T cells and a T-lymphopenic condition favorable for their expansion, leading to the development of autoimmune disease. It is likely that T_{reg} cells removed by neonatal thymectomy include those that were perinatally generated in an Aire-dependent manner.

Thus, developmental anomalies of thymic negative selection or T_{reg} cell generation (or both), and the resulting imbalance between T_{reg} cells and autoimmune T cells, can be causative of, and predispose to, autoimmune disease. Anomalies or variations of not only *Aire* but also other genes controlling T cell development might exert distinct or stronger effects early in life than in adults. How immunological self-tolerance and homeostasis is established during early life remains a developmentally interesting and medically important issue. ■

Perinatal window

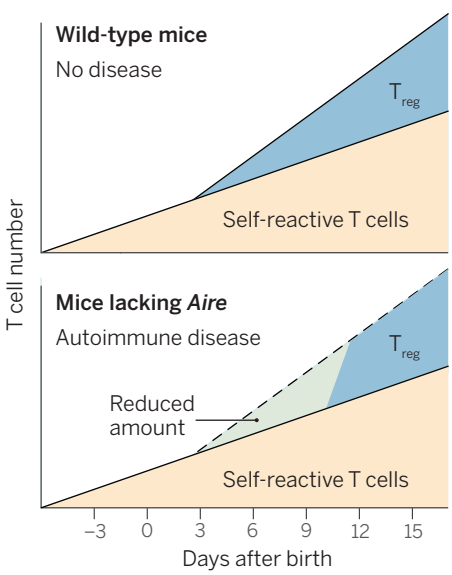

Department of Experimental Immunology, Immunology Frontier Research Center, Osaka University, Osaka 565-0871, Japan. E-mail: shimon@ifrec.osaka-u.ac.jp

REFERENCES

1. S. Yang, N. Fujikado, D. Kolodin, C. Benoist, D. Mathis, *Science* **348**, 589 (2015).
2. S. Sakaguchi, *Annu. Rev. Immunol.* **22**, 531 (2004).
3. E. S. Husebye, M. S. Anderson, *Immunity* **32**, 479 (2010).
4. B. Kyewski, L. Klein, *Annu. Rev. Immunol.* **24**, 571 (2006).
5. K. Aschenbrenner *et al.*, *Nat. Immunol.* **8**, 351 (2007).
6. M. Hinterberger *et al.*, *Nat. Immunol.* **11**, 512 (2010).
7. S. Malchow *et al.*, *Science* **339**, 1219 (2013).
8. J. S. Perry *et al.*, *Immunity* **41**, 414 (2014).
9. M. Guerau-de-Arellano, M. Martinic, C. Benoist, D. Mathis, *J. Exp. Med.* **206**, 1245 (2009).
10. G. Darrasse-Jèze, G. Marodon, B. L. Salomon, M. Catala, D. Klatzmann, *Blood* **105**, 4715 (2005).
11. M. Asano, M. Toda, N. Sakaguchi, S. Sakaguchi, *J. Exp. Med.* **184**, 387 (1996).
12. P. Romagnoli *et al.*, *J. Immunol.* **189**, 3831 (2012).

10.1126/science.aab2998

ILLUSTRATION: V. ALTOUNIAN/*SCIENCE*

Published by AAAS

BOOKS *et al.*

ANTHROPOLOGY

Cultivating human culture

Did food and fuel help shape our value systems?

By **Peter Turchin**

Foragers, Farmers, and Fossil Fuels
How Human Values Evolve
Ian Morris
Princeton University Press, 2015. 393 pp.

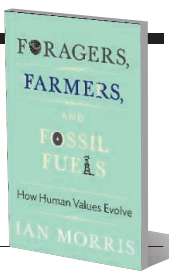

Ian Morris is a very unusual historian. Instead of tunneling into archives or digging up artifacts to answer narrow questions, he approaches history with a much wider lens. Looking at the big picture, he told Marc Parry of *The Chronicle of Higher Education*, "reveals patterns that play out over millennia, without historical actors really knowing what's going on" (*1*).

His first and wildly popular book, *Why the West Rules—for Now* (*2*), traced the development of the western and eastern regions of Eurasia over the past 15,000 years. The scope of *Foragers, Farmers, and Fossil Fuels* is similarly grand. In it, Morris asks why human values—including our attitudes toward equality, hierarchy, and violence—have changed so dramatically, and not always linearly, during the past 20,000 years.

Morris's explanation is unabashedly materialistic. Unlike Karl Marx and Friedrich Engels, however, he doesn't think that moral systems are superstructures over the forces of production. Instead, following anthropologist Leslie White, he argues that values are determined by technological systems—most importantly, those that enable the harvest of energy.

Which came first—farming or a shift in values?

Morris argues that "foraging values"—fierce egalitarianism, rejection of hierarchy, tolerance for high levels of violence—characterize societies that subsist by gathering and hunting. Farming societies, however, value hierarchy and are less tolerant of violence because these traits promote social stability, which is needed to cultivate fields. He argues that fossil fuel–driven societies see political and gender hierarchy as a bad thing because hierarchy stifles creativity and innovation, important attributes in these societies.

Such grand macrohistory is bound to raise the hackles of most historians. In an interesting approach, the book includes four critical chapters by three eminent humanities scholars and a fiction writer. One of them, the classicist Richard Seaford, predictably takes Morris to task for being too much "in the grip of deterministic quantification." This is not a criticism that I would level at this book. I have argued elsewhere that history needs to become an analytical and predictive science (*3*). To do that, we need precisely these kinds of grand theories. [Morris defends his quantitative, big picture approach to history (*1*) by stating, "there are people much weirder than me out there." I am cited in the very next line as "one of the most prominent" of these types of people.]

Grand theories, however, are just a first step. The critical part of history-as-science is determining the empirical adequacy of the theories—in plain language, testing them against data. Here's where, in my judgment, the book largely fails.

Yes, in taking a coarse-grained view of human evolution over the past 20,000 years, we do observe a correlation between human values and technological modes of production. But does the causal arrow operate from technology to morality? In my view, the evidence supports an alternative hypothesis—that shifting moral values lead to the development and adoption of new technologies (or that, perhaps, there is a dynamical feedback between the two).

Consider the transition from foraging to farming: Farming requires private ownership of land and crops, yet everything we know about foragers suggests that they rejected the idea that land and plants could be owned. Morris assumes that once humans understood how to grow crops, the families that switched to this mode of production inevitably outcompeted those that didn't. The rest—moral systems, large-scale societies, hierarchy, and inequality—"bubbled up" rather automatically. But a shift to agriculture meant long hours of backbreaking labor and poor health (as evidenced by declining stature). It also required abandonment of cherished values, such as egalitarianism and equal sharing. Furthermore, in a society where sharing is the norm, any forager passing by a crop field would feel completely entitled to harvest plants growing there. The institution of private property would have had to precede or coevolve with agriculture, not follow it (*4*).

There is also evidence that the transition to fossil-fuel economies was preceded, not followed, by a shift in social norms (*5*). Morris himself acknowledges that the Age of Enlightenment preceded the Industrial Revolution, for example. Furthermore, fossil-fuel economies were imposed on many societies in Africa and Asia during the 19th century, yet most have failed to develop "fossil-fuel values."

In the last chapter, responding to his critics, Morris writes, "in academia, criticism is the sincerest form of flattery." My critique is offered in the same spirit. I may disagree with some (or even many) ideas in it, but I have thoroughly enjoyed reading this excellent and thought-provoking book. More important, by putting forth a bold, clearly formulated hypothesis, Ian Morris has done a great service to the budding field of scientific history. We now need to test it against theoretical alternatives, something that we should be able to do on a massive scale very soon (*6*).

The reviewer is at the Department of Ecology and Environmental Biology, University of Connecticut, Storrs, CT 06269, USA. E-mail: peter.turchin@uconn.edu

REFERENCES

1. M. Parry, Quantitative History Makes a Comeback, *The Chronicle of Higher Education* (25 February 2013).
2. I. Morris, *Why the West Rules—for Now* (Farrar, Straus and Giroux, New York, 2010).
3. P. Turchin, *Nature* **454**, 34 (2008).
4. S. Bowles, J.-K. Choi, *Proc. Natl. Acad. Sci. USA* **110**, 8830 (2013).
5. G. Clark, *A Farewell to Alms: A Brief Economic History of the World* (Princeton Univ. Press, Princeton, NJ, 2007).
6. P. Turchin *et al.*, *Cliodynamics* **3**, 271 (2012).

10.1126/science.aaa9544

IMAGE: CARLOS E. SOLIVÉREZ/WIKICOMMONS

Downloaded from www.sciencemag.org on April 30, 2015

Published by AAAS

HISTORY OF OPTICS

Seeing optics in a new light

Johannes Kepler and the transition to modern optical theories

By **Christopher Dainty**

Until the 17th century, the science of optics focused mainly on explaining why and how we see things. Our understanding of light and vision was, effectively, that they were one and the same thing. The transition from "ancient" to "modern" theories of light occurred, in part, as a result of the publication of Johannes Kepler's theory of retinal image formation in 1604, which demonstrated that images are projected by the eye's lens onto the retina.

From Sight to Light is a scholarly text written by an eminent historian who argues that Kepler's theory was a radical break from the perspectivist tradition. This hypothesis contrasts with previous histories, which frame Kepler's theory as an incremental advance in a long-evolving field.

Since most readers of *Science*, and of this book, are likely to be scientists, it is important to note that the author is a historian and that the style of this book is therefore different from a scientific text. For a start, it is absolutely delightful to read, with an elegance far exceeding that of the overwhelming majority of scientific papers. The book holds one's attention and is difficult to put down. Some scientists, however, may find the pervasive presence of personal opinion and the subjective framework of the book's narrative problematic. The author, A. Mark Smith, clearly states that he is "telling a particular story, not necessarily the whole story, nor the 'true' story, nor the only story, nor even the best story."

Smith begins in the Greco-Roman period with a discussion of *Euclid's Optics*, the first known text to describe the geometry of vision. In this, and indeed in his descriptions of all subsequent theories, he provides detailed explanations and diagrams of the visual ray fields described by the early optical theorists. This is where having an expert in the history of science is so important: Few contemporary scientists would likely have the impartiality or patience to explain the ideas of these early thinkers so clearly.

No book on this topic can ignore the contributions of Ibn al-Haytham (965–1040), more familiarly known by the Latin name Alhacen, whose seven-volume treatise on optics is considered to have been a major contribution to the field. Smith has previously published definitive texts on Alhacen's contributions to optics, including his understanding of refraction (*1*, *2*). Yet, as he reveals in this book, Alhacen apparently showed no hint that it might be the cornea and lens of the eye that actually focused an image onto the retina.

It was Kepler who discovered that a real, inverted image was formed on the back of the eye on the light-sensitive retina. The properties of focusing and diverging lenses were known at that time, but his recognition of the eye as an optical system made his work a radical break from previous studies. Smith makes a persuasive case that this was indeed a breakthrough that marked the start of "modern" optics.

This book should be read together with the classic text *Theories of Vision from al-Kindi to Kepler* (reviewed in *Science* in 1976) (*3*, *4*). Both books are based on the same facts, but Lindberg and Smith ultimately disagree as to whether Kepler's discovery was incremental or radical.

I would recommend this book very highly for two reasons. First, because it provides an authoritative account of how the study of "sight" became that of "light" and highlights the contributions of scholars over many centuries. Second, and less obvious perhaps, is that it serves as an important reminder that "research" does not come in only one flavor and that we, as scientists, have a lot to learn from history.

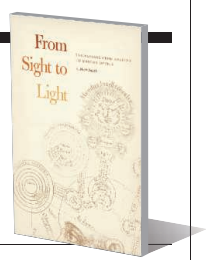

From Sight to Light
The Passage from Ancient to Modern Optics
A. Mark Smith
University of Chicago Press, 2015. 469 pp.

The reviewer is professor emeritus at the National University of Ireland Galway, Galway, Ireland. E-mail: chris.dainty@nuigalway.ie

REFERENCES

1. A. Smith, *Alhacen's Theory of Visual Perception* (American Philosophical Society, Philadelphia, 2001).
2. A. Smith, *Alhacen on the Principles of Reflection* (American Philosophical Society, Philadelphia, 2006).
3. D. Lindberg, *Theories of Vision from al-Kindi to Kepler* (Univ. Chicago Press, Chicago, 1976).
4. A. G. Molland, *Science* **194**, 1047 (1976).

10.1126/science.aab2222

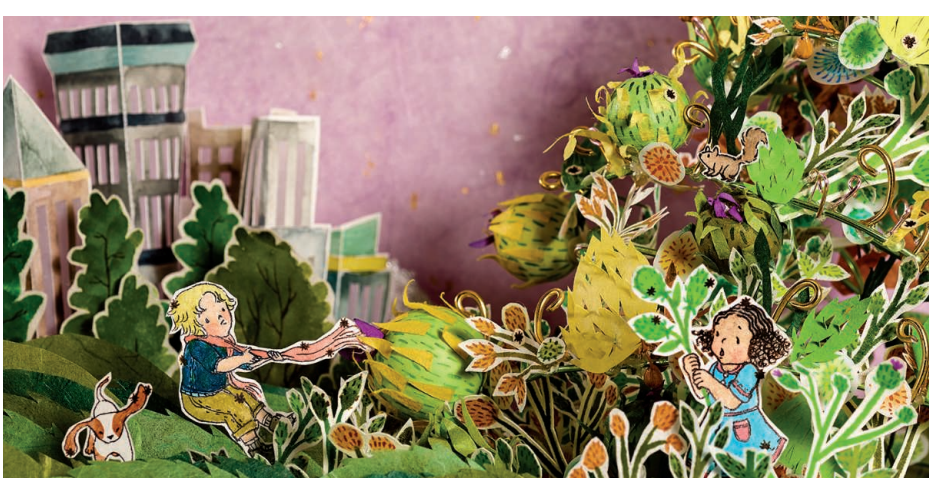

IMAGE: SOYEON KIM

Children's Book Week, the longest-running literacy initiative in the United States, will be held 4 to 10 May 2015.

Wild Ideas
Let Nature Inspire Your Thinking
By Elin Kelsey
Artist: Soyeon Kim
Owlkids Books, 2015. 32 pp.

What can hyenas teach us about cooperation? Who do baboons turn to for help? Drawing on observations gleaned from recent animal behavior research, *Wild Ideas* encourages young readers to look to the animal kingdom for inspiration the next time they encounter a seemingly unsolvable problem. Delightful dioramas bring the book's accessible prose to life.

10.1126/science.aab3116

Downloaded from www.sciencemag.org on April 30, 2015

Published by AAAS

Edited by **Jennifer Sills**

America's crisis of faith in science

FIFTY-THREE PERCENT OF Americans are not convinced that human activity is causing global warming (*1*). Why? The issue is faith, not facts. Shockingly few people can actually know—in any intelligent, meaningful way—that global warming is real. The rest of us do not have access to the huge quantity of data, and we wouldn't understand it if we did. We simply aren't competent to judge for ourselves what scientists are telling us. Often enough, scientists in one specialty aren't even competent to assess data and conclusions in another specialty. We cannot see climate change with our own eyes, yet we have faith in the scientific method. That is what gives science the right to an authoritative voice in public policy.

Others do not have this faith. Simply stating to them that they are ignoring "facts" is juvenile, naive, and ultimately ineffective. For those of us who are not global warming scientists ourselves, it is also arrogant to insist that others believe what we only know on faith ourselves. The real challenge for scientists and those who speak for them is to inspire the public's faith in science.

What does this mean in practice?

(i) Be more open about the data used to support conclusions. Make more data easily available for others, such as journalists, to review.

(ii) Be more open about the methods. This was a crucial element in the 2009 controversy over hacked e-mails from a UK climate research institute, which came to light just before an international conference on mitigating climate change (*2*, *3*). Legitimate debate among scientists was misunderstood by some of the public as evidence that the whole premise was unfounded.

(iii) Acknowledge the seriousness of scientific misconduct and do more to limit it. Such incidents may be rare, but they are highly consequential. They not only convince people that a particular scientific claim is false; they undermine the public's faith that science as an institution can be trusted to tell us what we can't see for ourselves.

(iv) Show more respect and less disdain for those who do not acknowledge

PHOTO: CARRI LEROY

OUTSIDE THE TOWER

Bringing science inside prison walls

No cell phone, no car keys, nothing in my pockets. I make my way through the metal detector and past the sentry posted in the armored box. I walk into the first of several sealed concrete rooms. Clangs and buzzes signal the closing of one door, the opening of another. I am in prison to talk about science.

There is some evidence that embracing the power of nature and learning about science can facilitate the rehabilitation of inmates, pro-social behavior, and relief of corrections fatigue in prison staff (*1*–*4*). I have always enjoyed translating science for new audiences, but never for students in prison before.

After traversing the maze of security, I stand before my first class, take a deep breath, and begin my talk about terrestrial-aquatic interactions. It is immediately clear that the discussion reaches the women on a personal level. Their eyes brighten when I ask them about their favorite river. They are engaged, attentive, and curious.

After presenting in-prison science lectures several times, I realized how little I needed to alter my material for incarcerated students. Their hunger for information overwhelms their lack of exposure to science education, and their questions are just as keen as those of my brightest college students. My favorite lecture was one that merged science and art. We brought paper, pencils, and specimens (plants, shells, insects, pinned butterflies) into the prison and taught the basics of scientific illustration. We gave the students time to observe their specimens, to ask questions, and to explore the morphology of life through multiple senses. In a gray world of sensory deprivation, we gave them moments with nature and a chance to observe the world like scientists.

Enhancing scientific literacy in society requires us to cross boundaries and serve new audiences. In my case, that meant literally crossing the most impermeable boundary in U.S. society. My biggest surprise was that physical boundaries are just those—talking about science transforms us from people on the inside versus the outside to just people talking about ideas.

Carri J. LeRoy

Sustainability in Prisons Project, The Evergreen State College, Olympia, WA 98505, USA.
E-mail: LeRoyC@evergreen.edu

REFERENCES

1. C. J. LeRoy, K. Bush, J. Trivett, B. Gallagher, *The Sustainability in Prisons Project: An Overview 2004–2012* (Gorham Publishing, Olympia, WA, 2012).
2. P. C. Little, *Environ. Educ. Res.* **21**, 365 (2015).
3. T. N. Kaye, K. B. Bush, C. Naugle, C. J. LeRoy, *Nat. Areas J.* **35**, 90 (2015).
4. Sustainability in Prisons Project (http://sustainabilityinprisons.org/)

Outside the Tower is an occasional feature highlighting science advocacy projects led by scientists and citizen scientists. How do you advocate for science? Tell us at submit2science.org.

Downloaded from www.sciencemag.org on April 30, 2015

Published by AAAS

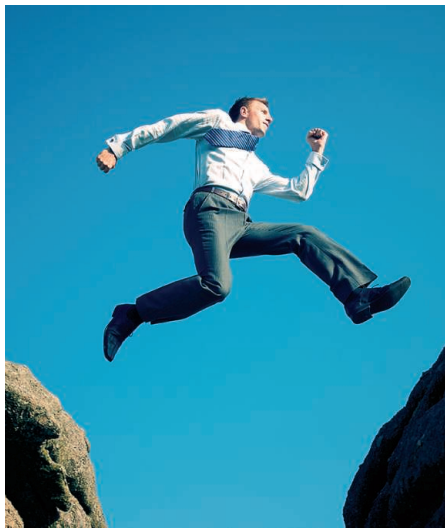

A leap of faith toward science.

established scientific theories. We are not justified in attributing traits of "stupid" and "hypocritical" to people just because they cannot see evolution or climate change with their own eyes and do not feel obliged to take someone else's word for it.

(v) Put more effort into public education in science. Perhaps the best way for more people to have faith in science is for more people to have firsthand experience with the scientific method, even on small scales, and more firsthand experience with scientists. In this way, more of society will understand how scientific facts come to be accepted and how they are checked and, if necessary, corrected.

(vi) Be more humble. During the 2013 State of the Union address, President Obama stated that global warming is a "fact" and that the science "was settled." What science is ever settled? And when did he observe it? If he went with his own direct experiences, he would have to admit that global temperatures have not risen significantly in the past decade (*4*). What he should have cited was the scientific consensus.

Scientists do not typically think it is their business to inspire faith. Their job is to provide facts. But to solve the pressing problems that require public acceptance of well-established science—from global warming to vaccinations to the increasing overuse of antibiotics—scientists must indeed inspire more public faith in their methods and their mutually enforced trustworthiness.

Todd L. Pittinsky

Stony Brook University, Port Jefferson, NY 11777, USA.
E-mail: todd.pittinsky@stonybrook.edu

REFERENCES

1. Pew Research Center, "Beyond red vs. blue: The political typology" (2014), section 7; www.people-press.org/2014/06/26/the-political-typology-beyond-red-vs-blue/.
2. J. Tierney, "E-mail fracas shows peril of trying to spin science," *The New York Times* (2009); www.nytimes.com/2009/12/01/science/01tier.html.
3. J. Tollefson, "Different method, same result: Global warming is real," *Nature* (2011); www.nature.com/news/2011/111020/full/news.2011.607.html.
4. www.climate.gov/news-features/climate-qa/why-did-earth's-surface-temperature-stop-rising-past-decade.

Beware study design measurement errors

I CONCUR WITH Leek and Peng ("What is the question?" Perspectives, 20 March, p. 1314) that careful alignment of statistical methodology to research questions will reduce the most common errors in data analysis. The data analysis flowchart they present is an elegant decision tree that should guide not only research scientists but also peer reviewers and journal editors. However, minimizing errors in data analysis is a necessary criterion but not sufficient.

Research results can be reproducible yet incorrect. As scientists, peer reviewers, and journal editors, we all need to be fully cognizant of the basic tenets of "measurement theory": precision, accuracy, reliability, and validity of data. This means that we also need to be cognizant of bias, which can be minimized most effectively during the study design phase. Measurement errors can constitute both random (variance) and nonrandom (bias) components. Increasing sample size in a study will reduce variance but will have no effect on bias, which can be much more insidious in research undertakings. Warren S. Sarle of the SAS Institute made an important distinction: "Mathematical statistics is concerned with the connection between inference and data. Measurement theory is concerned with the connection between data and reality. Both statistical theory and measurement theory are necessary to make inferences about reality" (*1*). An excellent framework for anticipating and addressing bias in experimental and observational studies is presented by David F. Ransohoff (*2*). I fully concur with Leek and Peng that "data analytic education" should be a key component of research training, but would like to additionally emphasize that fundamentals of study designs and measurement theory should also be covered in such research training.

Deepak B. Khatry

Arlington, VA 22205, USA.
E-mail: dkhatry@umich.edu

REFERENCES

1. W. S. Sarle, Measurement theory: Frequently asked questions (ftp://ftp.sas.com/pub/neural/measurement.html).
2. D. F. Ransohoff, *Nat. Rev. Cancer* **5**, 142 (2005).

PHOTO: © PESKYMONKEY/ISTOCKPHOTO.COM

Published by AAAS

Glass prisms like the one shown here (reputedly owned by Isaac Newton and now in the collection of the Whipple Museum of the History of Science, University of Cambridge) were used to split white light into its constituent colors.

PHOTO: © JOE MCNALLY. PHOTOGRAPHED AT THE WHIPPLE MUSEUM OF THE HISTORY OF SCIENCE, UNIVERSITY OF CAMBRIDGE

Frontiers in LIGHT & OPTICS

by **Ian Osborne**

Light, its interactions with materials, and our attempts at controlling those effects have held fascination for centuries. From the polishing of lustrous metals for mirrors to the recognition that glass could be worked to focus images to give us lenses and spectacles and the possibility of corrective vision, that fascination has had a practical bent. The development of telescopes and microscopes provided a view of the world far beyond our own physiological limitations, providing tools for the curious to pursue their scientific fields.

Our perception of light is limited to a very narrow band of the electromagnetic spectrum. Extending far beyond on either side of the visible wavelengths are the longer and shorter wavelengths of light that are exploited for myriad applications in communication, sensing, navigation, and imaging.

This special issue addresses modern developments in controlling and manipulating light: how light-based technologies are shrinking and becoming faster (Koenderink *et al.*, p. 516); how recent theoretical developments in the manipulation of light are being implemented to provide materials with properties not available in nature (Pendry *et al.*, p. 521); how the quantum properties of light are being exploited in new technologies (Walmsley, p. 525); and how new light sources are coming online that can probe the structure of matter on spatial and time scales that provide an exquisitely detailed picture of our microscopic world (Miao *et al.*, p. 530).

With light touching so heavily on our everyday lives, it is apt that the United Nations General Assembly has designated 2015 as the International Year of Light and Light-Based Technologies.

INSIDE

REVIEWS

Nanophotonics: Shrinking light-based technology *p. 516*

Transforming the optical landscape *p. 521*

Quantum optics: Science and technology in a new light *p. 525*

Beyond crystallography: Diffractive imaging using coherent x-ray light sources *p. 530*

RELATED ITEMS

▸ BOOKS *ET AL.* P. 509

Published by AAAS

REVIEW

Nanophotonics: Shrinking light-based technology

A. Femius Koenderink,[1] Andrea Alù,[1,2] Albert Polman[1]*

The study of light at the nanoscale has become a vibrant field of research, as researchers now master the flow of light at length scales far below the optical wavelength, largely surpassing the classical limits imposed by diffraction. Using metallic and dielectric nanostructures precisely sculpted into two-dimensional (2D) and 3D nanoarchitectures, light can be scattered, refracted, confined, filtered, and processed in fascinating new ways that are impossible to achieve with natural materials and in conventional geometries. This control over light at the nanoscale has not only unveiled a plethora of new phenomena but has also led to a variety of relevant applications, including new venues for integrated circuitry, optical computing, solar, and medical technologies, setting high expectations for many novel discoveries in the years to come.

Optics and the science of light is a lively field of research that continues to surprise decade after decade, with fundamental breakthroughs and disruptive applications. Communications technology has been revolutionized by the invention of the laser and the optical fiber, incandescent light bulbs are being replaced by efficient solid-state lighting, and solar energy technologies are on their way to price parity with fossil fuel–based power generation. A large number of these developments have resulted from increased control over the flow of light at length scales smaller than the wavelength. Squeezing light to nanoscale dimensions also opens the prospect of dense optical integrated circuits, which may overcome fundamental challenges related to bandwidth and energy dissipation in today's electronic integrated circuit technology. More broadly, the field of nanophotonics aims at overcoming Abbe's diffraction limit, developing technology able to manipulate light on a deep-subwavelength scale. As photons are shrunk to the nanometer scale, ultimately approaching the scale of the wave function of electrons, fundamental new science is expected, and important technological advances appear. In this article, we review recent highlights in the science and applications of nanophotonics, focusing on the ultraviolet (UV)/visible/near-infrared spectral range, and provide an outlook for the bright future of this research field.

Photonic crystals

The initial concept for on-chip miniaturization of light dates back to the late 1990s, when photonic crystals—periodic structures fabricated from high-refractive-index materials such as Si or GaAs—were proposed and realized (Fig. 1A). As the periodicity in these structures approaches the wavelength of light, a photonic bandgap can appear, analogous to the energy bandgap in a semiconductor. The propagation of light with a frequency in the band gap is then forbidden, except in localized regions created by a well-designed break in periodicity, such as line defects that can guide light, or point defects that confine light. Band structure engineering provides exquisite control over light dispersion—that is, over the relation between its frequency ω and its effective propagation constant $k = 2\pi/\lambda$—and thereby also over how fast signals of different wavelengths propagate, as given by the group velocity $d\omega/dk$. Slowing down light in waveguides, and confining it in optical nanocavities, can be used to create optical memories and enhance light switching and manipulation schemes based on ultrafast modulation of the local refractive index. Impressively, data transmission with just one femto-Joule of energy expenditure per bit was recently demonstrated by using this photonic crystal platform, and as many as 100 individually addressable and switchable optical cavities have been multiplexed to reach a low-power optical memory with nanosecond storage time (*1*).

Plasmonics

Confining light waves is much more difficult than confining electron waves because there is no optical equivalent to the Coulomb force, based on which deep electron traps can be created. Instead, the only parameter to shape light is the material dielectric constant ($\varepsilon = n^2$, where n is the refractive index), which is limited to the range $n = 1.3$ to 4.0 for nearly all dielectrics in the visible

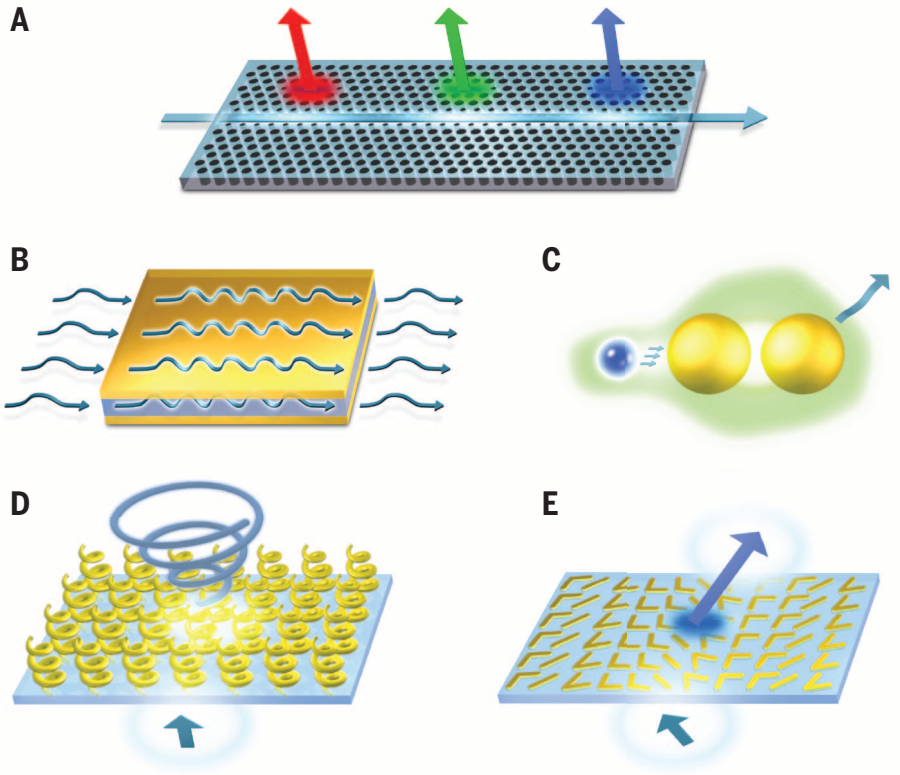

Fig. 1. Nanophotonic architectures. (**A**) 2D photonic crystal waveguide coupled to resonant cavities serves as a wavelength division multiplexer. (**B**) Metal-insulator-metal surface plasmon polariton waveguide strongly confines light and shrinks the wavelength. (**C**) Plasmonic dimer nanoantenna coupled to an optical emitter creates directional emission of light. (**D**) Metasurface composed of chiral antennas offers selectivity to circularly polarized light. (**E**) Metasurface composed of graded plasmonic or dielectric antenna geometries enables wavelength-dependent control over the reflection and refraction of the optical wave front.

[1]Center for Nanophotonics, FOM Institute AMOLF, Science Park 104, 1098 XG Amsterdam, Netherlands. [2]Department of Electrical and Computer Engineering, University of Texas at Austin, 1616 Guadalupe Street, UTA 7.215, Austin, TX 78712, USA.
*Corresponding author. E-mail: polman@amolf.nl

spectral range. Photonic crystals provide the ultimate confinement achievable with transparent materials: Light can be routed in waveguide circuits exactly at the diffraction limit. To go beyond, new strategies are necessary, one of which is provided by noble metals with large negative dielectric constants. This is a consequence of the fact that metals contain a large density of unbound electrons, which experience no restoring force upon being driven by an oscillating electric field. Light can propagate at a metal-dielectric interface in the form of surface plasmon polaritons, which are hybrid waves of photons and charge oscillations sustained by the electrons near the interface. When two of such interfaces are brought together in a metal-insulator-metal waveguide, light is strongly confined in the dielectric gap between them, allowing light confinement well beyond Abbe's limit (Fig. 1B). Moreover, as the gap shrinks, not just the lateral confinement increases, but also the effective in-plane wavelength is reduced as the dispersion of light is increasingly determined by the metal properties. For visible light with a free-space wavelength of 450 to 650 nm, an effective wavelength as small as 50 nm has been observed (*2*), and routing of light in such waveguides is subject only to the diffraction limit for this effective wavelength. The strong confinement in the dielectric gap also enhances the interaction with nonlinear or active materials placed in the gap. This has been exploited to realize plasmon lasers with modes that are tightly confined in two or three dimensions (*3*).

In a recent series of breakthroughs for nanophotonics, it was demonstrated that light can be hybridized with electrons in layers that are just one atomic layer thick, such as in graphene. Plasmons have been excited on graphene at mid-infrared frequencies (*4*, *5*), with wavelengths that are shrunk relative to free space by a factor of ~50. Graphene can be electrostatically gated to locally control its carrier concentration, and thereby its dielectric constant, promising a versatile platform for dynamically controlling plasmon propagation and reaching the ultimate confinement limit for optical integrated circuits.

Antennas for light

The unprecedented level of light concentration offered by plasmonic nanostructures suggests interesting new perspectives to interface light and matter, possibly even down to the level of illuminating a single molecule with a single photon. This level of control becomes possible as light is shrunk in all three dimensions. Optical antennas are nanophotonic elements designed to achieve this functionality, transducing free-space, far-field radiation to localized electromagnetic energy. The simplest nanoantenna is a single metal nanoparticle whose free electrons can support localized plasmon resonances at visible wavelengths, implying that its far-field excitation can result in a strongly localized near-field response. Reciprocally, an optically excited nanoparticle can efficiently radiate light in a controlled way.

A small isolated nanoparticle scatters as an electric point dipole, with a well-defined but broad angular distribution of radiation. Yet, tools borrowed from radio-frequency antenna design have allowed far-reaching control over the directivity of light radiation and scattering from proper arrangements of nanoantennas, and conversely over how far-field radiation drives near-field focusing in properly designed nanoclusters. Following these principles, antennas coupled to a single quantum emitter can result in highly directional beaming of spontaneous emission (*6*), and phased-array antennas coupled to efficient single-photon sources can serve as light-steering elements. Over 1000-fold brightness enhancement per fluorophore has been recorded in single-molecule experiments aimed at improving fluorescence microscopy in biological systems (*7*). Besides engineering emission directivity, antennas open a completely new regime for light-matter interaction strengths, especially in the case of dimer antennas with narrow gaps, through which plasmon modes can efficiently interact (Fig. 1C). A quantitative measure of the light-matter interaction enhancement around a nanoantenna is the Purcell factor: the spontaneous emission rate increase due to enhanced photon mode density in the antenna's optical near field. Recently, a Purcell factor as high as 1000 was reported in metallic nanoantennas with gaps in the order of just a few nanometers (*8*). The capability of plasmon antennas to transduce between light and molecules has large relevance for microscopy, such as in the case of observation of single molecules, and infrared vibrational spectroscopy by use of field enhancement at sharp metal tips (*9*).

Shrinking light and quantum photonics

As light is shrunk to smaller and smaller scales, its interaction with matter occurs over volumes that eventually become comparable with a single atomic unit cell. In these situations, classical models for describing optical interactions fail. In the dimer nanoantenna of Fig. 1C, for instance, classical electromagnetic theory would predict a diverging light intensity in the gap as the distance between particles approaches zero. For gaps below a few nanometers, however, quantum tunneling effects start dominating, and the nonlocality of the electron wave function, which extends across the gap, fundamentally limits the overall light intensity enhancement (*10*). As nanofabrication tools allow finer and finer control, such nanoscale quantum effects become increasingly relevant in experiments.

At these scales, our understanding of quantum optical effects also faces new challenges to properly describe the interaction of single emitters with single plasmons. For example, the Purcell factor has needed rewriting in plasmonics because the conventional definition of a resonant mode, and its associated cavity volume, must be revised as light shrinks to deep-subwavelength volumes at which optical absorption losses and quantum effects become dominant (*11*). Furthermore, in the case of very high Purcell factors, the characteristic spontaneous emission decay time can become comparable with a single cycle of the electromagnetic field, in which case Fermi's Golden Rule breaks down (*12*).

In this context, it is currently being debated whether the quantum mechanical regime of strong coupling can be reached with plasmons and single emitters. When a single emitter releases its energy as a quantum of light near a nanoresonator, the decay is not irreversible. Instead, the coupling may be made sufficiently strong to enable Rabi oscillations, coherently exchanging the excitation (*13*). This regime may enable ultrafast integrated quantum circuits based on single photons, with plasmons and emitters taking the role of information carriers and processors (*14*). The current state of the art in integrated quantum photonics has been reached in photonic crystals, in which single photon sources with near-unity efficiency have been reported (*15*), setting the stage for single-photon transistors and quantum-logic gates based on single-photon nonlinearities (*16*). These remarkable advances are opening a new paradigm for scalable, integrated quantum photonics.

Shrinking vector fields to boost magnetism and chirality

Antennas not only localize the photon energy density but also provide a way to control the vector nature of light at the nanoscale. The relevance of magnetic effects in optics is conventionally neglected for small objects because material magnetization rapidly vanishes as the frequency grows. This also implies that chiral effects such as circular dichroism and optical rotary power are inherently weak in ordinary matter because they require that distinct optical responses—such as an electric dipole plus a magnetic dipole response, or an electric dipole plus a quadrupole response—occur simultaneously in the same object with a controlled phase lag. Such magnetic and magnetoelectric effects can be boosted to become as strong as conventional electric responses by setting up scattering resonances in loop-shaped and helical antennas that carry circulating optical currents, or by pairing achiral resonances in strongly asymmetric geometries (*17*, *18*). These nanostructures may allow enhancement in the local chirality of the optical field so that enantiomers—molecular stereoisomers that are mirror images of each other—may be optically screened at the single-molecule level by placing them near a chiral antenna (*19*). Furthermore, helicity-dependent near-field enhancements may be used to control spin-polarized optical transitions.

Metamaterials and metasurfaces

The unprecedented opportunity to localize light at deep-subwavelength scales has not only been applied to isolated optical nanoresonators but has also led to the synthesis of optical metamaterials, artificial materials with an unusual optical response, formed by ordered or disordered collections of resonant nanoscale plasmonic scattering elements. Many unusual bulk optical responses have been theoretically prediced and experimentally verified on the basis of complex three-dimensional (3D) metallodielectric architectures by using nanoantennas as their basic elements. Remarkable nanofabrication advances

have allowed the realization of nanostructured materials with unusual optical responses such as, for example, a metamaterial slab composed of 3D chiral helix antennas (Fig. 1D) (*20*), offering large selectivity to circular polarization with a broadband response in an optical frequency band in which optical components filtering circular polarization do not exist. The fact that constituent antennas can carry both a strong electric and a strong magnetic response gives the opportunity to reach optical properties far outside the scope of naturally available refractive indices, permittivities, and permeabilities. Such materials can, for example, refract light in unexpected directions, as demonstrated in various geometries, most recently in the UV spectral range (*21*). Negative refraction has been a precursor to the broad paradigm of transformation optics (*22*), which is most popular for enabling invisibility cloaks that can make objects undetectable in a certain frequency band by wrapping them in a metamaterial shell with suitably graded electric and magnetic response. Strong frequency dispersion, as well as absorption that takes place in the constituent antennas, are fundamental constraints of passive metamaterials that have so far limited their practical applicability.

The need to overcome loss, combined with the continuous drive toward integration and large-area fabrication, has inspired a recent shift from 3D metamaterials toward 2D optical metasurfaces (Fig. 1E). Metasurfaces are planarized, ultrathin, patterned artificial surfaces that are designed to mimic the functionalities of conventional optics and metamaterials in two dimensions, avoiding absorption losses by light propagation in the third dimension. Strongly localized optical resonances induced by plasmonic nanoantennas enable abrupt phase and amplitude discontinuities, which can be tailored at will across the surface to provide a controllable transverse gradient, inducing anomalous refraction, reflection, and control over subwavelength structure of the impinging wavefront (*23*, *24*). This enables the realization of ultrathin lenses, beam steering devices, and generation of orbital angular momentum of light, to name just a few examples. A promising trend in metasurface design is the use of arrays of dielectric nanoscatterers that show geometric Mie-type resonances, avoiding absorption losses (*25*, *26*).

Recent work has shown that flat and ultrathin metamaterials may be used to engineer to a large extent both the spatial and spectral response of the impinging wavefront. In this sense, metasurfaces and metamaterials can operate as all-optical circuitry, processing the impinging signals at the nanoscale with nanocircuit elements that may form thin metasurfaces acting as complex operators (*27*). These concepts may lead to all-analog filtering, signal processing, and even computing functionalities performed as light interacts with these devices (*28*).

Probing nanoscale optical fields

Measuring light confinement is inherently difficult because the diffraction limit of conventional microscopy places a lower limit to imaging resolution. Yet, advances in nanophotonics research require new techniques to excite materials and probe them at the nanoscale. Although super-resolution microscopy tools such as photoactivated localization microscopy (PALM), stochastic optical reconstruction microscopy (STORM), and stimulated emission depletion (STED) have made it possible to circumvent Abbe's limit, they work best for specimens that are almost transparent and that can be functionalized with proper fluorescent markers. Nanophotonics research instead often requires a point detector, or a point source of vector fields that can be brought into the optical near field. Near-field scanning microscopy uses a sharp raster scanning probe to approach a nanostructure of interest to within 10 nm from its surface. The probe either acts as a scatterer that converts near fields into far-field light (*4*, *5*) or as a fiber-coupled source or detector. This technique has become so advanced in recent years that electric and magnetic field components of light can be separately imaged at a length scale far below the wavelength, and at femtosecond time scales (Fig. 2A) (*29*). Scanning emitter lifetime imaging microscopy can probe the optical density of states in two dimensions by use of a single fluorescent source attached to the end of a sharp fiber probe (*30*). Electron beam–induced excitation in a scanning/transmission electron microscope is another highly controllable way to study optical modes and resonances in polarizable metallic and dielectric nanostructures with deep-subwavelength spatial resolution (Fig. 2B). Cathodoluminescence spectroscopy enables spatial mapping of the radiative density of states in two dimensions by using the light emitted when a beam of fast electrons impinges on a sample (*31*). Conversely, electron energy loss spectroscopy (EELS) maps the kinetic energy lost by electrons during their interaction with photonic structures. EELS and CL have recently been demonstrated in tomography mode, imaging the localized surface plasmon modal field distribution of Au nanoparticles in three dimenions (*32*, *33*). Electron beam–induced optical images routinely provide a spatial resolution of ~5 nm, which is on par with the best optical super-resolution microscopy.

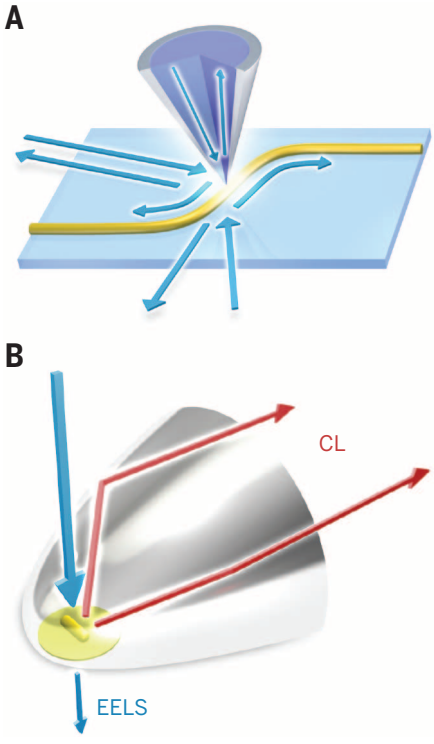

Fig. 2. Nanophotonic characterization techniques. (**A**) Near-field scanning optical microscopy—either in transmission, collection, or scattering mode—can measure the magnetic and electric field components of light at a 10- to 100-nm spatial resolution in the femtosecond time domain. (**B**) Resonant modes and light dispersion of plasmonic and dielectric nanostructures can be probed by means of electron irradiation, either by collecting the induced radiation (cathodoluminescence) or by measuring the EELS. The spatial resolution of these techniques is determined by the electron beam width: ~10 nm.

Practical applications of nanophotonics

Nanophotonics has already delivered many of the original promises dating back to when this research field started to develop around 10 years ago. One of the earliest nanophotonics discoveries to transcend the laboratory were chemically synthesized silica-core/Au-shell nanoparticles for applications in medical diagnostics and therapy (*34*). When introduced into the blood stream, these "nanoshells" are preferentially trapped in malicious tissues. When irradiated with a laser tuned to their plasmon resonance, the particles are locally heated, destroying the cells. This concept is presently being tested in clinical trials on humans for cancer treatment.

Molecular sensing and spectroscopy have motivated the drive to controllably shrink light to the size of a single molecule. It was found that optical hotspots in rough metal surfaces arising from localized surface plasmons result in a strong enhancement of the molecular Raman scattering signal, forming the basis for surface-enhanced Raman scattering (SERS), a well-established spectroscopy tool in chemistry. In a similar area, new sensors have been proposed based on the plasmon resonance wavelength shift caused by different molecular species placed in the plasmonic near field. Antibody-specific chemistry may also be used to bind or cluster plasmon particles by using the fact that gold is easily functionalized through thiol chemistry; commercial pregnancy tests today use this concept. An intriguing application of plasmonic light focusing is in DNA sequencing, in which a DNA molecule is transported through a small hole in a metal film, with the aim to read out the base-pair sequence through the subsequent detection of fluorescent markers that are selectively bound to different base pairs (*35*).

Lasers, solid-state lighting, and photovoltaics are also important fields in which nanophotonic

structures have enabled new designs for improved functionality. Photonic crystal lasers have now become so advanced that they can deliver power in the watt range (Fig. 3A) (*36*). The emission of light-emitting diodes (LEDs) is strongly enhanced if a suitably designed periodic array of Ag nanoparticles is embedded in the light-emitting phosphor (Fig. 3B). These nanostructures help to efficiently couple and scatter light from the UV pump LED into the phosphor material and, at the same time, aid the directional outcoupling of the phosphor emission, which enhances LED efficiency and brightness (*37*). Conversely, periodic and aperiodic metasurfaces composed of resonant plasmonic or dielectric nanoparticles can lead to improved light coupling and trapping into solar cells, supporting increased photovoltaic energy conversion efficiency, as well as thinner cell designs that can be made at lower cost (Fig. 3C) (*25*). Recently, efficient solar cells were realized by using InP nanowires (*38*). Here, the small radius of the wire enables efficient collection of electrical carriers. At the same time, optical resonances in the nanowire can lead to light concentration, increasing the photovoltage (*39*).

Metal nanowire networks have been developed as transparent electrically conducting coatings. Even though these nanowires suffer from ohmic losses owing to plasmon excitation, they show a beneficial tradeoff between optical transmission and electrical conduction and can be made at relatively low cost (Fig. 3D) (*40*). These nanowire networks are already finding applications in solar cells, computer display, and tablet technology, replacing the commonly used, expensive, and brittle indium-tin-oxide as a transparent top-contact.

The near-field focusing provided by plasmonic nanostructures has also found applications in heat-assisted magnetic recording (HAMR) for data storage, a technique in which the magnetic phase change in a recording medium is facilitated by a transient temperature increase (Fig. 3E). This increase is induced by an optical hotspot resulting from nanofocusing of plasmons onto a magnetic film (*41*). Plasmonic hole arrays have been demonstrated as color multiplexers in charge-coupled display (CCD) imaging systems (Fig. 3F) (*42*). Here, light within specific wavelength bands is guided to the matching light collection pixels on a CCD array and then converted to electrical signals. This represents an important advantage over the use of conventional color filters, in which a substantial portion of the impinging light is lost by absorption.

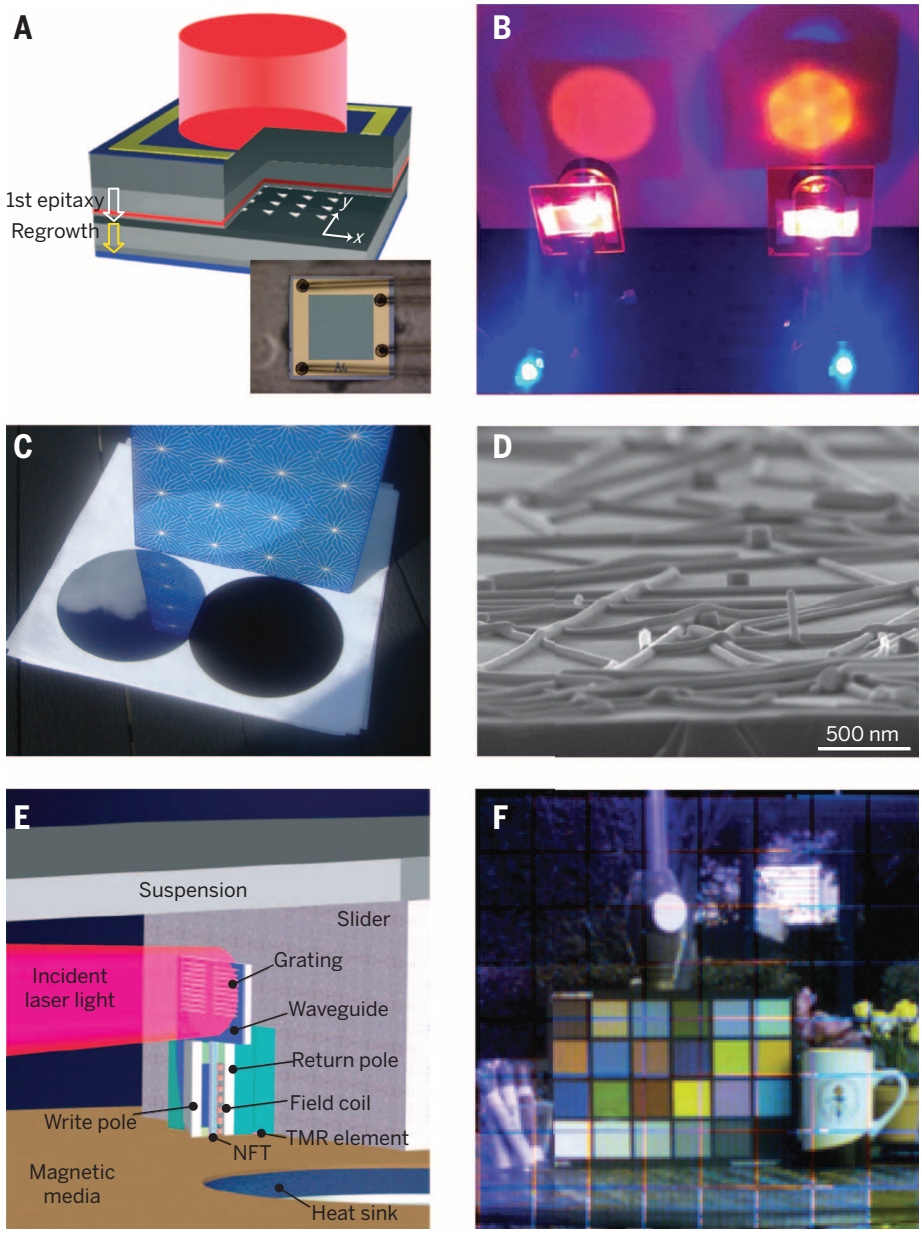

Fig. 3. Nanophotonic technologies and applications. (**A**) High-power photonic crystal laser. [Reprinted with permission from (*36*); copyright 2014, Nature Publishing Group] (**B**) LED without (left) and with (right) enhanced emission because of light scattering from embedded Ag nanoparticles. [Image: A. Nikitin, after (*37*), reprinted with permission; copyright 2013, Nature Publishing Group] (**C**) Black silicon wafer with (right) and without (left) dielectric optical metasurface for enhanced light coupling and trapping in solar cells. [Reprinted with permission from (*25*); copyright 2012, Nature Publishing Group]. (**D**) Transparent conducting nanowire network made from randomly dispersed chemically grown single-crystal Ag nanowires. [Reprinted with permission from (*40*); copyright 2012, Nature Publishing Group]. (**E**) Schematic of heat-assisted magnetic recording head with plasmonic light-focusing taper. [Reprinted with permission from (*41*); copyright, 2009, Nature Publishing Group] (**F**) Image taken by a plasmonic CCD chip with integrated plasmonic nanohole array for wavelength multiplexing. [Reprinted with permission from (*42*); copyright, 2013, American Chemical Society]

Future developments and perspectives

Nanophotonics provides a diverse set of tools to build on: Photonic crystals offer ultimate dispersion control and low-loss storage, whereas plasmonics is the platform of choice to control light on ultrafast time scales and ultrasmall length scales, matching optical interactions with single molecules. Metamaterials and metasurfaces provide the ultimate control over all properties of light. With the great control over light at the nanoscale that has now been achieved, the nanophotonics community is in an ideal position to bring the field another step further, by coupling light with other degrees of freedom at the nanoscale. Hybrid nanophotonics revolves around the simultaneous control of tightly confined light and phonons, electrons, spins, and/or excitons interacting with light. For example, when optical fields and acoustic vibrations are colocalized at the nanoscale, light can be used to control mechanical motion and vice versa, with optomechanical coupling strengths that are not achievable with other geometries (Fig. 4A). These interactions have, for example, been used for laser cooling of a nanomechanical

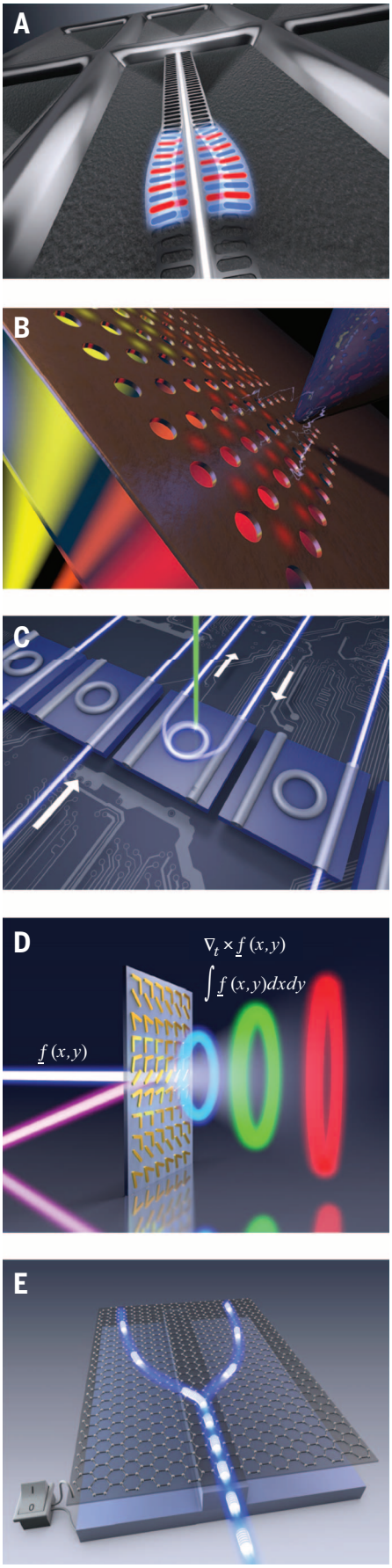

resonator to its quantum ground state (*43*). It has even been suggested that plasmon-enhanced SERS can be described by the dynamic backaction of the plasmon on a molecule's vibration, paving the way to a new form of molecular quantum optomechanics (*44*). Future hybrid nanophotonic systems hold the promise to couple electron spins with light, enabling integrated networks for quantum nanophotonics—for example, by using single-photon emission by color centers in diamond or defect centers in materials such as SiC (*45*).

Nanophotonics is also at the brink of making key contributions to the development of novel energy-conversion mechanisms. The recently discovered plasmoelectric effect in metal nanoparticles and hole arrays (*46*), in which optical illumination directly creates an electric potential by off-resonant excitation of a plasmonic structure (Fig. 4B), is being further explored to investigate how electrical power can be best generated. Another intriguing challenge is to harvest the excess energy of hot electrons excited in optically excited plasmonic nanostructures (*47*). This may find applications in energy harvesting and also plasmon-assisted surface catalysis for the generation of fuel (such as ethanol and hydrogen) from sunlight. More generally, plasmon-assisted photochemistry and catalysis is a research field with many opportunities to be explored.

An initial motivating factor for nanophotonics research was its direct impact on optoelectronic integration, aiming to bring together electronic and photonic length scales. The development of novel nanostructures that enable a nonreciprocal flow of light paves the way to on-chip all-optical isolation, in which light can only propagate in one direction, which is one of the missing components toward a fully integrated light-based communication system. Recent proposals and experimental demonstrations have shown that nonreciprocity can be indeed achieved by using a suitably designed spatiotemporal modulation of the local permittivity in waveguides and microring resonators (Fig. 4C) (*48*, *49*). Another interesting direction in this context lies in the exploration of the photonic equivalent of topological insulators. In such structures, unidirectional flow of light and reflectionless propagation robust to disorder may be achieved by designing periodic metasurfaces that support topologically nontrivial band diagrams (*50*).

Fig. 4. Nanophotonics future challenges and research fields. (**A**) Hybrid nanophotonics: coupling light with other degrees of freedom, such as mechanical motion. (**B**) Plasmoelectric effect converting sunlight to electrical power by using metallic nanostructures. (**C**) Nonreciprocal optical integrated circuit enables logic functions for optical computing. (**D**) Electrically tunable optical metasurface serves as wavelength division multiplexer in optical communication networks and may be operated as an analog computing metasurface. (**E**) Electrically tunable 2D graphene optoelectronic integrated circuit brings together optical and electronic length scales. [Illustrations are inspired by (*23*, *24*, *27*, *28*, *43*, *46*, *49*, *54*)]

Two further important ingredients for optoelectronic integration are access to strong nonlinearities within a very compact footprint and dynamic tunability and adaptability (*51*). The nonlinear optical response of materials is typically weak, and therefore large volumes are required to realize a measurable response. The recent observation of a giant nonlinear response from plasmonic metasurfaces coupled to intersubband transitions in semiconductors may open exciting venues for nonlinear nanophotonics (*52*). Similarly, one may ask how metasurfaces can enable new schemes for dynamically tunable integrated photonics. For example, can electrically tunable metasurfaces be used to steer and multiplex light on a chip, integrating an optical fiber communication system within an electronic integrated circuit? Also, how can "metatronic" optical signal processing and computing circuits be built and reconfigured by using building blocks with discrete optical functions (Fig. 4D)? Novel 2D materials and heterostructures based on graphene, MoS_2, and WSe_2 will play an important role in bringing light to the nanoscale, enabling 2D electrically tunable integrated optical nanocircuits (Fig. 4E) (*53*, *54*). It will be interesting to see to what degree of integration complexity optical and electronic functionality can ultimately be achieved on a chip by using these materials. A decisive factor will be to find the right tradeoff between light confinement and optical absorption losses.

The control over light at the nanoscale that scientists have achieved in recent years leads to a continuous stream of new fundamental insights in the interaction of light with matter at a deep-subwavelength scale. There is no doubt that this intense research activity promises a bright future for nanophotonics in the years to come.

REFERENCES AND NOTES

1. E. Kuramochi *et al.*, *Nat. Photonics* **8**, 474–481 (2014).
2. H. T. Miyazaki, Y. Kurokawa, *Phys. Rev. Lett.* **96**, 097401 (2006).
3. R. F. Oulton *et al.*, *Nature* **461**, 629–632 (2009).
4. J. Chen *et al.*, *Nature* **487**, 77–81 (2012).
5. Z. Fei *et al.*, *Nature* **487**, 82–85 (2012).
6. A. G. Curto *et al.*, *Science* **329**, 930–933 (2010).
7. D. Punj *et al.*, *Nat. Nanotechnol.* **8**, 512–516 (2013).
8. G. M. Akselrod *et al.*, *Nat. Photonics* **8**, 835–840 (2014).
9. R. Zhang *et al.*, *Nature* **498**, 82–86 (2013).
10. K. J. Savage *et al.*, *Nature* **491**, 574–577 (2012).
11. C. Sauvan, J. P. Hugonin, I. S. Maksymov, P. Lalanne, *Phys. Rev. Lett.* **110**, 237401 (2013).
12. X. W. Chen, M. Agio, V. Sandoghdar, *Phys. Rev. Lett.* **108**, 233001 (2012).
13. T. Schwartz, J. A. Hutchison, C. Genet, T. W. Ebbesen, *Phys. Rev. Lett.* **106**, 196405 (2011).
14. J. S. Fakonas, H. Lee, Y. A. Kelaita, H. A. Atwater, *Nat. Photonics* **8**, 317–320 (2014).
15. M. Arcari *et al.*, *Phys. Rev. Lett.* **113**, 093603 (2014).
16. D. Englund *et al.*, *Phys. Rev. Lett.* **108**, 093604 (2012).
17. E. Plum *et al.*, *Phys. Rev. Lett.* **102**, 113902 (2009).

18. I. Sersic, M. A. van de Haar, F. Bernal Arango, A. F. Koenderink, *Phys. Rev. Lett.* **108**, 223903 (2012).
19. M. Schäferling, D. Dregely, M. Hentschel, H. Giessen, *Phys. Rev. X* **2**, 031010 (2012).
20. J. K. Gansel *et al.*, *Science* **325**, 1513–1515 (2009).
21. T. Xu, A. Agrawal, M. Abashin, K. J. Chau, H. J. Lezec, *Nature* **497**, 470–474 (2013).
22. J. B. Pendry *et al.*, *Science* **348**, 521–524 (2015).
23. N. Yu *et al.*, *Science* **334**, 333–337 (2011).
24. X. Ni, N. K. Emani, A. V. Kildishev, A. Boltasseva, V. M. Shalaev, *Science* **335**, 427–427 (2012).
25. P. Spinelli, M. A. Verschuuren, A. Polman, *Nat. Commun.* **3**, 692 (2012).
26. D. Lin, P. Fan, E. Hasman, M. L. Brongersma, *Science* **345**, 298–302 (2014).
27. N. Engheta, *Science* **317**, 1698–1702 (2007).
28. A. Silva *et al.*, *Science* **343**, 160–163 (2014).
29. B. le Feber, N. Rotenberg, D. M. Beggs, L. Kuipers, *Nat. Photonics* **8**, 43–46 (2014).
30. M. Frimmer, Y. Chen, A. F. Koenderink, *Phys. Rev. Lett.* **107**, 23602 (2011).
31. R. Sapienza *et al.*, *Nat. Mater.* **11**, 781–787 (2012).
32. O. Nicoletti *et al.*, *Nature* **502**, 80–84 (2013).
33. A. Atre, B. J. M. Brenny, T. Coenen, A. Polman, J. A. Dionne, *Nat. Nanotechnol.* 10.1038/nnano.2015.39 (2015).
34. R. Bardhan, S. Lal, A. Joshi, N. J. Halas, *Acc. Chem. Res.* **44**, 936–946 (2011).
35. B. McNally *et al.*, *Nano Lett.* **10**, 2237–2244 (2010).
36. K. Hirose *et al.*, *Nat. Photonics* **8**, 406–411 (2014).
37. G. Lozano *et al.*, *Light: Sci. Appl.* **2**, e66 (2013).
38. J. Wallentin *et al.*, *Science* **339**, 1057–1060 (2013).
39. P. Krogstrup *et al.*, *Nat. Photonics* **7**, 306–310 (2013).
40. E. C. Garnett *et al.*, *Nat. Mater.* **11**, 241–249 (2012).
41. W. A. Challener *et al.*, *Nat. Photonics* **3**, 220–224 (2009).
42. S. P. Burgos, S. Yokogawa, H. A. Atwater, *ACS Nano* **7**, 10038–10047 (2013).
43. J. Chan *et al.*, *Nature* **478**, 89–92 (2011).
44. P. Roelli, C. Galland, N. Piro, T. J. Kippenberg, http://arxiv.org/abs/1407.1518 (2014).
45. B. J. Hausmann *et al.*, *Nano Lett.* **12**, 1578–1582 (2012).
46. M. T. Sheldon, J. van de Groep, A. M. Brown, A. Polman, H. A. Atwater, *Science* **346**, 828–831 (2014).
47. M. W. Knight, H. Sobhani, P. Nordlander, N. J. Halas, *Science* **332**, 702–704 (2011).
48. L. D. Tzuang, K. Fang, P. Nussenzveig, S. Fan, M. D. Lipson, *Nat. Photonics* **8**, 701–705 (2014).
49. D. L. Sounas, C. Caloz, A. Alù, *Nat. Commun.* **4**, 2407 (2013).
50. M. C. Rechtsman *et al.*, *Nature* **496**, 196–200 (2013).
51. M. Lapine, I. V. Shadrivov, Y. S. Kivshar, *Rev. Mod. Phys.* **86**, 1093–1123 (2014).
52. J. Lee *et al.*, *Nature* **511**, 65–69 (2014).
53. F. H. L. Koppens, D. E. Chang, F. J. García de Abajo, *Nano Lett.* **11**, 3370–3377 (2011).
54. A. Vakil, N. Engheta, *Science* **332**, 1291–1294 (2011).

ACKNOWLEDGMENTS

This work is part of the research program of the Foundation for Fundamental Research on Matter (FOM), which is part of the Netherlands Organisation for Scientific Research (NWO). It is also supported by the European Research Council and NanoNextNL, a research and technology program of the Dutch Ministry of Economic Affairs. A.A. was supported by the Royal Netherlands Academy of Arts and Sciences Visiting Professorship program and by the U.S. Office of Naval Research with Multidisciplinary University Research Initiative grant N00014-10-1-0942. A.P. is cofounder and co-owner of a Delmic BV, a startup company that commercializes a cathodoluminescence microscopy instrument. We gratefully acknowledge discussions with A. Lagendijk, K. Kuipers, J. Gómez Rivas, E. Garnett, E. Verhagen, B. Ehrler, the students and postdocs of AMOLF's Center for Nanophotonics, and many nanophotonics colleagues all over the world.

10.1126/science.1261243

REVIEW

Transforming the optical landscape

J. B. Pendry,[1]* Yu Luo,[2] Rongkuo Zhao[3]

Electromagnetism provides us with some of the most powerful tools in science, encompassing lasers, optical microscopes, magnetic resonance imaging scanners, radar, and a host of other techniques. To understand and develop the technology requires more than a set of formal equations. Scientists and engineers have to form a vivid picture that fires their imaginations and enables intuition to play a full role in the process of invention. It is to this end that transformation optics has been developed, exploiting Faraday's picture of electric and magnetic fields as lines of force, which can be manipulated by the electrical permittivity and magnetic permeability of surrounding materials. Transformation optics says what has to be done to place the lines of force where we want them to be.

The nature of light was revealed by Maxwell a century and a half ago. His equations stand today as an exact description of light, and all electromagnetic phenomena, at the classical level. It has long been known that Maxwell's equations are invariant under a coordinate transformation (*1*–*3*). If $\varepsilon(\mathbf{x}),\mu(\mathbf{x})$ are the permittivity and permeability tensors expressed in some coordinate frame, then a transformation to a new coordinate frame $\mathbf{x}'$ does not alter the form of Maxwell's equations but only changes the values of permittivity and permeability to be used. Formally we have

$$\varepsilon'^{i'j'} = [\det(\Lambda)]^{-1}\Lambda^{i'}_{i}\Lambda^{j'}_{j}\varepsilon^{ij}$$

$$\mu'^{i'j'} = [\det(\Lambda)]^{-1}\Lambda^{i'}_{i}\Lambda^{j'}_{j}\mu^{ij}$$

where

$$\Lambda^{j'}_{j} = \frac{\partial x^{j'}}{\partial x^{j}}$$

This simple mathematical statement has been elaborated over the past couple of decades into an intuitive working tool of electromagnetic theory (*4*–*8*). Here we give a physical interpretation of the equations and re-derive the formulae in an intuitive fashion, followed by examples of where transformation optics has been effectively applied.

Bald mathematical statements hide the real power of the transformation method, which is only revealed when we appeal to Michael Faraday's representation of electric and magnetic fields in terms of lines of force. In this scheme, the displacement field $\mathbf{D}(\mathbf{x})$ and the magnetic field $\mathbf{B}(\mathbf{x})$ are represented by field lines that begin and end on charges in the case of the displacement field and are continuous in the case of the magnetic field. Their density represents the field strength. A coordinate transformation can be thought of as a distortion of space, which moves the field lines around as if they were embedded in a block of rubber. As we distort the coordinates, we carry the field lines along too. This yields an intuitive picture of how to manipulate fields: Just as Snell's law tells how rays of light can be redirected and focused using the refractive index, transformation optics shows how field lines can be manipulated and gives an exact prescription for the values of $\varepsilon(\mathbf{x}),\mu(\mathbf{x})$, ensuring that the distorted field lines obey Maxwell's equations. Replacing the rays of Snell's law with Faraday's fields extends our powers of visualization into regimes untouched by Snell, such as the subwavelength electric fields found in plasmonic systems and even the regime of static electric and magnetic fields (*9*).

Not only does this manipulation apply to $\mathbf{D}$ and $\mathbf{B}$, but also to any electromagnetic quantity that is conserved and therefore represented by field lines: For example the Poynting vector representing the flow of energy serves as a generalization of the ray picture. Another example is the flow of charge either as an electrical current or as the trajectory of an individual particle.

The power of transformation

Here we give a few examples that demonstrate the power of the technique, but first let us make an alternate, intuitive, derivation of the transformation equations.

Consider an electric displacement field D_y, parallel to the y axis in a dielectric medium (as shown red in Fig. 1A). Next make a coordinate transformation in which one half of the space is uniformly compressed by a factor m (Fig. 1B. We then ask how the permittivity in the compressed medium must change. To calculate ε'_y, we require that E_y be continuous. Noting that owing to the compression, the lines of force have been pushed closer together and hence D'_y has been increased by a factor m^{-1}, $D_y/\varepsilon_y = D'_y/\varepsilon'_y = m^{-1}D_y/\varepsilon'_y$, and hence $\varepsilon'_y = m^{-1}\varepsilon_y$. The same argument for magnetic fields shows that $\mu'_y = m^{-1}\mu_y$.

To find ε'_x, consider an electric displacement field D_x, parallel to the x axis (as shown in cyan

[1]The Blackett Laboratory, Department of Physics, Imperial College London, London SW72AZ, UK. [2]Photonic Centre of Excellence (OPTIMUS), School of Electrical and Electronic Engineering, Nanyang Technological University, Nanyang Avenue 639798, Singapore. [3]National Science Foundation Nanoscale Science and Engineering Center, 3112 Etcheverry Hall, University of California, Berkeley, CA 94720, USA.
*Corresponding author. E-mail: j.pendry@imperial.ac.uk

18. I. Sersic, M. A. van de Haar, F. Bernal Arango, A. F. Koenderink, *Phys. Rev. Lett.* **108**, 223903 (2012).
19. M. Schäferling, D. Dregely, M. Hentschel, H. Giessen, *Phys. Rev. X* **2**, 031010 (2012).
20. J. K. Gansel *et al.*, *Science* **325**, 1513–1515 (2009).
21. T. Xu, A. Agrawal, M. Abashin, K. J. Chau, H. J. Lezec, *Nature* **497**, 470–474 (2013).
22. J. B. Pendry *et al.*, *Science* **348**, 521–524 (2015).
23. N. Yu *et al.*, *Science* **334**, 333–337 (2011).
24. X. Ni, N. K. Emani, A. V. Kildishev, A. Boltasseva, V. M. Shalaev, *Science* **335**, 427–427 (2012).
25. P. Spinelli, M. A. Verschuuren, A. Polman, *Nat. Commun.* **3**, 692 (2012).
26. D. Lin, P. Fan, E. Hasman, M. L. Brongersma, *Science* **345**, 298–302 (2014).
27. N. Engheta, *Science* **317**, 1698–1702 (2007).
28. A. Silva *et al.*, *Science* **343**, 160–163 (2014).
29. B. le Feber, N. Rotenberg, D. M. Beggs, L. Kuipers, *Nat. Photonics* **8**, 43–46 (2014).
30. M. Frimmer, Y. Chen, A. F. Koenderink, *Phys. Rev. Lett.* **107**, 23602 (2011).
31. R. Sapienza *et al.*, *Nat. Mater.* **11**, 781–787 (2012).
32. O. Nicoletti *et al.*, *Nature* **502**, 80–84 (2013).
33. A. Atre, B. J. M. Brenny, T. Coenen, A. Polman, J. A. Dionne, *Nat. Nanotechnol.* 10.1038/nnano.2015.39 (2015).
34. R. Bardhan, S. Lal, A. Joshi, N. J. Halas, *Acc. Chem. Res.* **44**, 936–946 (2011).
35. B. McNally *et al.*, *Nano Lett.* **10**, 2237–2244 (2010).
36. K. Hirose *et al.*, *Nat. Photonics* **8**, 406–411 (2014).
37. G. Lozano *et al.*, *Light: Sci. Appl.* **2**, e66 (2013).
38. J. Wallentin *et al.*, *Science* **339**, 1057–1060 (2013).
39. P. Krogstrup *et al.*, *Nat. Photonics* **7**, 306–310 (2013).
40. E. C. Garnett *et al.*, *Nat. Mater.* **11**, 241–249 (2012).
41. W. A. Challener *et al.*, *Nat. Photonics* **3**, 220–224 (2009).
42. S. P. Burgos, S. Yokogawa, H. A. Atwater, *ACS Nano* **7**, 10038–10047 (2013).
43. J. Chan *et al.*, *Nature* **478**, 89–92 (2011).
44. P. Roelli, C. Galland, N. Piro, T. J. Kippenberg, http://arxiv.org/abs/1407.1518 (2014).
45. B. J. Hausmann *et al.*, *Nano Lett.* **12**, 1578–1582 (2012).
46. M. T. Sheldon, J. van de Groep, A. M. Brown, A. Polman, H. A. Atwater, *Science* **346**, 828–831 (2014).
47. M. W. Knight, H. Sobhani, P. Nordlander, N. J. Halas, *Science* **332**, 702–704 (2011).
48. L. D. Tzuang, K. Fang, P. Nussenzveig, S. Fan, M. D. Lipson, *Nat. Photonics* **8**, 701–705 (2014).
49. D. L. Sounas, C. Caloz, A. Alù, *Nat. Commun.* **4**, 2407 (2013).
50. M. C. Rechtsman *et al.*, *Nature* **496**, 196–200 (2013).
51. M. Lapine, I. V. Shadrivov, Y. S. Kivshar, *Rev. Mod. Phys.* **86**, 1093–1123 (2014).
52. J. Lee *et al.*, *Nature* **511**, 65–69 (2014).
53. F. H. L. Koppens, D. E. Chang, F. J. García de Abajo, *Nano Lett.* **11**, 3370–3377 (2011).
54. A. Vakil, N. Engheta, *Science* **332**, 1291–1294 (2011).

ACKNOWLEDGMENTS

This work is part of the research program of the Foundation for Fundamental Research on Matter (FOM), which is part of the Netherlands Organisation for Scientific Research (NWO). It is also supported by the European Research Council and NanoNextNL, a research and technology program of the Dutch Ministry of Economic Affairs. A.A. was supported by the Royal Netherlands Academy of Arts and Sciences Visiting Professorship program and by the U.S. Office of Naval Research with Multidisciplinary University Research Initiative grant N00014-10-1-0942. A.P. is cofounder and co-owner of a Delmic BV, a startup company that commercializes a cathodoluminescence microscopy instrument. We gratefully acknowledge discussions with A. Lagendijk, K. Kuipers, J. Gómez Rivas, E. Garnett, E. Verhagen, B. Ehrler, the students and postdocs of AMOLF's Center for Nanophotonics, and many nanophotonics colleagues all over the world.

10.1126/science.1261243

REVIEW

Transforming the optical landscape

J. B. Pendry,[1]* Yu Luo,[2] Rongkuo Zhao[3]

Electromagnetism provides us with some of the most powerful tools in science, encompassing lasers, optical microscopes, magnetic resonance imaging scanners, radar, and a host of other techniques. To understand and develop the technology requires more than a set of formal equations. Scientists and engineers have to form a vivid picture that fires their imaginations and enables intuition to play a full role in the process of invention. It is to this end that transformation optics has been developed, exploiting Faraday's picture of electric and magnetic fields as lines of force, which can be manipulated by the electrical permittivity and magnetic permeability of surrounding materials. Transformation optics says what has to be done to place the lines of force where we want them to be.

The nature of light was revealed by Maxwell a century and a half ago. His equations stand today as an exact description of light, and all electromagnetic phenomena, at the classical level. It has long been known that Maxwell's equations are invariant under a coordinate transformation (*1*–*3*). If $\varepsilon(\mathbf{x}),\mu(\mathbf{x})$ are the permittivity and permeability tensors expressed in some coordinate frame, then a transformation to a new coordinate frame $\mathbf{x}'$ does not alter the form of Maxwell's equations but only changes the values of permittivity and permeability to be used. Formally we have

$$\varepsilon'^{i'j'} = [\det(\Lambda)]^{-1}\Lambda^{i'}_{i}\Lambda^{j'}_{j}\varepsilon^{ij}$$

$$\mu'^{i'j'} = [\det(\Lambda)]^{-1}\Lambda^{i'}_{i}\Lambda^{j'}_{j}\mu^{ij}$$

where

$$\Lambda^{j'}_{j} = \frac{\partial x^{j'}}{\partial x^{j}}$$

This simple mathematical statement has been elaborated over the past couple of decades into an intuitive working tool of electromagnetic theory (*4*–*8*). Here we give a physical interpretation of the equations and re-derive the formulae in an intuitive fashion, followed by examples of where transformation optics has been effectively applied.

Bald mathematical statements hide the real power of the transformation method, which is only revealed when we appeal to Michael Faraday's representation of electric and magnetic fields in terms of lines of force. In this scheme, the displacement field $\mathbf{D}(\mathbf{x})$ and the magnetic field $\mathbf{B}(\mathbf{x})$ are represented by field lines that begin and end on charges in the case of the displacement field and are continuous in the case of the magnetic field. Their density represents the field strength. A coordinate transformation can be thought of as a distortion of space, which moves the field lines around as if they were embedded in a block of rubber. As we distort the coordinates, we carry the field lines along too. This yields an intuitive picture of how to manipulate fields: Just as Snell's law tells how rays of light can be redirected and focused using the refractive index, transformation optics shows how field lines can be manipulated and gives an exact prescription for the values of $\varepsilon(\mathbf{x}),\mu(\mathbf{x})$, ensuring that the distorted field lines obey Maxwell's equations. Replacing the rays of Snell's law with Faraday's fields extends our powers of visualization into regimes untouched by Snell, such as the subwavelength electric fields found in plasmonic systems and even the regime of static electric and magnetic fields (*9*).

Not only does this manipulation apply to $\mathbf{D}$ and $\mathbf{B}$, but also to any electromagnetic quantity that is conserved and therefore represented by field lines: For example the Poynting vector representing the flow of energy serves as a generalization of the ray picture. Another example is the flow of charge either as an electrical current or as the trajectory of an individual particle.

The power of transformation

Here we give a few examples that demonstrate the power of the technique, but first let us make an alternate, intuitive, derivation of the transformation equations.

Consider an electric displacement field D_y, parallel to the y axis in a dielectric medium (as shown red in Fig. 1A). Next make a coordinate transformation in which one half of the space is uniformly compressed by a factor m (Fig. 1B. We then ask how the permittivity in the compressed medium must change. To calculate ε'_y, we require that E_y be continuous. Noting that owing to the compression, the lines of force have been pushed closer together and hence D'_y has been increased by a factor m^{-1}, $D_y/\varepsilon_y = D'_y/\varepsilon'_y = m^{-1}D_y/\varepsilon'_y$, and hence $\varepsilon'_y = m^{-1}\varepsilon_y$. The same argument for magnetic fields shows that $\mu'_y = m^{-1}\mu_y$.

To find ε'_x, consider an electric displacement field D_x, parallel to the x axis (as shown in cyan

[1]The Blackett Laboratory, Department of Physics, Imperial College London, London SW72AZ, UK. [2]Photonic Centre of Excellence (OPTIMUS), School of Electrical and Electronic Engineering, Nanyang Technological University, Nanyang Avenue 639798, Singapore. [3]National Science Foundation Nanoscale Science and Engineering Center, 3112 Etcheverry Hall, University of California, Berkeley, CA 94720, USA.
*Corresponding author. E-mail: j.pendry@imperial.ac.uk

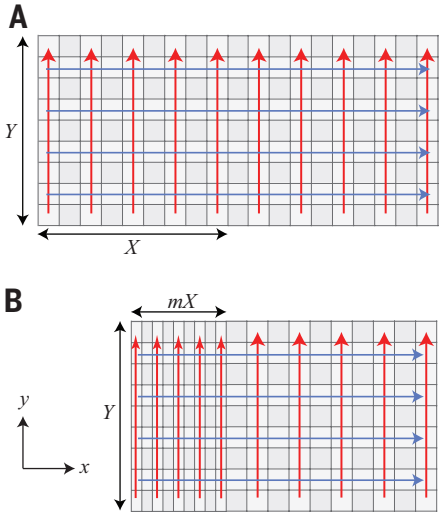

Fig. 1. Visualizing a transformation in the electric displacement fields. The field lines (**A**) before compression of half the coordinates and (**B**) after compression. The flux lines perpendicular to the axis of compression (red) are pushed closer together, whereas those parallel to the axis (blue) have their spacing and therefore the *D*-field intensity is unaltered.

in Fig. 1A). After compression of the coordinate system, this field is unaltered, $D'_x = D_x$ (Fig. 1B). To find ε'_x, we require that the work done by a test charge passing from one side of the compressed region to the other be unaltered by the compression. Because the charge traverses a region shortened by a factor m, the electric field E'_x must increase by a factor m^{-1}, and as D_x is unchanged, this requires that $\varepsilon'_x = m\varepsilon_x$.

The final result is simple: Compression along an axis by a factor of m decreases ε along that axis by a factor of m, and along the two perpendicular axes ε is increased by a factor of m^{-1}. Similarly for the permeability. In fact, this is the most general statement of the transformation, because the most general distortion of a local coordinate system can be represented as sequential compressions about three axes, followed by a rotation. So not only do we have an intuitive feel as to how field lines behave as we distort the coordinates, but we also get an intuitive feel for the changes in the electric and magnetic response of the transformed medium.

Example applications: Cloaking

Perhaps the most famous application of transformation optics has been the design of a cloak of invisibility (*10*–*15*). The technique is ideally suited to this task, because fields are only disturbed where the coordinates are distorted, so confining the distortion to the interior of the cloak itself leaves external fields undisturbed and therefore the act of cloaking undetected. However, early experimental realizations of cloaks were all much larger than the wavelength of radiation from which they were hiding, and could in principle, although with difficulty, have been designed using ray optics. More recently, cloaking principles have been applied to the near field, and in extremis to static magnetic fields, an instance where ray optics obviously has no application. The same transformation used for an optical cloak (*10*) was used to design a cloak for static magnetic fields (*15*) $r' = R_1 + r(R_2 - R_1)/R_2$, $\theta' = \theta$, $\phi' = \phi$, resulting in the following cloaking parameters for the permeability

$$\mu'_{r'} = \frac{R_2}{R_2 - R_1}\frac{(r' - R_1)^2}{r'^2}, \mu'_{\theta'} = \frac{R_2}{R_2 - R_1},$$
$$\mu'_{\phi'} = \frac{R_2}{R_2 - R_1}$$

Note how these parameters obey the compression rules derived above: Radial values of μ are decreased and angular ones increased.

The magnetic field cloak (Fig. 2C) is designed using these formulas with the simplification that because magnetic fields alone are assumed to be present, we need only adjust the permeability. The design strategy is to make a transformation that takes all the "space" inside the cloak and compress it in the radial direction into an annulus, leaving an empty inner space in which we can hide objects. As we have noted, compressing space increases the permeability perpendicular to the direction of compression and decreases the permeability along the direction of compression; in this instance, along the radius.

The latter specification was the key challenge that Narayana and Sata met (*15*). They built a cylindrical cloak for static magnetic fields using a novel design for the diamagnetic metamaterials demanded by the formula (*16*). They placed the cloak in a magnetic field created by two electromagnets and measured the fields inside and outside the cloak as a function of the current in the electromagnets (Fig. 2). They also measured the fields for three different devices, each of which excludes the magnetic field: (i) a superconducting screen that exploits the Meissner effect to exclude magnetic fields but, by repelling the fields into the surrounding space, distorts the external fields; (ii) a mumetal shield that attracts the field lines into the highly permeable metal but also distorts the external fields; and (iii) a cloak designed according the transformation optical principles, which excludes the magnetic fields in a fashion that does not distort the external fields. The measured data for the cloak confirm that the cloak not only excludes fields but is also undetectable.

There are several situations in which it may be desirable to hide a sensitive object from a magnetic field, but not to disturb the field outside the cloak. In this way, external functions of the field, such as resolving objects in a magnetic resonance imaging scan, are preserved. The solutions shown in Fig. 2, A and B, would not achieve this objective and would also result in mechanical forces on the cloak itself due to interaction with the induced dipole moment. In contrast, the true cloak has no dipole moment, and therefore no net force is exerted.

Nanophotonics

Plasmonics has also been a fruitful area of application, as reported in (*7*, *17*, *18*). The surfaces of metals such as gold and silver support density oscillations of the electrons, much like waves on a sea. These can couple to external radiation but have a much shorter wavelength. The plasmonic excitations are greatly influenced by the shape of the surface and in particular by any singularities such as sharp corners, touching surfaces, or other

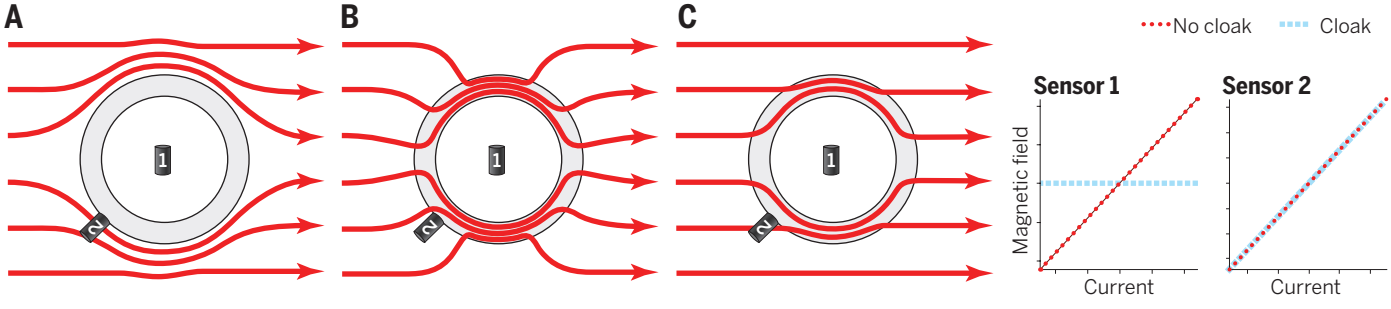

Fig. 2. Three schemes for excluding magnetic flux from an enclosed region of space. (**A**) A superconducting shell exploits the Meissner effect to exclude flux but results in a strong disturbance in the external field, which has to accommodate the excluded flux lines. (**B**) Mumetal is used to attract flux lines away from the central space but also results in a distortion of the external field. (**C**) A true magnetic cloak removes flux lines from the protected space but confines the displaced flux lines within the body of the cloak, leaving external fields unaltered. At right are the results of an experiment on the cloak shown in (C). A magnetic field generated by current in an electromagnet is applied to the cloak. Sensor 1 inside the cloak demonstrates zero flux inside the cloak; sensor 2 outside the cloak shows an undisturbed external field.

rough features, which tend to attract very high field intensities: They act as harvesting points for any incident radiation. This is the origin of surface-enhanced Raman spectroscopy, in which the intense field concentrations greatly increase the Raman signals from adsorbed molecules, sometimes by as much as 10^6. Without this effect, many molecules would be Raman-invisible at the surface.

By applying transformations to simple structures, such as plasmonic waveguides consisting of two parallel sheets of silver, many of the singular structures can be generated through a singular transformation and their spectra understood through the spectrum of the original simple waveguide. Thus, apparently diverse structures such as sharp edges, points, and nearly touching spheres can be shown to have a common origin and can in many cases be treated analytically. This deep understanding enables further properties of these structures to be elucidated, such as the dispersion forces acting at short range between surfaces that are otherwise out of physical contact (*19*, *20*). The origin of these forces lies in the zero point energy, $\hbar\omega/2$, of the electromagnetic modes, whose frequencies shift as surfaces approach. By transforming apparently complex surface configurations to simple waveguides, spectral shifts (invariant under a transformation) can be calculated analytically and the forces determined (*21*).

Two gold spheres in close proximity (Fig. 3) are shown to transform into two concentric spheres. The transformation consists of an inversion about a point carefully chosen so that the inverted structure comprises two concentric spheres. The highly symmetric geometry of the inverted structure leads to greatly simplified calculations—another instance of hidden symmetries.

This theory has been applied to the interaction between two gold nanospheres. First, the experimental permittivity of gold (*22*, *23*) was fitted using the Drude-like term for the lower frequencies and Lorentzian terms for higher frequencies, where core excitations in the gold are important. Data extending to 100 eV were fitted. Included in the calculation were nonlocal effects, which smear out surface charges and hence introduce a natural cutoff in wave vector, without which the forces would not saturate as the touching point is approached. On the right are the van der Waals energies calculated in the coordinate system of the concentric spheres. The calculations demonstrate the importance of going beyond the Drude approximation to the permittivity and also of including nonlocal corrections.

When investigating a system's properties, whether electromagnetic, electronic, or acoustic (to mention only three aspects), considerations of symmetry are often vital. In spectroscopy, symmetry classifies transitions, and when calculating the electronic properties of matter, symmetry is vital to simplifying computations because states are classified by wave vector, courtesy of Bloch's theorem. In contrast, disordered solids are still not well understood because of their lack of

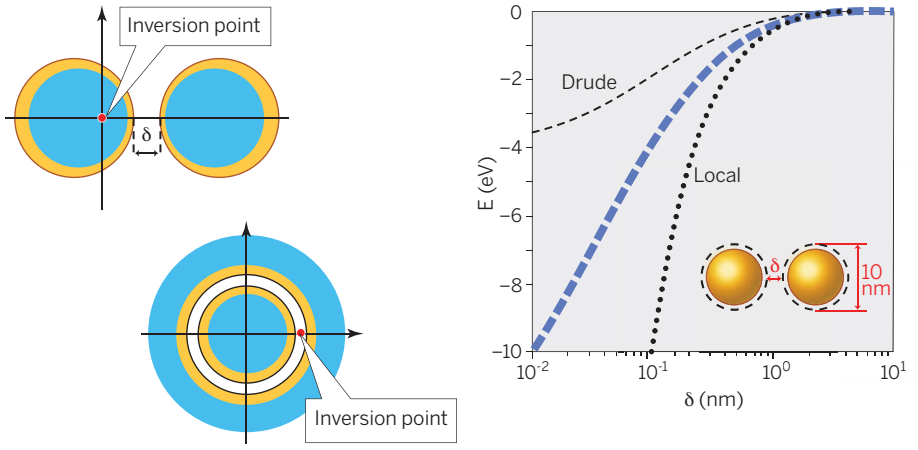

Fig. 3. van der Waals energy between two 10-nm-diameter gold nanoparticles as a function of the separation. For the blue dashed line, nonlocal effects are considered. The black dotted line shows the van der Waals energy calculated neglecting nonlocal effects. The energy considering nonlocal effects but neglecting the Lorentzian terms in the permittivity is shown by the black dashed line. δ represents the distance between the spheres.

symmetry. However, it is possible to start with a highly symmetric system, such as a planar plasmonic waveguide, whose properties are classified by a wave vector and are therefore well understood, thanks to the symmetry, and apply a transformation that destroys the geometric symmetry but leaves the spectroscopic properties intact. This we call a hidden symmetry (*24*). For example, the planar cross-section of the waveguide can be transformed variously into a knife edge, two cylinders in close proximity, or a crescent. All of these structures inherit the spectrum of the mother system: They have a common spectroscopic "DNA."

Electron microscopy

Yet another example of both insight and computational facility brought by transformation optics is found in electron energy-loss calculations. Electron microscope technology is highly developed and can image materials at the subnanometer level. In addition, by applying energy analysis to the emerging beam, it is possible to detect the electromagnetic spectrum of an object resolved at the nanoscale (*25*). This is a very powerful technique.

Figure 4 shows on the left an electron beam, typically 50 keV, passing close to a metallic nanostructure. Electrons lose energy and momentum to the surface plasmons of the metal, giving access to the electromagnetic spectrum of the structure. Electrons also have the advantage that, unlike photons, the excitations are not limited by a dipole selection rule. The electromagnetic field surrounding an electron in uniform motion is easily calculated, but in the past it has been generally supposed that the modes with which it interacts require a complex harmonic expansion involving many terms. However, a simple inversion about the touching point takes us to a highly

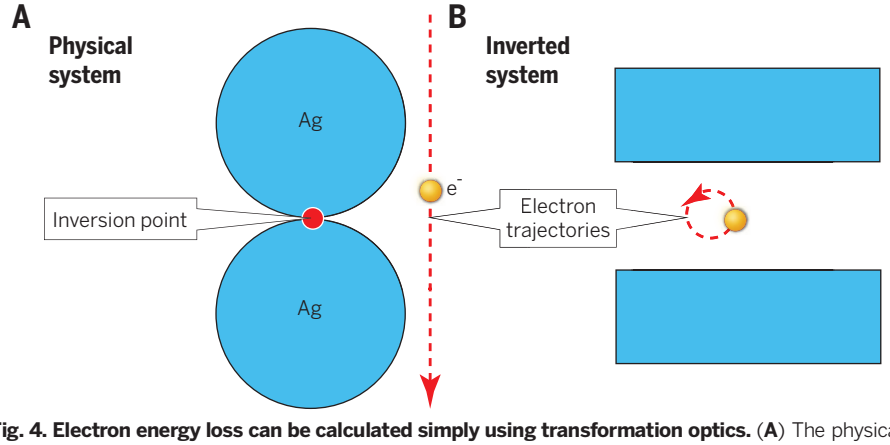

Fig. 4. Electron energy loss can be calculated simply using transformation optics. (**A**) The physical system with a high-energy electron passing close to a pair of touching nanowires represented as cylinders. (**B**) An inversion about the touching point takes points at the origin to infinity and points at infinity to the origin. The cylinders morph into a waveguide contained between two parallel metal plates, and the electron now makes a circular trajectory starting slowly at the origin, moving more rapidly at the farthest point from the origin, and slowing again before returning to the origin. The electromagnetic field of the electron is most simply calculated in (A) and that of the metallic system in (B).

symmetric planar waveguide, whose modes are easily calculated and which can immediately be transformed to the modes of the touching cylinders. The electron trajectory in the transformed frame maps to a circle traversed at a non-uniform rate, but that need not concern us because the field has already been simply calculated in the other frame. Hence the loss problem is easily solved in this way.

Perfect lensing

Another theoretical challenge to which transformation optics has been applied is the perfect lens. Veselago (*26*) made a study of the then-hypothetical materials that show negative refraction. He identified the necessary conditions for this effect, which comprise $\varepsilon < 0, \mu < 0$. Many years later, metamaterials have enabled his ideas to be realized (*27*–*30*). Among many suggestions from that earlier work was the possibility of focusing light using negative refraction: Veselago used the ray picture to show that light is naturally focused by a negative index slab of material (Fig. 5A). Of itself, this result is unremarkable: There are many devices that focus light, but an alternative derivation using transformation optics casts new light on the Veselago lens. We have discussed how compressing a region of space by a factor m results in ε and μ parallel to the compression being reduced by a factor of m; whereas in the perpendicular direction, ε and μ are increased by m^{-1}. Now let us push matters to an extreme: Infinite compression leads to infinities in one direction and zeros in the other, and going beyond that to negative values of m implies negative values of ε and μ if we take the mathematics seriously. If $m = -1$ we regain an isotropic system, but with $\varepsilon = -1$, $\mu = -1$, and hence according to Veselago, the refractive index is $n = -1$. In geometrical terms, we have folded space over onto itself (Fig. 5B). This means that according to the transformation, light passes through the same region of space three times, coming to the same focus each time. Furthermore, because transformation optics is exact at the level of Maxwell's equations, this is an exact statement, and the focus has the same level of perfection on each of the three manifolds. This conclusion was reached some time ago (*31*) by a more elaborate multiple-scattering treatment of the problem, with the conclusion that the Veselago lens is perfect in the sense that its resolution is limited only by the perfection of manufacture, not by fundamental constraints. This gives yet another instance in which transformation optics is not merely a tool for computation but provides insight and understanding of complex problems.

The apparent paradox of the light being in three places at once is resolved by the fact that the condition $n = -1$ can be satisfied exactly only at a single frequency, and therefore a causal interpretation in the time domain is not available.

Transformation optics has extended the concept of the perfect lens to the case of a magnifying lens. If we apply to the perfect lens a transformation

$$x = r_0 \exp(r'/R)\sin\theta' \cos\phi',$$
$$y = r_0 \exp(r'/R)\sin\theta' \sin\phi',$$
$$z = r_0 \exp(r'/R)\cos\theta'$$

then in the primed frame we have a spherically symmetric system shown in Fig. 5C, with the parameters

$$\varepsilon_x = \varepsilon_y = \varepsilon_z = +r_2^2/r_3^2, 0 < r < r_3$$
$$\varepsilon_x = \varepsilon_y = \varepsilon_z = -r_2^2/r^2, r_3 < r < r_2$$
$$\varepsilon_x = \varepsilon_y = \varepsilon_z = +1, r_2 < r < \infty$$

where r_1, r_2, r_3 are the radii of consecutive spheres, outermost to innermost. This new lens, colored in cyan, is described in more detail in (*5*, *32*, *33*) and has the property that everything inside the green inner sphere is perfectly imaged as a magnified object into the region within the outer magenta sphere, and conversely any object between the magenta sphere and the lens appears demagnified within the inner sphere. This leads to a paradox: An observer to the right of the lens would observe the red upper ray as having passed through the central region of the lens, because the theory says that it has to. In particular, if the region inside the green sphere were filled with a black material, to an external observer the whole of the large sphere outlined in magenta would appear black. The ray picture would say that this is not possible, because rays that do not strike the blue sphere cannot be refracted into the central sphere. This superficially logical statement is wrong: one of the many curious consequences of negative refraction. The paradox is resolved if we allow for optical tunneling between rays, which is allowed in the wave picture.

Concluding remarks

Transformation optics is a tool that can be applied across the entire electromagnetic spectrum. Here we have selected a few examples of its power. Already the concept has spread to acoustics (*34*) and other wavelike phenomena (*35*). In the future, we can expect many more applications as its utility comes to be recognized.

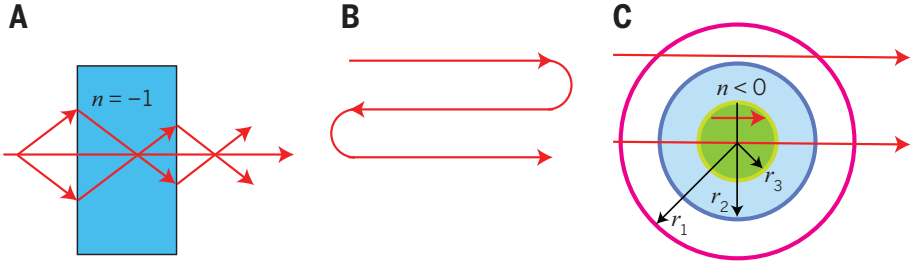

Fig. 5. Geometry and negative refraction. (**A**) The Veselago lens. (**B**) If negative refraction is interpreted as negative space, the light appears to move in a folded space. (**C**) Transformation to a system of spherical coordinates makes a perfect magnifying glass, which to an external observer makes everything within the green sphere appear within the magenta sphere in magnified form.

REFERENCES AND NOTES

1. E. G. Post, *Formal Structure of Electromagnetics: General Covariance and Electromagnetics* (Interscience Publishers, New York, 1962).
2. A. J. Ward, J. B. Pendry, *J. Mod. Opt.* **43**, 773–793 (1996).
3. D. M. Shyroki, http://arxiv.org/abs/physics/0307029v1 (2003).
4. U. Leonhardt, T. G. Philbin, *Progr. Opt.* **53**, 69–152 (2009).
5. H. Chen, C. T. Chan, P. Sheng, *Nat. Mater.* **9**, 387–396 (2010).
6. A. V. Kildishev, V. M. Shalaev, *Physics Uspekhi* **54**, 53 (2011).
7. J. B. Pendry, A. Aubry, D. R. Smith, S. A. Maier, *Science* **337**, 549–552 (2012).
8. N. B. Kundtz, D. R. Smith, J. B. Pendry, *Proc. IEEE* **99**, 1622–1633 (2011).
9. B. Wood, J. B. Pendry, *J. Phys. Condens. Matter* **19**, 076208 (2007).
10. J. B. Pendry, D. Schurig, D. R. Smith, *Science* **312**, 1780–1782 (2006).
11. U. Leonhardt, *Science* **312**, 1777–1780 (2006).
12. J. Li, J. B. Pendry, *Phys. Rev. Lett.* **101**, 203901 (2008).
13. A. Nicolet, F. Zolla, S. Guenneau, *Opt. Lett.* **33**, 1584–1586 (2008).
14. M. McCall, *Contemp. Phys.* **54**, 273–286 (2013).
15. S. Narayana, Y. Sato, *Adv. Mater.* **24**, 71–74 (2012).
16. F. Magnus *et al.*, *Nat. Mater.* **7**, 295–297 (2008).
17. A. Aubry, J. B. Pendry, in *Active Plasmonics and Tuneable Plasmonic Metamaterials*, A. V. Zayats, S. A. Maier, Eds. (Wiley, Hoboken, NJ, 2013), pp. 105–152.
18. Y. Luo, Z. Rongkuo, A. I. Fernandez-Dominguez, S. A. Maier, J. B. Pendry, *Inf. Sci.* **56**, 120401 (2013).
19. J. N. Israelachvili, *Intermolecular and Surface Forces* (Academic Press, Burlington, MA, ed. 3, 2011).
20. A. W. Rodriguez, F. Capasso, S. G. Johnson, *Nat. Photonics* **5**, 211–221 (2011).
21. Y. Luo, R. Zhao, J. B. Pendry, *Proc. Natl. Acad. Sci. U.S.A.* **111**, 18422–18427 (2014).
22. R. L. Olmon *et al.*, *Phys. Rev. B* **86**, 235147 (2012).
23. E. W. Palik, *Handbook of Optical Constants of Solids I* (Academic Press, San Diego, CA, 1985).
24. M. Kraft, J. B. Pendry, S. A. Maier, Y. Luo, *Phys. Rev. B* **89**, 245125 (2014).
25. T. Coenen, A. Polman, *ACS Nano* **8**, 7350–7358 (2014).
26. V. G. Veselago, *Sov. Phys. Usp.* **10**, 509–514 (1968).
27. J. B. Pendry, A. J. Holden, W. J. Stewart, I. Youngs, *Phys. Rev. Lett.* **76**, 4773–4776 (1996).
28. J. B. Pendry, A. J. Holden, D. J. Robbins, W. J. Stewart, *IEEE Trans. Microwave Theory* **47**, 2075–2084 (1999).
29. D. R. Smith, W. J. Padilla, D. C. Vier, S. C. Nemat-Nasser, S. Schultz, *Phys. Rev. Lett.* **84**, 4184–4187 (2000).
30. R. A. Shelby, D. R. Smith, S. Schultz, *Science* **292**, 77–79 (2001).
31. J. B. Pendry, *Phys. Rev. Lett.* **85**, 3966–3969 (2000).
32. J. B. Pendry, S. A. Ramakrishna, *J. Phys. Condens. Matter* **15**, 6345–6364 (2003).
33. W. H. Wee, J. B. Pendry, *New J. Phys.* **11**, 073033 (2009).
34. H. Chen, C. T. Chan, *J. Phys. D Appl. Phys.* **43**, 113001 (2010).
35. S. Brûlé, E. H. Javelaud, S. Enoch, S. Guenneau, *Phys. Rev. Lett.* **112**, 133901 (2014).

ACKNOWLEDGMENTS

We thank the following for support: the Gordon and Betty Moore Foundation (J.B.P.), the Royal Commission for the Exhibition of 1851 (R.Z.), and the Leverhulme Trust (Y.L. and J.B.P.). Helpful discussions with S. A. Maier and A. I. Fernandez-Dominguez are gratefully acknowledged.

10.1126/science.1261244

REVIEW

Quantum optics: Science and technology in a new light

I. A. Walmsley

Light facilitates exploration of quantum phenomena that illuminate the basic properties of nature and also enables radical new technologies based on these phenomena. The critical features of quantum light that underpin the opportunities for discovery and application are exceptionally low noise and strong correlations. Rapid progress in both science and technology has been stimulated by adopting components developed for optical telecommunications and networking, such as highly efficient detectors, integrated photonic circuits, and waveguide- or nanostructure-based nonlinear optical devices. These provide the means to generate new quantum states of light and matter of unprecedented scale, containing many photons with quantum correlations across space and time. Notably, networks with only several tens of photons are already beyond what can be efficiently analyzed by current computers.

Light has a notable property: it exhibits quantum features at room temperature. The reason is that the energy of a photon is both large enough that background blackbody radiation is negligible in ambient conditions and small enough to be easily detected in similar conditions. Further, it is possible to prepare quantum states of light relatively easily, to manipulate them using structures that are of the scale of the photon's wavelength (that is, its de Broglie wavelength), and to detect them by absorption. Quantum light provides distinctive features, such as reduced noise compared with classical optics, and correlations, especially entanglement, that are stronger than anything possible between classical light beams.

One consequence is that photonics has provided the impetus for many of the most far-reaching discoveries in quantum physics, yielding experimental evidence about quantum correlations that has changed the way in which we understand the natural world. For example, the inadequacy of local hidden variable models, tested by Bell inequalities, has been most convincingly demonstrated using quantum light. Another example is the recent demonstration that to a realist, wave functions are not simply descriptions of the state of knowledge of the observer (*1*).

Easily accessible quantum characteristics have also made quantum light a key enabler for emerging new technologies, primarily in new modes of information processing, including sensing, imaging, communications, simulation, and computation. Many of the cornerstone protocols of quantum information science were first realized optically, including teleportation and cryptography. Quantum optics is one of the most promising platforms for these new technologies, and it is driving forward the quantum information revolution.

Department of Physics, Clarendon Laboratory, University of Oxford, Oxford, OX1 3PU, UK.
E-mail: walmsley@physics.ox.ac.uk

The great strengths of photonics in these applications—the large information capacity per photon, the robustness to dephasing of superposition states, and the ability to move photons over very long distances—mean that optically based quantum networks inherit much of the ubiquity of their classical counterparts. However, there are costs that classical networks do not suffer. The very feature that photons can travel together across optical fibers without corrupting one another is evidence that they do not interact strongly with each other. This means that deterministic quantum operations are very difficult to engineer. Further, although photons retain their encoded information well when they make it to the receiver, they are easily absorbed or scattered, so that the information is lost along with the photon. In quantum networks, this cannot be remedied by means of conventional optical amplifiers, which add noise that corrupts the quantum aspects of the signal.

Recent advances in the laboratory have begun to make inroads into all of these challenges, building on and using concepts and fabrication methods that have been developed for classical optical communications and computing technologies.

Large quantum states

A current though long-standing challenge in photonics is constructing large quantum states out of light that attain a scale at which its quantum features cannot be studied by any other means. This is perhaps simply one modern version of the question raised by Schrödinger and others at the birth of quantum physics: Can a palpably macroscopic thing, such as a cat, exist simultaneously in two obviously distinct states?

The field of quantum information science has provided a new perspective for such questions. Quantum information systems are essentially macroscopic quantum machines robust to decoherence, the efficacy of which are evaluated by the cost, or the resources consumed, of performing functions. For example, when the quantum system is sufficiently complex, it is impossible to simulate efficiently with a conventional computer; hence it may be categorized as nonclassical. Recent work has shown that in the case of bosons scattered in a random network, this level of complexity can be reached with perhaps less than 100 particles.

Reaching this threshold with so few particles is promising for the development of bosonic systems capable of exploring a wide range of new physics areas that are expected to inform research in a number of fields dealing with complex quantum systems, such as materials science, condensed matter physics, chemistry, and biology—for instance, in the study of superconductivity and molecular dynamics. Fields that use large data sets, such as particle and astrophysics, and possibly health and social sciences, may realize new potential for exploiting this resource, perhaps by means of quantum machine learning (*2*).

Photons are bosons, of course, so there is a clear promise of new territory for exploration and innovation if one can bring together a few tens of photons, control their interactions, and count them. This is a feasible goal for the near future.

Light-based quantum technologies

Realizing photonic quantum states of this scale will open the door to new quantum technologies based on light, especially in secure communications, sensing (including metrology and imaging), simulation, and computation (*3*). Therefore, developments in the tools available for quantum optics will enable these new technologies, which promise radically new capabilities derived from design principles based on quantum mechanics rather than principles based on classical physics.

Light plays a central role in all of these applications because it is the ideal medium for transmitting quantum information. In some of these quantum technologies, light is the sole medium. It is known that an all-photonic quantum computer is possible in principle. For most technologies, hybrid approaches in which light and matter interact at the quantum level to realize new information processing machines are likely to be optimal.

As an example, among the simplest of these new technologies is the quantum random number generator (QRNG). The QRNG provides a string of numbers, the randomness of which is guaranteed by the laws of quantum mechanics. The simplest example of a QRNG is based on the observation that a single photon can register at only one detector (*4*). Thus, when the photon is incident on a beamsplitter, only one of two detectors looking at the output ports will fire. This will happen completely at random, because quantum mechanics does not allow us, even in principle, to predict to which detector the photon will go. This principle is at the heart of commercial devices (*5*) and finds application in the generation of PIN numbers, in Monte Carlo simulations, and unexpectedly, in lotteries.

Currently, improvements in QRNGs are being explored. Increases in bit rate could be achieved using large optical fields that can be measured

Downloaded from www.sciencemag.org on April 30, 2015

with fast semiconductor detectors, with continuous random phase arising from spontaneous emission or scattering. Full certification of randomness is possible by using entangled light beams, such as in the Randomness Beacon project at the U.S. National Institute for Standards and Technology.

Quantum communications

Quantum communication deals with the idea of transferring quantum states from one place to another. The underlying concept is that quantum states can share entanglement between several parties, and these correlations can encode information that is shared between the parties. (Fig. 1A). Such communication ranges from quantum cryptography to the "wiring" inside a quantum computer, in which quantum correlations are established between different parts of the machine.

The most advanced communication protocol is quantum key distribution (QKD), first developed in the 1980s (*6*). This protocol is a means for establishing a shared secret key between two remote parties and relies on the ability to communicate using quantum entities between these parties. Therefore, light plays a key role, as do optical fiber and free-space communication links. (Fig. 1B) The security arises from the inability to determine the unknown state of a single quantum particle, as well as the inability to make a replica of the particle. For instance, you cannot tell the unknown polarization of a single photon by any measurement procedure, nor can you make a second photon with exactly the same state of polarization. This makes it possible for two parties to have exactly the same set of random numbers and to be sure, to an acceptable degree, that no one else has them. They may then encode messages to one another using a one-time pad with certainty that their secrets will be safe.

The degree to which noise is acceptable arises from the inevitable imperfections of the optical link and detectors. Photons get lost and noise photons (perhaps from an eavesdropper) intrude, and detectors occasionally fire without a photon present. Environmental noise and intentional noise cannot be discriminated, so the sender and receiver must attribute all noise to a potential eavesdropper. Provided the noise is low enough, this approach guarantees that the two parties can communicate securely.

At its most advanced, QKD operates at high bit rates delivering real-time key distillation that provides high security even with finite key effects, authentication, and system errors (*7*). Further, QKD systems can operate in challenging conditions. For instance, secret keys have been established between a ground station and a moving aircraft, opening the door to secure satellite-based global communications in the near future (*8*).

Interestingly, there are versions of QKD protocols in which the sender of the message and the receiver do not have to trust the network or the supplier of photons. If they use entangled photons, then the sender and receiver can evaluate whether the network is trustworthy by using a subset of the photons to test the degree of entanglement. This allows key distribution in a way that is independent of the security of the stations or their inner workings. It is essentially device-independent and enables self-certification of both QKD and other protocols relying on randomness generation (*9*).

The capacity of light for carrying information is well known in telecommunications, which can operate with near-terahertz bandwidths by means of time-frequency encoding. Photons inherit all of these features, and there exists a possibility for an ultrahigh bandwidth quantum communications system in which each photon carries many bits (*10*, *11*).

The future in quantum communication will certainly include going beyond point-to-point transmissions and will deliver secure links across multimode networks (*12*). Such networks will require advanced protocols and some new quantum devices, such as memories, both to establish and to refine entanglement between nodes (*13*).

Quantum sensing

Quantum optics also provides a means to enhance sensors that use light (*14*). The precision of sensors that use classical light is limited by the signal-to-noise ratio of the measurements—often

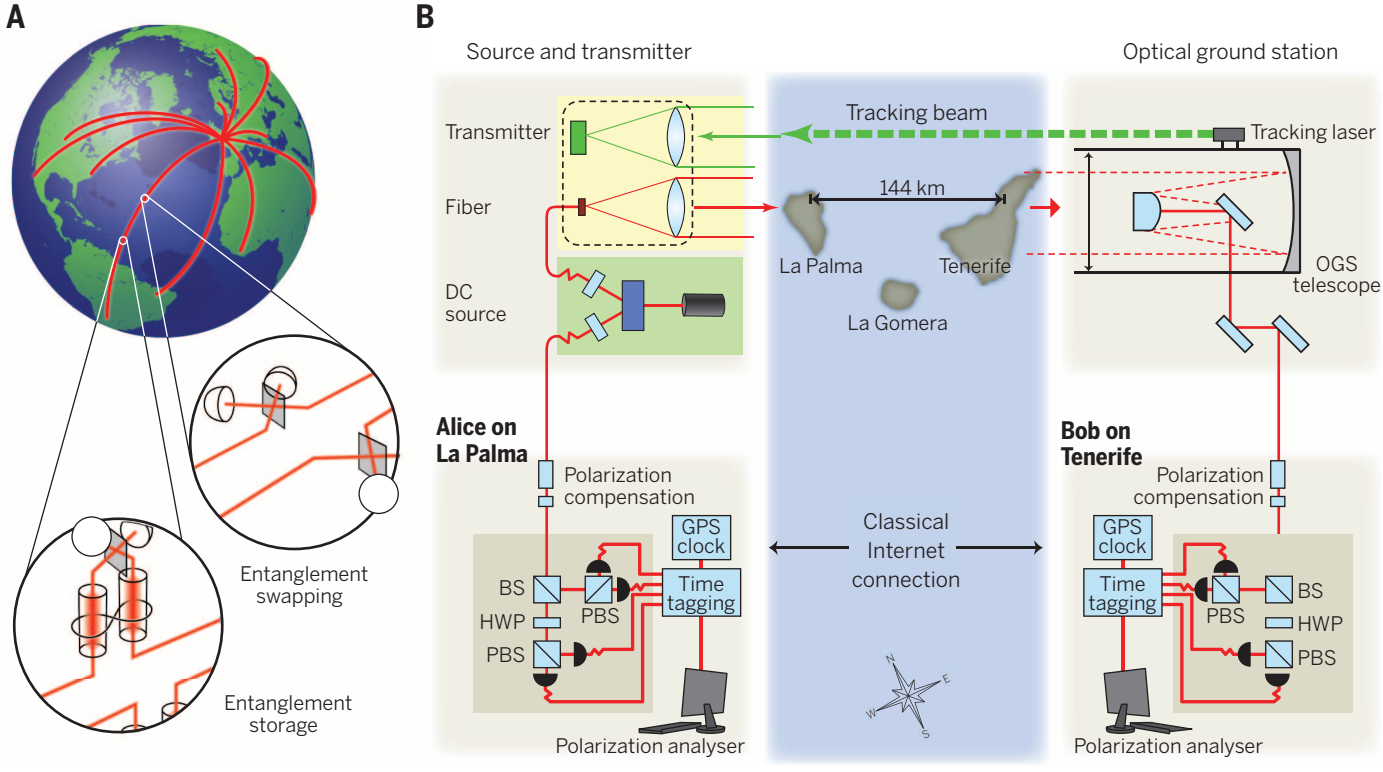

Fig. 1. Quantum communications networks. (**A**) Schematic of a long-distance repeater-based star network. Entanglement is stored in quantum memories along sublinks that are connected by entanglement-swapping operations based on linear optics and measurement. (**B**) A 144-km long-distance two-point quantum network for cryptographic key distribution based on shared entangled photon pairs between the sender (Alice) and the receiver (Bob). OGS, optical ground station; GPS, Global Positioning System; PBS, polarizing beam splitter; BS, beam splitter; HWP, half-wave plate. [From (*6*)]

the shot noise limit of photodetection, in which the "graininess" of photoelectron counts restricts the precision for a fixed intensity of light impinging on the sensor. The archetypal optical sensor measures a phase shift, which can be related to changes in refractive index in one arm of a two-path interferometer. Changes in index are related to changes in temperature, pressure, the presence of contaminant molecules, or other features of interest. In such a setup, shot noise sets the precision $\Delta\phi$ with which an optical phase shift ϕ can be measured using classical light. The precision scales as $N^{-1/2}$, where N is the mean number of photons used.

Quantum phenomena such as coherence and entanglement can be used to improve the sensitivity of measurements and thus to improve the precision of parameter estimation and the spatial and temporal resolution of imaging systems, as well as to provide the means to compensate automatically for aspects of the sensor components, such as dispersion. The most well known of these schemes is based on path entanglement: N photons arranged in a superposition of being in one path or the other. These states, labeled "N00N" states, provide an enhancement of precision such that $\Delta\phi$ scales as N^{-1}, the so-called Heisenberg limit. However, such entangled states are exceptionally sensitive to losses, so that it has not yet been possible to show true enhancement of precision after accounting for all of the photons that are put into the interferometer but do not make it through or are not detected.

Recent research has therefore focused on how the applications can be made robust against noise and imperfections that are found in real-world situations. It is now known what sorts of quantum states are useful—generally those that have some entanglement, but not the maximum possible for a given number of photons—although it is not always simple to generate the desired states (*15*). Further, it is impossible to achieve the Heisenberg limit when imperfections are present, though it is possible to improve things beyond the standard quantum limits for certain types of noise (*16*) and, more generally, to gain a substantial improvement in precision for a given amount of light. Improved precision has been demonstrated for gravitational wave sensors based on optical interferometers. Light that has very low noise in its field amplitude at certain points in the optical oscillation—a so-called squeezed state—is injected into the "empty" or vacuum input port of the interferometer. High-power light from a laser is injected into the other port. The replacement of no light at the vacuum port by squeezed light increases the signal-to-noise ratio of the measurements by 2.0 dB, so that the possibility of detecting gravity waves by this means is enhanced (*17*).

Attention is now turning to sensors that estimate several parameters. One application of this is the common situation in which there is technical noise in the parameter to be estimated. For instance, in an interferometer, where the phase shift due to a sample of material is to be determined, environmental fluctuations or temporal variations in the sample itself may cause the phase to change randomly. Therefore, both the mean and the variance of the phase shift are unknown quantities. In this case, the limits to the precision that quantum mechanics allows show some notable features. In particular, the joint estimation of several parameters is more efficient than estimating each separately (*18*, *19*).

Beyond this, imaging can be cast as a multiparameter estimation problem. For instance, in phase contrast microscopy, each pixel provides an estimate of the phase shift at that location in the image. Joint estimation of a collection of phase shifts is also more efficient than estimating each one independently (*20*, *21*). The quantum states required to achieve enhanced precision are not simple to make, so another strand of research seeks to understand how close to the quantum enhanced precision one can get using quantum light that can be feasibly generated in the laboratory (*22*).

An important use of these approaches is to apply them to distributed sensors, perhaps combining enhanced precision of multiple sensor readouts with secure polling of remote sensors. Time and frequency standards, light-based calibration, gravitometry, magnetometry, accelerometry, and imaging technologies such as microscopy are expected to benefit from these developments.

Quantum simulation and computation

It is perhaps not too great a leap to envision quantum light being useful for communications and sensing. After all, optical telecommunications and sensors are well-established technologies that we use every day. But, in principle, it is possible to build an entire computer out of light, in which photons not only play the role of transmitting information but also processing it (*23*). This idea is now more than a decade old, and it sparked a revival in thinking about quantum optical technologies for computation and simulation.

The goal of building a quantum computer using light remains a grand challenge, because the probabilistic nature of quantum operations and the imperfections leading to photon loss demand a tremendous overhead to ensure fault tolerance. Nonetheless, quantum photonics provides potentially one of the simplest routes into a quantum domain, relevant to both physics and computer science: a route in which the quantum states of the system cannot be simulated using conventional computer hardware and algorithms.

An important recent stimulus was the discovery of a new algorithm—boson sampling—that has both a well-defined computational complexity class and a clear physical implementation using light (*24*). This conjunction made it clear that it would be possible, with fewer than 100 photons, to generate quantum states, the photon statistics of which could not be efficiently computed using conventional machines. At the heart of this lies the photon bunching that arises from the bosonic nature of light.

This bunching manifests itself in the interference of two photons at a beam splitter. The input-output relationship for this optical element can be written as a 2-by-2 matrix relating the input fields to the output fields. The probability of obtaining a single photon at each of the output ports of the beam splitter when a single photon is put into each of the input ports is given by the permanent of the transfer matrix. (A permanent is similar to a determinant, but with each term carrying a positive sign rather than a negative sign associated with particular permutations of the terms being multiplied.) There are no known efficient algorithms for estimating permanents of arbitrary complex matrices. When this idea is applied to a random set of networks characterized by N-by-N matrices, then it is not possible to sample efficiently from the output photon distribution across the N output ports. When $N > 50$ or so, it is not possible to simulate the experiment using any computer currently available. This algorithm provides a prototype for a number of challenges related to computation, such as how to verify that the output of the devices is correct (*25*–*28*).

One avenue now being explored is whether such a program can be used as a quantum simulator. Quantum simulation uses controllable quantum systems to investigate the properties of other complex quantum systems and can tackle problems that are beyond the computational capability of any classical computer. Whether the boson sampling algorithm can be turned to such an application is not yet known, though several suggestions have been made. Further, small variations of the physical implementation, such as using nonlinear interaction between photons in some parts of the system, will open avenues to broader classes of quantum states and possibly realize new sorts of quantum algorithms with new applications.

Manipulating and measuring photons

The exciting visions for both science and technology promised by photonics indicate that there is still a great deal of work to be done on building efficient sources of quantum light. There are two main approaches to this task. One approach takes single atoms, excitons, color-center defects, or other single-particle light emitters to ensure that individual photons are emitted from the system one at a time. It is also possible to emit photons two at a time with careful design. In principle, this approach can produce a deterministic "on-demand" stream of photons (*29*).

The second approach is to use nonlinear optics to change the photon statistics of a light beam. For example, a laser pulse focused into an optical waveguide can undergo spontaneous scattering by means of four-wave mixing or parametric down-conversion and produce photons in pairs that are shifted in frequency from the pump laser. The photon pairs from such a source appear at random, though one of the photons can be used to "herald" the presence of the other. Both of

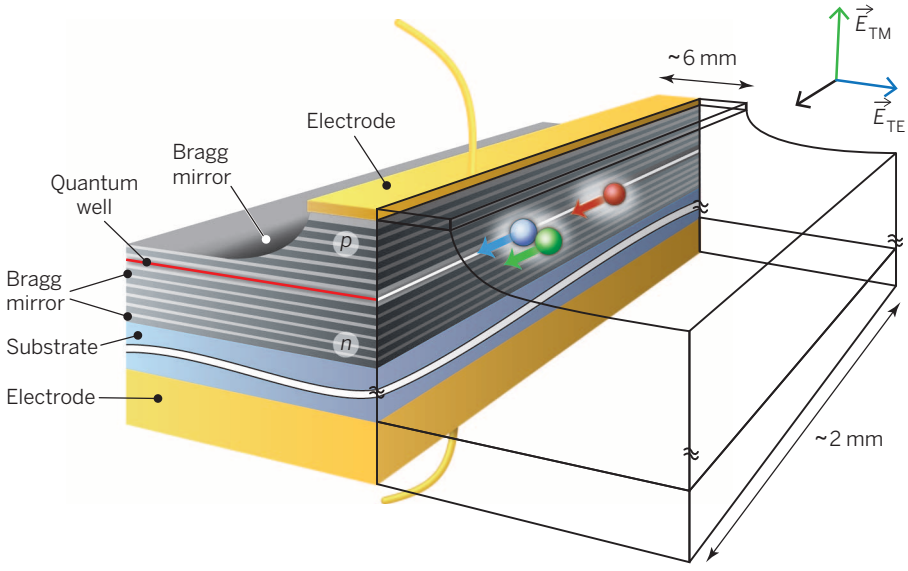

Fig. 2. An integrated quantum light source. An electrically driven semiconductor quantum-well laser generates photons (red) that are converted into telecommunications-wavelength photon pairs (blue and green) by intracavity spontaneous parametric down-conversion. [From (*32*)]

these approaches take advantage of the tremendous advances in integrated optical technology that have been developed over the past decade (*30*, *31*) (Fig. 2).

The challenges in both cases are to produce photons that are in pure quantum states and to capture them. A small loss or detector inefficiency can easily reduce the rate at which large photon numbers are detected. If the efficiency is 0.95, then the probability to detect 50 photons produced on demand simultaneously is less than 10%. Further, if the photons are not in pure states, they are, in principle, distinguishable from one another, and thus quantum interference between independent photons does not occur. As noted, this bosonic bunching is at the heart of building macroscopically complex quantum states.

The space-time field structure of the individual photons is therefore critical, and much effort has been devoted to building light sources that can be replicated many times, each of which produces photons of the same "shape" in pure states within a single mode having this shape. For single-emitter sources, this demands very-high-quality cavities, so that the Purcell enhancement overcomes any intrinsic dephasing of the emitting atom or exciton.

For nonlinear optical sources, careful management of the phase-matching and energy-matching conditions are required so that there is no hidden entanglement between unused or unobserved degrees of freedom. The use of waveguides—which provide a means to control dispersion of the interacting fields and, thus, the phase matching—has enabled a new class of high-purity single-photon and squeezed light sources (*30*, *31*). Further, integration of an entire quantum light source is now possible. For example, it was recently demonstrated that it is possible to produce photon pairs by combining an electrically driven optical pump laser and a downconverter on a single microchip, operating at room temperature (*32*).

To prepare complex photonic states, the photons must interact with one another. Therefore, a long-standing goal in quantum optics has been to explore the extension of nonlinear optics to the single-photon level, where the presence of just one photon can change the state of a second photon.

The key to achieving this is to make the volume of space occupied by the photon very small and to use the sharp optical resonances of cold atoms to provide an enhanced nonlinearity. Recently, much progress has been made using this approach by confining the light to the mode of a tiny optical cavity or to a waveguide. Conventional free-space cavities, cavities using modern fabrication methods based on photonic nanostructures coupled to optical fibers (Fig. 3), and tapered fibers embedded in a gas of cold atoms have all shown the possibility to control light by light. For example, an atom placed near the surface of a glass "bottle" resonator, the surface modes of which have a high quality factor, is able to couple very strongly to the optical field. A recent experiment showed a large photon-photon phase shift using an atom confined to a planar photonic band-gap cavity, itself coupled to a tapered optical fiber, which compressed the mode of the photon to a submicron diameter (*33*).

There is a second way to enable photons to interact nonlinearly: it uses linear optics as the means to bring photons together. Photodetection provides the nonlinear operation that selects appropriate outcomes from the bunching that occurs when photons collide in a linear network. Networks consisting of beam splitters bring together multiple photons, which, if they occupy identical modes with the same space-time field profiles, can be made to realize conditional operations, such as phase shifts at the level of single quanta.

The linear optical approach has the advantage that one can use low-loss guided-wave components developed for telecommunications and the very high bandwidth and wavelength diversity that is possible with light. But it has the disadvantage that the operations are probabilistic—the outcome sought does not always occur. This makes scaling the network impossible. The solution is to store the outcome of successful operations until other network operations are successful, then to concatenate the outcomes, and to repeat this process (*34*). The concept of network resynchronization by this approach borrows from well-known approaches for scaling imperfect communications networks, as well as modern telecommunications switching.

A photonic quantum memory, which interconverts "flying" optical and stationary long-lived material excitations (Fig. 1A), provides one way to address this problem. A quantum memory requires an enhanced interaction between light and atoms, which can be achieved either by placing

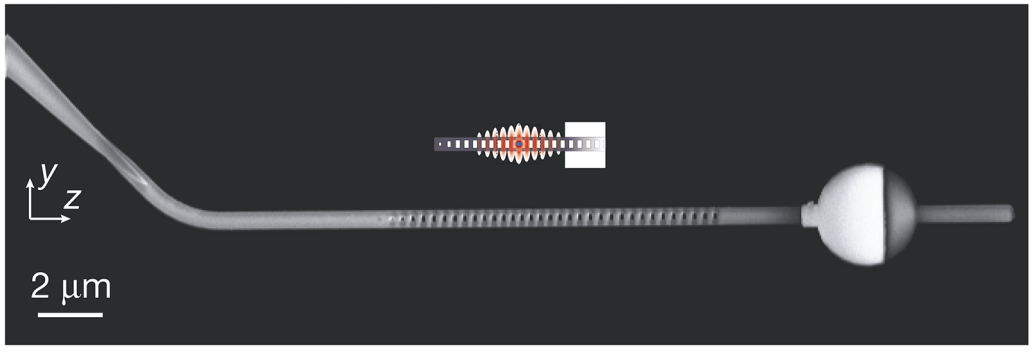

Fig. 3. A silicon nitride photonic crystal cavity provides an exceptionally small mode volume in which light from a tapered optical fiber (shown at left) interacts strongly with a single atom (indicated by the orange dot) held in a second light beam. The structure on the right is a heating pad for tuning the cavity resonance so that it coincides with the atomic optical resonance. [After (*33*)]

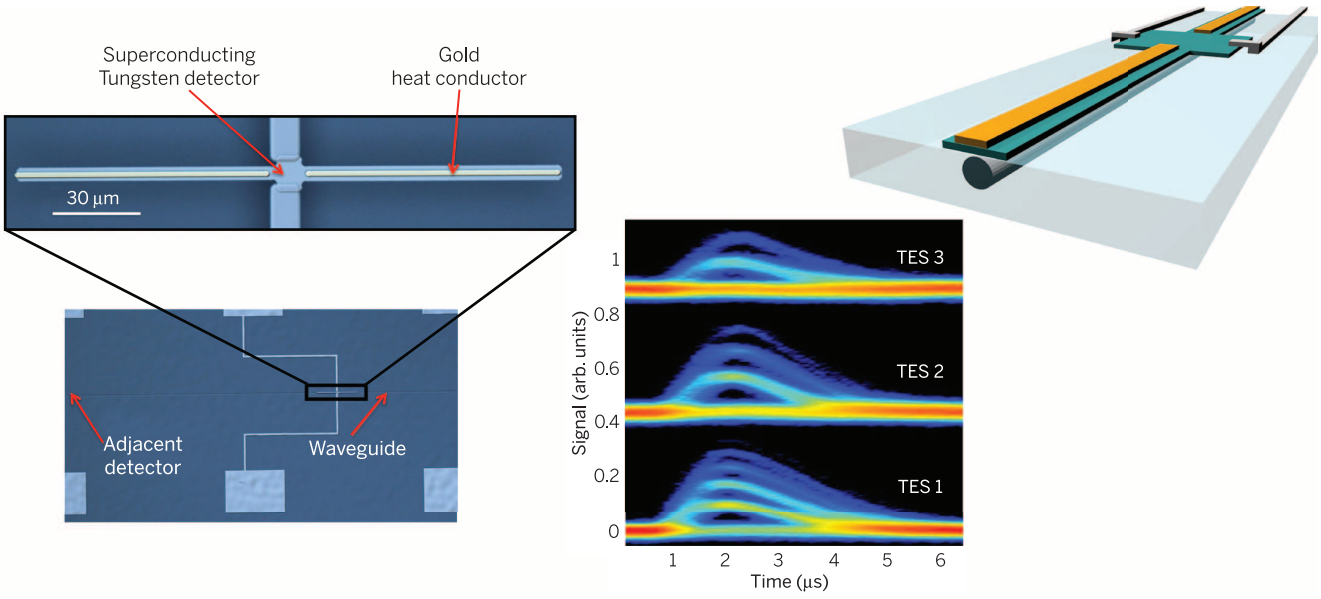

Fig. 4. A waveguide-based efficient photon-number resolving detector based on a superconductor (tungsten) biased near the transition edge. The evanescent field of the guide couples the light into the tungsten where it is absorbed. A gold wire conducts heat to the superconducting region, where the changes in resistance due to the change in temperature modifies the current through the device, which can be measured. Typical photocurrent pulses from three sequential detectors on a single waveguide enable up to 15 photons to be resolved with an efficiency of more than 85%. TES, transition-edge superconducting detectors. arb, arbitrary.

a single atom within a high-finesse optical cavity (*35*) or by using an ensemble of many thousands or millions of atoms (*36*). Several approaches to memories based on ensembles, including hot and cold atoms, as well as cryogenically cooled doped-insulating solids, have been studied, and it is now possible to store and retrieve light pulses with ~90% overall efficiency. Various schemes allow storage of broadband photons, though as yet with decreasing efficiency as the bandwidth increases. These are based on a form of either electromagnetically induced transparency or off-resonant Raman absorption into a metastable state or resonant absorption followed by transfer to this state.

The main outstanding problem with these memories is the noise level. As yet, only very few experiments have shown the storage and retrieval of single photons with low enough noise to preserve their character. Almost all of these experiments have been in cold atomic gases producing narrow-band photons. To date, only one demonstration has been in room-temperature memory. In this experiment, a terahertz-bandwidth photon was stored as a phonon in a vibrational mode in diamond, albeit with a short coherence time (*37*).

The current generation of cold-atom–based memories operates with high efficiency (>70%) and long storage times (>1 ms) and has the ability to store single photons (*38*). Nonetheless, the stringent requirements for broadband memories to be employed in long-distance quantum repeaters have not yet been met (*39*).

Using memories allows new operations, such as teleportation. This has been achieved by using the storage capabilities of the spins of color centers tied to nitrogen vacancies (NVs) in diamond at low temperature. Photons emitted from the NV center are correlated in polarization with the electronic spins residing there. A pair of photons emitted from two centers can interfere in an optical network and thus prepare an entangled state of the two NVs that can be used to teleport the state of a third NV (*40*).

The registration of individual photons or field amplitudes with very high efficiency is critical to scaling up a photonic quantum network. Notable advances in detectors have occurred over the past few years, so that now it is possible to count the number of photons in a pulse of light with efficiencies >95% and a range up to ~10 photons (*41*). This opens a wide swath of new types of quantum operations, such as state preparation based on heralding the vacuum state of no photons at all. Such operations are at the heart of entanglement-enhancing protocols such as distillation.

Very efficient means of detecting single photons have been achieved by means of both conventional absorptive detectors, in which the light causes an excitation of the detector material, as well as less conventional dispersive detection, in which the light causes a change in the medium without depositing energy in it.

Great strides have been made in detectors based on absorption by using the photon's energy to generate a change in the state of a superconducting material. For example, in transition-edge superconducting detectors, the change in temperature of a small piece of tungsten causes a change in the resistance of the material and thus a change in current, which is detected by a superconducting quantum interference device (Fig. 4). Alternatively in a nanowire detector, the resistance of a very narrow wire of niobium nitride suddenly changes upon absorption of a photon (*42*). Both types of detectors can be very efficient (*43*) and both need to operate at a temperature where the material is superconducting, so that cryogenic cooling to well below a few kelvin is needed.

Single-atom detectors allow the possibility of nondestructive measurement of single photons. An atom in an optical cavity can interact sufficiently strongly with a single photon to cause a shift in the relative phase of population in two metastable ground states. A measurement of a phase shift then signals that a photon has passed through the cavity and yet has not been absorbed (*44*). This is a new capability and promises new types of operations that will enhance the power of quantum networks by providing a means to implement a measurement-based nonlinearity for photon-photon interaction.

Conclusions

Despite the long history of quantum optics, light continues to be a medium that can deliver surprises, for both new science and new applications. The developments in optical technology, sources, guided-wave optics, and detectors have opened up promising vistas for this field, which will yield new modes of communication, sensing, and simulation based on light in the near future. The synergy of new discovery and technology that is central to science is as vital as ever for quantum optics.

REFERENCES AND NOTES

1. M. Ringbauer *et al.*, *Nat. Phys.* **11**, 249–254 (2015).
2. S. Garnerone, P. Zanardi, D. A. Lidar, *Phys. Rev. Lett.* **108**, 230506 (2012).
3. T. Calarco, P. Grangier, A. Wallraff, P. Zoller, *Nat. Phys.* **4**, 2–3 (2008).
4. B. Sanguinetti, A. Martin, H. Zbinden, N. Gisin, *Phys. Rev. X* **4**, 031056 (2014).
5. See, for example, www.idquantique.com/random-number-generators/products/quantis-usb.html.
6. H.-K. Lo, M. Curty, K. Tamaki, *Nat. Photonics* **8**, 595–604 (2014).
7. N. Walenta *et al.*, *New J. Phys.* **16**, 013047 (2014).
8. S. Nauerth *et al.*, *Nat. Photonics* **7**, 382–386 (2013).
9. U. Vazirani, T. Vidick, *Phys. Rev. Lett.* **113**, 140501 (2014).
10. I. Ali-Khan, C. J. Broadbent, J. C. Howell, *Phys. Rev. Lett.* **98**, 060503 (2007).
11. T. Zhong *et al.*, *New J. Phys.* **17**, 022002 (2015).
12. H. J. Kimble, *Nature* **453**, 1023–1030 (2008).
13. N. Sangouard, C. Simon, H. de Riedmatten, N. Gisin, *Rev. Mod. Phys.* **83**, 33–80 (2011).
14. V. Giovannetti, S. Lloyd, L. Maccone, *Nat. Photonics* **5**, 222–229 (2011).
15. R. Demkowicz-Dobrzański, L. Maccone, *Phys. Rev. Lett.* **113**, 250801 (2014).
16. R. Chaves, J. B. Brask, M. Markiewicz, J. Kołodyński, A. Acín, *Phys. Rev. Lett.* **111**, 120401 (2013).
17. H. Grote *et al.*, *Phys. Rev. Lett.* **110**, 181101 (2013).
18. M. G. Genoni, S. Olivares, M. G. A. Paris, *Phys. Rev. Lett.* **106**, 153603 (2011).
19. M. D. Vidrighin *et al.*, *Nat. Commun.* **5**, 3532 (2014).
20. P. C. Humphreys, M. Barbieri, A. Datta, I. A. Walmsley, *Phys. Rev. Lett.* **111**, 070403 (2013).
21. Y.-L. Zhang, H. Wang, L. Jing, L. Z. Mu, H. Fan, *Sci. Rep.* **4**, 7390 (2014).
22. M. Lang, C. Caves, *Phys. Rev. A* **90**, 025802 (2014).
23. P. Kok *et al.*, *Rev. Mod. Phys.* **79**, 135–174 (2007).
24. S. Aaronson, A. Arkhipov, in *Proceedings of the 43rd Annual ACM Symposium on Theory of Computing* (Association for Computing Machinery, New York, 2011), pp. 333–342.
25. J. B. Spring *et al.*, *Science* **339**, 798–801 (2013).
26. M. A. Broome *et al.*, *Science* **339**, 794–798 (2013).
27. M. Tillman *et al.*, *Nat. Photonics* **7**, 540–544 (2013).
28. A. Crespi *et al.*, *Nat. Photonics* **7**, 545–549 (2013).
29. C. L. Salter *et al.*, *Nature* **465**, 594–597 (2010).
30. J. B. Spring *et al.*, *Opt. Express* **21**, 13522–13532 (2013).
31. M. Förtsch *et al.*, *Nat. Commun.* **4**, 1818 (2013).
32. F. Boitier *et al.*, *Phys. Rev. Lett.* **112**, 183901 (2014).
33. D. E. Chang, V. Vuletic, M. D. Lukin, *Nat. Photonics* **8**, 685–694 (2014).
34. J. Nunn *et al.*, *Phys. Rev. Lett.* **110**, 133601 (2013).
35. H. P. Specht *et al.*, *Nature* **473**, 190–193 (2011).
36. Y. O. Dudin, L. Li, A. Kuzmich, *Phys. Rev. A* **87**, 031801(R) (2013).
37. D. G. England, P. J. Bustard, J. Nunn, R. Lausten, B. J. Sussman, *Phys. Rev. Lett.* **111**, 243601 (2013).
38. D.-S. Ding, Z. Y. Zhou, B. S. Shi, G. C. Guo, *Nat. Commun.* **4**, 2527 (2013).
39. W. J. Munro, K. Azuma, K. Tamaki, K. Nemoto, *IEEE J. Select. Top. Quant. Elec.* **21**, 6400813 (2015).
40. W. Pfaff *et al.*, *Science* **345**, 532–535 (2014).
41. A. E. Lita, A. J. Miller, S. W. Nam, *Opt. Express* **16**, 3032–3040 (2008).
42. J. J. Renema *et al.*, *Phys. Rev. Lett.* **112**, 117604 (2014).
43. F. Marsili *et al.*, *Nat. Photonics* **7**, 210–214 (2013).
44. A. Reiserer, S. Ritter, G. Rempe, *Science* **342**, 1349–1351 (2013).

ACKNOWLEDGMENTS

I acknowledge support from the UK Engineering and Physical Sciences Research Council, the UK Quantum Technology Network, the European Commission through the Marie Curie Actions, the European Research Council, and the U.S. European Office of Aerospace Research and Development. I thank J. Nunn and W. S. Kolthammer for insightful discussions and helpful comments on the manuscript.

10.1126/science.aab0097

REVIEW

Beyond crystallography: Diffractive imaging using coherent x-ray light sources

Jianwei Miao,[1]* Tetsuya Ishikawa,[2] Ian K. Robinson,[3,4] Margaret M. Murnane[5]

X-ray crystallography has been central to the development of many fields of science over the past century. It has now matured to a point that as long as good-quality crystals are available, their atomic structure can be routinely determined in three dimensions. However, many samples in physics, chemistry, materials science, nanoscience, geology, and biology are noncrystalline, and thus their three-dimensional structures are not accessible by traditional x-ray crystallography. Overcoming this hurdle has required the development of new coherent imaging methods to harness new coherent x-ray light sources. Here we review the revolutionary advances that are transforming x-ray sources and imaging in the 21st century.

The x-ray science community has witnessed two revolutionary developments over the past two decades. First, large- and small-scale coherent x-ray sources, including advanced synchrotron sources, x-ray free electron lasers (XFELs), and high harmonic generation (HHG) sources, are under rapid development worldwide (*1*–*3*). Compared with the previous generations of x-ray sources, the new light sources have remarkable properties. XFELs increase the coherent x-ray flux by nine orders of magnitude, while tabletop HHG sources generate a coherent x-ray supercontinuum that spans the entire electromagnetic spectrum from the ultraviolet (UV) to the kilo–electron volt (keV) region, covering 12 octaves of bandwidth. In addition, HHG and XFEL pulses are extremely short, ranging from tens of attoseconds to hundreds of femtoseconds. Second, a new approach to x-ray crystallography, known as coherent diffractive imaging (CDI), enables structure determination of noncrystalline specimens and nanocrystals with a resolution limited only by the spatial frequency of the diffracted waves (*4*). Moreover, CDI enables simultaneous amplitude and phase contrast imaging. In recent years, the combination of powerful coherent x-ray light sources and CDI methods, coupled with advanced x-ray detectors and computational algorithms, has opened up new research frontiers in the physical and biological sciences that are simply not attainable with conventional x-ray crystallography (*5*–*19*). Here, we review progress in CDI and the advanced x-ray light sources that are allowing this new imaging modality to blossom. We highlight the exciting scientific discoveries that were enabled by these new capabilities and look forward with great anticipation to the new frontiers in imaging that are emerging.

[1]Department of Physics and Astronomy and California NanoSystems Institute, University of California, Los Angeles, CA 90095, USA. [2]RIKEN SPring-8 Center, Kouto 1-1-1, Sayo, Hyogo 679-5148, Japan. [3]London Centre for Nanotechnology, University College London, 17-19 Gordon Street, WC1H 0AH, UK. [4]Research Complex at Harwell, Harwell Campus, Didcot, Oxford OX11 0DE, UK. [5]JILA, University of Colorado, and National Institute of Standards and Technology (NIST), Boulder, Boulder, CO 80309, USA.
***Corresponding author. E-mail: miao@physics.ucla.edu**

Coherent diffractive imaging methods

In a traditional microscope, a lens is used to collect the light scattered by a sample and thereby recover an image. However, in the x-ray region, the use of lenses introduces a severe limitation because diffractive x-ray optics must be used, and these are far from perfect. Although x-ray microscopes with ~10-nm spatial resolution have been demonstrated, ~25 nm is more typical—which is nowhere near the wavelength limit (*20*). CDI avoids this limitation by illuminating an object with a coherent laser-like beam and collecting the scattered light on a detector (Fig. 1, A to E). The image of the object can then be recovered with an advanced phase retrieval algorithm by taking advantage of the fact that the diffracted wave is proportional to the Fourier transform of the object (*4*). However, although the magnitude squared of the Fourier transform can be measured by a detector, the phase information is lost. This constitutes the well-known phase problem associated with recovering an image from a diffraction pattern. For a noncrystalline specimen, the diffraction pattern is continuous and can be sampled at a frequency finer than the Nyquist interval (the inverse of the specimen size). For a noise-free diffraction pattern, when the number of independently sampled intensity points is larger than (or equal to) the number of unknown variables associated with a specimen, the phase information is in principle encoded inside the diffraction intensity (*21*) and can usually be retrieved by iterative algorithms (*22*, *23*). Furthermore, because no optics is inserted between the specimen and detector, CDI represents the most photon-efficient x-ray imaging modality (*24*).

By combining phase retrieval algorithms (Box 1) and coherent x-ray sources, several CDI methods have now been developed in both transmission and reflection modes, including plane-wave CDI (PCDI), Bragg CDI (BCDI), ptychographic CDI (ptychography), Fresnel CDI, reflection CDI, sparsity CDI, and others (*5*–*18*, *25*, *26*). Figure 1, A to

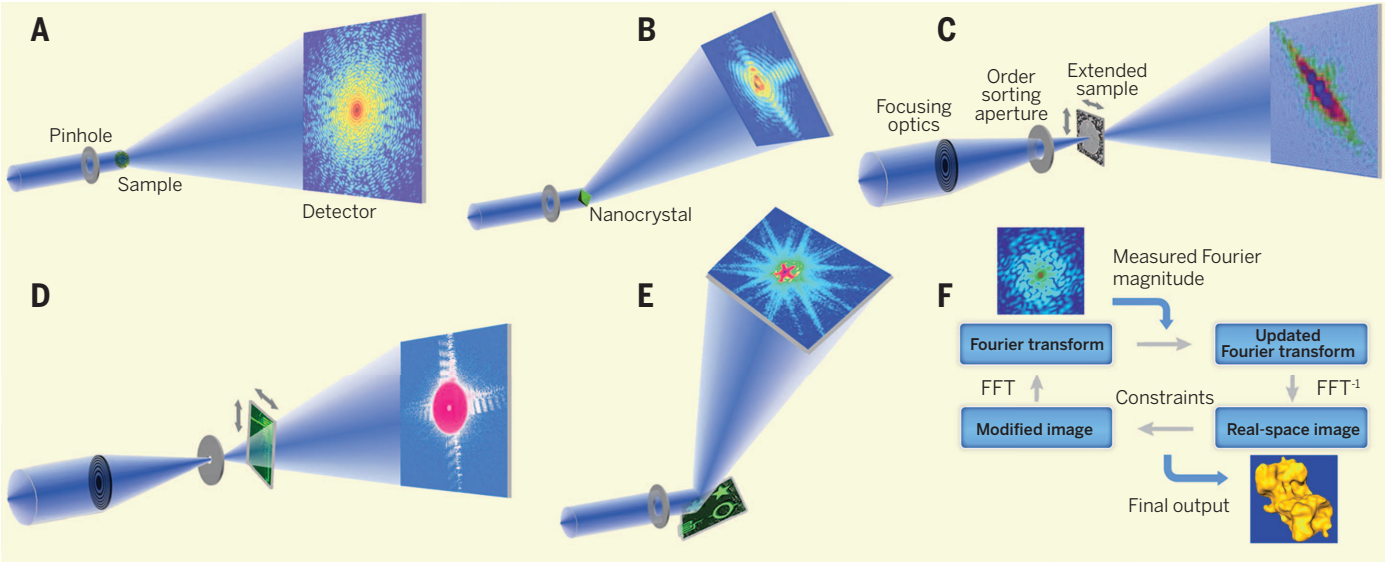

Fig. 1. Schematic layout of five main CDI methods and iterative phase retrieval algorithms. (**A**) Plane-wave CDI: A plane wave illuminates a sample, and an oversampled diffraction pattern is measured by a detector. (**B**) Bragg CDI: The diffraction pattern surrounding a Bragg peak is acquired from a nanocrystal. (**C**) Ptychographic CDI: A coherent x-ray probe is generated by an aperture or focusing optics. An extended sample is scanned through the probe on a 2D grid, and diffraction patterns are collected from a series of partially overlapping regions. (**D**) Fresnel CDI: A sample is positioned in front of (or behind) the focal spot of a coherent x-ray wave, and the Fresnel diffraction pattern is measured by a detector. (**E**) Reflection CDI: A coherent x-ray wave is specularly reflected off a sample on a substrate, and the diffraction intensity around the reflected beam is collected by a detector. (**F**) Phase retrieval algorithms iterate back and forth between real and reciprocal space. In each iteration, various constraints, including support, positivity (i.e., electron density cannot be negative), or partially overlapping regions, are enforced in real space, while the measured Fourier magnitude is updated in reciprocal space. Usually, after hundreds to thousands of iterations, the correct phase information can be recovered.

E, shows the schematic layout of the five major CDI methods to date. In the original PCDI, a plane wave illuminates an object in transmission, and the diffraction pattern is measured by an area detector (Fig. 1A). To satisfy the oversampling criterion, either an isolated object or a finite illumination had to be implemented. To obtain 3D structural information, a tilt series of diffraction patterns is acquired over various sample orientations and then phased to obtain a 3D image (*6*, *11*). Because PCDI is insensitive to sample drift and vibration, it achieved the highest 2D and 3D spatial resolution (≈2 and 5.5 nm, respectively) of any x-ray imaging method (*27*, *28*). In BCDI, a coherent beam of x-rays illuminates a nanocrystal, and the diffraction pattern surrounding a Bragg peak is measured (Fig. 1B) (*5*, *8*). Inversion of the diffraction pattern yields a complex 3D image, whose phase is related to the displacement and strain field of the crystal lattice. Furthermore, BCDI is also useful for powder and polycrystalline samples, where many randomly oriented grains are in the beam at the same time. Because the Bragg peak of each grain will be in a different location in reciprocal space, individual grains can be isolated from their neighbors.

Ptychography brings powerful new imaging capabilities because it can image an extended sample in either reflection or transmission modes, with near-wavelength spatial resolution (≈1.3 λ) horizontally and subnanometer (sub-nm) resolution vertically (*18*, *29*). In ptychography, the sample is scanned on a 2D grid to collect a series of diffraction patterns from partially overlapping regions (Fig. 1C). This additional redundancy in the diffraction data enables robust image reconstruction with quantitative phase contrast (*12*), while also extracting the complex x-ray illumination beam, correcting for errors in the scanning stages, and improving the convergence of the iterative phase retrieval process (*13*, *18*). In Fresnel CDI, a sample is illuminated by a curved wavefront through defocusing of an x-ray beam, and the resulting Fresnel diffraction pattern is measured by a detector (Fig. 1D). If the incident beam is independently characterized and the geometrical dimensions of the experiment are accurately determined, the exit wave at the sample can be quantitatively reconstructed by using an iterative algorithm with fast convergence (*10*).

CDI has also been successfully implemented in reflection mode, giving beautiful 3D height maps of a surface, with near-wavelength transverse resolution, sub-nm vertical resolution, and very high phase and amplitude contrast due to the short wavelength of the illumination light (*18*, *26*, *30*, *31*). Moreover, the geometry is very simple: A coherent x-ray beam illuminates a sample, and the diffracted light can then be collected with very high numerical aperture (Fig. 1E). When combined with powerful ptychographic imaging, high-quality images of extended samples can be obtained (*18*). Reflection CDI is complementary to other imaging modalities, such as scanning electron microscopy (SEM) and atomic force

Box 1. Iterative phase retrieval algorithms.

A common feature of these algorithms requires iterating between real and reciprocal space (*23*), consisting of the following four steps in each iteration (Fig. 1F): (i) The algorithms usually start with a random phase set as the initial guess. By combining this random phase set with the measured Fourier magnitude and then applying an inverse fast Fourier transform (FFT), an initial image is computed; (ii) depending on oversampling of the diffraction intensity, a support (i.e., a boundary slightly larger than the sample envelope) can be estimated from the image. The electron density outside the support of the image is reduced, while the negative electron density inside the support is modified—for example, by setting to zero, depending on the algorithm; (iii) by applying a FFT to the updated image, a new Fourier transform is generated; and (iv) by replacing its magnitude with the measured data, a better estimate of the Fourier transform is obtained and used for the next iteration. This process is then repeated, and each iteration is characterized by an error metric, defined as the difference between the calculated and measured Fourier magnitudes. Usually, after hundreds to thousands of iterations, the correct phase set can be retrieved.

microcopy (AFM), allowing for long (>3 cm) working distances, less damage, and higher-contrast imaging than other approaches.

A revolution in coherent x-ray light sources

In the past decade, there has also been a revolution in the development of both large-scale and tabletop coherent x-ray sources (Fig. 2). Large-scale x-ray sources are based on high-energy accelerators, which emit x-rays with varying degrees of coherence (*23*). When the first so-called third-generation x-ray synchrotron facilities were designed, it was widely believed that undulators for hard x-rays would require high-energy electron beams. As a result, the first third-generation facilities used electron storage rings with energies of 6 to 8 GeV and low-emittance electron beams to enhance the brightness of the undulator radiation (*23*). However, despite their small source size and long source-sample distance, these third-generation facilities radiated only a small amount of spatially coherent light (≈0.1% of total). Nevertheless, by using a small aperture, this small fraction of spatially coherent light could be extracted and used to perform the first CDI experiment at the National Synchrotron Light Source (*4*). A maturation of undulator technology enabled the development of higher harmonics and shorter-period undulators, which can produce hard x-rays without requiring high-energy storage rings. Thus, lower energy (~3 GeV), medium-sized storage rings are now used for hard x-ray sources where a wide variety of CDI activities are now in progress. Another new and important trend of accelerator-based advanced x-ray sources is the use of a new magnetic lattice, known as a multi-bend-achromat, to more tightly focus the electron beam, further reduce its emittance, and increase the x-ray brilliance (*23*).

At the turn of the 21st century, brighter XFEL sources were developed (*23*) based on self-amplified spontaneous emission (SASE) (Fig. 2A, inset) (*1*, *2*). When a low-emittance, high-density, and high-energy electron bunch is injected into a long undulator (~100 m), it initially emits synchrotron radiation. The emitted photons travel at the speed of the light inside the undulator, which is only slightly faster than the velocity of the high-energy electron bunch. As a result, the radiation interacts back with the electron bunch. If the undulator is designed such that the interaction makes the faster electrons slower and slower electrons faster, the electron bunch density is periodically modulated by the radiation, a process called microbunching. The process exponentially increases the intensity of the emitted radiation, as well as the interaction between the radiation and the electron bunch, introducing "gain" in a manner similar to that of a conventional laser. At the end of the long undulator, the gain is saturated and an extremely intense XFEL pulse is produced. The peak brightness of the XFEL pulse is 10^9 times higher than that of the most powerful third-generation source (Fig. 2A), while their pulse duration ranges from tens to hundreds of femtoseconds, although with lower repetition rate and some timing jitter.

In parallel with advances in large-scale coherent x-ray facilities, the same revolution that visible lasers underwent in the 1960s is now happening for tabletop coherent x-ray sources. Interestingly, the first tabletop-scale coherent soft x-ray source was not based on creating a population inversion to support laser action, but was rather based on nonlinear optics. In nonlinear optics, the high electric fields that are present in a focused laser beam can drive electrons in a highly irregular (anharmonic) motion that reradiates harmonics of the driving laser light at much shorter wavelengths. In HHG, the laser field intensity must be sufficient to tunnel ionize the atoms used as the nonlinear medium, by suppressing the Coulomb field that normally binds the electron to the ion. For the few-femtosecond time interval during which this is happening, the laser-driven quantum wave function of the electron can radiate coherent high-harmonic x-rays. If x-rays from a macroscopic number of atoms interfere constructively to generate a laser-like beam, in a process called phase matching, HHG can have spectacular temporal and spatial coherence. This is because of the ultra-precise timing relationship between the laser and x-ray fields that are synchronized to less than 1 attosecond.

Although its physical manifestation is very different, HHG can also be thought of as a coherent laser-driven version of the Röntgen x-ray tube. However, the full power of femtosecond lasers for manipulating the quantum wave function of an electron is now being realized. By changing the color and polarization of the driving laser, the HHG spectrum, pulse duration, and polarization can be controlled (*3*, *32*, *33*), thus making it possible to generate x-ray bursts with durations from tens of attoseconds to tens of femtoseconds, with a coherent bandwidth spanning 12 octaves, from <100 meV to ≈1 keV. One recent surprising finding is that longer-wavelength mid-infrared lasers can generate shorter-wavelength bright x-ray beams. Using 4-μm driving lasers, for example, HHG emerges as a broad coherent supercontinuum, spanning the entire electromagnetic spectrum from the ultraviolet to the soft x-ray keV region of

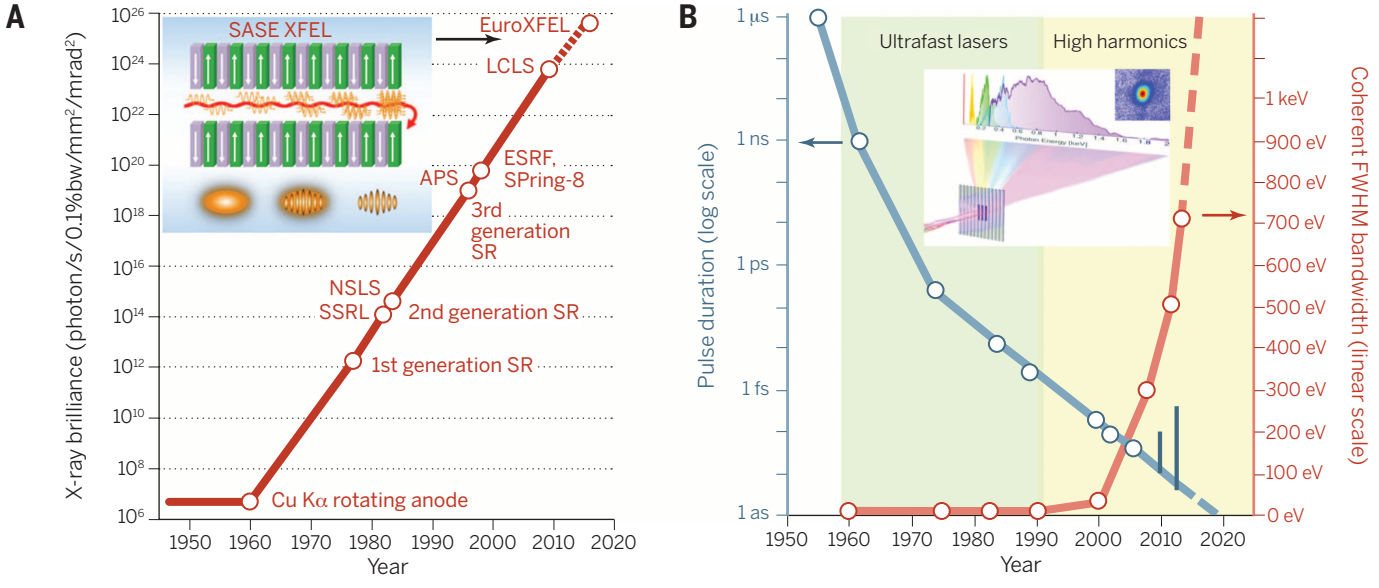

Fig. 2. Revolution in coherent x-ray sources. (**A**) The x-ray brilliance of coherent light sources has improved by 20 orders of magnitude in 6 decades (brilliance is a measure of coherent x-ray flux). The inset shows the SASE process to produce extremely intense and ultrashort XFEL pulses. (**B**) Progress in tabletop coherent bandwidth and pulse duration as a function of year. Coherent high harmonics can generate an x-ray supercontinuum or a series of narrowband peaks spanning the UV to the keV region, supporting the shortest bursts of light to date. The vertical lines show both the transform-limited pulse duration and the chirped isolated bursts that emerge when HHG is driven by infrared lasers. The inset shows the HHG spectrum and laser-like beam. FWHM, full width at half maximum.

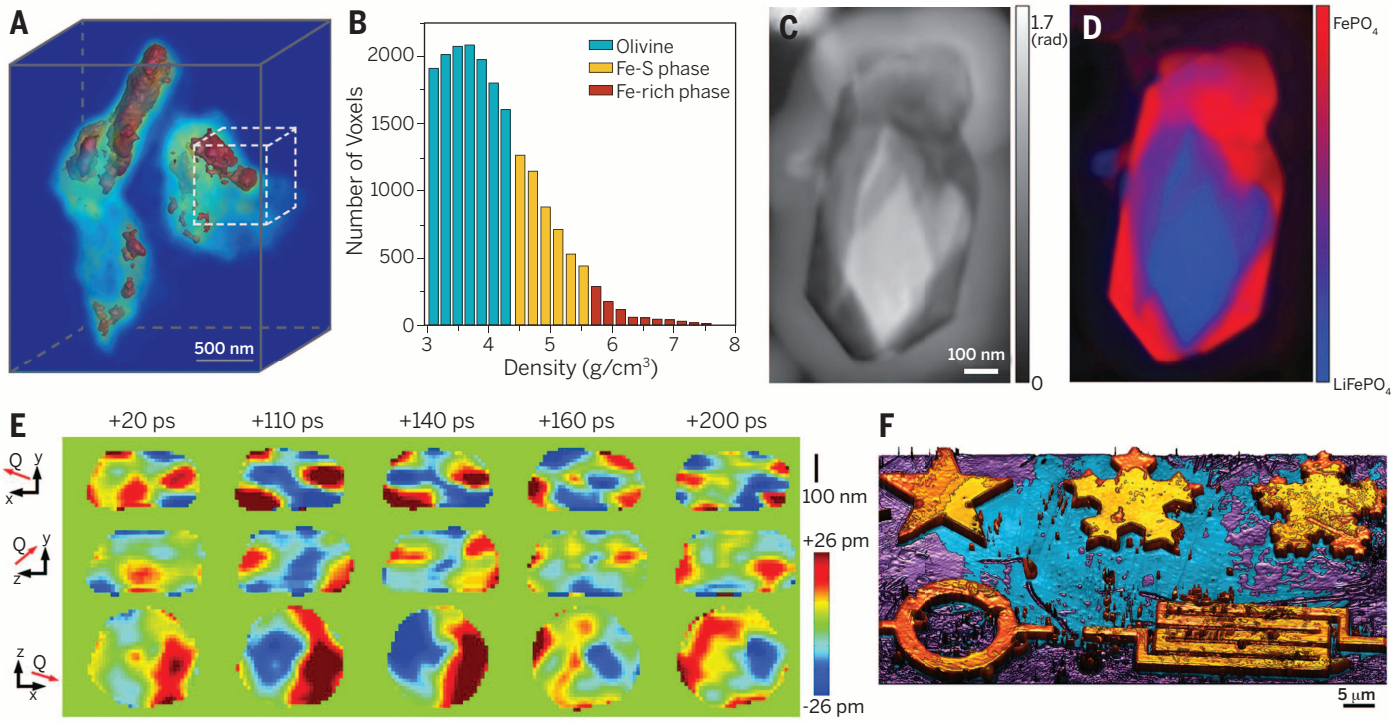

Fig. 3. Physical science applications of diffractive imaging methods with coherent x-rays. (**A**) 3D morphology of Fe-rich and Fe-S phases in an olivine matrix (*37*). (**B**) Histogram of the Fe-rich phase, Fe-S phase, and olivine distribution within a dotted-line cube in (A). (**C**) Phase of the ptychographic reconstruction of a partially delithiated nanoplate of $LiFePO_4$ (*40*). (**D**) Chemical composition image of the nanoplate showing the distribution of two chemical species: $LiFePO_4$ and $FePO_4$. (**E**) 3D imaging of lattice dynamics in a gold nanocrystal (*17*). Orthogonal cut through the center of the nanocrystal showing the displacement as a function of delay time at three different directions. The **Q** vector represents the direction of the displacement field. (**F**) 3D profile of a ptychographic reconstruction with spatial resolution of <1.3 λ horizontally and sub-nm vertically, which was acquired by using a tabletop HHG source with <1-min exposure time (*18*).

the spectrum to wavelengths <8 Å. Moreover, these x-rays emerge as isolated attosecond bursts, which are predicted to scale to the subattosecond (i.e., zeptosecond) regime with longer-wavelength lasers (*33*). In contrast, using intense UV driving lasers, HHG emerges as a series of bright narrowband peaks, with ≈10-fs pulse duration. Finally, by manipulating the electron wave function with bichromatic (two-color) circularly polarized counter-rotating laser beams, it is now possible to produce bright circularly polarized harmonics that complement the bright linearly polarized HHG beams that have been available for 20 years (*32*).

The powerful quantum coherence of HHG makes it ideal for imaging the fastest dynamics relevant to function in atoms, molecules, nanosystems, and materials, at multiple atomic sites simultaneously. HHG is complementary to the powerful XFEL machines, because it can be driven by a small-scale (≈mJ energy) laser at very high repetition rates (1 to 100 kHz). Although the pulse energies are lower than those available at XFELs (nJ versus mJ), the repetition rates are higher and are ideal for several exciting applications discussed below (*3*, *32*–*36*).

Multidisciplinary science enabled by coherent x-ray light sources and diffractive imaging

CDI is ideally suited for quantitative 3D characterization of materials at the nanoscale: X-rays have a larger penetration depth than electrons, so that destructive sample preparation can often be avoided. Moreover, by quantifying the incident and diffracted x-ray flux, CDI can extract the mass density and thus distinguish different phases in materials in three dimensions (*37*). Furthermore, the presence of core shell x-ray absorption provides chemical contrast, while their polarization can be exploited to provide magnetic contrast and molecular orientation. Thus, CDI enables nanoscale chemical, elemental, and magnetic mapping of complex matter (*38*–*40*). Finally, the high temporal resolution of the new coherent x-ray sources such as HHG and XFELs already make it possible to capture the fastest charge, spin, and lattice motions in matter, on multiple length and time scales.

In recent work, PCDI was used to quantitatively image a molten Fe-rich alloy and crystalline olivine sample, which was synthesized at 6 GPa and 1800°C to mimic the conditions of Earth's upper mantle (*37*). Figure 3A shows the 3D morphology of the Fe-rich and Fe-S phases in an olivine matrix in which the molten Fe exhibits varied shapes and sizes. A histogram of the 3D mass density distribution of the sample indicates that the Fe-rich and Fe-S phases change continuously instead of abruptly (Fig. 3B)—owing to local temperature, pressure, geometry, and microscopic percolation mechanisms, which are difficult to probe with other imaging techniques.

In other exciting developments, Fig. 3C shows a ptychographic image of a partially delithiated nanoplate of $LiFePO_4$, a material with broad potential application in electrochemical energy storage (*40*). By acquiring multiple images across the Fe L-shell x-ray absorption edge and using them as input to principal-component and singular-value decomposition analysis, a chemical composition image of the partially delithiated nanoplate is obtained, showing the distribution of two chemical species: $LiFePO_4$ and $FePO_4$ (Fig. 3D). The resolution of this chemical image (~18 nm) is nearly an order of magnitude higher than the probe size (150 nm) and more than three times better than that of state-of-the-art scanning transmission x-ray microscopy (*20*). These results suggest that the (de)lithiation reaction of $LiFePO_4$ is two-phase, where both phases coexist in these submicrometer nanoplates.

BCDI's unique ability to image displacement (strain) fields in 3D also has widespread applications in materials science and nanoscience. For example, it was used to understand the structural principles of metal nanoparticles (*5*, *8*) and to obtain quantitative 3D images of the full strain tensor when the projections from three or more noncoplanar Bragg peaks are combined to yield the full vectorial displacement field (*41*). XFELs also provide sufficient coherent x-ray flux in a single monochromatic femtosecond pulse to record a slice through the BCDI diffraction pattern of a nanocrystal. A pump-probe BCDI experiment was carried out on 300-nm-diameter Au nanocrystals (*17*). The nanocrystals were first excited by an 800-nm Ti-sapphire infrared laser pulse

and then followed by snapshot imaging of the excited state with XFEL BCDI. Provided that both laser and x-ray pulses were kept below their damage thresholds, full 3D diffraction patterns could be built up as a function of delay time from the same nanocrystal. In this way, movies were captured of the strain associated with whole-crystal vibrations, with a 200-ps period (Fig. 3E). Two simple dilation breathing modes and a previously unknown shear mode were identified (*17*).

Using tabletop HHG, full-field coherent imaging in both reflection and transmission geometries has been demonstrated, with record spatial resolution of 22 nm (transverse) and 6 Å (axial) (*18*, *42*). Figure 3F shows a ptychographic image of a surface, with spatial resolution <1.3 λ or 40 nm horizontally, 6 Å vertically, and acquired with <1 min of x-ray exposure time (*18*). Moreover, the phase contrast in CDI is enhanced owing to the use of extreme ultraviolet (λ = 30 nm) illumination. Compared with SEM or AFM, HHG-based CDI enables higher-contrast full-field imaging with less sample damage, with long working distances (≈3 to 10 cm), automatic correction for imperfect scanning stages, and femtosecond time resolution (≈10 fs).

Several discoveries have been made recently simply by monitoring the time-dependent HHG diffraction from a material after excitation by a laser pulse, to uncover which mechanisms are responsible for nanoscale energy, charge, and spin transport (*19*, *35*). One remarkable demonstration of this capability showed that the cooling rate for a nanometer-size heat source depends on its proximity to other sources, cooling more rapidly when spaced close together than when isolated. This finding represents fundamentally new materials science directly relevant to the design of future energy-efficient nanosystems (*19*, *36*). Real-time imaging in 3D through opaque materials will represent a powerful capability for understanding functional nanosystems.

For biological applications, CDI is complementary to optical and electron microscopies in terms of spatial resolution, sample thickness, contrast mechanism, and quantitative capability. By using novel imaging technologies and labeling techniques, superresolution fluorescence microscopy can study dynamic processes in living cells at the tens-of-nanometers level, but it requires labeling of specific molecules and can accommodate limited sample thickness. To achieve considerably higher resolution, electron microscopy is the method of choice, but it is limited to imaging thinner samples, owing to the short penetration depth of electrons. Compared with superresolution and electron microscopy, CDI has three distinctive features. First, because of the large penetration depth of x-rays, CDI can image whole biological cells without the need of sectioning. Second, CDI takes advantage of the phase shift (contrast) of the intrinsic density in biological specimens that enables quantitative 3D imaging of the entire contents of cells and cellular organelles by using their natural contrast. Finally, by avoiding the use of lenses, the resolution of CDI is limited only by the spatial frequency of the diffracted waves from the sample.

Using third-generation synchrotrons, CDI has been used to image whole cells, cellular organelles, viruses, and biological materials, with spatial resolution down to ~11 nm (*7*, *43*–*48*). As an example, Fig. 4A shows the 3D mass density distribution of a whole, unstained yeast spore cell in which the 3D structure of intercellular organelles is quantitatively identified (*44*). Figure 4, B and C, shows the 3D image of an unstained human chromosome, as well as the first coherent diffraction pattern ever measured from a single, unstained

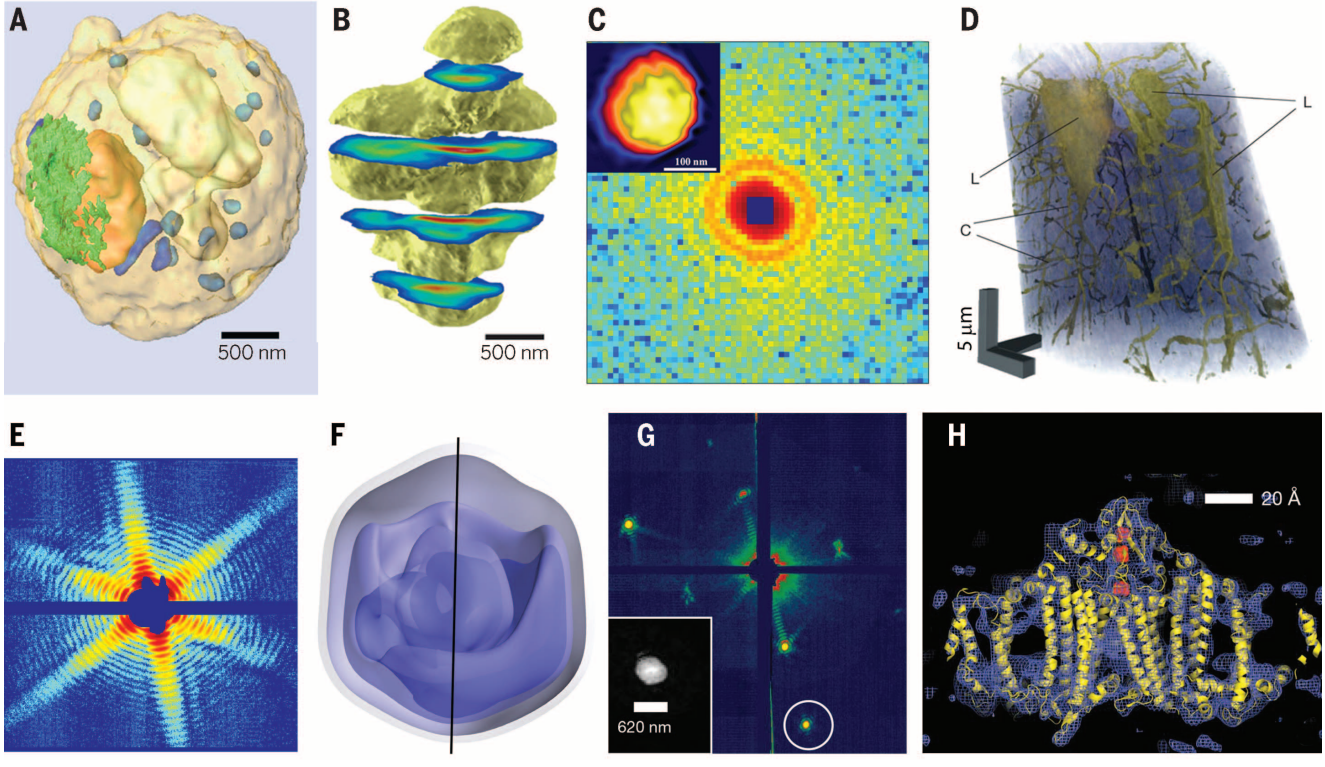

Fig. 4. Biological applications of diffractive imaging methods with coherent x-rays. (**A**) 3D mass density distribution of a whole, unstained yeast spore cell, showing nucleus (orange), endoplasmic reticulum (green), vacuole (white), mitochondria (blue), and granules (light blue) (*44*). (**B**) 3D image of an unstained human chromosome where the highest electron density is around the centromere (in red) (*46*). (**C**) First coherent x-ray diffraction pattern measured from a single, unstained herpesvirus virion and its reconstructed structure (inset), where the capsid is in yellow (*47*). (**D**) Quantitative 3D measurements of the osteocyte lacunae (L) and the connecting canaliculi (C) in a bone matrix (*15*). (**E**) A representative diffraction pattern of a giant mimivirus particle collected with a single LCLS pulse, where the symmetry of the diffraction pattern is clearly visible (*16*). (**F**) 3D structure of the mimivirus reconstructed from 198 diffraction patterns with higher density in blue and lower density in white (*50*). The vertical line represents the pseudo-fivefold axis. (**G**) Coherent x-ray diffraction pattern collected from a photosystem I nanocrystal using the LCLS, where the interference pattern between the Bragg peaks is visible owing to the finite size of the nanocrystal (*54*). (Inset) Real-space image of the nanocrystal reconstructed from the circled Bragg shape transform. (**H**) $2mF_o - DF_c$ electron density map at 1.0σ (purple mesh), obtained from diffraction intensities with more than 15,000 photosystem I nanocrystals (the refined model shown in yellow).

virus particle and its reconstructed structure (*46*, *47*). CDI has also been applied to study biological composite materials, including nanoscale imaging of mineral crystals in bone at different stages of mineralization (*48*) and quantitative 3D measurements of the osteocyte lacunae and the connecting canaliculi in a bone matrix (Fig. 4D) (*15*).

Using XFELs, CDI has been applied to measure the diffraction patterns of biological samples with single extremely intense and short x-ray pulses before the onset of radiation damage (diffraction-before-destruction) (*9*, *49*). Two important directions have been pursued. One is to perform diffractive imaging of live cells, cellular organelles, and virus particles with a resolution down to ~18 nm (*16*, *50*–*53*), which is presently limited by the x-ray flux density on the sample. Figure 4E shows a representative diffraction pattern of a giant mimivirus particle measured with a single Linac Coherent Light Source (LCLS) pulse (*16*). Using 198 diffraction patterns, the 3D structure of the mimivirus was reconstructed, revealing a nonuniform internal structure (Fig. 4F) (*50*). The other uses nanometer- to micrometer-sized protein crystals to substantially increase the resolution of diffraction patterns from single XFEL pulses (Fig. 4, G and H) (*54*). This method, known as serial femtosecond crystallography, has achieved a highest resolution of 1.6 Å (*55*) and also been applied to the structure determination of proteins that are difficult to grow as large crystals, such as membrane proteins (*56*, *57*).

Looking forward

Looking into the future for this 2015 Year of Light, we can already identify three research frontiers in imaging science and applications using small and large-scale coherent x-ray light sources. First, by taking advantage of the extremely short XFEL and HHG pulses, CDI is ideally suited to probe functioning systems at the nanoscale—at multiple sites simultaneously. A new form of CDI—hyperspectral imaging based on ptychography (*12*)—makes it possible to retrieve an image at several different x-ray wavelengths simultaneously, encoding instantaneous charge and spin information. Recently, dynamic CDI has been applied to image coherent acoustic phonons in nanocrystals, nanofabricated structures undergoing laser ablation, and standing surface acoustic waves in a piezoelectric substrate with spatial resolutions of tens of nanometers and temporal resolutions of picoseconds to <10 fs (*17*, *34*, *35*, *58*, *59*). With further improvement in experimental design, dynamic CDI should be able to achieve spatial resolutions <10 nm and temporal resolutions of 10 fs. Such a powerful imaging technique with high spatial-temporal resolutions is expected to profoundly expand our understanding of a wide range of dynamic phenomena, ranging from phase transitions, charge transfer, transport, nucleation, melting, superheating, crack and shock formation to lattice and grain boundary dynamics, as well as materials discovery of transient "hidden" phases of matter.

Second, as the wavelength of x-rays is on the order of the size of an atom, scientists have long dreamed of the development of atomic-resolution x-ray microscopy. However, the highest resolution presently attainable by any x-ray imaging method is ~2 nm in 2D and ~5.5 nm in 3D (*27*, *28*). With the rapid development of coherent light sources that promise to increase the x-ray brilliance by several orders of magnitude (Fig. 2A), CDI may achieve atomic resolution for radiation hard samples. Although electron microscopy can routinely image crystalline materials at atomic resolution, x-rays have several distinctive properties compared to electrons: (i) X-rays interact with the electron density rather than the Coulomb potential of an atom; (ii) dynamical scattering is usually negligible, allowing study of thick specimens; and (iii) the sample can be placed in an ambient environment. Thus, the potential ability to achieve atomic-resolution CDI, coupled with elemental, chemical, and magnetic specificity, would find broad applications in both fundamental and applied science.

Finally, one of the ultimate goals of CDI is to achieve high-resolution single-particle imaging (SPI)—for example, of protein complexes—without the need of crystallization. Using extremely intense and ultrashort XFEL pulses, coherent x-ray diffraction patterns can be collected from single protein complexes based on the diffraction-before-destruction scheme (*49*). These diffraction patterns can then be assembled into 3D patterns from which a 3D image follows after inversion (*60*–*62*). Numerical simulations show that with ~10^5 to 10^6 identical copies of large protein molecules, the 3D structure of the molecules can be determined at near-atomic resolution (*60*). Recent XFEL experiments have demonstrated the feasibility of the SPI method but at much lower resolution (*16*, *50*–*53*). To improve the spatial resolution, the XFEL pulse intensity has to be increased by two to three orders of magnitude. Recent work has suggested that the combination of self-seeding (using x-rays from the first half of the undulator to seed the second half via a monochromator) and undulator tapering (a gradual reduction in the field strength of an undulator to preserve the resonance wavelength) can achieve a 100-fold increase of the XFEL peak power (*23*). The increase in the XFEL pulse flux, coupled with large dynamic-range detectors, could realize the potential of SPI at higher resolution.

REFERENCES AND NOTES

1. P. Emma *et al.*, *Nat. Photonics* **4**, 641–647 (2010).
2. T. Ishikawa *et al.*, *Nat. Photonics* **6**, 540–544 (2012).
3. T. Popmintchev *et al.*, *Science* **336**, 1287–1291 (2012).
4. J. Miao, P. Charalambous, J. Kirz, D. Sayre, *Nature* **400**, 342–344 (1999).
5. I. K. Robinson, I. A. Vartanyants, G. J. Williams, M. A. Pfeifer, J. A. Pitney, *Phys. Rev. Lett.* **87**, 195505 (2001).
6. J. Miao *et al.*, *Phys. Rev. Lett.* **89**, 088303 (2002).
7. J. Miao *et al.*, *Proc. Natl. Acad. Sci. U.S.A.* **100**, 110–112 (2003).
8. M. A. Pfeifer, G. J. Williams, I. A. Vartanyants, R. Harder, I. K. Robinson, *Nature* **442**, 63–66 (2006).
9. H. N. Chapman *et al.*, *Nat. Phys.* **2**, 839–843 (2006).
10. G. J. Williams *et al.*, *Phys. Rev. Lett.* **97**, 025506 (2006).
11. H. N. Chapman *et al.*, *J. Opt. Soc. Am. A Opt. Image Sci. Vis.* **23**, 1179–1200 (2006).
12. J. M. Rodenburg *et al.*, *Phys. Rev. Lett.* **98**, 034801 (2007).
13. P. Thibault *et al.*, *Science* **321**, 379–382 (2008).
14. K. S. Raines *et al.*, *Nature* **463**, 214–217 (2010).
15. M. Dierolf *et al.*, *Nature* **467**, 436–439 (2010).
16. M. M. Seibert *et al.*, *Nature* **470**, 78–81 (2011).
17. J. N. Clark *et al.*, *Science* **341**, 56–59 (2013).
18. M. D. Seaberg *et al.*, *Optica* **1**, 39–44 (2014).
19. M. E. Siemens *et al.*, *Nat. Mater.* **9**, 26–30 (2010).
20. A. Sakdinawat, D. Attwood, *Nat. Photonics* **4**, 840–848 (2010).
21. J. Miao, D. Sayre, H. N. Chapman, *J. Opt. Soc. Am. A Opt. Image Sci. Vis.* **15**, 1662–1669 (1998).
22. J. R. Fienup, *Opt. Lett.* **3**, 27–29 (1978).
23. See supplementary text in supplementary materials on *Science* Online.
24. X. Huang *et al.*, *Opt. Express* **17**, 13541–13553 (2009).
25. A. Szameit *et al.*, *Nat. Mater.* **11**, 455–459 (2012).
26. T. Sun, Z. Jiang, J. Strzalka, L. Ocola, J. Wang, *Nat. Photonics* **6**, 586–590 (2012).
27. Y. Takahashi *et al.*, *Phys. Rev. B* **82**, 214102 (2010).
28. R. Xu *et al.*, *Nat. Commun.* **5**, 4061 (2014).
29. A. M. Maiden, J. M. Rodenburg, *Ultramicroscopy* **109**, 1256–1262 (2009).
30. I. K. Robinson *et al.*, *Phys. Rev. B* **60**, 9965–9972 (1999).
31. S. Roy *et al.*, *Nat. Photonics* **5**, 243–245 (2011).
32. O. Kfir *et al.*, *Nat. Photonics* **9**, 99–105 (2015).
33. C. Hernández-García *et al.*, *Phys. Rev. Lett.* **111**, 033002 (2013).
34. E. Turgut *et al.*, *Phys. Rev. Lett.* **110**, 197201 (2013).
35. D. Rudolf *et al.*, *Nat. Commun.* **3**, 1037 (2012).
36. K. M. Hoogeboom-Pot *et al.*, *Proc. Natl. Acad. Sci. U.S.A.* 10.1073/pnas.1503449112 (2015).
37. H. Jiang *et al.*, *Phys. Rev. Lett.* **110**, 205501 (2013).
38. C. Song *et al.*, *Phys. Rev. Lett.* **100**, 025504 (2008).
39. A. Tripathi *et al.*, *Proc. Natl. Acad. Sci. U.S.A.* **108**, 13393–13398 (2011).
40. D. A. Shapiro *et al.*, *Nat. Photonics* **8**, 765–769 (2014).
41. M. C. Newton, S. J. Leake, R. Harder, I. K. Robinson, *Nat. Mater.* **9**, 120–124 (2010).
42. M. D. Seaberg *et al.*, *Opt. Express* **19**, 22470–22479 (2011).
43. D. Shapiro *et al.*, *Proc. Natl. Acad. Sci. U.S.A.* **102**, 15343–15346 (2005).
44. H. Jiang *et al.*, *Proc. Natl. Acad. Sci. U.S.A.* **107**, 11234–11239 (2010).
45. J. Nelson *et al.*, *Proc. Natl. Acad. Sci. U.S.A.* **107**, 7235–7239 (2010).
46. Y. Nishino, Y. Takahashi, N. Imamoto, T. Ishikawa, K. Maeshima, *Phys. Rev. Lett.* **102**, 018101 (2009).
47. C. Song *et al.*, *Phys. Rev. Lett.* **101**, 158101 (2008).
48. H. Jiang *et al.*, *Phys. Rev. Lett.* **100**, 038103 (2008).
49. R. Neutze, R. Wouts, D. van der Spoel, E. Weckert, J. Hajdu, *Nature* **406**, 752–757 (2000).
50. T. Ekeberg *et al.*, *Phys. Rev. Lett.* **114**, 098102 (2015).
51. T. Kimura *et al.*, *Nat. Commun.* **5**, 3052 (2014).
52. M. Gallagher-Jones *et al.*, *Nat. Commun.* **5**, 3798 (2014).
53. M. F. Hantke *et al.*, *Nat. Photonics* **8**, 943–949 (2014).
54. H. N. Chapman *et al.*, *Nature* **470**, 73–77 (2011).
55. J. Tenboer *et al.*, *Science* **346**, 1242–1246 (2014).
56. J. Kern *et al.*, *Science* **340**, 491–495 (2013).
57. W. Liu *et al.*, *Science* **342**, 1521–1524 (2013).
58. A. Barty *et al.*, *Nat. Photonics* **2**, 415–419 (2008).
59. J.-D. Nicolas *et al.*, *J. Appl. Cryst.* **47**, 1596–1605 (2014).
60. J. Miao, K. O. Hodgson, D. Sayre, *Proc. Natl. Acad. Sci. U.S.A.* **98**, 6641–6645 (2001).
61. R. Fung, V. Shneerson, D. K. Saldin, A. Ourmazd, *Nat. Phys.* **5**, 64–67 (2009).
62. N.-T. D. Loh, V. Elser, *Phys. Rev. E Stat. Nonlin. Soft Matter Phys.* **80**, 026705 (2009).

ACKNOWLEDGMENTS

We thank C. Pellegrini and J. M. Rodenburg for stimulating discussions and H. Jiang, J. Zhou, Y. Yang, and D. Adams for help with the figures and references. J.M. and M.M.M. acknowledge support from the Defense Advanced Research Projects Agency PULSE program through a grant from AMRDEC. J.M. thanks support from NSF (grant DMR-1437263). M.M.M. thanks support from NSF, DOE, and SRC. I.K.R. acknowledges support from an ERC "Advanced" grant. The University of Colorado and the University of Michigan have patents coauthored by M.M.M. in the area of high harmonic sources: U.S. Patent 8,462,824 (2013) and U.S. Patent 6151155 (2000).

SUPPLEMENTARY MATERIALS

www.sciencemag.org/content/348/6234/530/suppl/DC1
Supplementary Text
References (*63*–*92*)

10.1126/science.aaa1394

RESEARCH

Ultracold rubidium atoms in a two-dimensional optical lattice

Brown et al., *p. 540*

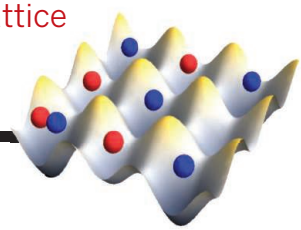

IN *SCIENCE* JOURNALS

Edited by **Stella Hurtley**

Artist's impression of a magnetic monopole

QUANTUM GASES

Making a monopole in an atomic gas

Some "grand unified theories" of physics predict the existence of the so-called magnetic monopole. No such particles have been seen, but analogs of monopoles may be observable in quantum fluids. Ray *et al*. created such an analog in a gas of ultracold ^{87}Rb atoms with three spin states at their disposal. The authors used a protocol involving external magnetic fields with particular spatial distributions to create and observe a monopole-like spin texture in the gas. — JS

Science, this issue p. 544

THREE-BODY PHYSICS

Helium caught in the act of triangulating

Helium is the noblest of noble gases, almost completely unattracted to itself or any other chemical element. Of course, when quantum mechanics comes into play, that "almost" is an inevitable caveat. For several decades, researchers have been intrigued by a theoretically predicted Efimov state composed of three helium atoms held loosely together in a triangle. Kunitski *et al*. now report experimental realization of that state and detection of its acute triangular geometry (see the Perspective by Kornilov). Beyond completing a long quest in helium studies, the results shed light on three-body physics more broadly. — JSY

Science, this issue p. 551; see also p. 498

IONIC INTERACTIONS

Ions' response to hydrophobic surfaces

The strength of interactions between ions depends on their solvation environment. Schellman postulated in the 1950s that when aqueous solvated ions approached a hydrophobic surface (such as a parts of a protein surface), interactions between ions would be enhanced. Chen *et al*. experimentally tested this theory by studying the dissociation of organic ions bonded by salt bridges after the addition of acid. The ion pairs were held by tethers at different distances from hydrophobic surfaces. The salt bridge was stronger when it was closer to the hydrophobic surface. — PDS

Science, this issue p. 555

BACTERIAL DIVISION

Pop goes the coccus

Daughter cell separation in *Staphylococcus aureus* proceeds much like the cracking of an egg. So say Zhou *et al*., who examined dividing cells with millisecond precision using high-speed videomicroscopy. Rather than proceeding gradually, tiny imperfections in the mother cell wall were seen to crack open, leaving two daughter cells linked by a hinge. — SMH

Science, this issue p. 574

BRAIN COMPUTATION

How the brain sorts and routes messages

How do higher brain areas communicate with each other? Do they send out all computations equally to all target areas and leave the recipient to extract the needed and relevant information? Or does the transmitting region package and route computations differentially to distinct target areas, depending on the content? Ciocchi *et al*. found that the ventral hippocampus routes

ILLUSTRATION: HEIKKA VALJA

Published by AAAS

anxiety-related information preferentially to the prefrontal cortex and goal-related information preferentially to the nucleus accumbens. Hippocampal neurons with multiple projections were more involved in a variety of behavioral tasks and in memory consolidation. — PRS

Science, this issue p. 560

STRESS SIGNALING

Seeing stress signaling in living mice

Stress activates the eIF2α-ATF4 pathway to reduce global protein production while enhancing targeted gene expression, which helps cells adapt and survive. Activation of this pathway is associated with various pathologies, such as tissue fibrosis after injury. Chaveroux *et al.* developed transgenic mice in which the activation of this pathway could be monitored at the whole-animal level and at the tissue and cellular level. Activation was tissue-specific, depending on the initiating stress. Chemically induced liver fibrosis correlated with activation of the eIF2α-ATF4 pathway by a specific kinase. — NRG

Sci. Signal. **8**, rs5 (2015).

BIOMECHANICS

A beetle's internal bomb

Bombardier beetles shoot a toxic pulse at potential predators and other harassers. The toxic spray is created by a chemical reaction that occurs inside the beetle's body. Although the details of the reaction are known, how the beetle is able to precisely combine the chemicals at appropriate times and release the pulse at regular intervals has remained a mystery. Arndt *et al*. used synchrotron x-ray imagery to observe the process as it occurs within live beetles. Expansion and contraction of an internal expansion membrane facilitate the precise cyclic injection of reactants and the subsequent ejection of toxic sprays that keep the beetle's predators at bay. — SNV

Science, this issue p. 564

RETROTRANSPOSONS

Keeping jumping genes out of harm's way

The genomes of most eukaryotes, including our own, are jam-packed with parasitic mobile DNA elements. Most are nonfunctional remnants, but a few are still active, capable of jumping about in our DNA, potentially causing serious damage to our genes. Nevertheless, they avoid landing in and disrupting coding regions. For example, in yeast, the retrotransposon Ty1 is targeted away from protein genes to positions upstream of yeast RNA polymerase III genes. Bridier-Nahmias *et al*. show that Ty1 is targeted to these "safe havens" through an interaction between a Ty1-encoded protein that controls its genome jumping activity and a subunit of the yeast RNA polymerase III complex. — GR

Science, this issue p. 585

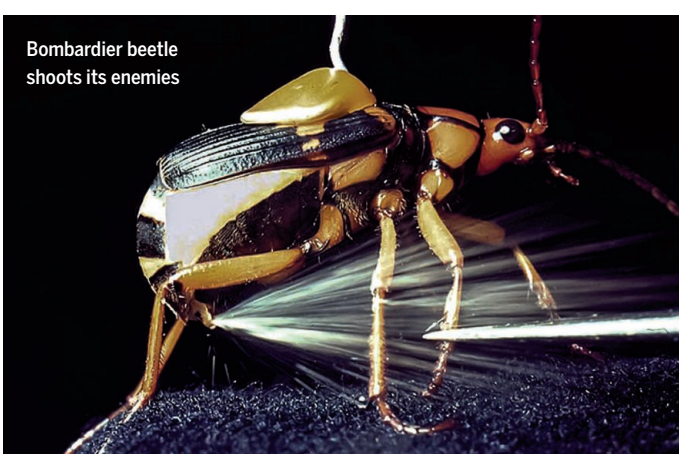

Bombardier beetle shoots its enemies

PHOTO: (LEFT TO RIGHT) T. EISNER *ET AL. PNAS* **96**, 17 (17 AUGUST 1999) © 2015 NATIONAL ACADEMY OF SCIENCES; © GLOBALP/ISTOCKPHOTO

IN OTHER JOURNALS

Edited by **Sacha Vignieri** *and* **Jesse Smith**

Groups of hair cells influence each other's growth through quorum sensing

CELL BEHAVIOR

Sense-ible hair

Could restoring hair growth depend on group behavior? Chen *et al.* report that damaged and healthy hair follicles grow cooperatively. The authors found that plucking 200 hairs in a specific pattern and density on the back of a mouse elicited not only the regrowth of the injured follicles but also the growth of up to five times that number of nearby uninjured follicles. Injured follicles release CCL2, a factor that recruits macrophages to the damaged area, and these secrete tumor necrosis factor–α, which stimulates stem cells in both plucked and unplucked follicles. The process reflects quorum sensing, where a population of cells communicates and coordinates behavior of the group through a signaling mechanism. — LC

Cell **161**, 277 (2015).

NONCODING RNAS

Signaling stress

Small nucleolar RNAs (snoRNAs)—small noncoding RNAs better known for their roles as sequence guides for modification of other RNAs—may function to promote elimination of damaged cells undergoing metabolic stress. Youssef *et al.* explored RNA binding partners of the protein kinase PKR (protein kinase RNA–activated) and found them to be enriched in snoRNAs. Such binding activated PKR and was increased in cells treated with palmitic acid to mimic the metabolic stress seen in obese animals. Thus, snoRNAs appear to link metabolic stress to the activation of PKR, which in turn inhibits protein synthesis and promotes the death of stressed cells. — LBR

Proc. Natl. Acad. Sci. U.S.A. 10.1073/pnas.1424044112 (2015).

T CELLS

T cells require mRNA modifications

T cells are important components of our immune system that recognize and respond to immune threats. Stimulation of

Published by AAAS

ALSO IN *SCIENCE* JOURNALS

Edited by **Stella Hurtley**

DNA REPAIR

Uncrossing covalently linked DNA strands

DNA interstrand cross-links (ICLs) covalently link the two strands of the double helix. ICL mutations are difficult to repair, because the two DNA strands cannot be separated and so one strand cannot be used as a template to repair the other. Räschle *et al*. developed a mass spectrometry–based method to systematically analyze a time series of all the proteins recruited to repair ICLs in *Xenopus* egg extracts. They found many of the known factors required for ICL repair. They also found a number of new factors, two of which define a new repair pathway for ICL mutations. — GR

Science, this issue p. 539

QUANTUM SIMULATION

Simulating magnetism out of equilibrium

A major goal of quantum simulation is to help us understand problems that are difficult to describe analytically or solve with conventional computers. This goal has been very challenging to reach experimentally, requiring, for example, extremely low temperatures to determine the effects of quantum magnetism in equilibrium. Brown *et al*. studied a nonequilibrium system of ultracold ^{87}Rb atoms in a two-dimensional optical lattice. They monitored the atoms' dynamics after a sudden change in the lattice parameters and were able to reach a regime where the magnetic interactions dominated the dynamics. — JS

Science, this issue p. 540

FERROELECTRICS

Getting closure in ferroelectric films

Ferroelectric materials have a spontaneous electric polarization that can be manipulated for applications. The polarization is usually not uniform throughout the material, and for nanosized ferroelectrics, polarization can be quite complex. Using scanning transmission electron microscopy, Tang *et al*. found that in thin films of the ferroelectric $PbTiO_3$, the polarization vector rotated in space, forming a closed loop, the so-called flux closure. The flux closure structures formed an array, with the period dependent on the width of the thin film, and caused the buildup of considerable strain within the crystal lattice of the material — JS

Science, this issue p. 547

EXTINCTIONS

Recognizing the threat of additive risk

Humans are accelerating the extinction rates of species in both terrestrial and marine environments. However, species extinctions have occurred across time for a variety of other reasons. Finnegan *et al*. looked at the extinction rates across marine species over the past 23 million years to determine intrinsic extinction rates and what traits or regions correspond to the highest rates. Combining patterns of intrinsic extinction with regions of high anthropogenic threat revealed taxa and areas, particularly in the tropics, where the risk of extinction will be especially high. — SNV

Science, this issue p. 567

CLIMATE CHANGE

Predicting extinction in a changing world

There is great interest in understanding how species might respond to our changing climate, but predictions have varied greatly. Urban looked at over 130 studies to identify the level of risk that climate change poses to species and the specific traits and characteristics that contribute to risk (see the Perspective by Hille Ris Lambers). If climate changes proceed as expected, one in six species could face extinction. Several regions, including South America, Australia, and New Zealand, face the greatest risk. Understanding these patterns will help us to prepare for, and hopefully prevent, climate-related loss of biodiversity. — SNV

Science, this issue p. 571; see also p. 501

STRUCTURAL BIOLOGY

Changing shape to destroy RNA

Clustered regularly interspaced short palindromic repeats (CRISPRs) together with CRISPR-associated (Cas) proteins form an adaptive immune system that helps bacteria and archaea defend themselves against invading viruses and plasmids. CRISPR RNAs (crRNAs) target CRISPR-Cas protein complexes to the invaders, bringing about their destruction. Taylor *et al*. used cryo–electron microscopy to determine the structure of a 12-subunit CRISPR-Cas protein complex with crRNA from *Thermus thermophilus*, in the presence and absence of single-stranded target RNA. Binding to the target RNA causes a change in shape of the CRISPR-Cas complex that results in target recognition and destruction. — GR

Science, this issue p. 581

PROTEIN DYNAMICS

A hierarchy of protein motions

Functioning proteins are not static but explore complex conformational energy landscapes. Lewandowski *et al*. used multinuclear solid-state nuclear magnetic resonance experiments to measure protein motion over a broad range of temperatures and time scales. Above 160 K there was a strong coupling between solvent and protein motion. The hierarchy of motions as the temperature increased revealed the dynamic modes that relate solvent, side-chain, and backbone motion. — VV

Science, this issue p. 578

IMMUNE TOLERANCE

Early T cells keep autoimmunity at bay

A major challenge faced by the immune system is to react to foreign substances, such as microbes, while simultaneously tolerating the self. Upsetting this balance leads to autoimmunity. Regulatory T cells (T_{regs}), are a subset of immune cells that help to maintain this balance. Yang *et al*. found that murine T_{reg} cells generated very early in life are distinct from those generated in older animals and play an especially important role in keeping autoimmunity in check (see the Perspective by Tanaka and Sakaguchi). These changes are due to differences in the way T_{regs} develop in the thymus in newborn versus adult mice. — KLM

Science, this issue p. 589; see also p. 506

CONSERVATION

Large herbivore loss threatens biodiversity

Large herbivores (100 kg or larger) are suffering dramatic population declines and range contractions worldwide. These losses alter their native ecosystems. Ripple *et al.* review data on all 76 species of large herbivores. Population declines lead to range contractions, often because of conversion of land to other purposes. Populations of large herbivores should be increased and wildlife trade controlled wherever possible to

0501elSIOr1.indd 538-B 4/28/15 10:40 AM

prevent further range contraction and extinction. These approaches should help to restore normal ecological function and biological diversity. — TEL

Sci. Adv. 10.1126/sciadv.1400103 (2015).

ENVIRONMENT

How rivers respond to dam removals

Globally, dam building is experiencing a renaissance in the quest for hydropower. However, over the past 40 years, more than 1000 dams have been removed in the United States because they have filled with sediment or have become unsafe or inefficient. Dams are also being taken down in other parts of the world. In a Perspective, O'Connor *et al.* explore how rivers have responded to these dam removals. Many dam removals have improved ecosystem function and have avoided catastrophic consequences, but most of these dams have been relatively small. As larger dams are increasingly removed, there is a need for longer-term, systematic monitoring. — JFU

Science, this issue p. 496

CONSERVATION ECOLOGY

Humans and animals vying for space in the air

Human uses of the airspace are increasingly conflicting with wildlife, such as migrating or foraging birds. Flying aircraft are frequently struck by birds, and wind turbines and other human-made structures cause millions of animal deaths each year. In a Perspective, Lambertucci *et al.* outline such aerial conflicts between human activities and wildlife. Innovative methods aimed at reducing these conflicts include adjusting wind turbine speeds upon radar detection of animal movements and using ultraviolet light to deter birds from windows. These and other measures must be applied at the regional scale to protect migrating species effectively. Judicious management of the airspace should also include airspace reserves in areas with high densities of aerial wildlife. — JFU

Science, this issue p. 502

BIOENGINEERING

Personalized implants provide a 4D fix

The three-dimensional (3D) printing revolution is in full swing, with printed kidneys, cars, and body armor. Now, 3D is entering into the fourth dimension—time—which renders 4D materials adaptable and enduring. In pediatric medicine, 4D implants are particularly relevant: As the patient grows, so should the material. Morrison *et al.* used 3D printing to create personalized splints for three pediatric patients with tracheobronchomalacia, a condition in which airways collapse during normal breathing. In all three patients, the 4D devices were stable and functional after 1 month, and one has stayed in place for 30 months. This pilot trial shows that the fourth dimension is becoming a reality for regenerative medicine. — MLF

Sci. Transl. Med. **7**, 285ra64 (2015).

Published by AAAS

anxiety-related information preferentially to the prefrontal cortex and goal-related information preferentially to the nucleus accumbens. Hippocampal neurons with multiple projections were more involved in a variety of behavioral tasks and in memory consolidation. — PRS

Science, this issue p. 560

STRESS SIGNALING

Seeing stress signaling in living mice

Stress activates the eIF2α-ATF4 pathway to reduce global protein production while enhancing targeted gene expression, which helps cells adapt and survive. Activation of this pathway is associated with various pathologies, such as tissue fibrosis after injury. Chaveroux *et al.* developed transgenic mice in which the activation of this pathway could be monitored at the whole-animal level and at the tissue and cellular level. Activation was tissue-specific, depending on the initiating stress. Chemically induced liver fibrosis correlated with activation of the eIF2α-ATF4 pathway by a specific kinase. — NRG

Sci. Signal. **8**, rs5 (2015).

BIOMECHANICS

A beetle's internal bomb

Bombardier beetles shoot a toxic pulse at potential predators and other harassers. The toxic spray is created by a chemical reaction that occurs inside the beetle's body. Although the details of the reaction are known, how the beetle is able to precisely combine the chemicals at appropriate times and release the pulse at regular intervals has remained a mystery. Arndt *et al*. used synchrotron x-ray imagery to observe the process as it occurs within live beetles. Expansion and contraction of an internal expansion membrane facilitate the precise cyclic injection of reactants and the subsequent ejection of toxic sprays that keep the beetle's predators at bay. — SNV

Science, this issue p. 564

RETROTRANSPOSONS

Keeping jumping genes out of harm's way

The genomes of most eukaryotes, including our own, are jam-packed with parasitic mobile DNA elements. Most are nonfunctional remnants, but a few are still active, capable of jumping about in our DNA, potentially causing serious damage to our genes. Nevertheless, they avoid landing in and disrupting coding regions. For example, in yeast, the retrotransposon Ty1 is targeted away from protein genes to positions upstream of yeast RNA polymerase III genes. Bridier-Nahmias *et al*. show that Ty1 is targeted to these "safe havens" through an interaction between a Ty1-encoded protein that controls its genome jumping activity and a subunit of the yeast RNA polymerase III complex. — GR

Science, this issue p. 585

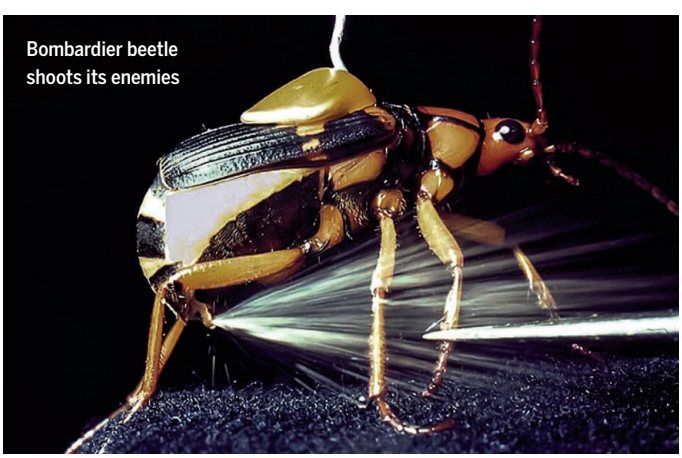

Bombardier beetle shoots its enemies

PHOTO: (LEFT TO RIGHT) T. EISNER *ET AL. PNAS* **96**, 17 (17 AUGUST 1999) © 2015 NATIONAL ACADEMY OF SCIENCES; © GLOBALP/ISTOCKPHOTO

IN OTHER JOURNALS

Edited by **Sacha Vignieri** *and* **Jesse Smith**

Groups of hair cells influence each other's growth through quorum sensing

CELL BEHAVIOR

Sense-ible hair

Could restoring hair growth depend on group behavior? Chen *et al.* report that damaged and healthy hair follicles grow cooperatively. The authors found that plucking 200 hairs in a specific pattern and density on the back of a mouse elicited not only the regrowth of the injured follicles but also the growth of up to five times that number of nearby uninjured follicles. Injured follicles release CCL2, a factor that recruits macrophages to the damaged area, and these secrete tumor necrosis factor–α, which stimulates stem cells in both plucked and unplucked follicles. The process reflects quorum sensing, where a population of cells communicates and coordinates behavior of the group through a signaling mechanism. — LC

Cell **161**, 277 (2015).

NONCODING RNAS

Signaling stress

Small nucleolar RNAs (snoRNAs)—small noncoding RNAs better known for their roles as sequence guides for modification of other RNAs—may function to promote elimination of damaged cells undergoing metabolic stress. Youssef *et al.* explored RNA binding partners of the protein kinase PKR (protein kinase RNA–activated) and found them to be enriched in snoRNAs. Such binding activated PKR and was increased in cells treated with palmitic acid to mimic the metabolic stress seen in obese animals. Thus, snoRNAs appear to link metabolic stress to the activation of PKR, which in turn inhibits protein synthesis and promotes the death of stressed cells. — LBR

Proc. Natl. Acad. Sci. U.S.A. 10.1073/pnas.1424044112 (2015).

T CELLS

T cells require mRNA modifications

T cells are important components of our immune system that recognize and respond to immune threats. Stimulation of

Downloaded from www.sciencemag.org on April 30, 2015

Published by AAAS

A central control center allows octopuses to move their heads and eight arms independently

NEUROSCIENCE

Managing eight arms

How does the octopus control its long and flexible arms? Levy *et al.* used kinematic analysis, filming animals as they maneuvered, and found that octopuses evolved a unique way of efficiently generating and controlling crawling. They can crawl in any direction relative to their body orientation, a feature found only in animals with radial organization, such as starfish. However, in contrast to those animals, octopuses control the direction in which the body faces, independently of the crawling direction. Octopuses can thus change the crawling direction while maintaining a fixed gaze direction, or rotate their body while continuing to crawl in the same direction. This indicates the existence of a sophisticated central command generator in the motor centers of the octopus brain. — PRS

Curr. Biol. **25**, 10.1016/j.cub.2015.02.064 (2015).

T cells results in up-regulation of the RNA binding protein CELF2 (CUGBP, Elav-like family member 2). This gene is associated with posttranscriptional modifications of RNAs, including alternative splicing. Mallory *et al*. show that in response to T cell stimulation, expression of CELF2 is up-regulated and its transcripts are stabilized, ensuring an increase in the availability of this RNA. Furthermore, this up-regulation of CELF2 is associated with specific alternative exon transcripts and isoform expression within stimulated T cells. These results suggest that regulation of specific transcriptomes is important for mounting an immune response. — LMZ

Proc. Natl. Acad. Sci. U.S.A. 10.1073/pnas.1423695112 (2015).

MATERIALS SCIENCE

Seeing sonic hot spots

Mechanical impact can detonate explosives, but how impact heats these materials to initiate reactions has been unclear. You *et al*. used mild ultrasound irradiation to study composite materials —small crystals of sucrose or table salt in rubber—while performing thermal imaging. Uncoated particles remained unheated, but particles that had a coating that could delaminate (a polyethylene glycol layer that liquefies or Teflon) heated very rapidly (up to ~22,000 K per second). Delamination allows the particle to move and friction-heat against the matrix, an effect that authors also saw in samples of polymer-bonded explosive (PBX). — PDS

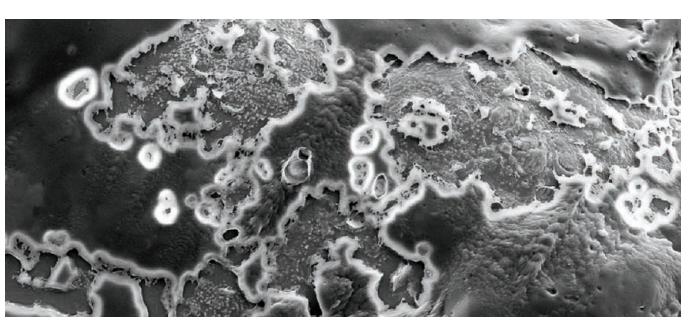

PTFE coatiing on an NaCl crystal degraded by ultrasonic heating

Nat. Commun. 10.1038/ncomms7581 (2015).

MINERAL PHYSICS

Strength to put a stop to sinking slabs

Tectonic plates plunging toward Earth's core can unexpectedly stop sinking in the middle of the mantle. Marquardt and Miyagi provide a potential explanation involving the abundant mantle mineral ferropericlase. Their x-ray diffraction experiments revealed a large increase in the strength of ferropericlase with increased pressure. This translates to a viscosity increase at mid-mantle depths, providing a rheological barrier that subducted ocean lithosphere cannot easily penetrate. This mechanism of slab stagnation may also explain some of the mantle's well-known chemical heterogeneity. — BG

Nat. Geosci. 10.1038/ngeo2393 (2015).

ANTIBIOTICS

Extent of children's antibiotic exposure

Antibiotics are widely used in human and veterinary medicine and in personal care products, so people are increasingly exposed to them in the environment and in food. How high is the resulting antibiotic burden? Wang *et al.* measured the concentrations of 18 representative antibiotics in the urine of 1064 schoolchildren from three economically and geographically distinct areas in eastern China. They show that 58.3% of samples contained at least one antibiotic and that more than 20% of samples contained more than one. A lack of suitable analytical methods for some commonly used antibiotics means that the total antibiotic burden is likely to be even higher. Based on contamination data for the aquatic environment, exposures of children in the United States and Europe may be similar to those in this study. — JFU

Environ. Sci. Technol. 10.1021/es5059428 (2015).

PHOTOS: (TOP TO BOTTOM) © AURIGADESIGN/ISTOCKPHOTO; S. YOU *ET AL. NATURE COMMUNICATIONS* **6** (2 APRIL 2015) © NATURE PUBLISHING GROUP

Published by AAAS

RESEARCH ARTICLE SUMMARY

DNA REPAIR

Proteomics reveals dynamic assembly of repair complexes during bypass of DNA cross-links

Markus Räschle, Godelieve Smeenk, Rebecca K. Hansen, Tikira Temu, Yasuyoshi Oka, Marco Y. Hein, Nagarjuna Nagaraj, David T. Long, Johannes C. Walter, Kay Hofmann, Zuzana Storchova, Jürgen Cox, Simon Bekker-Jensen,* Niels Mailand,* Matthias Mann*

INTRODUCTION: DNA damage encountered during DNA replication represents a major challenge to the integrity of the genome. Because replicative polymerases are unable to synthesize across DNA lesions, prolonged stalling of replisomes can lead to replication fork collapse, giving rise to gross genomic alterations. Cells have evolved intricate responses that orchestrate the reorganization of the replication fork necessary for overcoming such roadblocks, but the full set of factors involved in these processes has not been defined. Here, we performed unbiased proteomic analyses of the dynamically changing protein landscape at damaged chromatin undergoing DNA replication. This yielded mechanistic insights into the pathways that ensure genomic stability during perturbed DNA replication.

RATIONALE: We combined the powerful and well-established *Xenopus* egg extract system for cell-free DNA replication with quantitative mass spectrometry to develop CHROMASS (chromatin mass spectrometry), a simple yet robust method for the unbiased analysis of chromatin composition. Using bifunctional cross-linkers, compounds commonly applied in chemotherapy, we systematically monitored the assembly and disassembly of protein complexes on replicating chromatin containing DNA interstrand cross-links (ICLs).

RESULTS: We show that replication of ICL-containing chromatin templates triggers recruitment of more than 90 DNA repair and genome maintenance factors. Addition of replication inhibitors revealed the subset of proteins that accumulate in a strictly replication-dependent fashion. The quantitative readout by CHROMASS is highly lesion-specific, as the known repair factors enriched on psoralen–cross-linked templates had previously been linked to ICL repair or specific branches of DNA damage signaling. In contrast, virtually none of the proteins involved in unrelated DNA repair pathways (e.g., base excision repair or nonhomologous end joining) showed damage-specific enrichment. The temporal profiles of hundreds of proteins across an extensive time course and a variety of perturbations provided a data-rich resource that could be mined to identify previously unknown genome maintenance factors. Among such hits, we identified SLF1 and SLF2 and showed that they physically link RAD18 with the SMC5/6 complex. This defines a linear RAD18-SLF1-SLF2 recruitment pathway for the SMC5/6 complex to RNF8/RNF168-generated ubiquitylations at damaged DNA in vertebrate cells. We found that SLF2 is a distant ortholog of yeast NSE6, an SMC5/6-associated factor that is essential for targeting this complex to damaged DNA to promote faithful repair of the lesions. Consistent with pivotal functions of SMC5/6 in the suppression of replication stress-induced, illegitimate recombination intermediates, depletion of SLF1 or SLF2 led to mitotic errors and compromised cell survival in response to genotoxic agents.

CONCLUSIONS: CHROMASS enables rapid and unbiased time-resolved insights into the chromatin interaction dynamics of entire DNA repair pathways. Combined with specific perturbations, CHROMASS allows systems-level interrogation of the consequences of inactivating particular aspects of the repair process. We compiled comprehensive proteome-wide profiles of dynamic protein interactions with damaged chromatin. These can be mined to pinpoint genome stability maintenance factors, exemplified here by the identification of SLF1 and SLF2, which define a recruitment pathway for the SMC5/6 complex. CHROMASS can be applied to other chromatin-associated pathways and may also shed light on the dynamics of posttranslational modifications governing the regulation of these processes. ■

ON OUR WEB SITE

Read the full article at http://dx.doi.org/10.1126/science.1253671

The list of author affiliations is available in the full article online.
*Corresponding author. E-mail: simon.bekker-jensen@cpr.ku.dk (S.B.-J.); niels.mailand@cpr.ku.dk (N.M.); mmann@biochem.mpg.de (M.M.)
Cite this article as M. Räschle *et al.*, *Science* **348**, 1253671 (2015). DOI: 10.1126/science.1253671

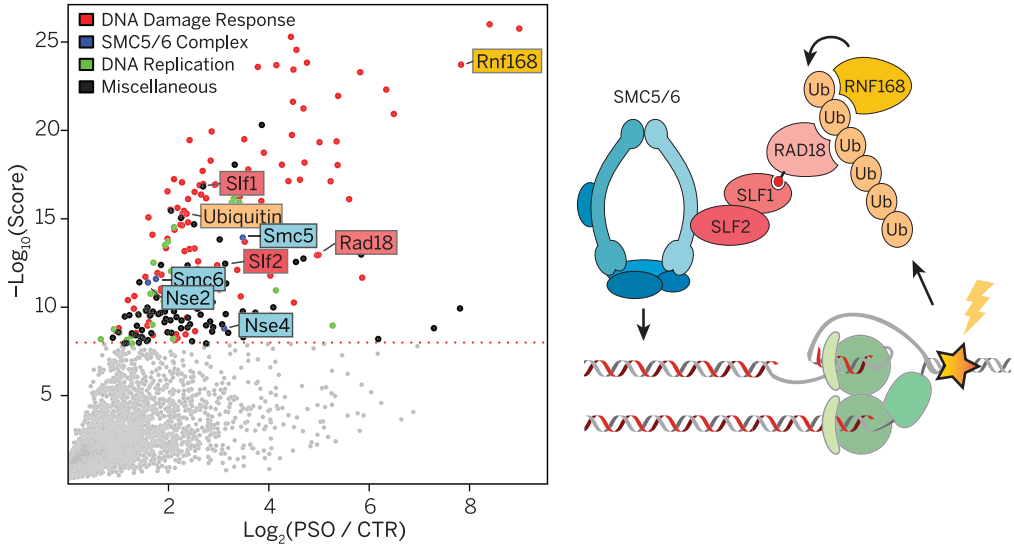

CHROMASS analysis of proteins recruited to stalled replication forks reveals a specific set of DNA repair factors involved in the replication stress response. Among these, SLF1 and SLF2 are found to bridge the SMC5/6 complex to RAD18, thereby linking SMC5/6 recruitment to ubiquitylation products formed at various DNA lesions.

RESEARCH ARTICLE

DNA REPAIR

Proteomics reveals dynamic assembly of repair complexes during bypass of DNA cross-links

Markus Räschle,[1] Godelieve Smeenk,[2] Rebecca K. Hansen,[2] Tikira Temu,[1] Yasuyoshi Oka,[2] Marco Y. Hein,[1] Nagarjuna Nagaraj,[1] David T. Long,[3] Johannes C. Walter,[3] Kay Hofmann,[5] Zuzana Storchova,[4] Jürgen Cox,[1] Simon Bekker-Jensen,[2]* Niels Mailand,[2]* Matthias Mann[1,6]*

DNA interstrand cross-links (ICLs) block replication fork progression by inhibiting DNA strand separation. Repair of ICLs requires sequential incisions, translesion DNA synthesis, and homologous recombination, but the full set of factors involved in these transactions remains unknown. We devised a technique called chromatin mass spectrometry (CHROMASS) to study protein recruitment dynamics during perturbed DNA replication in *Xenopus* egg extracts. Using CHROMASS, we systematically monitored protein assembly and disassembly on ICL-containing chromatin. Among numerous prospective DNA repair factors, we identified SLF1 and SLF2, which form a complex with RAD18 and together define a pathway that suppresses genome instability by recruiting the SMC5/6 cohesion complex to DNA lesions. Our study provides a global analysis of an entire DNA repair pathway and reveals the mechanism of SMC5/6 relocalization to damaged DNA in vertebrate cells.

Cellular genomes are particularly susceptible to DNA damage during S phase of the cell cycle, when unrepaired lesions interfere with DNA replication. Several genetically distinguishable pathways have evolved to bypass these roadblocks, involving processing of the stalled replication forks, translesion synthesis (TLS), and homologous recombination (HR) (*1*–*3*). Defects in these pathways can lead to genomic rearrangements and cancer predisposition syndromes in higher eukaryotes (*3*, *4*). Among DNA lesions, ICLs are particularly difficult to repair because they affect both strands of the DNA, thereby precluding mechanisms that use an intact complementary strand as a template. Replication of plasmids containing a defined ICL in *Xenopus* egg extracts provided insight into the stepwise bypass of these complex lesions (*5*). After collision of the replisome with the ICL, the leading-strand DNA polymerase stalls 20 to 40 nucleotides from the cross-link because of steric hindrance by the Mcm2-7 replicative DNA helicase, which unwinds the parental strands ahead of the polymerase. Upon unloading of the helicase and dual incision of one parental strand, leading-strand synthesis advances beyond the ICL. Finally, the incised sister molecule is repaired by HR (*6*). In agreement with this mechanism, replication-dependent ICL repair in *Xenopus* egg extracts consistently requires the Fanconi anemia protein Fancd2, the Polζ subunit Rev7, and the Rad51 recombinase (*5*–*7*). The response to ICL-stalled replication forks also triggers an extensive DNA damage response (DDR) that synchronizes repair status with cell cycle progression and promotes recruitment of the repair machinery. This involves extensive chromatin modifications that serve as docking marks for protein recruitment and change the chromatin architecture to make it permissive for homology-directed repair. However, the factors involved in coordinating all these steps have not yet been defined in an unbiased fashion.

Higher-order chromosome structure is regulated by the SMC (structural maintenance of chromosome) proteins, SMC1 to SMC6 (*8*). They form heterodimeric complexes involved in sister chromatid cohesion (SMC1/3), chromosome condensation (SMC2/4), and DNA repair (SMC5/6) (*9*). Like cohesin, the SMC5/6 complex localizes along chromosomes. Local accumulation of SMC5/6 is also observed at DNA double-strand breaks (DSBs) (*10*) and at stalled replication forks (*11*, *12*), where it regulates the outcome of HR (*13*). Consistent with this notion, loss of the essential SMC5/6 complex leads to spontaneous chromosomal aberrations and chromosome segregation errors, which are increased strongly by drugs that interfere with DNA replication. In budding and fission yeast, four non-SMC elements (NSE1 to NSE4) stably associate with SMC5/6, conferring ubiquitin and SUMO E3 ligase activity to the complex. In contrast, the NSE5/6 heterodimer only loosely associates with SMC5/6 and appears to be specifically required for its recruitment to DSBs and stalled replication forks (*11*, *14*). So far, no functional orthologs of NSE5/6 have been identified in higher eukaryotes, which raises the question of how the SMC5/6 complex is recruited to DNA lesions in these species.

Dynamic recruitment of DNA repair factors to stalled replication forks

To systematically monitor protein recruitment during ICL repair, we developed chromatin mass spectrometry (CHROMASS) (fig. S1A). In brief, psoralen–cross-linked or undamaged sperm chromatin is replicated in *Xenopus* egg extracts, isolated by sedimentation through a sucrose cushion, and analyzed by a high-performance single-run mass spectrometry workflow (*15*, *16*). Using recently developed algorithms (*17*), CHROMASS accurately quantifies the recruitment of factors to chromatin. Even at a single time point, as many as 146 known DDR factors were readily detected, 72 of which showed significant enrichment on the damaged chromatin over the undamaged control [relative change >1.5; false discovery rate (FDR) < 0.05] (Fig. 1A and table S1). Consistent with ICL repair being strictly dependent on replication in this system (*5*), the recruitment of most DDR factors was sensitive to the replication inhibitor geminin (Fig. 1B and table S1). In total, we analyzed 160 chromatin pellets representing 37 different time points and/or perturbations (fig. S1B). The three independent replicates that we measured for each condition showed a high degree of correlation (median R^2 = 0.92; fig. S2A). Of 5730 quantified proteins, 1349 were specifically enriched on chromatin (fig. S2B and table S1). Intensity profiles of these proteins across all perturbations provide a data-rich resource that can be mined for new insights into chromatin biology.

To analyze the recruitment kinetics of known DNA replication and ICL repair factors, we isolated psoralen–cross-linked chromatin from repair-competent extracts at 15-min intervals. Replication of this damaged template triggered a transient checkpoint response that peaked at 30 min (Fig. 1C), indicating that replication forks reached the ICLs within that time (*5*, *7*). Consistently, most replication initiation and elongation factors peaked early, between 15 and 30 min, whereas most DNA repair factors accumulated only after fork collision with the ICL (Fig. 1D). Concomitant with the unloading of replicative DNA polymerases around 45 min, TLS polymerases (Polκ, Polη, Rev1/3/7), the entire Fanconi core complex, and the Xpf and Fan1 nucleases (*18*) became enriched on the damaged chromatin. This was followed by the recruitment of the Brca1-A complex, indicating the loading of the HR machinery. Finally, at around 75 min, the Fanci-Fancd2 complex peaked on the chromatin. Given that this complex regulates the incision

[1]Department of Proteomics and Signal Transduction, Max Planck Institute of Biochemistry, 82152 Martinsried, Germany. [2]Ubiquitin Signaling Group, Department of Disease Biology, Novo Nordisk Foundation Center for Protein Research, University of Copenhagen, DK-2200 Copenhagen, Denmark. [3]Howard Hughes Medical Institute and Department of Biological Chemistry and Molecular Pharmacology, Harvard Medical School, Boston, MA 02115, USA. [4]Maintenance of Genome Stability Group, Max Planck Institute of Biochemistry, 82152 Martinsried, Germany. [5]Institute of Genetics, University of Cologne, 50674 Cologne, Germany. [6]Novo Nordisk Foundation Center for Protein Research, Proteomics Program, University of Copenhagen, DK-2200 Copenhagen, Denmark.
*Corresponding author. E-mail: simon.bekker-jensen@cpr.ku.dk (S.B.-J.); niels.mailand@cpr.ku.dk (N.M.); mmann@biochem.mpg.de (M.M.)

and TLS step during ICL repair (*19*, *20*), the late peak of Fanci-Fancd2 was surprising. We speculate that this reflects an additional function of the complex, possibly related to the retention of Fancd2 at ultrafine bridges that become visible only in mitosis (*21*). This global analysis provides detailed insights into the dynamics of protein recruitment to replication forks stalled at ICLs and suggests a highly orchestrated assembly of the repair machinery to ensure a safe handover of potentially dangerous repair intermediates to downstream processes (*16*).

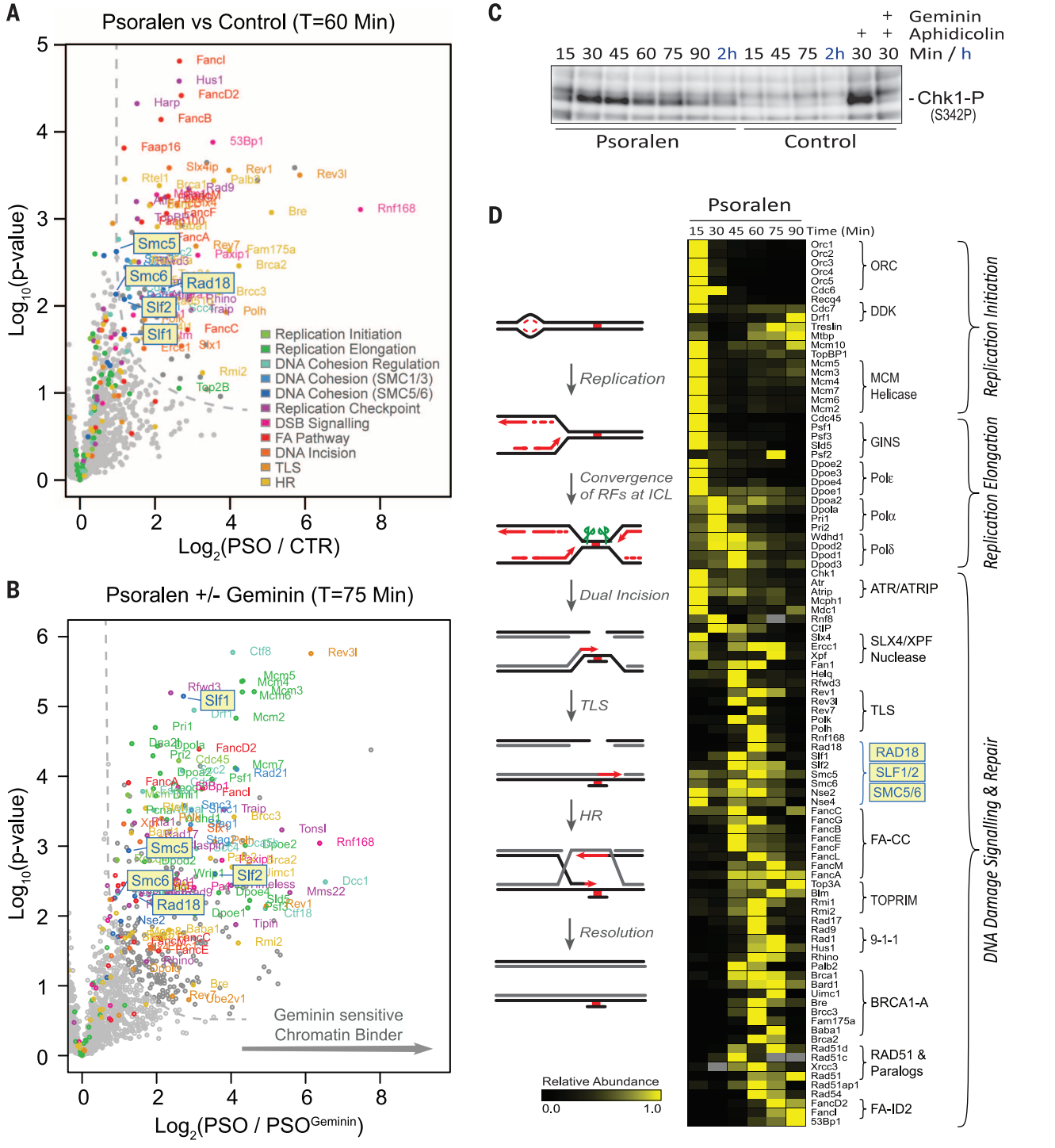

Fig. 1. Dynamic recruitment of proteins to replication forks stalled at psoralen cross-links. Chromatin was replicated in *Xenopus* egg extract and analyzed by CHROMASS. (**A**) Analysis of protein recruitment to psoralen–cross-linked chromatin compared to an undamaged control. The volcano plot shows the mean difference of the protein intensity plotted against the *P* value. Dashed lines indicate the significance cutoff (*16*). (**B**) Protein recruitment to psoralen–cross-linked chromatin in the presence or absence of the replication inhibitor geminin. (**C**) Analysis of DNA damage checkpoint activation by probing total extracts with antibodies raised against phospho-CHK1. (**D**) CHROMASS analysis of chromatin pellets from the same reactions shown in (C). The heat map shows the relative abundance of the median intensity from three biological replicates calculated for each protein. See table S2 for intensities of all quantified proteins. A model for ICL repair is shown at the left. The same sample was analyzed in (A), (C), and (D).

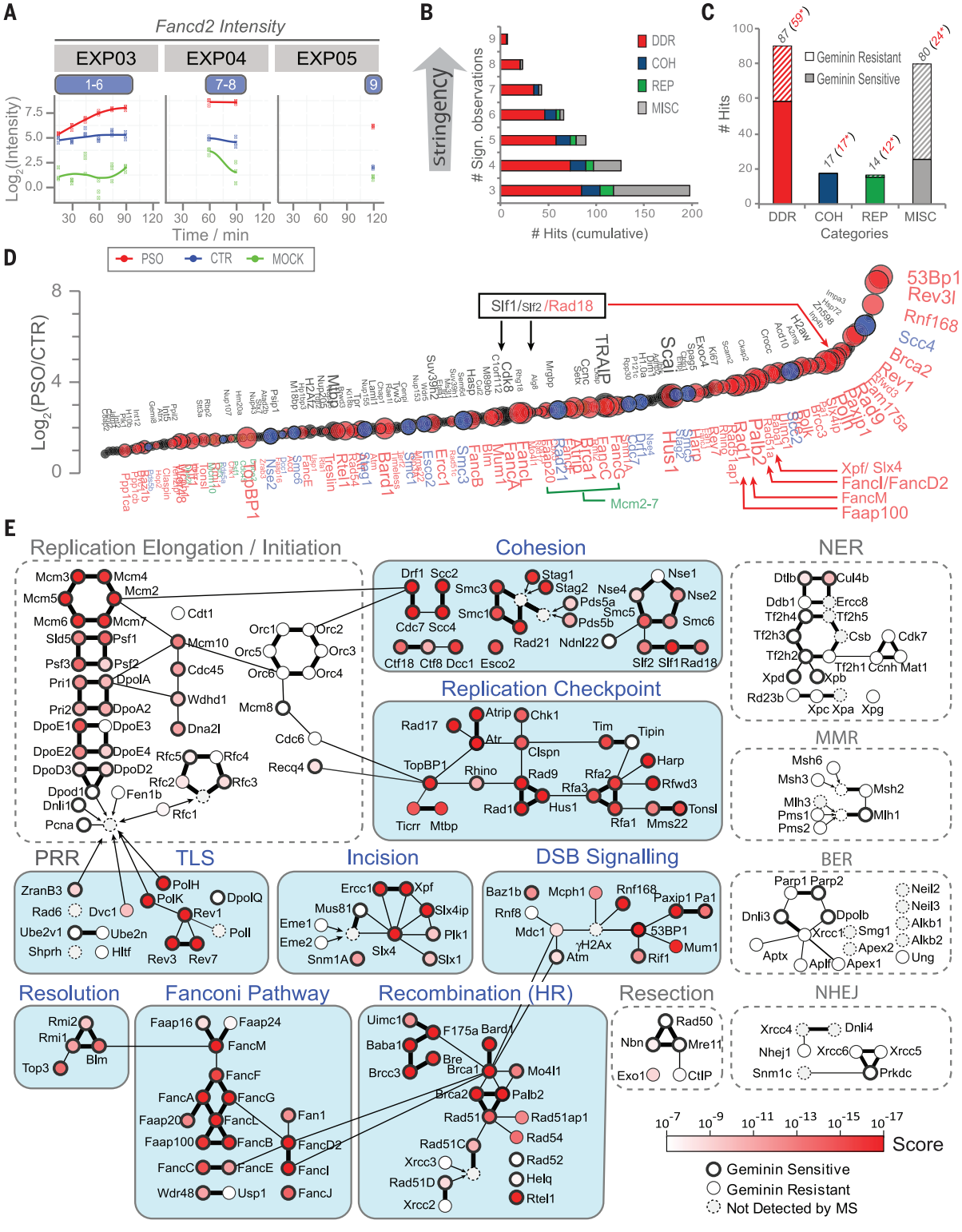

Fig. 2. Pathway analysis reveals comprehensive proteomic coverage of the ICL repair pathway. (**A**) Time points evaluated for the identification of all damage-specific chromatin binders. Representative intensity profile of FancD2 on psoralen–cross-linked chromatin (red), undamaged chromatin (blue), or a mock control lacking chromatin (green) plotted against time. (**B**) The cumulative number of hits in each category plotted against the number of significant observations (table S1), in which a protein was found to be significantly enriched on psoralen–cross-linked chromatin relative to undamaged chromatin and a mock reaction. DDR, DNA damage response; COH, cohesion; REP, DNA replication; MISC, miscellaneous. See table S1 for assignment to categories. (**C**) Replication dependency of damage-specific chromatin binder with at least three significant observations. (**D**) Maximal intensity ratio (PSO/CTR) plotted against the rank of the protein. Dot and label sizes reflect the number of significant observations. (**E**) Mapping a global score for damage-specific enrichment (*16*) onto a schematic protein interaction network. Low coverage may indicate module members that are not involved in the response to cross-linking agents.

Identification of damage-specific chromatin binders

Using robust statistical algorithms (*22*), we next identified for each time point of EXP03-05 (see Fig. 2A and fig. S1B) all proteins with significant enrichment on psoralen–cross-linked chromatin over both undamaged chromatin and a mock control (relative change >1.5; FDR > 0.05). For each protein, we analyzed how often it scored as a damage-specific chromatin binder in the nine evaluated time points (labeled 1 to 9 in Fig. 2A; see also table S1) (*16*). Only seven proteins were enriched in all nine conditions (Fig. 2B, top bar), whereas the majority of hits scored only in a subset of the analyzed time points. The highest-scoring

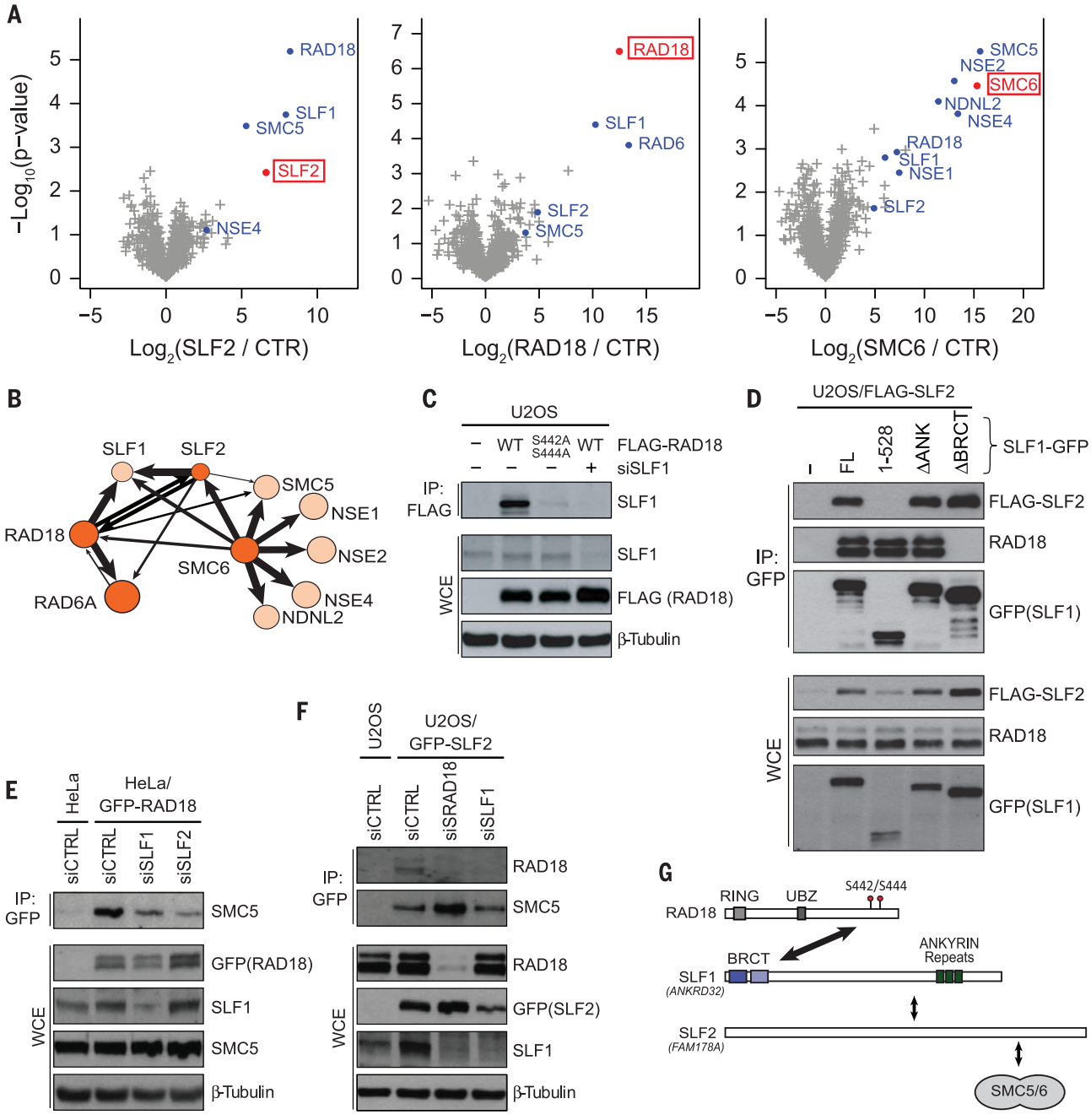

Fig. 3. SLF1 and SLF2 physically link RAD18 to the SMC5/6 complex. (**A**) Green fluorescent protein (GFP) pulldowns from HeLa (BAC) cells expressing SLF2, RAD18, or SMC6 as GFP fusion proteins under their endogenous promoter were analyzed by QUBIC (*24*). (**B**) Protein interactions identified in (A). Circle size indicates absolute copy number in HeLa cells (see fig. S7C). Baits are shown in dark orange. Arrow size indicates relative intensities of interactors. (**C**) U2OS cells left untreated or transfected with SLF1 siRNA were transfected with indicated FLAG-RAD18 constructs. Whole-cell extracts (WCE) were subjected to FLAG immunoprecipitation (IP) and immunoblotted with antibodies to SLF1, FLAG, and β-tubulin. (**D**) U2OS/FLAG-SLF2 cells were transfected with indicated SLF1 constructs. Interactions among SLF1, SLF2, and RAD18 were analyzed by immunoblotting GFP IPs with the indicated antibodies. (**E**) GFP IPs from HeLa or HeLa/GFP-RAD18 (BAC) cells transfected with indicated siRNAs were immunoblotted with antibody to SMC5. Knockdown efficiency of the SLF2 siRNA is shown in fig. S6F. (**F**) GFP IPs from U2OS cells transfected with the indicated siRNAs, followed by transfection with empty vector or GFP-SLF2 plasmid, were immunoblotted with antibodies to RAD18 and SMC5. (**G**) Schematic depiction of human SLF1 and SLF2 proteins. Conserved BRCT and ankyrin repeat (ANK) domains in SLF1 are highlighted. Interactions among RAD18, SLF1, SLF2, and SMC5/6 are indicated by double-headed arrows.

proteins were almost exclusively known DDR factors. Although the number of identified repair factors increased steadily with decreasing stringency, the overall number of hits increased disproportionately. Therefore, only hits scoring in at least three experimental conditions were included in subsequent analyses. Among the 198 proteins fulfilling these criteria, 87 had previously been implicated in the DDR (red), 17 in sister chromatid cohesion, and 14 in DNA replication (Fig. 2C). The observed maximal damage-specific enrichment of proteins ranged from a factor of 1.5 up to a factor of >400 (Fig. 2D).

To gain further statistical power from these independent experiments (Fig. 2A), we computed a global score for the damage-specific enrichment by means of an FDR-controlled approach (*16*). Mapping this global score onto a protein-protein interaction network indicated comprehensive coverage of known protein modules implicated in ICL repair (Fig. 2E; see also fig. S3). In contrast, virtually none of the factors involved in unrelated repair pathways—such as nonhomologous end joining, base excision repair, mismatch repair, or postreplicative repair—were robustly enriched on psoralen–cross-linked chromatin. Together with the temporal profiles, these analyses provide a systems-wide proteomic survey of protein recruitment to ICL-stalled replication forks.

To further characterize the damage-specific chromatin binders, we determined whether their recruitment was suppressed in the presence of the replication inhibitor geminin. Although recruitment of the majority of known DDR and replication factors required prior DNA replication, only 24 of the 80 miscellaneous hits showed geminin-sensitive accumulation (Fig. 2, C and E, and figs. S3B and S4). Among these, we identified Ankrd32 and Fam178a, which we refer to as SLF1 and SLF2 (Smc5/6 localization factors 1 and 2), respectively. Both proteins showed prominent enrichment on psoralen–cross-linked chromatin (fig. S3A), and their accumulation peaked together with the early ICL repair factors (see Fig. 1D). Across the entire data set, their intensity profiles clustered most tightly with that of Rad18 (fig. S5). Notably, Rad18, but not its binding partner Rad6 (*2*, *23*), accumulates strongly on cross-linked DNA (Fig. 2E and table S1); this finding suggests that, together with SLF1 and SLF2, RAD18 might play a noncatalytic role in the response to stalled replication forks that is distinct from its RAD6-dependent function as a ubiquitin ligase required for the polymerase switch during postreplicative repair (*2*).

The RAD18-SLF1-SLF2 complex recruits SMC5/6 to DNA lesions

We next set out to investigate the potential function of SLF1 and SLF2 in the DNA damage response in human cells. Quantitative bacterial artificial chromosome interactomics (QUBIC) (*24*) confirmed strong and specific interactions among RAD18, SLF1, and SLF2 (Fig. 3, A and B, and fig. S6A). These unbiased experiments also suggested association with components of the SMC5/6 complex. Indeed, when SMC6 was used as bait, RAD18, SLF1, and SLF2 were specifically detected in the pulldowns (Fig. 3A, right, and fig. S6A). Furthermore, the highly abundant RAD6 protein was recovered efficiently in RAD18 but not in SLF2 nor SMC6 pulldowns, and unlike

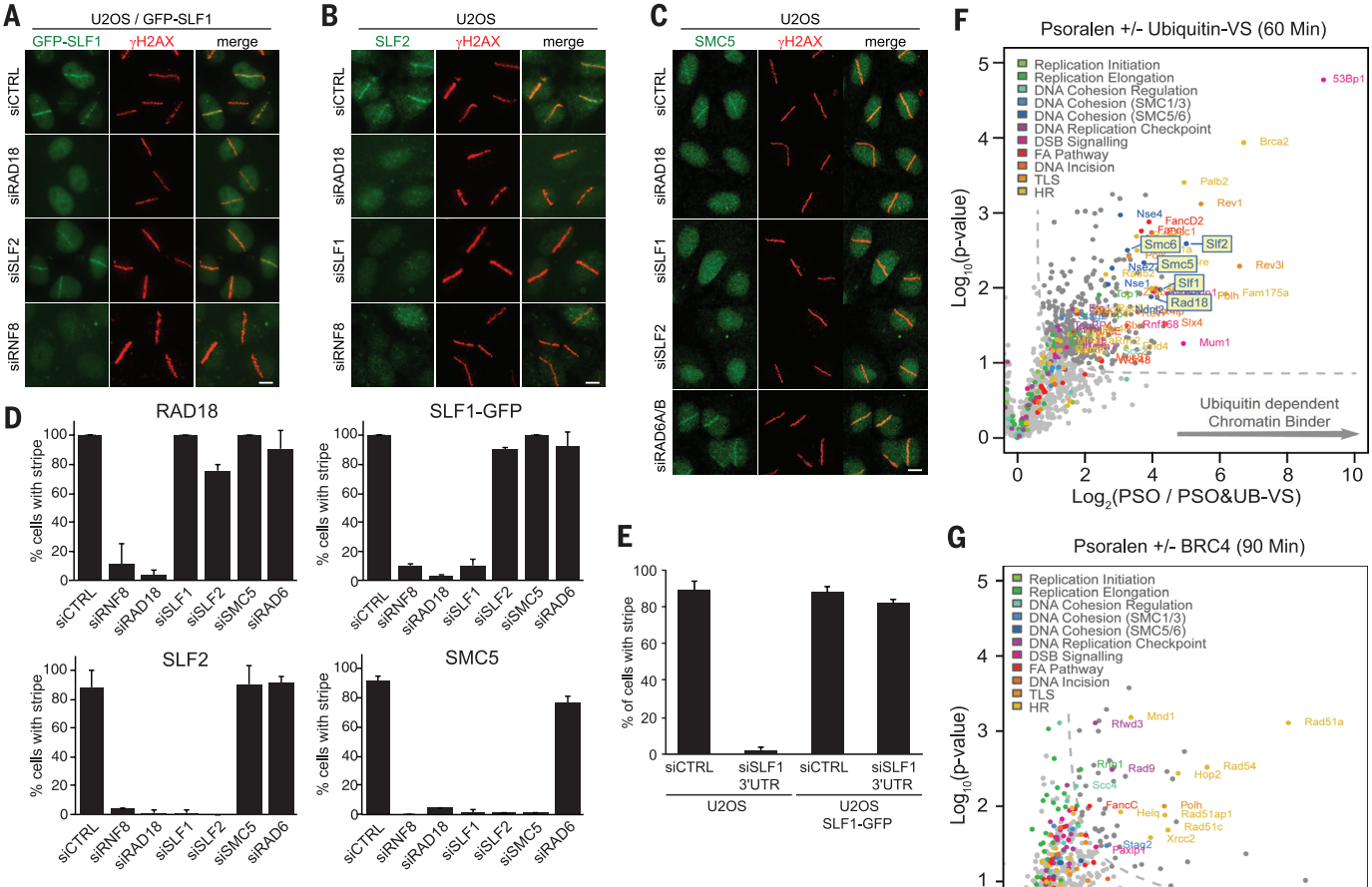

Fig. 4. The RAD18-SLF1-SLF2 complex promotes ubiquitin-dependent recruitment of SMC5/6 to sites of DNA damage. (**A**) U2OS/GFP-SLF1 cells transfected with indicated siRNAs were exposed to laser microirradiation, fixed 1 hour later, and immunostained with γ-H2AX antibody. Scale bar, 10 μm. (**B** and **C**) U2OS cells treated as in (A) were coimmunostained with antibody to SLF2 or SMC5, respectively. Scale bar, 10 μm. (**D**) Quantification of data shown in (A) to (C) and fig. S8A. At least 75 cells were counted per data point [mean ± SEM (error bars); $N = 2$]. (**E**) U2OS or U2OS/GFP-SLF1 cells were processed as in (B). At least 100 cells were counted per data point [mean ± SEM (error bars); $N = 2$]. See also fig. S8D. (**F**) CHROMASS analysis of protein recruitment to psoralen–cross-linked chromatin in the presence or absence of ubiquitin vinyl sulfone. (**G**) Protein recruitment to psoralen–cross-linked chromatin in the presence or absence of BRC4 peptide.

RAD18, neither SLF1, SLF2, nor any components of the SMC5/6 complex were strongly enriched in RAD6 pulldowns (fig. S6B). These findings suggest that RAD18 forms two distinct complexes in HeLa cells: one with RAD6, and another with SLF1 and SLF2 that interacts with the entire SMC5/6 complex in a sub-stoichiometric fashion.

To delineate the molecular nature of the RAD18-SLF1-SLF2-SMC5/6 complex, we confirmed interactions by coimmunoprecipitation. Consistent with work showing that the isolated tandem BRCT repeat of SLF1 recognizes two phosphorylated serine residues located in the C terminus of RAD18 (25), only the wild type, but not mutant RAD18 (S442A/S444A), interacted with full-length SLF1 (Fig. 3C, fig. S6, C to E, and fig. S7). Deletion of the N-terminal tandem BRCT repeat from SLF1 abrogated RAD18 interaction, although this mutant still bound SLF2 (Fig. 3D). In agreement with a linear organization of the RAD18-SLF1-SLF2-SMC5/6 complex, depletion of SLF1 or SLF2 strongly reduced the amount of SMC5 in RAD18 pulldowns (Fig. 3E). Furthermore, knockdown of SLF1 abolished the interaction between RAD18 and SLF2 (Fig. 3F), whereas depletion of SLF2 did not affect the association of RAD18 with SLF1. We therefore conclude that SLF1 and SLF2 physically link RAD18 to the SMC5/6 complex (Fig. 3G).

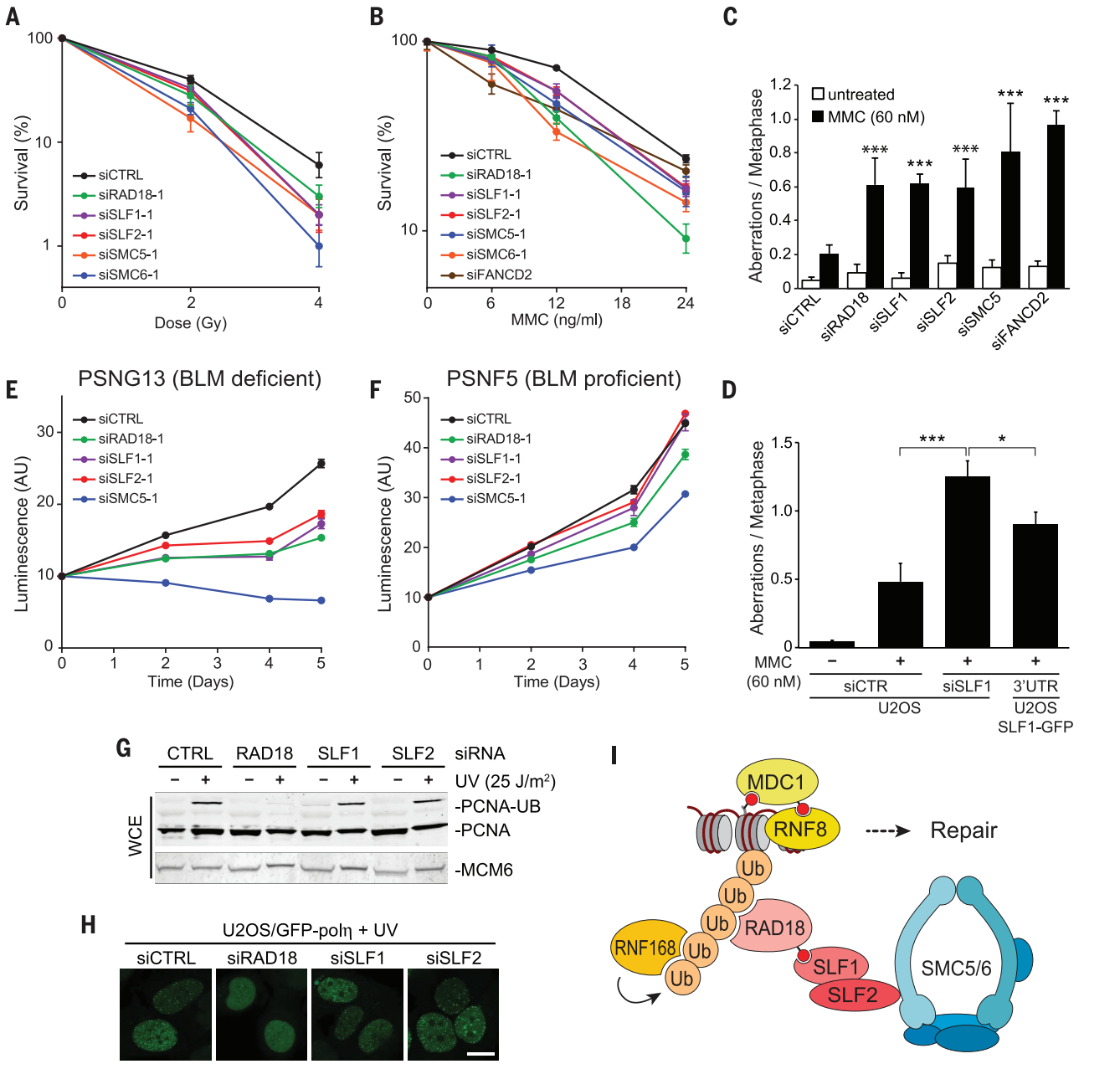

Fig. 5. Role of the RAD18-SLF1-SLF2 complex in genome stability maintenance after DNA damage. (**A**) Clonogenic survival of U2OS cells after exposure to ionizing radiation (mean ± SEM; $N = 3$). See also fig. S10A for an independent set of siRNAs. (**B**) Clonogenic survival of U2OS cells exposed to MMC (mean ± SEM; $N = 3$). (**C**) Chromosomal aberrations of U2OS cells exposed to MMC; 50 metaphases were analyzed per condition (mean ± SD; $N = 2$; ***$P < 0.001$, nonparametric t test, all tested against the siCTRL treated with MMC). (**D**) As in (E), except that either U2OS or U2OS/GFP-SLF1 cells were used (mean ± SD; $N = 2$; ***$P < 0.001$, *$P < 0.05$, nonparametric t test). (**E** and **F**) Proliferation of PSNG13 or PSNF5 cells (mean ± SD; $N = 3$). See also fig. S10D. (**G**) U2OS were exposed to ultraviolet (UV) irradiation. After 6 hours, extracts were analyzed by immunoblotting with antibodies to PCNA and MCM6. (**H**) U2OS/GFP-polη cells were treated as in (G) and analyzed by confocal microscopy. Scale bar, 10 μm. (**I**) Model of RAD18-SLF1-SLF2–mediated recruitment of the SMC5/6 complex to damaged DNA.

To investigate the role of the RAD18-SLF1-SLF2-SMC5/6 complex in the DNA damage response, we asked whether these proteins are physically recruited to laser-induced DNA lesions. Consistent with the accumulation of RAD18 at DSB sites (*26*) and our physical interaction studies, RAD18, SLF1, SLF2, SMC5, and SMC6 were all recruited to laser-induced DSBs (Fig. 4, A to D, and fig. S8A), as well as to ICLs induced by laser-activated psoralen (fig. S8B). Depletion of SLF1 abolished SLF2 recruitment to DSB sites but not vice versa, further confirming that SLF1 links RAD18 to SLF2 within the complex (Fig. 4D and fig. S8C).

The expression of ectopic SLF1 in cells treated with an SLF1 small interfering RNA (siRNA) targeting the 3′ untranslated region fully restored SLF2 recruitment to laser-induced DNA lesions (Fig. 4E and fig. S8D). Neither SLF1 nor SLF2 depletion impaired RAD18 accumulation at the break sites (Fig. 4D and fig. S8A), but each of these factors was required for SMC5/6 recruitment, further demonstrating the linear relationship among the components of this pathway (Fig. 4, A to D, and fig. S8A).

RAD18 has been shown to accumulate at DSBs via its UBZ domain, which recognizes ubiquitylation products formed at DNA lesions when RNF8, MDC1, and RNF168 are present (*26*–*29*). Consistently, recruitment of RAD18, SLF1, SLF2, and SMC5/6 to microlaser-induced DNA lesions required RNF8, MDC1, and RNF168, but did not require either RAP80 or 53BP1, which function downstream in separate branches of the DSB response (fig. S8, B and D). Likewise, damage recruitment of SLF2 or SMC6 was abolished in cells treated with the proteasome inhibitor MG132, which efficiently depletes the pool of free ubiquitin (*30*) (fig. S9, C and D). In the *Xenopus* system, depletion of free ubiquitin also abrogated recruitment of all components of the Smc5/6 recruitment cascade, as well as many DNA repair factors known to accumulate at stalled replication forks in a ubiquitin-dependent fashion (Fig. 4F) (*31*). Because depletion of ubiquitin specifically interferes with early steps of ICL repair without affecting DNA replication (*32*), these results demonstrate a pivotal role of ubiquitin in the assembly of repair complexes at stalled replication forks.

To further demonstrate how CHROMASS can generate additional insights into chromatin biology via targeted perturbations, we sought to specifically inhibit the HR branch of ICL repair. We added a Brca2-derived peptide (BRC4) to the extract to specifically block the loading of the Rad51 recombinase and formation of recombination intermediates (*6*). At 90 min, the levels of Rad51 were reduced by a factor of 16 in the presence of BRC4 (Fig. 4G). Recruitment of several Rad51-associated HR factors (Rad51ap1, Rad51c, Xrcc2, Rad54, Mnd1, and Hop2) was similarly reduced. Furthermore, Polη showed a robust decrease, indicating a potential role of this TLS polymerase in HR-associated DNA synthesis. In contrast, addition of the BRC4 peptide did not reveal differential recruitment of enzymes involved in the processing of recombination intermediates, such as Holliday junction resolvases. Thus, dissolution by the Blm-TopoIIIa-Rmi1-Rmi2 (BTRR) complex, which is recruited early to stalled replication forks by FancM (*33*), might be the preferred pathway in this system. Our targeted perturbation experiment also demonstrates that the HR branch and the SMC5/6 recruitment cascade are independent pathways.

The SMC5/6 pathway protects cells from replication-associated genotoxic stress

We next examined the impact of compromised RAD18-SLF1-SLF2 function on the maintenance of genome integrity after DNA damage. Depletion of SLF1 or SLF2 increased the sensitivity of U2OS cells to DSB-inducing agents such as ionizing radiation (Fig. 5A and fig. S10A). The degree of hypersensitivity of SLF1- or SLF2-depleted cells to ionizing radiation was comparable to that of cells lacking RNF8 or RNF168 (*31*, *34*), both of which are required for RAD18-SLF1-SLF2 recruitment to DSB sites. In addition, loss of SLF1 or SLF2 function sensitized cells to ionizing radiation to an extent similar to that of RAD18 or SMC6 depletion (Fig. 5A), consistent with the notion that RAD18, SLF1, SLF2, and SMC5/6 function in a linear pathway. Furthermore, depletion of any component of the SMC5/6 recruitment pathway resulted in mild sensitivity to mitomycin C (MMC) (Fig. 5B). Knockdown of RAD18, SLF1, SLF2, or SMC5 enhanced MMC-induced chromosomal aberrations observed in metaphase spreads, comparable to the effect of depleting FANCD2 (Fig. 5C). Ectopic expression of siRNA-insensitive SLF1 in cells treated with SLF1 siRNA significantly reduced MMC-induced chromosomal aberrations (Fig. 5D, asterisks).

The SMC5/6 complex contains a number of non-SMC proteins, collectively referred to as NSE (non-SMC element) proteins (*9*). Whereas the SMC5/6 and NSE1 to NSE4 subunits are highly conserved across all kingdoms of life, homologs of the NSE5/6 heterodimer have diverged considerably between budding and fission yeast and have not been identified in higher eukaryotes. Using advanced sequence analysis tools (*16*), we unambiguously found NSE6 to be a member of the SLF2 gene family despite weak overall sequence conservation (fig. S10, B and C). NSE1 to NSE4 are essential proteins in yeast, like SMC5 and SMC6; by contrast, NSE5 and NSE6 appear to promote SMC5/6 complex functions only during genotoxic stress, in particular related to S phase–specific DNA lesions (*11*, *35*). However, deletion of Rqh1 or Mus81 in nse6 or in hypomorphic nse1, nse2, or nse3 mutants results in synthetic lethality, indicating that dissolution and resolution of HR structures becomes critical in cells with compromised SMC5/6 function (*35*). To test whether this is also the case in human cells, we depleted SMC5/6 pathway proteins from PSNG13 cells, which are unable to dissolve recombination intermediates because of mutations in the BLM helicase (Rqh1 homolog). Depletion of RAD18, SLF1, SLF2, and SMC5 strongly reduced the proliferation of PSNG13 cells relative to BLM-complemented PSNF5 cells (Fig. 5E and fig. S10D). Consistent with an involvement of the SMC5/6 pathway in the resolution of recombination intermediates or the avoidance of illegitimate recombination events (*11*, *36*), knockdown of SLF1 or SLF2 enhanced the rate of sister chromatid exchanges (fig. S10E). Moreover, depletion of SLF1 or SLF2 from U2OS cells significantly increased the frequency of ultrafine bridges and other abnormalities in anaphase cells (fig. S10, F and G, asterisks). From these lines of evidence, we conclude that SLF1 and SLF2 are important for genome stability maintenance in human cells.

RAD18 facilitates bypass of DNA damage encountered by the replication machinery by promoting the monoubiquitylation of the replication processivity factor PCNA (*37*). However, we found that both SLF1 and SLF2 were dispensable for replication block–induced PCNA monoubiquitylation and recruitment of the TLS polymerase Polη to stalled replication forks (Fig. 5, G and H). Likewise, knockdown of SLF1 or SLF2 did not affect FANCD2 monoubiquitylation in response to DNA damage (fig. S10H). Thus, we conclude that the RAD18-SLF1-SLF2 complex selectively promotes the function of SMC5/6 in HR, whereas it is not required for RAD18-mediated bypass of replication-blocking lesions.

In addition to the sequence similarity between NSE6 and SLF2 (fig. S10, B and C), we note a considerable analogy between the pathways governing recruitment of the SMC5/6 complex to DNA damage sites in yeast and humans. For instance, Rtt107, a BRCT repeat–containing protein like SLF1, has been shown to mediate SMC5/6 recruitment to DSBs in budding yeast (*14*). Moreover, the fission yeast ortholog of Rtt107, Brc1, is a high-copy suppressor of SMC5/6 deficiency in a manner requiring a noncatalytic function of RAD18 (*38*, *39*). Given these parallels, we propose that the SMC5/6 recruitment pathway has rapidly evolved to protect cells from replication-associated genotoxic stress.

Combined with existing data, our study suggests that we now know many of the players in postreplicative ICL repair. However, delineating their regulation and potential involvement in related repair pathways remains a challenging task. CHROMASS can be applied to other chromatin-associated processes, and with further development, it offers the perspective to also identify regulatory posttranslational modifications of the chromatin-bound factors in a global manner.

REFERENCES AND NOTES

1. D. Branzei, M. Foiani, Maintaining genome stability at the replication fork. *Nat. Rev. Mol. Cell Biol.* **11**, 208–219 (2010). doi: 10.1038/nrm2852; pmid: 20177396
2. J. E. Sale, Competition, collaboration and coordination—determining how cells bypass DNA damage. *J. Cell Sci.* **125**, 1633–1643 (2012). doi: 10.1242/jcs.094748; pmid: 22499669
3. A. J. Deans, S. C. West, DNA interstrand crosslink repair and cancer. *Nat. Rev. Cancer* **11**, 467–480 (2011). doi: 10.1038/nrc3088; pmid: 21701511
4. S. P. Jackson, J. Bartek, The DNA-damage response in human biology and disease. *Nature* **461**, 1071–1078 (2009). doi: 10.1038/nature08467; pmid: 19847258
5. M. Räschle *et al.*, Mechanism of replication-coupled DNA interstrand crosslink repair. *Cell* **134**, 969–980 (2008). doi: 10.1016/j.cell.2008.08.030; pmid: 18805090

6. D. T. Long, M. Räschle, V. Joukov, J. C. Walter, Mechanism of RAD51-dependent DNA interstrand cross-link repair. *Science* **333**, 84–87 (2011). doi: 10.1126/science.1204258; pmid: 21719678
7. P. Knipscheer *et al*., The Fanconi anemia pathway promotes replication-dependent DNA interstrand cross-link repair. *Science* **326**, 1698–1701 (2009). pmid: 19965384
8. K. Jeppsson, T. Kanno, K. Shirahige, C. Sjögren, The maintenance of chromosome structure: Positioning and functioning of SMC complexes. *Nat. Rev. Mol. Cell Biol.* **15**, 601–614 (2014). doi: 10.1038/nrm3857; pmid: 25145851
9. J. M. Murray, A. M. Carr, Smc5/6: A link between DNA repair and unidirectional replication? *Nat. Rev. Mol. Cell Biol.* **9**, 177–182 (2008). doi: 10.1038/nrm2309; pmid: 18059412
10. G. De Piccoli *et al*., Smc5-Smc6 mediate DNA double-strand-break repair by promoting sister-chromatid recombination. *Nat. Cell Biol.* **8**, 1032–1034 (2006). doi: 10.1038/ncb1466; pmid: 16892052
11. D. E. Bustard *et al*., During replication stress, non-SMC element 5 (NSE5) is required for Smc5/6 protein complex functionality at stalled forks. *J. Biol. Chem.* **287**, 11374–11383 (2012). doi: 10.1074/jbc.M111.336263; pmid: 22303010
12. J. H. Barlow *et al*., Identification of early replicating fragile sites that contribute to genome instability. *Cell* **152**, 620–632 (2013). doi: 10.1016/j.cell.2013.01.006; pmid: 23352430
13. J. Torres-Rosell *et al*., SMC5 and SMC6 genes are required for the segregation of repetitive chromosome regions. *Nat. Cell Biol.* **7**, 412–419 (2005). doi: 10.1038/ncb1239; pmid: 15793567
14. G. P. Leung, L. Lee, T. I. Schmidt, K. Shirahige, M. S. Kobor, Rtt107 is required for recruitment of the SMC5/6 complex to DNA double strand breaks. *J. Biol. Chem.* **286**, 26250–26257 (2011). doi: 10.1074/jbc.M111.235200; pmid: 21642432
15. N. Nagaraj *et al*., System-wide perturbation analysis with nearly complete coverage of the yeast proteome by single-shot ultra HPLC runs on a bench top Orbitrap. *Mol. Cell. Proteomics* **11**, M111.013722 (2012). doi: 10.1074/mcp.M113.031591; pmid: 24942700
16. See supplementary materials on *Science* Online.
17. J. Cox *et al*., Accurate proteome-wide label-free quantification by delayed normalization and maximal peptide ratio extraction, termed MaxLFQ. *Mol. Cell. Proteomics* **13**, 2513–2526 (2014). doi: 10.1074/mcp.M113.031591; pmid: 24942700
18. J. M. Svendsen *et al*., Mammalian BTBD12/SLX4 assembles a Holliday junction resolvase and is required for DNA repair. *Cell* **138**, 63–77 (2009). doi: 10.1016/j.cell.2009.06.030; pmid: 19596235
19. K. Kratz *et al*., Deficiency of FANCD2-associated nuclease KIAA1018/FAN1 sensitizes cells to interstrand crosslinking agents. *Cell* **142**, 77–88 (2010). doi: 10.1016/j.cell.2010.06.022; pmid: 20603016
20. C. MacKay *et al*., Identification of KIAA1018/FAN1, a DNA repair nuclease recruited to DNA damage by monoubiquitinated FANCD2. *Cell* **142**, 65–76 (2010). doi: 10.1016/j.cell.2010.06.021; pmid: 20603015
21. K. L. Chan, T. Palmai-Pallag, S. Ying, I. D. Hickson, Replication stress induces sister-chromatid bridging at fragile site loci in mitosis. *Nat. Cell Biol.* **11**, 753–760 (2009). doi: 10.1038/ncb1882; pmid: 19465922
22. V. G. Tusher, R. Tibshirani, G. Chu, Significance analysis of microarrays applied to the ionizing radiation response. *Proc. Natl. Acad. Sci. U.S.A.* **98**, 5116–5121 (2001). doi: 10.1073/pnas.091062498; pmid: 11309499
23. J.-R. Lin, M. K. Zeman, J.-Y. Chen, M.-C. Yee, K. A. Cimprich, SHPRH and HLTF act in a damage-specific manner to coordinate different forms of postreplication repair and prevent mutagenesis. *Mol. Cell* **42**, 237–249 (2011). doi: 10.1016/j.molcel.2011.02.026; pmid: 21396873
24. N. C. Hubner *et al*., Quantitative proteomics combined with BAC TransgeneOmics reveals in vivo protein interactions. *J. Cell Biol.* **189**, 739–754 (2010). doi: 10.1083/jcb.200911091; pmid: 20479470
25. T. Liu *et al*., RAD18-BRCTx interaction is required for efficient repair of UV-induced DNA damage. *DNA Repair* **11**, 131–138 (2012). doi: 10.1016/j.dnarep.2011.10.012; pmid: 22036607
26. J. Huang *et al*., RAD18 transmits DNA damage signalling to elicit homologous recombination repair. *Nat. Cell Biol.* **11**, 592–603 (2009). doi: 10.1038/ncb1865; pmid: 19396164
27. S. Panier *et al*., Tandem protein interaction modules organize the ubiquitin-dependent response to DNA double-strand breaks. *Mol. Cell* **47**, 383–395 (2012). doi: 10.1016/j.molcel.2012.05.045; pmid: 22742833
28. C. M. Helchowski, L. F. Skow, K. H. Roberts, C. L. Chute, C. E. Canman, A small ubiquitin binding domain inhibits ubiquitin-dependent protein recruitment to DNA repair foci. *Cell Cycle* **12**, 3749–3758 (2013). doi: 10.4161/cc.26640; pmid: 24107634
29. S. Bekker-Jensen, N. Mailand, Assembly and function of DNA double-strand break repair foci in mammalian cells. *DNA Repair* **9**, 1219–1228 (2010). doi: 10.1016/j.dnarep.2010.09.010; pmid: 21035408
30. N. P. Dantuma, T. A. Groothuis, F. A. Salomons, J. Neefjes, A dynamic ubiquitin equilibrium couples proteasomal activity to chromatin remodeling. *J. Cell Biol.* **173**, 19–26 (2006). doi: 10.1083/jcb.200510071; pmid: 16606690
31. C. Doil *et al*., RNF168 binds and amplifies ubiquitin conjugates on damaged chromosomes to allow accumulation of repair proteins. *Cell* **136**, 435–446 (2009). doi: 10.1016/j.cell.2008.12.041; pmid: 19203579
32. D. T. Long, V. Joukov, M. Budzowska, J. C. Walter, BRCA1 promotes unloading of the CMG helicase from a stalled DNA replication fork. *Mol. Cell* **56**, 174–185 (2014). doi: 10.1016/j.molcel.2014.08.012; pmid: 25219499
33. A. J. Deans, S. C. West, FANCM connects the genome instability disorders Bloom's syndrome and Fanconi anemia. *Mol. Cell* **36**, 943–953 (2009). doi: 10.1016/j.molcel.2009.12.006; pmid: 20064461
34. N. Mailand *et al*., RNF8 ubiquitylates histones at DNA double-strand breaks and promotes assembly of repair proteins. *Cell* **131**, 887–900 (2007). doi: 10.1016/j.cell.2007.09.040; pmid: 18001824
35. S. Pebernard, J. Wohlschlegel, W. H. McDonald, J. R. Yates 3rd, M. N. Boddy, The Nse5-Nse6 dimer mediates DNA repair roles of the Smc5-Smc6 complex. *Mol. Cell. Biol.* **26**, 1617–1630 (2006). doi: 10.1128/MCB.26.5.1617-1630.2006; pmid: 16478984
36. I. Miyabe, T. Morishita, T. Hishida, S. Yonei, H. Shinagawa, Rhp51-dependent recombination intermediates that do not generate checkpoint signal are accumulated in *Schizosaccharomyces pombe* rad60 and smc5/6 mutants after release from replication arrest. *Mol. Cell. Biol.* **26**, 343–353 (2006). doi: 10.1128/MCB.26.1.343-353.2006; pmid: 16354704
37. N. Mailand, I. Gibbs-Seymour, S. Bekker-Jensen, Regulation of PCNA-protein interactions for genome stability. *Nat. Rev. Mol. Cell Biol.* **14**, 269–282 (2013). doi: 10.1038/nrm3562; pmid: 23594953
38. D. M. Sheedy *et al*., Brc1-mediated DNA repair and damage tolerance. *Genetics* **171**, 457–468 (2005). doi: 10.1534/genetics.105.044966; pmid: 15972456
39. K. M. Lee *et al*., Brc1-mediated rescue of Smc5/6 deficiency: Requirement for multiple nucleases and a novel Rad18 function. *Genetics* **175**, 1585–1595 (2007). doi: 10.1534/genetics.106.067801; pmid: 17277362

ACKNOWLEDGMENTS

We thank A. Hyman and I. Poser for providing BAC cell lines; I. Hickson for providing BLM-deficient and -corrected cells; J. Huang for reagents; J. Cox, F. Gnad, M. Oroshi, R. Scheltema, and C. Schaab for bioinformatics support; S. Schmalbrock, A. Sewo Pires de Campos, C. Kuffer, and A. Kutznetsova for help with microscopy; K. Mayr, I. Paron, G. Sowa, S. Kroiss, B. Splettstösser, and people from the Max Planck animal facility for support; and S. Gruber, B. Pfander, M. Steger, M. Wierer, and F. Coscia for discussion and reading the manuscript. Supported by the Center for Integrated Protein Research Munich (CIPSM), the Novo Nordisk Foundation, the Danish Medical Research Council, the Danish Cancer Society, the Lundbeck Foundation, the Bundesministerium für Bildung und Forschung (grant FKZ01GS0861, DiGtoP consortium) and the European Committees Marie Skłodowska-Curie actions (grant PIEF-GA-2012-330675) and 7th Framework Program PROSPECTS (HEALTH-F4-2008-201648). J.C.W. was supported by NIH grant HL098316. J.C.W. is an investigator of the Howard Hughes Medical Institute. The mass spectrometry data have been deposited at Proteome Exchange: http://proteomecentral.proteomexchange.org.

SUPPLEMENTARY MATERIALS

www.sciencemag.org/content/348/6234/1253671/suppl/DC1
Materials and Methods
Supplementary Text
Figs. S1 to S10
Tables S1 and S2
References (*40*–*51*)

20 March 2014; accepted 19 March 2015
10.1126/science.1253671

REPORTS

QUANTUM SIMULATION

Two-dimensional superexchange-mediated magnetization dynamics in an optical lattice

R. C. Brown, R. Wyllie,* S. B. Koller, E. A. Goldschmidt, M. Foss-Feig, J. V. Porto†

The interplay of magnetic exchange interactions and tunneling underlies many complex quantum phenomena observed in real materials. We study nonequilibrium magnetization dynamics in an extended two-dimensional (2D) system by loading effective spin-1/2 bosons into a spin-dependent optical lattice and use the lattice to separately control the resonance conditions for tunneling and superexchange. After preparing a nonequilibrium antiferromagnetically ordered state, we observe relaxation dynamics governed by two well-separated rates, which scale with the parameters associated with superexchange and tunneling. With tunneling off-resonantly suppressed, we observe superexchange-dominated dynamics over two orders of magnitude in magnetic coupling strength. Our experiment will serve as a benchmark for future theoretical work as the detailed dynamics of this 2D, strongly correlated, and far-from-equilibrium quantum system remain out of reach of current computational techniques.

The interplay of spin and motion underlies some of the most intriguing and poorly understood behaviors in many-body quantum systems (*1*). A well-known example is the onset of superconductivity in cuprate compounds when mobile holes are introduced into an otherwise insulating two-dimensional (2D) quantum magnet (*2*). Understanding this behavior is particularly challenging because the insulating state has strong quantum spin fluctuations, and the introduction of holes impedes the use of numerically exact techniques for quantum-correlated systems in more than one dimension. Ultracold atoms in optical lattices realize tunable, idealized models of such behavior and can naturally operate in a regime where the quantum motion (tunneling) of particles and magnetic interactions (superexchange) appear simultaneously (*3*, *4*).

For ultracold atoms in equilibrium, the extremely small energy scale associated with superexchange interactions makes the observation of magnetism challenging, and short-range antiferromagnetic correlations resulting from superexchange have only recently been observed (*5*, *6*). Out-of-equilibrium superexchange-dominated dynamics has been demonstrated in isolated pairs of atoms (*7*), in 1D systems with single-atom spin impurities (*8*), and recently in the decay of spin-density waves (*9*). However, the perturbative origin of superexchange in these systems implies that it must be weak compared with tunneling, and thus the manifestation of superexchange requires extremely low motional entropy. Dipolar gases (*10*) and ultracold polar molecules (*11*) in lattices provide a promising route toward achieving large (nonperturbative) magnetic interactions (*12*), but technical limitations in these systems currently complicate the simultaneous observation of motional and spin-exchange effects.

Here, we study the magnetization dynamics of pseudospin-1/2 bosons in a 2D optical lattice after a global quench from an initially antiferromagnetically ordered state (*13*). The dynamics we observe are governed by a bosonic t-J model (*14*, *15*) and occur in a parameter regime where quantitatively accurate calculations are not currently possible. Using a checkerboard optical lattice, we continuously tune the magnetization dynamics from a tunneling-dominated regime into a regime where superexchange is dominant, even at relatively high motional entropies. We observe decay of the antiferromagnetic order with clearly identifiable time scales that correspond to the underlying Hamiltonian parameters for tunneling and superexchange. In contrast to the oscillatory dynamics observed in isolated pairs of atoms (*7*), we observe exponential decay of the magnetization. Some damping of the dynamics can be attributed to the extended, many-body nature of the experiment, but the degree of the expected damping is difficult to quantify because a full theoretical description of nonequilibrium 2D systems is lacking. This experiment bridges the gap between studies of nonequilibrium behavior in systems with exclusively motional (*16*–*20*) or spin (*21*, *22*) degrees of freedom, demonstrating the requisite control to explore the intriguing intermediate territory in which they coexist. In addition, the techniques that we demonstrate lay the groundwork for adiabatic preparation of low-entropy spin states relevant for studies of equilibrium quantum magnetism (*23*, *24*).

Our experiment uses two hyperfine states (denoted by ↑ and ↓) of ultracold ^{87}Rb atoms trapped

Joint Quantum Institute, National Institute of Standards and Technology (NIST), and University of Maryland, Gaithersburg, MD 20899, USA.
*Present address: Quantum Systems Division, Georgia Tech Research Institute, Atlanta, GA 30332, USA. †Corresponding author. E-mail: porto@jqi.umd.edu

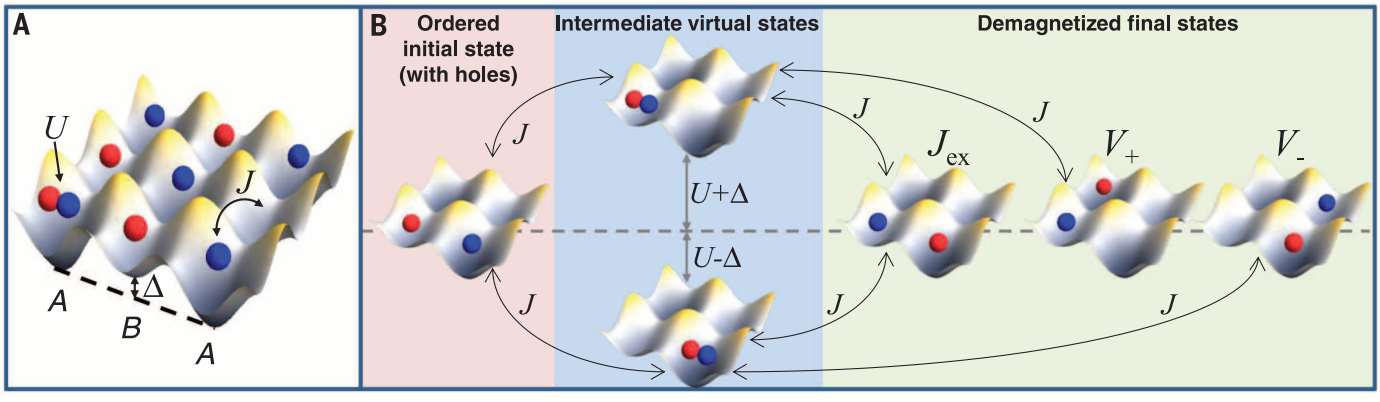
A
U
J
Δ
A
B
A
B
Ordered initial state (with holes)
Intermediate virtual states
Demagnetized final states
J
U+Δ
U-Δ
J
J
J

in a dynamically controlled, 2D checkerboard optical lattice (*25*) composed of two sublattices, *A* and *B* (Fig. 1A). For most experimental conditions presented here, our system is well described by a Bose-Hubbard model (*3*) characterized by a nearest-neighbor tunneling energy J, and an onsite interaction energy $U > 0$. In addition, we use the lattice to apply an energy offset $\Delta_\sigma = \Delta + \delta_\sigma$ between the *A* and *B* sublattices, consisting of a spin-independent part Δ and a spin-dependent part δ_σ acting as a staggered magnetic field, $\sigma \in \{\uparrow, \downarrow\}$ (*26*). All of these parameters can be dynamically controlled, which we exploit to prepare initial states with 2D antiferromagnetic order and to observe the resulting dynamics after a quench to different values of J, U, Δ, and δ_σ.

At unit filling, for $U \gg J$ and $\Delta_\sigma = 0$, double occupation at each site is allowed only virtually, and the Bose-Hubbard model can be mapped onto a ferromagnetic Heisenberg model (*4*, *27*) with a nearest-neighbor magnetic interaction strength J_{ex} that is second-order in the tunneling energy. In the presence of hole impurities, first-order tunneling (with the much larger energy scale J) must be included, which substantially modifies the dynamics even at low hole concentrations (*9*). The offset Δ_σ provides the flexibility to tune the relative importance of first-order tunneling and second-order superexchange processes. For example, below unit filling, if $|U - \Delta| \gg J$ and δ_σ, the Bose-Hubbard model can be mapped onto a bosonic t-J model with a staggered energy offset.

$$H = -J \sum_{\langle i,j\rangle,\sigma} a^\dagger_{i\sigma} a_{j\sigma} - \sum_{j\in A,\sigma} \Delta_\sigma a^\dagger_{j\sigma} a_{j\sigma}$$
$$-J_{ex} \sum_{\langle i,j\rangle} \mathbf{S}_i \cdot \mathbf{S}_j - \sum_{\langle i,j,k\rangle,\sigma\sigma'} V_j (a^\dagger_{i\sigma} \boldsymbol{\tau}_{\sigma\sigma'} a_{k\sigma'}) \cdot \mathbf{S}_j \quad (1)$$

The local spin operators are defined as $\mathbf{S}_i = \frac{1}{2} \sum_{\sigma\sigma'} a^\dagger_{i\sigma} \boldsymbol{\tau}_{\sigma\sigma'} a_{i\sigma'}$, where $a_{i\sigma}$ ($a^\dagger_{i\sigma}$) annihilates (creates) a hardcore boson of spin σ on site i, and $\boldsymbol{\tau}$ is a vector of Pauli matrices. The notation $\langle i,j\rangle$ indicates that the sum over i and j is restricted to nearest neighbors, and $\langle i,j,k\rangle$ indicates that the sum is restricted to sites i,j,k, such that $i \neq k$ are both nearest neighbors of j. The superexchange energy $J_{ex} = 4J^2U/(U^2 - \Delta^2)$ (Fig. 1B) can be either ferromagnetic ($U > \Delta$) or antiferromagnetic ($U < \Delta$) (*7*). The last term in Eq. 1 describes hole-mediated exchange, where an atom on site k interacts via superexchange with an atom on site j, while simultaneously hopping to site i (Fig. 1B). Here, $V_j = V_\pm \equiv J^2/(U \pm \Delta)$, where $-(+)$ applies when j is in the lower (higher) energy sublattice. In writing Eq. 1, we have ignored second-order processes (*28*, *29*) that conserve sublattice magnetization (*30*). When $|\Delta| \lesssim J$, first-order tunneling is resonant and dominates the magnetization dynamics except at extremely low hole densities. For $|\Delta| \gg J$, however, first-order tunneling is effectively suppressed, in which case superexchange dominates the magnetization dynamics. (The frequently ignored V_j term should be included for a quantitative description at nonzero hole density.) Superexchange is resonant when $|\delta_\sigma| \lesssim J_{ex}$ but is suppressed when $|\delta_\sigma| \gg J_{ex}$. The values of J, U, Δ, and δ_σ are determined from an experimentally calibrated model of the lattice (*30*). Inhomogeneity in the system—arising, for example, from trap curvature—primarily enters the model via inhomogeneities in the parameters Δ and δ_σ.

The experiments begin with $12(1) \times 10^3$ ^{87}Rb atoms loaded into a square 3D optical lattice with one atom per site (*30*), initially spin-polarized in the state $|\uparrow\rangle$. We use the hyperfine states $|\uparrow\rangle \equiv |F = 1, m_F = -1\rangle$ and $|\downarrow\rangle \equiv |1, +1\rangle$ to represent the pseudospin-1/2 system. (F and m_F are the quantum numbers labeling the total angular momentum and its projection along the quantization axis, respectively.) The 3D lattice is composed of a vertical lattice along z, which confines the atoms to an array of independent 2D planes, along with the dynamic 2D checkerboard lattice in the x-y plane. The vertical lattice depth is typically $V_z \approx 35E_R$, held constant throughout the experiment, and the 2D lattice depth is initially $V_{xy} \approx 30E_R$ with no staggered offset, $\Delta_\sigma = 0$ (the recoil energy $E_R = h^2/(2m\lambda^2)$, $E_R/h = 3.47$ kHz, where m is the mass of ^{87}Rb and $\lambda = 813$ nm). The atoms occupy roughly 13 to 15 2D planes, with the central plane containing 800 to 1100 atoms. The ratio of surface lattice sites to total lattice sites of the trapped cloud is ≈15% and sets a zero-temperature lower bound for the number of sites with neighboring holes. Based on spectroscopic measurements and assuming a thermal distribution (*30*), we estimate the hole density at the center of the cloud to be about 8%.

To measure the spin population independently on each sublattice, we map the four spin/sublattice states $|A\uparrow\rangle$, $|A\downarrow\rangle$, $|B\uparrow\rangle$ and $|B\downarrow\rangle$ onto four distinct Zeeman states and determine their populations with absorption imaging (Fig. 2A). To perform the experiment, we start with a spin-polarized configuration (Fig. 2B) and construct an initial state with staggered magnetization by applying the addressing offset δ_σ and transferring the *B*-site atoms to $|\downarrow\rangle$ (Fig. 2C). After returning δ_σ to zero, we initiate dynamics by quenching to a given configuration with lattice

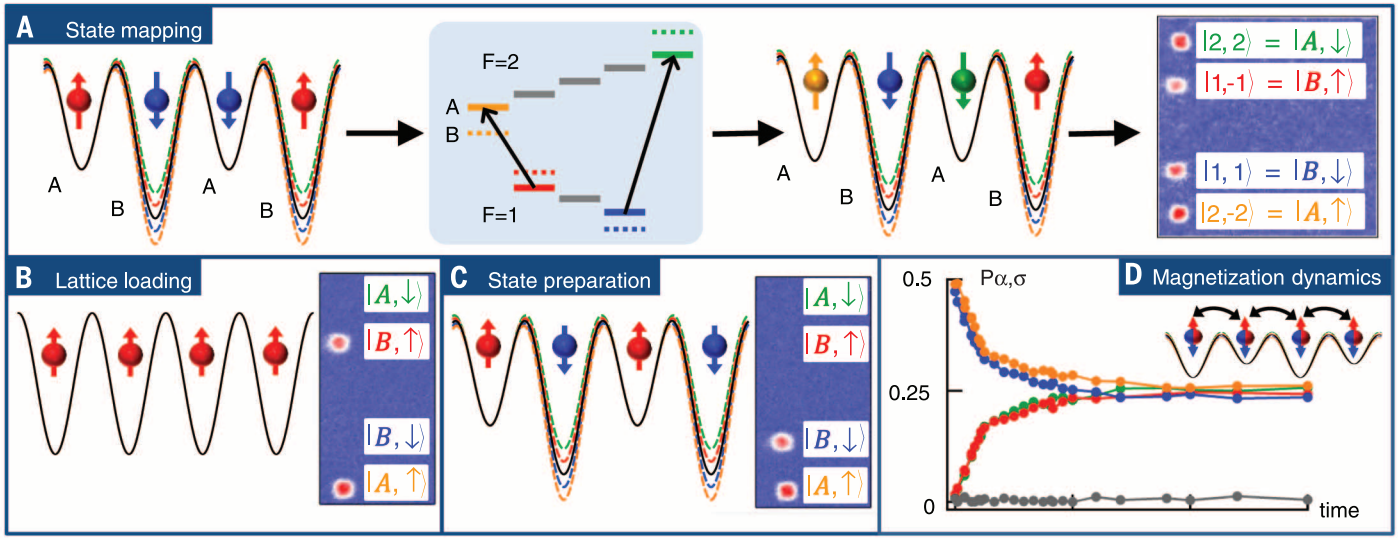

Fig. 2. Experimental sequence. (**A**) Spin/sublattice mapping. Atoms in $|\uparrow\rangle$ (red) or $|\downarrow\rangle$ (blue) occupy either the *A* or B sublattice (shown on the left). Applying a spin-dependent addressing offset to the *B* sublattice spectroscopically resolves the *A* and *B* sublattices (colored lines correspond to the potentials and energy levels seen by different hyperfine states). The $|A, \uparrow\rangle$ and $|A, \downarrow\rangle$ populations are microwave transferred to two different hyperfine states (yellow and green respectively), and the four mapped populations are measured by absorption imaging after Stern-Gerlach separation (shown on the right). (**B**) Initial lattice loading: a spin-polarized $|\uparrow\rangle$ unit filled Mott insulator. (**C**) Microwave state preparation. B sites are microwave-transferred from $|\uparrow\rangle$ to $|\downarrow\rangle$ using techniques similar to those employed for the state readout shown in (A). (**D**) Time evolution. After the lattice is quenched to a specific configuration, the spin/sublattice populations are measured as a function of time (including the nonparticipating $m_F = 0$ hyperfine state shown in gray).

depth V_{xy} and offsets Δ and δ_σ (Fig. 2D). The ramp time for the quench of 200 μs was chosen to be fast with respect to subsequent dynamics but slow enough to avoid band excitation. After a variable hold time t, we freeze the dynamics by raising V_{xy} to $\approx 30E_R$ and read out the populations $P_{\alpha,\sigma}$, from which we determine the staggered magnetization M_s and the sublattice population difference P_{A-B}.

$$M_s(t) \equiv P_{A,\uparrow}(t) + P_{B,\downarrow}(t) - P_{A,\downarrow}(t) - P_{B,\uparrow}(t),$$
$$P_{A-B}(t) \equiv P_{A,\uparrow}(t) + P_{A,\downarrow}(t) - P_{B,\uparrow}(t) - P_{B,\downarrow}(t). \quad (2)$$

The exchange terms in Eq. 1 conserve P_{A-B}, whereas the first-order tunneling does not, allowing for population transport between sublattices. We also monitor the total spin imbalance $P_{\uparrow-\downarrow}$ and the $m_F = 0$ population to quantify unwanted spin-changing processes that drive the atoms out of the pseudospin-1/2 manifold containing $|\uparrow\rangle$ and $|\downarrow\rangle$. The measured time for depopulation of the pseudospin-1/2 states is greater than 6 s, and the atom number lifetime in the lattice is greater than 3 s.

For the lattice parameters studied in this paper, the magnetization dynamics is well described by exponential decay, with decay time scales ranging between 0.5 ms and 500 ms. Example decay curves are shown in Fig. 3A for a lattice depth $V_{xy} \approx 15E_R$ and different offsets Δ. For some V_{xy} and Δ, the exponential decay clearly occurs on two well-separated time scales (Fig. 3A, inset): a fast time scale, τ_f, which dominates the behavior in shallow lattices when $\Delta \approx 0$ or $\Delta \approx U$, and a slow time scale, τ_s, which dominates the behavior in deep lattices with larger offset, $|\Delta| \gg U, J$.

To investigate the faster time scale, we measure M_s and P_{A-B} at a fixed decay time for different Δ, as shown in Fig. 3B for $V_{xy} = 15(0.5)\, E_R$. The 5-ms decay time (vertical line in Fig. 3A, inset) was chosen so that nearly all of the fast decay but little of the slow decay occurred. The fast magnetization decay reveals resonant features at $\Delta = 0$ and U, with the decay rate at $\Delta = 0$ twice as fast as at $\Delta = U$. (Near the resonance at $\Delta = U$, the condition $|U-\Delta| \gg J$ is not satisfied and the system must be described with the full Bose-Hubbard Hamiltonian, rather than Eq. 1.) In addition, P_{A-B} shows sublattice transport from B to A sites at $\Delta = U$, indicative of resonant first-order tunneling. At $\Delta \approx 0$ the demagnetizing sublattice transport $B \rightarrow A$ and $A \rightarrow B$ are balanced. We theoretically estimate the expected width of the $\Delta = U$ resonance in P_{A-B} to be $5J/h = 110$ Hz (*30*), which is narrower than the 530(60) Hz width that we observe experimentally, suggesting inhomogeneous broadening. We note, however, that the observed broadening is beyond what is expected from the measured trap curvature and is inconsistent with estimates of light-shift inhomogeneity from spectroscopic measurements (*30*). A residual δ_σ could account for the width.

The measured decay times τ_f for a range of lattice depths are plotted against the calculated tunneling time h/J in Fig. 3C, showing a decay rate linear in J/h, with $h/(J\tau_f) = 22(2)$. This slope is comparable to a simple theoretical estimate taking only resonant tunneling into account, which predicts $h/(J\tau_f) \approx 2\pi\sqrt{2z} \approx 18$, with $z = 4$ the lattice coordination number. Given the relatively large hole density near the surface of the cloud, the agreement with a noninteracting estimate is not surprising, although we would expect interactions to reduce the decay rate.

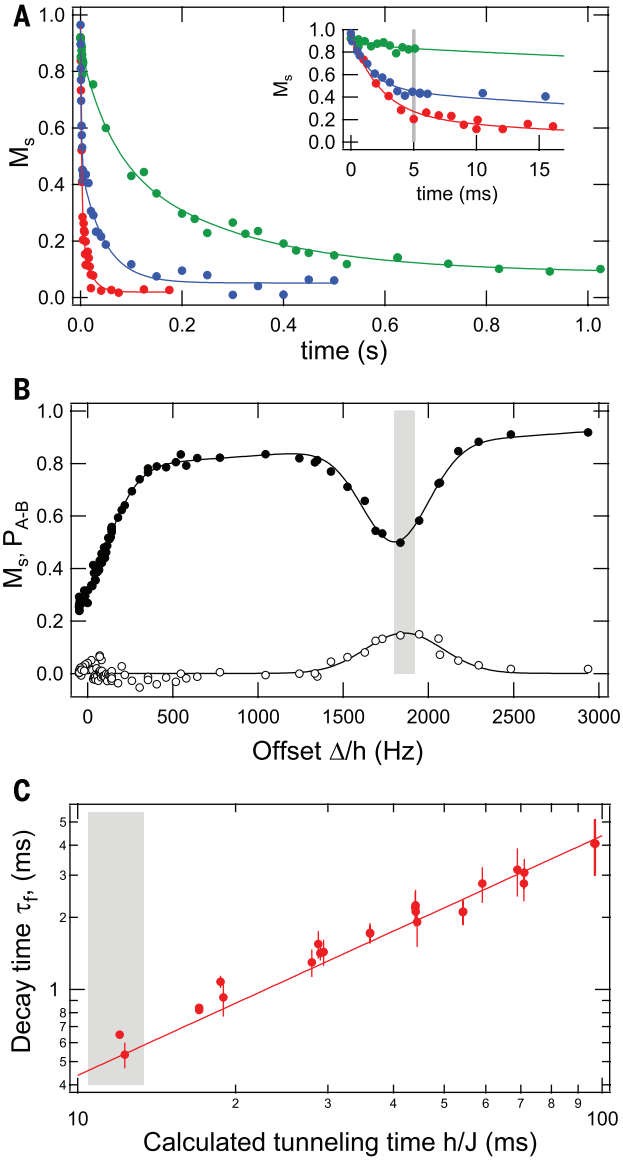

Fig. 3. Identification and control of tunneling. (**A**) Decay of magnetization at a lattice depth of $15E_R$ for different offsets Δ/h of 1000 Hz (green), 300 Hz (blue), and −50 Hz (red). (Inset) Short time evolution, with two time scales ($\tau_f \approx$ 2 ms and $\tau_s \approx$ 50 ms), both visible in the Δ/h = 300 Hz (blue) trace. The solid lines are double exponential fits. The vertical gray line indicates the fixed decay time at which the data in (B) were taken. (**B**) Magnetization M_s (filled circles) and sublattice population P_{A-B} (open circles) as a function of Δ at a fixed wait time of 5 ms $\gtrsim \tau_f$ after the quench. The fast magnetization decay is resonant at $\Delta = 0$ and $\Delta = U$, whereas sublattice transport occurs only near $\Delta = U$. The vertical gray band represents the calculated U with an uncertainty due to parameter extraction from the two-band model (*30*). (**C**) The fast time scale, τ_f, versus calculated tunneling time scale h/J for different lattice depths and $\Delta \lesssim J$. The solid line is $\tau_f = (h/J)/22$, and the gray band represents the uncertainty in the location of the 2D superfluid-insulator transition reported in (*31*). Error bars, ±1 SD statistical uncertainties from fitting.

To investigate the slow dynamics, we measure the magnetization decay time τ_s for $\Delta > U$, where first-order tunneling is negligible and superexchange should dominate the dynamics. To determine the dependence of τ_s on the spin-dependent staggered offset δ_σ, we measure the remaining staggered magnetization M_s and population difference P_{A-B} after a fixed wait time $\approx \tau_s$, as shown in Fig. 4A for a lattice depth 9.4(3) E_R and offset $\Delta/h = 4.3(2)$ kHz. As expected for superexchange dynamics, the magnetization decay is resonant in δ_σ. The full width at half maximum of the Lorentzian fit to the resonance is 126(14) Hz,

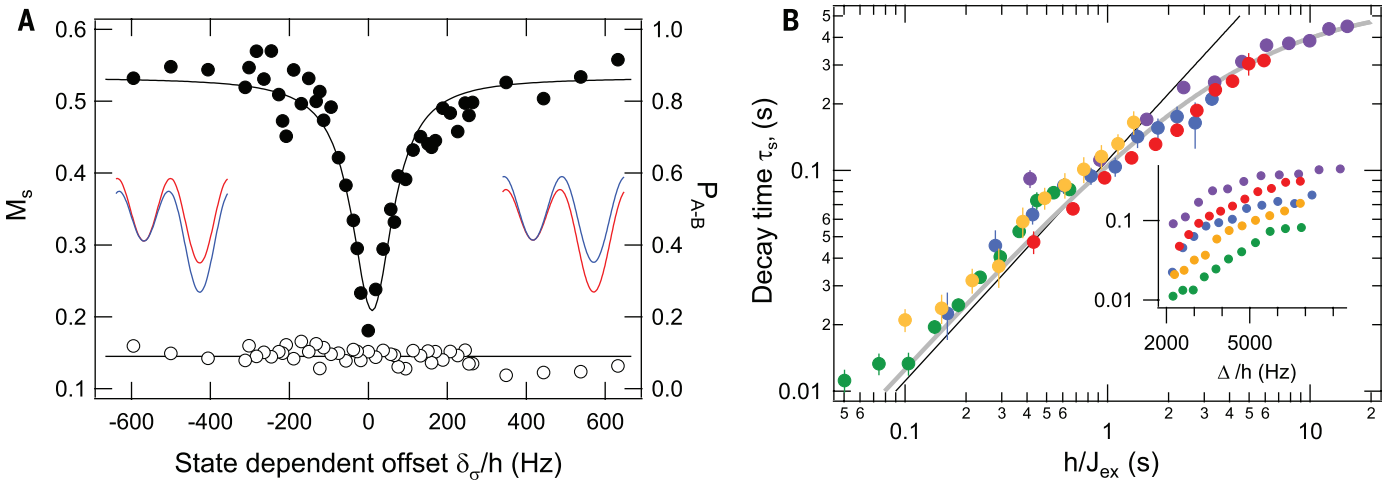

Fig. 4. Resonant superexchange. (**A**) Magnetization (filled circles) and sublattice population difference (open circles) at a fixed wait time of 70 ms versus spin-dependent energy offset δ_σ for $V_{xy} = 9.4\,E_R$ and $\Delta/h = 4.3$ kHz. The initial and final states of the second-order processes are resonant when $\delta_\sigma = 0$, resulting in increased magnetization decay. Lattice potentials (blue and red solid lines) show the sign change of δ_σ across resonance for a fixed offset $\Delta > U$. (**B**) Measured slow decay time τ_s versus calculated superexchange time h/J_{ex}. The filled purple, red, blue, yellow, and green markers represent lattice depths of 14.7, 13.2, 11.3, 9.4, and 7.5 E_R, respectively. (Inset) Measured slow decay rate versus applied staggered offset Δ. The decay time scale, τ_s, collapses with h/J_{ex} over roughly two orders of magnitude in J_{ex}. The black line is a perturbative estimate of the scaling, which was checked in small systems by comparing to exact diagonalization averaged over hole-induced disorder (*30*). The gray line is a fit to a saturated linear dependence of τ_s on h/J_{ex}.

considerably narrower than the observed tunneling resonances shown in Fig. 3B, and is most likely dominated by inhomogeneous broadening (second-order exchange processes are sensitive to inhomogeneity in both Δ and δ_σ). Figure 4A also shows that there is negligible sublattice transport associated with the demagnetization resonance. We note that at these values of Δ, the ground state of the system would have all atoms on the lower sublattice, and the conservation of P_{A-B} indicates that the spin dynamics occurs within a metastable manifold with respect to population.

Figure 4B shows the measured resonant decay times τ_s versus calculated h/J_{ex} for different V_{xy} and Δ, with $\delta_\sigma = 0$ and Δ chosen to be larger than U but considerably less than the next excited band. The decay time τ_s collapses to a single curve over two orders of magnitude in h/J_{ex}. The solid gray line through the data is a fit to $\tau_s = (AJ_{ex}/h + \Gamma_0)^{-1}$, where Γ_0 is needed to capture the apparent saturation of τ_s at large h/J_{ex}; the fitted values are $A = 7.8(4)$ and $\Gamma_0^{-1} = 0.57(2)$s. A quantitative calculation of the decay rate in 2D, including the effects of holes, is extremely challenging. However, a short-time perturbative calculation supports the experimental observation that τ_s scales with the single energy scale h/J_{ex}, which is not a priori expected given the existence of other ($V_\pm$) energy scales in the Hamiltonian (*30*). Surprisingly, the perturbative calculations suggest that the decay rate is nearly independent of hole density, which can be attributed to the approximate cancellation of two competing effects of holes: they decrease the rate of superexchange dynamics but simultaneously open new demagnetization channels through the hole-mediated spin-exchange term in Eq. 1. We therefore compare the data to an analytical estimate, strictly valid at unit filling, of $A \approx 2\pi\sqrt{z/2} \approx 9$ (black line in Fig. 4B). The empirically determined time scale Γ_0^{-1} (beyond which deviations from linear scaling become apparent in Fig. 4B) is shorter than the measured times for depopulation of the pseudospin manifold or loss of atoms. For times substantially larger than Γ_0^{-1}, interplane tunneling may also play a role in the short-time magnetization dynamics. This background decay rate may also be related to the nonzero relaxation processes observed outside the $\delta_\sigma = 0$ resonance in Fig. 4A. The mechanism for this off-resonant decay is not clear, but because the initial and final states differ in energy by substantially more than J_{ex}, it must arise from energy-nonconserving processes such as noise-assisted relaxation or doublon production (*20*). Corrections to J_{ex} caused by excited-band virtual processes (*8*), which we estimate to be on the order of 10 to 20% at the largest Δ and smallest V_{xy} shown in Fig. 4B, may partially explain the observed saturation.

The scaling and resonant behavior of the fast and slow relaxation processes clearly reveal their origin as first-order tunneling and superexchange, respectively. For $\Delta \gg J$, our experiment realizes an unusual situation where tunneling, which is only active within a given sublattice, is comparable in strength to the superexchange coupling. This feature—which is crucial to our ability to observe superexchange-dominated dynamics—may have interesting implications for the equilibration of a doped antiferromagnetic state, because it determines the extent to which entropy (initially introduced in the motional degrees of freedom) is shared by the spin degrees of freedom. For smaller but nonzero Δ, the ability to observe both tunneling and superexchange, often simultaneously and at experimentally accessible entropies, opens exciting opportunities to explore the nonequilibrium interplay of spin exchange and motion. Understanding the detailed dynamics of this strongly correlated, 2D quantum system is a formidable challenge, which may require the development of new theoretical techniques.

REFERENCES AND NOTES

1. A. Auerbach, *Interacting Electrons and Quantum Magnetism* (Springer, New York, 1994).
2. D. J. Scalapino, *Rev. Mod. Phys.* **84**, 1383–1417 (2012).
3. D. Jaksch, C. Bruder, J. I. Cirac, C. W. Gardiner, P. Zoller, *Phys. Rev. Lett.* **81**, 3108–3111 (1998).
4. L.-M. Duan, E. Demler, M. D. Lukin, *Phys. Rev. Lett.* **91**, 090402 (2003).
5. D. Greif, T. Uehlinger, G. Jotzu, L. Tarruell, T. Esslinger, *Science* **340**, 1307–1310 (2013).
6. R. A. Hart *et al.*, *Nature* **519**, 211–214 (2015).
7. S. Trotzky *et al.*, *Science* **319**, 295–299 (2008).
8. T. Fukuhara *et al.*, *Nature* **502**, 76–79 (2013).
9. S. Hild *et al.*, *Phys. Rev. Lett.* **113**, 147205 (2014).
10. A. de Paz *et al.*, *Phys. Rev. Lett.* **111**, 185305 (2013).
11. B. Yan *et al.*, *Nature* **501**, 521–525 (2013).
12. A. V. Gorshkov *et al.*, *Phys. Rev. Lett.* **107**, 115301 (2011).
13. P. Barmettler, M. Punk, V. Gritsev, E. Demler, E. Altman, *Phys. Rev. Lett.* **102**, 130603 (2009).
14. M. Boninsegni, *Phys. Rev. Lett.* **87**, 087201 (2001).
15. A. B. Kuklov, B. V. Svistunov, *Phys. Rev. Lett.* **90**, 100401 (2003).
16. M. Cheneau *et al.*, *Nature* **481**, 484–487 (2012).
17. M. Gring *et al.*, *Science* **337**, 1318–1322 (2012).
18. T. Langen, R. Geiger, M. Kuhnert, B. Rauer, J. Schmiedmayer, *Nat. Phys.* **9**, 640–643 (2013).
19. T. Kinoshita, T. Wenger, D. S. Weiss, *Nature* **440**, 900–903 (2006).
20. N. Strohmaier *et al.*, *Phys. Rev. Lett.* **104**, 080401 (2010).
21. P. Richerme *et al.*, *Nature* **511**, 198–201 (2014).
22. P. Jurcevic *et al.*, *Nature* **511**, 202–205 (2014).
23. A. S. Sørensen *et al.*, *Phys. Rev. A* **81**, 061603 (2010).
24. M. Lubasch, V. Murg, U. Schneider, J. I. Cirac, M.-C. Bañuls, *Phys. Rev. Lett.* **107**, 165301 (2011).
25. J. Sebby-Strabley, M. Anderlini, P. S. Jessen, J. V. Porto, *Phys. Rev. A* **73**, 033605 (2006).
26. P. J. Lee *et al.*, *Phys. Rev. Lett.* **99**, 020402 (2007).
27. Strictly speaking, the validity of Eq. 1 also requires $|\Delta - U/2| \gg J^2/\Delta$ and $|\Delta - 3U/2| \gg J^2/|U - \Delta|$ to avoid

narrower second-order resonances that are associated with double and triple occupancy, respectively.
28. S. Fölling *et al.*, *Nature* **448**, 1029–1032 (2007).
29. F. Meinert *et al.*, *Science* **344**, 1259–1262 (2014).
30. Materials and methods are available as supplementary materials on *Science* Online.
31. I. B. Spielman, W. D. Phillips, J. V. Porto, *Phys. Rev. Lett.* **100**, 120402 (2008).

ACKNOWLEDGMENTS

This work was partially supported by the Army Research Office's atomtronics Multidisciplinary University Research Initiative and NIST. M.F.F. and E.A.G. acknowledge support from the National Research Council Research Associateship program. We thank B. Grinkemeyer for his contributions to the data taking effort, E. Tiesinga and S. Paul for discussions about tight-binding models, and A. V. Gorshkov and S. Sugawa for a critical reading of the manuscript.

SUPPLEMENTARY MATERIALS

www.sciencemag.org/content/348/6234/540/suppl/DC1
Materials and Methods
Figs. S1 to S3
References (*32*–*35*)

28 October 2014; accepted 27 March 2015
10.1126/science.aaa1385

QUANTUM GASES

Observation of isolated monopoles in a quantum field

M. W. Ray,[1]* E. Ruokokoski,[2] K. Tiurev,[2] M. Möttönen,[2,3]† D. S. Hall[1]

Topological defects play important roles throughout nature, appearing in contexts as diverse as cosmology, particle physics, superfluidity, liquid crystals, and metallurgy. Point defects can arise naturally as magnetic monopoles resulting from symmetry breaking in grand unified theories. We devised an experiment to create and detect quantum mechanical analogs of such monopoles in a spin-1 Bose-Einstein condensate. The defects, which were stable on the time scale of our experiments, were identified from spin-resolved images of the condensate density profile that exhibit a characteristic dependence on the choice of quantization axis. Our observations lay the foundation for experimental studies of the dynamics and stability of topological point defects in quantum systems.

Two structures are topologically equivalent if they can be continuously transformed into one another (*1*, *2*), such as the letters O and P. Topological defects exist in a physical system if its state is not topologically equivalent to its ground state. Such defects can decay or disappear only as a result of globally nontrivial transformations, rendering them long-lived and ubiquitous in the universe.

Line defects are among the most common topological structures. In classical physics, for example, dislocations in a crystal lattice (*3*) can determine the strength and hardness of materials. In quantum physics, a line defect in a complex-valued order parameter is accompanied by a phase winding of an integer multiple of 2π. These quantized vortices are regarded as the hallmark of superfluidity (*4*, *5*) and constitute a versatile tool in the study of quantum physics. In contrast, the roles played by point defects in three-dimensional superfluids and superconductors remain less explored experimentally, although related objects such as skyrmion solitons and boojums at domain interfaces have been observed (*6*–*9*).

Homotopy theory (*2*, *10*) is a mathematical tool that classifies topological point defects according to the behavior of the order parameter on closed surfaces. Evaluation of the second homotopy group reveals whether point defects can occur. Nematic liquid crystals (*11*) and colloids (*12*) are examples of classical systems for which the second homotopy group is nontrivial and point defects have been observed [see also (*13*)]. Quantum systems described by multidimensional fields are also predicted to support point defects as stable elementary particles (*2*). The magnetic monopole (*14*, *15*) that emerges under broken symmetry in grand unified theories (*16*) is one such example.

The polar phase of a spin-1 Bose-Einstein condensate (BEC) permits the existence of topological point defects in the quantum mechanical order parameter (*17*, *18*). Although these defects are not elementary particles, they are analogous quantum objects often referred to as monopoles.

In our experiments, we create a topological point defect in the spin-1 order parameter of an ^{87}Rb BEC using a method originally suggested in (*19*) and used to create Dirac monopoles in a ferromagnetic BEC in (*20*) [see related work in (*21*)]. The key technical difference relative to (*20*) is that the condensate is initialized in its polar phase. This seemingly minor modification leads to a topological excitation with properties that are fundamentally different from those of the recently observed Dirac monopole. The Dirac monopole is not a pointlike topological defect in the order parameter, as the second homotopy group of the ferromagnetic phase contains only the identity element (*22*). Consequently, Dirac monopoles are attached to at least one terminating nodal line (*23*), which renders the energetics and dynamics of the excitation similar to those of vortices. No such nodal line is attached to the point defect structure we create here in the order parameter field, and hence we refer to it as an isolated monopole.

A spin-1 condensate can be described by the order parameter

$$\Phi(\mathbf{r}) = \sqrt{n(\mathbf{r})}\exp[i\phi(\mathbf{r})]\zeta(\mathbf{r}) \qquad (1)$$

where n is the particle density, ϕ is the scalar phase, and the spinor is represented by a normalized complex-valued vector $\zeta = (\zeta_{+1}\ \zeta_0\ \zeta_{-1})^T$. Here, $\zeta_m = \langle m|\zeta\rangle$ is the mth spinor component along the quantization axis z. The most general polar order parameter, for which the local spin vanishes, is given by

$$\Phi = \frac{\sqrt{n}\,\exp(i\phi)}{\sqrt{2}}\begin{pmatrix} -\exp(-i\alpha)\,\sin\beta \\ \sqrt{2}\,\cos\beta \\ \exp(i\alpha)\,\sin\beta \end{pmatrix} = \frac{\sqrt{n}\,\exp(i\phi)}{\sqrt{2}}\begin{pmatrix} -d_x + id_y \\ \sqrt{2}d_z \\ d_x + id_y \end{pmatrix} \qquad (2)$$

where the Euler angles $\beta(\mathbf{r})$ and $\alpha(\mathbf{r})$ refer to the spin rotation of a spinor $(0\,1\,0)^T$ about the y and z axes, respectively, and $\hat{\mathbf{d}}$ is a three-dimensional

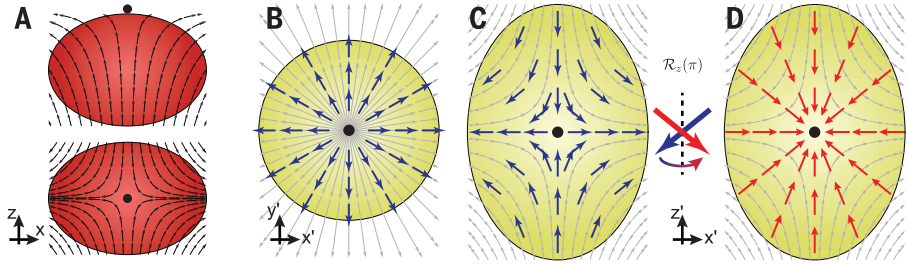

Fig. 1. Schematic representation of the experiment. (**A**) Magnetic field lines as B_z is decreased. The zero point of the magnetic field is shown as a black dot. (**B** to **D**) Cross sections through the condensate in the $x'y'$ plane (B) and in the $x'z'$ plane (C) showing the nematic vector field (thick arrows) defining our isolated monopole structure, which is related to the hedgehog monopole structure (D) by a rotation of π about the z' axis, $\mathcal{R}_z(\pi)$. The primed coordinates are defined as $x' = x$, $y' = y$, and $z' = 2z$; the gray arrows depict magnetic field lines.

[1]Department of Physics and Astronomy, Amherst College, Amherst, MA 01002, USA. [2]QCD Labs, COMP Centre of Excellence, Department of Applied Physics, Aalto University, FI-00076 Aalto, Finland. [3]Low Temperature Laboratory (OVLL), Aalto University, FI-00076 Aalto, Finland.
*Present address: Department of Physics and Astronomy, Union College, Schenectady, NY 12308, USA. †Corresponding author. E-mail: mikko.mottonen@aalto.fi

narrower second-order resonances that are associated with double and triple occupancy, respectively.
28. S. Fölling *et al.*, *Nature* **448**, 1029–1032 (2007).
29. F. Meinert *et al.*, *Science* **344**, 1259–1262 (2014).
30. Materials and methods are available as supplementary materials on *Science* Online.
31. I. B. Spielman, W. D. Phillips, J. V. Porto, *Phys. Rev. Lett.* **100**, 120402 (2008).

ACKNOWLEDGMENTS

This work was partially supported by the Army Research Office's atomtronics Multidisciplinary University Research Initiative and NIST. M.F.F. and E.A.G. acknowledge support from the National Research Council Research Associateship program. We thank B. Grinkemeyer for his contributions to the data taking effort, E. Tiesinga and S. Paul for discussions about tight-binding models, and A. V. Gorshkov and S. Sugawa for a critical reading of the manuscript.

SUPPLEMENTARY MATERIALS

www.sciencemag.org/content/348/6234/540/suppl/DC1
Materials and Methods
Figs. S1 to S3
References (*32*–*35*)

28 October 2014; accepted 27 March 2015
10.1126/science.aaa1385

QUANTUM GASES

Observation of isolated monopoles in a quantum field

M. W. Ray,[1]* E. Ruokokoski,[2] K. Tiurev,[2] M. Möttönen,[2,3]† D. S. Hall[1]

Topological defects play important roles throughout nature, appearing in contexts as diverse as cosmology, particle physics, superfluidity, liquid crystals, and metallurgy. Point defects can arise naturally as magnetic monopoles resulting from symmetry breaking in grand unified theories. We devised an experiment to create and detect quantum mechanical analogs of such monopoles in a spin-1 Bose-Einstein condensate. The defects, which were stable on the time scale of our experiments, were identified from spin-resolved images of the condensate density profile that exhibit a characteristic dependence on the choice of quantization axis. Our observations lay the foundation for experimental studies of the dynamics and stability of topological point defects in quantum systems.

Two structures are topologically equivalent if they can be continuously transformed into one another (*1*, *2*), such as the letters O and P. Topological defects exist in a physical system if its state is not topologically equivalent to its ground state. Such defects can decay or disappear only as a result of globally nontrivial transformations, rendering them long-lived and ubiquitous in the universe.

Line defects are among the most common topological structures. In classical physics, for example, dislocations in a crystal lattice (*3*) can determine the strength and hardness of materials. In quantum physics, a line defect in a complex-valued order parameter is accompanied by a phase winding of an integer multiple of 2π. These quantized vortices are regarded as the hallmark of superfluidity (*4*, *5*) and constitute a versatile tool in the study of quantum physics. In contrast, the roles played by point defects in three-dimensional superfluids and superconductors remain less explored experimentally, although related objects such as skyrmion solitons and boojums at domain interfaces have been observed (*6*–*9*).

Homotopy theory (*2*, *10*) is a mathematical tool that classifies topological point defects according to the behavior of the order parameter on closed surfaces. Evaluation of the second homotopy group reveals whether point defects can occur. Nematic liquid crystals (*11*) and colloids (*12*) are examples of classical systems for which the second homotopy group is nontrivial and point defects have been observed [see also (*13*)]. Quantum systems described by multidimensional fields are also predicted to support point defects as stable elementary particles (*2*). The magnetic monopole (*14*, *15*) that emerges under broken symmetry in grand unified theories (*16*) is one such example.

The polar phase of a spin-1 Bose-Einstein condensate (BEC) permits the existence of topological point defects in the quantum mechanical order parameter (*17*, *18*). Although these defects are not elementary particles, they are analogous quantum objects often referred to as monopoles.

In our experiments, we create a topological point defect in the spin-1 order parameter of an ^{87}Rb BEC using a method originally suggested in (*19*) and used to create Dirac monopoles in a ferromagnetic BEC in (*20*) [see related work in (*21*)]. The key technical difference relative to (*20*) is that the condensate is initialized in its polar phase. This seemingly minor modification leads to a topological excitation with properties that are fundamentally different from those of the recently observed Dirac monopole. The Dirac monopole is not a pointlike topological defect in the order parameter, as the second homotopy group of the ferromagnetic phase contains only the identity element (*22*). Consequently, Dirac monopoles are attached to at least one terminating nodal line (*23*), which renders the energetics and dynamics of the excitation similar to those of vortices. No such nodal line is attached to the point defect structure we create here in the order parameter field, and hence we refer to it as an isolated monopole.

A spin-1 condensate can be described by the order parameter

$$\Phi(\mathbf{r}) = \sqrt{n(\mathbf{r})}\exp[i\phi(\mathbf{r})]\zeta(\mathbf{r}) \qquad (1)$$

where n is the particle density, ϕ is the scalar phase, and the spinor is represented by a normalized complex-valued vector $\zeta = (\zeta_{+1}\ \zeta_0\ \zeta_{-1})^T$. Here, $\zeta_m = \langle m|\zeta\rangle$ is the mth spinor component along the quantization axis z. The most general polar order parameter, for which the local spin vanishes, is given by

$$\Phi = \frac{\sqrt{n}\,\exp(i\phi)}{\sqrt{2}}\begin{pmatrix} -\exp(-i\alpha)\,\sin\beta \\ \sqrt{2}\,\cos\beta \\ \exp(i\alpha)\,\sin\beta \end{pmatrix} = \frac{\sqrt{n}\,\exp(i\phi)}{\sqrt{2}}\begin{pmatrix} -d_x + id_y \\ \sqrt{2}d_z \\ d_x + id_y \end{pmatrix} \qquad (2)$$

where the Euler angles $\beta(\mathbf{r})$ and $\alpha(\mathbf{r})$ refer to the spin rotation of a spinor $(0\,1\,0)^T$ about the y and z axes, respectively, and $\hat{\mathbf{d}}$ is a three-dimensional

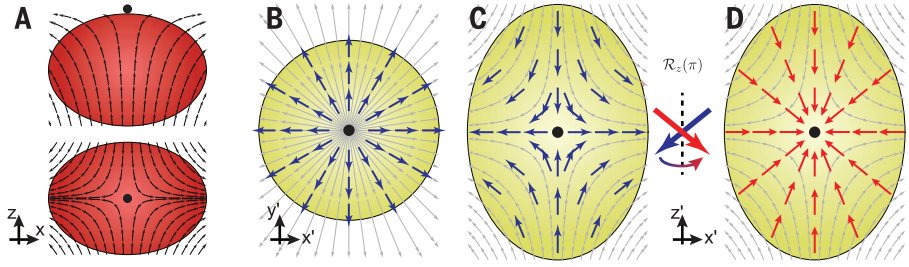

Fig. 1. Schematic representation of the experiment. (**A**) Magnetic field lines as B_z is decreased. The zero point of the magnetic field is shown as a black dot. (**B** to **D**) Cross sections through the condensate in the $x'y'$ plane (B) and in the $x'z'$ plane (C) showing the nematic vector field (thick arrows) defining our isolated monopole structure, which is related to the hedgehog monopole structure (D) by a rotation of π about the z' axis, $\mathcal{R}_z(\pi)$. The primed coordinates are defined as $x' = x$, $y' = y$, and $z' = 2z$; the gray arrows depict magnetic field lines.

[1]Department of Physics and Astronomy, Amherst College, Amherst, MA 01002, USA. [2]QCD Labs, COMP Centre of Excellence, Department of Applied Physics, Aalto University, FI-00076 Aalto, Finland. [3]Low Temperature Laboratory (OVLL), Aalto University, FI-00076 Aalto, Finland.
*Present address: Department of Physics and Astronomy, Union College, Schenectady, NY 12308, USA. †Corresponding author. E-mail: mikko.mottonen@aalto.fi

Downloaded from www.sciencemag.org on April 30, 2015

real-valued unit vector field known as the nematic vector. Equation 2 shows that the polar spin-1 condensate is simply described by the mean-field order parameter

$$\Psi(\mathbf{r}) = \sqrt{n(\mathbf{r})}\exp[i\phi(\mathbf{r})]\hat{\mathbf{d}}(\mathbf{r}) \qquad (3)$$

with its topological properties determined by the factor $\exp[i\phi(\mathbf{r})]\hat{\mathbf{d}}(\mathbf{r})$ (*24*). Note that any unitary spin rotation imposed on the order parameter in Eq. 2 corresponds to an identical rotation of $\hat{\mathbf{d}}$. Thus, the nematic vector $\hat{\mathbf{d}}$ follows adiabatic changes in the external magnetic field, much as the direction of the spin follows the field in the ferromagnetic case.

The initial atom number in the optically trapped ^{87}Rb BEC is $N \approx 2.1 \times 10^5$ with calculated radial and axial Thomas-Fermi radii $R = 7.2\ \mu$m and $Z = 5.4\ \mu$m, respectively, and corresponding optical trapping frequencies $\omega_r \approx 2\pi \times 124$ Hz and $\omega_z \approx 2\pi \times 164$ Hz, respectively. The creation process begins with $\hat{\mathbf{d}}$ aligned with a uniform magnetic field $\mathbf{B}_b(t) = B_x(t)\hat{\mathbf{x}} + B_y(t)\hat{\mathbf{y}} + B_z(t)\hat{\mathbf{z}}$ (*24*). We use $\mathbf{B}_b(t) = B_z(t)\hat{\mathbf{z}}$ here, but the experimental results are independent of the choice of direction. A quadrupole magnetic field $\mathbf{B}_q(\mathbf{r}) = b_q(x\hat{\mathbf{x}} + y\hat{\mathbf{y}} - 2z\hat{\mathbf{z}})$ of strength $b_q = 3.7$ G/cm is then introduced; the zero point

$$\mathbf{r}_0(t) = \frac{-B_x(t)\hat{\mathbf{x}} - B_y(t)\hat{\mathbf{y}} + \frac{B_z(t)\hat{\mathbf{z}}}{2}}{b_q} \qquad (4)$$

of the total magnetic field $\mathbf{B}(\mathbf{r},t) = \mathbf{B}_q(\mathbf{r}) + \mathbf{B}_b(t)$ is initially located well outside the condensate. We then change $\mathbf{B}_b$ until $\mathbf{r}_0$ lies near the center of the condensate (Fig. 1A). This "creation ramp" is carried out nearly adiabatically ($dB_z/dt = -0.25$ G/s)—that is, $\hat{\mathbf{d}}(\mathbf{r},t) \approx \hat{\mathbf{B}}(\mathbf{r},t)$—thereby creating the isolated monopole structure in the order parameter field shown in Fig. 1, B and C. Nonadiabatic excitations and spin-exchange collisions are measured to be relatively small (~10%) for the experimental parameter values used here.

To select a quantization axis for imaging the monopole structure, we apply a "projection ramp" in which the magnetic bias field is rapidly increased to $|\mathbf{B}_b|/b_q >> \{R, Z\}$ along a direction of our choice, $\hat{\mathbf{z}}_p$, leaving the nematic vector essentially unchanged. Subsequently, the spinor components quantized along this axis, $\langle m_p|\zeta\rangle$, are spatially separated and imaged in both the vertical ($\hat{\mathbf{z}}$) and horizontal ($\hat{\mathbf{y}}$) directions (*24*). In Fig. 2, A and D, we show the corresponding experimentally obtained particle densities in the simple case $\hat{\mathbf{z}}_p = -\hat{\mathbf{z}}$. The theory [Eq. 2 with $\hat{\mathbf{d}}(\mathbf{r},t) = \hat{\mathbf{B}}_q(\mathbf{r})$] predicts hollow-core vortices of opposite unit circulations in the $m = \pm 1$ components along z, in agreement with the observed density "holes" in Fig. 2D. The unit phase winding and the opposite circulations of the two vortices are experimentally confirmed using interferometric techniques (*24*) (figs. S1 and S2). Furthermore, the data in Fig. 2, A and C, are in qualitative agreement with Eq. 2 because the particle density in the $m = 0$ component $n|\zeta_0|^2 \propto d_z^2$ vanishes in the $z = 0$ plane, and the other two components $n|\zeta_{\pm 1}|^2 \propto d_x^2 + d_y^2$ accumulate in its vicinity. This agreement constitutes the primary evidence for the existence of the monopole.

We modeled the experimental creation and imaging process numerically by solving the full three-dimensional dynamics of the mean-field spinor order parameter from the spin-1 Gross-Pitaevskii equation (*19*). Figures 2 and 3 show one-to-one comparisons of the numerically obtained particle density distributions to the experimental results without any free parameters. The good quantitative agreement between the simulations and the experiments reinforces the congruence between the experiments and the results of the analytic theory, thereby providing complementary evidence for the realization of an isolated monopole structure in the order parameter. Discrepancies between the numerical and experimental results—for example, the density peak in the $m = 0$ component in Fig. 2F—may arise from the experimental noise and the choice of imaging technique that are not taken fully into account in the simulations (*24*).

Particle densities identical to those shown in Fig. 2 for our isolated monopole are expected for the topologically equivalent hedgehog monopole structure shown in Fig. 1D, as the only difference between the spinors of the two configurations is the sign of the $m = \pm 1$ components (see Eq. 2 and Fig. 1, C and D). In fact, after the projection ramp $\hat{\mathbf{z}}_p = \pm\hat{\mathbf{z}}$, the order parameter oscillates between the two configurations because of the 350-kHz Larmor precession of the nematic vector about $\hat{\mathbf{z}}$. Because the other condensate dynamics occur on much longer time scales, the experiment also accurately produces the hedgehog monopole, as confirmed by the numerical simulations shown in fig. S3.

One characteristic feature of a quantum mechanical point defect is that arbitrary rotations of a properly chosen coordinate system, $\mathcal{D}$, can be compensated by rotations in the order parameter space, $\hat{\mathcal{D}}$, and vice versa. We study whether the created point defect has this property by imposing a spin rotation $\hat{\mathcal{D}}_p$ on the spin state of the defect $|\zeta\rangle$ such that we choose the direction of the projection ramp, $\hat{\mathbf{z}}_p$, defined by

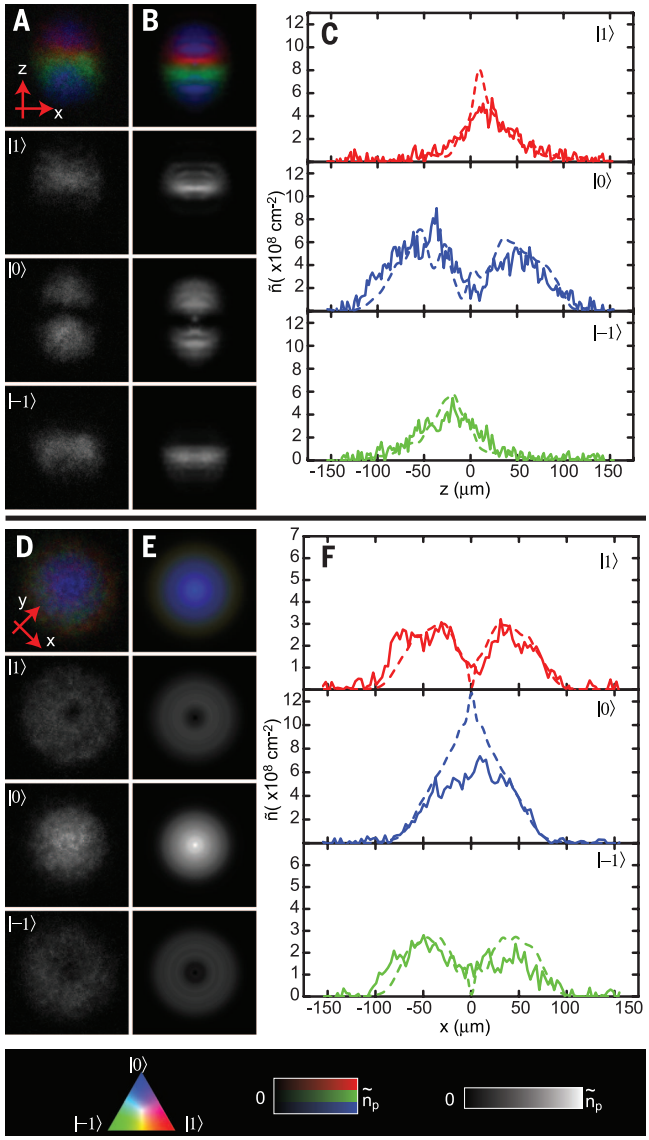

Fig. 2. Experiment compared to numerical simulations following a projection ramp along –*z*. (**A** and **D**) Experimentally obtained images of the condensate taken along the horizontal (*y*) axis (A) and the vertical (*z*) axis (D). (**B** and **E**) Results of the corresponding numerical simulations. In each panel, the top image gives a false-color composite, in which the color intensity represents the particle density of each spinor component integrated along the respective imaging axis. The lower three sets of images show the densities for the individual components. (**C** and **F**) Quantitative comparison of experimental (solid lines) and simulated (dashed lines) column density, $\tilde{n}$, for cross sections. The field of view is 288 μm × 288 μm for images along the horizontal axis and 219 μm × 219 μm for those along the vertical axis. The peak column density in all images is $\tilde{n}_p = 12.9 \times 10^8$ cm^{-2}. Color and intensity scales are shown at bottom of figure.

the coordinate rotation $(x_p, y_p, z_p) = \mathcal{D}_p^{-1}(x, y, z)$. The projection of the original spinor onto the new z_p-quantized basis is equal to the projection of the rotated spinor onto the z-quantized basis:

$$\langle m_p|\zeta\rangle = \langle m_p|\hat{\mathcal{D}}_p^{\dagger}\hat{\mathcal{D}}_p|\zeta\rangle = \langle m|\hat{\mathcal{D}}_p|\zeta\rangle \quad (5)$$

Thus, the rotational compensation property given above demands that there exists a rotation $\mathcal{D}_v$ into a new coordinate system $(x_v, y_v, z_v) = \mathcal{D}_v(x, y, z)$ such that Eq. 2, with (x, y, z) replaced by (x_v, y_v, z_v), yields the observed spinor components. Below, we analytically find the new coordinate system for both the hedgehog monopole and our isolated monopole in the case of an arbitrary projection axis, and show matching experimental observations.

The hedgehog monopole is characterized by the nematic vector $\hat{\mathbf{d}}_h = -\hat{\mathbf{r}}'$, where the primed coordinates are defined as $(x', y', z') = (x, y, 2z)$. Because the radial vectors in any two rotated coordinate systems coincide, $\hat{\mathbf{r}}'(x'_p, y'_p, z'_p) = \hat{\mathbf{r}}'_p(x'_p, y'_p, z'_p)$, we can choose $(x'_v, y'_v, z'_v) = (x'_p, y'_p, z'_p)$ (i.e., $\mathcal{D}_v = \mathcal{D}_p^{-1}$). Together with Eq. 2, this shows that the vortices in the $m_p = \pm 1$ components of the hedgehog configuration always align with the projection axis $\hat{\mathbf{z}}_p$. To find how the vortices will be oriented in the case of our isolated monopole, we make use of the property that the hedgehog monopole is obtained from the isolated monopole configuration by a continuous π-rotation about the z axis (Fig. 1, C and D); that is, $\hat{\mathcal{R}}_z(\pi)|\zeta_m\rangle = |\zeta_h\rangle$ and $\mathcal{R}_z(\pi)\hat{\mathbf{d}}_m = \hat{\mathbf{d}}_h$. By writing the observed spinor component as

$$\begin{aligned}\langle m_p|\zeta_m\rangle &= \langle m_p|\hat{\mathcal{R}}_z(\pi)^{\dagger}\hat{\mathcal{R}}_z(\pi)|\zeta_m\rangle \\ &= [\langle m_p|\hat{\mathcal{R}}_z(\pi)^{\dagger}]|\zeta_h\rangle \end{aligned} \quad (6)$$

we find that a proper choice of the new coordinate system is $(x_v, y_v, z_v) = \mathcal{R}_z(\pi)(x_p, y_p, z_p)$. Thus, the vortices are aligned with $\hat{\mathbf{z}}_v = \mathcal{R}_z(\pi)\hat{\mathbf{z}}_p$.

The isolated monopole (Fig. 1, B and C) is topologically equivalent to the hedgehog structure (Fig. 1D) and has the same topological charge and stability properties. However, the fact that the projection axis and the vortex axis are not always aligned makes the isolated monopole an ideal object to demonstrate that the observed vortices are not technical artifacts of the projection ramp. The corresponding experimental results are shown in Fig. 4. In agreement with the result $\hat{\mathbf{z}}_v = \mathcal{R}_z(\pi)\hat{\mathbf{z}}_p$ derived above, we observe that the two axes, $\hat{\mathbf{z}}_v$ and $\hat{\mathbf{z}}_p$, are parallel when they lie in the xy plane (Fig. 4A) and rotate in opposite directions in the xz plane (Fig. 4B).

Both monopole structures are expected to exhibit an instability toward a formation of a vortex ring (*25*). Although this and other instabilities (*26*, *27*) occur slowly enough not to disturb the creation and imaging process (*24*), observation of the resulting decay dynamics and implementation of a system in their absence are interesting research directions. Furthermore, studies of the interaction between monopoles and other topological defects, such as domain walls and skyrmions (*7*), may yield additional insights into high-energy physics and cosmology (*28*). A related goal is to create a topological point defect that also generates the synthetic magnetic field of a monopole, thereby combining the scenarios of Dirac (*23*), 't Hooft (*14*), and Polyakov (*15*). Finally, the observation of non-Abelian monopoles (*29*, *30*) remains an important goal.

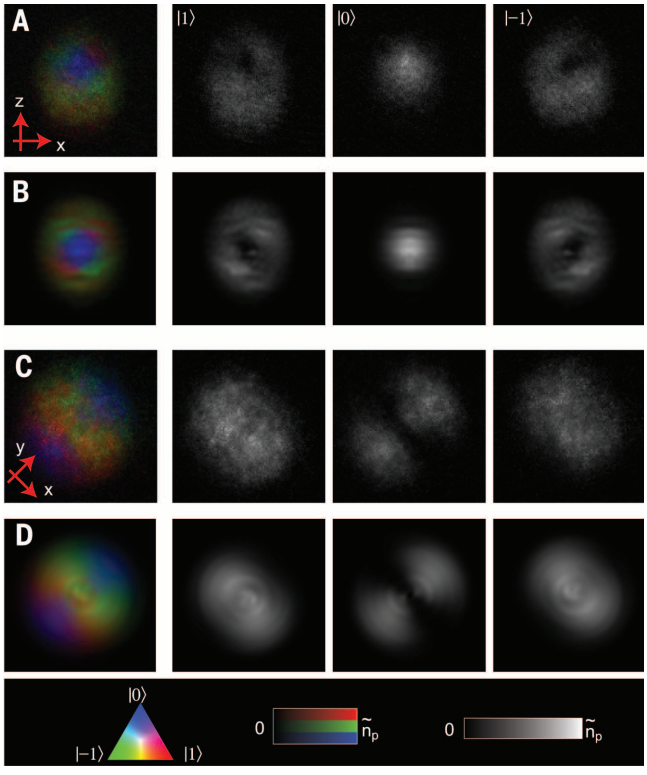

Fig. 3. Experiment compared to numerical simulations following a projection ramp along –*y*. (**A**) Experimentally obtained images of the condensate taken along the horizontal (y) axis. (**B**) Results of the corresponding numerical simulations. See Fig. 2 for further description. (**C** and **D**) As above, but for images taken along the vertical (z) axis. The field of view is 288 μm × 288 μm in (A) and (B), 219 μm × 219 μm in (C) and (D). The peak column density is $\tilde{n}_p = 12.9 \times 10^8$ cm^{-2}.

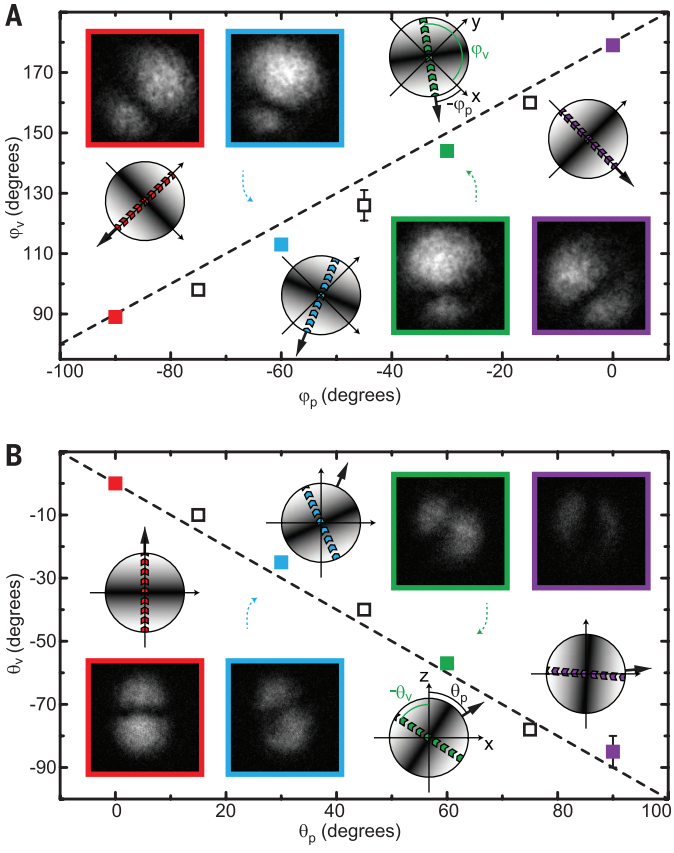

Fig. 4. Experimental results for different choices of the projection axis. (**A**) The angle of the vortices in the $|m = \pm 1\rangle$ states, φ_v, resulting from projections in the xy plane with azimuthal angle φ_p. Condensates are imaged along the z axis and φ_v is extracted from the alignment of the density profile in the $|m = 0\rangle$ state, as shown in the insets (see also figs. S4 to S7). Typical uncertainties are indicated by the error bars shown. The dashed line shows the theoretical result. The black arrows in the insets show the projection axes, z_p, and the chevrons show the expected orientation of the vortex axes, z_v. (**B**) Same as (A) but for angles θ_v resulting from projections in the xz plane with polar angle θ_p and imaging axis y.

REFERENCES AND NOTES

1. N. D. Mermin, *Rev. Mod. Phys.* **51**, 591–648 (1979).
2. M. Nakahara, *Geometry, Topology and Physics* (Taylor & Francis, Boca Raton, FL, 2003).
3. N. W. Ashcroft, N. D. Mermin, *Solid State Physics* (Harcourt, Orlando, FL, 1976).
4. R. J. Donnelly, *Quantized Vortices in Helium II* (Cambridge Univ. Press, Cambridge, 1991).
5. A. L. Fetter, *Rev. Mod. Phys.* **81**, 647–691 (2009).
6. J. Y. Choi, W. J. Kwon, Y. I. Shin, *Phys. Rev. Lett.* **108**, 035301 (2012).
7. P. Milde *et al.*, *Science* **340**, 1076–1080 (2013).
8. R. Blaauwgeers *et al.*, *Nature* **404**, 471–473 (2000).
9. R. Blaauwgeers *et al.*, *Phys. Rev. Lett.* **89**, 155301 (2002).
10. G. Toulouse, M. Kléman, *J. Phys. Lett.* **37**, 149–151 (1976).
11. I. Chuang, R. Durrer, N. Turok, B. Yurke, *Science* **251**, 1336–1342 (1991).
12. B. Senyuk *et al.*, *Nature* **493**, 200–205 (2013).
13. S. T. Bramwell *et al.*, *Nature* **461**, 956–959 (2009).
14. G. 't Hooft, *Nucl. Phys. B* **79**, 276–284 (1974).
15. A. M. Polyakov, *JETP Lett.* **20**, 194 (1974).
16. J. Preskill, *Annu. Rev. Nucl. Part. Sci.* **34**, 461–530 (1984).
17. H. T. C. Stoof, E. Vliegen, U. Al Khawaja, *Phys. Rev. Lett.* **87**, 120407 (2001).
18. F. Zhou, *Int. J. Mod. Phys. B* **17**, 2643–2698 (2003).
19. V. Pietilä, M. Möttönen, *Phys. Rev. Lett.* **103**, 030401 (2009).
20. M. W. Ray, E. Ruokokoski, S. Kandel, M. Möttönen, D. S. Hall, *Nature* **505**, 657–660 (2014).
21. J. Y. Choi, S. Kang, S. W. Seo, W. J. Kwon, Y. I. Shin, *Phys. Rev. Lett.* **111**, 245301 (2013).
22. Y. Kawaguchi, M. Ueda, *Phys. Rep.* **520**, 253–381 (2012).
23. P. A. M. Dirac, *Proc. R. Soc. London Ser. A* **133**, 60–72 (1931).
24. See supplementary materials on *Science* Online.
25. J. Ruostekoski, J. R. Anglin, *Phys. Rev. Lett.* **91**, 190402 (2003).
26. W. Zhang, D. L. Zhou, M.-S. Chang, M. S. Chapman, L. You, *Phys. Rev. Lett.* **95**, 180403 (2005).
27. L. E. Sadler, J. M. Higbie, S. R. Leslie, M. Vengalattore, D. M. Stamper-Kurn, *Nature* **443**, 312–315 (2006).
28. M. O. Borgh, J. Ruostekoski, *Phys. Rev. Lett.* **109**, 015302 (2012).
29. J. Ruseckas, G. Juzeliūnas, P. Ohberg, M. Fleischhauer, *Phys. Rev. Lett.* **95**, 010404 (2005).
30. V. Pietilä, M. Möttönen, *Phys. Rev. Lett.* **102**, 080403 (2009).

ACKNOWLEDGMENTS

Supported by NSF grant PHY-1205822, the Academy of Finland through its Centres of Excellence Program (grant 251748) and grants 135794 and 272806, the Finnish Doctoral Programme in Computational Sciences, and the Magnus Ehrnrooth Foundation. We thank CSC-IT Center for Science Ltd. (project no. ay2090) and Aalto Science-IT project for computational resources, M. Nakahara and M. Krusius for discussions concerning this work, and N. H. Thomas and S. J. Vickery for experimental assistance. All data used to support the conclusions of this work are presented in this manuscript and the supplementary materials. M.W.R. and D.S.H. developed and conducted the experiments and analyzed the data. E.R. and K.T. performed the numerical simulations under the guidance of M.M., who provided the initial ideas and suggestions for the experiment. All authors discussed both experimental and theoretical results and commented on the manuscript.

SUPPLEMENTARY MATERIALS

www.sciencemag.org/content/348/6234/544/suppl/DC1
Materials and Methods
Supplementary Text
Figs. S1 to S11
Reference (*31*)

3 July 2014; accepted 24 March 2015
10.1126/science.1258289

FERROELECTRICS

Observation of a periodic array of flux-closure quadrants in strained ferroelectric $PbTiO_3$ films

Y. L. Tang,[1]* Y. L. Zhu,[1]* X. L. Ma,[1]† A. Y. Borisevich,[2] A. N. Morozovska,[3] E. A. Eliseev,[4] W. Y. Wang,[1] Y. J. Wang,[1] Y. B. Xu,[1] Z. D. Zhang,[1] S. J. Pennycook[5,6]

Nanoscale ferroelectrics are expected to exhibit various exotic domain configurations, such as the full flux-closure pattern that is well known in ferromagnetic materials. Here we observe not only the atomic morphology of the flux-closure quadrant but also a periodic array of flux closures in ferroelectric $PbTiO_3$ films, mediated by tensile strain on a $GdScO_3$ substrate. Using aberration-corrected scanning transmission electron microscopy, we directly visualize an alternating array of clockwise and counterclockwise flux closures, whose periodicity depends on the $PbTiO_3$ film thickness. In the vicinity of the core, the strain is sufficient to rupture the lattice, with strain gradients up to 10^9 per meter. Engineering strain at the nanoscale may facilitate the development of nanoscale ferroelectric devices.

Atomic-scale information is of critical importance for understanding intrinsic characteristics of advanced functional materials such as ferroelectrics, magnets, superconductors, and catalysts. For example, it is often the small deviations from symmetry in atom positions and the resultant strains that allow ferroelectric oxides, used in computer memory chips, to store charge and information or to resonate with magnets as composite multiferroics. Ferroelectric crystals feature asymmetric or polar structures that are switchable under an external field, holding promise for random access memories, thin-film capacitors, and actuators (*1*). For integration into silicon chips, practical ferroelectric memories take the form of nanoscale films (*1*). Nanoscale ferroelectrics have been predicted to undergo unusual phase transitions and exhibit distinctive domain patterns, such as closure quadrants with closed head-tail dipole moments, known as flux closures (*2*–*7*). These flux-closure domains should be switchable and may give rise to an unusually high density of bits (*2*), and they can undergo vortex-polarization phase transformation (*6*). These domains are also predicted to be potentially useful as mechanical sensors and transducers (*7*). Similar domains are well known in ferromagnetic materials (*8*–*10*), and their topological properties and dynamics are under investigation (*9*, *10*). However, in ferroelectric materials, particularly in tetragonal ferroelectrics, the coupling of polarization to spontaneous strain would be so pronounced that formation of a closure quadrant with its resultant severe disclination strains could be impossible (*11*, *12*). Although closure quadrants were reported recently in tetragonal ferroelectric $BaTiO_3$ (*13*–*16*), $PbZr_{0.42}Ti_{0.58}O_3$ (*17*), and PZN-12PT (*18*), they are mostly composed of shape-conserving 90° stripe domains or twins within each quadrant to accommodate the disclination strains. In such cases, the closure quadrants may not always involve continuous dipole rotations, as have been observed directly in half of a closure quadrant in $PbZr_{0.2}Ti_{0.8}O_3$ (*19*) and $BiFeO_3$ (*20*) by aberration-correction transmission electron microscopy (TEM) or scanning TEM (STEM). The atomic-scale characterization based on STEM imaging has been validated to be capable of directly displaying ionic displacement maps (*19*–*24*), whereas approaches based on piezoresponse force microscopy are not able to do so because of lower spatial resolution (*11*, *14*–*18*, *25*, *26*).

In this study, we have grown $PbTiO_3$/$SrTiO_3$ (PTO/STO) multilayer films on a $GdScO_3$ substrate with a lattice parameter larger than the a value of PTO (*27*). Using aberration-corrected high-angle annular dark-field (HAADF) Z-contrast STEM imaging, we visualize, at the atomic scale, the existence of periodic twin-free flux-closure quadrants.

$PbTiO_3$ has a tetragonal structure (Fig. 1A). Both the oxygen octahedra and the Ti^{4+} have displacements from the center of the Pb^{2+} tetragonal cell that give rise to the spontaneous polarization (Fig. 1, B and C). The shifts of Ti^{4+} (denoted as δ_{Ti} in Fig. 1B) can be used to determine the polarizations of PTO unit cells. In HAADF images, the Pb^{2+} columns appear as the brightest dots because the intensity of atom columns is approximately proportional to Z^2, where Z is the atomic number (*20*, *21*, *23*, *24*). The Ti^{4+} columns show weaker contrast. The displacement vectors of Ti^{4+} (δ_{Ti}) relative to the center of mass of the

[1]Shenyang National Laboratory for Materials Science (SYNL), Institute of Metal Research, Chinese Academy of Sciences, Wenhua Road 72, 110016 Shenyang, China. [2]Oak Ridge National Laboratory, Materials Science and Technology Division, Oak Ridge, TN 37831-6071, USA. [3]Institute of Physics, National Academy of Sciences of Ukraine, 46 pr. Nauky, 03028 Kyiv, Ukraine. [4]Institute for Problems of Materials Sciences, National Academy of Sciences of Ukraine, 3 Krjijanovskogo, 03142 Kyiv, Ukraine. [5]Department of Materials Science and Engineering, University of Tennessee, Knoxville, TN 37996-2200, USA. [6]Department of Materials Science and Engineering, National University of Singapore, Singapore 117576, Singapore.
*These authors contributed equally to this work. †**Corresponding author. E-mail: xlma@imr.ac.cn**

Downloaded from www.sciencemag.org on April 30, 2015

four nearest Pb^{2+} neighbors (Fig. 1C) can be determined by fitting them as two-dimensional (2D) Gaussian peaks, based on the HAADF-STEM images (*19*–*24*, *27*, *28*). The δ_{Ti} vector in each unit cell is opposite to the polarization direction of PTO (Fig. 1 and figs. S1 and S2).

A low-magnification high-resolution HAADF-STEM image of a PTO/STO film shows that the contrast in each PTO layer is basically uniform, indicating the homogeneity of chemical compositions (Fig. 1D). Slight variation of the contrast implies the existence of domain walls. The domain structure was characterized by geometric phase analysis (GPA) (*21*, *27*, *29*). The out-of-plane strain ε_{yy} shown in Fig. 1E displays a clear spatial arrangement of the domain patterns. The domains in the upper PTO layer (in red, *c* domains, with *c* axis along the out-of-plane direction) form a 2D periodic sinusoidal array, whereas the domains with triangular configurations give rise to another periodic array (in green, *a* domains, with *c* axis along the in-plane direction).

Four typical areas (labeled as 1, 2, 3, and 4 in Fig. 1D) are magnified in Fig. 2A, which shows the atomically resolved HAADF-STEM images corresponding to these four areas. The atomic structures in each image depict the positions of Ti^{4+} and Pb^{2+} columns by red and yellow circles, respectively. For example, on the left side of area 2, the δ_{Ti} is upward, whereas on the right side of the image, the δ_{Ti} is downward. The yellow arrows denote the reversed δ_{Ti} directions, which are also the directions of spontaneous polarization (*22*, *24*). The opposite local polarization directions indicate the presence of two domains in a 180° orientation relation; the corresponding domain walls are marked by red dashed lines. At the bottom interface of PTO/STO, in-plane δ_{Ti} vectors are discernable; thus two 90° domain walls are outlined (blue dashed lines). Such in-plane displacement may play an important role in stabilizing this ferroelectric domain configuration (*4*, *19*). The 90° domain walls for areas 1 and 4 are denoted by green dashed lines. Figure 2B displays a superposition of the $-\delta_{Ti}$ vectors mapping with the atomic images in Fig. 2A. The $-\delta_{Ti}$ vectors are marked with an arrow located at the Ti^{4+} columns. The combined δ_{Ti} configurations in areas 1 and 2 form a flux-closure pattern (closure quadrant); the same is true for combined areas 3 and 4. Such a closure configuration is almost the same as that predicted in ferromagnetic materials in (*12*) and in ferroelectrics in (*30*). The combination of 1 and 2 forms a counterclockwise flux closure, whereas the combination of 3 and 4 leads to a clockwise flux closure. The same closure patterns can be identified in other areas. Because the order parameter of each flux closure—the toroid moment **G**, defined by the sum of cross-multiplication of radial vector $\mathbf{R_i}$ and local dipole $\mathbf{p_i}$—can be uniquely assigned (*2*), an antiparallel configuration of the **G** can be determined for a periodic closure pattern. The dynamic interactions of the periodic closures are of technological importance, as explored recently in $BaTiO_3$ platelets, although the closures are still composed of shape-conserving 90° stripe domains within each quadrant to accommodate the disclination strains (*16*).

The long-range strains in these ferroelectric closure quadrants show interesting disclination characteristics. Based on the HAADF-STEM images, the in-plane and out-of-plane strains and lattice rotations [rigid-body rotation of crystal lattice (*21*, *29*)] are determined by GPA (Fig. 3). The *c* lattice strains (that is, the in-plane strain ε_{xx} in the triangle domains in Fig. 3, A to C, and the out-of-plane strain ε_{yy} in the sinusoidal array in Fig. 3, D to F) have a strong local maximum around the vertices of the triangle domains, leading to a giant *c* lattice strain gradient. Away from the vertex, the strain gradient estimated in the triangle domain is ~4×10^6 m^{-1} (Fig. 3C). The lattice rotations are also spatially inhomogeneous (Fig. 3, G to I); in each single domain, the lattice rotation changes continuously (Fig. 3, H and I). Sudden jumps of lattice rotations (red arrows in Fig. 3, H and I) can be used to locate the 180° domain walls in HAADF-STEM images. 3D illustrations of the *c* lattice strain mappings (fig. S3) indicate a giant strain gradient that appears like a "volcano" at the vertices of the flux closure.

Strains close to the vertex can be interpreted from the point of view of ferroelectric theory. Strains and strain gradients corresponding to the vertex derived from the HAADF images and calculated using the Landau-Ginsburg-Devonshire (LGD) framework are given in figs. S4 to S10. A strain gradient reaching ~10^9 m^{-1} near the vertices can be identified (fig. S5). The analysis of the results suggests that most of the considerable deformation that the material undergoes in the vicinity of the vertices (for instance, the peaks in Fig. 3, B and C) and around domain walls can be attributed to the ferroelectric-electrostrictive contribution, which is not surprising given the large *c*/*a* ratio of the $PbTiO_3$. However, the shear strain

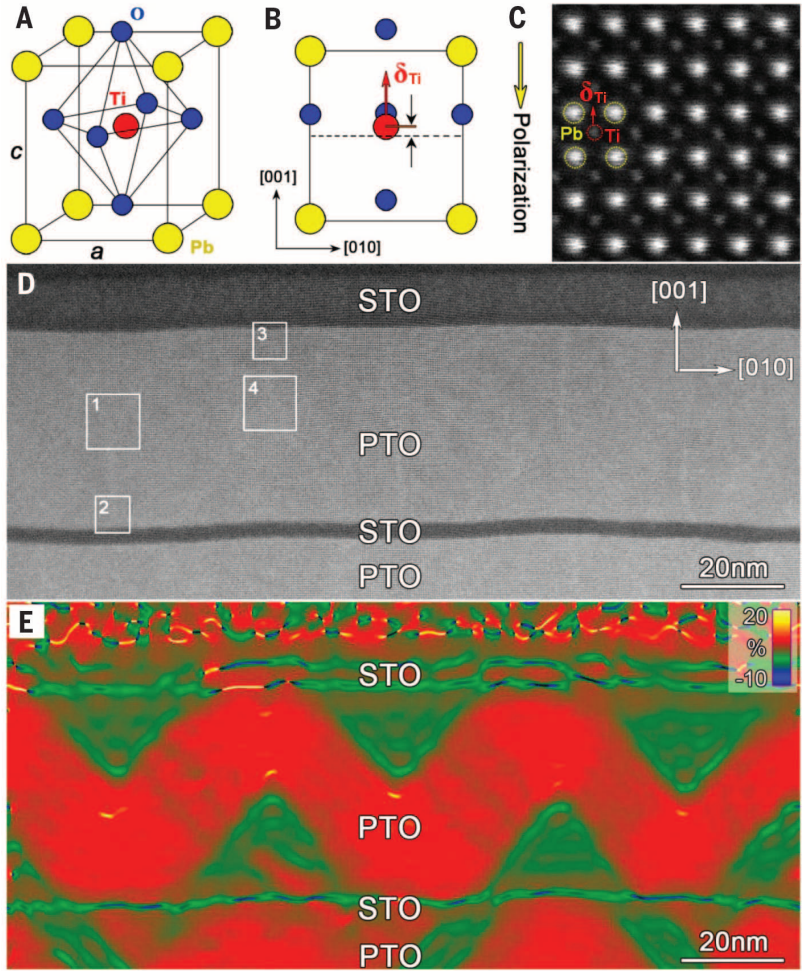

Fig. 1. Long-range periodic disclination pairs in a ferroelectric $PbTiO_3$ layer. (**A**) Schematic perspective view of the unit cell of $PbTiO_3$ (yellow, Pb; red, Ti; blue, O). (**B**) Projection of the unit cell along the [100] direction. (**C**) HAADF-STEM image of the $PbTiO_3$ crystal along [100]. (**D**) Low-magnification high-resolution HAADF-STEM image showing the upper $PbTiO_3$ layer in a $SrTiO_3$(10 nm)/$PbTiO_3$(36 nm)/$SrTiO_3$(3 nm)/$PbTiO_3$(28 nm)/$GdScO_3$ multilayer. Boxes labeled with numbers 1 to 4 denote typical areas. (**E**) GPA analysis of the STEM data reveals the out-of-plane strain ε_{yy}. The *c* domains are associated with an abrupt elongation of the out-of-plane lattice parameter (red areas) and exhibit a sinusoidal array. The domains (in green), with triangular head-to-head configurations having a smaller ε_{yy}, are *a* domains.

at the 180° domain wall appears to arise from a flexoelectric contribution

$$u_5 \approx \frac{-F_{44}P_S}{R_c \cosh^2(x_1/R_c)}$$

where u_5 is the shear strain component, F_{44} is a component of the flexoelectric tensor, P_S is the spontaneous polarization, R_c is the correlation radius (width of a domain wall), and x_1 is the coordinate normal to the 180° domain wall. In fact, the flexoelectric coefficient F_{44} can be directly estimated from the experimental data. The offset, which indicates the relative shift between two neighboring 180° domains, can be expressed as

$$\delta u_2 = 2F_{44}P_S$$

which is similar to the expression given in (*31*). Experimentally, we observe offsets as large as ~1.5 to 2 Å (fig. S11); together with the spontaneous polarization of 0.75 C m^{-2}, this gives us an estimate of $F_{44} \approx 10^{-10}$ C^{-1} m^3, which is within an order of magnitude of values previously reported (*31*, *32*).

Moreover, the lattice strain reaches extremely high values left and right of the core of the vertex (Fig. 2). At the core itself, the Pb columns appear to have bifurcated into two partial columns, possibly forming a small sliver of PbO. We expect large disclination stress in this region, the magnitude of which is roughly Eu, where E is Young's modulus and u is strain. The strain is much larger in the polar direction than in the nonpolar direction, consistent with the anisotropic elastic constants reported in (*33*). Using an average value of elastic constant c_{33} ~ 80 GPa in (*33*, *34*) as an estimate of E, with the observed dilatation reaching 25% in the core region, the stresses would appear to reach the order of 20 GPa. The theoretical shear strength σ_{theor} of a material can be estimated from

$$\sigma_{theor} = \sqrt{\frac{E\gamma}{a}}$$

where γ is the surface energy and a the lattice parameter. Using γ ~ 1 J m^{-2} (*35*) gives σ_{theor} ~ 14 GPa, suggesting that the lattice has ruptured because the disclination stresses exceeded the material's maximum shear strength. This lattice rupture is a general phenomenon at the vertex in this study (see fig. S12 for other examples).

For the whole multilayer structure, the periodic arrangement of the closure-quadrant arrays is characterized by two fundamental aspects. Structurally, the disclination pairs are arranged in a reversed manner, known as strain-compensating hetero-disclination pairs (*36*), whereas the clockwise and counterclockwise flux closures are stacked in an alternating fashion. This arrangement helps to relax the long-range strains in the disclinations (*36*), consequently stabilizing the closure quadrants. Nevertheless, a large strain gradient remains (Fig. 3). The disclination strain at the vertex here is up to 25%, which is more than one order of magnitude larger than that in rhombohedral $BiFeO_3$ ferroelectric, where the maximal disclination strain at the core is 1.5% (*26*). At the atomic level, our results show convincing evidence of the compatibility of disclinations and closure quadrants in a ferroelectric, even with strong tetragonality.

The periodic array of closure quadrants is occasionally absent in our PTO/STO multilayers. Figure 4A is a low-magnification TEM image of another PTO/STO film displaying an overview of the periodic array of the closure quadrants in both of the 20-nm PTO layers. Figure 4B shows a schematic illustration of the periodic closure quadrants.

By comparing PTO films with various thicknesses, we have derived the stabilization condition for such periodic closure quadrants (*27*). The thickness of each single PTO layer is the most important factor scaling the periodicity of the closure quadrants in tensile strained PTO/STO multilayers. We find that the thicknesses in which closure quadrants may occur are within the range of 15 to 36 nm. Thinner PTO tends to be fully strained without obvious domain structures, whereas thicker PTO tends to form alternating a/c domains (*21*) (figs. S13 to S16). In the present PTO/STO multilayer structures, each layer of PTO could be composed of such periodic closure quadrants. For example, in Fig. 4A, each of the two PTO layers is ~20 nm thick, and both layers contain the periodic closure quadrants. This indicates that, by repeatedly introducing STO layers, it is possible to fabricate extremely thick PTO/STO films that are composed of periodic disclination pairs in all PTO sublayers. Meanwhile, we find that the period of the closure-quadrant array w is strongly correlated with the PTO thickness d (Fig. 4C, following a linear relationship). In particular, for each PTO thickness, the ratio of period/thickness is ~1.45; i.e., $w \approx \sqrt{2}d$.

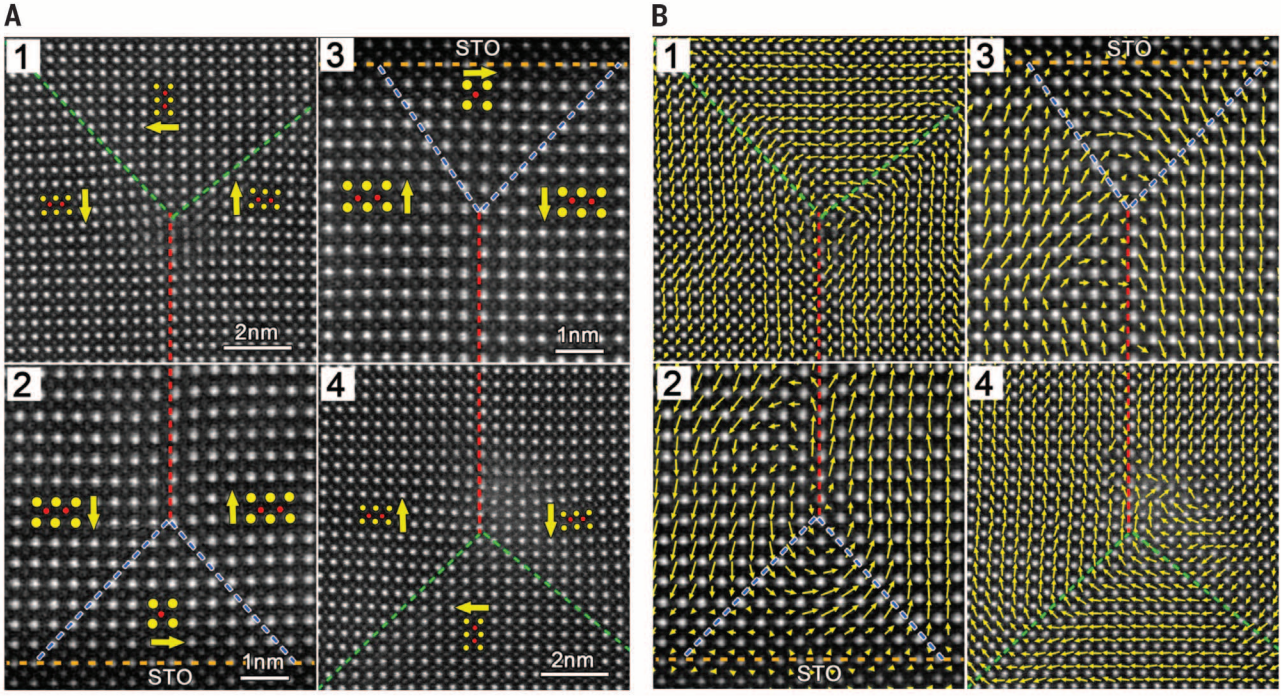

Fig. 2. Superposition of HAADF-STEM images and Ti^{4+} displacement vector maps showing the closure quadrants. (**A**) Atomically resolved HAADF-STEM images corresponding to the areas labeled as 1, 2, 3, and 4 in Fig. 1D. The red and yellow circles denote the positions of Ti^{4+} and Pb^{2+} columns, respectively. Arrows denote reversed Ti^{4+} displacement directions. (**B**) Superposition of reversed δ_{Ti} vectors with experimental images. The δ_{Ti} vectors corresponding to PTO unit cells are shown as yellow arrows superimposed on the atomic image of Fig. 2A. The green and blue dashed lines indicate the 90° domain walls in areas 1 and 4, as well as 2 and 3, respectively. The red dashed lines indicate the 180° domain walls.

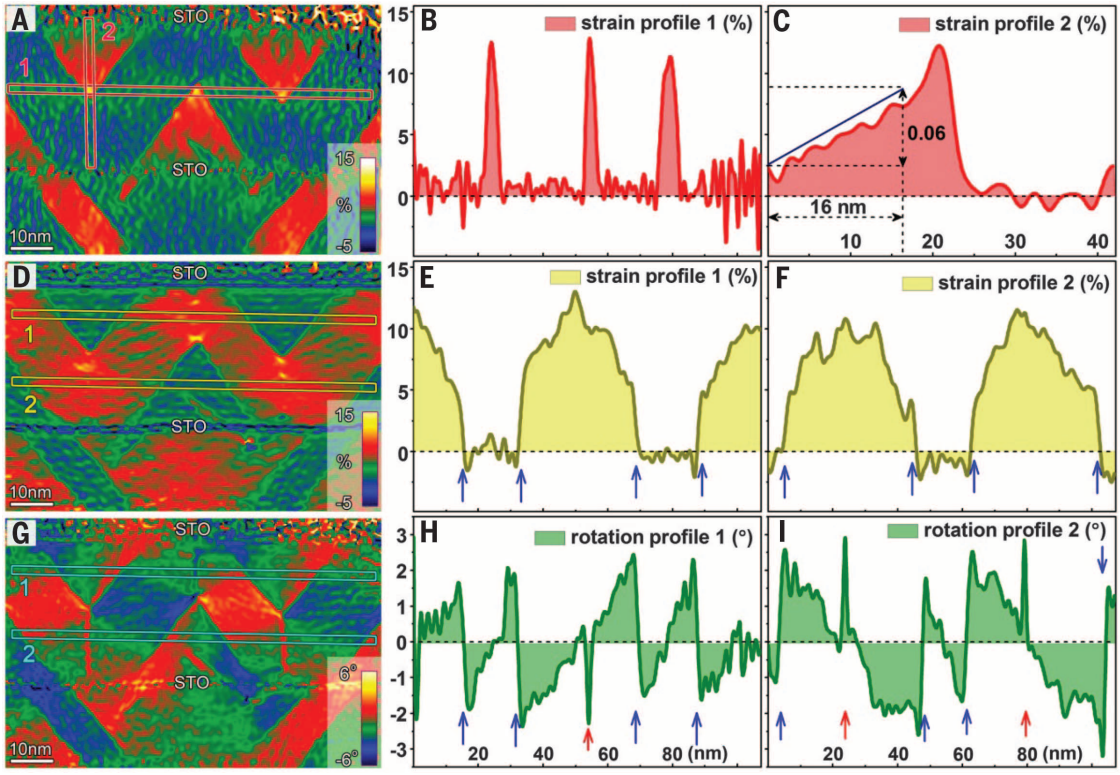

Fig. 3. Strain mappings of the periodic disclination pairs. (**A** to **C**) In-plane strain (ε_{xx}) maps and corresponding line profiles of areas 1 and 2 [labeled in (A)]. (**D** to **F**) Out-of-plane strain (ε_{yy}) maps and corresponding line profiles of areas 1 and 2 [labeled in (D)]. (**G** to **I**) Lattice rotation maps and corresponding line profiles of areas 1 and 2 [labeled in (G)]. Note the very inhomogeneous distribution of the strains and lattice rotations. The continuous, giant *c* lattice strain gradient estimated in the triangle domain in (C) is ~4 × 10^6 m^{-1}. Blue arrows in (E), (F), (H), and (I) denote the strain-rotation abrupt change points indicating the 90° domain walls. Red arrows in (H) and (I) denote the rotation maximal points indicating the 180° domain walls.

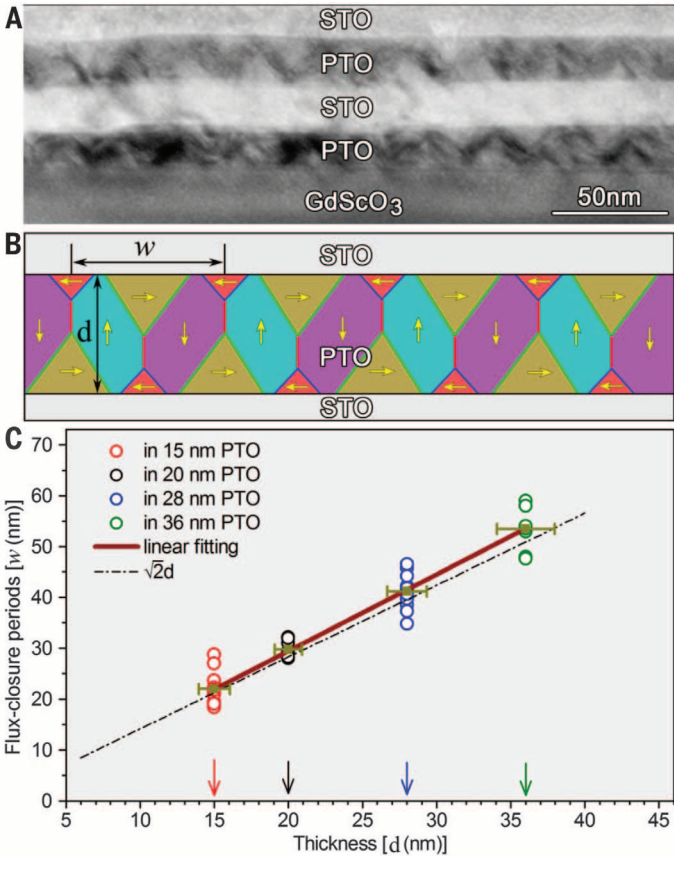

Fig. 4. Variation of flux-closure period with $PbTiO_3$ thicknesses. (**A**) Cross-sectional TEM image showing an overview of a $SrTiO_3$(10 nm)/$PbTiO_3$(20 nm)/$SrTiO_3$(20 nm)/$PbTiO_3$(20 nm)/$GdScO_3$ multilayer. Two flux-closure arrays align periodically in both $PbTiO_3$ layers. (**B**) Schematic showing the flux-closure domain configuration based on the experimental data in Figs. 1 to 3. Because not all of the 90° domain walls in Fig. 2A are visible in the strain maps, the 90° domain walls were denoted by green (visible) and blue (invisible) dashed lines, respectively. (**C**) Linear relationship between the thicknesses (*d*) and the periods (*w*) of closure-quadrant arrays in $PbTiO_3$ layers on $GdScO_3$. The linear fit is close to $\sqrt{2}d$.

According to Kittel's law, stripe-domain widths are predominantly determined by the bulk domain energy E_d, the domain-wall energy E_w, and the film thickness *d* (*11*, *37*). This law was further extended for all ferroics, and a universal square root dependence $w \propto \sqrt{d}$ was deduced (*11*, *38*), where *w* is the domain period. However, the situation in the present study cannot be understood as simple 90°/180° stripe domains (*37*, *38*) because of the substantial nonuniform disclination strains that result from the configuration of the flux closures. In (*39*) it was theoretically demonstrated that, for films with a specific thickness range, the energy associated with disclination strains breaks the square root law, and a new linear law $w \propto \alpha + \beta d$ (where α and β are experiment-determined specific coefficients) is preferred. Our experimental results support the linear law with $\alpha = 0$ and $\beta = \sqrt{2}$.

Our results indicate that giant strain gradients can be preserved within a very thick PTO/STO film by simply increasing the PTO/STO period. This may provide opportunities for exploring various functionalities induced by strain gradients—such as the catalytic efficiency (*40*) of perovskite oxides—and other material properties that are tunable by elastic strains (*41*).

The results also extend the potential of employing epitaxial strain for modulating ferroelectric domain patterns. Designs based on controllable ferroelectric closure quadrants could be fabricated for investigating their dynamics and flexoelectric responses and, in turn, may assist future development of nanoscale ferroelectric devices such as high-density memories and high-performance energy-harvesting devices.

REFERENCES AND NOTES

1. J. F. Scott, *Science* **315**, 954–959 (2007).
2. I. I. Naumov, L. Bellaiche, H. Fu, *Nature* **432**, 737–740 (2004).
3. I. Kornev, H. Fu, L. Bellaiche, *Phys. Rev. Lett.* **93**, 196104 (2004).
4. P. Aguado-Puente, J. Junquera, *Phys. Rev. Lett.* **100**, 177601 (2008).
5. B.-K. Lai *et al.*, *Phys. Rev. Lett.* **96**, 137602 (2006).
6. I. Naumov, H. Fu, *Phys. Rev. Lett.* **98**, 077603 (2007).
7. W. J. Chen, Y. Zheng, B. Wang, *Sci. Rep.* **2**, 00796 (2012).
8. T. Shinjo, T. Okuno, R. Hassdorf, K. Shigeto, T. Ono, *Science* **289**, 930–932 (2000).
9. N. Romming *et al.*, *Science* **341**, 636–639 (2013).
10. N. Nagaosa, Y. Tokura, *Nat. Nanotechnol.* **8**, 899–911 (2013).
11. G. Catalan, J. Seidel, R. Ramesh, J. F. Scott, *Rev. Mod. Phys.* **84**, 119–156 (2012).
12. C. Kittel, *Rev. Mod. Phys.* **21**, 541–583 (1949).
13. A. Schilling *et al.*, *Nano Lett.* **9**, 3359–3364 (2009).
14. L. J. McGilly, A. Schilling, J. M. Gregg, *Nano Lett.* **10**, 4200–4205 (2010).
15. R. G. P. McQuaid, L. J. McGilly, P. Sharma, A. Gruverman, J. M. Gregg, *Nat. Commun.* **2**, 404 (2011).
16. R. G. P. McQuaid, A. Gruverman, J. F. Scott, J. M. Gregg, *Nano Lett.* **14**, 4230–4237 (2014).
17. L. J. McGilly, J. M. Gregg, *Nano Lett.* **11**, 4490–4495 (2011).
18. L.-W. Chang, V. Nagarajan, J. F. Scott, J. M. Gregg, *Nano Lett.* **13**, 2553–2557 (2013).
19. C.-L. Jia, K. W. Urban, M. Alexe, D. Hesse, I. Vrejoiu, *Science* **331**, 1420–1423 (2011).
20. C. T. Nelson *et al.*, *Nano Lett.* **11**, 828–834 (2011).
21. G. Catalan *et al.*, *Nat. Mater.* **10**, 963–967 (2011).
22. C. L. Jia *et al.*, *Nat. Mater.* **7**, 57–61 (2008).
23. Y. L. Tang *et al.*, *Sci. Rep.* **4**, 04115 (2014).
24. P. Gao *et al.*, *Nat. Commun.* **4**, 3791 (2013).
25. N. Balke *et al.*, *Nat. Nanotechnol.* **4**, 868–875 (2009).
26. N. Balke *et al.*, *Nat. Phys.* **8**, 81–88 (2012).
27. Materials and methods are available as supplementary materials on *Science* Online.
28. S. M. Anthony, S. Granick, *Langmuir* **25**, 8152–8160 (2009).
29. M. J. Hÿtch, E. Snoeck, R. Kilaas, *Ultramicroscopy* **74**, 131–146 (1998).
30. D. J. Srolovitz, J. F. Scott, *Phys. Rev. B* **34**, 1815–1819 (1986).
31. A. K. Tagantsev, L. E. Cross, J. Fousek, in *Domains in Ferroic Crystals and Thin Films* (Springer, New York, 2010), chap. 6, pp. 300–304.
32. A. K. Tagantsev, *Phase Transit.* **35**, 119–203 (1991).
33. Y. Liu *et al.*, *Mater. Sci. Eng. A* **472**, 269–272 (2008).
34. A. G. Kalinichev, J. D. Bass, B. N. Sun, D. A. Payne, *J. Mater. Res.* **12**, 2623–2627 (1997).
35. G. C. C. Costa, P. Saradhi Maram, A. Navrotsky, *J. Am. Ceram. Soc.* **95**, 3254–3262 (2012).
36. N. D. Mermin, *Rev. Mod. Phys.* **51**, 591–648 (1979).
37. C. Kittel, *Phys. Rev.* **70**, 965–971 (1946).
38. A. L. Roitburd, *Phys. Status Solidi A* **37**, 329–339 (1976).
39. N. A. Pertsev, A. G. Zembilgotov, *J. Appl. Phys.* **78**, 6170–6180 (1995).
40. J. Suntivich, K. J. May, H. A. Gasteiger, J. B. Goodenough, Y. Shao-Horn, *Science* **334**, 1383–1385 (2011).
41. D. Yu, J. Feng, J. Hone, *MRS Bull.* **39**, 157–162 (2014).

ACKNOWLEDGMENTS

This work is supported by the National Natural Science Foundation of China (grants 51231007 and 51171190) and the National Basic Research Program of China (grants 2014CB921002 and 2009CB623705). A.N.M. and E.A.E. acknowledge financial support from the National Academy of Science of the Ukraine; A.Y.B. and S.J.P. thank the U.S. Department of Energy, Office of Basic Energy Sciences, Materials Sciences and Engineering Division for financial support. The authors at SYNL are grateful to B. Wu and L. X. Yang of this laboratory for their technical support on the Titan platform of the aberration-corrected scanning transmission electron microscope. Author contributions: Y.L.Z. and X.L.M. conceived the project of interfacial characterization in oxides by using aberration-corrected STEM; Y.L.T. performed the thin-film growth and TEM observations; W.Y.W. provided some of the TEM images used in the supplementary materials; Y.J.W. carried out digital analysis of the STEM data; Y.B.X. and Z.D.Z. contributed to the thin-film growth; A.N.M. and E.A.E. participated in the ferroelectric theoretical analysis based on the LGD framework; and A.Y.B. and S.J.P. contributed to STEM-HAADF imaging data analysis, particularly to the calculation of the strain-gradient components near the vertex core. All authors participated in discussion and interpretation of the data. Correspondence and requests for materials should be addressed to X.L.M.

SUPPLEMENTARY MATERIALS

www.sciencemag.org/content/348/6234/547/suppl/DC1
Materials and Methods
Supplementary Text
Figs. S1 to S16
Table S1
References (*42*–*56*)

11 August 2014; accepted 24 March 2015
10.1126/science.1259869

THREE-BODY PHYSICS

Observation of the Efimov state of the helium trimer

Maksim Kunitski,[1]* Stefan Zeller,[1] Jörg Voigtsberger,[1] Anton Kalinin,[1] Lothar Ph. H. Schmidt,[1] Markus Schöffler,[1] Achim Czasch,[1] Wieland Schöllkopf,[2] Robert E. Grisenti,[1,3] Till Jahnke,[1] Dörte Blume,[4] Reinhard Dörner[1]*

Quantum theory dictates that upon weakening the two-body interaction in a three-body system, an infinite number of three-body bound states of a huge spatial extent emerge just before these three-body states become unbound. Three helium (He) atoms have been predicted to form a molecular system that manifests this peculiarity under natural conditions without artificial tuning of the attraction between particles by an external field. Here we report experimental observation of this long-predicted but experimentally elusive Efimov state of $^4He_3$ by means of Coulomb explosion imaging. We show spatial images of an Efimov state, confirming the predicted size and a typical structure where two atoms are close to each other while the third is far away.

Ever since the early days of celestial mechanics, the three-body problem has posed a major challenge to physicists. In the early 20th century, the failure to find a stable solution for the classical helium (He) atom (two electrons and a nucleus) heralded the demise of Niels Bohr's program of semiclassical atomic physics (*1*). Quantum mechanics then added yet another surprising twist to the three-body problem, when in 1970 Vitaly Efimov predicted the appearance of an infinite series of stable three-body states of enormous spatial extents (*2*). These Efimov states are predicted to exist for short-range interactions such as the van der Waals force between atoms or the strong force between nucleons. When the potential becomes so shallow that the last two-body bound state is on the verge of becoming unbound or is unbound, then three particles stick together to form Efimov states. This three-body behavior does not depend on the details of the underlying two-body interactions. This makes the Efimov effect a universal phenomenon, with important applications in particle, nuclear (*3*, *4*), atomic (*4*), condensed-matter (*5*), and biological physics (*6*).

[1]Institut für Kernphysik, Goethe-Universität Frankfurt am Main, Max-von-Laue-Straße 1, 60438 Frankfurt am Main, Germany. [2]Department of Molecular Physics, Fritz-Haber-Institut, Faradayweg 4-6, 14195 Berlin, Germany. [3]GSI Helmholtz Centre for Heavy Ion Research, Planckstraße 1, 64291 Darmstadt, Germany. [4]Department of Physics and Astronomy, Washington State University, Pullman, WA 99164-2814, USA.
***Corresponding author. E-mail: kunitski@atom.uni-frankfurt.de (M.K.); doerner@atom.uni-frankfurt.de (R.D.)**

Figure 1 summarizes two facets of Efimov's prediction: the energy spectrum and the structure of an Efimov state. Figure 1A shows how the two- and three-body binding energies (the binding energy of an atomic cluster is defined as the energy needed to separate all constituents of the cluster to infinite distances) change as the depth of the two-body potential is increased. As indicated by the arrow above Fig. 1A, the depth of the two-body potential increases along the horizontal axis. As the depth increases, the s-wave scattering length a changes from negative values to infinitely large values to positive values. Negative a values correspond to the domain where shallow two-body bound states do not exist. For positive a, a shallow two-body bound state, the dimer (blue solid line in Fig. 1A), exists. Bound three-body states (called trimers) exist in the green-shaded area. The extremely weakly bound three-body states close to threshold (solid red line labeled "1st ES" and the dashed black line labeled "2nd ES") are Efimov states, which have been predicted to possess remarkable characteristics that are intricately related to the discrete scale invariance of the underlying three-body Hamiltonian. Key characteristics of Efimov states are their unusual extent and structure. Figure 1B shows the calculated structure of the state labeled 1st ES for $\mathrm{sign}(a)|a|^{-1/2} = 0$; i.e., for the ideal and universal case where the two-body scattering length is infinitely large and the dimer binding energy is equal to zero. For comparison, the size and shape of the ground state trimer (labeled "GS" in Fig. 1A) are depicted in Fig. 1C. The hypothetical ideal

Efimov trimer extends out to 300 Å (1 Å = 0.1 nm); i.e., the Efimov trimer is about 100 times larger than a typical chemically bound triatomic molecule. Moreover, the ideal Efimov state is highly diffuse and does not display a predominantly equilateral triangular or linear shape.

Despite their relevance across different subfields of physics, these spatially extended and weakly bound trimer states have proven extremely challenging to prepare and detect, and experimental evidence for the Efimov effect was reported only in 2006 (*7*) (36 years after its theoretical prediction), stimulating a great deal of continued experimental activity. Experimental signatures to date have come from loss measurements or spectroscopy on trapped cold-atom systems. In experiments of this type, the two-body interaction is tuned in the vicinity of a Feshbach resonance through the application of an external magnetic field. Signatures of the Efimov effect are then obtained by monitoring the atom loss from the trap due to the formation of Efimov trimers at scattering lengths for which the trimer energy coincides with that of three free atoms (these scattering lengths are marked by asterisks in Fig. 1A). The most direct probe of Efimov trimers to date comes from radiofrequency spectroscopy on an ultracold three-component lithium gas, which yielded the binding energies of an Efimov trimer for different two-body interaction strengths (*8*, *9*). An experimental exploration of the size and shape of Efimov states requires a setup where the trimer is sufficiently long-lived and can be imaged selectively. These two demands prove challenging for cold-atom experiments. The experiments reported in this work circumvent these challenges by working with a different species, namely ^{4}He, and a completely different experimental approach.

The He trimer is a paradigmatic molecular system that is believed to support an Efimov state. In fact, it was already predicted in 1977 to be a prime candidate with which to study Efimov physics (*10*). Theoretical calculations based on the currently most accurate He-He potential (*11*) predict two bound states for the He trimer, the ground and excited states, with binding energies of 131.84 and 2.6502 mK, respectively (*12*). These states occur naturally along the vertical dashed line in Fig. 1A at a scattering length of a = 90.4 Å (*11*). The excited state has one node in the hyperradial coordinate, indicating a vibrational excitation that is reminiscent of a breathing mode in classical triatomic molecules. Our calculations, shown by the green and red lines in Fig. 1A, conclude, in agreement with earlier works (*4*, *10*, *13*–*16*), that an artificial strengthening of the pair interaction (see the right pointing arrow above Fig. 1A) renders the excited state of the He trimer less strongly bound with respect to the dimer, thus confirming the Efimov character of the trimer state. This character is further supported by the appearance of a second Efimov state upon an artificial weakening of the true two-body He-He potential (dashed black line labeled 2nd ES in Fig. 1A).

The energy ratio of two neighboring Efimov states for infinitely large s-wave scattering length is 22.7[2]. Correspondingly, the excited state is about 22.7 larger than the ground state (Fig. 1, B and C). The energy ratio decreases when the scattering length takes finite positive values. For the scattering length corresponding to He, Efimov's radial law predicts an energy ratio of 5.0[2]. The energy ratio of the ground and excited state of the true He trimers is larger than predicted by Efimov's theory, namely 7.0[2], owing to the fact that the ground state of the He trimer is not an Efimov state.

Because of the very low binding energy, the ^{4}He trimer lacks rotational states, which implies that common structural experimental tools such as rotational spectroscopy cannot be applied. The ^{4}He trimer ground state was observed experimentally in 1996 by Schöllkopf and Toennies (*17*), using matter-wave diffraction of He clusters from a transmission grating. Concerted experimental efforts, however, did not provide any evidence for the existence of the excited state of the ^{4}He trimer (*18*, *19*).

Here we report experimental observation of the Efimov state of the He trimer; the creation of this stable state in a "natural" field-free environment allows us to directly investigate the structural aspects of Efimov physics and take real-space images of the square of the wave function of an Efimov state using Coulomb explosion imaging. The obtained experimental distributions are in good agreement with those obtained from full first-principles quantum-mechanical calculations (*20*, *21*) that use the currently most accurate He-He potential published by Cencek *et al.* (*11*).

The He clusters were prepared in a molecular beam under supersonic expansion of gaseous He at a temperature of 8 K through a 5-μm nozzle. The cluster yields were tuned by varying the nozzle back-pressure. He trimers were selected from the molecular beam by means of matter-wave diffraction (*17*). The selection removed an overwhelming fraction of He monomers that dominates the molecular beam under all expansion conditions. All three atoms of a trimer were then singly ionized by a strong ultrashort laser field (30 fs, 780 nm, >3 × 10^{15} W/cm^2). Because the ionization process is essentially instantaneous, the quantum-mechanical probability distributions

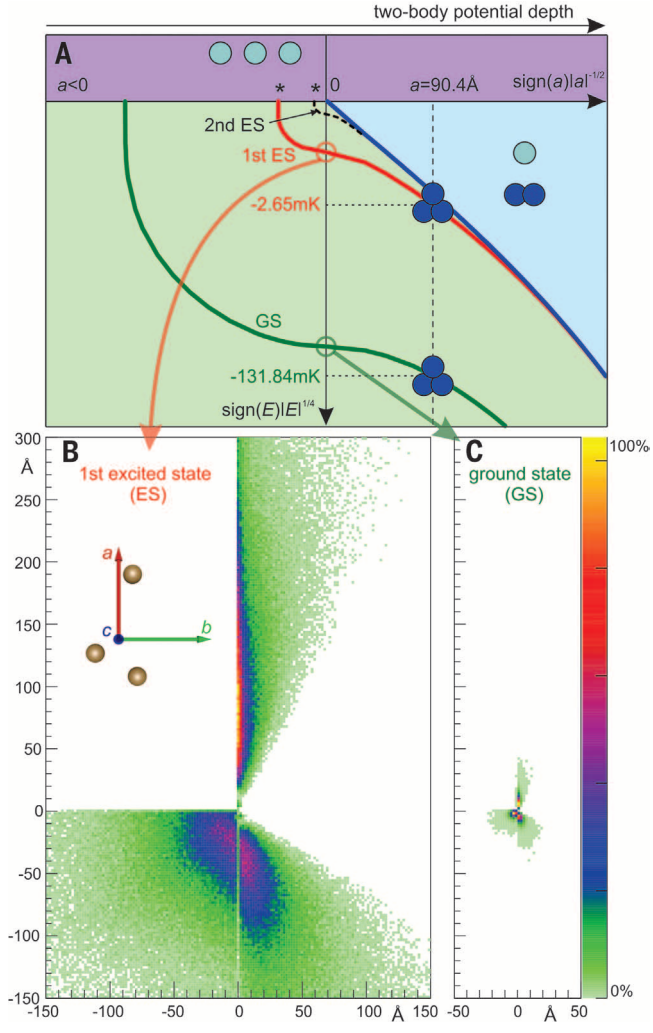

Fig. 1. Theoretical basis for the Efimov state of the He trimer. (**A**) Dependence of the binding energies [sign(E) × $|E|^{1/4}$] of the ground (GS) and first excited (1st ES) states of the He trimer on the scattering length [sign (a) × $|a|^{-1/2}$] calculated by artificially scaling the He-He potential. The blue line on the positive scattering length side shows the binding energy of the He dimer. The vertical dashed line corresponds to the naturally occurring ^{4}He system with a two-body scattering length of 90.4 Å (*11*). (**B** and **C**) Theoretical structures of the excited and ground states of the hypothetical He trimer corresponding to the scaled He-He potential with an infinite scattering length. The structures are plotted in the principal axis frame (abc) as shown in the inset. The center of mass of the trimer was shifted to the origin, and the structures were rotated so that the principal axis with the smallest moment of inertia (shown by the red vector a in the inset) lay along the y axis. Additionally, if required, the structure was mirrored with respect to the x or y axis in order to get one He atom in the first quadrant and the other two in the third and fourth quadrants, so that the second quadrant is always empty. The linear color scale encodes the number of entries.

of the neutral trimers provide the initial configurations for the subsequent Coulomb explosion (*22*) of the triply charged trimers. The momenta acquired during the explosion of the ions were measured by cold target recoil ion momentum spectroscopy (*23*, *24*). From these momentum vectors, the initial spatial geometry of the three charged fragments at the instant of ionization was reconstructed using Newton's equation of motion (for details, see the supplementary materials). A simple global observable related to the structure is the total kinetic energy of all three ions [kinetic energy release (KER)]. In the Coulomb explosion, the total potential energy of the three charges with interparticle distances R_{ij} is converted into KER (in atomic units)

$$\mathrm{KER} = 1/R_{12}+1/R_{13}+1/R_{23} \qquad (1)$$

The measured KER distributions corresponding to the He trimer at two different nozzle backpressures are depicted in Fig. 2A. At a pressure of 1.7 bar (Fig. 2A, blue curve), only one peak with a maximum at 5 eV is observed. This peak corresponds to the ground state of the He trimer, with an average He-He distance of 10.4 Å (*25*). At a lower nozzle pressure of 330 mbar (Fig. 2A, black curve), an additional peak with a maximum at 0.57 eV emerges. This low-energy feature corresponds to structures that are about eight times larger than those of the ground state. Such large spatial extent (≈80 Å) has been predicted for the excited state of the ^{4}He trimer (*12*, *26*, *27*). Indeed, the KER distribution (Fig. 2A, violet curve) calculated from the full quantum-mechanical probability distribution of the excited He trimer using Eq. 1 resembles the experimental observation (difference spectrum in red, Fig. 2A) very closely.

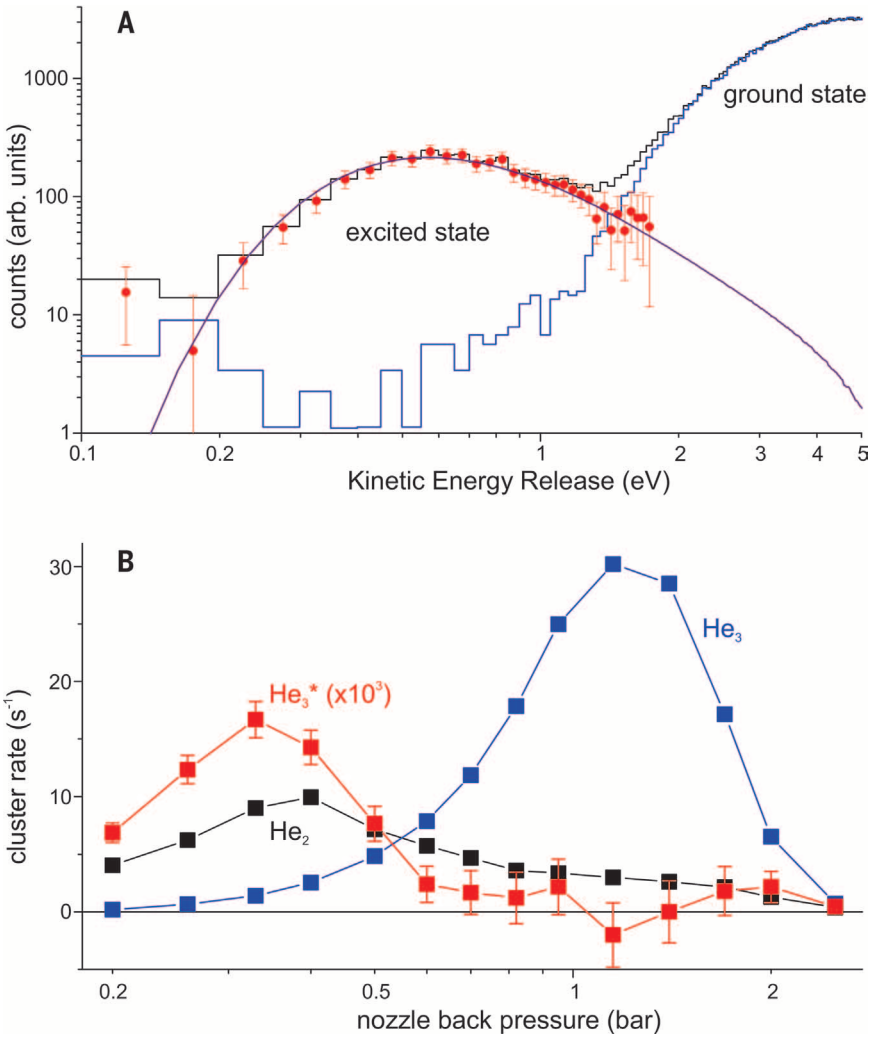

Fig. 2. Experimental observation of the He_3 excited state. (**A**) The KER distributions of Coulomb exploded ^{4}He trimers. The experimental distributions correspond to the mixture of the ground and excited states (black, expansion conditions: 8 K, 330 mbar) and to the ground state only (blue, expansion conditions: 8 K, 1.7 bar). The difference spectrum is shown in red with error bars (corresponding to a confidence interval of 95%). The ground-state–only distribution (blue) is normalized so that it agrees with the mixture distribution (black) for KER around 3 to 5 eV. The theoretical KER distribution for the excited state of the ^{4}He trimer, obtained from our full quantum-mechanical calculation, is shown in violet. Note the logarithmic scale on both axes. arb., arbitrary units. (**B**) Dependence of the ^{4}He cluster rates on the back pressure at a temperature of 8 K for a nozzle with a 5-μm orifice. The very low rate of the He_3 excited state (red) is scaled by a factor of 10^3. The background caused by ground-state structures has been subtracted from the excited-state rate. The error bars correspond to a confidence interval of 68%. The rates for the He_3 ground state and He_2 are shown in blue and black, respectively.

As Fig. 2A shows, the yield of the $^4He_3$ excited state is sensitive to the expansion conditions. The detailed analysis of the pressure dependence shows that the maximum rate of the excited state of the ^{4}He trimer is achieved not at pressures with the highest yield of the ground state of the trimer, but rather at pressures that favor dimer formation (Fig. 2B). This might be an indication that two He dimers are required for the formation of the excited He trimer during the supersonic expansion; the formation mechanism of the ground-state trimer is seeded primarily by collisions between one He dimer and two He monomers (*28*). Another interpretation of the observed pressure dependence of the excited state yield might be an increased collision-induced breakup rate of excited trimers in an expansion at higher pressures due to increased translational temperatures (*28*). The highest ratio of the excited- to the ground-state He trimer populations of about 4% was found at the lowest pressure used in the experiment, namely at 200 mbar. At a pressure with the maximum yield of the trimer ground state, we could not detect any contribution of the excited state. This very weak relative yield of the excited state explains why it was not observed in the experiment of Toennies and co-workers (*19*), with an estimated detection limit of 6%.

Figure 2 establishes unambiguously that the He trimer excited state is stable and can be prepared reliably in an experiment. In order to deduce quantitative information about the structural properties of the excited He trimer from the measured momenta, we used classical mechanics to invert the Coulomb explosion [see (*25*) and the supplementary materials for details]. Unfortunately, there is an ambiguity of momentum-to-structure relation in the small region of the structural space. This results in the reconstruction of some number of irrelevant geometries. In order to overcome this issue, the irrelevant structures were filtered out during reconstruction (for details, see the supplementary materials).

Figure 3 shows the reconstructed pair distance distributions for the excited state (red and black) and the ground state (blue) of He_3. The red and black distributions differ in how the excited-state structures are separated from the ground-state structures. The separation is necessary because the wave functions of both states overlap spatially in the range of lower pair distances, and the ground state always dominates in the experiment. By applying a filter in the momentum space (for details, see the supplementary materials), we were able to choose momenta that mainly relate to the excited state of He_3 (Fig. 3, black). However, some

structures of the excited state have been cut by the filter, resulting in the discrepancy below a pair distance of 50 Å. An alternative way of obtaining the excited-state distribution is subtraction of the reconstructed distribution of the ground state from the distribution of the mixture of the ground and excited states (Fig. 3, red). This approach still fails to give an accurate reproduction of the distribution in the lower pair distance range, because of the overwhelming amount of the ground state, whose distribution spreads up to 50 Å (Fig. 3, blue). At larger distances (>100 Å), however, both

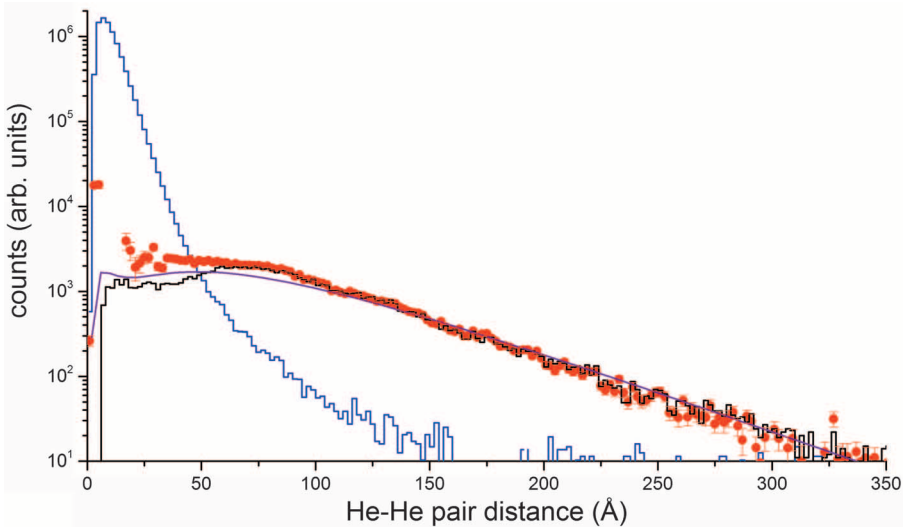

Fig. 3. Pair distance distributions $P_{pair}(R)$ of the He_3 excited state. The red circles represent the difference between the mixture of the excited- and ground-state distribution (measured at a nozzle pressure of 330 mbar and a temperature of 8 K) and the ground-state–only distribution (1.7 bar, 8 K, blue line). The error bars correspond to a confidence interval of 68%. The ground-state distribution was normalized to the quantity of ground-state structures under conditions where the excited state was measured (300 mbar, 8 K). The black histogram corresponds to the distribution that was obtained from the measured momenta of the ground- and excited-state mixture by filtering out the structures with higher KERs (for details, see the supplementary materials). Experimental distributions have been reconstructed from the measured momenta, using Newtonian mechanics to invert the Coulomb explosion. The theoretical pair distance distribution of the excited He trimer is shown in purple.

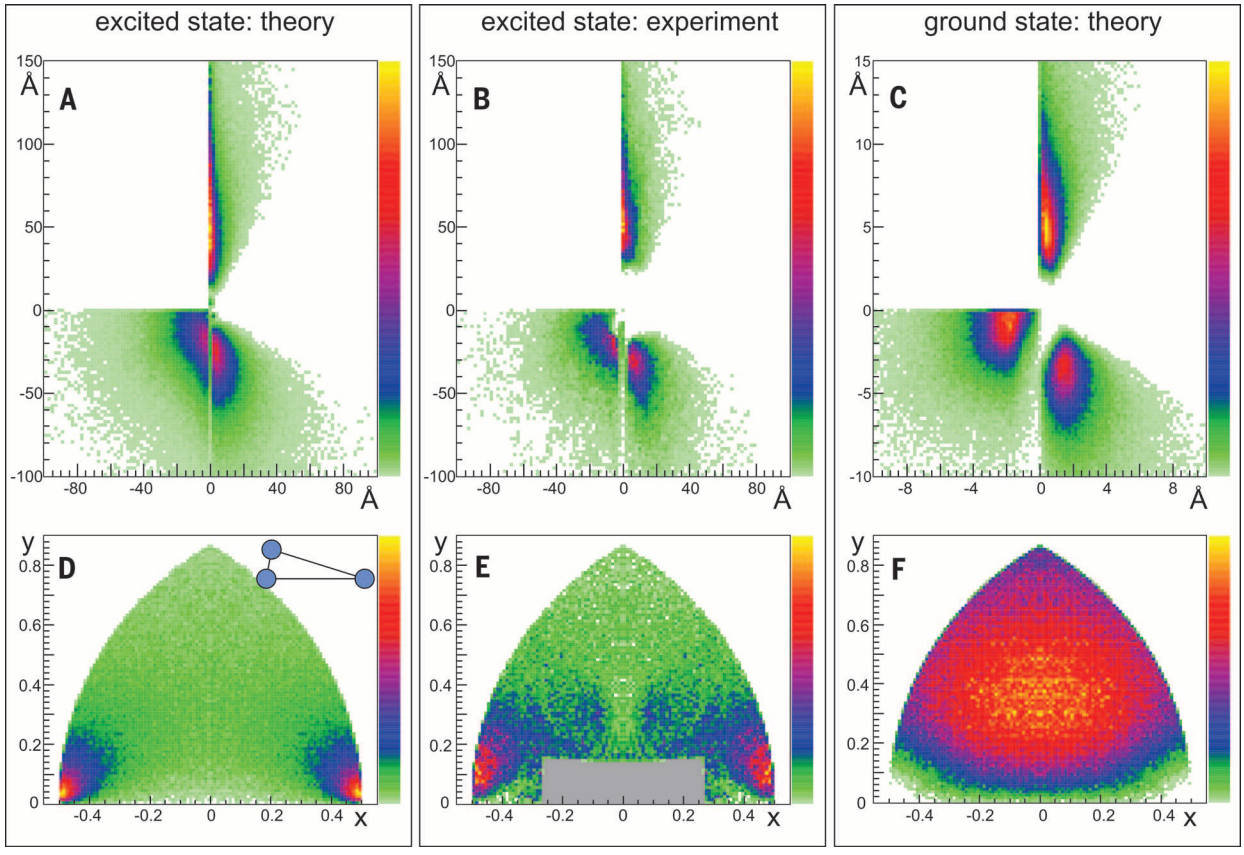

Fig. 4. Structures of the He trimer. (**A** and **B**), respectively, show the theoretical and experimental excited-state structure; (**C**) shows the theoretical ground state. Note the different scale for the ground state structure. For the plots, the center of mass of the trimer was shifted to the origin. The structures were rotated so that the principal axis with the smallest moment of inertia lay along the *y* axis. Additionally, if required, the structure was mirrored with respect to the *x* or *y* axis in order to get one He atom in the first quadrant and the other two in the third and fourth quadrants. The corresponding normalized structures are plotted in (**D** to **F**). The structures are normalized to the largest pair distance and subsequently located so that the two atoms with the largest pair distance get coordinates (−0.5,0) and (0.5,0) and the position of the third atom is plotted. The gray rectangle in (E) relates to structures that were cut during the reconstruction (see the supplementary materials for details). The linear color scale encodes the number of entries. The typical structure of the excited state of the He_3 is sketched in the upper right corner of (D).

experimental pair distance distributions of the excited state are nearly identical and match the theoretical distribution (Fig. 3, violet) very well.

The measured pair distribution (Fig. 3) can be used to extract the binding energy of the excited state. The excited He_3 exists mainly in the classically forbidden region well outside the two-body interaction potential well. Therefore, the asymptotic part of the pair distance distribution $P_{pair}(R)$ can be approximated by an exponential decay function (*12*)

$$P_{pair}(R) \propto e^{-2\sqrt{2\mu\Delta B/\hbar^2}R} \quad (2)$$

where R denotes the He-He distance, $\mu = 2 \times m_{He}/3$ is the reduced mass of the He trimer, and ΔB is the difference between the binding energies of the excited trimer state and the dimer ground state. Fitting the falling edge of the reconstructed pair distance distribution (black curve, Fig. 3) by Eq. 2 yields ΔB of 0.98 ± 0.2 mK (for details, see the supplementary materials). Given a theoretical prediction for the dimer binding energy of 1.62 mK (*11*), we obtain a binding energy of the trimer excited state of 2.6 ± 0.2 mK. This is in excellent agreement with our theoretical value of 2.65 mK, as well as with a theoretical value of 2.6502 mK from (*12*).

Having established the spatial extent of the He_3 Efimov state, we now discuss its geometric shape revealed by the structural plots shown in Fig. 4. The plots in the upper row [(A) to (C)] of Fig. 4 are generated in the center-of-mass coordinate frame, with the principal axis of the smallest moment of inertia chosen to lie along the y axis as proposed by Nielsen *et al.* (*26*). In the plots of the lower row [(D) to (F)] of Fig. 4, the interparticle distances of each reconstructed geometry were initially normalized to the largest of the three interparticle distances. Subsequently, the two atoms with the largest pair distance were placed at positions (–0.5,0) and (0.5,0), and the position of the third atom was plotted. In these plots, the equilateral triangle corresponds to the $(x,y) = (0, \sqrt{3}/2)$, and linear configurations have $y = 0$. The structure in which two particles are close to each other, with the third particle being far away, corresponds to (x,y) being close to (–0.5,0) or (0.5,0).

The geometry of the Efimov state is remarkably different from that of the ground state. Whereas the ground state corresponds to an almost randomly distributed cloud of particles (*25*), the excited Efimov state is dominated by configurations in which two atoms are close to each other and the third one farther away, in the classically forbidden region of the two-body interaction potential. According to theory, the average value of the smallest angle in the triangle is 18°. This typical structure of the $^4He_3$ excited state is in accordance with the prediction of Nielsen and coworkers (*26*) and in line with a dimer-like pair model proposed by Hiyama and Kamimura (*29*), which explains the asymptotic behavior of the excited state of the He_3. More generally, the typical structure revealed by Fig. 4 is an intrinsic property of all Efimov states with positive two-body scattering length. Comparison with Fig. 1B shows that the geometrical structure of the real He_3 exited state is similar to the one of the hypothetical He trimer with an infinite scattering length, although the amount of triangles with a small acute angle is reduced in the latter case (see also fig. S7).

We have reported the observation of the elusive Efimov state of the ^{4}He trimer by means of Coulomb explosion imaging of mass-selected clusters. We have found that the dominant structure of an Efimov state with positive two-body scattering length is a triangle with a relatively small acute angle. This has important consequences for how Efimov states are formed and possibly excited, as it is the geometry that defines the Franck-Condon overlap with continuum as well as with bound states. Having demonstrated the ability to experimentally image the quantum-mechanical probability distribution of Efimov trimers, this work opens the door for quantitative studies of Efimov physics beyond the geometric scaling properties and energetics. Extensions of the imaging approach to the four-body sector appear feasible.

REFERENCES AND NOTES

1. D. Wintgen, K. Richter, G. Tanner, *Chaos Interdiscip. J. Nonlinear Sci.* **2**, 19–33 (1992).
2. V. Efimov, *Phys. Lett. B* **33**, 563–564 (1970).
3. P. F. Bedaque, H.-W. Hammer, U. van Kolck, *Nucl. Phys. A.* **676**, 357–370 (2000).
4. E. Braaten, H.-W. Hammer, *Phys. Rep.* **428**, 259–390 (2006).
5. Y. Nishida, Y. Kato, C. D. Batista, *Nat. Phys.* **9**, 93–97 (2013).
6. T. Pal, P. Sadhukhan, S. M. Bhattacharjee, *Phys. Rev. Lett.* **110**, 028105 (2013).
7. T. Kraemer *et al.*, *Nature* **440**, 315–318 (2006).
8. T. Lompe *et al.*, *Science* **330**, 940–944 (2010).
9. S. Nakajima, M. Horikoshi, T. Mukaiyama, P. Naidon, M. Ueda, *Phys. Rev. Lett.* **106**, 143201 (2011).
10. T. K. Lim, S. K. Duffy, W. C. Damer, *Phys. Rev. Lett.* **38**, 341–343 (1977).
11. W. Cencek *et al.*, *J. Chem. Phys.* **136**, 224303 (2012).
12. E. Hiyama, M. Kamimura, *Phys. Rev. A* **85**, 062505 (2012).
13. T. Cornelius, W. Glöckle, *J. Chem. Phys.* **85**, 3906–3912 (1986).
14. B. D. Esry, C. D. Lin, C. H. Greene, *Phys. Rev. A* **54**, 394–401 (1996).
15. E. A. Kolganova, A. K. Motovilov, W. Sandhas, *Few-Body Syst.* **51**, 249–257 (2011).
16. P. Naidon, E. Hiyama, M. Ueda, *Phys. Rev. A* **86**, 012502 (2012).
17. W. Schöllkopf, J. P. Toennies, *Science* **266**, 1345–1348 (1994).
18. G. C. Hegerfeldt, T. Köhler, *Phys. Rev. Lett.* **84**, 3215–3219 (2000).
19. R. Brühl *et al.*, *Phys. Rev. Lett.* **95**, 063002 (2005).
20. D. Blume, C. H. Greene, B. D. Esry, *J. Chem. Phys.* **113**, 2145–2158 (2000).
21. D. Blume, C. H. Greene, B. D. Esry, *J. Chem. Phys.* **141**, 069901 (E) (2014).
22. Z. Vager, R. Naaman, E. P. Kanter, *Science* **244**, 426–431 (1989).
23. J. Ullrich *et al.*, *Rep. Prog. Phys.* **66**, 1463–1545 (2003).
24. O. Jagutzki *et al.*, *Nucl. Sci. IEEE Trans. On* **49**, 2477–2483 (2002).
25. J. Voigtsberger *et al.*, *Nat Commun.* **5** (2014).
26. E. Nielsen, D. V. Fedorov, A. S. Jensen, *J. Phys. At. Mol. Opt. Phys.* **31**, 4085–4105 (1998).
27. D. Blume, C. H. Greene, *J. Chem. Phys.* **112**, 8053–8067 (2000).
28. L. W. Bruch, W. Schöllkopf, J. P. Toennies, *J. Chem. Phys.* **117**, 1544–1566 (2002).
29. E. Hiyama, M. Kamimura, *Phys. Rev. A* **85**, 022502 (2012).

ACKNOWLEDGMENTS

The experimental work was supported by a Reinhart Koselleck project of the Deutsche Forschungsgemeinschaft. The financial support of the Goethe-University Frankfurt am Main is gratefully acknowledged. D.B. acknowledges support by the U.S. National Science Foundation through grant number PHY-1205443. Authors thank J. Williams for the proofreading of the manuscript. Raw data are archived at the Goethe-University Frankfurt am Main and are available upon request.

SUPPLEMENTARY MATERIALS

www.sciencemag.org/content/348/6234/551/suppl/DC1
Materials and Methods
Figs. S1 to S7
References (*30*–*32*)

23 December 2014; accepted 25 March 2015
10.1126/science.aaa5601

IONIC INTERACTIONS

Subnanoscale hydrophobic modulation of salt bridges in aqueous media

Shuo Chen,[1] Yoshimitsu Itoh,[1]* Takuya Masuda,[2] Seishi Shimizu,[3] Jun Zhao,[4] Jing Ma,[4] Shugo Nakamura,[5] Kou Okuro,[1] Hidenori Noguchi,[2,6,7] Kohei Uosaki,[2,6,7] Takuzo Aida[1,8]*

Polar interactions such as electrostatic forces and hydrogen bonds play an essential role in biological molecular recognition. On a protein surface, polar interactions occur mostly in a hydrophobic environment because nonpolar amino acid residues cover ~75% of the protein surface. We report that ionic interactions on a hydrophobic surface are modulated by their subnanoscale distance to the surface. We developed a series of ionic head groups—appended self-assembled monolayers with C2, C6, C8, and C12 space-filling alkyl chains, which capture a dendritic guest via the formation of multiple salt bridges. The guest release upon protonolysis is progressively suppressed when its distance from the background hydrophobe changes from 1.2 (C2) to 0.2 (C12) nanometers, with an increase in salt bridge strength of ~3.9 kilocalories per mole.

Oppositely charged polar residues often conjugate to form ion pairs at interfaces of biomolecules, as well as in nonbiological systems (*1*, *2*). Despite the general importance of ion pairing in biological phenomena (*3*), effects of interfaces on ion-pairing interactions have not been well understood to date (*2*, *4*, *5*). In relation to this point, a prime issue is how diversity of biomolecular recognition has developed from a limited variety

Downloaded from www.sciencemag.org on April 30, 2015

of polar residues on protein surfaces. Considering that ~75% of protein surface is covered by nonpolar amino acid residues, ion-paring interactions on hydrophobic solid surfaces must deserve in-depth investigations. However, only a few theoretical studies have been reported on this subject (*2*, *6*), whereas effects of air–water and liquid–water interfaces on ion pairing have been studied both theoretically and experimentally (*4*, *5*). On the basis of a dielectric continuum model of solvents, Schellman postulated in the 1950s that ion pairing in aqueous media, when approaching a hydrophobic surface, would be enhanced (*6*). However, the theoretical scenario of Schellman lacks direct experimental support, despite its frequent use in interpreting and simulating protein structures (*7*). Recently, by using an atomic force microscopy (AFM) technique, Ma *et al.* quantified how hydrophobic interactions are modulated by proximal ions (*8*). In contrast, we focus here on how ionic interactions are modulated by proximal hydrophobes. Obtaining experimental evidence for this issue is equally important but experimentally difficult because solid ideas are needed to construct ion pairs at a defined distance from a hydrophobic surface and to quantify their strengths in aqueous media.

Lahann *et al.* (*9*) reported a voltage-responsive mixed self-assembled monolayer (SAM) and showed that an ionic head group incorporated into the SAM moved electrostatically in response to an applied voltage in an electrolyte solution. This achievement led to a variety of interesting applications, such as DNA detection (*10*), protein recognition (*11*), and cell adhesion (*12*). For our studies, we used mixed SAMs (tethered onto a highly doped silicon wafer electrode via silanization) (*13*, *14*), in which a fluorescent reporter molecule with an ionic head group is embedded in alkyl group layers of different chain lengths. The reporter consists of fluorescein isothiocyanate (FITC), an anionic fluorescent motif, bound to a flexible hydrophilic tetraethylene glycol (TEG) linker. We designed a series of self-assembled fluorescent monolayers—$fSAM_{C2}$, $fSAM_{C6}$, $fSAM_{C8}$, and $fSAM_{C12}$—in which the reporters are dispersed in hosting SAMs that are composed of C2, C6, C8, and C12 space-filling alkyl chains (1:1 feed molar ratio), respectively (Fig. 1A). The $fSAM_{C2}$ was unambiguously characterized by electronic absorption, fluorescence emission, and x-ray photoelectron spectroscopies (figs. S8 and S12). The area-per-molecule density, in terms of FITC, is 2.9 nm^2 (fig. S8), in which the FITC-TEG units are dispersed homogeneously, as confirmed by the absence of concentration-dependent quenching in the fluorescence decay profile being analogous to that of FITC in dilute solution (fig. S10). The length effect of the space-filling alkyl chains on the densities and dispersities of the FITC head groups was found to be negligible, as shown by the similar area-per-molecule FITC density (2.8 nm^2) (fig. S9) and fluorescence decay profile (fig. S11) for $fSAM_{C12}$ compared with those of $fSAM_{C2}$. In $fSAM_{C2}$ with space-filling ethyl groups, the FITC head groups are 1.2 nm above

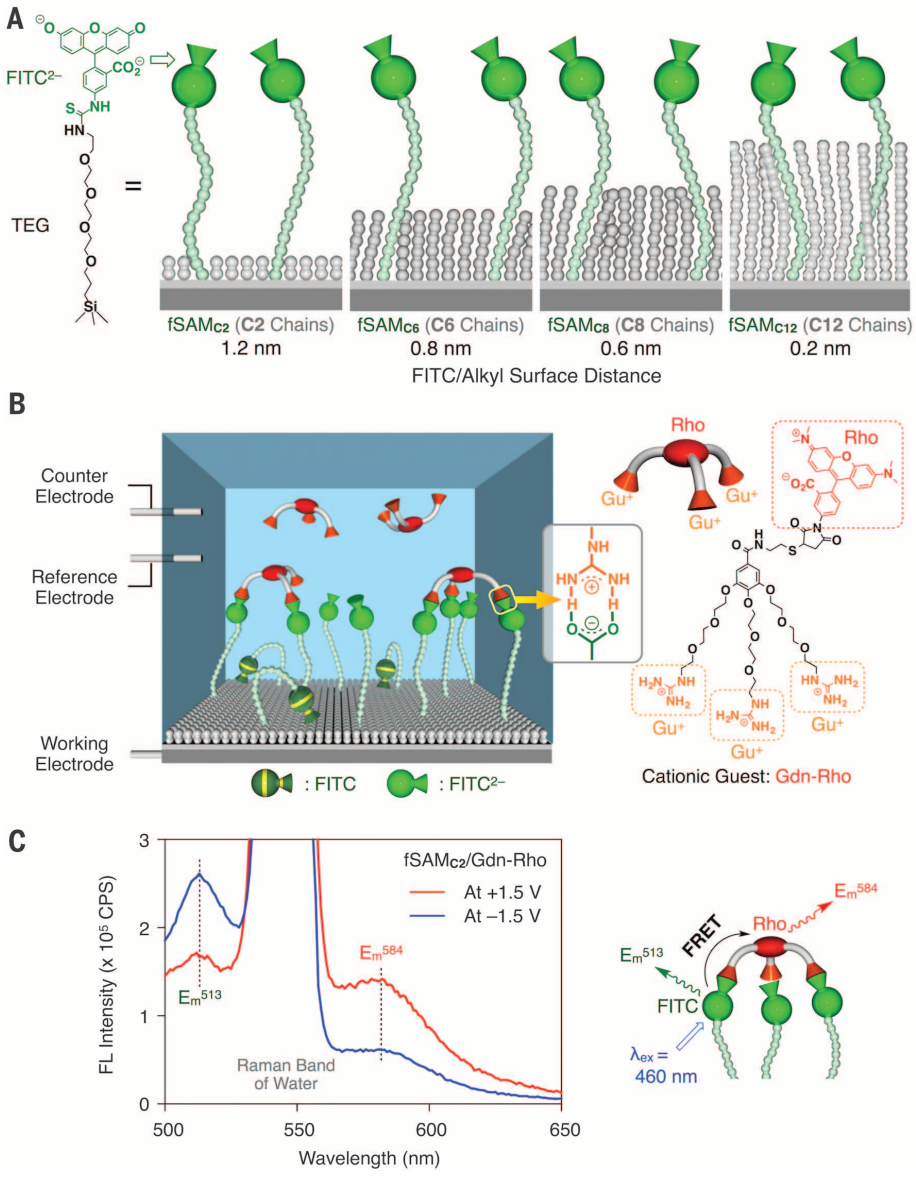

Fig. 1. Design of voltage-responsive fSAMs for guest capture and release. (**A**) Schematic representations of the structures of $fSAM_{C2}$, $fSAM_{C6}$, $fSAM_{C8}$, and $fSAM_{C12}$ that carry fluorescein isothiocyanate (FITC) head groups via a hydrophilic TEG linker in C2, C6, C8, and C12 space-filling alkyl chains on a silicon substrate, respectively. The ellipsometric thickness of $fSAM_{C2}$ in deionized water at +1.5 V (ionized FITC), together with the alkyl chain lengths upon extended conformation, was used for estimating the FITC head group/alkyl surface distances in fSAMs. (**B**) Schematic representation of a three-electrode system for investigating voltage-responsive behaviors of $fSAM_{C2}$ conjugated with Gdn-Rho. Gdn-Rho carries a rhodamine (Rho) dye at its focal core and three guanidinium ions (Gu^+) at the termini of hydrophilic triethylene glycol chains. This dendritic structure allows Gdn-Rho to be salt-bridged with the FITC head groups of $fSAM_{C2}$, leading to FRET. (**C**) In situ front-face fluorescence spectra (λ_{ex} = 460 nm) of $fSAM_{C2}$/Gdn-Rho at –1.5 V (blue curve) and +1.5 V (red curve) (versus Ag/AgCl). FRET takes place from FITC to Rho when $fSAM_{C2}$ conjugates Gdn-Rho.

[1]Department of Chemistry and Biotechnology, School of Engineering, The University of Tokyo, 7-3-1 Hongo, Bunkyo-ku, Tokyo 113-8656, Japan. [2]Global Research Center for Environment and Energy based on Nanomaterials Science (GREEN), National Institute for Materials Science (NIMS), Tsukuba 305-0044, Japan. [3]York Structural Biology Laboratory, Department of Chemistry, University of York, Heslington, York YO10 5DD, UK. [4]Collaborative Innovation Center of Chemistry for Life Sciences, School of Chemistry and Chemical Engineering, Nanjing University, Nanjing 210093, P. R. China. [5]Department of Biotechnology, Graduate School of Agricultural and Life Sciences, The University of Tokyo, 1-1-1 Yayoi, Bunkyo-ku, Tokyo 113-8657, Japan. [6]International Center for Materials Nanoarchitectonics (WPI-MANA), National Institute for Materials Science (NIMS), Tsukuba 305-0044, Japan. [7]Graduate School of Chemical Science and Engineering, Hokkaido University, Sapporo 060-0810, Japan. [8]RIKEN Center for Emergent Matter Science, 2-1 Hirosawa, Wako, Saitama 351-0198, Japan.
***Corresponding author. E-mail: itoh@macro.t.u-tokyo.ac.jp (Y.I.); aida@macro.t.u-tokyo.ac.jp (T.A.)**

the hydrophobic SAM surface and thus should possess spatial freedom for conformational changes (Fig. 1A) (*9*, *15*). In contrast, in $fSAM_{C12}$, the FITC-TEG units are sterically constrained by the surrounding dodecyl chains (*9*, *15*), leaving the FITC head groups just above the hydrophobic surface (Fig. 1A).

The carboxylate moiety of the FITC head groups can form salt bridges with guanidinium ions (Gu^+) introduced from the solution phase. We did not use the free Gu^+ ions but tethered them in groups of three via TEG chains to a rhodamine (Rho) dye in a water-soluble dendritic guest molecule Gdn-Rho (scheme S2), thus creating multiple salt bridges for stable complexation (Fig. 1B) (*16*–*18*). We initially chose $fSAM_{C2}$ and $fSAM_{C12}$ to investigate how fSAMs would capture and release Gdn-Rho in response to a pH change or voltage change in deionized water (Fig. 1B). In either case, an increase in H^+ concentration, by the addition of an acid or an electrically generated H^+ gradient (*19*–*21*), should lead to protonolysis of the salt bridge constructed on the hydrophobic SAM surface. To visualize the voltage responses of these fSAMs, we took advantage of the pH-sensitive fluorescence emission of the FITC head groups. FITC is more emissive when its anionic groups are ionized (*22*, *23*), and its fluorescence intensity also changes as a result of the voltage-driven positional change of the FITC motif relative to the electrode surface (*24*). When bound to a Gu^+ pendant of Gdn-Rho via the salt-bridge formation (Fig. 1B), the FITC head group underwent a change in its fluorescence emission profile (Fig. 1C).

We conducted pH titrations of $fSAM_{C2}$ and $fSAM_{C12}$ and confirmed that both of them predictably modulated the intensity of their fluorescence emission in response to an applied change in pH (Fig. 2, A and B). The titration profiles are similar to one another, with inflection points at pH 6.1 and 5.8 for $fSAM_{C2}$ and $fSAM_{C12}$, respectively. Nevertheless, in a low pH range, at which the anionic FITC head groups are protonated, $fSAM_{C2}$ is much less emissive than $fSAM_{C12}$. This contrasting behavior is a reflection of the difference in the conformational freedom of the FITC-TEG units in $fSAM_{C2}$ and $fSAM_{C12}$ (Fig. 1A). Protonation both attenuates the fluorescence of FITC anionic head groups (*22*) and makes them become hydrophobic (*23*), causing them to interact with the hydrophobic alkyl chains. In the case of $fSAM_{C2}$, the TEG linkers to the FITC head groups can fold toward the surface, which further attenuated the fluorescence via the distance-dependent nonradiative energy transfer to the electrode (*24*). In contrast, it is unlikely that $fSAM_{C12}$ permits this type of conformational change and nonradiative energy transfer because of steric congestion (Fig. 1A).

With these inherent behaviors in mind, we applied an alternating voltage of ±1.5 V (all voltages reported are versus Ag/AgCl) to $fSAM_{C2}$ and $fSAM_{C12}$ in order to examine their responses to an applied voltage through protonation and deprotonation of the FITC head groups. As confirmed with cyclic voltammetry (figs. S13 and S14), the native dielectric SiO_2 layer (~2 nm) maintained an intense electric field and prevented electrochemical disruption of the SAMs over a wide potential range from −1.5 V to +1.5 V. To sensitively and quantitatively monitor the responses of these fSAMs to an electrically generated H^+ gradient, we used a dedicated in situ analytical technique of front-face fluorescence spectroscopy (*25*), which allows for monitoring the fluorescence spectral features of solid surfaces in fluid media. A homemade sample cell with a solution chamber and a quartz window (fig. S1) allowed the SAM sample to be immersed in water and also assembled in a three-electrode electrochemical system. When an electrode was immersed in deionized water, application of a potential generated a H^+ gradient in close proximity to the electrode surface (*19*–*21*). This electrical method can cleanly modulate the local pH near the SAM surface without the addition of an acid or a base.

The FITC fluorescence of $fSAM_{C2}$ was remarkably enhanced and attenuated at applied voltages of +1.5 V and −1.5 V, respectively (Fig. 3A). As expected from the difference in the conformational dynamics of their FITC-TEG units, $fSAM_{C2}$, analogous to the case of pH titration, was much less emissive than $fSAM_{C12}$ when its local pH was lowered by application of a voltage of −1.5 V (Fig. 3, A and B). To directly confirm whether the FITC-TEG units in $fSAM_{C2}$ underwent a voltage-responsive conformational change, we performed in situ ellipsometry using a homemade sample cell (fig. S2) (*26*). As shown in Fig. 3C, the ellipsometric thickness of $fSAM_{C2}$ decreased considerably from 1.2 to 0.3 nm when the applied voltage was switched from +1.5 V to −1.5 V, and vice versa. In sharp contrast, $fSAM_{C12}$

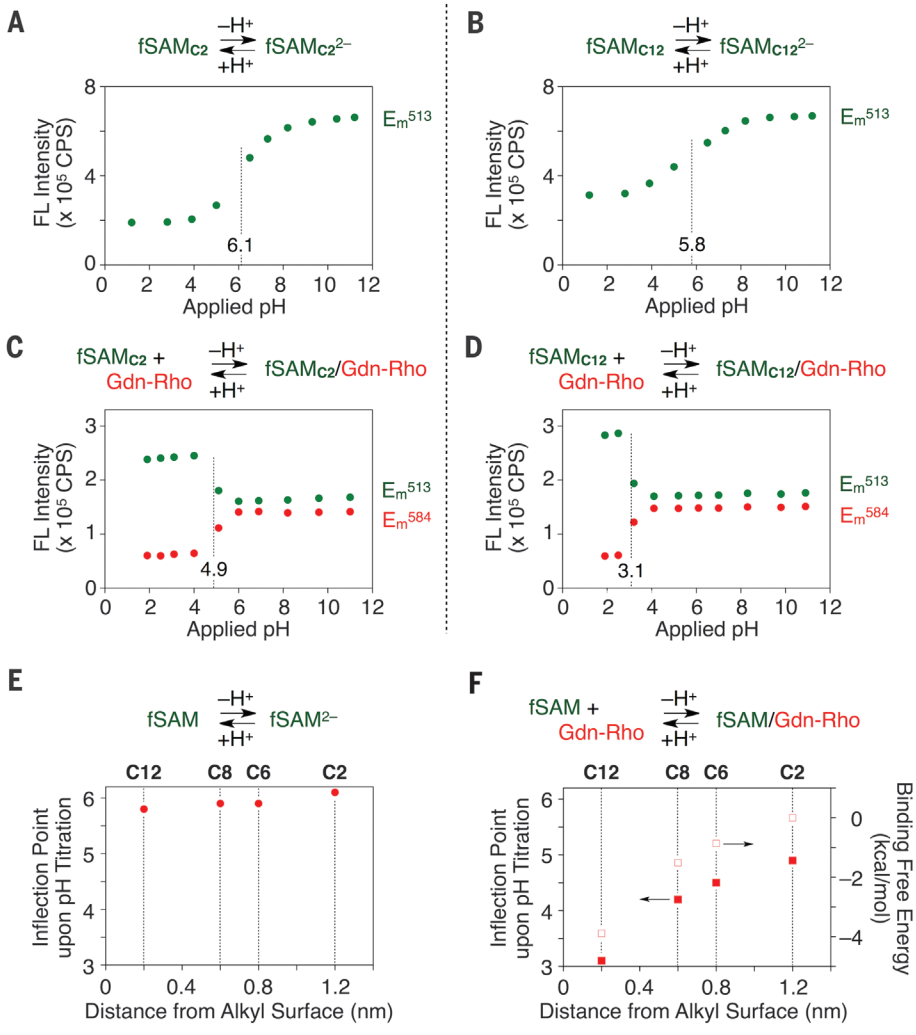

Fig. 2. pH-Responsive features of fSAMs in the presence and absence of Gdn-Rho. (**A** and **B**) pH-Responsive fluorescence intensity changes at 513 nm (λ_{ex} = 460 nm) of (A) $fSAM_{C2}$ and (B) $fSAM_{C12}$ (**C** and **D**) pH-Responsive fluorescence intensity changes at 513 nm and 584 nm (λ_{ex} = 460 nm) of (C) $fSAM_{C2}$ and (D) $fSAM_{C12}$ in an aqueous solution of Gdn-Rho (10 nM). (**E**) Inflection points upon pH titration of $fSAM_{C2}$, $fSAM_{C6}$, $fSAM_{C8}$, and $fSAM_{C12}$. (**F**) Inflection points upon pH titration of $fSAM_{C2}$, $fSAM_{C6}$, $fSAM_{C8}$, and $fSAM_{C12}$ in the presence of Gdn-Rho (red squares) and their binding free energies derived from pH titration profiles (open squares).

exhibited a minimal voltage-responsive thickness change (Fig. 3D), indicating that its FITC-TEG units did not substantially change their conformation because of the steric congestion from the dodecyl chains.

We next investigated whether $fSAM_{C2}$ could capture and release water-soluble cationic guest Gdn-Rho through a multivalent salt bridge in response to an applied voltage (Fig. 4, A and B). When this interaction occurs, fluorescence resonance energy transfer (FRET) should take place from the FITC head groups to a Rho dye attached to the core of the dendrimer (Fig. 1C). To confirm the binding of Gdn-Rho to $fSAM_{C2}$, the SAM was incubated overnight in an aqueous solution of Gdn-Rho (10 nM) before performing front-face fluorescence spectroscopy. Upon excitation at 460 nm, the Rho emission at 584 nm was enhanced, whereas the FITC emission at 513 nm was decreased (Fig. 4C). The resulting $fSAM_{C2}$/Gdn-Rho conjugate appeared to be rather stable because its FRET profile hardly changed after rinsing with water (fig. S15, A, C, and E). In sharp contrast, a nonionic SAM composed solely of ethyl groups was unable to capture Gdn-Rho (fig. S15, B, D, and F), indicating the primary role of the salt bridges in the binding of Gdn-Rho to $fSAM_{C2}$.

When a negative voltage of –1.5 V was applied to the $fSAM_{C2}$/Gdn-Rho conjugate in order to lower the local pH at the surface, a substantial decrease in the Rho emission at 584 nm was observed, along with an increase in the FITC emission at 513 nm (Fig. 4C). Thus, electrical liberation of Gdn-Rho from $fSAM_{C2}$ switched off the FRET from FITC to Rho. This spectral change occurred sigmoidally with time and reached a plateau in 15 min. We attributed this voltage-responsive guest release to the protonolysis of the salt bridges (*16*, *17*) between $fSAM_{C2}$ and Gdn-Rho upon electrically lowering the local pH (Fig. 4A). Subsequently, when the applied voltage was then switched to +1.5 V so as to increase the local pH around $fSAM_{C2}$, the inverse fluorescence spectral change resulted (Fig. 4C). As a consequence, $fSAM_{C2}$ recaptured Gdn-Rho by reforming the salt bridges (Fig. 4A). Such a voltage-responsive guest capture/release event could be repeated multiple times (Fig. 4C).

The Rho unit at the focal core of the dendritic guest did not contribute to the electric response because the guest release profile from $fSAM_{C2}$ was essentially the same as that in Fig. 4C when Gdn-OMe (scheme S3) was used as the guest instead of Gdn-Rho (fig. S18). The voltage-responsive guest capture and release, realized with $fSAM_{C2}$, was the goal of our initial investigation because such electrically operable SAMs have never been reported. However, analogous experiments with $fSAM_{C12}$, a long-alkyl version of $fSAM_{C2}$, helped elucidate intriguing fundamental insights (Fig. 4, B and D). Similar to $fSAM_{C2}$, long-chain $fSAM_{C12}$ could capture Gdn-Rho (Fig. 4B) and afforded an analogous FRET profile (figs. S15 and S16). However, in stark contrast, $fSAM_{C12}$ did not release Gdn-Rho when a negative voltage of –1.5 V was applied to its conjugate (Fig. 4, B and D). Furthermore, no change in the FRET profile was observed even upon prolonged application of this negative voltage (Fig. 4D).

Given this distinctly different behavior of $fSAM_{C12}$, we performed a pH titration, along with $fSAM_{C2}$, in the presence of Gdn-Rho without an applied voltage (Fig. 2, C and D). Much to our surprise, the release of Gdn-Rho from $fSAM_{C12}$ occurred at a pH value of 3.1 (Fig. 2D), which is a much more acidic condition than that for $fSAM_{C2}$ (pH = 4.9) (Fig. 2C). Hence, the salt bridges formed on $fSAM_{C12}$ with Gdn-Rho were much more tolerant to protonolysis than those on $fSAM_{C2}$. This result is intriguing, considering that the pH titration profiles of $fSAM_{C2}$ (Fig. 2A) and $fSAM_{C12}$ (Fig. 2B) are nearly the same. We estimated the binding free energy ($\Delta\mu$) of the fSAM/Gdn-Rho conjugates based on the Clausius–Clapeyron equation (*13*), where $\Delta\mu$ is assumed to depend on pH as well as on the length of the alkyl chain, l, as follows:

$$\partial\Delta\mu/\partial l = (-\partial\Delta\mu/\partial \mathrm{pH})(d\mathrm{pH}/dl)$$

Strikingly, $\Delta\mu$ for $fSAM_{C12}$ is as much as 3.9 kcal/mol (at pH = 4.9) greater than that for $fSAM_{C2}$ (Fig. 2F, open squares). In other words, the stability of the salt bridge increases by as much as 3.9 kcal/mol when the distance of the binding site from the hydrophobic surface decreases by 1.0 nm. This value is ~1.7 times as large as the roughly estimated strength of a hydrogen bond in liquid water, 2.25 kcal/mol (*27*).

To systematically investigate how the strength of the salt bridge changed with increasing distance from the hydrophobic surface, we evaluated $fSAM_{C6}$ and $fSAM_{C8}$ that had hexyl and octyl groups as the space-filling alkyl chains, respectively (fig. S19). As shown in Fig. 2F (red squares), the release of Gdn-Rho from $fSAM_{C6}$ and $fSAM_{C8}$ took place at pH values of 4.5 and 4.2, respectively. The pH value for the guest release changed nonlinearly with the distance of the FITC head group from the alkyl surface (Fig. 2F, red squares), whereas the pH titration profiles of the varying fSAMs hardly showed any such distance dependency (Fig. 2E). We calculated $\Delta\mu$ values of $fSAM_{C2}$, $fSAM_{C6}$, $fSAM_{C8}$, and $fSAM_{C12}$ with Gdn-Rho (*13*) from their titration profiles (Fig. 2F and fig. S19, G and H) and plotted in Fig. 2F (open squares), where the binding stability of the guest clearly increased nonlinearly in an upwardly convex manner when its distance from the hydrophobic surface decreased from 1.2 to 0.8, 0.6, and 0.2 nm (the method of estimation is provided in the caption of Fig. 1A). Consistent with these experimental results, molecular dynamics simulations with real (fig. S21) and simplified (fig. S22) models of the fSAM/Gdn-Rho conjugates for calculating their binding energies (*13*) suggested that the guest binding is stabilized with the increase of the alkyl chain length.

The formation of a salt bridge between a carboxylate ion and a guanidinium ion in aqueous media is accompanied by the dehydration of both ions (*5*, *16*, *17*). In turn, protonolysis of the salt bridge involves rehydration of its ionic parents through the formation of new hydrogen bonds with proximal water molecules. This rehydration event is energetically demanding if water molecules

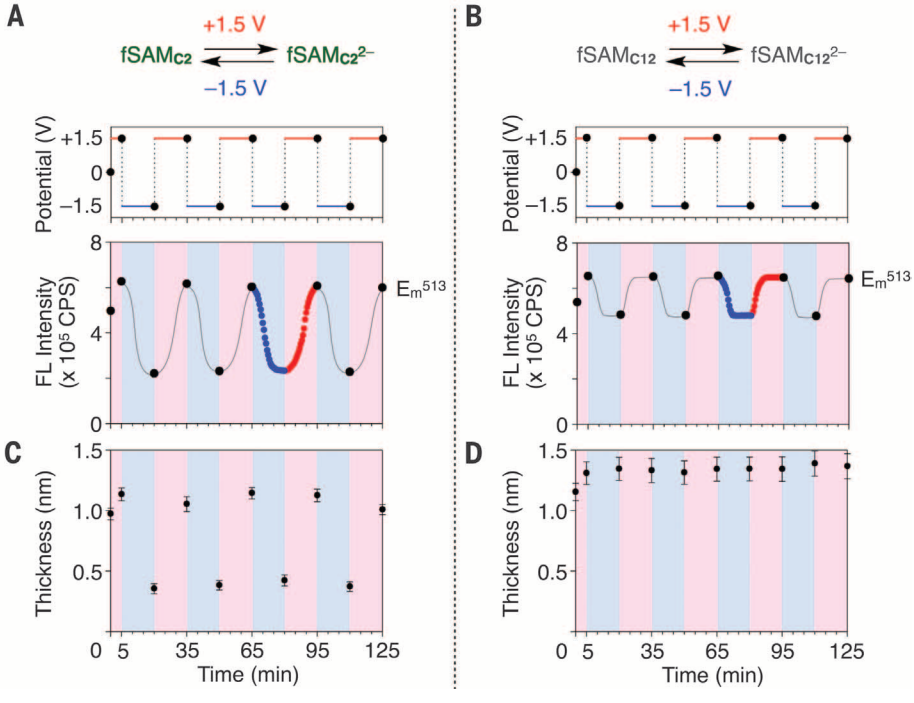

Fig. 3. Voltage-responsive features of $fSAM_{C2}$ and $fSAM_{C12}$. (**A** and **B**) Fluorescence intensity changes at 513 nm (λ_{ex} = 460 nm) of (A) $fSAM_{C2}$ and (B) $fSAM_{C12}$ in response to the switching of an applied voltage between –1.5 and +1.5 V (versus Ag/AgCl) in deionized water. (**C** and **D**) Ellipsometric thickness changes of (C) $fSAM_{C2}$ and (D) $fSAM_{C12}$ in response to the switching of an applied voltage between –1.5 and +1.5 V (versus Ag/AgCl) in deionized water.

that surround the salt bridge are tightly hydrogen-bonded together. On the basis of AFM studies, Teschke *et al*. reported that from 0 to 10 nm, the local water permittivity progressively decreases the nearer the water molecules are to a hydrophobic surface (*28*). This trend originates from a reinforced hydrogen-bond network among water molecules (*29*, *30*), which is analogous to the case of those on a hydrophobic protein surface (*31*).

As described previously, the salt bridges in the $fSAM_{C12}$/Gdn-Rho conjugate are located just above the hydrophobic SAM surface (Fig. 4B), where water molecules are supposed to be more tightly hydrogen bonded than those in the bulk state. Thus, the rehydration of salt bridges is rather energetically demanding. In contrast, this energetic problem seems to be much less important for $fSAM_{C2}$, in which the salt bridges constructed on $fSAM_{C2}$ are more than 1 nm away from its hydrophobic surface (Fig. 4A), where water molecules appear to be hydrogen-bonded in the same manner as those in the bulk state (*32*, *33*). Why, then, do the pH titration profiles of fSAMs not differ from one another (Fig. 2E), despite the very different protonolytic behaviors of their salt bridges with Gdn-Rho (Fig. 2F, red squares)? As speculated from the rapid diffusion of H^+ in ice (*34*), this small cation is singular because its hydration and dehydration require only a minimal rearrangement of proximal water molecules. The hydrophobic effect on proximal ionic interactions, which we found serendipitously through the use of voltage-responsive SAMs, supports the long-standing theory of Schellman (*6*) and suggests how nature might have harnessed a limited variety of polar residues to create diverse recognition patterns in biomolecular systems.

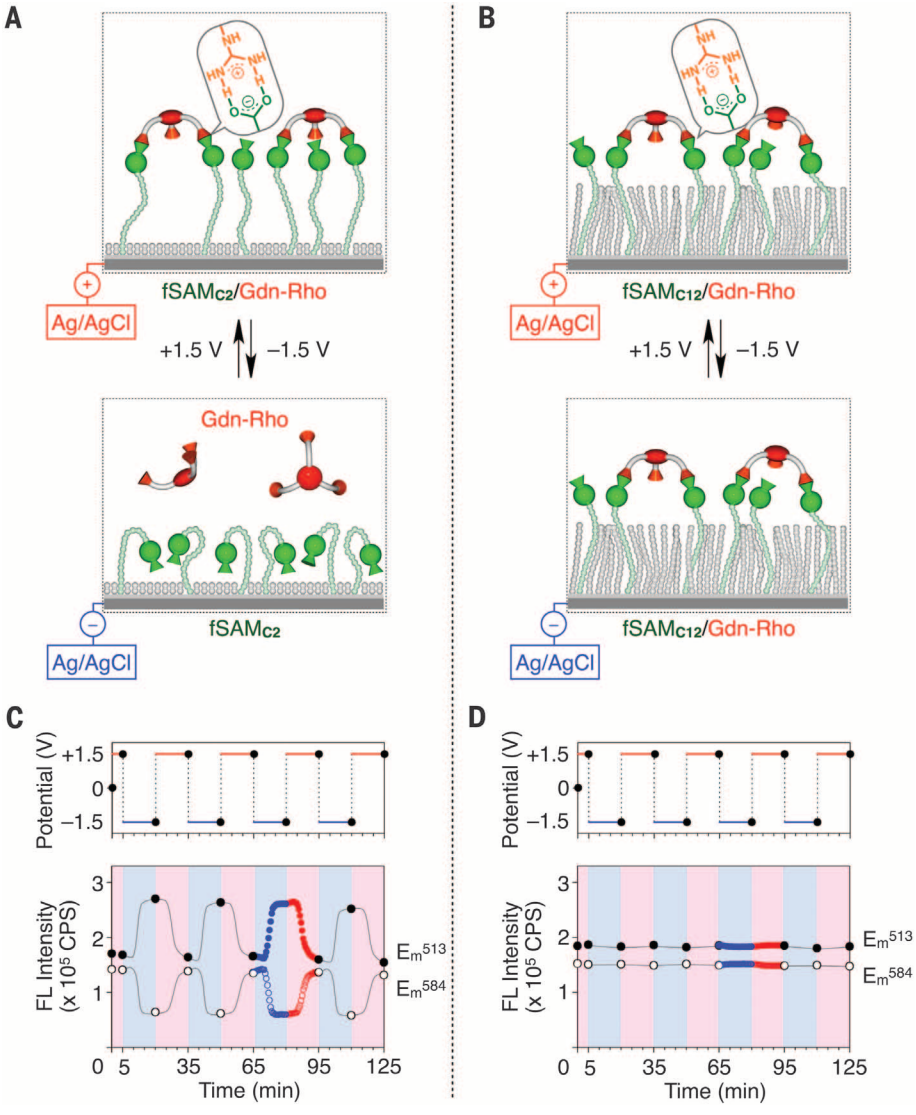

Fig. 4. Voltage-responsive features of $fSAM_{C2}$ and $fSAM_{C12}$ in the presence of Gdn-Rho. (**A** and **B**) Schematic representations of the voltage-responsive features of (A) $fSAM_{C2}$/Gdn-Rho and (B) $fSAM_{C12}$/Gdn-Rho. (**C** and **D**) Fluorescence intensity changes at 513 and 584 nm (λ_{ex} = 460 nm) of (C) $fSAM_{C2}$ and (D) $fSAM_{C12}$ in response to the switching of an applied voltage between −1.5 and +1.5 V (versus Ag/AgCl) in an aqueous solution of Gdn-Rho (10 nM).

REFERENCES AND NOTES

1. D. H. Williams, E. Stephens, D. P. O'Brien, M. Zhou, *Angew. Chem. Int. Ed.* **43**, 6596–6616 (2004).
2. I. Chorny, K. A. Dill, M. P. Jacobson, *J. Phys. Chem. B* **109**, 24056–24060 (2005).
3. K. A. Dill, J. L. MacCallum, *Science* **338**, 1042–1046 (2012).
4. V. Venkateshwaran, S. Vembanur, S. Garde, *Proc. Natl. Acad. Sci. U.S.A.* **111**, 8729–8734 (2014).
5. P. Jungwirth, D. J. Tobias, *Chem. Rev.* **106**, 1259–1281 (2006).
6. J. A. Schellman, *J. Phys. Chem.* **57**, 472–475 (1953).
7. M. Schaefer, M. Karplus, *J. Phys. Chem.* **100**, 1578–1599 (1996).
8. C. D. Ma, C. Wang, C. Acevedo-Vélez, S. H. Gellman, N. L. Abbott, *Nature* **517**, 347–350 (2015).
9. J. Lahann *et al*., *Science* **299**, 371–374 (2003).
10. U. Rant *et al*., *Proc. Natl. Acad. Sci. U.S.A.* **104**, 17364–17369 (2007).
11. C. L. Yeung *et al*., *Adv. Funct. Mater.* **20**, 2657–2663 (2010).
12. C. C. A. Ng *et al*., *Angew. Chem. Int. Ed.* **51**, 7706–7710 (2012).
13. Materials and methods are available as supplementary materials on *Science* Online.
14. S. Onclin, B. J. Ravoo, D. N. Reinhoudt, *Angew. Chem. Int. Ed.* **44**, 6282–6304 (2005).
15. M. Luo, A. Amegashie, A. Chua, G. K. Olivier, J. Frechette, *J. Phys. Chem. C* **116**, 13964–13971 (2012).
16. B. Dietrich, D. L. Fyles, T. M. Fyles, J.-M. Lehn, *Helv. Chim. Acta* **62**, 2763–2787 (1979).
17. M. Valtiner, S. H. Donaldson Jr., M. A. Gebbie, J. N. Israelachvili, *J. Am. Chem. Soc.* **134**, 1746–1753 (2012).
18. Q. Wang *et al*., *Nature* **463**, 339–343 (2010).
19. A. J. Bard, L. R. Faulkner, *Electrochemical Methods: Fundamentals and Applications* (Wiley, New York, ed. 2, 2001).
20. R. Morrow, D. R. McKenzie, *Proc. R. Soc. A* **468**, 18–34 (2012).
21. I. Burgess, B. Seivewright, R. B. Lennox, *Langmuir* **22**, 4420–4428 (2006).
22. M. M. Martin, L. Lindqvist, *J. Lumin.* **10**, 381–390 (1975).
23. H. Diehl, R. Markuszewski, *Talanta* **32**, 159–165 (1985).
24. A. P. Alivisatos, M. F. Arndt, S. Efrima, D. H. Waldeck, C. B. Harris, *J. Chem. Phys.* **86**, 6540–6549 (1987).
25. E. A. McArthur, T. Ye, J. P. Cross, S. Petoud, E. Borguet, *J. Am. Chem. Soc.* **126**, 2260–2261 (2004).
26. Y. Han, H. Noguchi, K. Sakaguchi, K. Uosaki, *Langmuir* **27**, 11951–11957 (2011).
27. A. Ben-Naim, *Statistical Thermodynamics for Chemists and Biochemists* (Plenum, New York, 1992).
28. O. Teschke, E. F. de Souza, *Appl. Phys. Lett.* **82**, 1126–1128 (2003).
29. S. Nihonyanagi *et al*., *J. Am. Chem. Soc.* **133**, 16875–16880 (2011).
30. Y. R. Shen, V. Ostroverkhov, *Chem. Rev.* **106**, 1140–1154 (2006).
31. P. W. Snyder, M. R. Lockett, D. T. Moustakas, G. M. Whitesides, *Eur. Phys. J. Spec. Top.* **223**, 853–891 (2014).
32. D. Chandler, *Nature* **437**, 640–647 (2005).
33. P. Ball, *Chem. Rev.* **108**, 74–108 (2008).
34. I. Presiado, J. Lal, E. Mamontov, A. I. Kolesnikov, D. Huppert, *J. Phys. Chem. C* **115**, 10245–10251 (2011).

ACKNOWLEDGMENTS

We thank N. Matubayashi from Division of Chemical Engineering, Graduate School of Engineering Science, Osaka University for valuable discussion. We also thank E. Silver for generous discussion. This work was supported by the Japan Society for the Promotion of Science (JSPS) through its Funding Program for World-Leading Innovative R&D on Science and Technology (FIRST Program). Y. I. acknowledges the Ministry of Education, Culture, Sports, Science and Technology (MEXT), Japan, Grant-in-Aid for Young Scientists B. S.N. is partly supported by the Platform for Drug Discovery, Informatics, and Structural Life Science from MEXT, Japan. K.U. and H.N. thank the World Premier International Research Center (WPI) Initiative on Materials Nanoarchitectonics from MEXT, Japan. J.M. is supported by the National Natural Science Foundation of China (no. 21273102).

SUPPLEMENTARY MATERIALS

www.sciencemag.org/content/348/6234/555/suppl/DC1
Materials and Methods
Figs. S1 to S22
Schemes S1 to S4
Tables S1 and S2
References (*35*–*47*)

23 January 2015; accepted 20 March 2015
10.1126/science.aaa7532

BRAIN COMPUTATION

Selective information routing by ventral hippocampal CA1 projection neurons

S. Ciocchi,[1]* J. Passecker,[1] H. Malagon-Vina,[1] N. Mikus,[1] T. Klausberger[1,2]*

The hippocampus computes diverse information involving spatial memory, anxiety, or reward and directly projects to several brain areas. Are different computations transmitted to all downstream targets uniformly, or does the hippocampus selectively route information according to content and target region? By recording from ventral hippocampal CA1 neurons in rats during different behavioral tasks and determining axonal projections with optogenetics, we observed subsets of neurons changing firing at places of elevated anxiety or changing activity during goal approach. Anxiety-related firing was selectively increased in neurons projecting to the prefrontal cortex. Goal-directed firing was most prominent in neurons targeting the nucleus accumbens; and triple-projecting neurons, targeting the prefrontal cortex, amygdala, and nucleus accumbens, were most active during tasks and sharp wave/ripples. Thus, hippocampal neurons route distinct behavior-contingent information selectively to different target areas.

Learning processes require precise neuronal communication across distributed brain networks. The dorsal hippocampus is primarily associated with spatial navigation and episodic memory, whereas the ventral hippocampus is implicated in affective and motivated behaviors as well (*1*). Along the septotemporal axis of the hippocampus, CA1 projection neurons classically target the subiculum and entorhinal cortex (*2*). In the ventral CA1 hippocampus (vCA1), additional projections have been described (*2*), such as to the medial prefrontal cortex (mPFC), nucleus accumbens (Acb), and amygdala (Amy). We asked whether the hippocampus transmits all of its computations equally to those target areas, ceding their interpretation to those areas, or rather routes distinct representations selectively to different brain areas according to information content?

We recorded the activity of vCA1 neurons from rats (n = 4) during an anxiety task, spatial exploration, and goal-directed navigation, all within single experimental sessions (Fig. 1A). After each session, we determined the projections of recorded cells with optogenetics (*3*). For this, vCA1 was previously (4 to 5 weeks before) injected with an adeno-associated virus expressing channelrhodopsin-2 fused to enhanced yellow fluorescent protein (ChR2-eYFP) under the control of a neuron-specific promoter. In addition to vCA1 somata and dendrites, ChR2-eYFP was expressed in vCA1 projection fibers and synaptic boutons targeting the mPFC, Acb, or Amy (Fig. 1B). Blue light pulses were delivered via optic fibers placed above the mPFC, Acb, or Amy, while recording single-unit activity and antidromically evoking spikes in vCA1 (Fig. 1A and fig. S1). Antidromic spikes were defined by early-latency, low-spike jitter and a high-fidelity response to

[1]Center for Brain Research, Department for Cognitive Neurobiology, Medical University Vienna, Spitalgasse 4, 1090 Vienna, Austria. [2]Medical Research Council, Anatomical Neuropharmacology Unit, Oxford University, Mansfield Road, Oxford OX1 3TH, UK.
*Corresponding author. E-mail: stephane.ciocchi@meduniwien.ac.at (S.C.); thomas.klausberger@meduniwien.ac.at (T.K.)

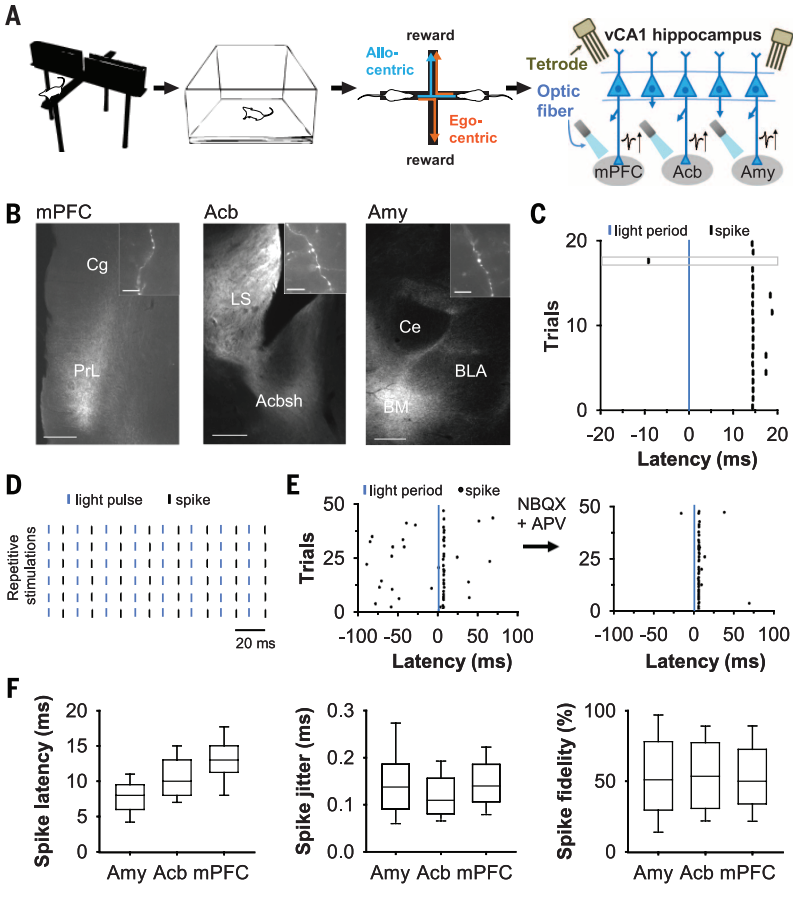

Fig. 1. Optogenetic identification of vCA1 projection neurons. (**A**) Behavioral tasks and antidromic activation of single units in vCA1 by photostimulating ChR2-expressing vCA1 axons in the mPFC, Acb, or Amy. (**B**) ChR2-immunopositive vCA1 axons targeting the mPFC, Acb, and Amy. Scale bar, 500 μm; in insets, 10 μm. Cg, cingulate cortex; PrL, prelimbic cortex; LS, lateral septum; Acbsh, nucleus accumbens shell; Ce, central amygdala; BLA, basolateral amygdala; BM, basomedial amygdala. (**C**) Low-jitter, high-fidelity, and early-latency response of a vCA1 neuron upon light stimulation (blue) in the Acb. Spike collision is shown at trial 18. (**D**) Reliable firing after 50-Hz stimulation. (**E**) Local infusion of NBQX/D-AP5 (APV) reduces spontaneous but not light-induced firing. (**F**) Spike latency, jitter, and fidelity in vCA1 projections targeting the Amy (n = 21 neurons), Acb (n = 79), or mPFC (n = 52). Plots indicate median, quartiles, and range.

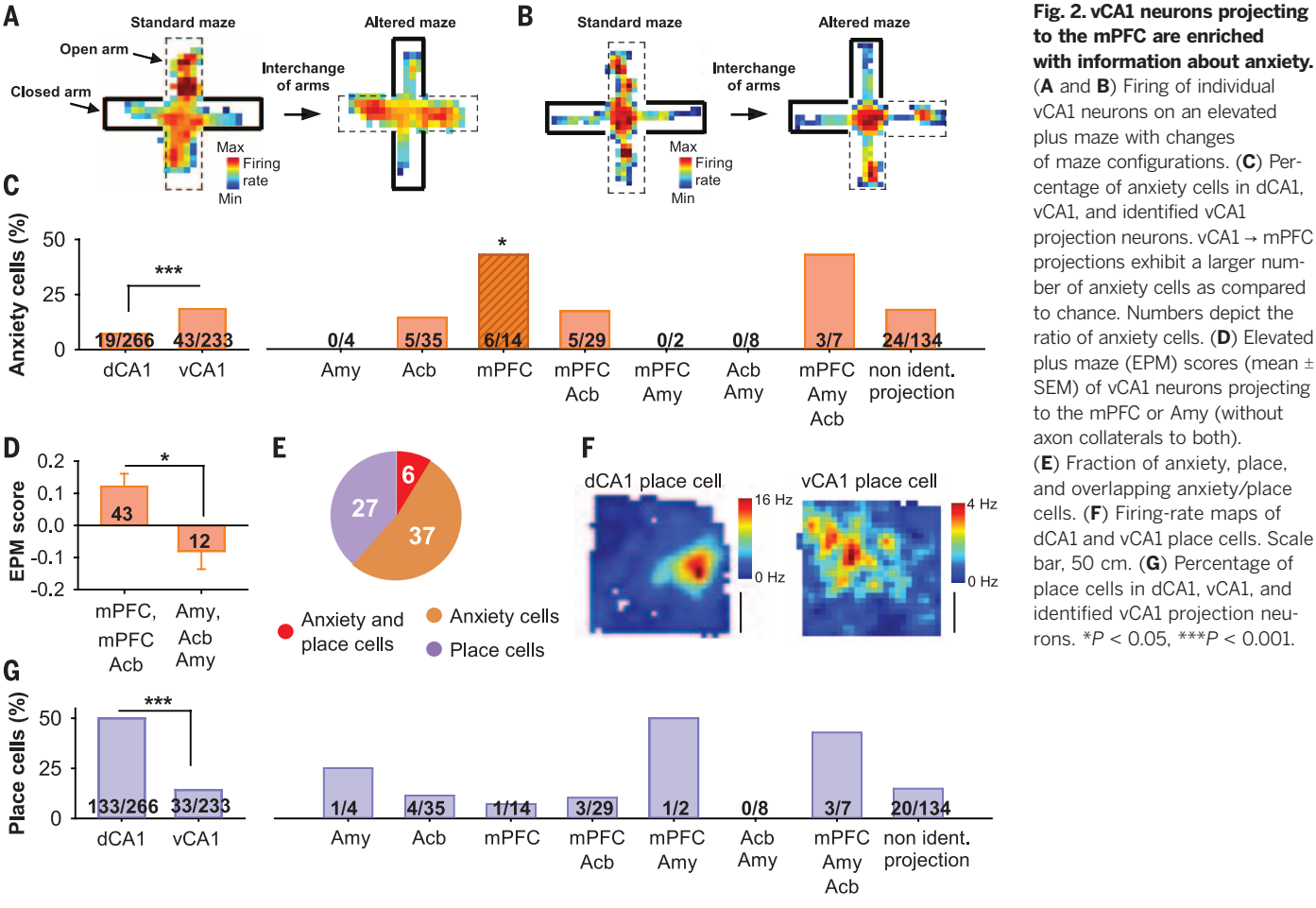

Fig. 2. vCA1 neurons projecting to the mPFC are enriched with information about anxiety. (**A** and **B**) Firing of individual vCA1 neurons on an elevated plus maze with changes of maze configurations. (**C**) Percentage of anxiety cells in dCA1, vCA1, and identified vCA1 projection neurons. vCA1 → mPFC projections exhibit a larger number of anxiety cells as compared to chance. Numbers depict the ratio of anxiety cells. (**D**) Elevated plus maze (EPM) scores (mean ± SEM) of vCA1 neurons projecting to the mPFC or Amy (without axon collaterals to both). (**E**) Fraction of anxiety, place, and overlapping anxiety/place cells. (**F**) Firing-rate maps of dCA1 and vCA1 place cells. Scale bar, 50 cm. (**G**) Percentage of place cells in dCA1, vCA1, and identified vCA1 projection neurons. *P < 0.05, ***P < 0.001.

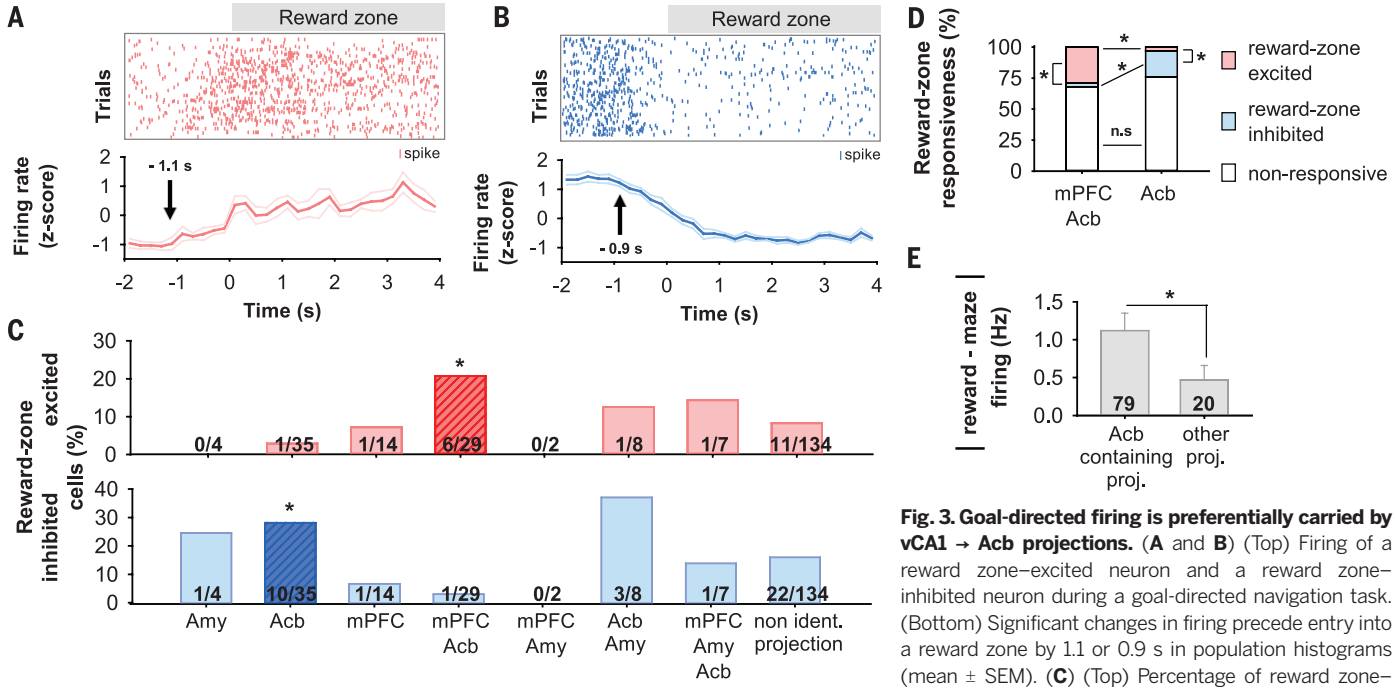

Fig. 3. Goal-directed firing is preferentially carried by vCA1 → Acb projections. (**A** and **B**) (Top) Firing of a reward zone–excited neuron and a reward zone–inhibited neuron during a goal-directed navigation task. (Bottom) Significant changes in firing precede entry into a reward zone by 1.1 or 0.9 s in population histograms (mean ± SEM). (**C**) (Top) Percentage of reward zone–excited and reward zone–inhibited neurons among vCA1 projection types. Neurons projecting to the mPFC and Acb are preferentially enriched in reward zone–excited neurons, whereas vCA1 → Acb projections are preferentially enriched in reward zone–inhibited neurons. (**D**) Proportions of reward zone–excited and reward zone–inhibited neurons among vCA1 → Acb/mPFC and vCA1 → Acb projections. (**E**) Absolute difference (mean ± SEM) of firing in reward zone and maze for neurons with or without projections to the Acb. *P < 0.05, n.s.: not significant.

light (Fig. 1, C and F, and figs. S2 to S4). Spike-collision tests (Fig. 1C, right) and entrainment by 50-Hz photostimulation (Fig. 1D) were also used. In control experiments under anesthesia, local application of D-(-)-2-amino-5-phosphonopentanoic acid (D-AP5, a competitive *N*-methyl-D-aspartate receptor antagonist) and 2,3-dioxo-6-nitro-1,2,3,4-tetrahydrobenzo[*f*]quinoxaline-7-sulfonamide (NBQX, a competitive AMPA receptor antagonist) preserved antidromic but not spontaneous spiking (Fig. 1E and fig. S5), indicating that antidromic spikes are not generated via multisynaptic pathways. The spike waveforms of antidromic and spontaneous spikes recorded during behavior were similar (fig. S6). Using stringent criteria (fig. S7), we identified 99 out of 233 units (42%) as vCA1 projection neurons targeting the Amy, Acb, and/or mPFC.

During recording sessions, naïve rats were placed onto an elevated plus maze with two open and two closed arms. Rats spent less time in and made fewer entries into open arms (more anxiogenic) versus closed arms (less anxiogenic, fig. S8A). We discovered that a subset of vCA1 neurons fired with different frequency whenever the rat was located in open arms as compared to closed arms (Fig. 2, A and B). Their firing rates were positively correlated in open and closed arms but negatively correlated across different types of arm (fig. S8, B and C). When the positions of closed and open arms were exchanged, the neurons maintained their firing respective to anxiety levels (Fig. 2, A and B, and fig. S8D). Using an elevated plus maze/neurophysiological score for such firing patterns (*4*), we found more neurons with anxiety-related firing in vCA1 than in the dorsal CA1 hippocampus (dCA1, Fig. 2C). Using a bootstrap analysis (see supplementary methods and results) and combining for each neuron elevated plus maze scores and axonal projection sites, we observed that the vCA1-to-mPFC projection was selectively enriched with vCA1 anxiety-related neurons (Fig. 2C). Absolute levels of anxiety-related firing were larger in vCA1 neurons projecting to the mPFC than in those targeting the Amy (shared projections to both targets not counted, Fig. 2D). Most cells with anxiety-related firing had higher firing in the open arm (fig. S8E), and elevated plus maze scores of individual neurons correlated with the frequency of visited open/closed arms (fig. S8F).

Next, rats were placed in a large open field (180 × 180 cm) to detect place cells in vCA1. Consistent with the reported lower spatial information content across the septotemporal axis of the hippocampus (*5*, *6*), vCA1 place cells had larger place fields (Fig. 2F and fig. S9) and less spatial tuning and stability than dCA1 place cells (fig. S9). Place cells in vCA1 were less numerous than dCA1 place cells (Fig. 2G); vCA1 anxiety-related neurons had little overlap with place cells (Fig. 2E). We found that vCA1 projections carrying spatial information directly targeted the Amy, Acb, and mPFC, although none of the projection types were significantly enriched with place cells (Fig. 2G).

Next, rats performed a goal-directed navigation with changing rules (fig. S10A). None of the vCA1 projection types were specifically recruited after a rule change. However, we observed that a subset of vCA1 neurons increased firing, whereas another subset decreased firing when animals approached the reward zone (Fig. 3, A and B). Changes in firing rates were progressive, observed across behavioral conditions (fig. S10B), and occurred before the entry into the reward zone, suggesting that these firing patterns were not simply a mere consequence of reward consumption. Firing rates of vCA1 neurons were not correlated with speed or acceleration (fig. S11). Reward zone–excited neurons were preferentially observed among vCA1 double projections targeting the mPFC and Acb, whereas reward zone–inhibited neurons were enriched in vCA1 projections targeting the Acb (Fig. 3, C and D). The firing of vCA1 neurons projecting to the Acb was more strongly modulated during entry into reward zone compared to other projection neurons (Fig. 3E and fig. S12).

We observed that neurons with triple projections targeting the mPFC, Amy, and Acb showed the most prominent behavior-dependent firing during the three tasks altogether and exhibited higher firing during behavioral tasks (Fig. 4A and fig. S13). The higher firing of these cells was also present before task performance (Fig. 4B). We observed that vCA1 triple projections were recruited most during sharp wave/ripples (Fig. 4C), suggesting that vCA1 triple projections contribute chiefly to vCA1-dependent memory consolidation (*7*).

We have shown that specialized projection pathways in vCA1 route behaviorally relevant information to distinct neural networks (Fig. 4D, fig. S14, and table S1). Our application of strict conditions to accept antidromic spike activation and the lack of synaptic inputs to vCA1 from the Acb and mPFC suggest a reliable classification of projection types. Although ChR2 was universally expressed in vCA1 neurons at the recording sites, we cannot exclude the possibility that some projections remained undetected with our method. However, such unaccounted projections could not generate the significant differences between cell groups described here, and any unaccounted-for projections within our data set would have led to an underestimation of observed differences. Also, despite the behavioral control experiments

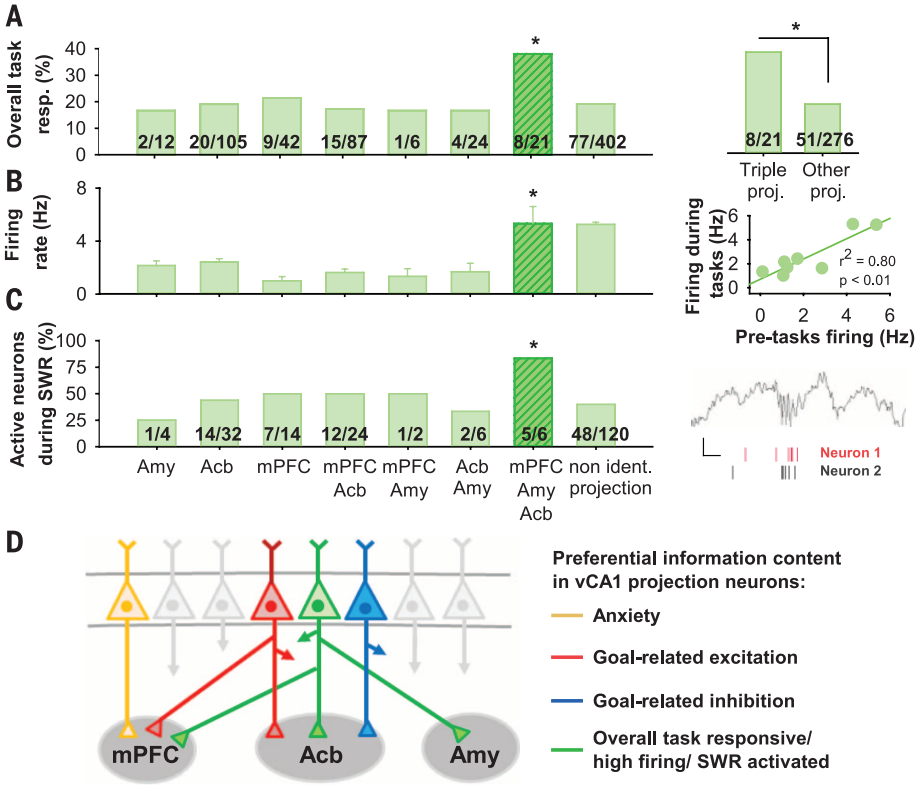

Fig. 4. Preferential recruitment of vCA1 triple projections during behavior and sharp wave/ripples. (**A**) (Left) Higher overall behavioral responsiveness of vCA1 triple projections as compared to chance and (right) to other pooled vCA1 projections. Numbers indicate the ratio of task responses in each group (a neuron responding to three tasks counts 3; for alternative plotting, see fig. S13). (**B**) (Left) Higher firing rates (mean ± SEM) of vCA1 triple projection cells during behavioral tasks (non-identified projections include interneurons). (Right) Pre-task and during-task firing are positively correlated across projection types. (**C**) (Left) Preferential recruitment of triple projections during sharp wave/ripples. SWR, sharp wave/ripples. Numbers indicate the ratio of sharp wave/ripples to active neurons in each group. (Right) Firing of neurons during sharp wave/ripples. Scale bar, 40 ms, 100 μV. (**D**) Schematic showing preferential information content of identified vCA1 projection neurons. *$P < 0.05$.

performed, it can never be fully excluded that the anxiety- and goal-related firing described here may reflect more complex aspects and computations of the vCA1 network.

The mPFC and Amy are involved in anxiety behavior, receiving direct inputs from vCA1 (*2*, *4*, *8*). We demonstrated that anxiety-related activity is preferentially supported by vCA1 → mPFC projections, in agreement with described theta-frequency synchronization between the ventral hippocampus and mPFC during anxiety behavior (*9*). Nevertheless, the Amy could receive anxiety-related signals indirectly and processed them via the mPFC (*10*, *11*). We hypothesize that vCA1 → Amy projections may rather contribute to contextual fear memories (*12*). Our results support a differential contribution of the dorsal and ventral hippocampus to spatial and anxiety behaviors (*1*, *13*–*15*). Neural representations of space and anxiety coexist in vCA1 but are conveyed by distinct vCA1 projection types, which may receive segregated space and anxiety inputs from the Amy (*16*) or entorhinal cortex (*17*, *18*). Alternatively, this segregation could be boosted by local parvalbumin-positive basket cells, which differentially inhibit CA1 projections targeting the Amy or mPFC (*19*). Additionally, projection type–specific plasticity could fine-tune the formation of place or anxiety neurons in vCA1 (*20*–*23*). Context-dependent fear renewal, conditioned place preference, or spatial working memory require spatial information to reach the Amy, Acb, or mPFC, respectively (*24*–*26*). We have demonstrated that place cells among vCA1 projection neurons indiscriminately target these areas and may support spatially driven cognitive processes. The wide-ranging presence of spatial information along the septotemporal axis of the hippocampus may coordinate the expression of interference and generalization, pertaining to mnemonic processes (*27*, *28*).

We found two types of neuronal response among vCA1 projection neurons, with consistent trial-by-trial discharges in anticipation of reward outcomes, which were observed under numerous behavioral conditions, suggesting that this may be a universal phenomenon among subsets of vCA1 projection neurons. Goal-directed firing is conveyed to the Acb and mPFC by distinct vCA1 projections and may tune corticostriatal loops for goal-directed behavior (*29*, *30*).

Our results indicate that higher cortical areas, such as the vCA1, communicate with other brain areas not by transmitting all of their computations equally but by routing the information according to content and recipient.

REFERENCES AND NOTES

1. M. S. Fanselow, H. W. Dong, *Neuron* **65**, 7–19 (2010).
2. L. A. Cenquizca, L. W. Swanson, *Brain Res. Brain Res. Rev.* **56**, 1–26 (2007).
3. J. H. Jennings *et al.*, *Nature* **496**, 224–228 (2013).
4. A. Adhikari, M. A. Topiwala, J. A. Gordon, *Neuron* **71**, 898–910 (2011).
5. M. W. Jung, S. I. Wiener, B. L. McNaughton, *J. Neurosci.* **14**, 7347–7356 (1994).
6. K. B. Kjelstrup *et al.*, *Science* **321**, 140–143 (2008).
7. G. Girardeau, M. Zugaro, *Curr. Opin. Neurobiol.* **21**, 452–459 (2011).
8. K. M. Tye *et al.*, *Nature* **471**, 358–362 (2011).
9. A. Adhikari, M. A. Topiwala, J. A. Gordon, *Neuron* **65**, 257–269 (2010).
10. E. Likhtik, J. M. Stujenske, M. A. Topiwala, A. Z. Harris, J. A. Gordon, *Nat. Neurosci.* **17**, 106–113 (2014).
11. R. P. Vertes, *Synapse* **51**, 32–58 (2004).
12. C. A. Orsini, J. H. Kim, E. Knapska, S. Maren, *J. Neurosci.* **31**, 17269–17277 (2011).
13. S. Royer, A. Sirota, J. Patel, G. Buzsáki, *J. Neurosci.* **30**, 1777–1787 (2010).
14. D. M. Bannerman *et al.*, *Nat. Rev. Neurosci.* **15**, 181–192 (2014).
15. K. G. Kjelstrup *et al.*, *Proc. Natl. Acad. Sci. U.S.A.* **99**, 10825–10830 (2002).
16. A. C. Felix-Ortiz *et al.*, *Neuron* **79**, 658–664 (2013).
17. T. van Groen, P. Miettinen, I. Kadish, *Hippocampus* **13**, 133–149 (2003).
18. S. J. Zhang *et al.*, *Science* **340**, 1232627 (2013).
19. S. H. Lee *et al.*, *Neuron* **82**, 1129–1144 (2014).
20. S. A. Hussaini, K. A. Kempadoo, S. J. Thuault, S. A. Siegelbaum, E. R. Kandel, *Neuron* **72**, 643–653 (2011).
21. C. S. Kim, P. Y. Chang, D. Johnston, *Neuron* **75**, 503–516 (2012).
22. A. Arszovszki, Z. Borhegyi, T. Klausberger, *Front. Neuroanat.* **8**, 53 (2014).
23. A. R. Graves *et al.*, *Neuron* **76**, 776–789 (2012).
24. S. Maren, J. A. Hobin, *Learn. Mem.* **14**, 318–324 (2007).
25. G. D. Carr, N. M. White, *Life Sci.* **33**, 2551–2557 (1983).
26. M. W. Jones, M. A. Wilson, *PLOS Biol.* **3**, e402 (2005).
27. R. W. Komorowski *et al.*, *J. Neurosci.* **33**, 8079–8087 (2013).
28. A. T. Keinath *et al.*, *Hippocampus* **24**, 1533–1548 (2014).
29. J. E. Lisman, A. A. Grace, *Neuron* **46**, 703–713 (2005).
30. S. Ruediger, D. Spirig, F. Donato, P. Caroni, *Nat. Neurosci.* **15**, 1563–1571 (2012).

ACKNOWLEDGMENTS

We thank P. Schönenberger [Institute of Science and Technology (IST), Klosterneuburg, Austria] and S. Wolff (Harvard Medical School, Boston, USA) for helpful discussions on the optogenetic strategy; T. Asenov (IST) for three-dimensional printing of microdrives; R. Tomioka (Kumamoto University, Japan) for help in setting up the behavioral and electrophysiological experiments; E. Borok and R. Hauer for technical help with histology; all the members of the Klausberger lab for insightful discussions; and P. Somogyi, T. Viney, and M. Lagler for commenting on an earlier version of the manuscript. We thank Penn Vector Core from the University of Pennsylvania for the adeno-associated virus (AAV). The use of the AAV is disclosed by an materials transfer agreement between the University of Pennsylvania and the Medical University of Vienna. This work was supported in part by grant 242689 of the European Research Council and grant SCIC03 of the Vienna Science and Technology Fund. The authors declare that the research was conducted in the absence of any commercial or financial relationships that could be construed as a potential conflict of interest. Some of the original data are shown in the supplementary materials; all other data are available upon request from the corresponding authors.

SUPPLEMENTARY MATERIALS

www.sciencemag.org/content/348/6234/560/suppl/DC1
Materials and Methods
Figs. S1 to S14
Table S1
References (*31*–*38*)

18 November 2014; accepted 1 April 2015
10.1126/science.aaa3245

BIOMECHANICS

Mechanistic origins of bombardier beetle (Brachinini) explosion-induced defensive spray pulsation

Eric M. Arndt,[1] Wendy Moore,[2] Wah-Keat Lee,[3] Christine Ortiz[1]*

Bombardier beetles (Brachinini) use a rapid series of discrete explosions inside their pygidial gland reaction chambers to produce a hot, pulsed, quinone-based defensive spray. The mechanism of brachinines' spray pulsation was explored using anatomical studies and direct observation of explosions inside living beetles using synchrotron x-ray imaging. Quantification of the dynamics of vapor inside the reaction chamber indicates that spray pulsation is controlled by specialized, contiguous cuticular structures located at the junction between the reservoir (reactant) and reaction chambers. Kinematics models suggest passive mediation of spray pulsation by mechanical feedback from the explosion, causing displacement of these structures.

When threatened, bombardier beetles (Fig. 1A) expel a hot spray from their pygidial glands (*1*, *2*). The spray contains *p*-benzoquinones (*3*), chemical irritants commonly employed by arthropods (*4*). However, bombardier beetles are unique in using an internal explosive chemical reaction to simultaneously synthesize, heat, and propel their sprays (*2*, *3*). The spray dynamics have been investigated by high-speed photography of the spray, spray impact force measurements, recordings of explosion sounds, and simulations (*5*–*7*). Species in the tribe Brachinini (brachinines) achieve spray temperatures of ~100°C (*2*), with ranges of several centimeters (*1*) and velocities of ~10 m/s via a "biological pulse jet" (*5*), where the spray consists of a rapid succession of pulses formed in discrete explosions. Pulse repetition rates of 368 to 735 Hz were measured from audio recordings for *Stenaptinus insignis* (*5*).

[1]Department of Materials Science and Engineering, Massachusetts Institute of Technology (MIT), Cambridge, MA 02139-4307, USA. [2]Department of Entomology, The University of Arizona, Tucson, AZ 85721-0036, USA. [3]National Synchrotron Light Source II, Brookhaven National Laboratory, Upton, NY 11973-5000, USA.
***Corresponding author. E-mail: cortiz@mit.edu**

performed, it can never be fully excluded that the anxiety- and goal-related firing described here may reflect more complex aspects and computations of the vCA1 network.

The mPFC and Amy are involved in anxiety behavior, receiving direct inputs from vCA1 (*2*, *4*, *8*). We demonstrated that anxiety-related activity is preferentially supported by vCA1 → mPFC projections, in agreement with described theta-frequency synchronization between the ventral hippocampus and mPFC during anxiety behavior (*9*). Nevertheless, the Amy could receive anxiety-related signals indirectly and processed them via the mPFC (*10*, *11*). We hypothesize that vCA1 → Amy projections may rather contribute to contextual fear memories (*12*). Our results support a differential contribution of the dorsal and ventral hippocampus to spatial and anxiety behaviors (*1*, *13*–*15*). Neural representations of space and anxiety coexist in vCA1 but are conveyed by distinct vCA1 projection types, which may receive segregated space and anxiety inputs from the Amy (*16*) or entorhinal cortex (*17*, *18*). Alternatively, this segregation could be boosted by local parvalbumin-positive basket cells, which differentially inhibit CA1 projections targeting the Amy or mPFC (*19*). Additionally, projection type–specific plasticity could fine-tune the formation of place or anxiety neurons in vCA1 (*20*–*23*). Context-dependent fear renewal, conditioned place preference, or spatial working memory require spatial information to reach the Amy, Acb, or mPFC, respectively (*24*–*26*). We have demonstrated that place cells among vCA1 projection neurons indiscriminately target these areas and may support spatially driven cognitive processes. The wide-ranging presence of spatial information along the septotemporal axis of the hippocampus may coordinate the expression of interference and generalization, pertaining to mnemonic processes (*27*, *28*).

We found two types of neuronal response among vCA1 projection neurons, with consistent trial-by-trial discharges in anticipation of reward outcomes, which were observed under numerous behavioral conditions, suggesting that this may be a universal phenomenon among subsets of vCA1 projection neurons. Goal-directed firing is conveyed to the Acb and mPFC by distinct vCA1 projections and may tune corticostriatal loops for goal-directed behavior (*29*, *30*).

Our results indicate that higher cortical areas, such as the vCA1, communicate with other brain areas not by transmitting all of their computations equally but by routing the information according to content and recipient.

REFERENCES AND NOTES

1. M. S. Fanselow, H. W. Dong, *Neuron* **65**, 7–19 (2010).
2. L. A. Cenquizca, L. W. Swanson, *Brain Res. Brain Res. Rev.* **56**, 1–26 (2007).
3. J. H. Jennings *et al.*, *Nature* **496**, 224–228 (2013).
4. A. Adhikari, M. A. Topiwala, J. A. Gordon, *Neuron* **71**, 898–910 (2011).
5. M. W. Jung, S. I. Wiener, B. L. McNaughton, *J. Neurosci.* **14**, 7347–7356 (1994).
6. K. B. Kjelstrup *et al.*, *Science* **321**, 140–143 (2008).
7. G. Girardeau, M. Zugaro, *Curr. Opin. Neurobiol.* **21**, 452–459 (2011).
8. K. M. Tye *et al.*, *Nature* **471**, 358–362 (2011).
9. A. Adhikari, M. A. Topiwala, J. A. Gordon, *Neuron* **65**, 257–269 (2010).
10. E. Likhtik, J. M. Stujenske, M. A. Topiwala, A. Z. Harris, J. A. Gordon, *Nat. Neurosci.* **17**, 106–113 (2014).
11. R. P. Vertes, *Synapse* **51**, 32–58 (2004).
12. C. A. Orsini, J. H. Kim, E. Knapska, S. Maren, *J. Neurosci.* **31**, 17269–17277 (2011).
13. S. Royer, A. Sirota, J. Patel, G. Buzsáki, *J. Neurosci.* **30**, 1777–1787 (2010).
14. D. M. Bannerman *et al.*, *Nat. Rev. Neurosci.* **15**, 181–192 (2014).
15. K. G. Kjelstrup *et al.*, *Proc. Natl. Acad. Sci. U.S.A.* **99**, 10825–10830 (2002).
16. A. C. Felix-Ortiz *et al.*, *Neuron* **79**, 658–664 (2013).
17. T. van Groen, P. Miettinen, I. Kadish, *Hippocampus* **13**, 133–149 (2003).
18. S. J. Zhang *et al.*, *Science* **340**, 1232627 (2013).
19. S. H. Lee *et al.*, *Neuron* **82**, 1129–1144 (2014).
20. S. A. Hussaini, K. A. Kempadoo, S. J. Thuault, S. A. Siegelbaum, E. R. Kandel, *Neuron* **72**, 643–653 (2011).
21. C. S. Kim, P. Y. Chang, D. Johnston, *Neuron* **75**, 503–516 (2012).
22. A. Arszovszki, Z. Borhegyi, T. Klausberger, *Front. Neuroanat.* **8**, 53 (2014).
23. A. R. Graves *et al.*, *Neuron* **76**, 776–789 (2012).
24. S. Maren, J. A. Hobin, *Learn. Mem.* **14**, 318–324 (2007).
25. G. D. Carr, N. M. White, *Life Sci.* **33**, 2551–2557 (1983).
26. M. W. Jones, M. A. Wilson, *PLOS Biol.* **3**, e402 (2005).
27. R. W. Komorowski *et al.*, *J. Neurosci.* **33**, 8079–8087 (2013).
28. A. T. Keinath *et al.*, *Hippocampus* **24**, 1533–1548 (2014).
29. J. E. Lisman, A. A. Grace, *Neuron* **46**, 703–713 (2005).
30. S. Ruediger, D. Spirig, F. Donato, P. Caroni, *Nat. Neurosci.* **15**, 1563–1571 (2012).

ACKNOWLEDGMENTS

We thank P. Schönenberger [Institute of Science and Technology (IST), Klosterneuburg, Austria] and S. Wolff (Harvard Medical School, Boston, USA) for helpful discussions on the optogenetic strategy; T. Asenov (IST) for three-dimensional printing of microdrives; R. Tomioka (Kumamoto University, Japan) for help in setting up the behavioral and electrophysiological experiments; E. Borok and R. Hauer for technical help with histology; all the members of the Klausberger lab for insightful discussions; and P. Somogyi, T. Viney, and M. Lagler for commenting on an earlier version of the manuscript. We thank Penn Vector Core from the University of Pennsylvania for the adeno-associated virus (AAV). The use of the AAV is disclosed by an materials transfer agreement between the University of Pennsylvania and the Medical University of Vienna. This work was supported in part by grant 242689 of the European Research Council and grant SCIC03 of the Vienna Science and Technology Fund. The authors declare that the research was conducted in the absence of any commercial or financial relationships that could be construed as a potential conflict of interest. Some of the original data are shown in the supplementary materials; all other data are available upon request from the corresponding authors.

SUPPLEMENTARY MATERIALS

www.sciencemag.org/content/348/6234/560/suppl/DC1
Materials and Methods
Figs. S1 to S14
Table S1
References (*31*–*38*)

18 November 2014; accepted 1 April 2015
10.1126/science.aaa3245

BIOMECHANICS

Mechanistic origins of bombardier beetle (Brachinini) explosion-induced defensive spray pulsation

Eric M. Arndt,[1] Wendy Moore,[2] Wah-Keat Lee,[3] Christine Ortiz[1]*

Bombardier beetles (Brachinini) use a rapid series of discrete explosions inside their pygidial gland reaction chambers to produce a hot, pulsed, quinone-based defensive spray. The mechanism of brachinines' spray pulsation was explored using anatomical studies and direct observation of explosions inside living beetles using synchrotron x-ray imaging. Quantification of the dynamics of vapor inside the reaction chamber indicates that spray pulsation is controlled by specialized, contiguous cuticular structures located at the junction between the reservoir (reactant) and reaction chambers. Kinematics models suggest passive mediation of spray pulsation by mechanical feedback from the explosion, causing displacement of these structures.

When threatened, bombardier beetles (Fig. 1A) expel a hot spray from their pygidial glands (*1*, *2*). The spray contains *p*-benzoquinones (*3*), chemical irritants commonly employed by arthropods (*4*). However, bombardier beetles are unique in using an internal explosive chemical reaction to simultaneously synthesize, heat, and propel their sprays (*2*, *3*). The spray dynamics have been investigated by high-speed photography of the spray, spray impact force measurements, recordings of explosion sounds, and simulations (*5*–*7*). Species in the tribe Brachinini (brachinines) achieve spray temperatures of ~100°C (*2*), with ranges of several centimeters (*1*) and velocities of ~10 m/s via a "biological pulse jet" (*5*), where the spray consists of a rapid succession of pulses formed in discrete explosions. Pulse repetition rates of 368 to 735 Hz were measured from audio recordings for *Stenaptinus insignis* (*5*).

[1]Department of Materials Science and Engineering, Massachusetts Institute of Technology (MIT), Cambridge, MA 02139-4307, USA. [2]Department of Entomology, The University of Arizona, Tucson, AZ 85721-0036, USA. [3]National Synchrotron Light Source II, Brookhaven National Laboratory, Upton, NY 11973-5000, USA.
***Corresponding author. E-mail: cortiz@mit.edu**

Downloaded from www.sciencemag.org on April 30, 2015

It is well known that brachinines' ability to produce internal explosions is facilitated by the two-chambered construction of their pygidial glands (*3*) (Fig. 1, B to E). Each of the beetle's two pygidial glands comprises a reservoir chamber (RSC), reaction chamber (RXC), and exit channel (EC), which vents near the abdomen tip (Fig. 1B). The distal ends of the exit channels curve dorsally to form reflector plates (Fig. 1B, RP) used for spray aiming (*8*). An interchamber valve (Fig. 1, D and E, ICV) is contiguous with the walls of the reaction and reservoir chambers and separates the chambers' contents when closed (*2*). The pygidial glands are constructed of cuticle, a composite of chitin, proteins, and waxes (*9*) that protects the beetle from the toxic chemicals, high temperatures, and high pressures during explosions. The muscle-enveloped, flexible reservoir chamber (*5*) stores an aqueous reactant solution of ~25% hydrogen peroxide and ~10% *p*-hydroquinones (*3*), along with ~10% alkanes as a nonreactive second liquid phase (*10*). Valve muscles (Fig. 1D, VM) span between the valve and the reservoir chamber to facilitate valve opening. During spray emission, reactant solution flows from the reservoir chamber into the reaction chamber, where it reacts with a solution of peroxidase and catalase enzymes (*11*) to form *p*-benzoquinones and explosively liberate oxygen gas, water vapor, and heat, propelling a hot, noxious spray out the exit channel.

The mechanism of brachinines' spray pulsation has not been understood because previous studies, relying on external observations, have not probed internal dynamics. Here, we investigate this open question through optical and scanning electron microscopy to obtain new insights into the pygidial gland anatomy and synchrotron x-ray imaging (*12*–*16*) at up to 2000 frames per second (fps) to directly observe the internal dynamics of spray pulsation in live beetles (*Brachinus elongatulus*) (*17*). These experiments provide an understanding of how explosions are initiated inside the pygidial glands and allow identification of the specific gland structures that mediate spray pulsation. An understanding of how brachinine pygidial glands produce (and survive) repetitive explosions could provide new design principles for technologies such as blast mitigation and propulsion.

Optical microscopy reveals that the reaction chamber exhibits dramatic spatial heterogeneity in cuticle sclerotization (Fig. 1C), corresponding to regions with different flexibility/rigidity (*18*) and, presumably, functional importance. The cuticle of most of the reaction chamber is tan or brown, implying heavy sclerotization and therefore high stiffness, which would serve to limit wall deflection and protect the beetle's internal tissues from the explosions. However, several regions are colorless (stained blue in Fig. 1, B and C, to increase contrast) and, hence, lightly sclerotized and compliant. These regions include the reaction

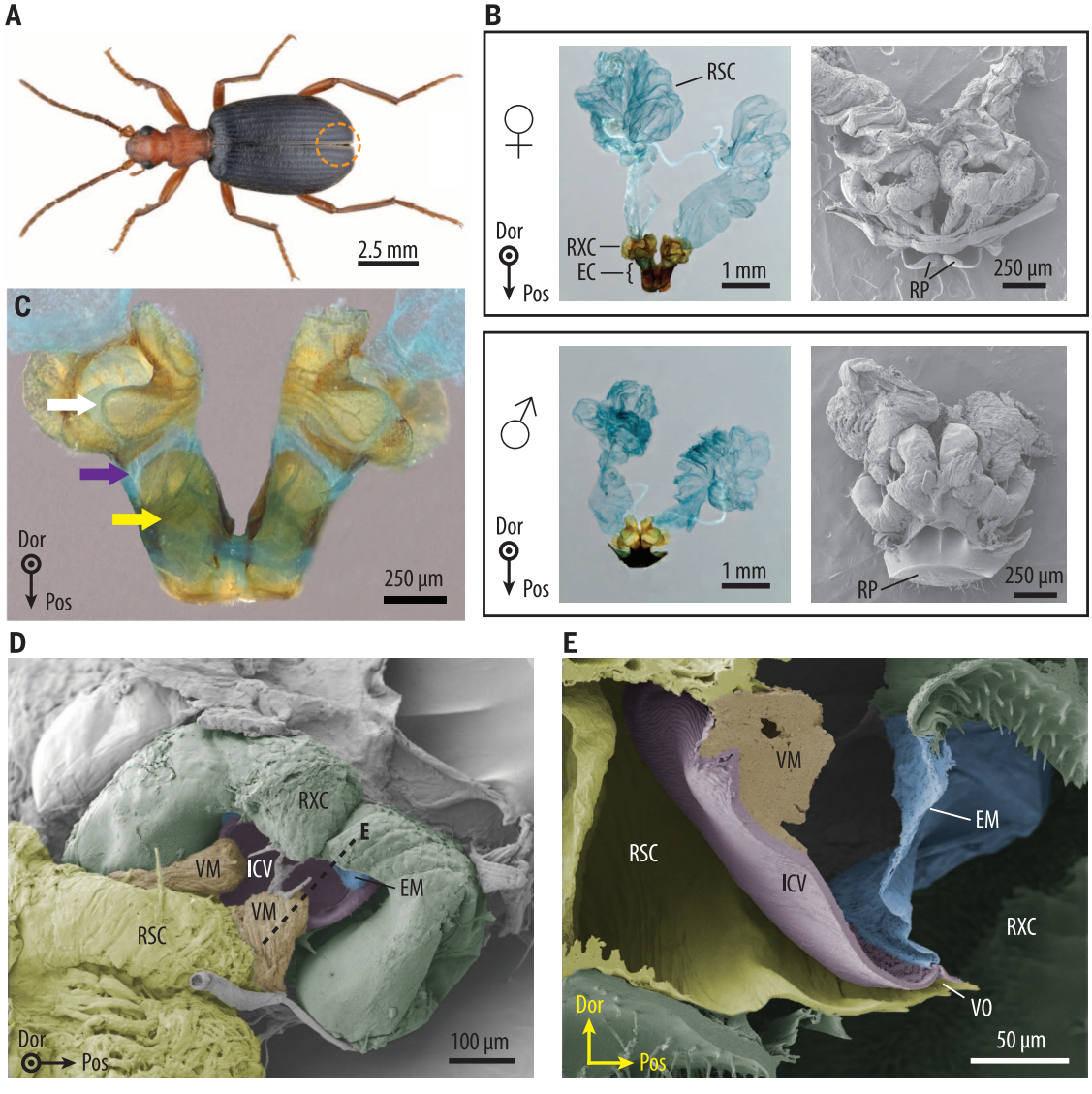

Fig. 1. *Brachinus elongatulus* pygidial gland morphology. (**A**) Dorsal view. Dashed circle indicates location of pygidial glands. (**B**) Female (top) and male (bottom) pygidial glands: optical micrographs, chlorazol black staining (left) and SEM (right). Features are indicated: reservoir chamber (RSC), reaction chamber (RXC), exit channel (EC), and reflector plate (RP). (**C**) Female pygidial glands stained as in (B) showing rigid (highly sclerotized, brown/tan) and flexible (lightly sclerotized, stained blue) regions. Lightly sclerotized regions are identified: reaction chamber midline crease (white arrow); junction between reaction chamber and exit channel (purple arrow); exit channel dorsal membrane (yellow arrow). (**D**) False-color SEM showing valve muscles (VM), interchamber valve (ICV), and expansion membrane (EM). Other features labeled as in (B). Cross section shown in (E) is approximately normal to dashed line. (**E**) False-color SEM of cross section through interchamber region. The interchamber valve is observed in a closed conformation. Labels and colorization correspond to (D), with additional indication for the valve opening (VO).

chamber's dorsal midline crease and the junction between the reaction chamber and the exit channel (Fig. 1C). Similarly, the dorsal part of the exit channel is membranous and lightly sclerotized, whereas the ventral part is thick and heavily sclerotized (Fig. 1C) (*6*). Scanning electron microscopy (SEM) of the interchamber region in cross section (Fig. 1E) reveals that the cuticle that connects the valve to the dorsal part of the reaction chamber [hereafter called the expansion membrane (EM)] is very thin (~200 nm) and wrinkled, suggesting high flexibility.

Vapor formation during each explosion is clearly seen in the x-ray video as a bright region within the reaction chamber (Fig. 2A and movie S1). In the first pulse, vapor forms in the reaction chamber and propagates toward the exit channel. With each subsequent pulse, the vapor pocket initially expands slightly within the reaction chamber (implied by increased area) and then quickly contracts slightly as gas is ejected (Fig. 2A, first five pulses shown). Average pulsation rates calculated for 35 instances of gland activity from 18 sprays (median number of explosions, 13; range, 2 to 46) ranged from 341 to 976 Hz (median, 667 Hz; mean ± SD, 698 ± 146 Hz) (fig. S1 and table S2). A linear fit to active time versus number of pulses predicts a pulsation rate of 650 Hz (R^2 = 0.88). These results are consistent with external experimental measurements of *S. insignis* (*5*) and approach the maximum rates reported for cyclic insect motions such as wing beats, measured as high as 1000 Hz for midges (*19*).

Each explosion corresponds to the injection of a reactant droplet into the reaction chamber, which can sometimes be seen as a dark circle in relief against bright vapor (Fig. 2B and movie S2). Maximum diameters measured 208 ± 7 μm (mean ± SD) for four clearly visualized droplets. Assuming sphericity, the droplet volume is calculated to be 4.7 ± 0.5 nL, and the mass is estimated as 5.5 ± 0.6 μg. Based on the theoretical heat of reaction of 0.8 J/mg (*2*), the estimated energy release for each explosion is 4×10^{-3} J, and this energy liberates heat, boils water, and to a lesser extent provides the kinetic energy of the spray pulse. Estimating the spray pulse mass as equivalent to the droplet mass and taking 10 m/s for the spray exit velocity (*5*), the kinetic energy of a spray pulse is calculated to be 3×10^{-7} J. Equating this energy to work done by pressure, the average overpressure in the reaction chamber is estimated as 20 kPa, producing wall tensile stresses of ~1 MPa. For comparison, cuticle tensile strengths are typically tens to hundreds of megapascals (*20*). The time required to expel a pulse is estimated as 0.1 ms from the spray velocity and gland dimensions, consistent with the fact that explosions typically occur within single 2000-fps video frames (0.5 ms).

During each explosion, vapor is observed to fill a convex region between the reservoir and reaction chambers (Fig. 2A) that exceeds the dimensions of the reaction chamber indicated by microscopy (fig. S2), suggesting outward displacement of the expansion membrane driven by the explosion overpressure. Using the convex vapor shape as a proxy, the stretched expansion membrane can be modeled as a hemi-ellipsoid (fig. S2), and its maximum extension is found to be ~280% (see the supplementary text). For comparison, some insect cuticles exhibit recoverable extensions of 1000% (*21*). Based on the estimated overpressure and the estimated mass of the hemolymph displaced as the expansion membrane displaces into the body cavity, the expansion occurs with a maximum velocity of 6 m/s, attaining maximum displacement in 0.06 ms (supplementary text), consistent with the observation that expansion occurs within one video frame (0.5 ms). About one video frame after expansion is observed, the explosion reaction stops and vapor in the interchamber region contracts (e.g., Fig. 2A, frame 16), implying that the expansion membrane has returned to its unexpanded shape.

The exit channel of an active gland remains vapor-filled, and therefore open, throughout the entire pulse cycle (Fig. 2A and movies S1 to S3), possibly due to shape or mechanical characteristics (e.g., viscoelasticity) of its dorsal membrane, indicating that control of spray pulsation is accomplished by the reaction chamber inlet structures alone through opening and closing of the interchamber valve, as hypothesized previously (*5*). Typical cyclic mechanisms in insects (e.g., flapping flight and tymbal sound production) use multiple muscle sets that alternately contract or cuticular structures serving as springs (*22*), whereas the bombardier beetle possesses only valve-opening muscles and the valve is contiguous with flexible structures on all sides (i.e., reservoir chamber and expansion membrane). Hence, valve closure during each pulse cycle likely occurs passively due to mechanical feedback from the explosion, such as dynamic pressure from fluid (hemolymph) displaced by the expansion membrane, or impingement of the pressurized expansion membrane directly onto the valve, or a

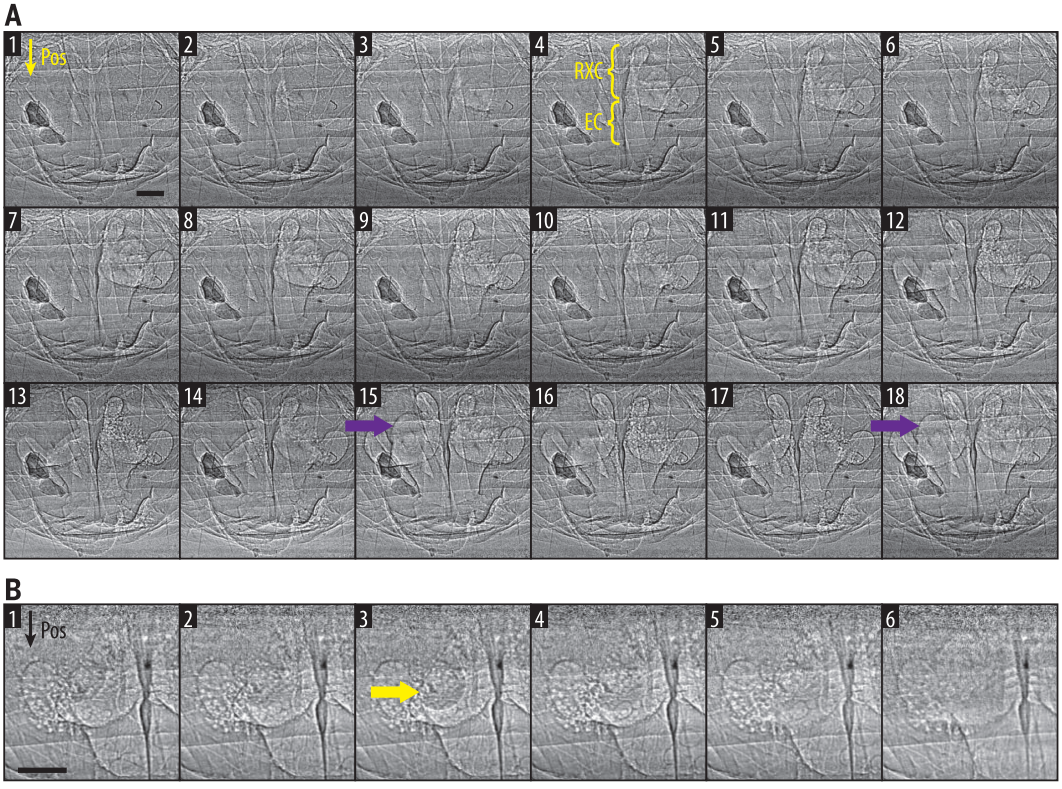

Fig. 2. Internal dynamics revealed by x-ray imaging. (**A**) First five pulses of a spray; successive frames from 2000-fps video of a male beetle. Scale bar is 200 μm. Location of right reaction chamber (RXC) and exit channel (EC) indicated in frame 4. Right and left exit channels are open starting in frames 4 and 11, respectively. Arrows indicate dramatic displacement of the expansion membrane. Dark objects at left are external debris. (**B**) Reactant droplet (arrow) entering reaction chamber and exploding; successive frames from 2000-fps video of a male beetle. Scale bar is 200 μm.

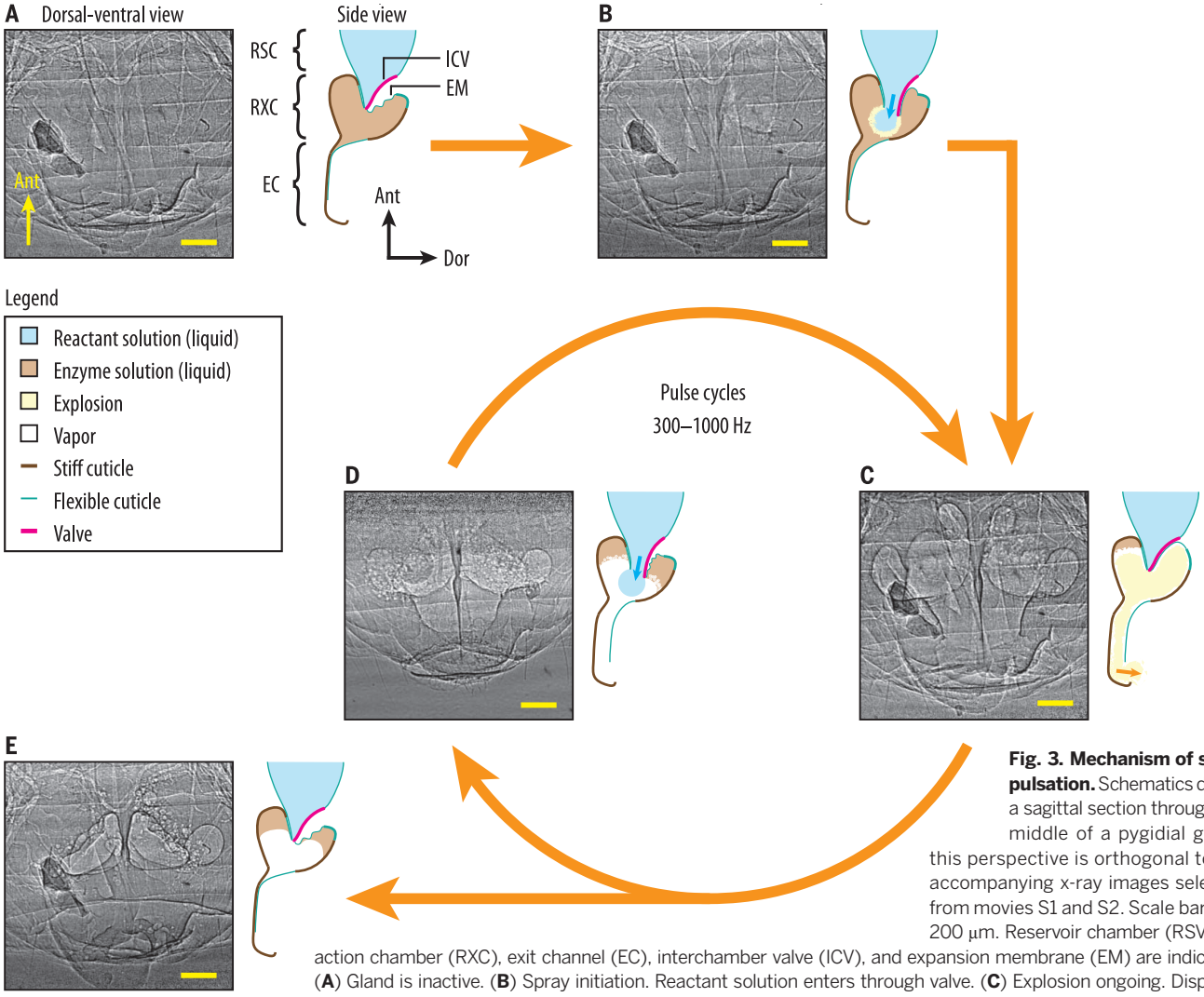

Fig. 3. Mechanism of spray pulsation. Schematics depict a sagittal section through the middle of a pygidial gland; this perspective is orthogonal to the accompanying x-ray images selected from movies S1 and S2. Scale bars are 200 μm. Reservoir chamber (RSV), reaction chamber (RXC), exit channel (EC), interchamber valve (ICV), and expansion membrane (EM) are indicated. (**A**) Gland is inactive. (**B**) Spray initiation. Reactant solution enters through valve. (**C**) Explosion ongoing. Displacement of expansion membrane closes the valve. A spray pulse is ejected. (**D**) Explosion ceases. Expansion membrane relaxes and valve reopens, permitting fresh reactant solution to enter. The process repeats C-D-C-D-C-D, and so on, with each "C-D" corresponding to one pulse cycle. (**E**) Spraying concluded. The exit channel closes and a vapor pocket remains in the reaction chamber.

combination of both. Simple kinematics models of these scenarios incorporating valve dimensions, the vapor expansion profile, and estimated overpressure discussed above predict forces that are sufficient to close the valve (supplementary online text).

Once the spray pulse is released and the overpressure in the reaction chamber drops, the load on the valve is removed, allowing it to reopen and permit a fresh reactant droplet to enter. It is not known whether the valve-opening muscles contract continually for the duration of spraying or once per pulse cycle, but both scenarios are compatible with passive valve closure and the capabilities of insect muscles (*19*).

The data presented suggest the following mechanism for spray pulsation (Fig. 3): The reservoir chamber musculature contracts for the duration of spraying to apply a continuous pressure to the reactant solution, and the valve muscles also contract, opening the interchamber valve and forcing a reactant droplet into the reaction chamber (Fig. 3B). The droplet explodes upon contacting the reaction chamber enzymes (Fig. 3C), producing high-pressure vapor that propels a spray pulse out of the exit channel. Explosion overpressure displaces the expansion membrane and closes the interchamber valve, thereby interrupting the flow of reactants. After the explosion, the pressure in the reaction chamber decreases, the expansion membrane relaxes, the valve reopens, and a fresh reactant droplet enters, starting a new pulse cycle (Fig. 3D). Eventually, the reservoir and valve muscles relax, causing spraying to cease. The exit channel's dorsal membrane relaxes and collapses into its ventral trough, and some quantity of vapor generally remains in the reaction chamber as a pocket surrounded by numerous bubbles (Fig. 3E).

The pulsed spray mechanism of brachinine bombardier beetles is remarkably elegant and effective, protecting these beetles from nearly all predators (and incautious humans). The passive mediation of pulsation by mechanical feedback from the explosion is advantageous because it provides automatic regulation of reactant use. Further, the evolutionary change from a continuous defensive spray (exhibited by close relatives of the brachinines) to a pulsed spray required only relatively minor changes to the reaction chamber inlet structures rather than the evolution of novel valve-closing muscles.

REFERENCES AND NOTES

1. T. Eisner, *J. Insect Physiol.* **2**, 215–220 (1958).
2. D. J. Aneshansley, T. Eisner, J. M. Widom, B. Widom, *Science* **165**, 61–63 (1969).
3. H. Schildknecht, K. Holoubek, K. H. Weis, H. Krämer, *Angew. Chem. Int. Ed. Engl.* **3**, 73–82 (1964).
4. M. S. Blum, *Chemical Defenses of Arthropods* (Academic Press, New York, 1981).
5. J. Dean, D. J. Aneshansley, H. E. Edgerton, T. Eisner, *Science* **248**, 1219–1221 (1990).
6. N. Beheshti, A. C. Mcintosh, *Bioinspir. Biomim.* **2**, 57–64 (2007).
7. A. James, K. Morison, S. Todd, *J. R. Soc. Interface* **10**, 20120801 (2013).
8. T. Eisner, D. J. Aneshansley, *Proc. Natl. Acad. Sci. U.S.A.* **96**, 9705–9709 (1999).
9. S. O. Andersen, *Annu. Rev. Entomol.* **24**, 29–59 (1979).

10. T. Eisner *et al.*, *J. Insect Physiol.* **23**, 1383–1386 (1977).
11. H. Schildknecht, *Angew. Chem. Int. Ed. Engl.* **9**, 1–9 (1970).
12. M. W. Westneat *et al.*, *Science* **299**, 558–560 (2003).
13. J. J. Socha, M. W. Westneat, J. F. Harrison, J. S. Waters, W.-K. Lee, *BMC Biol.* **5**, 6 (2007).
14. J. J. Socha *et al.*, *J. Exp. Biol.* **211**, 3409–3420 (2008).
15. M. W. Westneat, J. J. Socha, W.-K. Lee, *Annu. Rev. Physiol.* **70**, 119–142 (2008).
16. W.-K. Lee, J. J. Socha, *BMC Physiol.* **9**, 2 (2009).
17. Materials and methods are available as supplementary materials on *Science* Online.
18. J. F. V. Vincent, J. E. Hillerton, *J. Insect Physiol.* **25**, 653–658 (1979).
19. O. Sotavalta, *Biol. Bull.* **104**, 439–444 (1953).
20. J. F. V. Vincent, U. G. K. Wegst, *Arthropod Struct. Dev.* **33**, 187–199 (2004).
21. J. F. V. Vincent, *Proc. R. Soc. London Ser. A* **188**, 189–201 (1975).
22. R. F. Chapman, *The Insects: Structure and Function* (Cambridge Univ. Press, Cambridge, ed. 5, 1998).

ACKNOWLEDGMENTS

Use of the Advanced Photon Source was supported by the U.S. Department of Energy, Office of Science, Office of Basic Energy Sciences, under contract DE-AC02-06CH11357. This work was supported in part by the U.S. Army Research Laboratory and the U.S. Army Research Office through the MIT Institute of Soldier Nanotechnologies under contract W911NF-13-D-0001 and in part by the National Science Foundation through the MIT Center for Materials Science and Engineering under contract DMR-08-19762. This research was funded in part by the U.S. Department of Defense, Office of the Director, Defense Research and Engineering, through the National Security Science and Engineering Faculty Fellowship awarded to C.O. under contract N00244-09-1-0064; in part by the National Science Foundation through funding awarded to W.M. under contract DEB-0908187; and in part by the U.S. Department of Energy, Office of Science, Office of Basic Energy Sciences, under contract DE-SC0012704. Experiment data are available for download from DSpace@MIT (https://dspace.mit.edu); please cite this collection using the handle hdl.handle.net/1721.1/96123.

SUPPLEMENTARY MATERIALS

www.sciencemag.org/content/348/6234/563/suppl/DC1
Materials and Methods
Supplementary Text
Figs. S1 to S3
Tables S1 and S2
Movies S1 to S3
References (*23*–*32*)

12 September 2014; accepted 16 March 2015
10.1126/science.1261166

EXTINCTIONS

Paleontological baselines for evaluating extinction risk in the modern oceans

Seth Finnegan,[1]*† Sean C. Anderson,[2]† Paul G. Harnik,[3]† Carl Simpson,[4] Derek P. Tittensor,[5,6,7] Jarrett E. Byrnes,[8] Zoe V. Finkel,[9] David R. Lindberg,[1] Lee Hsiang Liow,[10] Rowan Lockwood,[11] Heike K. Lotze,[7] Craig R. McClain,[12] Jenny L. McGuire,[13] Aaron O'Dea,[14] John M. Pandolfi[15]

Marine taxa are threatened by anthropogenic impacts, but knowledge of their extinction vulnerabilities is limited. The fossil record provides rich information on past extinctions that can help predict biotic responses. We show that over 23 million years, taxonomic membership and geographic range size consistently explain a large proportion of extinction risk variation in six major taxonomic groups. We assess intrinsic risk—extinction risk predicted by paleontologically calibrated models—for modern genera in these groups. Mapping the geographic distribution of these genera identifies coastal biogeographic provinces where fauna with high intrinsic risk are strongly affected by human activity or climate change. Such regions are disproportionately in the tropics, raising the possibility that these ecosystems may be particularly vulnerable to future extinctions. Intrinsic risk provides a prehuman baseline for considering current threats to marine biodiversity.

Overfishing, habitat loss, pollution, climate change, and ocean acidification (*1*–*4*) pose intensifying threats to marine ecosystems, leading to concerns that a wave of marine extinctions may be imminent (*5*–*10*). In contrast to the terrestrial realm (*11*–*13*), little is known about the distribution of extinction vulnerability among marine taxa. Formal threat assessments have been conducted for a small and taxonomically biased subset of marine species (*5*, *9*). These assessments are based primarily on the current distribution of species and their exposure to modern threats (*14*–*17*), but longer-term baseline data are a key component of any forecasting effort (*18*, *19*). Knowledge of past extinction patterns is critical for predicting the factors that will determine future extinction vulnerability.

This knowledge can only come from the fossil record. Historical records are fragmentary for the marine realm, and few extinctions have been directly documented (*5*, *20*). However, thick sequences of fossil-rich marine sediments are widespread on all continents (*21*, *22*) and chronicle the waxing, waning, and extinction of taxa within many ecologically important groups. The environmental drivers of current and future extinctions may differ from those of the past (*5*), but the considerable variation in rates and drivers of extinction over geological time scales (10^5 to 10^7 years) (*5*) provides an opportunity to determine whether there are predictors of extinction vulnerability that have remained consistent despite this variation. Such predictors can complement current risk assessments by identifying taxa that we expect to be especially vulnerable to extinction, given the macroevolutionary histories of taxa with similar characteristics. Here we construct models of extinction risk—defined as the probability of a fossil taxon being classified as extinct on the basis of its similarity to other fossil taxa that went extinct over the same interval of time—and use these models to evaluate the baseline extinction vulnerabilities of extant marine taxa. We use the term "intrinsic risk" to refer to paleontologically calibrated estimates of baseline vulnerability for modern taxa.

We base our intrinsic risk evaluation on analyses of observed extinctions over the past 23 million years (Neogene-Pleistocene). We chose this interval to maximize faunal and geographic comparability between the modern and fossil data sets. The Neogene-Pleistocene fossil record is dominated by groups that are still extant and diverse, with continental configurations relatively similar to those of the present day. This interval also encompasses multiple extinction pulses and major changes in climatic and oceanographic conditions (e.g., contraction of the tropics, glacial-interglacial cycles, and associated changes in sea surface temperature and sea level) and is thus ideal for evaluating the consistency of extinction risk predictors. Using the Paleobiology Database (*23*), we analyzed Neogene-Pleistocene extinctions in six major marine taxonomic groups (bivalves, gastropods, echinoids, sharks, mammals, and scleractinian corals) for a total of 2897 fossil genera (table S1). We focused on these groups because they are generally well preserved in the fossil record (fig. S1) and are comparatively well sampled in modern coastal environments. Furthermore, these groups include several speciose

[1]Department of Integrative Biology, University of California, Berkeley, CA 94720, USA. [2]Department of Biological Sciences, Simon Fraser University, Burnaby, British Columbia V5A 1S6, Canada. [3]Department of Earth and Environment, Franklin and Marshall College, Lancaster, PA 17604, USA. [4]Department of Paleobiology, National Museum of Natural History, Washington, DC 20013, USA. [5]United Nations Environment Programme World Conservation Monitoring Centre, Cambridge CB3 0DL, UK. [6]Computational Science Laboratory, Microsoft Research, Cambridge CB1 2FB, UK. [7]Department of Biology, Dalhousie University, Halifax, Nova Scotia B3H 4R2, Canada. [8]Department of Biology, University of Massachusetts, Boston, MA 02125, USA. [9]Environmental Science Program, Mount Allison University, Sackville, New Brunswick E4L 1A5, Canada. [10]Center for Ecological and Evolutionary Synthesis, Department of Biosciences, University of Oslo, Blindern, N-0316 Oslo, Norway. [11]Department of Geology, College of William and Mary, Williamsburg, VA 23187, USA. [12]National Evolutionary Synthesis Center, Durham, NC 27705, USA. [13]School of Environmental and Forest Sciences, University of Washington, Seattle, WA 98195, USA. [14]Smithsonian Tropical Research Institute, 0843-03092, Balboa, Republic of Panamá. [15]Australian Research Council Centre of Excellence for Coral Reef Studies, School of Biological Sciences, University of Queensland, St. Lucia, QLD 4072, Australia. ***Corresponding author. E-mail: sethf@berkeley.edu** †These authors contributed equally to this work.

clades that exhibit well-known global marine biodiversity gradients and collectively represent a broad sample of marine ecological, phylogenetic, and functional diversity (*24*, *25*).

Geographic range size (*26*, *27*) and taxonomic identity (*27*, *28*) are some of the most consistent predictors of extinction risk in the marine fossil record—the former presumably because wide-ranging taxa are less susceptible to habitat loss and local disturbances, and the latter because many traits that influence extinction risk are correlated with phylogeny (*29*). We therefore evaluated seven metrics of geographic distribution and occurrence frequency [Fig. 1 and table S2 (*30*)] as potential predictors of extinction risk for fossil genera in four Neogene-Pleistocene subintervals (Early Miocene, Middle Miocene, Late Miocene, Plio-Pleistocene). Ideally, risk would be assessed for species, but species durations and geographic ranges in the fossil record are often poorly known. Hence, in keeping with many previous paleobiological analyses, we analyzed genera and included the number of species per genus as a potential extinction predictor [Fig. 1 (*30*)]. Strong positive correlations between fossil and modern predictor values for the 1163 genera that are sampled in both the Plio-Pleistocene fossil record and modern biogeographic databases suggest that relative differences among genera in these characteristics are not systematically distorted by the vagaries of fossil preservation [fig. S2 (*30*)]. To represent taxonomic identity and its correlates, we included membership in taxonomic subgroups of ordinal to familial rank as predictors [Fig. 1 (*30*)].

We used generalized boosted regression models (GBMs), which perform well when relationships between predictor and response variables are nonlinear (*31*), to evaluate extinction risk in each Neogene-Pleistocene subinterval (*30*). All subinterval models performed significantly better than chance (AUC = 0.71 to 0.82) when predicting one-third of the data that were withheld when building test models (fig. S3). A model built on the entire Neogene-Pleistocene data set correctly identified genera that went extinct as having higher risk than those that survived in 87% (±1%) of cases (table S3) (*30*). Partial dependence plots show that many extinction risk patterns are common to all subintervals (Fig. 1). Geographic range size (great circle distance) and especially taxonomic group have a strong influence on extinction risk in all subintervals (Fig. 1 and fig. S4). The consistency of between-group differences throughout the Neogene-Pleistocene interval implies that important extinction risk factors are phylogenetically conserved (*29*). An alternative hypothesis, that between-group extinction risk differences reflect differences in preservation potential, is not supported (fig. S5).

We further evaluated the consistency of extinction risk patterns across geological time by comparing the extinction risk of a genus estimated by a model calibrated on the subinterval in which it was sampled to the extinction risk of the same genus estimated by a model calibrated on a different subinterval (fig. S6). Spearman rank-order correlations of genus extinction risk estimates for the 12 comparisons range from 0.70 to 0.79 (all $P < 0.001$, fig. S6). Thus, all subinterval-specific models yield similar and strongly correlated genus risk predictions despite subinterval-to-subinterval variation in the environmental drivers of extinction and in the sampling of the fossil record.

The consistency of extinction risk patterns through more than 23 million years suggests that the fossil record can provide meaningful constraints on the distribution of intrinsic risk across modern marine genera. We therefore measured the same predictors that were included in the paleontological models (Fig. 1) for 2615 extant marine genera belonging to the same six taxonomic groups that are recorded either in the OBIS database (*32*) or in species range maps (*33*, *34*) [fig. S7 and table S1 (*30*)]. Before calculating geographic range predictors, we smoothed sampling heterogeneity across regions using a minimum bounding box procedure (*35*) to interpolate genus occurrences within 12 coastal biogeographic

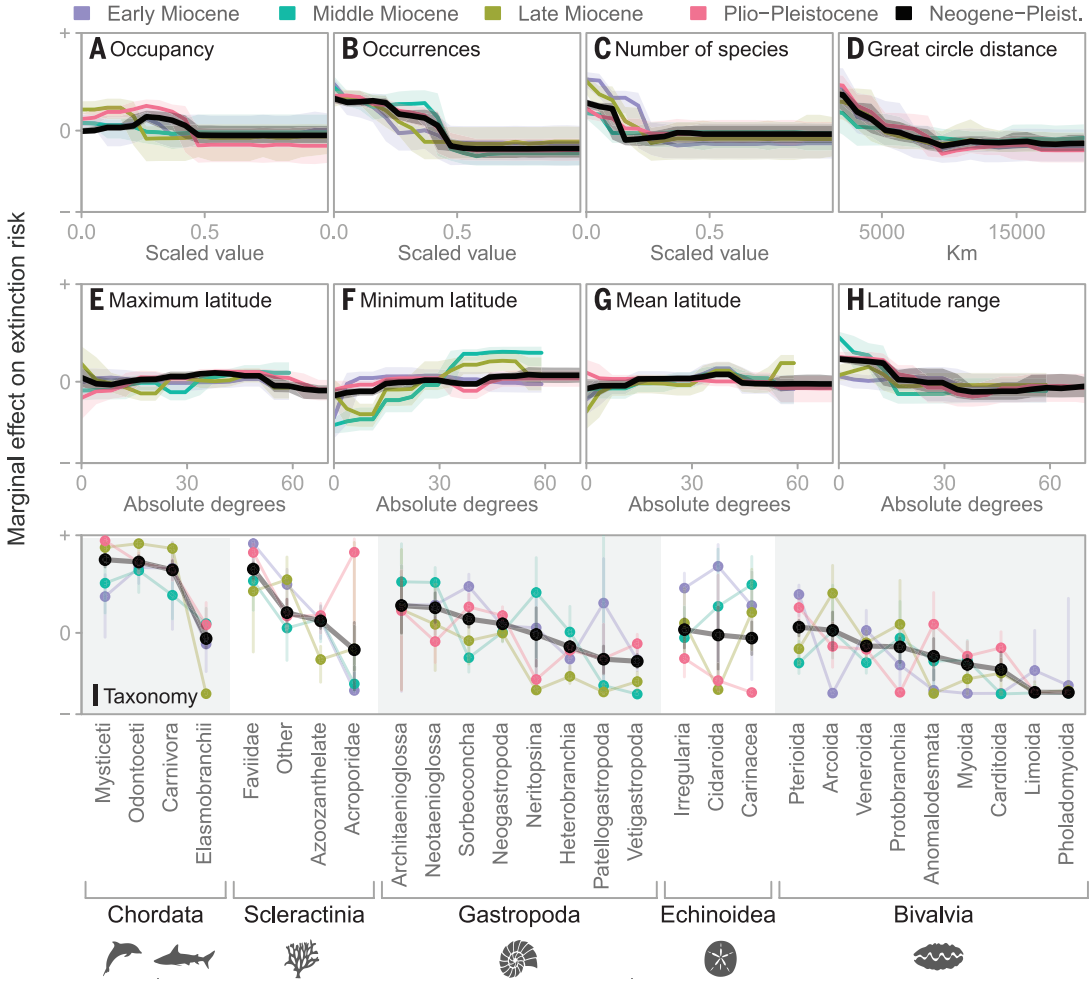

Fig. 1. Predictors of extinction risk in the marine fossil record. (**A** to **I**) Panels show scaled marginal influence of predictors on genus extinction risk for subinterval models and a model based on the entire Neogene-Pleistocene (lines: median; shaded regions: 80% confidence interval). *y*-axis values above 0 indicate a tendency for genera with a given predictor value to go extinct, and values below 0 indicate a tendency to survive. Occupancy, occurrences, and number of species per genus were log transformed and rescaled within each subinterval to reduce the effects of differential sampling intensity.

realms (*36*) [fig. S7 (*30*)]. We then used the model built on the entire Neogene-Pleistocene (Fig. 1) to predict intrinsic risk for contemporary genera (fig. S8). We averaged intrinsic risk predictions for all genera sampled in 62 coastal biogeographic provinces (*36*) (fig. S9) to map the modern distribution of intrinsic risk (Fig. 2).

Our maps show that many provinces with the highest mean intrinsic risk are located in the tropics, particularly in the diverse tropical Indo-Pacific and Western Atlantic (Fig. 2). This pattern is not driven by innate differences in extinction regime between tropical and extratropical environments—genera with exclusively extratropical distributions exhibit higher proportional extinction than those with ranges that include the tropics in most Neogene-Pleistocene subintervals [Fig. 1F and fig. S10D (*23*)]. The elevated mean intrinsic risk of some tropical provinces instead reflects the macroecological and macroevolutionary characteristics of some tropical genera. Tropical

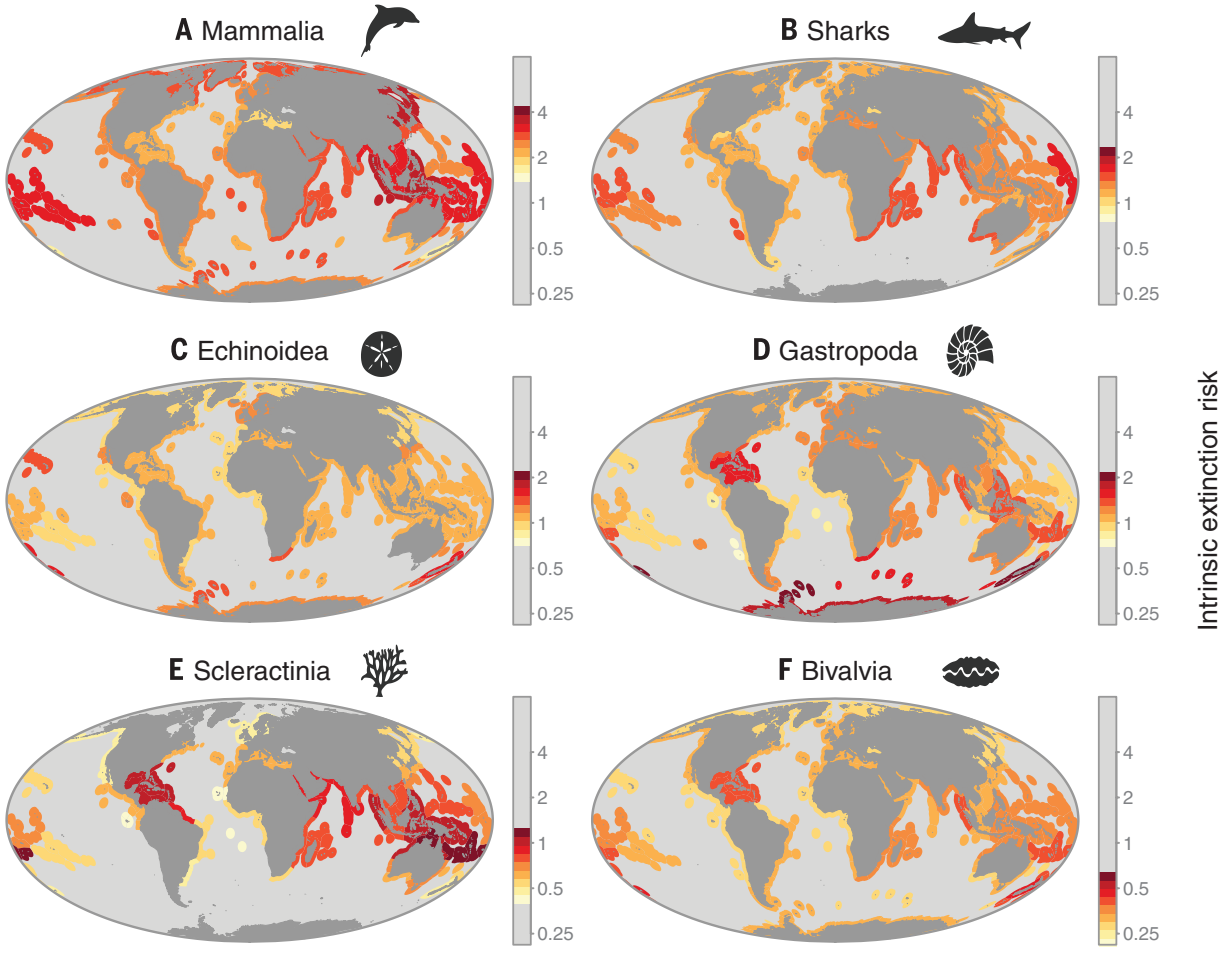

Fig. 2. Geographic distribution of mean intrinsic risk for present-day genera across coastal biogeographic provinces for six major taxonomic groups. (**A** to **F**) Scale bars indicate mean intrinsic risk as a multiple of the geometric mean across all groups. Color scales indicate a fixed threefold range of intrinsic risk centered on the geometric mean risk for a given group.

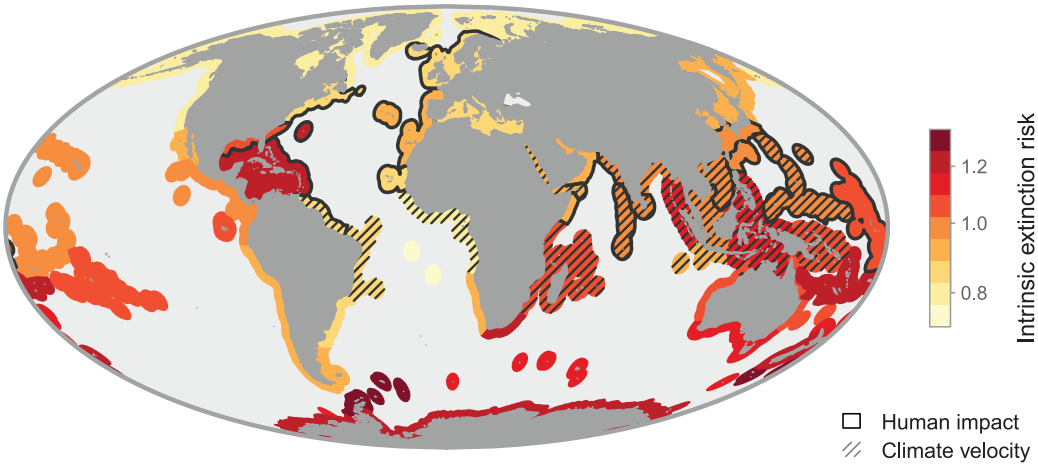

Fig. 3. Hotspots of human impact and velocity of climate change overlaid on mean intrinsic risk. Colored regions indicate mean intrinsic extinction risk of all genera that occur in a given province as a multiple of the geometric mean risk across all provinces. Outlined and hatched provinces indicate areas above the 80th percentile for mean human impact (*2*) and velocity of climate change (*1*), respectively.

provinces generally host a greater proportion of genera belonging to relatively extinction-prone groups such as faviid corals and also tend to have proportionally more genera with narrow geographic ranges [fig. S11 (*30*)]. The latter pattern may be driven by habitat heterogeneity in regions with numerous islands and associated reefs (*37*), which have been argued to promote endemism (*38*). In the polar regions, the mean intrinsic risk of gastropods is high in the Antarctic relative to that of the Arctic (Fig. 2), again reflecting high endemicity in this province (*39*, *40*), isolated for more than 30 million years by circumpolar currents (*41*).

We highlight these large-scale patterns but caution against overinterpreting province-to-province variation. The range of intrinsic risk within a given province far exceeds the range of mean intrinsic risk between provinces (fig. S12). Furthermore, sampling is taxonomically and geographically uneven in both the Paleobiology Database (*42*, *43*) and OBIS (*24*), and such heterogeneity could bias our understanding of intrinsic risk distributions by distorting the observed geographic ranges of fossil and extant genera. It is possible, for example, that heavily sampled provinces contain a greater proportion of "pseudoendemic" genera that have not been sampled in other provinces in which they occur. Some groups exhibit positive relationships between modern sampling effort (as measured by total genus occurrences in OBIS) and mean intrinsic risk of provinces (figs. S13 and S14), but the same broad-scale geographic patterns of intrinsic risk remain after accounting for this relationship (fig. S15). Omitting all genera sampled in only a single province reduces the number of modern genera by 14% but likewise does not substantially alter broad-scale mean intrinsic risk patterns (fig. S16). Omitting the bounding-box interpolation procedure results in greater heterogeneity among adjacent provinces but also does not change the broad-scale regional differences (fig. S17). Genera with very few occurrences necessarily have limited geographic ranges, but genera with three or more occurrences exhibit the full range of great circle distances (fig. S18). Raising the minimum number of occurrences required for including a genus in the modern data set has relatively little effect on differences in intrinsic risk across provinces (figs. S19 and S20). In the fossil calibration data, marginal effects of predictor variables on extinction risk are relatively stable even when poorly preserved genera are excluded (figs. S21 to S24). Thus, per-genus and interprovincial intrinsic risk patterns are generally conserved when a variety of culls are applied to the fossil data to address potential biases arising from incomplete sampling (figs. S25 and S26).

The preceding analyses suggest that the broad-scale intrinsic risk patterns that we report are unlikely to be artifacts of sampling heterogeneity or our modeling approach, but rather reflect the expected distribution of extinction risk if the extinction risk patterns of the past 23 million years are projected onto modern fauna. Our intrinsic risk predictions can thus be used as a baseline for determining which genera would be most at risk, and which regions would face the greatest losses, under a prehuman extinction regime. Human activity is increasingly altering the structure and function of marine ecosystems (*3*), and the degree to which future extinction patterns will resemble those of the past depends on how contemporary stresses and intrinsic risk interact.

To delineate the geographic distribution of potential interactions, we compared the mean intrinsic risk of genera in each province with assessments of anthropogenic impact (*2*) and velocity of climate change (*1*) (Fig. 3 and fig. S27). Provinces characterized by the coincidence of high intrinsic risk and rapid climate shifts or elevated human impacts are located primarily in the tropics and subtropics (Fig. 3). Extratropical provinces in the Northern Hemisphere are characterized by low mean intrinsic risk and variable but often high human impact, whereas extratropical provinces in the Southern Hemisphere tend to combine high mean intrinsic risk and comparatively low current threats (Fig. 3).

The implications of these broad-scale patterns for the future of coastal marine ecosystems will depend on how intrinsic risk and current threats interact to determine future extinction risk. For example, additive interactions would lead to extinction rates in some tropical regions exceeding those expected from human impacts alone, whereas multiplicative interactions would also raise the prospect of unforeseen ecological consequences (*44*). In other cases, such as the highly impacted coastal ecosystems of the North Atlantic, anthropogenic impacts may dwarf intrinsic risk effects and leave a distinctly human fingerprint on future extinctions.

Understanding how intrinsic risk and current threats interact will involve disentangling the traits that underlie intrinsic risk differences. Potentially important life-history and ecological correlates of taxonomic identity include body size, larval mode, fecundity, life span, habitat preference, and trophic position, all of which are important predictors in modern risk assessments (*17*). Examining differences in the evolutionary lability of these traits across taxa (*29*) may also illuminate the drivers of intrinsic risk variation and inform predictions about the potential response times of taxa to current and future environmental change.

Our approach provides a flexible analytical framework that can be extended to incorporate additional risk predictors as data become available, and can be adapted to focus on specific taxa or regions of interest where exceptionally complete fossil records coincide with detailed modern censuses of marine populations. Integrating modern threat assessments with long-term baseline data provided by the fossil record has potential to inform conservation planning—identifying taxa and ecosystems of potential conservation concern and teasing apart the ways in which extinction regimes in modern human-impacted ecosystems differ from those that prevailed in the geologic past.

REFERENCES AND NOTES

1. M. T. Burrows *et al.*, *Science* **334**, 652–655 (2011).
2. B. S. Halpern *et al.*, *Science* **319**, 948–952 (2008).
3. J. B. C. Jackson, *Proc. Natl. Acad. Sci. U.S.A.* **105** (suppl. 1), 11458–11465 (2008).
4. J. M. Pandolfi, S. R. Connolly, D. J. Marshall, A. L. Cohen, *Science* **333**, 418–422 (2011).
5. P. G. Harnik *et al.*, *Trends Ecol. Evol.* **27**, 608–617 (2012).
6. L. McClenachan, A. B. Cooper, K. E. Carpenter, N. K. Dulvy, *Conserv. Lett.* **5**, 73–80 (2012).
7. T. P. Hughes *et al.*, *Science* **301**, 929–933 (2003).
8. N. Dulvy, Y. Sadovy, J. Reynolds, *Fish Fish.* **4**, 25–64 (2003).
9. T. J. Webb, B. L. Mindel, *Curr. Biol.* **25**, 506–511 (2015).
10. D. J. McCauley *et al.*, *Science* **347**, 1255641 (2015).
11. K. E. Jones, A. Purvis, J. L. Gittleman, *Am. Nat.* **161**, 601–614 (2003).
12. M. Cardillo, G. M. Mace, J. L. Gittleman, A. Purvis, *Proc. Natl. Acad. Sci. U.S.A.* **103**, 4157–4161 (2006).
13. I. P. Owens, P. M. Bennett, *Proc. Natl. Acad. Sci. U.S.A.* **97**, 12144–12148 (2000).
14. C. M. Roberts *et al.*, *Science* **295**, 1280–1284 (2002).
15. V. Parravicini *et al.*, *Ecol. Lett.* **17**, 1101–1110 (2014).
16. N. K. Dulvy *et al.*, *eLife* **3**, e00590 (2014).
17. A. D. Davidson *et al.*, *Proc. Natl. Acad. Sci. U.S.A.* **109**, 3395–3400 (2012).
18. J. S. Clark *et al.*, *Science* **293**, 657–660 (2001).
19. L. Bromham, R. Lanfear, P. Cassey, G. Gibb, M. Cardillo, *Proc. Biol. Sci.* **279**, 4024–4032 (2012).
20. N. K. Dulvy, J. K. Pinnegar, J. D. Reynolds, *Holocene Extinctions*, S. T. Turvey, Ed. (Oxford Univ. Press, Oxford, 2009), pp. 129–150.
21. A. B. Ronov, *Int. Geol. Rev.* **24**, 1365–1388 (1982).
22. S. E. Peters, *J. Geol.* **114**, 391–412 (2006).
23. J. Alroy *et al.*, *Science* **321**, 97–100 (2008).
24. D. P. Tittensor *et al.*, *Nature* **466**, 1098–1101 (2010).
25. J. W. Valentine, D. Jablonski, A. Z. Krug, K. Roy, *Paleobiology* **34**, 169–178 (2008).
26. M. Foote, J. S. Crampton, A. G. Beu, R. A. Cooper, *Paleobiology* **34**, 421–433 (2008).
27. P. G. Harnik, C. Simpson, J. L. Payne, *Proc. Biol. Sci.* **279**, 4969–4976 (2012).
28. S. C. Wang, A. M. Bush, *Paleobiology* **34**, 434–455 (2008).
29. A. Purvis, J. L. Gittleman, T. M. Brooks, *Phylogeny and Conservation* (Cambridge Univ. Press, Cambridge, 2005).
30. See supplementary materials and methods on *Science* Online.
31. J. Elith, J. R. Leathwick, T. Hastie, *J. Anim. Ecol.* **77**, 802–813 (2008).
32. OBIS, Data from the Ocean Biogeographic Information System. Intergovernmental Oceanographic Commission of UNESCO. http://www.iobis.org (consulted on 12 September 2012).
33. L. O. Lucifora, V. B. García, B. Worm, *PLOS ONE* **6**, e19356 (2011).
34. J. Schipper *et al.*, *Science* **322**, 225–230 (2008).
35. C. L. Belanger *et al.*, *Proc. Natl. Acad. Sci. U.S.A.* **109**, 14046–14051 (2012).
36. M. D. Spalding *et al.*, *Bioscience* **57**, 573 (2007).
37. C. Mora, D. R. Robertson, *Ecology* **86**, 1771–1782 (2005).
38. W. Renema *et al.*, *Science* **321**, 654–657 (2008).
39. A. Clarke, *J. Exp. Mar. Biol. Ecol.* **366**, 48–55 (2008).
40. K. Linse, H. J. Griffiths, D. K. Barnes, A. Clarke, *Deep Sea Res. Part II Top. Stud. Oceanogr.* **53**, 985–1008 (2006).
41. M. Lyle, S. Gibbs, T. C. Moore, D. K. Rea, *Geology* **35**, 691 (2007).
42. J. W. Valentine, D. Jablonski, A. Z. Krug, S. K. Berke, *Paleobiology* **39**, 1–20 (2012).
43. D. A. Vilhena, A. B. Smith, *PLOS ONE* **8**, e74470 (2013).
44. D. F. Doak *et al.*, *Ecology* **89**, 952–961 (2008).

ACKNOWLEDGMENTS

This work is a product of the Determinants of Extinction in Ancient and Modern Seas Working Group supported by the National Evolutionary Synthesis Center (NSF grant EF-0905606). Additional support was provided by the Natural Sciences and Engineering Research Council of Canada (to H.K.L., S.C.A., and Z.V.F.); the National System of Investigators of the National Secretariat for Science, Technology and Innovation of Panama (to A.O.); the Australian Research Council Centre of Excellence for Coral Reef Studies (to J.M.P.); and the Deutsche Forschungsgemeinschaft (grant KI 806/7-1 to C.S.). We thank the contributors to the Paleobiology Database and to OBIS. We also thank four anonymous reviewers for insightful comments that substantially improved the quality of the manuscript. This article is Paleobiology Database contribution no. 227. All scripts and data used to conduct analyses are available at https://github.com/seananderson/paleobaselines

SUPPLEMENTARY MATERIALS

www.sciencemag.org/content/348/6234/567/suppl/DC1
Materials and Methods
Figs. S1 to S27
Tables S1 to S3
References (*45*–*75*)

10 January 2015; accepted 23 March 2015
10.1126/science.aaa6635

CLIMATE CHANGE

Accelerating extinction risk from climate change

Mark C. Urban*

Current predictions of extinction risks from climate change vary widely depending on the specific assumptions and geographic and taxonomic focus of each study. I synthesized published studies in order to estimate a global mean extinction rate and determine which factors contribute the greatest uncertainty to climate change–induced extinction risks. Results suggest that extinction risks will accelerate with future global temperatures, threatening up to one in six species under current policies. Extinction risks were highest in South America, Australia, and New Zealand, and risks did not vary by taxonomic group. Realistic assumptions about extinction debt and dispersal capacity substantially increased extinction risks. We urgently need to adopt strategies that limit further climate change if we are to avoid an acceleration of global extinctions.

We critically need to know how climate change will influence species extinction rates in order to inform international policy decisions about the biological costs of failing to curb climate change and to implement specific conservation strategies to protect the most threatened species. Current predictions about extinction risks vary widely, suggesting that anywhere from 0 to 54% of species could become extinct from climate change (*1*–*4*). Studies differ in particular assumptions, methods, species, and regions and thus do not encompass the full range of our current understanding. As a result, we currently lack consistent, global estimates of species extinctions attributable to future climate change.

To provide a more comprehensive and consistent analysis of predicted extinction risks from climate change, I performed a meta-analysis of 131 published predictions (table S1). I focused on multispecies studies so as to exclude potential biases in single-species studies. I estimated the global proportion of species threatened in a Bayesian Markov chain Monte Carlo (MCMC) random-effects meta-analysis that incorporated variation among and within studies (*5*) and with each study weighted by sample size (*6*). I evaluated how extinction risk varied depending on future global temperature increases, taxonomic groups, geographic regions, endemism, modeling techniques, dispersal assumptions, and extinction thresholds. I used credible intervals (CIs) that do not overlap with zero and a deviance information criterion (DIC) greater than four to assess statistical support for factors. The majority of studies estimated correlations between current distributions and climate so as to predict suitable habitat under future climates. A smaller number of studies determined extinction risks by using process-based models of physiology or demography (15%), species-area relationships (5%), or expert opinion (4%). Species were predicted to become extinct if their range fell below a minimum threshold. An important caveat is that most of these models ignore many factors thought to be important in determining future extinction risks such as species interactions, dispersal differences, and evolution.

Overall, 7.9% of species are predicted to become extinct from climate change; (95% CIs, 6.2 and 9.8) (Fig. 1). Results were robust to model type, weighting scheme, statistical method, potential publication bias, and missing studies (fig. S1 and table S2) (*6*). This proportion supports an estimate from a 5-year synthesis of studies (*7*). Its divergence from individual studies (*1*–*4*) can be explained by their specific assumptions and taxonomic and geographic foci. These differences provide the opportunity to understand how divergent factors and assumptions influence extinction risk from climate change.

The factor that best explained variation in extinction risk was the level of future climate change. The future global extinction risk from climate change is predicted not only to increase but to accelerate as global temperatures rise (regression coefficient = 0.53; CIs, 0.46 and 0.61) (Fig. 2). Global extinction risks increase from 2.8% at present to 5.2% at the international policy target of a 2°C post-industrial rise, which most experts believe is no longer achievable (*8*). If the Earth warms to 3°C, the extinction risk rises to 8.5%. If we follow our current, business-as-usual trajectory [representative concentration pathway (RCP) 8.5; 4.3°C rise], climate change threatens one in six species (16%). Results were robust to alternative data transformations and were bracketed by models with liberal and conservative extinction thresholds (figs. S2 and S3 and table S3).

Regions also differed significantly in extinction risk (ΔDIC = 12.6) (Fig. 3 and table S4). North America and Europe were characterized by the lowest risks (5 and 6%, respectively), and South America (23%) and Australia and New Zealand (14%) were characterized by the highest risks. These latter regions face no-analog climates (*9*) and harbor diverse assemblages of endemic species with small ranges. Extinction risks in Australia and New Zealand are further exacerbated by small land masses that limit shifts to new habitat (*10*). Poorly studied regions might face higher risks, but insights are limited without more research (for example, only four studies in Asia). Currently, most predictions (60%) center on North America and Europe, suggesting a need to refocus efforts toward less studied and more threatened regions.

Endemic species with smaller ranges and certain taxonomic groups such as amphibians and reptiles are predicted to face greater extinction risks (*11*, *12*). I estimated that endemic species face a 6% greater extinction risk relative to models that include both species endemic and non-endemic to the study region (ΔDIC = 8.3). Extinction risks also rose faster with preindustrial temperature rise for models with endemic species (ΔDIC = 8.2) (fig. S4). In contrast to predictions, extinction risks did not vary significantly by taxonomic group (ΔDIC = 0.7) (Fig. 4). One explanation is that trait variation at finer taxonomic scales might play a more important role in modulating extinction risks (*13*). Also, typical approaches for quantifying extinction risks likely do not capture the full range of differences among taxonomic groups.

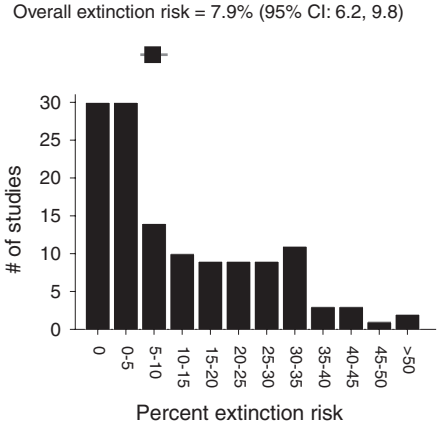

Fig. 1. Histogram of percent extinction risks from climate change for 131 studies. Percent extinction risk refers to the predicted percent of species extinctions in each study, averaged across all model assumptions. The meta-analysis estimated mean with 95% CIs is also shown.

Department of Ecology and Evolutionary Biology, University of Connecticut, 75 North Eagleville Road, Unit 3043, Storrs, CT 06269, USA.
*Corresponding author. E-mail: mark.urban@uconn.edu

Downloaded from www.sciencemag.org on April 30, 2015

Key model assumptions altered predictions of future extinction risk. For instance, extinction debts occur when species decline to the point that they are committed to extinction, but not yet extinct (*14*). Studies differed in how much habitat loss was assumed to commit a species to extinction, commonly applying habitat loss thresholds of 100, 95, and 80%. Extinction thresholds were second only to expected climate change in explaining variable extinction risks. Decreasing the extinction threshold from 100% (no extinction debt) to 80% increased risk from 5 to 15% (ΔDIC = 144.1) (Fig. 4), and lower thresholds increased the rise in extinction risk with future temperatures (interaction ΔDIC = 5.9) (fig. S2). The applicability of these thresholds will depend on species-specific characteristics such as generation time and initial population size. We urgently need to understand how range reductions determine future extinction risk better in order to predict accurately both the number and timing of future extinctions (*15*).

Species must disperse into newly suitable habitats as fast as climates shift across landscapes (*16*, *17*). Modelers variously assume no dispersal, dispersal only into contiguous habitats, dispersal based on each species' ability, or universal dispersal regardless of distance or ability. Modelers usually assume no dispersal and universal dispersal and presume that the true value lies between these extremes. I found that assumptions about dispersal significantly affected extinction risks (ΔDIC = 68.5) (Fig. 4). Species-specific dispersal increased extinction risk from 6%, assuming universal dispersal to 10%. Assuming no dispersal increased risk further to 12%. Extinction risks increase more rapidly with temperature rise assuming no- and species-specific dispersal (interaction ΔDIC = 6.1) (fig. S5). Incorporating more realistic species-specific dispersal

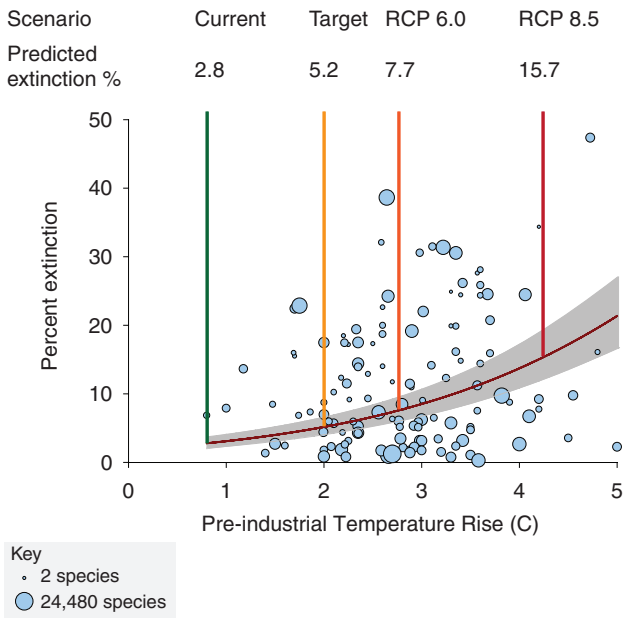

Fig. 2. Predicted extinction risks from climate change accelerate with global temperature rise. The gray band indicates 95% CIs. Preindustrial rise was calculated by using standard methods (*27*). Circles indicate posterior means with area proportional to $\log_{10}$ sample size (bottom left, key). Extinction risks for four scenarios are provided: the current postindustrial temperature rise of 0.8°C (*5*), the policy target of 2°C, and RCPs 6.0 and 8.5.

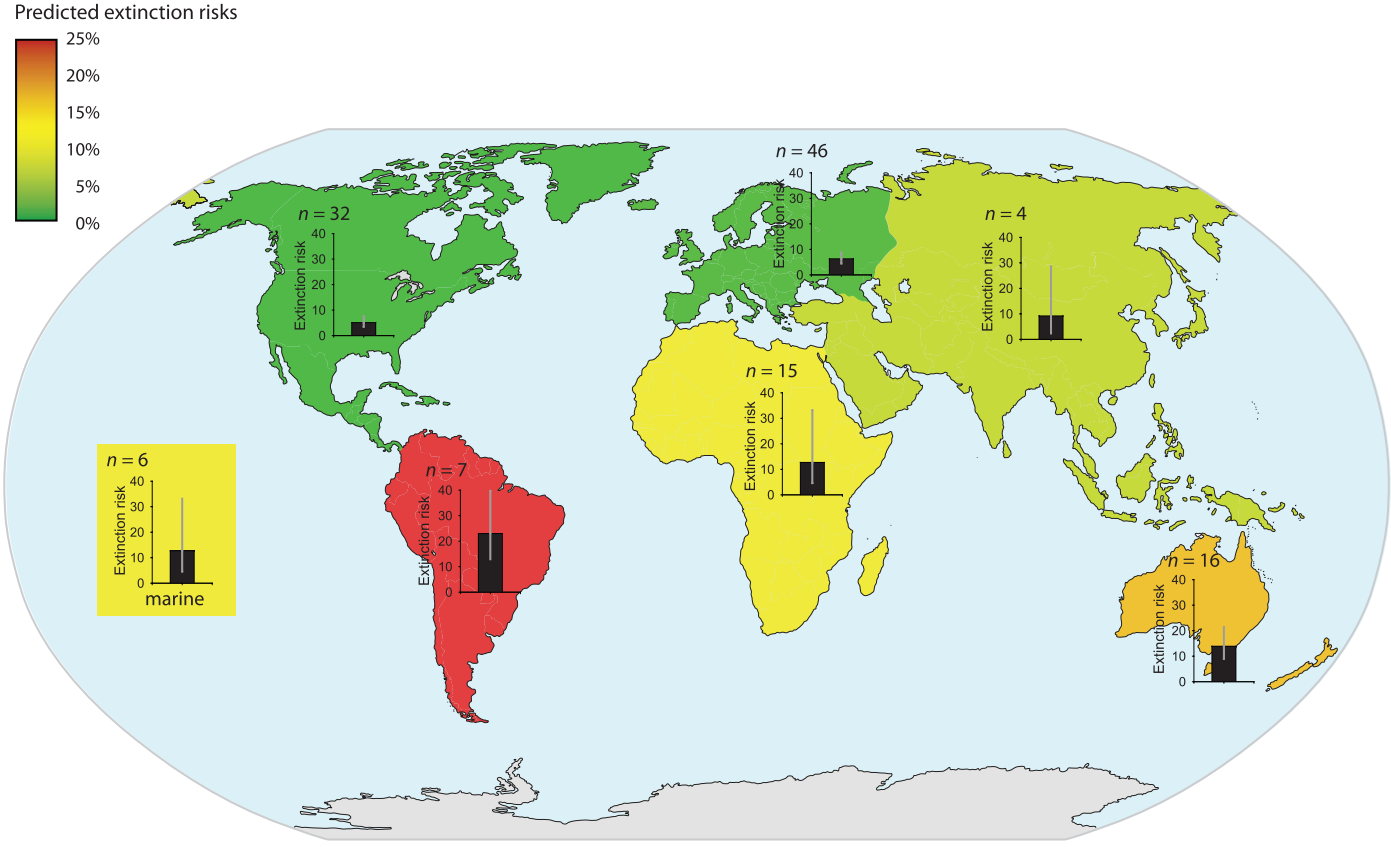

Fig. 3. Predicted extinction risks from climate change differ by region. The highest risks characterized South America, Australia, and New Zealand (14 to 23%), and the lowest risks characterized North America and Europe (5 to 6%). Colors indicate relative risk. Bar graphs with 95% CIs and number of studies (*n*) are displayed.

abilities resulted in extinction risks midway between the no- and universal-dispersal assumptions as expected.

Modelers apply different techniques to predict future extinctions, ranging from correlations between current distributions and climate (species distribution, niche, or climate envelope models) to sophisticated mechanistic models. I found only a marginal effect of modeling technique on extinction risk (ΔDIC = 3.4). The largest extinction risks originated from results based on species-area relationships (22%) and expert opinion (18%). The lowest risks originated from mechanistic (8%) and species distribution models (7%). Species-area models explicitly incorporate an extinction debt and also can overestimate extinction risks because of a sampling artifact (*18*). The high risk associated with expert opinion could stem from a broader biological understanding, more pessimistic outlook, or greater uncertainty when translating qualitative indicators into quantitative classifications of extinction risk.

Here, I provide a global assessment of climate change–induced extinction risks and the factors that influence them. However, I emphasize that extinction risks are likely much smaller than the total number of species influenced by climate change. Even species not threatened directly by extinction could experience substantial changes in abundances, distributions, and species interactions, which in turn could affect ecosystems and their services to humans (*19*). Already, changes in species' phenologies, range margins, and abundances are evident (*20*, *21*). Extinctions, although still uncommon, are increasingly attributed to climate change (*22*).

At the same time, we must cautiously interpret the predictions underlying this meta-analysis. The majority of studies extrapolate correlations between current climate and species distributions to novel conditions and omit important biological mechanisms, including species interactions, evolution, landscape dispersal barriers, habitat degradation, and intraspecific trait variation (*23*). Depending on the mechanism, its consideration can either increase or decrease predicted risks. For instance, evolution can decrease extinction risks by allowing populations to adapt to changing climates (*24*), whereas anthropogenic landscape barriers can increase risks by limiting dispersal into newly suitable habitats (*25*). Next-generation models for estimating extinction risks should incorporate these factors in order to increase biological realism and therefore the accuracy of future predictions.

In 1981, Hansen and colleagues predicted that the signal of global climate change would soon emerge from the stochastic noise of weather (*26*). Thirty years later, we are reaching a similar threshold for the effects of climate change on biodiversity. Extinction risks from climate change are expected not only to increase but to accelerate for every degree rise in global temperatures. The signal of climate change–induced extinctions will become increasingly apparent if we do not act now to limit future climate change.

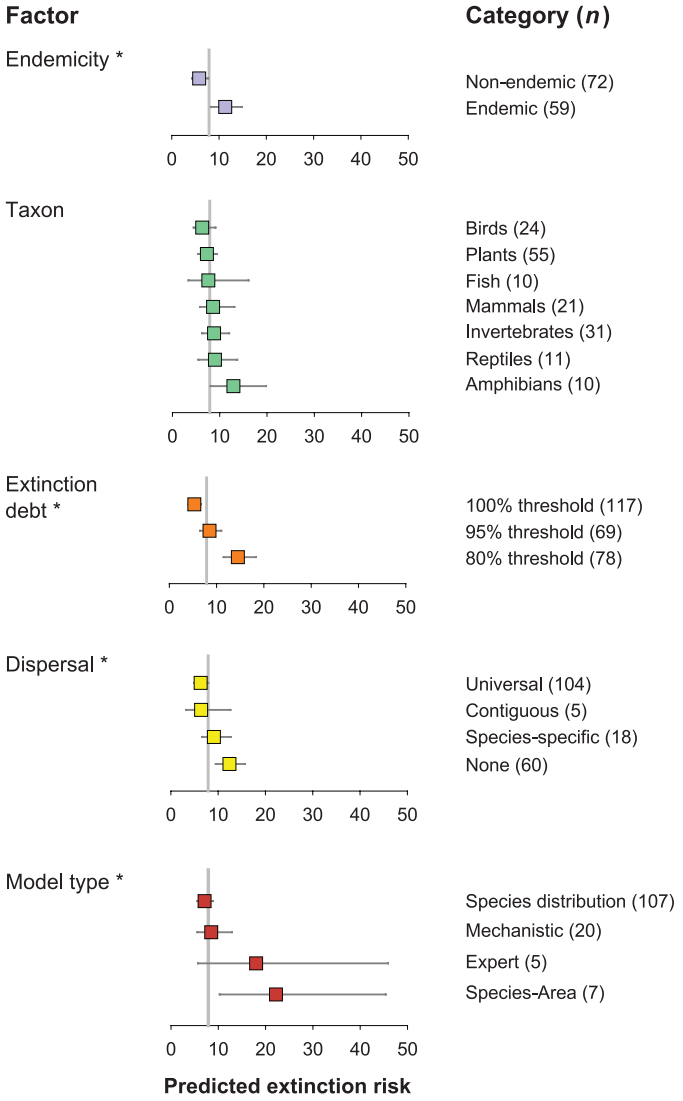

Fig. 4. Predicted extinction risks from climate change depend on model characteristics. The asterisk indicates model support (ΔDIC > 4) for each factor separately, and number of studies is included in parentheses. Categories within each factor are listed in order of increasing extinction risk. The gray vertical reference line indicates mean overall extinction risk. Bars represent 95% CIs.

REFERENCES AND NOTES

1. J. R. Malcolm, C. Liu, R. P. Neilson, L. Hansen, L. Hannah, *Conserv. Biol.* **20**, 538–548 (2006).
2. C. D. Thomas *et al.*, *Nature* **427**, 145–148 (2004).
3. R. Warren *et al.*, *Nature Clim. Change* **3**, 678–682 (2013).
4. W. B. Foden *et al.*, *PLOS ONE* **8**, e65427 (2013).
5. S. Nakagawa, E. S. Santos, *Evol. Ecol.* **26**, 1253–1274 (2012).
6. Materials and methods are available as supplementary materials on *Science* Online.
7. I. M. Maclean, R. J. Wilson, *Proc. Natl. Acad. Sci. U.S.A.* **108**, 12337–12342 (2011).
8. S. Fuss *et al.*, *Nature Clim. Change* **4**, 850–853 (2014).
9. J. W. Williams, S. T. Jackson, J. E. Kutzbach, *Proc. Natl. Acad. Sci. U.S.A.* **104**, 5738–5742 (2007).
10. S. E. Williams, E. E. Bolitho, S. Fox, *Proc. Biol. Sci.* **270**, 1887–1892 (2003).
11. B. Sinervo *et al.*., *Science* **328**, 894–899 (2010).
12. J. W. Gibbon *et al.*, *Bioscience* **50**, 653–666 (2000).
13. A. L. Angert *et al.*, *Ecol. Lett.* **14**, 677–689 (2011).
14. S. T. Jackson, D. F. Sax, *Trends Ecol. Evol.* **25**, 153–160 (2010).
15. J. C. Stanton, K. T. Shoemaker, R. G. Pearson, H. R. Akcakaya, *Glob. Change Biol.* **21**, 1066–1077 (2015).
16. C. A. Schloss, T. A. Nuñez, J. J. Lawler, *Proc. Natl. Acad. Sci. U.S.A.* **109**, 8606–8611 (2012).
17. S. R. Loarie *et al.*, *Nature* **462**, 1052–1055 (2009).
18. F. He, S. P. Hubbell, *Nature* **473**, 368–371 (2011).
19. J. J. Lawler *et al.*, *Ecology* **90**, 588–597 (2009).
20. C. Parmesan, G. Yohe, *Nature* **421**, 37–42 (2003).
21. G. R. Walther *et al.*, *Nature* **416**, 389–395 (2002).
22. A. E. Cahill *et al.*, *Proc. Biol. Sci.* **280**, 20121890 (2013).
23. L. B. Buckley *et al.*, *Ecol. Lett.* **13**, 1041–1054 (2010).
24. A. A. Hoffmann, C. M. Sgrò, *Nature* **470**, 479–485 (2011).
25. P. Opdam, D. Wascher, *Biodivers. Conserv.* **117**, 285–297 (2004).
26. J. Hansen *et al.*, *Science* **213**, 957–966 (1981).
27. R. Warren, J. Price, A. Fischlin, S. de la Nava Santos, G. Midgley, *Clim. Change* **106**, 141–177 (2011).

ACKNOWLEDGMENTS

The data reported in this paper are tabulated in the supplementary materials. Research was supported by NSF DEB-1119877 and PLR-1417754 and the James S. McDonnell Foundation. I thank M. Tingley, J. Urban, and all the authors of the studies who made this meta-analysis possible.

SUPPLEMENTARY MATERIALS

www.sciencemag.org/content/348/6234/571/suppl/DC1
Materials and Methods
Supplementary Text
Figs. S1 to S5
Tables S1 to S4
References (*28*–*174*)

16 December 2014; accepted 17 March 2015
10.1126/science.aaa4984

BACTERIAL DIVISION

Mechanical crack propagation drives millisecond daughter cell separation in *Staphylococcus aureus*

Xiaoxue Zhou,[1,2,3]* David K. Halladin,[2,3,4]* Enrique R. Rojas,[2,3,5]* Elena F. Koslover,[2,3] Timothy K. Lee,[5] Kerwyn Casey Huang,[4,5] Julie A. Theriot[2,3,4]†

When *Staphylococcus aureus* undergoes cytokinesis, it builds a septum, generating two hemispherical daughters whose cell walls are only connected via a narrow peripheral ring. We found that resolution of this ring occurred within milliseconds ("popping"), without detectable changes in cell volume. The likelihood of popping depended on cell-wall stress, and the separating cells split open asymmetrically, leaving the daughters connected by a hinge. An elastostatic model of the wall indicated high circumferential stress in the peripheral ring before popping. Last, we observed small perforations in the peripheral ring that are likely initial points of mechanical failure. Thus, the ultrafast daughter cell separation in *S. aureus* appears to be driven by accumulation of stress in the peripheral ring and exhibits hallmarks of mechanical crack propagation.

Most bacteria propagate through binary fission, a process that is highly coordinated and tightly controlled to pass on genetic material equally to the two daughter cells and to regulate cell size and shape. Much of our knowledge of bacterial cell division comes from rod-shaped bacteria, which double their cell length before cytokinesis (*1*, *2*); relatively less is known about cell division in bacteria with other shapes. *Staphylococcus aureus*, a model system for round bacteria, is a Gram-positive pathogen well recognized for its virulence and antibiotic resistance (*3*, *4*). To divide, *S. aureus* builds a septum, generating two hemispherical daughter cells (*5*, *6*). After construction, the septal wall exists as two flat, parallel plates, and the walls of the two daughter cells are connected only through a narrow peripheral ring (Fig. 1A) (*7*). Presumably, resolution of this peripheral wall ring leads to daughter cell separation, which is accompanied by a shape conversion of the daughter cells from hemispheres to spheres. This shape change has previously been assumed to occur through expansion of the septum to twice its original surface area, which would double the cell volume (*5*, *8*). It remains unclear how exactly the peripheral ring is resolved to allow the daughter cells to separate, particularly given that the *S. aureus* cell wall is quite thick (20 to 30 nm) (*9*).

Previous video microscopy–based observations of *S. aureus* cell division have described daughter cell separation as a dramatic "popping" event with no detectable intermediate stages (*10*, *11*). To address the time scale and mechanism of the popping, we used phase contrast microscopy with a temporal resolution of 1 ms. At this frame rate, we occasionally observed intermediate stages of popping, whereas most separations occurred within one or two frames (<2 ms, or $1/10^6$ of the cell cycle) (Fig. 1B and movie S1). This rapid separation of the daughter cells with drastic shape change contrasts sharply with the gradual morphological changes commonly associated with cell division in other bacteria (*12*), suggesting that daughter cell separation in *S. aureus* must not be solely dependent on enzyme-mediated cell-wall remodeling. Rather, the millisecond daughter-cell separation suggests the involvement of mechanical forces (*13*). One possibility is that the peripheral ring connecting the two daughter cells is under substantial mechanical stress before separation, so that if a random point on this ring were to fail, a crack would propagate around the periphery, separating the daughter cells but leaving them connected by a hinge point roughly opposite the position of the initial point of material failure. The observed rate of daughter-cell separation (~1 μm/ms) is well within the range of crack propagation speeds for soft biological materials (*14*, *15*).

An essential feature of mechanical crack propagation is its dependence on stress in the material (*16*, *17*). The primary source of stress in the bacterial cell wall is turgor pressure (*18*). Indeed, removing turgor pressure in *S. aureus* by disrupting the cytoplasmic membrane resulted in an average decrease in cell volume of >20% (fig. S1 and movie S2), indicating that the cell wall is normally under substantial mechanical stress. If cell-wall stress and consequent mechanical failure are contributing factors to the ultrafast cell separation, then altering turgor pressure should influence the likelihood of separation. To test this hypothesis, we exposed an unsynchronized, growing population of cells to oscillatory changes in medium osmolarity over a range of 100 to 500 mM in order to modulate turgor pressure and cell-wall stress and recorded the time of popping with respect to the phase of the oscillatory cycle for hundreds of individual popping events. We observed a large dose-dependent enrichment of popping events during the intervals when medium osmolarity was being lowered (downshift), which corresponds to an increase in turgor pressure and cell-wall stress, and a depletion of popping events during the intervals when medium osmolarity was being raised (upshift) (Fig. 1C and fig. S2). Thus, an externally induced increase in cell-wall stress promotes popping, whereas a decrease in wall stress delays popping, confirming the involvement of cell-wall stress in determining the likelihood of popping.

A further prediction of the stress-driven crack propagation model in which failure is initiated at one random point along the periphery is that after splitting, when stress has been released, the two daughter cells will remain connected at a hinge point opposite the initial site of failure. To probe the relative orientation of the two daughter cells after popping, we tracked the fate of the outer wall (Fig. 1A) relative to the septal wall after cell separation using fluorescent wheat germ agglutinin (WGA) and three-dimensional (3D) structured illumination microscopy (3D SIM). WGA binds to *N*-acetylglucosamine residues in the cell wall (*19*) and does not penetrate into the septum because of its size and can therefore be used to selectively label the *S. aureus* outer wall (*20*). In nearly all of the daughter cell pairs observed (39 of 40), the two sections of the previous outer wall were still partially connected after cell separation, and in all cases (40 of 40) they appeared to have rotated around a hinge (Fig. 1D, 10 min, and movie S3). In addition, we followed WGA-labeled live cells with epifluorescence microscopy and observed two WGA labeling patterns after popping: the hinged pattern as observed with 3D SIM (Fig. 1E, left) and a nonhinged pattern (Fig. 1E, right) that resembles the labeling pattern reported previously (*20*). By correlating epifluorescence microscopy to scanning electron microscopy (SEM), we realized that the nonhinged pattern corresponds to cells with their hinge points oriented at the top or bottom surface of the cells relative to the coverslip (Fig. 1F). Thus, daughter-cell separation in *S. aureus* is achieved through mechanical crack propagation that initiates at some point around the peripheral ring, connecting the two daughter cells, and rapidly propagates circumferentially, resulting in a hinge-like rotation.

Given that popping occurs so quickly, we questioned whether cell volume and surface area change during this process. It has been suggested that cell volume doubles at the moment of cell separation as a result of the septum expanding to cover one-half of the new spherical cell (*8*, *21*), which would require substantial water influx over a very short time frame. To address this question, we tracked growth of individual *S. aureus* cells

[1]Department of Chemistry, Stanford University, Stanford, CA 94305, USA. [2]Department of Biochemistry, Stanford University School of Medicine, Stanford, CA 94305, USA. [3]Howard Hughes Medical Institute (HHMI), Stanford University School of Medicine, Stanford, CA 94305, USA. [4]Department of Microbiology and Immunology, Stanford University School of Medicine, Stanford, CA 94305, USA. [5]Department of Bioengineering, Stanford University, Stanford, CA 94305, USA.
*These authors contributed equally to this work. †Corresponding author. E-mail: theriot@stanford.edu

Downloaded from www.sciencemag.org on April 30, 2015

using the membrane dye FM 4-64 (Life Technologies, Grand Island, NY), and estimated cell volume and surface area from the 2D cell outlines by assuming a prolate cell shape (Fig. 2A). Overlaying the 2D cell outlines from different stages in the cell cycle (Fig. 2B, inset) revealed that a growing *S. aureus* cell increases both its volume and surface area throughout the cell cycle, accompanied by an overall increase in the cell aspect ratio after a small initial decrease (Fig. 2B). This small initial decrease corresponded to a phase in which the two daughter cells gradually (within minutes) became more round and more separated after popping. Following single cells and their progeny, we observed a continuous increase in cell volume for each microcolony over several generations (Fig. 2C), which is consistent with the continuous exponential volume increase that has been described for *E. coli* and other bacteria (*22*). With respect to this continuous growth, the volume change upon popping is negligible on average (Fig. 2D). Consistent with this, using 3D deconvolution fluorescence microscopy with a *S. aureus* strain expressing cytoplasmic green fluorescent protein (GFP), we observed only minimal changes in cell volume and GFP intensity (fig. S3) after cell separation. Last, we estimated changes in cell surface area from 2D cell outlines by assuming a prolate cell shape, which revealed a modest net decrease in surface area upon popping (Fig. 2E and fig. S4), which is consistent with a geometric conversion from hemi-ellipsoidal to ellipsoidal shape, given constant volume. A decrease in surface area during popping indicates that the cell wall must have been under tensile stress before popping, which is in line with the hypothesis that cell-wall stress contributes to daughter-cell separation.

We next questioned whether the septum expands to become one half of the new daughter's surface (*8*, *21*), given that the total surface area decreases upon popping. To determine the relative contributions of the previous outer wall and septum to the surface of the new daughter, we used WGA pulse-chase labeling and 3D SIM as described above. We found that ~73% of the new daughter's surface was represented by the old wall regardless of cell size (or stage in the cell cycle) (fig. S5), similar to the ratio before cell separation (Fig. 2F), indicating that the septum constitutes only ~1/4 of the new daughter's surface and does not expand noticeably in surface area upon popping, which is contrary to the doubling of septal surface area assumed previously (*8*).

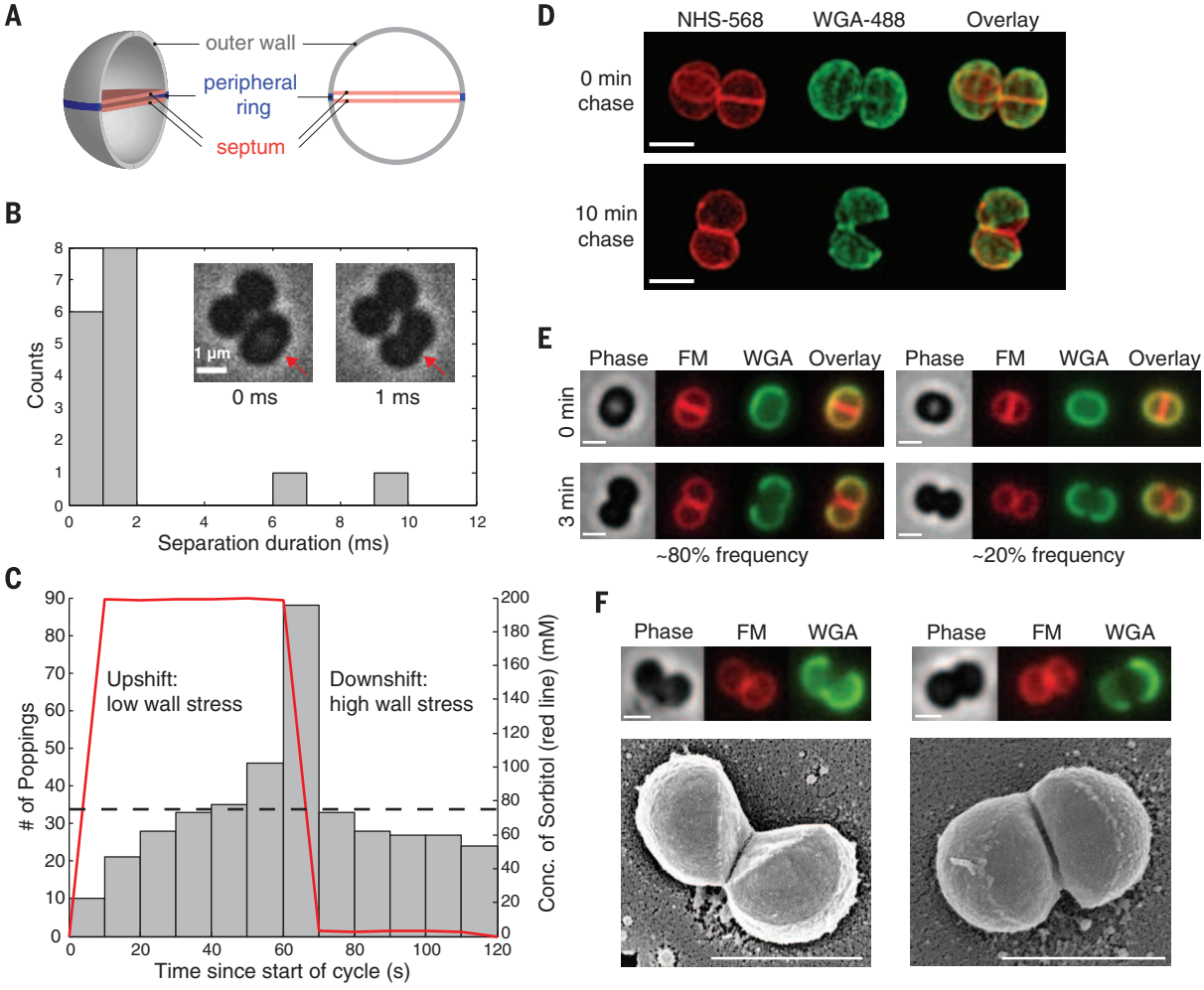

Fig. 1. Daughter cell separation in *S. aureus* occurs within milliseconds with characteristics of mechanical crack propagation. (**A**) A schematic diagram of the cell wall before daughter cell separation. (**B**) Snapshots of *S. aureus* strain Newman "popping" (inset) and histogram of daughter cell separation duration captured by means of phase contrast microscopy at 1000 frames/s (n = 16 popping events). (**C**) Distribution of cumulative counts of popping events plotted over the 2-min oscillatory period for 200 mM osmotic shocks. The red line denotes the concentration of sorbitol in the medium, and the dashed line denotes average popping counts, assuming a uniform distribution (n = 400 popping events). (**D**) 3D SIM images of fixed Newman cells labeled with fluorescent WGA (WGA-488, green), which marks the outer wall and followed by 0 or 10 min of growth in the absence of WGA. Cell surfaces and septa were stained with an amine reactive dye (NHS-568, red). (**E**) Time-lapse epifluorescence images of Newman cells labeled with WGA (green) before (0 min) and after (3 min) popping. Corresponding phase-contrast (gray), membrane staining with FM 4-64 (red), and overlay of WGA and FM signals are also displayed. Two types of old wall geometry after popping were observed: hinged (left, ~80%) and nonhinged (right, ~20%). (**F**) Correlative light and SEM on Newman cells labeled with WGA followed by 10-min chase showing the two types of WGA labeling patterns as in (E). Scale bars, 1 µm.

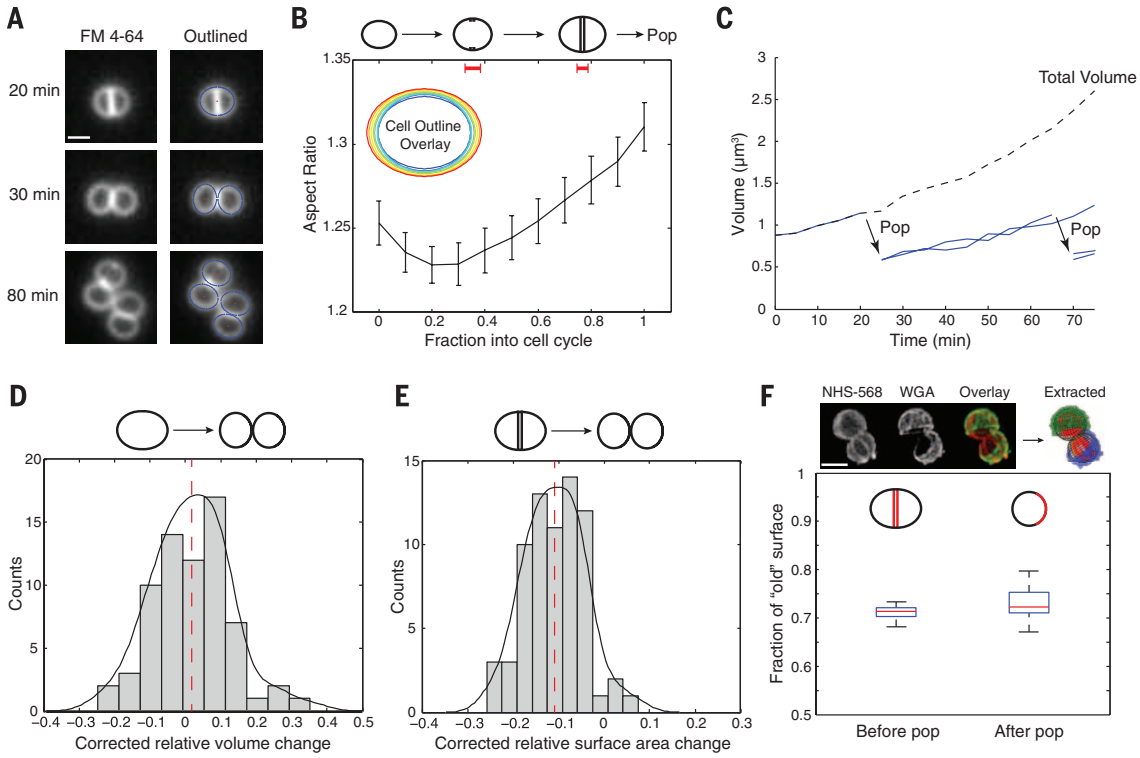

Fig. 2. Cell volume increases continuously throughout the cell cycle. (**A**) Time-lapse images of *S. aureus* cells stained with FM 4-64 (left) and outlined by fitting with ellipses (right). (**B**) Average aspect ratio of *S. aureus* cells throughout the cell cycle (from immediately after previous popping to ready-to-pop) and overlay of the cell outlines (inset) from a typical cell at different points of the cell cycle colored from blue (early) to red (late). Error bars denote standard errors (n = 27 cells). Red bars on top indicate the time fraction into the cell cycle when septation starts (left, 0.35 ± 0.03 SEM) and completes (right, 0.77 ± 0.02 SEM), respectively (n = 26 cells). (**C**) Representative traces of cell volume as a function of time following a microcolony starting from a single cell; solid blue traces indicate cell volumes of individual cells before popping, and the dashed black line denotes the total cell volume of all the cells present at a given time. Cell volume and surface area were estimated from the 2D cell outlines by fitting to ellipses and assuming prolate cell shapes (that each cell was rotationally symmetric around the long axis). (**D** and **E**) Distribution of relative changes in (D) volume and (E) surface area during popping, after correcting for baseline growth rate. The black solid line represents kernel density estimate of the distribution, and the red dashed line denotes the average (2 ± 10% SD for volume, −11 ± 6.5% SD for surface area; n = 69 division events). (**F**) (Top) 3D SIM images and corresponding extracted data (fig. S5); (bottom) fraction of old surface before (0.71 ± 0.01 SD; n = 15 cells) and after (0.73 ± 0.03 SD; n = 36 cells) popping. Cells were modeled as ellipsoids, and the contribution of the old, WGA-labeled wall to the daughter cells' total surface area was measured by fitting a plane to the old/new boundary (fig. S5A). Scale bars, 1 μm.

Additionally, the finding that the previous outer wall makes up ~3/4 of the new daughter's cell wall (as opposed to half) suggests that there must be new wall synthesis in the outer wall as well as at the septum to sustain the continuous surface expansion required for cell size homeostasis generation after generation.

Because our data suggest that accumulation of stress in the cell wall plays an important role in the ultrafast daughter cell separation, we sought to model the stress distribution in the cell wall before popping using a continuum elastostatic approach. On the basis of previous cryogenic electron microscopy data (*7*) and constraints determined by our experimental measurements on cell volume and surface area, we built a 3D finite element model of a "ready-to-pop" *S. aureus* cell wall as a prolate ellipsoidal shell with two separated septal plates that are connected with a peripheral ring (fig. S6). We assumed that the peripheral ring does not grow as much as the rest of the cell once septation begins because it is not in direct contact with the cytoplasmic membrane where new wall material is incorporated (supplementary text 1 and fig. S7). After inflating the modeled cell wall with a uniform turgor pressure in both compartments, we calculated the von Mises stress (a criterion for material failure) for the entire surface. Indeed, the von Mises stress at the peripheral ring was found to be higher than elsewhere in the outer wall (Fig. 3, A and B, and movie S6). The high von Mises stress in the

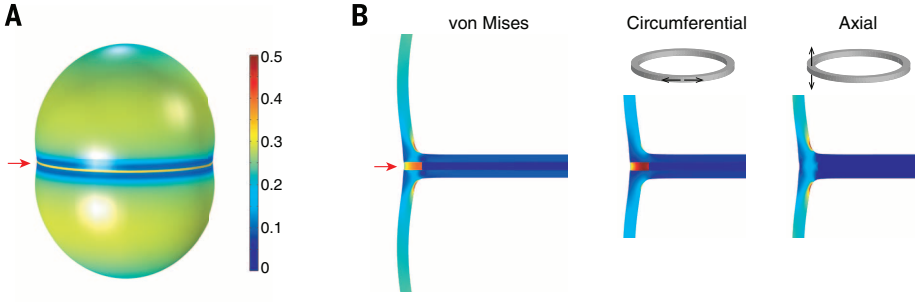

Fig. 3. High stress in the peripheral ring prepares the cell for popping. (**A**) von Mises stress distribution in the "ready-to-pop" *S. aureus* cell wall (fig. S6, state 3) modeled as a linear elastic material (details of model construction are provided in the supplementary materials). Color represents the relative magnitude of stress. The stress at the peripheral ring (red arrow), where the cell wall splits open during popping, is higher than elsewhere in the outer wall. (**B**) Enlarged views of a cut-through slice of the cell in (A) shows high von Mises stress at the peripheral ring (red arrow) as well as the stress distribution in the circumferential and axial directions, respectively.

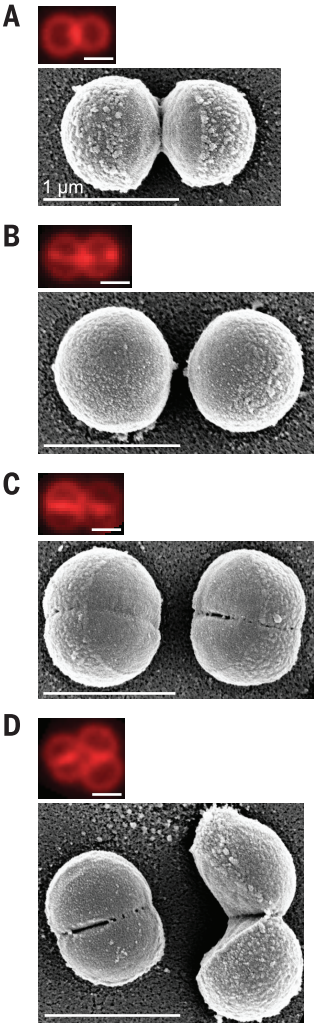

Fig. 4. Correlative SEM reveals cell cycle–dependent early signs of mechanical fracture. (**A** to **D**) Representative correlative fluorescence (top) and SEM images (bottom) of *S. aureus* Newman cells stained with FM 4-64, showing the cell surface features at different stages of the cell cycle. Ninety-eight percent (n = 54 cells) of the cells with visible holes [blind analysis (supplementary materials, materials and methods)] had completed septa, whereas only 49% (n = 108 cells) of the cells with completed septa had holes.

peripheral ring was mostly due to the high circumferential stress (Fig. 3B, supplementary text 2, and fig. S8) resulting from differential growth of the peripheral ring compared with the rest of the cell wall. The axial stress, which results mainly from turgor pressure (fig. S9), is actually lower in the peripheral ring than elsewhere (Fig. 3B). Modeling a series of intermediate stages throughout the growth and division cycle that includes the growth of the septum resulted in an increase in the overall cell aspect ratio during growth (movie S6), which is similar to our experimental observations (Fig. 2B).

Last, we examined the cell surface closely with high-resolution SEM in order to search for potential features of mechanical failure or fracture, and we noticed structures in a subpopulation of cells that appeared to be perforation-like holes and cracks along the peripheral ring. Similar structures have been observed with atomic force microscopy on hydrated live cells (*23*). To determine whether the appearance of these structures was cell-cycle dependent, we correlated SEM with fluorescence microscopy on FM 4-64–stained cells. The holes and cracks were observed mostly on cells at later stages in the cell cycle with completed septa (Fig. 4, A to D). Specifically, 53 out of 54 cells with visible holes had completed septa (98%), whereas only 53 of 108 cells with completed septa had holes (49%), suggesting that the holes are formed after the septum is completed. Enrichment of WGA binding at the peripheral ring region was also observed when holes were present (fig. S10), suggesting that these holes are true structural changes permitting access of large proteins through the wall that are excluded at earlier stages. These perforations are likely points of mechanical failure that could initiate a propagating crack. Although the axial stress necessary for circumferential crack propagation is relatively low at the peripheral ring, the presence of perforations will lead to locally high stresses at the tips of the cracks (*24*) that could be sufficient to drive propagation. Consistent with this hypothesis, the distribution of the perforation lengths observed with SEM featured a cutoff length so that most perforations were <40 nm in size, which may correspond to the critical length above which cracks propagate (fig. S11A).

One candidate for creating these perforations is the enzymatic activity of cell-wall hydrolases that include Atl. Atl is the major autolysin in *S. aureus* and has been shown to localize at the peripheral ring region before daughter-cell separation (*25*, *26*). In addition, *atl* null mutant cells form large clusters, indicating the involvement of this hydrolase in daughter cell separation (*27*). However, we found that the Δ*atl* mutant still forms perforations at the peripheral ring and pops with a similar millisecond time scale as that of the wild type (fig. S12) but remains associated longer after popping, giving rise to the characteristic clustering phenotype, in which individual cells in the large clusters are nearly normal sizes and shapes. It remains possible that other cell-wall hydrolases are responsible for generating the perforations we observe. However, another interesting possibility is that the perforations themselves have a mechanical origin. Given that the peripheral ring is under high circumferential stress and that the distribution of spacings between the perforations is distinctly peaked, indicating some periodicity to their locations (fig. S11B), it is plausible that perforations could form because of periodic thinning and necking of the peripheral ring under tension (supplementary text 3), a phenomenon of plastic instability observed for expanding ductile rings (*28*, *29*).

We have described a new model for the *S. aureus* cell cycle (fig. S14) in which cell growth happens continuously throughout the cycle, and the final resolution of the peripheral ring connecting the two daughter cells happens within a few milliseconds, with characteristics of mechanical crack propagation. It appears that this crack propagation is initiated by the perforations formed in the peripheral ring, which may result from a combination of mechanical stress and hydrolase activities, and is driven by axial wall stress originating from turgor pressure to propagate around the peripheral ring and complete daughter-cell separation. The previous outer wall of the mother cell is still partially connected immediately after cell separation, giving rise to the hinge-like off-center attachment between daughter cells. This off-center attachment has been noted before (*11*, *30*) and could explain the irregular cluster shape of *Staphylococcus* despite the fact that successive divisions occur in alternating perpendicular planes (*11*, *31*, *32*). The mechanical crack propagation-driven model for *S. aureus* daughter-cell separation described here demonstrates how a biological system with appropriate geometrical design can use mechanical forces to achieve large-scale morphological changes.

REFERENCES AND NOTES

1. L. J. Wu, J. Errington, *Nat. Rev. Microbiol.* **10**, 8–12 (2012).
2. A. Typas, M. Banzhaf, C. A. Gross, W. Vollmer, *Nat. Rev. Microbiol.* **10**, 123–136 (2012).
3. T. J. Foster, *Nat. Rev. Microbiol.* **3**, 948–958 (2005).
4. H. de Lencastre, D. Oliveira, A. Tomasz, *Curr. Opin. Microbiol.* **10**, 428–435 (2007).
5. M. G. Pinho, M. Kjos, J. W. Veening, *Nat. Rev. Microbiol.* **11**, 601–614 (2013).
6. R. D. Turner, W. Vollmer, S. J. Foster, *Mol. Microbiol.* **91**, 862–874 (2014).
7. V. R. Matias, T. J. Beveridge, *Mol. Microbiol.* **64**, 195–206 (2007).
8. S. J. Seligman, M. R. Pincus, *J. Theor. Biol.* **124**, 275–292 (1987).
9. V. R. Matias, T. J. Beveridge, *J. Bacteriol.* **188**, 1011–1021 (2006).
10. E. P. Previc, *J. Theor. Biol.* **27**, 471–497 (1970).
11. H. Tzagoloff, R. Novick, *J. Bacteriol.* **129**, 343–350 (1977).
12. A. J. Egan, W. Vollmer, *Ann. N. Y. Acad. Sci.* **1277**, 8–28 (2013).
13. J. M. Skotheim, L. Mahadevan, *Science* **308**, 1308–1310 (2005).
14. T. Baumberger, C. Caroli, D. Martina, *Nat. Mater.* **5**, 552–555 (2006).
15. T. Baumberger, O. Ronsin, *J. Chem. Phys.* **130**, 061102 (2009).
16. A. A. Griffith, *Philos. Trans. R. Soc. Lond., A Contain. Pap. Math. Phys. Character* **221**, 163–198 (1921).
17. E. H. Dill, in *Continuum Mechanics: Elasticity, Plasticity, Viscoelasticity* (CRC Press, Boca Raton, FL, 2007), pp. 239–251.
18. E. Rojas, J. A. Theriot, K. C. Huang, *Proc. Natl. Acad. Sci. U.S.A.* **111**, 7807–7812 (2014).
19. M. Wagner, *Immunobiology* **156**, 57–64 (1979).
20. M. G. Pinho, J. Errington, *Mol. Microbiol.* **50**, 871–881 (2003).
21. R. D. Turner *et al.*, *Nat. Commun.* **1**, 1 (2010).
22. M. Godin *et al.*, *Nat. Methods* **7**, 387–390 (2010).
23. A. Touhami, M. H. Jericho, T. J. Beveridge, *J. Bacteriol.* **186**, 3286–3295 (2004).
24. J. Schijve, *Fatigue of Structures and Materials* (Springer, New York, ed. 2, 2009).
25. S. Yamada *et al.*, *J. Bacteriol.* **178**, 1565–1571 (1996).
26. T. Baba, O. Schneewind, *EMBO J.* **17**, 4639–4646 (1998).
27. M. Sugai *et al.*, *J. Bacteriol.* **177**, 1491–1496 (1995).
28. J. M. Walsh, *J. Appl. Phys.* **56**, 1997–2006 (1984).
29. F. Zhou, J. F. Molinari, K. T. Ramesh, *Int. J. Impact Eng.* **33**, 880–891 (2006).
30. K. Amako, A. Umeda, *J. Ultrastruct. Res.* **58**, 34–40 (1977).
31. T. Koyama, M. Yamada, M. Matsuhashi, *J. Bacteriol.* **129**, 1518–1523 (1977).

ACKNOWLEDGMENTS

We thank P. A. Levin for strain Newman; A. Cheung for RN6390Δ*spa*; W. M. Nauseef for plasmid pCM29; J. Bose and K. W. Bayles for UAMS-1 and UAMS-1 Δ*atl*; J. Mulholland and L. Joubert in the Cell Sciences Imaging Facility at Stanford for technical assistance with 3D SIM (funded by National Center for Research Resources award number 1S10OD01227601) and SEM; S. Lou and L. Harris for help with the blind SEM analysis; M. Pinho, F. Chang, and L. Cegelski for discussions; and J. Shaevitz, D. Fisher, L. Harris, and the anonymous reviewers for helpful comments on the manuscript. X.Z. was supported by a Stanford Interdisciplinary Graduate Fellowship; D.K.H. was supported by the Stanford Cell and Molecular Biology Training Grant (T32-GM007276); E.R.R. was supported by a Distinguished Postdoctoral Fellowship from the Simbios NIH Center for Biomedical Computation (U54-GM072970); E.F.K. was supported by the James S. McDonnell Foundation Postdoctoral Fellowship Award in Studying Complex Systems; T.K.L. was supported by a Siebel Scholars Graduate Fellowship and an NIH Biotechnology Training Grant; K.C.H. was funded by a NIH Director's New Innovator Award (DP2OD006466); and J.A.T. was funded by HHMI, the National Institute of Allergy and Infectious Diseases (R01-AI36929) and the Stanford Center for Systems Biology (P50-GM107615).

SUPPLEMENTARY MATERIALS

www.sciencemag.org/content/348/6234/574/suppl/DC1
Materials and Methods
Supplementary Text
Figs. S1 to S14
Table S1
References (*32*–*36*)
Movies S1 to S7

27 October 2014; accepted 25 March 2015
10.1126/science.aaa1511

PROTEIN DYNAMICS

Direct observation of hierarchical protein dynamics

Józef R. Lewandowski,[1]*† Meghan E. Halse,[1]‡ Martin Blackledge,[2]* Lyndon Emsley[1,3]*

One of the fundamental challenges of physical biology is to understand the relationship between protein dynamics and function. At physiological temperatures, functional motions arise from the complex interplay of thermal motions of proteins and their environments. Here, we determine the hierarchy in the protein conformational energy landscape that underlies these motions, based on a series of temperature-dependent magic-angle spinning multinuclear nuclear-magnetic-resonance relaxation measurements in a hydrated nanocrystalline protein. The results support strong coupling between protein and solvent dynamics above 160 kelvin, with fast solvent motions, slow protein side-chain motions, and fast protein backbone motions being activated consecutively. Low activation energy, small-amplitude local motions dominate at low temperatures, with larger-amplitude, anisotropic, and functionally relevant motions involving entire peptide units becoming dominant at temperatures above 220 kelvin.

Proteins must traverse complex conformational energy landscapes to perform their physiological function. This is achieved through thermally activated fluctuations (*1*), and when specific molecular motions cease at low temperatures, function also ceases or becomes reduced (*2*, *3*). Understanding the hierarchy of these motions thus holds the key to understanding how proteins function on a molecular level at physiological temperatures. Contrary to expectations, and despite large differences in structure and function between proteins of different families, dynamic properties appear to exhibit common general features, in particular apparent transitions between different dynamic regimes as a function of temperature. These transitions are thought to occur as a result of coupling between proteins and the surrounding solvent (*4*).

Observing and understanding protein dynamic transitions has been a focus of many fields of research over the past 40 years, including neutron scattering (*5*), Mössbauer spectroscopy (*4*, *6*), Terahertz spectroscopy (*7*), dielectric spectroscopy (*4*), differential scanning calorimetry (*8*), x-ray crystallography (*2*, *9*), and molecular dynamics simulation (*10*, *11*). This relative wealth of information has not, however, led to a consensus picture of dynamical transitions and their origins, with different techniques detecting distinct processes, leading to apparently contradictory descriptions (*12*, *13*). This may be due to the widely varying conditions required for the diverse techniques or to the sensitivity of the different physical measurements to dynamics occurring on different time scales.

Here we measure, in a single sample, a set of 13 different nuclear magnetic resonance (NMR) observables that are sensitive to dynamics occurring on different time scales and in different parts of the system over temperatures from 105 to 280 K in the fully hydrated crystalline protein GB1, a small globular protein specifically binding to antibodies. The analysis of multiple probes that report on the different structural components of this complex system allows us to develop a complete and coherent picture of the dynamic processes across the whole temperature range, as

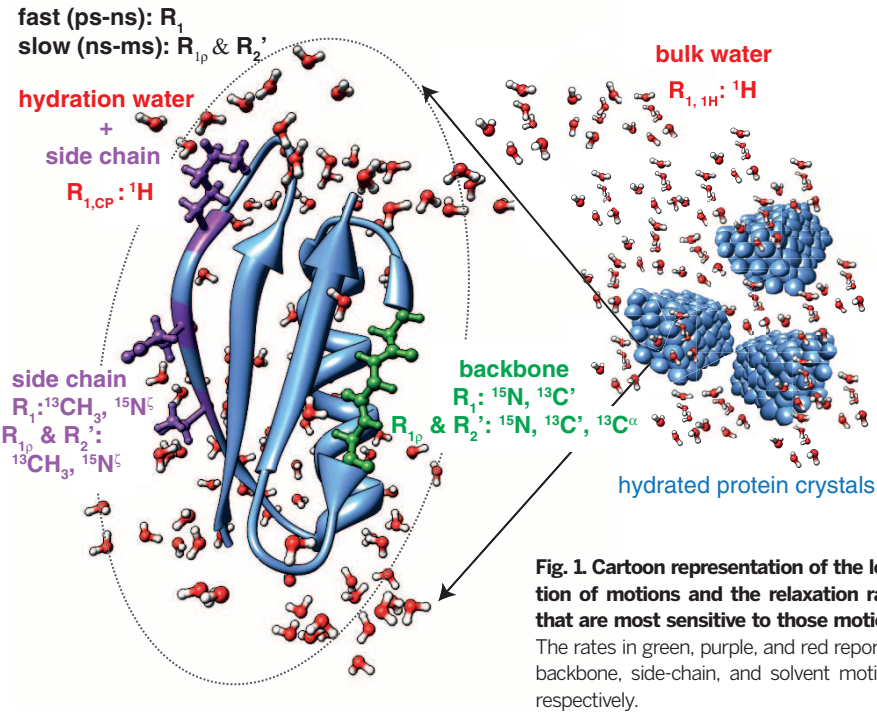

Fig. 1. Cartoon representation of the location of motions and the relaxation rates that are most sensitive to those motions. The rates in green, purple, and red report on backbone, side-chain, and solvent motions, respectively.

[1]Université de Lyon, Institut de Sciences Analytiques (CNRS/ENS-Lyon/UCB-Lyon 1), Centre de Résonance Magnétique Nucléaire à Très Hauts Champs, 69100 Villeurbanne, France. [2]Université Grenoble Alpes, Institut de Biologie Structurale (IBS), F-38044 Grenoble, France; CNRS, IBS, F-38044 Grenoble, France; CEA, IBS, F-38044 Grenoble, France. [3]Institut des Sciences et Ingénierie Chimiques, Ecole Polytechnique Fédérale de Lausanne (EPFL), CH-1015 Lausanne, Switzerland.
***Corresponding author. E-mail: j.r.lewandowski@warwick.ac.uk (J.R.L.); martin.blackledge@ibs.fr (M.B.); lyndon.emsley@epfl.ch (L.E.)** †Present address: Department of Chemistry, University of Warwick, Coventry CV4 7AL, UK. ‡Present address: Department of Chemistry, University of York, York YO10 5DD, UK.

well as to rationalize previous observations from other techniques. Our findings support strong coupling between protein and solvent dynamics above 160 K, with motions in the solvent, protein backbone, and side-chain being activated as temperature increases. The generally observed dynamic transitions are found to report on thermal activation of processes concerning different components of the system, with higher activation energies enabling anisotropic, functionally important backbone motions, coupled to side-chain and solvent motions, becoming dominant above 220 K.

As illustrated in Fig. 1, the key to generating this complete picture is the measurement of different ^{1}H, ^{13}C, and ^{15}N relaxation rates (*14*) from a single sample. This allows us to determine different dominant rotational motional modes that affect bulk solvent, hydration water, protein side chains, and protein backbone in a site-specific manner. Analysis of longitudinal (R_1) and transverse ($R_{1\rho}$ and R_2') relaxation rates identifies changes in picosecond-nanosecond and nanosecond-millisecond motions (see Fig. 1).

Figure 2 shows experimentally determined longitudinal relaxation rates from backbone, side chain, and solvent as a function of temperature. Transverse relaxation rates are presented in Fig. 3. A similar pattern is seen in all cases. As temperature increases, abrupt changes in the experimental relaxation rates are observed, suggesting that different motions dominate the measured relaxation within distinct temperature ranges. The origin of this behavior was analyzed by fitting the measured ^{1}H, ^{15}N, and ^{13}C relaxation rates to a sum of Arrhenius terms (see Materials and Methods in the supplementary materials), describing the superposition of distinct motional processes with different activation energies (Figs. 2 and 3 and tables S3 and S4). Each individual process is fitted with three parameters: the activation energy E_a (Figs. 2F and 3F and table S2), the characteristic time scale, and a constant that accounts for the amplitude of the relaxation active interaction associated with this process (and a constant term accounting for coherent contributions to transverse relaxation rates). The expressions for relaxation rates are based on Redfield theory, the validity of which in the concerned regime has been discussed previously (*15*). We assume a constant amplitude motion throughout each range, which although physically unrealistic, provides an effective amplitude reporting on a broad mean.

Remarkably, the measured rates can be accurately reproduced over the whole temperature range by invoking one to three (typically two) distinct motional processes. The apparent transitions with respect to temperature report on thermal activation of new motional modes, which rapidly become dominant for relaxation rates measured above the transition temperature.

Based on the changes in the observed trends for longitudinal and transverse relaxation rates in Figs. 2 and 3, we are able to identify three key transitions: TI at ~195 K, above which transverse relaxation reports on slow motions dominated by a mode with E_a > 20 kJ/mol; TII at ~220 K, above which longitudinal relaxation reports on fast motions dominated by a mode with E_a ~30 kJ/mol; and TIII at ~250 K, above which faster side-chain motions with E_a ~30 kJ/mol dominate longitudinal methyl relaxation.

The observation of TI to TIII dynamic boundaries is dependent on the location of the "spy" nuclei—i.e., whether specific relaxation rates probe solvent, protein side-chain, or protein backbone motions. ^{1}H relaxation rates report on both bulk solvent and hydration water and detect dynamical transitions for fast motions at two out of three transition temperatures (TI and TII).

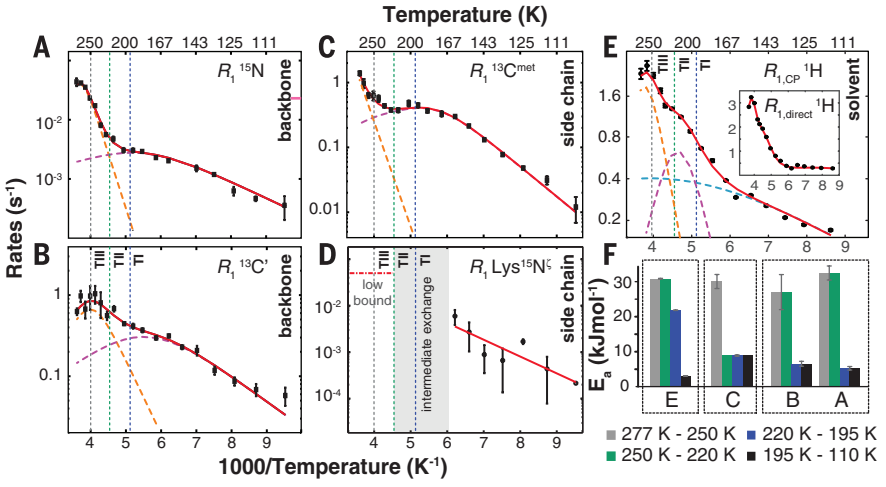

Fig. 2. Measured bulk longitudinal relaxation rates in hydrated nanocrystalline [U-^{13}C,^{15}N]GB1 as a function of temperature. Rates in (**A** to **E**) (points with error bars reflecting fitting uncertainties) are sensitive to picosecond-nanosecond motions of protein backbone [(A) and (B)], side chain [(C) to (E)], and solvent (E). Lines of best-fit over the entire temperature range are shown in red. Two components for protein motions and three components for solvent motions were justified statistically [P < 0.05 compared with a single (and two) component model]. The individual components with distinct E_a obtained from a global fit over each type of nucleus are indicated with dashed lines. The E_a for the components dominating the relaxation rates in different temperature ranges in (A) to (E) are shown in (**F**). The dynamic transitions TI, TII, and TIII, identified as the temperature where a higher activation energy mode becomes dominant, are shown by vertical dotted lines.

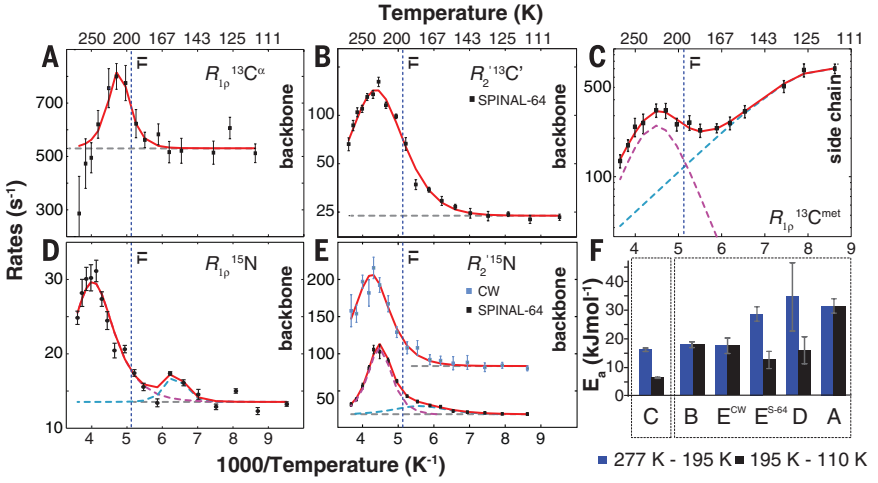

Fig. 3. Bulk transverse relaxation measurements in hydrated nanocrystalline [U-^{13}C,^{15}N]GB1 as a function of temperature. (**A** to **E**) Transverse relaxation rates (points with error bars reflecting fitting uncertainties) report on nanosecond-millisecond motions of protein backbone [(A) (B), (D), and (E)] and side chain (**F**). Lines of best-fit over the entire temperature range are shown in red. Two components were justified statistically (P < 0.05 compared with a single component model) for backbone ^{15}N R_2' and methyl side chain. Components with distinct average activation energies obtained from a global fit over all temperatures are indicated with dashed lines. The offset accounting for coherent contributions is shown as a horizontal gray dashed line. E_a for components dominating the relaxation rates in different temperature ranges in panels (A) to (E) are shown in (F). The dynamic transition TI (195 K), identified as the temperature at which a higher activation energy mode becomes dominant, is shown by a vertical dotted line.

Hydrophobic protein side chains, observed through methyl groups, show a clear fast-motional transition at TIII. For hydrophilic protein side chains—represented by lysine side chains—170 K and TII delineate an intermediate exchange regime, where the resonances are not observed in the spectra. ^{15}N and $^{13}C'$ R_1 rates detect a major transition in fast backbone dynamics at TIII. Finally, TI seems to involve slow motions of both protein side chain and backbone but is more pronounced for the side chains.

^{15}N relaxation rates can be used to quantitatively determine motional amplitudes (see supplementary text S4), thereby providing a physical link between the activation energies and amplitudes of motions. Estimation of the median amplitude ($1\text{-}S^2$) associated with the two backbone dynamic regimes probed by ^{15}N longitudinal relaxation (Fig. 2A) reveals a significantly higher amplitude (0.012) for the high-E_a component than for the low-E_a component (0.0008). Remarkably, the amplitude of the high-E_a component is consistent with S^2 values extrapolated from temperature-dependent solution state studies of GB1 (*16*, *17*). This mode can therefore be assigned to the anisotropic backbone fluctuations commonly measured at room temperature in solution and solid-state proteins.

The comparison of the observed dynamical transitions at different locations of the protein-solvent system, and the associated changes in the average activation energies for the dominant motional modes, provide (together with findings from other studies in the literature) the coherent picture for the dynamic transitions in protein behavior summarized in Fig. 4.

In the region below 160 K, translations and rotations of solvent molecules are arrested (*8*) and protein motions are decoupled from the dynamics of the solvent, as evidenced by large differences in the activation energies for the dominant motional modes of solvent and protein (Fig. 2F). In this regime, fast motions involving fluctuations of atoms in side chains in local energy wells (e.g., three-site hops for methyl groups) are dominant (*18*), with the available thermal energy being insufficient to sample different side-chain rotameric states. Backbone conformations are frozen in a quasicontinuum of noninterchanging substates, unambiguously identifying the origin of the broadening of protein NMR signals at low temperatures (supplementary text S11). The amplitude of motions within these states is very small but increases gradually, concomitant with dynamics getting faster, as temperature increases from 110 to 160 K.

Solvent rotations, which become active at ~160 K (*8*) and dominate solvent relaxation rates above TI (~195 K), allow side chains to access different rotameric states (*19*). This has an especially dramatic effect on hydrophilic side chains (probed by lysines), which are affected by the forming and breaking of hydrogen bonds to fluctuating solvent molecules (resulting in a chemical exchange process leading to the disappearance of the lysine resonances from the spectra). The side-chain motions that become dominant above TI, and which are characterized by higher E_a values compared with the local rotations, are slow in nature and thus detected by transverse relaxation only (Fig. 3F). At TI, backbone motions with higher activation energies are also detected by transverse relaxation, but the transition from low E_a to high E_a motions is less pronounced than for side chains.

At TII (~220 K), larger-amplitude, nanosecond time scale anisotropic backbone peptide motions (*20*), with substantially increased activation energies, become the dominant source of longitudinal relaxation. These motions are accompanied by the unfreezing of hydration water at TII (~220 K), corresponding to the onset of translational diffusion of the solvent (*21*). The observed motions represent the dominant modes that are pervasive at physiological temperatures, providing access to rare conformational jumps sampling different regions of Ramachandran space and functionally important conformational rearrangements. The higher E_a associated with motions that become dominant above TII (~220 K) very likely reports on more collective modes, involving at least entire peptide planes, or possibly multiple amino acids, as was suggested in the case of myoglobin (*9*, *10*). We note that correlated motions traversing the entire β sheet of protein GB1, culminating in larger-amplitude excursions of the hydrogen bonding moieties that form the interaction interface with the physiological partner Fab, were observed with correlation times in the nanosecond to microsecond range at 298 K (*20*, *22*, *23*). At room temperature, nanosecond motions dominate both longitudinal and transverse relaxation processes in crystalline GB1 (*22*). The very similar range of activation energies for dominant backbone and solvent motions in this range suggests strong coupling of these modes above TII (~220 K). The observed sequence of motional mode activations strongly suggests a correlation between low-E_a and high-E_a motions, supporting the idea that at room temperature, fast motions facilitate slow motions.

Finally, larger-amplitude fast side-chain motions start visibly contributing to relaxation around TII and become dominant at TIII (~250 K). Notably, these motions are characterized by an E_a very similar to the E_a for the fast solvent and backbone motions in this regime (E_a ~ 30 kJ/mol), providing further evidence for strong coupling between protein and solvent motions at physiological temperatures, as well as the large-scale nature of these motions extending over several moieties.

Our observations reconcile divergent interpretations from techniques that are individually sensitive to dynamic phenomena occurring on different time scales and at different locations in protein-solvent systems (supplementary text S6 to S10). The average activation energies for the dominant motional modes determined here compare very well to those determined from a wide variety of experimental techniques and provide insight into their physical origin. The findings from other approaches, which support our conclusions, are presented in the supplementary materials.

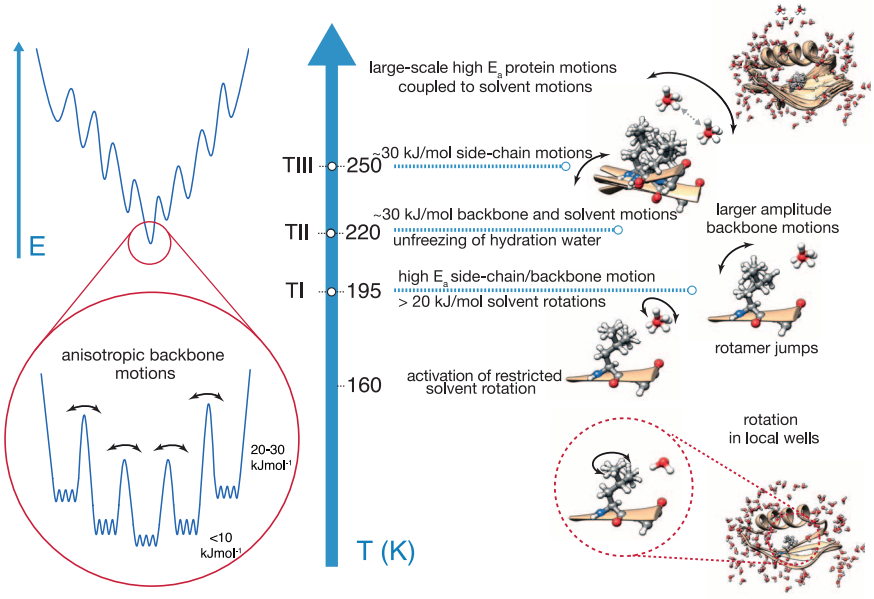

Fig. 4. Summary of hierarchical dynamic behavior of the protein-solvent system as observed by solid-state NMR in a microcrystalline globular protein GB1. The approximate temperature for the transitions between dominant dynamic modes is indicated on the blue axis. The image in the top right corner represents an ensemble extracted from a 200-ns molecular dynamics simulation in a crystalline environment (*24*). The left panel presents a simplified representation of the link between small- and larger-amplitude backbone motional modes. At low temperatures, the protein backbone is constrained to small-amplitude modes separated by low-energy barriers, within substates separated by high barriers. As temperature increases, these modes are dynamically sampled, enabling larger-amplitude anisotropic modes.

In summary, simultaneous measurement of the temperature dependence of 13 different spin relaxation probes reporting on dynamic modes distributed throughout the solvated microcrystalline protein allows for a unified description of the essential conformational energy surface, relating the amplitude and activation of solvent, sidechain, and backbone motions in a hierarchical distribution, as well as unambiguous identification of NMR line broadening at cryogenic temperatures.

REFERENCES AND NOTES

1. H. Frauenfelder, S. G. Sligar, P. G. Wolynes, *Science* **254**, 1598–1603 (1991).
2. B. F. Rasmussen, A. M. Stock, D. Ringe, G. A. Petsko, *Nature* **357**, 423–424 (1992).
3. R. M. Daniel *et al.*, *Biophys. J.* **75**, 2504–2507 (1998).
4. H. Frauenfelder *et al.*, *Proc. Natl. Acad. Sci. U.S.A.* **106**, 5129–5134 (2009).
5. W. Doster, S. Cusack, W. Petry, *Nature* **337**, 754–756 (1989).
6. F. Parak, H. Formanek, *Acta Crystallogr. A* **27**, 573–578 (1971).
7. J. R. Knab, J. Y. Chen, Y. F. He, A. G. Markelz, *Proc. IEEE* **95**, 1605–1610 (2007).
8. H. Jansson, R. Bergman, J. Swenson, *J. Phys. Chem. B* **115**, 4099–4109 (2011).
9. M. Weik, J. P. Colletier, *Acta Crystallogr. D Biol. Crystallogr.* **66**, 437–446 (2010).
10. D. Vitkup, D. Ringe, G. A. Petsko, M. Karplus, *Nat. Struct. Biol.* **7**, 34–38 (2000).
11. M. Tarek, D. J. Tobias, *Phys. Rev. Lett.* **88**, 138101 (2002).
12. W. Doster, *Eur. Biophys. J. Biophy.* **37**, 591–602 (2008).
13. P. W. Fenimore *et al.*, *Chem. Phys.* **424**, 2–6 (2013).
14. J. R. Lewandowski, *Acc. Chem. Res.* **46**, 2018–2027 (2013).
15. N. Giraud *et al.*, *J. Am. Chem. Soc.* **127**, 18190–18201 (2005).
16. D. Idiyatullin, I. Nesmelova, V. A. Daragan, K. H. Mayo, *J. Mol. Biol.* **325**, 149–162 (2003).
17. M. J. Seewald *et al.*, *Protein Sci.* **9**, 1177–1193 (2000).
18. E. R. Andrew, R. Gaspar, W. Venart, *Biopolymers* **17**, 1913–1925 (1978).
19. A. L. Lee, A. J. Wand, *Nature* **411**, 501–504 (2001).
20. G. Bouvignies *et al.*, *Proc. Natl. Acad. Sci. U.S.A.* **102**, 13885–13890 (2005).
21. K. Wood *et al.*, *J. Am. Chem. Soc.* **130**, 4586–4587 (2008).
22. J. R. Lewandowski, H. J. J. Sass, S. Grzesiek, M. Blackledge, L. Emsley, *J. Am. Chem. Soc.* **133**, 16762–16765 (2011).
23. P. R. L. Markwick, G. Bouvignies, M. Blackledge, *J. Am. Chem. Soc.* **129**, 4724–4730 (2007).
24. L. Mollica *et al.*, *J. Phys. Chem. Lett.* **3**, 3657–3662 (2012).

ACKNOWLEDGMENTS

We thank S. Grzesiek and H. J. Sass for providing [U-^{13}C,^{15}N]GB1. We acknowledge support from Agence Nationale de la Recherche (ANR PCV 2007 Protein Motion, ComplexDynamics ANR Blanc 2012 SIMI7), the Access to Research Infrastructures Activity in the Seventh Framework Program of the European Commission (BioNMR 261863), and Swiss National Science Foundation grant 31-132857. J.R.L. acknowledges support from the European Union International Reintegration Grant (PIRG03-GA-2008-231026) and startup funds from University of Warwick. All data used to support conclusions in this manuscript are provided in the supplementary materials.

SUPPLEMENTARY MATERIALS

www.sciencemag.org/content/348/6234/578/suppl/DC1
Materials and Methods
Supplementary Text
Figs. S1 to S6
Tables S1 to S4
References (*25*–*79*)

5 January 2015; accepted 24 March 2015
10.1126/science.aaa6111

STRUCTURAL BIOLOGY

Structures of the CRISPR-Cmr complex reveal mode of RNA target positioning

David W. Taylor,[1,2]* Yifan Zhu,[3]* Raymond H. J. Staals,[3]† Jack E. Kornfeld,[1] Akeo Shinkai,[4,5] John van der Oost,[3] Eva Nogales,[1,2,6,7]‡ Jennifer A. Doudna[1,2,6,8,9]‡

Adaptive immunity in bacteria involves RNA-guided surveillance complexes that use CRISPR (clustered regularly interspaced short palindromic repeats)–associated (Cas) proteins together with CRISPR RNAs (crRNAs) to target invasive nucleic acids for degradation. Whereas type I and type II CRISPR-Cas surveillance complexes target double-stranded DNA, type III complexes target single-stranded RNA. Near-atomic resolution cryo–electron microscopy reconstructions of native type III Cmr (CRISPR RAMP module) complexes in the absence and presence of target RNA reveal a helical protein arrangement that positions the crRNA for substrate binding. Thumblike β hairpins intercalate between segments of duplexed crRNA:target RNA to facilitate cleavage of the target at 6-nucleotide intervals. The Cmr complex is architecturally similar to the type I CRISPR-Cascade complex, suggesting divergent evolution of these immune systems from a common ancestor.

Bacteria and archaea defend themselves against infection using adaptive immune systems comprising CRISPR (clustered regularly interspaced short palindromic repeats) arrays and CRISPR-associated (Cas) genes (*1*). A defining feature of CRISPR-Cas systems is the use of Cas proteins in complex with small CRISPR RNAs (crRNAs) to identify and cleave complementary target sequences in foreign DNA (*2*, *3*). Whereas type I and type II CRISPR–Cas systems recognize target sequences in double-helical DNA that is locally unwound to enable DNA target strand cleavage (*4*, *5*), type III systems bind and cleave single-stranded RNA target sequences (*6*, *7*).

The effector complex of the type III system from *Thermus thermophilus* (Cmr) is a 12-subunit assembly composed of six Cmr subunits (Cmr1–6) and a crRNA with a stoichiometry of $Cmr1_2 2_1 3_1 4_4 5_3 6_1$:$crRNA_1$ (*7*). The Cmr complex binds to target RNA that is complementary to the bound 40- or 46-nucleotide (nt) crRNA and cleaves the target at 6-nt intervals measured from the 5′ end of the crRNA sequence (*7*, *8*). Although structural studies revealed an overall capsule-like architecture of the Cmr complex (*7*), the molecular basis of subunit assembly, crRNA binding, and single-stranded RNA (ssRNA) target recognition and cleavage by the intact surveillance complex remains unknown.

We performed cryo–electron microscopy (cryo-EM) of the intact ~350-kD Cmr complex in the absence and presence of target ssRNA. We purified endogenous apo-Cmr (containing a crRNA) and used this sample for stepwise assembly with a 56-nt biotinylated ssRNA target followed by purification using streptavidin affinity chromatography. Cryo-EM micrographs of frozen-hydrated samples of both apo-Cmr and target-bound Cmr showed monodisperse particles with wormlike features (fig. S1). Using Leginon (*9*), we acquired ~7000 and ~4000 micrographs and automatically picked ~700,000 and ~300,000 apo- and target-bound Cmr particles, respectively (*10*). After three-dimensional (3D) classification and single-particle reconstruction (supplementary materials and methods) (*11*), we obtained structures of intact apo-Cmr and target-bound Cmr at ~4.1 and 4.4 Å resolution (figs. S1 and S2) from a final set of 250,000 and 175,000 particles, respectively. Additionally, we obtained the structure of a smaller apo-Cmr species revealed during our 3D classification at ~4.4 Å resolution from a second class of ~100,000 particles.

The structure of intact apo-Cmr resembles a capsule in which a central, double-helical core of four Cmr4 subunits and three Cmr5 subunits is capped by a Cmr2–Cmr3 heterodimer at one end and Cmr1–Cmr6 at the other (Fig. 1A). The 5′-handle of the crRNA, an invariant sequence derived from the repeat, is held in the Cmr2–Cmr3 heterodimer. An α-helical bundle within Cmr2 makes extensive contacts with the bottom Cmr5

[1]Howard Hughes Medical Institute, University of California, Berkeley, CA 94720, USA. [2]California Institute for Quantitative Biosciences, University of California, Berkeley, CA 94720, USA. [3]Laboratory of Microbiology, Department of Agrotechnology and Food Sciences, Wageningen University, 6703 HB Wageningen, Netherlands. [4]RIKEN SPring-8 Center, Hyogo 679-5148, Japan. [5]RIKEN Structural Biology Laboratory, Kanagawa 230-0045, Japan. [6]Department of Molecular and Cell Biology, University of California, Berkeley, CA 94720, USA. [7]Life Sciences Division, Lawrence Berkeley National Laboratory, Berkeley, CA 94720, USA. [8]Department of Chemistry, University of California, Berkeley, CA 94720, USA. [9]Physical Biosciences Division, Lawrence Berkeley National Laboratory, Berkeley, CA 94720, USA.
*These authors contributed equally to this work. †Present address: Department of Microbiology and Immunology, University of Otago, Post Office Box 56, Dunedin 9054, New Zealand. **‡Corresponding author. E-mail: doudna@berkeley.edu (J.A.D.); enogales@lbl.gov (E.N.)**

geometry in their interactions with substrate sequences, leading to a lack of continuous double-helix formation between guide RNA and target strands. That RecA employs similar discontiguous DNA-DNA interactions for homology searches (*18*) hints at a common mode of substrate recognition among genome surveillance complexes. Although type II CRISPR-Cas9-RNA-ssDNA crystal structures contain a canonical crRNA-DNA helix (*19*, *20*), crRNA could form a discontinuous helix with one strand of dsDNA targets during sequence interrogation, consistent with tolerance of large 5′ end extensions on the crRNA (*21*). In the related type III CRISPR-Csm complex, discontinuous helix formation might occur during association with topologically constrained R loops formed during transcription (*22*).

REFERENCES AND NOTES

1. B. Wiedenheft, S. H. Sternberg, J. A. Doudna, *Nature* **482**, 331–338 (2012).
2. R. Barrangou *et al.*, *Science* **315**, 1709–1712 (2007).
3. S. J. Brouns *et al.*, *Science* **321**, 960–964 (2008).
4. M. M. Jore *et al.*, *Nat. Struct. Mol. Biol.* **18**, 529–536 (2011).
5. M. Jinek *et al.*, *Science* **337**, 816–821 (2012).
6. C. R. Hale *et al.*, *Cell* **139**, 945–956 (2009).
7. R. H. Staals *et al.*, *Mol. Cell* **52**, 135–145 (2013).
8. C. R. Hale, A. Cocozaki, H. Li, R. M. Terns, M. P. Terns, *Genes Dev.* **28**, 2432–2443 (2014).
9. C. Suloway *et al.*, *J. Struct. Biol.* **151**, 41–60 (2005).
10. G. C. Lander *et al.*, *J. Struct. Biol.* **166**, 95–102 (2009).
11. S. H. Scheres, *J. Struct. Biol.* **180**, 519–530 (2012).
12. R. N. Jackson *et al.*, *Science* **345**, 1473–1479 (2014).
13. S. Mulepati, A. Héroux, S. Bailey, *Science* **345**, 1479–1484 (2014).
14. C. Benda *et al.*, *Mol. Cell* **56**, 43–54 (2014).
15. F. DiMaio, M. D. Tyka, M. L. Baker, W. Chiu, D. Baker, *J. Mol. Biol.* **392**, 181–190 (2009).
16. B. Wiedenheft *et al.*, *Nature* **477**, 486–489 (2011).
17. M. L. Hochstrasser *et al.*, *Proc. Natl. Acad. Sci. U.S.A.* **111**, 6618–6623 (2014).
18. Z. Chen, H. Yang, N. P. Pavletich, *Nature* **453**, 489–4 (2008).
19. C. Anders, O. Niewoehner, A. Duerst, M. Jinek, *Nature* **513**, 569–573 (2014).
20. H. Nishimasu *et al.*, *Cell* **156**, 935–949 (2014).
21. O. W. Ryan *et al.*, *eLife* **3**, e03703 (2014).
22. G. W. Goldberg, W. Jiang, D. Bikard, L. A. Marraffini, *Nature* **514**, 633–637 (2014).

ACKNOWLEDGMENTS

The structures of intact apo-Cmr, smaller apo-Cmr, and target-bound Cmr have been deposited into the EMDataBank with accession codes EMD-2898, EMD-2899, and EMD-2900, respectively. We thank R. Louder, S. Howes, E. Kellogg, R. Zhang, P. Grob, Y. He, T. Houweling, Z. Yu, and M. J. de la Cruz for expert electron microscopy assistance. D.W.T is a Damon Runyon Fellow supported by the Damon Runyon Cancer Research Foundation (DRG-2218-15). R.H.J.S. was supported by the University of Otago's Division of Health Sciences Career Development postdoctoral fellowship. Y.Z. and J.v.d.O. received financial support from the Netherlands Organisation for Scientific Research (NWO), via a Gravitation grant to the Soehngen Institute for Anaerobic Microbiology (024.002.002) and an ALW-TOP project (854.10.003), respectively. This work was supported in part by Japan Society for the Promotion of Science KAKENHI grant 25440013 (to A.S.). J.A.D and E.N. are Howard Hughes Medical Institute Investigators. The *T. thermophilus* Cmr complex and *T. thermophilus* strain–producing Cmr6-His protein are available from A.S. under a material transfer agreement with RIKEN.

SUPPLEMENTARY MATERIALS

www.sciencemag.org/content/348/6234/581/suppl/DC1
Materials and methods
Figs. S1 to S3
Table S1
Movies S1 to S3
References (*23*–*29*)

9 December 2014; accepted 11 March 2015
Published online 2 April 2015;
10.1126/science.aaa4535

RETROTRANSPOSONS

An RNA polymerase III subunit determines sites of retrotransposon integration

Antoine Bridier-Nahmias,[1,2]* Aurélie Tchalikian-Cosson,[1]* Joshua A. Baller,[3,4] Rachid Menouni,[1] Hélène Fayol,[1] Amando Flores,[5]† Ali Saïb,[1,2] Michel Werner,[5] Daniel F. Voytas,[3] Pascale Lesage[1]‡

Mobile genetic elements are ubiquitous. Their integration site influences genome stability and gene expression. The Ty1 retrotransposon of the yeast *Saccharomyces cerevisiae* integrates upstream of RNA polymerase III (Pol III)–transcribed genes, yet the primary determinant of target specificity has remained elusive. Here we describe an interaction between Ty1 integrase and the AC40 subunit of Pol III and demonstrate that AC40 is the predominant determinant targeting Ty1 integration upstream of Pol III–transcribed genes. Lack of an integrase-AC40 interaction dramatically alters target site choice, leading to a redistribution of Ty1 insertions in the genome, mainly to chromosome ends. The mechanism of target specificity allows Ty1 to proliferate and yet minimizes genetic damage to its host.

A balance exists between the short-term detrimental effects of transposable elements as mutagens and the long-term, positive role they play as agents of genome plasticity and evolution (*1*). Integration site choice (ISC), important for this balance, is typically not random and often occurs in genomic regions where insertion is benign. For retrotransposons—that is, obligate genomic parasites—integration preferentially occurs in gene-poor regions, probably the consequence of selection for mechanisms that favor nondeleterious insertions. Ty1, the most active and abundant *Saccharomyces cerevisiae* long terminal repeat (LTR) retrotransposon, preferentially integrates within a 1-kb window upstream of polymerase III (Pol III)–transcribed genes (*2*). Ty1 targeting requires a functional Pol III promoter in the target gene (*2*–*4*) and is influenced by the chromatin-remodeling factor Isw2 and the Bdp1 subunit of TFIIIB (*5*, *6*). However, the primary determinant of Ty1 ISC and its contribution in protecting the genome from deleterious insertions is still unknown.

To identify Pol III protein interactors, we performed yeast two-hybrid screens using the 17 Pol III subunits as bait and a library of yeast DNA as prey. We identified a specific interaction between the AC40 subunit and a region of Ty1 that encompasses the C terminus of integrase (IN) and the N terminus of reverse transcriptase (Fig. 1A). The screen also recovered the same domain in Ty2 and Ty4, consistent with similar integration preferences for these three elements (*7*). Hemagglutinin (HA)–tagged AC40 (AC40-HA) coimmunoprecipitated IN when ectopically expressed, either as a streptavidine fusion (IN-Strep) (Fig. 1B) or from a functional Ty1 element (Fig. 1C) (see supplementary materials and methods).

The INs of several retrotransposons and retroviruses interact with a cellular DNA-bound protein to mediate ISC (*8*–*14*). Ty1 IN has two phylogenetically conserved regions [an N-terminal zinc-binding domain and a catalytic core with the $DDX_{35}E$ motif (D, Asp; X, any amino acid; E, Glu)] and a less-conserved C terminus containing a nuclear localization signal required for IN nuclear localization and efficient retrotransposition (Fig. 1A) (*15*, *16*). A two-hybrid assay confirmed the interaction between AC40 and full-length IN ($IN_{1\text{-}635}$) and revealed that the IN N terminus and catalytic core were dispensable ($IN_{193\text{-}635}$). The last C-terminal 57 amino acids were necessary and

[1]Université Paris Diderot, Sorbonne Paris Cité, INSERM U944, CNRS UMR 7212, Institut Universitaire d'Hématologie, Hôpital St. Louis, 75010 Paris, France. [2]Department CASER Conservatoire National des Arts et Métiers (Cnam), 75003 Paris, France. [3]Department of Genetics, Cell Biology and Development and Center for Genome Engineering, University of Minnesota, Minneapolis, MN 55455, USA. [4]Minnesota Supercomputing Institute, University of Minnesota, Minneapolis, MN 55455, USA. [5]IBiTec-S, Institut de Biologie Intégrative de la Cellule (I2BC), Commissariat à l'Energie Atomique et aux Energies Alternatives (CEA), CNRS, Université Paris-Sud, CP 22, CEA-Saclay, 91191 Gif-sur-Yvette, France.
*These authors contributed equally to this work. †Present address: Centro Andaluz de Biología del Desarrollo, Consejo Superior de Investigaciones Científicas/Universidad Pablo de Olavide, Seville, Spain. ‡Corresponding author. E-mail: pascale.lesage@inserm.fr

Downloaded from www.sciencemag.org on April 30, 2015

sufficient (Fig. 1A, IN_{1-578} versus $IN_{578-635}$), indicating that the Ty1 targeting domain is located at the IN C terminus.

Because AC40 is an essential protein, we addressed its role in Ty1 ISC using the *Schizosaccharomyces pombe rpc40*$^{+}$ ortholog of *RPC40*, which encodes AC40. The *S. pombe* AC40 (AC40sp) restored viability of *S. cerevisiae* cells lacking AC40 and sustained normal Pol III transcription (figs. S1 and S2) (*17*). However, Gal4 binding domain (GBD)–AC40sp, when expressed at levels similar to GBD-AC40, did not show two-hybrid interaction with Ty1 IN (Fig. 1A and fig. S1D), implying that AC40sp and Ty1 IN do not interact or do so very poorly. Therefore, AC40sp was used as a loss-of-interaction mutant. We first determined the role of AC40 in Ty1 integration at Pol III–transcribed genes by using a quantitative assay that relies on a *URA3* gene located upstream of the tRNA gene *tG(GCC)B*, a hotspot of Ty1 integration. In this assay, Ty1 insertions upstream of *tG(GCC)B* inactivate *URA3*, resulting in Ura^{-} cells that grow on 5FOA plates (see supplementary materials). Endogenous Ty1 retrotransposition was induced at 20°C, a temperature permissive for Ty1 retrotransposition, in *rpc40Δ* strains expressing AC40 or AC40sp at similar levels (fig. S1B). A ~3.5-fold decrease in the number of $5FOA^{R}$ colonies per cell was observed in the presence of AC40sp (Fig. 2A). The fraction of $5FOA^{R}$ cells

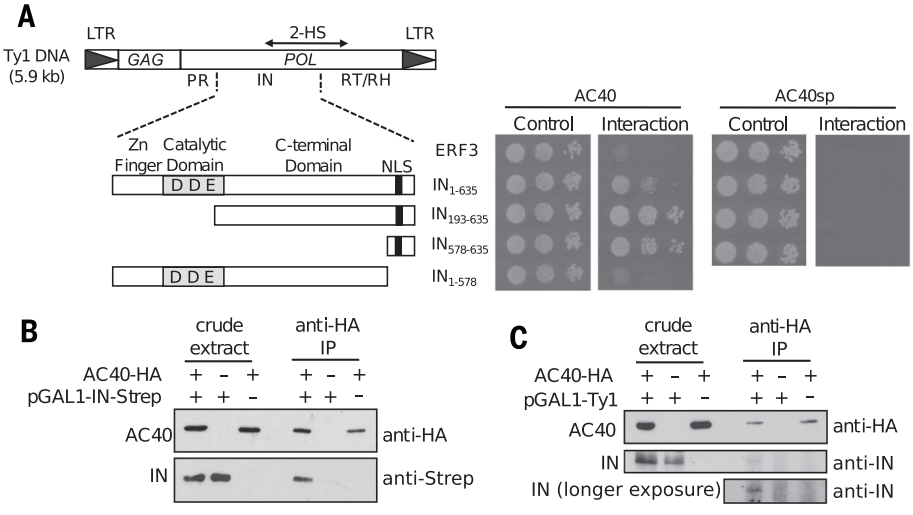

Fig. 1. Ty1 IN interacts with AC40 but not AC40sp. (**A**) Two-hybrid interaction between Ty1-IN and AC40 or AC40sp. (Left) Ty1 *GAG* and *POL* ORFs are flanked by two LTRs. PR, protease; IN, integrase; RT/RH, reverse transcriptase ribonuclease H. The two-headed arrow indicates Ty1 sequences recovered in the two-hybrid screen (2-HS) with AC40 as bait (coordinates 2706 to 4342 in Ty1-H3). Different Ty1-IN regions were fused to the Gal4 activation domain; AC40 or AC40sp were fused to the GBD. NLS, nuclear localization signal. (Right) Cells were plated onto nonselective (Control) or selective (Interaction) media to detect interactions. (**B**) Coimmunoprecipitation of AC40-HA and IN-Strep expressed from the *GAL1* galactose-inducible promoter. IP, immunoprecipitation. (**C**) Coimmunoprecipitation of AC40-HA and IN expressed from a galactose-inducible functional Ty1 element. Immunoprecipitation of protein extracts was performed with anti-HA magnetic beads coupled to immunoglobulin G. Proteins were revealed with 12CA5 anti-HA, anti-Strep, and 8B11 anti-IN antibodies.

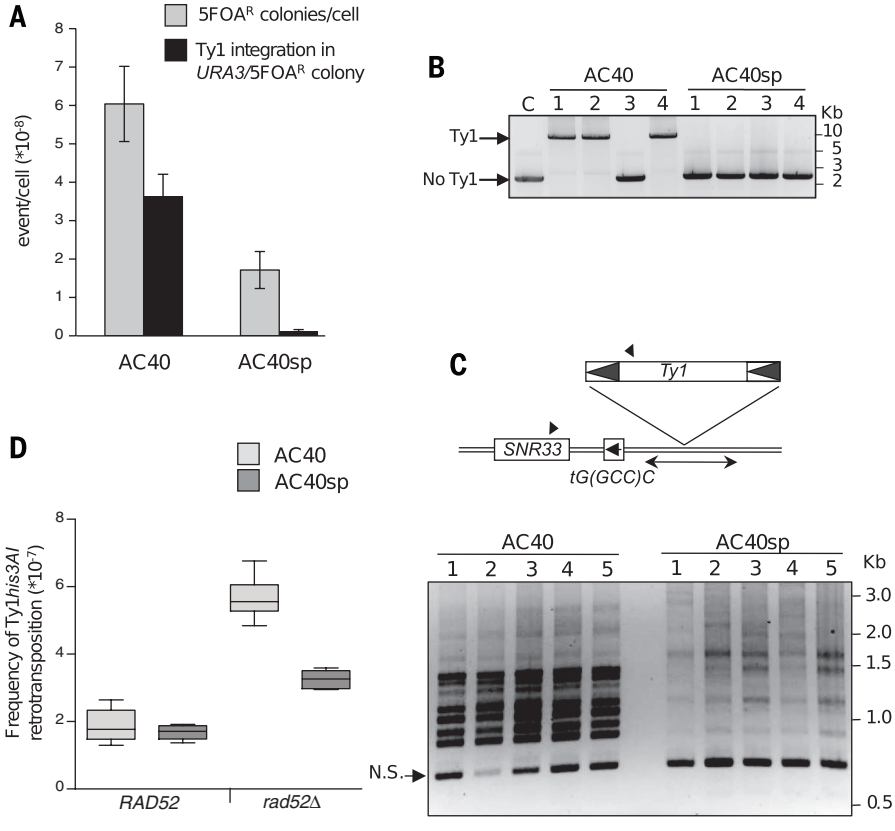

Fig. 2. The AC40-IN interaction is important for Ty1 targeting upstream of two tRNA genes but not for overall Ty1 mobility. (**A**) Ty1 integration into the *URA3-tG(GCC)B* locus. The histogram shows the average frequency of $5FOA^{R}$ colonies obtained from independent cultures at 20°C of strains expressing AC40 and AC40sp, respectively (gray bar), and of Ty1 insertions in *URA3*/$5FOA^{R}$ colonies identified by polymerase chain reaction (PCR) (black bars) with standard errors. (**B**) PCR analysis of $5FOA^{R}$ colonies obtained from the cultures in (A) to detect Ty1 insertions in *URA3*. Representative PCR results from four colonies per strain are shown. A 6-kb band indicates a Ty1 element; a 2.5-kb band indicates no insertion. The negative control (labeled "C") represents a strain grown at 30°C. (**C**) Detection of Ty1 insertions upstream of *tG(GCC)C* in five independent cultures at 20°C of AC40 and AC40sp strains, expressing Ty1 from the *GAL1* promoter. (Top) The *tG(GCC)C* locus and experimental design. PCR reactions were carried out with primers specific for *tG(GCC)C* and Ty1 (arrowheads). Ty1 insertion occurs with equal frequency in both orientations (*3*, *4*). (Bottom) Only insertion events in the opposite orientation to *tG(GCC)C* were analyzed by PCR. N.S., a nonspecific band corresponding to amplification of a fragment from adjacent Ty1 and Ty2 elements. (**D**) Frequency of Ty1*his3AI* retrotransposition. Box plots display data from six independent cultures of *RAD52* or *rad52Δ* strains expressing AC40 or AC40sp (number of His^{+} prototrophs divided by the total number of cells).

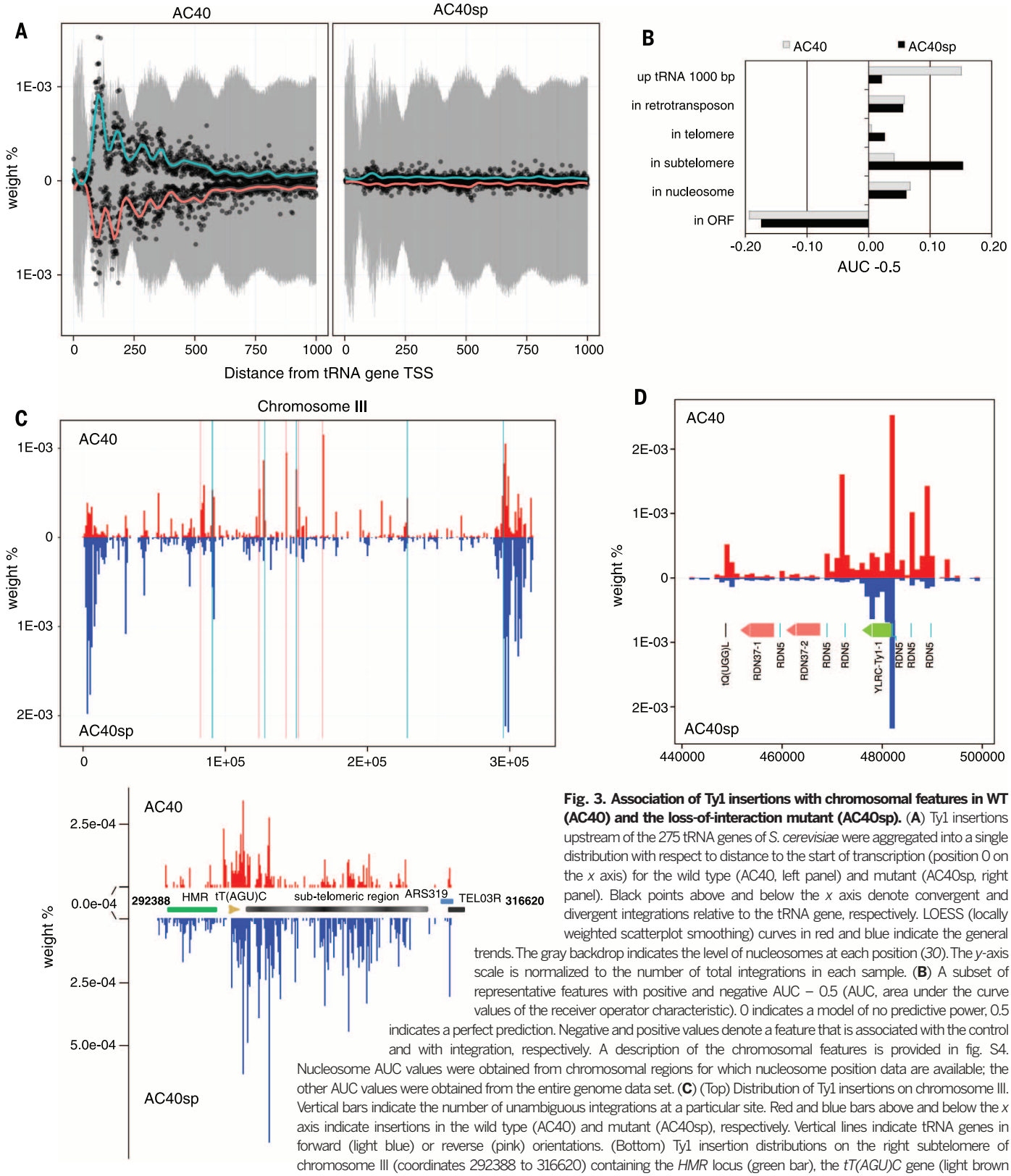

Fig. 3. Association of Ty1 insertions with chromosomal features in WT (AC40) and the loss-of-interaction mutant (AC40sp). (**A**) Ty1 insertions upstream of the 275 tRNA genes of *S. cerevisiae* were aggregated into a single distribution with respect to distance to the start of transcription (position 0 on the *x* axis) for the wild type (AC40, left panel) and mutant (AC40sp, right panel). Black points above and below the *x* axis denote convergent and divergent integrations relative to the tRNA gene, respectively. LOESS (locally weighted scatterplot smoothing) curves in red and blue indicate the general trends. The gray backdrop indicates the level of nucleosomes at each position (*30*). The *y*-axis scale is normalized to the number of total integrations in each sample. (**B**) A subset of representative features with positive and negative AUC – 0.5 (AUC, area under the curve values of the receiver operator characteristic). 0 indicates a model of no predictive power, 0.5 indicates a perfect prediction. Negative and positive values denote a feature that is associated with the control and with integration, respectively. A description of the chromosomal features is provided in fig. S4. Nucleosome AUC values were obtained from chromosomal regions for which nucleosome position data are available; the other AUC values were obtained from the entire genome data set. (**C**) (Top) Distribution of Ty1 insertions on chromosome III. Vertical bars indicate the number of unambiguous integrations at a particular site. Red and blue bars above and below the *x* axis indicate insertions in the wild type (AC40) and mutant (AC40sp), respectively. Vertical lines indicate tRNA genes in forward (light blue) or reverse (pink) orientations. (Bottom) Ty1 insertion distributions on the right subtelomere of chromosome III (coordinates 292388 to 316620) containing the *HMR* locus (green bar), the *tT(AGU)C* gene (light brown triangle), a large region with nonessential genes (gray bar), an autonomously replicating sequence (ARS) (blue bar), and the telomere TEL03R (black bar). The *x* axis denotes the position along the chromosome at 1000-bp (top) and 100-bp resolution (bottom). The *y*-axis scale shows the percentage of total integrations in the genome per bin. (**D**) Distribution of Ty1 insertions at the *RDN1* locus encoding ribosomal RNA genes. All Ty1 integrations occurring in 100 to 200 repeats are attributed to two repeats (*RDN37-1* and *RDN37-2*), leading to an apparent large peak of integration (see fig. S6, chromosome XII). The total number of integration events in this region was normalized to the expected number of repeats to correct for this effect. The *tQ(GUUC)L* gene, *RDN37-1* and *RDN37-2* repeats, Pol III–transcribed *RDN5* repeats, and *YLRCTy1-1* are depicted. The *x* axis denotes the position along the chromosome at 1000-bp resolution. Vertical red and blue bars and the *y* axis are as in (C).

arising from Ty1 integration in cells expressing AC40sp was ~30-fold lower than in AC40-expressing cells (Fig. 2, A and B). Therefore, AC40-IN interaction is crucial for Ty1 integration at this reporter gene.

We further demonstrated the role of AC40 in Ty1 ISC by analyzing unselected insertions at the tRNA gene *tG*(*GCC*)*C*, another Ty1 integration hotspot, in strains that express a galactose-inducible Ty1 element (Fig. 2C). In the presence of AC40, we observed a ~70–base pair (bp) periodic banding pattern characteristic of Ty1 insertion in nucleosomal DNA upstream of tRNA genes (*3*, *4*, *18*). In cultures expressing AC40sp, this pattern was dramatically altered, showing both a major decrease in Ty1 integration and an apparent relaxed periodicity between hotspots (Fig. 2C). The same alteration was observed in AC40sp-expressing cells for endogenous Ty1 elements (fig. S3). Hence, AC40-IN interaction is critical for Ty1 integration specificity upstream of Pol III–transcribed genes.

To establish whether Ty1 integration frequency depends on the AC40-IN interaction, we used a chromosomal Ty1 element marked with a *his3AI* reporter gene, which confers His^+ prototrophy to cells upon retrotransposition (see supplementary materials). Frequencies of His^+ cells generated in strains expressing AC40 or AC40sp were similar (Fig. 2D). In the loss-of-interaction mutant, an overrepresentation of Ty1*HIS3* insertions could be due to homologous recombination (HR) with endogenous elements (*19*). His^+ events were slightly higher in *rad52Δ* HR–deficient mutant cells, consistent with previous studies showing that although the Rad52 pathway contributes to Ty1 HR, it globally inhibits Ty1 retrotransposition (*20*). Notably, the frequency of IN-dependent integration was twofold lower in AC40sp cells compared with AC40 cells, suggesting that a higher proportion of Ty1 insertions might be due to recombination in the absence of interaction. However, this slight decrease cannot explain the dramatic effect observed on Ty1 integration at *URA3-tG*(*GCC*)*B*. Altogether, these results indicate that the AC40-IN interaction is required for the canonical Ty1 targeting pattern upstream of two representative tRNA genes, but the interaction does not influence integration efficiency. Therefore, the interaction with AC40 could function specifically to restrict Ty1 integration upstream of Pol III–transcribed genes to prevent potentially harmful insertions at secondary genomic targets.

We compared the genome-wide Ty1 integration patterns in the wild-type (WT) and AC40sp mutant strains. The WT strain exhibited a typical pattern at Pol III–transcribed genes (*3*, *4*), whereas the loss-of-interaction mutant displayed a fundamentally different profile with a slight bias toward integration near tRNA genes (Fig. 3A), probably due to residual interaction between IN and AC40sp. To determine whether other genomic features influence Ty1 ISC in the absence of the AC40-IN interaction, we used single (Fig. 3B) and multidimensional (fig. S4) logistic regression models to associate genomic features with integration hotspots. Ty1 insertions in the WT strain were associated with upstream regions of tRNA genes or features associated with these sites, such as preexisting retrotransposons (Fig. 3B and fig. S5). Regions with well-positioned nucleosomes were also favored and open reading frames (ORFs) avoided. In the AC40sp mutant, tRNA genes were no longer the primary targeting determinant but nucleosomes were still favored. Telomeres and subtelomeric regions of all chromosomes were also preferred targets in the WT and even more so in the mutant (Fig. 3, B and C, and figs. S5 and S6). Noteworthy, Ty5, a related yeast retrotransposon, also targets heterochromatin by specifically interacting with the heterochromatin protein Sir4 (*9*). Thus, an interaction between Ty1 IN and heterochromatin proteins could be involved in Ty1's secondary ISC.

We identified a direct interaction between Ty1 IN and the Pol III subunit AC40 that determines Ty1 ISC upstream of Pol III genes. Previous studies indicated that Ty1 integration requires a functional Pol III promoter, in agreement with our characterization of AC40 as a cofactor of Ty1 integration. The retroelements Ty3 of *S. cerevisiae* and TRE5-A of *Dictyostelium discoideum* also integrate at Pol III–transcribed genes, but their targeting involves an interaction with TFIIIB (*21*, *22*). AC40 is located at the periphery of the Pol III complex in close proximity to the upstream region (*23*), which may explain why Ty1 integrates mostly upstream of Pol III–transcribed genes and rarely downstream. Ty1 does not integrate near or into genes transcribed by Pol I, which also contain AC40 (Fig. 3D) (*3*, *4*). The AC40-IN interaction could require additional Pol III–specific cofactor(s). Notably, AC40 in Pol III is in close contact with TFIIIB (*24*), which contains Bdp1, a protein required for the Isw2-dependent periodic integration of Ty1 (*6*). This cofactor could participate directly or indirectly in the interaction. Ty1 integrates preferentially in nucleosomes, and Pol III promoters have a relatively open structure with well-organized nucleosomes (*25*, *26*) as opposed to Pol I genes, which are either actively transcribed or packed into a tight, repressive nucleosomal structure (*27*)—chromatin states that might disfavor Ty1 integration.

The Pol III transcription complex is regulated by nutrient and stress signaling pathways (*28*). As a result, Ty1 may potentially act as a mutagenic agent under conditions that affect AC40-IN interaction or Pol III transcription (fig. S7). Our work reveals that Ty1 also targets subtelomeres, especially in the absence of AC40-IN interaction. Yeast chromosome ends contain nonessential fast-evolving gene families generally needed to respond to environmental changes (*29*). Therefore, targeting Ty1 integration to subtelomeres could further protect the yeast genome from Ty1 mobility, while potentially promoting evolutionary adaptation and gene innovation in response to stress.

REFERENCES AND NOTES

1. H. L. Levin, J. V. Moran, *Nat. Rev. Genet.* **12**, 615–627 (2011).
2. S. E. Devine, J. D. Boeke, *Genes Dev.* **10**, 620–633 (1996).
3. J. A. Baller, J. Gao, R. Stamenova, M. J. Curcio, D. F. Voytas, *Genome Res.* **22**, 704–713 (2012).
4. L. Mularoni *et al.*, *Genome Res.* **22**, 693–703 (2012).
5. M. E. Gelbart, N. Bachman, J. Delrow, J. D. Boeke, T. Tsukiyama, *Genes Dev.* **19**, 942–954 (2005).
6. N. Bachman, M. E. Gelbart, T. Tsukiyama, J. D. Boeke, *Genes Dev.* **19**, 955–964 (2005).
7. J. M. Kim, S. Vanguri, J. D. Boeke, A. Gabriel, D. F. Voytas, *Genome Res.* **8**, 464–478 (1998).
8. J. Kirchner, C. M. Connolly, S. B. Sandmeyer, *Science* **267**, 1488–1491 (1995).
9. W. Xie *et al.*, *Mol. Cell. Biol.* **21**, 6606–6614 (2001).
10. Y.-E. E. Leem *et al.*, *Mol. Cell* **30**, 98–107 (2008).
11. A. Engelman, P. Cherepanov, *PLOS Pathog.* **4**, e1000046 (2008).
12. J. De Rijck *et al.*, *Cell Rep.* **5**, 886–894 (2013).
13. S. S. Gupta *et al.*, *J. Virol.* **87**, 12721–12736 (2013).
14. A. Sharma *et al.*, *Proc. Natl. Acad. Sci. U.S.A.* **110**, 12036–12041 (2013).
15. M. A. Kenna, C. B. Brachmann, S. E. Devine, J. D. Boeke, *Mol. Cell. Biol.* **18**, 1115–1124 (1998).
16. S. P. Moore, L. A. Rinckel, D. J. Garfinkel, *Mol. Cell. Biol.* **18**, 1105–1114 (1998).
17. G. V. Shpakovski, E. K. Shematorova, *Curr. Genet.* **36**, 208–214 (1999).
18. N. Bachman, Y. Eby, J. D. Boeke, *Genome Res.* **14**, 1232–1247 (2004).
19. G. Sharon, T. J. Burkett, D. J. Garfinkel, *Mol. Cell. Biol.* **14**, 6540–6551 (1994).
20. A. J. Rattray, B. K. Shafer, D. J. Garfinkel, *Genetics* **154**, 543–556 (2000).
21. L. Yieh, G. Kassavetis, E. P. Geiduschek, S. B. Sandmeyer, *J. Biol. Chem.* **275**, 29800–29807 (2000).
22. T. Chung, O. Siol, T. Dingermann, T. Winckler, *Mol. Cell. Biol.* **27**, 8492–8501 (2007).
23. C. Fernández-Tornero *et al.*, *Nature* **502**, 644–649 (2013).
24. A. Vannini, P. Cramer, *Mol. Cell* **45**, 439–446 (2012).
25. K. Brogaard, L. Xi, J.-P. Wang, J. Widom, *Nature* **486**, 496–501 (2012).
26. Y. Kumar, P. Bhargava, *BMC Genomics* **14**, 402 (2013).
27. K. Merz *et al.*, *Genes Dev.* **22**, 1190–1204 (2008).
28. R. D. Moir, I. M. Willis, *Biochim. Biophys. Acta* **1829**, 361–375 (2013).
29. C. A. Brown, A. W. Murray, K. J. Verstrepen, *Curr. Biol.* **20**, 895–903 (2010).
30. N. Kaplan *et al.*, *Nature* **458**, 362–366 (2009).

ACKNOWLEDGMENTS

We thank J. Boeke, S. Moore, and M. Riva for reagents; C. Conesa, J. Curcio, O. Lefèbvre, and members of the laboratory for stimulating discussions; M. Bazin, D. Davoine, M. Saunier, and M. Zitouni for contributions during their training; and E. Fabre, H. de Thé, and J. Recht for critical reading of the manuscript. This work was supported by CNRS, INSERM, Université Paris Diderot Sorbonne Paris Cité, Agence nationale de recherches sur le sida et les hépatites virales (grant AO 2008-01), Agence Nationale de la Recherche (grant 13-BSV3-0012-01), and the European Union through the FP7 project HIVINNOV (grant 305137). A.B.-N. was supported by a CNRS Ph.D. fellowship and a European Molecular Biology Organization Short-Term Fellowship (ASTF 17-2013) (to work in D.F.V.'s lab) and A.T.-C. by a Ph.D. fellowship from the Ministère de l'Enseignement Supérieur et de la Recherche.

SUPPLEMENTARY MATERIALS

www.sciencemag.org/content/348/6234/585/suppl/DC1
Materials and Methods
Figs. S1 to S7
Tables S1 and S2
References (*31*–*48*)

23 July 2014; accepted 11 March 2015
10.1126/science.1259114

IMMUNE TOLERANCE

Regulatory T cells generated early in life play a distinct role in maintaining self-tolerance

Siyoung Yang,[1,2]* Noriyuki Fujikado,[1]* Dmitriy Kolodin,[1] Christophe Benoist,[1,3]† Diane Mathis[1,3]†

Aire is an important regulator of immunological tolerance, operating in a minute subset of thymic stromal cells to induce transcripts encoding peptides that guide T cell selection. Expression of Aire during a perinatal age window is necessary and sufficient to prevent the multiorgan autoimmunity characteristic of Aire-deficient mice. We report that Aire promotes the perinatal generation of a distinct compartment of Foxp3$^+$CD4$^+$ regulatory T (T_{reg}) cells, which stably persists in adult mice. This population has a role in maintaining self-tolerance, a transcriptome and an activation profile distinguishable from those of T_{regs} produced in adults. Underlying the distinct T_{reg} populations are age-dependent, Aire-independent differences in the processing and presentation of thymic stromal-cell peptides, resulting in different T cell receptor repertoires. Our findings expand the notion of a developmentally layered immune system.

Individuals with APECED (autoimmune polyendocrinopathy–candidiasis–ectodermal dystrophy) have a mutation in the gene encoding Aire. Such individuals, and mice lacking Aire, develop multiorgan autoimmune disease. Aire promotes immunological tolerance by inducing, specifically in thymic medullary epithelial cells (MECs), a large repertoire of mRNA transcripts encoding proteins characteristic of differentiated cell types (peripheral-tissue antigens, PTAs), such as insulin or casein-α. Peptides derived from these proteins are displayed on major histocompatibility complex (MHC) molecules at the MEC surface. The MHC:PTA-peptide complexes negatively select thymocytes whose antigen (Ag) receptors (T cell receptors, TCRs) are engaged too avidly. In addition, MECs can positively select Foxp3$^+$CD4$^+$ regulatory T (T_{reg}) cells (*1*, *2*), at least some of them in an Aire-dependent manner (*3*, *4*). Cross-presentation of Aire-induced PTAs by thymic dendritic cells (DCs) also occurs and can promote either negative or positive selection (*4*, *5*). Aire's presence during the first few weeks of life is necessary and sufficient to guard against the autoimmune disease characteristic of *Aire*-knockout (KO) mice (*6*). We sought to uncover the root of this unexpected finding.

To compare the effectiveness of clonal deletion in perinatal and adult mice, we examined the thymus of young and old *Aire*-WT (wild-type) and *Aire*-KO animals expressing (i) membrane-bound ovalbumin driven by the rat insulin promoter (RIP-mOva), and thereby within MECs; and (ii) TCRs that recognize a peptide of ovalbumin presented by MHC-II molecules (OT-II) (*7*, *8*). In both perinatal and adult mice, Aire-dependent clonal deletion was readily evident (fig. S1).

As a first step in comparing the T_{reg} compartments, we enumerated Foxp3$^+$CD4$^+$ T cells in the thymus of progressively older *Aire*-WT and -KO mice (Fig. 1A and fig. S2A). Although a few T_{regs} were detected in the thymus of WT individuals 2 days after birth, a substantial population was evident only on day 4, and it gradually increased through day 35. KO mice showed a similar pattern of T_{reg} accumulation in the thymus, but their fractional representation was reduced relative to WT littermates through day 35, and their numbers until day 10. Results were similar in the periphery (fig. S2, A and B).

To address the relative importance of the T_{reg} compartments for the maintenance of immunological tolerance, we used a NOD.*Foxp3-DTR* system to deplete T_{regs} during the day 0 to 10 or day 35 to 45 age window and followed the mice until 15 weeks of age (or loss of ≥ 20% body weight). Depletion of T_{regs} during the 0- to 10-day window resulted in significant weight reduction by 16 days of age (even though T_{reg} numbers were normal by days 11 to 12) and ≥20% weight loss in all mice by 24 days (Fig. 1B). All individuals showed the multiorgan autoimmunity typical of *Aire*-KO mice on the NOD genetic background (Fig. 1B and fig. S3). In contrast, T_{reg} ablation during the 35- to 45-day window had no significant effect on either weight gain or survival, although there were some mild manifestations of autoimmunity in scattered individuals (figs. S3 and S4).

We next performed a complementation experiment to rule out the trivial explanation that perinatal mice are nonspecifically perturbed by the repeated injection of diphtheria toxin (DT). Addition of T_{regs} from 20-day-old T_{reg}-replete, but not T_{reg}-depleted, donors to recipients perinatally depleted of T_{regs} resulted in a marked improvement in the autoimmune manifestations (figs. S5 and S6). To confirm that the critical perinatally generated T_{reg} population was, indeed, Aire-dependent, we transferred T_{regs} isolated from 20-day-old *Aire*-WT or -KO mice into either T_{reg}-depleted (Fig. 1, C and D) or *Aire*-KO (fig. S7) perinates. For both types of recipient, only the perinatal T_{regs} from WT mice protected against development of the characteristic "Aire-less" autoimmune disease. Thus, Aire promotes the generation of T_{reg} cells during the perinatal age window. Mice lacking these cells phenocopy *Aire*-KO mice; exhibiting a spectrum of pathology that differs substantially from that of mice either constitutively lacking T_{regs} or depleted of them as adults (*9*–*11*).

An inducible T_{reg} lineage-tracer system (*12*) allowed us to explore the functional and phenotypic properties of perinatally generated T_{regs}. In NOD-backcrossed Foxp3$^{eGFP\text{-}Cre\text{-}ERT2}$xR26Y mice, all Foxp3$^+$CD4$^+$ cells express green fluorescent protein (GFP); treatment with tamoxifen turns on expression of yellow fluorescent protein (YFP) in the T_{regs} extant during drug coverage, rendering them GFP/YFP double-positive thereafter. We first used this system to examine the stability of T_{regs} made perinatally. Lineage-tracer mice were injected with tamoxifen from days 0 to 10 or 35 to 45, and their splenic T_{reg} compartment was analyzed 1 day, 1 week, or 8 weeks later (Fig. 2). The adult-tagged and perinate-tagged T_{reg} populations were both readily discernible the day after termination of tamoxifen, constituting about a quarter of the Foxp3$^+$CD4$^+$ compartment. For adult-tagged T_{regs}, this fraction remained similar throughout the period examined. In contrast, perinate-tagged T_{regs} dwindled to a minor component of the Foxp3$^+$CD4$^+$ compartment between 1 and 8 weeks after cessation of labeling. This reduction in fractional representation was a dilution effect as total T_{reg} numbers increased exponentially during this time. Indeed, the actual numbers of perinate-tagged T_{regs} were very stable over the 2 months examined.

The persistence of the tagged T_{reg} populations permitted us to address the functionality of perinatally generated T_{regs} by conducting a four-way comparison (as schematized in fig. S8A). Mice were treated with tamoxifen from 0 to 10 or 35 to 45 days and were then left unmanipulated until 60 days of age, at which time the GFP$^+$YFP$^+$ (tagged) T_{reg} and GFP$^+$YFP$^-$ (bulk) T_{reg} populations were sorted and transferred into newborn *Aire*-KO mice. According to all criteria evaluated, disease was not affected by the introduction of adult-tagged T_{regs} or control bulk T_{reg} population (Fig. 2, B to D, and fig. S8B). In contrast, an addition of perinate-tagged T_{regs} resulted in a substantial reversal of the typical *Aire*-KO pathology (but with substitution of the insulitis characteristic of classical NOD mice) (Fig. 2E and fig. S8B). These findings argue that the T_{reg} population generated perinatally has distinct functional properties that persist within the adult environment.

We also sorted GFP$^+$YFP$^+$ and GFP$^+$YFP$^-$ CD4$^+$ T cells from 8- to 10-week-old mice whose T_{regs}

[1]Division of Immunology, Department of Microbiology and Immunobiology, Harvard Medical School, Boston, MA 02115, USA. [2]Aging Intervention Research Center, Korea Research Institute of Bioscience and Biotechnology (KRIBB), 125 Gwahak-ro, Yuseong-gu, Daejeon, 305-806, South Korea. [3]Evergrande Center for Immunologic Diseases, Harvard Medical School and Brigham and Women's Hospital, Boston MA 02115, USA.
*These authors contributed equally to this work. †Corresponding author. E-mail: cbdm@hms.harvard.edu

Downloaded from www.sciencemag.org on April 30, 2015

had been labeled between 0 and 10 or 35 and 45 days after birth and analyzed their transcriptomes. Distinct sets of genes were either over- (pink) or underexpressed (green) in T_{reg} cells tagged perinatally versus the bulk T_{reg} population of the same mice, but were not differentially transcribed in mice whose T_{regs} were labeled as adults (Fig. 3A and table S1). Overlaying the standard T_{reg} signature on a volcano plot comparing the two labeled T_{reg} populations revealed an overrepresentation of T_{reg} "up" genes in perinate-tagged T_{regs} (Fig. 3B). Indeed, these T_{regs} performed better than the three comparator populations in a typical in vitro suppression assay (Fig. 3C), perhaps reflecting higher transcription of genes, such as *Fgl2*, *Ebi3*, *Pdcd1*, and *Icos* (table S1A), previously implicated in T_{reg} effector function (*13*–*16*). The perinate-tagged T_{reg} population was in a more activated state (Fig. 3D), which fit with its higher content of $CD44^{hi}CD62L^{lo}$ cells (Fig. 3E). It was also more proliferative, as indicated by fractions of EdU-incorporating and of $Ki67^{+}$ cells higher than those of the three comparator populations (Fig. 3F). Indeed, the top pathways overrepresented in perinate-tagged T_{regs} according to Gene-Set Enrichment Analysis (GSEA) were related to DNA replication and cell division (e.g., Fig. 3G). We confirmed the elevated expression of a number of functionally relevant genes at the protein level (Fig. 3H and fig. S9).

Lastly, we sought a molecular or cellular explanation for the distinct T_{reg} compartments generated in perinatal and adult mice. We first used a mixed fetal-liver:bone-marrow chimera approach to rule out the possibility that T cell precursors derived from fetal liver hematopoietic stem cells, which service the developing immune system for the first few weeks after birth (*17*), are predisposed to yield T_{regs} with particular properties, assessing both reconstitution efficiencies and gene-expression profiles (fig. S10).

To facilitate comparison of the repertoires of Aire-dependent PTA transcripts in perinatal and adult MECs, we generated Adig reporter mice, which express GFP under the dictates of *Aire* promoter and enhancer elements (*18*), on either an *Aire*-WT or -KO background. $GFP^{+}MHC\text{-}II^{hi}$ cells were isolated from thymic stroma of <3-day-old or 5-week-old animals, and gene-expression profiling was performed. The fraction of Aire $^{+}MHC\text{-}II^{hi}$ MECs and the Aire mean fluorescence intensity (MFI) were indistinguishable in mice of the two ages (fig. S11, A and B). The repertories of Aire-dependent MEC transcripts were also extremely similar (fig. S11C).

Next, we asked whether the similar repertoires of PTA transcripts might still yield distinct sets of MHC-presented peptides, owing to different Ag-processing and presentation machinery in mice of the two ages, which need not be Aire dependent. Transcripts encoding several molecules implicated in generating or regulating the repertoire of peptides bound to MHC-II or -I molecules were differentially expressed in perinatal

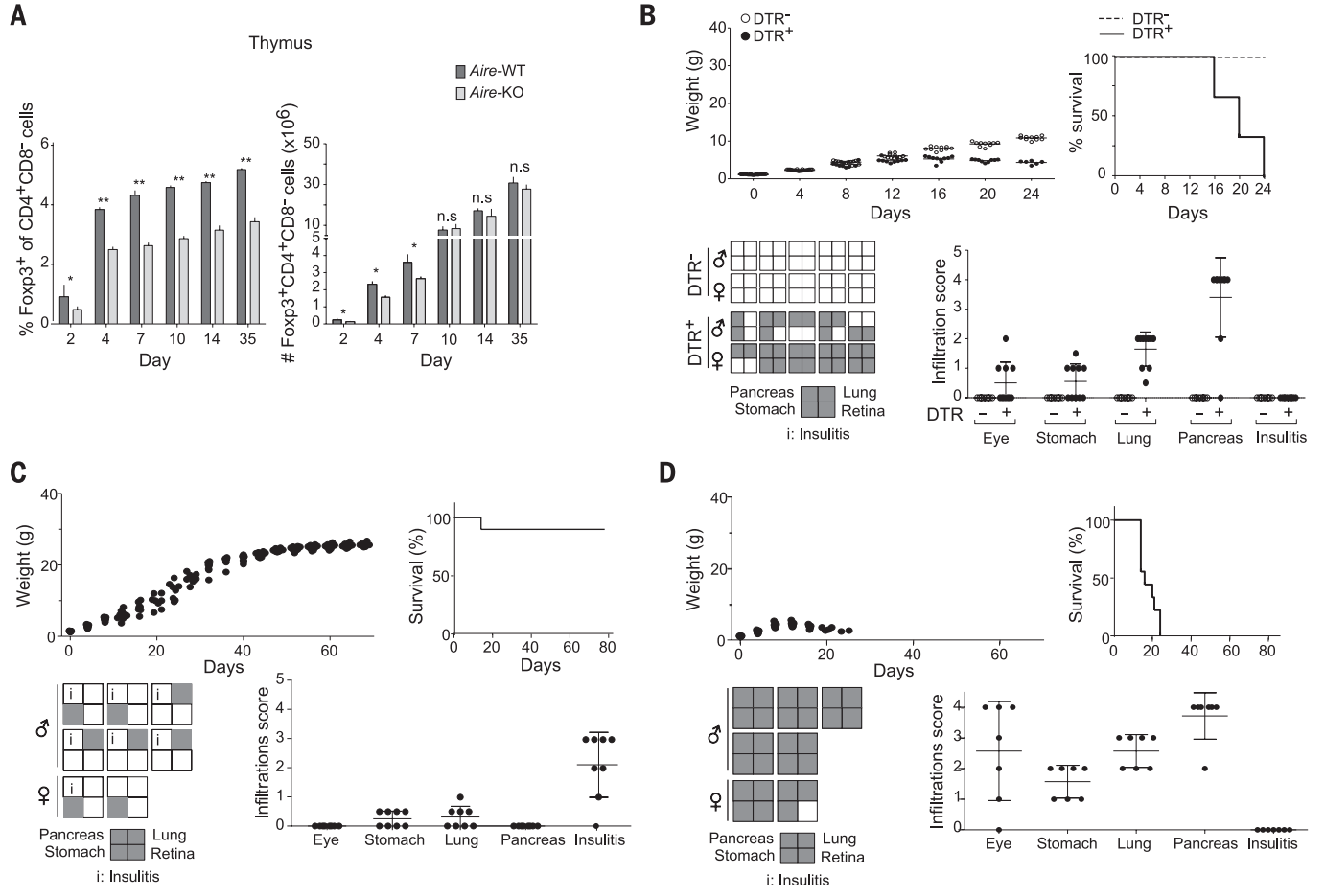

Fig. 1. A perinatal T_{reg} population that is Aire dependent and guards against the autoimmune manifestations typical of *Aire*-KO mice. (**A**) Summary data for fractional representation (left) and numbers (right) of $Foxp3^{+}CD4^{+}CD8^{-}$ thymocytes from *Aire*-WT or -KO mice of increasing age. $^{*}P \leq 0.05$, $^{**}P \leq 0.01$ (Student's *t* test); n.s, not significant; $n = 5$. Examples of corresponding dot-plots can be found in fig. S2A. (**B**) T_{reg} depletion in perinates. Perinatal (0.5 days after birth) NOD.*Foxp3-DTR*$^{+}$ mice or DTR^{-} littermates were treated every other day until day 10 with DT and then followed for manifestations of autoimmune disease. Perinates were examined <24 days after birth because of wasting in the DTR^{+} littermates. Upper left: weight curves. Upper right: survival curves; mice were killed if their weight fell to <20% of that of their DTR^{-} littermates. Lower left: presence (shaded) or absence of organ infiltrates; "i" indicates that insulitis replaced infiltration of the exocrine pancreas. Lower right: severity of organ infiltration (scored as indicated in the supplementary materials and methods). $n = 9$. (**C** and **D**) NOD.*Foxp3.DTR*$^{+}$ mice perinatally depleted of T_{regs} as in (B) were supplemented on days 12 and 19 with T_{regs} isolated from 20-day-old *Aire*-WT (C) or -KO (D) littermates. Cohorts were followed until 70 days of age. $n = 9$. The experimental setup was otherwise the same as in (B).

and adult MECs (Fig. 4A). The data on *H2-O* transcripts drew our attention because DO is known to inhibit the activity of DM, an "editor" needed for dislodging the invariant chain (CD74) derivative, CLIP, and other peptides from the Ag-binding groove of a maturing MHC-II molecule, enabling effective loading of a diverse repertoire of peptides (*19*, *20*). Transcripts encoding both DO chains were expressed at a significantly lower level in perinatal than in adult MECs, independently of Aire (Fig. 4B); perinatal MECs also had reduced amounts of intracellular DO complexes (Fig. 4C). In addition, they displayed higher intracellular amounts of DM complexes (Fig. 4E). Co-plotting intracellular amounts of the two complexes at the single-cell level revealed a subset of perinatal MECs with reduced DO and enhanced DM expression (Fig. 4F). A lower DO:DM ratio should promote more effective replacement of CLIP by other peptides. Indeed, a higher percentage of perinatal MECs displayed low amounts of or no CLIP (37.6 ± 6.4% versus 20.9 ± 2.2%), and the CLIP MFI was lower for perinatal MECs (761.7 ± 78.7%

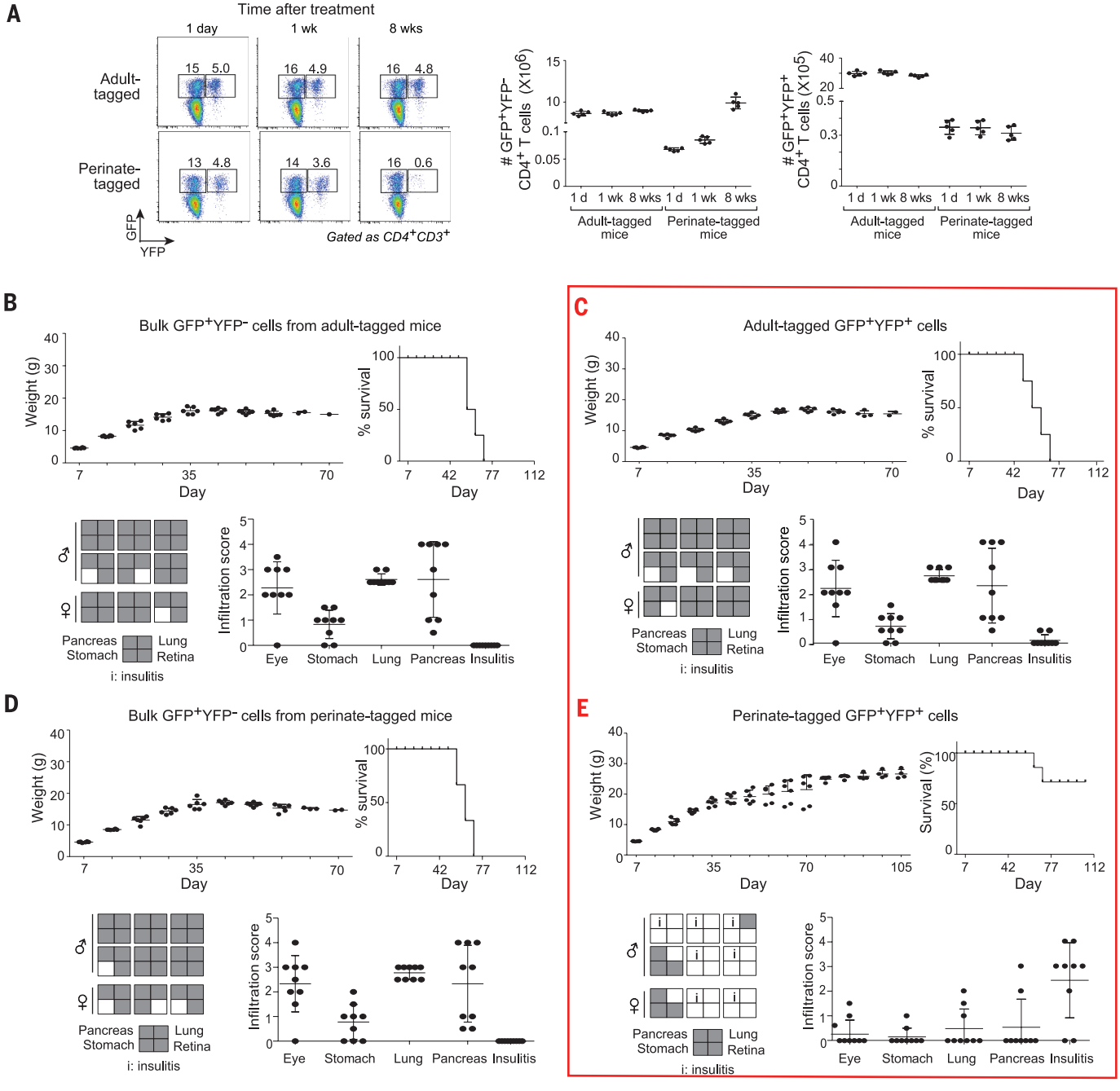

Fig. 2. Stability and function of perinate- versus adult-tagged T_{regs}. (**A**) Tamoxifen was administered from 0 to 10 or 35 to 45 days of age; at various times later, splenocytes were analyzed for GFP and YFP expression by flow cytometry. Left: representative flow-cytometric dot-plots. Numbers represent percentages of $CD4^+3^+$ cells in the designated gates. Center: summary data on numbers of GFP^+YFP^- bulk T_{regs}. Right: corresponding data on GFP^+YFP^+ perinate-tagged or adult-tagged T_{regs} from the same mice. $n = 5$. (**B** to **E**) T_{regs} (1.5×10^5) were transferred into *Aire*-KO mice on days 0.5, 3, and 7 after birth, and the recipients were monitored until 16 weeks of age. A four-way comparison as schematized in fig. S8A: GFP^+YFP^+ T_{regs} tagged from 35 to 45 days of age and isolated from a 60-day-old mouse (C), GFP^+YFP^- bulk T_{regs} from the same mouse (B), GFP^+YFP^+ T_{regs} tagged from 0 to 10 days of age and isolated from a 60-day-old mouse (E), and GFP^+YFP^- bulk T_{regs} from the same mouse (D). Data organized as in Fig. 1B. The key comparison is boxed.

versus 1019.0 ± 54%) (Fig. 4G). Thus, the repertoires of peptides presented by perinatal and adult MECs are different, the latter appearing to be more limited.

Aire-dependent PTAs can be "cross-presented" by myeloid-lineage cells in the vicinity (*4*, *5*), primarily MHC-II^{hi}CD8α^+ DCs (*4*). Interestingly, this cell type was present in strongly reduced amounts in thymi from perinatal mice (Fig. 4H). Because the splenic MHC-II^{hi}CD8α^+ DC subset showed an even more extreme age dependence, it is unlikely that this difference is Aire dependent.

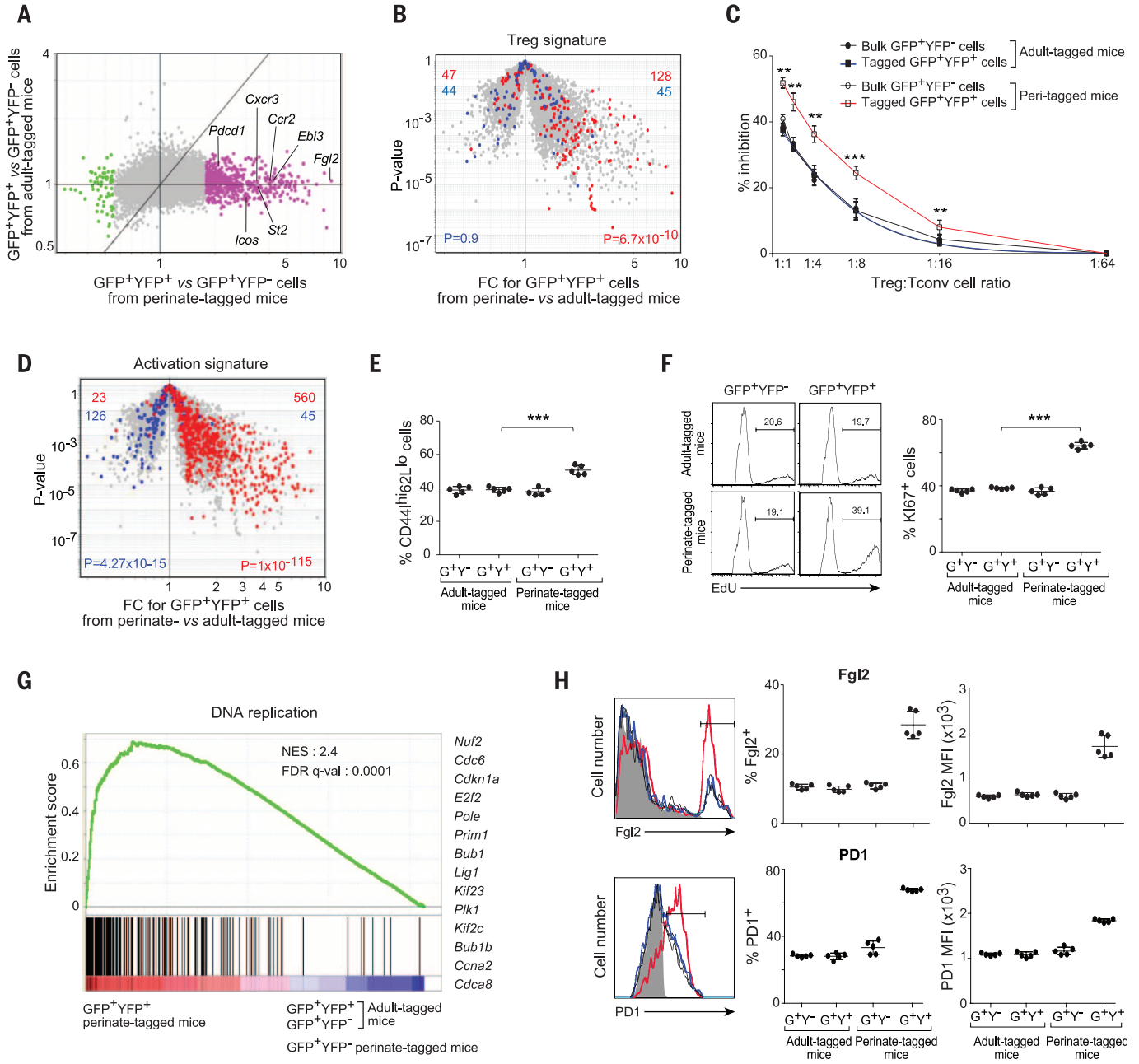

Fig. 3. A distinct transcriptome in perinate-tagged T_{regs}. The same type of four-way comparison used in Fig. 2 was performed except that the sorted cells were analyzed for diverse phenotypic features. (**A**) FC/FC plots comparing perinate-tagged GFP$^+$YFP$^+$ cells versus bulk GFP$^+$YFP$^-$ cells from the same mice (*x* axis) and adult-tagged GFP$^+$YFP$^+$ cells versus bulk GFP$^+$YFP$^-$ cells from the same mice (*y* axis). Pink dots denote transcripts overrepresented in perinate-tagged GFP$^+$YFP$^+$ cells; green dots indicate underrepresented transcripts. (**B**) *P*-value versus FC volcano plot comparing gene expression of perinate-tagged GFP$^+$YFP$^+$ and adult-tagged GFP$^+$YFP$^+$ cells. Red and blue dots indicate up- and down-regulated T_{reg} signature genes, respectively (*31*). *P*-values from the chi-squared test. (**C**) Classical in vitro suppression assay on the four sorted T_{reg} populations. $^{**}P \le 0.01$, $^{***}P \le 0.001$ (Student's *t* test). (**D**) Same volcano plot as in (B), except that up- (red) and down- (blue) regulated activation signature genes (*31*) are superimposed. (**E**) Summary data on late activation marker (CD44^{hi}CD62L^{lo}) expression in the four T_{reg} populations. $n = 5$. $^{***}P \le 0.001$ (Students' *t* test). (**F**) EdU uptake (left) and Ki67 expression (right) by the four T_{reg} populations. $^{***}P \le 0.001$. (**G**) GSEA of transcripts increased in the perinate-tagged GFP$^+$YFP$^+$ relative to the adult-tagged control T_{reg} populations. NES, normalized enrichment score. FDR q-val, false discovery rate. Representative transcripts showing increased expression are shown on the right. (**H**) Flow cytometric confirmation of gene overexpression in perinate-tagged T_{regs}. For Fgl2 and PD1: Left: representative flow-cytometric histograms; red, perinate-tagged; blue, adult-tagged; black, control bulk populations; gray shading, isotype-control antibody; bar indicates marker positivity. Center: summary data for percentage of the four T_{reg} populations expressing the marker; Right: summary data for marker MFI in the marker-positive population.

Such differences in the Ag processing and presentation machinery of MECs from perinatal and adult mice suggested that their T_{reg} TCR repertoires might diverge. We constrained the inventory of TCRs to be examined by using an approach that had proven fruitful in the past (*21*, *22*). BDC2.5 is a $V_\alpha1^+V_\beta4^+$ T helper cell specificity directed at a pancreatic Ag presented by A^{g7} molecules; hence, generation of T_{regs} in BDC2.5/NOD mice is dependent on rearrangement of an endogenous *Tcra* gene and thymic selection on the resulting second TCRαβ complexes. The fixed $V_\beta4^+$ chain constrains the TCR repertoire, and the analysis is further delimited by sorting individual cells expressing $V_\alpha2$. We sequenced 281 $V_\alpha2^+$ TCR CDR3 regions from splenic T_{regs} of three individual BDC2.5/NOD adults and another 232 from the corresponding population of three individual perinates. This restricted, but parallel, slice of the TCR repertoire was clearly different in the two age groups. Perinate T_{reg} TCRs

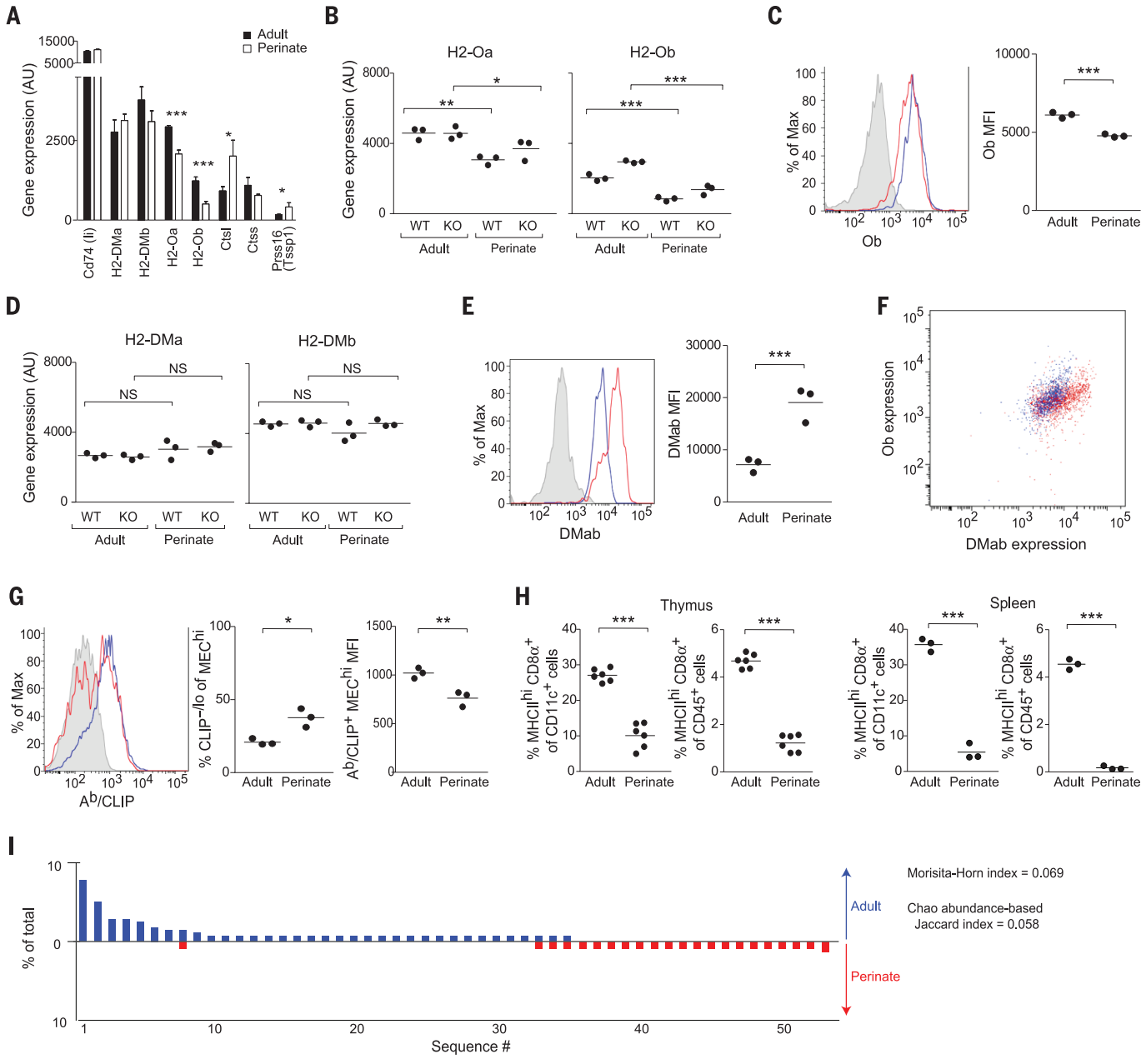

Fig. 4. Age-dependent, Aire-independent differences in the processing and presentation of MEC-generated peptides. (**A**) Microarray-based quantification of transcripts encoding a set of proteins involved in processing and presentation of MHCII-bound peptides. (**B**) Microarray-based quantification of DOa and DOb in MEC^{hi} from *Aire*-WT or -KO adults or perinates. (**C**) Intracellular expression of DOb protein. Left: representative flow-cytometric histograms. Red, perinate; blue, adult; gray shading, negative control staining. Right: summary MFI data. (**D** and **E**) Same as in (B) and (C) except that DMa and DMb were examined. (**F**) Coordinate intracellular staining of DOb and DMab. (**G**) Surface expression of Ab:CLIP complexes on MEC^{hi}. Left: representative flow-cytometric histograms. Red, perinate; blue, adult; gray shading, negative control staining. Center: summary data for percentage of MEC^{hi} expressing little or no CLIP. Right: summary data for MFI. (**H**) Flow cytometric quantification of $MHC^{hi}CD8\alpha^+$ DCs in perinatal versus adult thymus (left) and spleen (right). Summary data for representation in the $CD11c^+$ (left) and $CD45^+$ (right) compartments. (**I**) High-frequency $V\alpha2^+$ TCRs from 5-week-old (upper) and 4-day-old (lower) BDC2.5/NOD females. These sequences correspond to those in table S2. Bars represent frequency of each sequence. (A to H) $^*P < 0.05$, $^{**}P < 0.01$, $^{***}P < 0.001$ (Student's *t* test). $n = 3$ to 6.

were less clonally expanded (fig. S12A), had shorter CDR3α stretches (fig. S12B) and, as expected (*23*), had fewer *Tcra* N-region additions (fig. S12C). To permit a more statistically robust assessment, we focused on repeat sequences. There were many more repeated sequences in the adult mice, and very low values were obtained for both the Morisita-Horn index (0.069 on a scale from 0 to 1) and the Chao abundance-based Jaccard index (0.058 on a scale from 0 to 1), indicating that the two repertoires were very different (table S2 and Fig. 4I).

Thus, our data highlight Aire's ability to promote the generation of a distinct compartment of $Foxp3^+CD4^+$ T_{regs} as the explanation for its importance during the perinatal age window. Given the age-dependent differences in Ag processing machinery and presenting cells that we documented, juvenile and older mice are likely to have distinct repertoires of both Aire-dependent and Aire-independent T_{regs}, selected primarily on Ag:MHC complexes encountered on MECs. These findings add to, rather than negate, Aire's role in clonal deletion of self-reactive thymocytes, established in multiple experimental contexts (*4*, *5*, *24*, *25*).

There are notable similarities in the autoimmune diseases provoked by constitutive genetic ablation of *Aire*, thymectomy at 3 days of age, and perinatal depletion of Foxp3-expressing cells—in particular, the pattern of target tissues on different genetic backgrounds (*26*, *27*) (Fig. 1). Our studies yield a unifying explanation for these phenocopies: The perinatally generated, Aire-dependent T_{reg} compartment is particularly proficient at protecting a defined set of tissues from autoimmune attack, and there may be little overlap with the tissues guarded by adult T_{regs}. This notion is consistent with the observations that mice that underwent a thymectomy 3 days after birth exhibit multiorgan autoimmune disease but do not have a numerically diminished T_{reg} compartment when they get older (*28*, *29*), and that mice constitutively devoid of T_{regs} or inducibly depleted of them as adults show a very different spectrum of pathologies (*9*–*11*). Such a dichotomy could also explain why the autoimmune disease characteristic of both APECED patients and *Aire*-KO mice is restricted to such a limited set of tissues. An important implication of this dichotomy is that therapies based on transfer of T_{regs} isolated from adult donors may not be able to impact a particular subset of autoimmune diseases. Thus, our findings extend the notion of a "layered" immune system (*30*).

REFERENCES AND NOTES

1. K. Aschenbrenner *et al.*, *Nat. Immunol.* **8**, 351–358 (2007).
2. M. Hinterberger *et al.*, *Nat. Immunol.* **11**, 512–519 (2010).
3. S. Malchow *et al.*, *Science* **339**, 1219–1224 (2013).
4. J. S. Perry *et al.*, *Immunity* **41**, 414–426 (2014).
5. R. T. Taniguchi *et al.*, *Proc. Natl. Acad. Sci. U.S.A.* **109**, 7847–7852 (2012).
6. M. Guerau-de-Arellano, M. Martinic, C. Benoist, D. Mathis, *J. Exp. Med.* **206**, 1245–1252 (2009).
7. M. S. Anderson *et al.*, *Immunity* **23**, 227–239 (2005).
8. Materials and methods are available as supplementary materials on *Science* Online.
9. J. D. Fontenot *et al.*, *Immunity* **22**, 329–341 (2005).
10. J. M. Kim, J. P. Rasmussen, A. Y. Rudensky, *Nat. Immunol.* **8**, 191–197 (2007).
11. Z. Chen, C. Benoist, D. Mathis, *Proc. Natl. Acad. Sci. U.S.A.* **102**, 14735–14740 (2005).
12. Y. P. Rubtsov *et al.*, *Science* **329**, 1667–1671 (2010).
13. I. Shalev *et al.*, *J. Immunol.* **180**, 249–260 (2008).
14. L. W. Collison *et al.*, *Nature* **450**, 566–569 (2007).
15. M. J. Polanczyk, C. Hopke, A. A. Vandenbark, H. Offner, *Int. Immunol.* **19**, 337–343 (2007).
16. I. Gotsman *et al.*, *Circulation* **114**, 2047–2055 (2006).
17. F. Jotereau, F. Heuze, V. Salomon-Vie, H. Gascan, *J. Immunol.* **138**, 1026–1030 (1987).
18. J. M. Gardner *et al.*, *Science* **321**, 843–847 (2008).
19. E. D. Mellins, L. J. Stern, *Curr. Opin. Immunol.* **26**, 115–122 (2014).
20. Y. O. Poluektov, A. Kim, S. Sadegh-Nasseri, *Front. Immunol.* **4**, 260 (2013).
21. J. Wong, D. Mathis, C. Benoist, *J. Exp. Med.* **204**, 2039–2045 (2007).
22. J. Nishio, M. Feuerer, J. Wong, D. Mathis, C. Benoist, *J. Exp. Med.* **207**, 1879–1889 (2010).
23. M. Bogue, S. Gilfillan, C. Benoist, D. Mathis, *Proc. Natl. Acad. Sci. U.S.A.* **89**, 11011–11015 (1992).
24. D. Mathis, C. Benoist, *Annu. Rev. Immunol.* **27**, 287–312 (2009).
25. K. Kisand, P. Peterson, *Ann. N. Y. Acad. Sci.* **1246**, 77–91 (2011).
26. W. Jiang, M. S. Anderson, R. Bronson, D. Mathis, C. Benoist, *J. Exp. Med.* **202**, 805–815 (2005).
27. K. S. Tung, Y. Y. Setiady, E. T. Samy, J. Lewis, C. Teuscher, *Curr. Top. Microbiol. Immunol.* **293**, 209–247 (2005).
28. H. C. Dujardin *et al.*, *Proc. Natl. Acad. Sci. U.S.A.* **101**, 14473–14478 (2004).
29. E. T. Samy, K. M. Wheeler, R. J. Roper, C. Teuscher, K. S. Tung, *J. Immunol.* **180**, 4366–4370 (2008).
30. L. A. Herzenberg, L. A. Herzenberg, *Cell* **59**, 953–954 (1989).
31. J. A. Hill *et al.*, *Immunity* **27**, 786–800 (2007).

ACKNOWLEDGMENTS

We thank A. Rudensky, M. Anderson, and A. Lichtman for providing valuable mouse strains; F. Depis and H.-K. Kwon for insightful discussions; and A. Ortiz-Lopez, L. Denu, and K. Hattori for technical assistance. The data presented in this paper are tabulated in the main paper and in the supplementary materials. Microarray data can be found at Gene Expression Omnibus under accession numbers GSE66332 and GSE66402. This work was supported by NIH grant R01 DK060027 (to D.M.). S.Y., N.F., and D.K. were supported by fellowships from the National Research Foundation of Korea (NRF-2013M3A9B6076413), Japan Society for the Promotion of Science, and National Science Foundation, respectively.

SUPPLEMENTARY MATERIALS

www.sciencemag.org/content/348/6234/589/suppl/DC1
Materials and Methods
Figs. S1 to S12
Tables S1 and S2
References (*32*–*42*)

15 January 2015; accepted 4 March 2015
Published online 19 March 2015;
10.1126/science.aaa7017

PNAS Congratulates 2014 Cozzarelli Prize Recipients

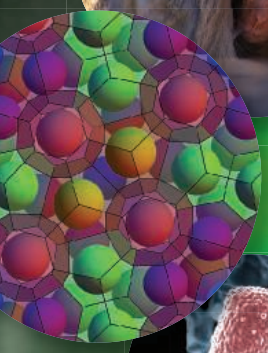

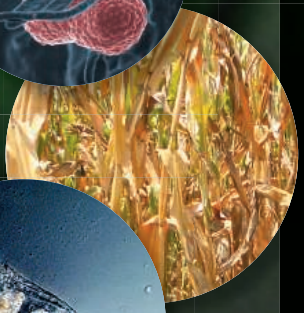

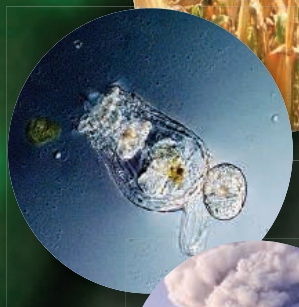

PNAS has selected six outstanding PNAS papers for the 2014 Cozzarelli Prize. The award was established in 2005 as the PNAS Paper of the Year Prize and renamed the Cozzarelli Prize in 2007 to honor late PNAS Editor-in-Chief Nicholas R. Cozzarelli. Papers receiving the Cozzarelli Prize were chosen from the more than 3,500 research articles published by PNAS in 2014 and represent the six broadly defined classes under which the National Academy of Sciences is organized.

CLASS I: PHYSICAL AND MATHEMATICAL SCIENCES

High-precision timeline for Earth's most severe extinction

Seth D. Burgess, Samuel Bowring, and Shu-zhong Shen (2014) *Proc Natl Acad Sci USA* 111(9):3316–3321

CLASS II: BIOLOGICAL SCIENCES

A propagating ATPase gradient drives transport of surface-confined cellular cargo

Anthony G. Vecchiarelli, Keir C. Neuman, and Kiyoshi Mizuuchi (2014) *Proc Natl Acad Sci USA* 111(13):4880–4885

CLASS III: ENGINEERING AND APPLIED SCIENCES

Sphericity and symmetry breaking in the formation of Frank–Kasper phases from one component materials

Sangwoo Lee, Chris Leighton, and Frank S. Bates (2014) *Proc Natl Acad Sci USA* 111(50): 17723–17731

CLASS IV: BIOMEDICAL SCIENCES

Transfer of noncoding DNA drives regulatory rewiring in bacteria

Yaara Oren, Mark B. Smith, Nathan I. Johns, Millie Kaplan Zeevi, Dvora Biran, Eliora Z. Ron, Jukka Corander, Harris H. Wang, Eric J. Alm, and Tal Pupko (2014) *Proc Natl Acad Sci USA* 111(45):16112–16117

CLASS V: BEHAVIORAL AND SOCIAL SCIENCES

Neural and cognitive characteristics of extraordinary altruists

Abigail A. Marsh, Sarah A. Stoycos, Kristin M. Brethel-Haurwitz, Paul Robinson, John W. VanMeter, and Elise M. Cardinale (2014) *Proc Natl Acad Sci USA* 111(42):15036–15041

CLASS VI: APPLIED BIOLOGICAL, AGRICULTURAL, AND ENVIRONMENTAL SCIENCES

China's international trade and air pollution in the United States

Jintai Lin, Da Pan, Steven J. Davis, Qiang Zhang, Kebin He, Can Wang, David G. Streets, Donald J. Wuebbles, and Dabo Guan (2014) *Proc Natl Acad Sci USA* 111(5):1736–1741

PNAS

www.pnas.org

Podcast interviews with the authors will be available at:
pnas.org/site/misc/cozzarelliprize.xhtml

AAAS 2016 ANNUAL MEETING | WASHINGTON, DC FEBRUARY 11–15

Global Science Engagement

Science is a global endeavor that advances when knowledge is both generated and shared. Increasingly, scientists and engineers are working both within and outside of national boundaries on local and global issues.

Challenges necessitating innovation and international scientific collaboration are abundant in food and water security, sustainable development, infectious disease and health, climate change, natural disasters, and energy. Countries with varying levels of development, education, and scientific capacity may have different goals and expectations for international scientific engagement.

What elements make international collaboration successful and sustainable? What engagement opportunities are available, and what are the responsibilities of researchers, entrepeneurs, educators, and policymakes in global scientific endeavors?

Career Development Workshops

Share your expertise. Help others advance in science and technology careers by submitting a career development workshop proposal. Workshops are designed for scientists, engineers, and students at different career stages with varying skillsets and needs.

The deadline for submitting proposals is May 11.

aaas.org/meetings

eppendorf & Science

PRIZE FOR NEURO BIOLOGY

2014 Winner
Eiman Azim, Ph.D.
Columbia University
For research on skilled limb movement

Application Deadline
June 15, 2015

Call for Entries

Eppendorf & Science Prize for Neurobiology
The annual Eppendorf & Science Prize for Neurobiology is an international award which honors young scientists for their outstanding contributions to neurobiological research based on methods of molecular and cell biology. The winner and finalists are selected by a committee of independent scientists, chaired by Science's Senior Editor, Dr. Peter Stern. To be eligible, you must be 35 years of age or younger.

You could be next to win this prize and to receive
> Prize money of US$25,000
> Publication of your work in Science
> Full support to attend the Prize Ceremony held in conjunction with the Annual Meeting of the Society for Neuroscience in the USA
> An invitation to visit Eppendorf in Hamburg, Germany

It's easy to apply!

Learn more at: www.eppendorf.com/prize

eppendorf Science AAAS

AAAS® and Science® are registered trademarks of the American Association for the Advancement of Science, USA. Eppendorf® and the Eppendorf logo are registered trademarks of Eppendorf AG Germany. U.S. Design Patents are listed on www.eppendorf.com/ip. All rights reserved, including graphics and images. Copyright © 2015 by Eppendorf AG. Kurstin Roe Photography.

CALL FOR APPLICATIONS

CHANEL

RECHERCHE ET TECHNOLOGIE

RESEARCH AND TECHNOLOGY

CHANEL-CERIES RESEARCH AWARD 2015

The CHANEL-CERIES Research Award of 40,000€ is intended to honor a scientific researcher with a proven track record in fundamental or clinical research work, for a one-year period, on the subject of

PHYSIOLOGY OR BIOLOGY OF HEALTHY SKIN AND/OR ITS REACTIONS TO ENVIRONMENTAL FACTORS

Previous Award Winners

2014 Julia A. Segre, Ph.D., Bethesda, USA
2013 Robert L. Modlin, M.D., Los Angeles, USA
2012 Martin Röcken, M.D., Ph.D., Tübingen, Germany
2011 Joke A. Bouwstra, Ph.D., Leiden, Netherlands
2010 Howard Y. Chang, M.D., Ph.D., Stanford, USA
2009 Sabine Werner, Ph.D., Zurich, Switzerland
2008 Paul A. Khavari, M.D., Ph.D., Stanford, USA
2007 Richard L. Gallo, M.D., Ph.D., San Diego, USA
2006 Irwin McLean, Ph.D., DSc, FRSE, Dundee, Scotland, UK
2005 Masayuki Amagai, M.D., Ph.D., Tokyo, Japan
2004 Thomas Schwarz, M.D., Kiel, Germany
2003 Angela M. Christiano, Ph.D., New York, USA
2002 Dennis R. Roop, Ph.D., Houston, USA
2001 Fiona M. Watt, D.Phil., London, UK
2000 Michael Karin, Ph.D., San Diego, USA
1999 Jonathan Rees, M.D., Edinburgh, UK
1998 Jean Krutmann, M.D., Düsseldorf, Germany
1997 Jens-Michael Schröder, Ph.D., Kiel, Germany
1996 Akira Takashima, M.D., Ph.D., Dallas, USA

DEADLINE FOR APPLICATIONS: JUNE 1, 2015

http://research-technology.chanel.com/research-awards

Lambda TLED™
Transmitted Light Source

High-output white light LED!

NEW!

FEATURES

- >10,000 hour lifetime
- <25µsecs on-off time
- TTL control (with polarity switch)
- Very stable output
- Compact stand-alone design
- Easy installation

SUTTER INSTRUMENT

PHONE: 415.883.0128 | FAX: 415.883.0572
EMAIL: INFO@SUTTER.COM | WWW.SUTTER.COM

AAAS *Travels*

Istanbul & Cappadocia

Including the Ancient Cities of Ephesus & Troy
September 29–October 10, 2015

Discover sites important to the heritage of Western Civilization on this great adventure to Istanbul and the fascinating caves at Cappadocia. In Istanbul, see the splendid Topkapi Palace and immense Blue Mosque & St. Sophia. In Cappadocia see the Rock-Cut Monastery, the fascinating Goreme Valley, and the earliest settlement in Anatolia. $3,995 + air

For a detailed brochure, call (800) 252-4910
All prices are per person twin share + air

BETCHART EXPEDITIONS Inc.
17050 Montebello Rd, Cupertino, CA 95014
Email: AAASInfo@betchartexpeditions.com
www.betchartexpeditions.com

New SuperScript® IV RT offers supercharged sensitivity and specificity to the heart of cDNA synthesis, for any sample, fast.

Choose to supercharge your RT at
lifetechnologies.com/ssiv

life technologies

A Thermo Fisher Scientific Brand

For Research Use Only. Not for use in diagnostic procedures. © 2015 Thermo Fisher Scientific Inc. All rights reserved.
All trademarks are the property of Thermo Fisher Scientific and its subsidiaries unless otherwise specified. CO013282 0315

Trace Gas Analysis System

PTR-TOF systems are capable of measuring trace gas samples in real-time with a high mass resolving power. The new "fastGC" module adds an optional chemical separation step before the analysis. The module consists of a short GC column with an advanced heating concept for ultrafast heating and equally fast cooling rates which makes this pre-separation step nearly real-time. A full PTR-TOF spectrum can be acquired every 100 ms—18,000 times faster than a typical GC spectrum—and contains several hundred compounds separated according to their chemical composition. Separating compounds with the same composition (isomers) remains, however, the domain of GC. The fastGC add-on provides a quick chemical preseparation step for the PTR-TOF systems. The fastGC module is integrated with the PTR-TOF and the normal sample gas inlet is utilized. This allows researchers to perform real-time measurements and add fastGC runs at time points of interest for enhanced separation and identification.

Ionicon
For info: +43-512-214-800
www.ionicon.com

Mutation Surveyor Software

Mutation Surveyor software is compatible with all major sequencing platforms and chemistries. Included in version 5.0 is a new variant knowledge database, which allows users to track variants by chromosomal position, indicate false-positives and other chemistry/sequencing artifacts, and query the variant information from popular databases such as dbSNP, dbNSFP, and COSMIC. Also incorporated in Mutation Surveyor software version 5.0 is a user management system, which enables administrators to set up password-protected user names, control access rights, and generate a user audit trail for each analysis project. Access rights for each user are determined by the administrator, providing assurance that unauthorized individuals do not accidentally alter a project or change the analysis parameters established by the laboratory. User management also provides user ID and organization in the header of the final reports. Each change to the project is captured by user and time stamped.

Soft Genetics
For info: 888-791-1270
www.softgenetics.com

Colony Counter/ID System

A vibrant new automated colony counting and chromogenic identification system, Protos 3, allows walk-away colony counts, as well as accurate identification of colonies cultured on chromogenic plates. What makes the new Protos 3 outperform other commercial colony counters is the system's ability to count colonies in seconds and identify microbial species by their color on chromogenic plates. This is a great time saver, providing accurate, objective, and fully traceable GLP-compliant results. The stylish, yet practical Protos 3, which comes in bright red, attaches easily to a computer and requires minimal training to set up. Users simply input their plate identification and click. The Protos 3, featuring a highly sensitive CCD camera combined with unique three color LED lighting, rapidly images an infinite number of colony colors on one plate and detects colonies as small as 0.043 mm. The Protos 3's powerful software then generates true to life counts and plate images.

Synbiosis
For info: +44-(0)-1223-727125
www.synbiosis.com/protos-3

Cleanroom Furniture

A brand new range of chemical-resistant lab furniture has been unveiled. The range is built from Trespa Toplab Base—a brand of high-pressure laminate plate—giving an attractive appearance and a range of inherent benefits. As well as being chemical-resistant and antistatic, it has low dirt pick-up, is easy to clean, and is scratch-resistant, making it ideal for use in a controlled lab environment. The robust cleanroom furniture can be created bespoke to requirements and a core range of sub-assemblies will be kept in stock for a short delivery time. These include a step-over bench, wall mounted shelving, and a selection of tables with options including shelving and upstands. The UK-manufactured products are ideal for use in in all Connect 2 Cleanrooms modular cleanrooms including the recently introduced modular pre-engineered version of the FM Approved Puracore wall and ceiling panel system. All products have a Trespa Toblab Base surface finish with mild steel powder coated legs.

Connect 2 Cleanrooms
For info: +44-(0)-1524-813022
www.connect2cleanrooms.com

Reverse Transcriptase

A novel, thermostable reverse transcriptase, WarmStart RTx Reverse Transcriptase, has been specifically designed for nucleic acid detection. WarmStart RTx is reversibly inhibited at room temperature, and is activated when warmed above 40°C, enabling researchers to set up their reactions at room temperature with no background reverse transcriptase activity. Maximum activity is reached at 55°C, enabling high-temperature cDNA synthesis. This results in more consistent target detection across different RNA targets. WarmStart RTx Reverse Transcriptase builds upon NEB's portfolio of enzymes for nucleic acid detection, including Hot Start Taq DNA Polymerase, Q5 Hot Start High Fidelity DNA Polymerase, Bst 2.0 WarmStart DNA Polymerase, and Antarctic Thermolabile UDG.

New England Biolabs
For info: 800-632-5227
www.neb.com/m0380

Electronically submit your new product description or product literature information! Go to www.sciencemag.org/products/newproducts.dtl for more information.

Newly offered instrumentation, apparatus, and laboratory materials of interest to researchers in all disciplines in academic, industrial, and governmental organizations are featured in this space. Emphasis is given to purpose, chief characteristics, and availability of products and materials. Endorsement by *Science* or AAAS of any products or materials mentioned is not implied. Additional information may be obtained from the manufacturer or supplier.

63 north

KNOWLEDGE FOR A BETTER WORLD

THE ONSAGER FELLOWSHIPS

12 tenure-track positions available at NTNU

The Norwegian University of Science and Technology (NTNU) is Norway's primary institution for educating the future's engineers and scientists. The university also has strong programmes in the social sciences, teacher education, the arts and humanities, medicine, architecture and fine art. NTNU's cross-disciplinary research delivers creative innovations that have far-reaching social and economic impact and that help contribute to a better world.

The Onsager Fellowship programme at NTNU is designed to attract the most talented scholars with an established reputation for high quality research and a commitment to learning and teaching at the university level.

APPLY FOR A TENURE-TRACK POSITION AS AN ASSOCIATE PROFESSOR IN:

- Linguistics
- Robotic vision
- Molecular biodiversity
- Medicine – bioinformatics
- Medicine – molecular biology
- Statistical machine learning
- Theoretical condensed matter physics
- Inorganic or hybrid functional materials
- Safety and reliability of complex systems
- Marine structures for the future – marine technology
- Zero emission refurbishment of the built environment
- Economics of natural resources and quantitative peace research

More info at: www.ntnu.edu/onsagerfellowship

Closing date: 25 May.

NTNU – Trondheim
Norwegian University of Science and Technology

TOP RESEARCH DEMANDS BRILLIANT MINDS
– WE'RE ALWAYS LOOKING FOR THE BEST

NEW ENGLAND BioLabs® Inc.

On the mend.

NEBNext® FFPE DNA Repair Mix from New England Biolabs®

While archiving of clinical materials as Formalin-Fixed, Paraffin-Embedded (FFPE) samples is common, it causes significant damage to the sample's DNA. As a result, such samples can be difficult to sequence. The cocktail of enzymes in the NEBNext FFPE DNA Repair Mix repairs multiple types of damage that are common among FFPE samples, thereby improving yields and overall library success rates.

Make sure your sample's DNA is on the mend before your next sequencing experiment!

Effect of FFPE DNA Repair Mix on library yields

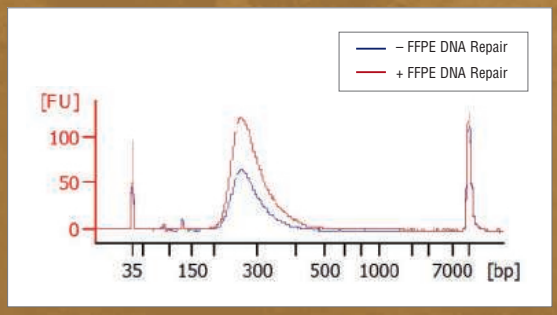

An example of Agilent Bioanalyzer® traces of libraries prepared from stomach tumor FFPE DNA that was treated with the FFPE DNA Repair Mix, or was untreated, before library construction. Yield improvements of 101% to 458% have been observed.

Visit www.neb.com/M6630 to learn more.

NEW ENGLAND BIOLABS®, NEB® and NEBNext® are registered trademarks of New England Biolabs, Inc.
BIOANALYZER® is a registered trademark of Agilent Technologies, Inc.

ScienceCareers online @sciencecareers.org

Science Careers Advertising

For full advertising details, go to ScienceCareers.org and click For Employers, or call one of our representatives.

Tracy Holmes
Worldwide Associate Director
Science Careers
Phone: +44 (0) 1223 326525

THE AMERICAS

E-mail: advertise@sciencecareers.org
Fax: 202 289 6742

Tina Burks
Phone: 202 326 6577

Nancy Toema
Phone: 202 326 6578

Marci Gallun
Sales Administrator
Phone: 202 326 6582

Online Job Posting Questions
Phone: 202 312 6375

EUROPE / INDIA / AUSTRALIA / NEW ZEALAND / REST OF WORLD

E-mail: ads@science-int.co.uk
Fax: +44 (0) 1223 326532

Axel Gesatzki
Phone: +44 (0) 1223 326529

Sarah Lelarge
Phone: +44 (0) 1223 326527

Kelly Grace
Phone: +44 (0) 1223 326528

JAPAN

Katsuyoshi Fukamizu (Tokyo)
E-mail: kfukamizu@aaas.org
Phone: +81 3 3219 5777

Hiroyuki Mashiki (Kyoto)
E-mail: hmashiki@aaas.org
Phone: +81 75 823 1109

CHINA / KOREA / SINGAPORE / TAIWAN / THAILAND

Ruolei Wu
Phone: +86 186 0082 9345
E-mail: rwu@aaas.org

All ads submitted for publication must comply with applicable U.S. and non-U.S. laws. *Science* reserves the right to refuse any advertisement at its sole discretion for any reason, including without limitation for offensive language or inappropriate content, and all advertising is subject to publisher approval. *Science* encourages our readers to alert us to any ads that they feel may be discriminatory or offensive.

ScienceCareers
FROM THE JOURNAL SCIENCE AAAS

ScienceCcareers.org

中国科学院上海巴斯德研究所
INSTITUT PASTEUR OF SHANGHAI
CHINESE ACADEMY OF SCIENCES

Director-General Position at Institut Pasteur of Shanghai, Chinese Academy of Sciences (IPS-CAS), Shanghai, China

The Chinese Academy of Sciences (CAS) invites applications for the position of Director-General of the Institut Pasteur of Shanghai, CAS (IPS-CAS).

I. About IPS-CAS

IPS-CAS, an independent legal entity jointly founded by CAS, Institut Pasteur and Shanghai Municipal Government in 2004, focuses on the studies of Virology, Immunology, and Vaccinology etc. IPS-CAS has played an important role in the promotion of science and technology development in China, functioning as the epicenter to promote Sino-French friendship and science/technology cooperation since its inception.

For more information, please visit: **http://english.shanghaipasteur.cas.cn/**

II. Job description

1. IPS-CAS practices the responsibility system by the Director General (DG) of the Institute in management. The DG's responsibility includes the execution of the decisions made by the Board of Directors and CAS, the organization and administration of the overall issues of the Institute including its daily management.
2. Manage the Institute in accordance with the policies decided by the Board of Directors and CAS and within the limits of the annual budget.
3. Define and determine the scientific objectives and issues of research of the Institute under the guidance of the Scientific Advisory Board in consultation with the Scientific Co-Director and manage the research, development, public relation/health and academic activities of the Institute.
4. Prepare the annual budget of the Institute and ensure its submission to the Board of Directors.
5. Prepare the scientific reports and annual report of the Institute and ensure their submission to the Board of Directors on a regular basis.
6. The term of the DG is 5 years and it can be renewed once with the decision/proposal of the Board of Directors and the approval of CAS management.

III. Eligibility

1. Applicants are expected to have the confidence and determination to promote the development of IPS-CAS and achieve its objectives in light of the guiding principles of CAS in the coming years.
2. Should be leaders of integrity, democratic in their style of work, and open to different views.
3. Should have remarkable capacity for strategic thinking, macroscopic decision-making and overall control with an emancipated mind, a spirit of pioneering, innovation and enterprise, and a sense of responsibility.
4. Must hold a doctoral degree and professorship or equivalent in a world-class university or research institution with a globally recognized record of academic accomplishment in basic and applied research in health sciences with particular emphasis in the area of infectious diseases.
5. Their research interest should be in line with the major academic directions of IPS-CAS and in principle they must have around 10 years of experience in leading scientific research projects and managing S&T teams.
6. They shall hold Chinese passport to qualify for the position of legal representative of a state-owned research institute.
7. He or she shall work at IPS-CAS for full time.

III. Application Materials

1. Please fill in the application downloaded from **http://www.pe.cas.cn/xwdt/rczp/201504/t20150416_4338307.html**
2. Applicants are expected to submit a 3,000- word written report in both Chinese and English, providing:

An overview of your experience and information about your major academic achievements.

Your understanding of the positioning, philosophy, S&T layout, and strategy for the development of IPS-CAS in light of CAS planning and initiatives.

Your advantages and shortcomings.

IV. Application Submission

Please email your applications to the Human Resources Department of CAS and confirm by telephone.

V. Application Deadline

Applications are accepted from **April 16 to May 27, 2015**.

VI. Contact Information:

JI Kuixian or SONG Qi
Human Resources Department, CAS
E-mail: kxji@cashq.ac.cn or qsong@cashq.ac.cn
Tel. 86-10-68597472, or 86-10-68597449

EMBL

The European Molecular Biology Laboratory offers a highly collaborative, uniquely international culture. It fosters top quality, interdisciplinary research by promoting a vibrant environment consisting of young independent research groups with access to outstanding graduate students and postdoctoral fellows. Significant core funding and limited teaching responsibilities allow EMBL group leaders to undertake ambitious, farsighted research programmes and provide a scientific environment that is particularly attractive for researchers with families.

Group Leader
Epigenetics and Mouse Genetics
at EMBL Monterotondo, Italy

The Scientific Programme of EMBL emphasises experimental analysis at multiple levels of biological organisation, from the molecule to the organism, as well as Computational Biology, Bioinformatics and Systems Biology. Within this overall structure, the EMBL Monterotondo Unit applies a wide range of modern technologies to diverse problems of whole organism biology. Currently, its research groups address areas of neurobiology, epigenetics, developmental biology and developmental genetics and are supported by state-of-the-art core facilities in histology, recombineering/gene editing, flow cytometry, microscopy, and mouse transgenesis.

EMBL Monterotondo benefits from close interactions with groups at EMBL Heidelberg in the Developmental Biology, Genome Biology, Cell Biology and Biophysics, and Structural and Computational Biology Units with whom it shares core facilities in high-throughput sequencing, advanced light and electron microscopy, small molecule screening, protein production, and mass spectroscopy. EMBL Monterotondo groups also have access to research activities at the EMBL-EBI (European Bioinformatics Institute) in Hinxton, UK, and structural biology expertise at EMBL Hamburg and Grenoble.

EMBL is searching for a Group Leader to head up an independent research group in the EMBL Monterotondo Unit in Rome. We seek dynamic and interactive individuals having recently completed their post-doctoral training with an excellent scientific track record and demonstrated experience or interest in the general area of epigenetics and developmental biology. We encourage applications from scientists working on diverse questions relating to mammalian organismal biology that would benefit from the mouse as an experimental system and the use of modern genetic and genomic approaches.

EMBL is an inclusive, equal opportunity employer offering attractive working conditions and benefits appropriate to an international research organisation. The remuneration package comprises a competitive salary, a comprehensive pension scheme, medical, educational and other social benefits, as well as financial support for relocation and installation, including for family. Female candidates are strongly encouraged to apply.

Please apply online through **www.embl.org/jobs** and include a cover letter, CV and a concise description of research interests and future research plans. Please also arrange for 3 letters of recommendation to be emailed to **references@embl.de** at the latest by 31 May 2015.

Interviews are planned for 26 June 2015.

Further information about the position can be obtained from the Head of the Monterotondo Unit Philip Avner (**philip.avner@embl.it**).

An initial contract of 5 years will be offered to the successful candidate. This is foreseen to be extended to a maximum of 9 years, subject to an external review.

Further details on Group Leader appointments can be found under **www.embl.org/gl_faq**.

www.embl.org

ScienceCareers online @sciencecareers.org

ScienceCareers online @sciencecareers.org

Director Position

Biodiversity Research Center
Academia Sinica, Taiwan

Academia Sinica, Taiwan, invites applications and nominations for the position of Director of the Biodiversity Research Center (BRC). The initial appointment is for a period of three years (renewable for a second term), and will also carry the title of Research Fellow.

As the pre-eminent academic research institution in Taiwan, Academia Sinica is devoted to basic and applied research in life sciences, mathematics and physical sciences, humanities, and social sciences. BRC currently consists of 19 laboratories engaging in the following four focal areas of research: "Marine Biodiversity and Ecosystems", "Terrestrial Biodiversity and Ecosystems", "Evolutionary Genetics and Genomics", and "Microbial Diversity and Bioinformatics". BRC is well funded and equipped with modern research facilities managed by experienced research specialists. BRC maintains a high research standard with a high-quality publication record. For details about Academia Sinica and BRC, please see **http://www.sinica.edu.tw** and **http://biodiv.sinica.edu.tw/**, respectively.

Interested candidates should have a PhD or equivalent degree, with outstanding research accomplishments and demonstrated leadership ability. Besides pursuing a rigorous research program at BRC, the successful candidate is expected to build on the existing strengths of BRC, develop new research thrusts, and provide intellectual leadership in biodiversity research in Taiwan.

Applications including complete curriculum vitae, a publication list, and research accomplishments, or nominations with a brief rationale for recommendation and contact information, should be submitted to **Dr. Tao-shih Hsieh, Academia Sinica, 128 Academia Road, Section 2, Nankang, Taipei 115, Taiwan** or by Email to **charity@gate.sinica.edu.tw**. Letters of recommendation will be requested on the applicant's behalf. Screening of applications/nominations will begin **June 1st, 2015**, and will continue until the position is filled.

MAX-PLANCK-GESELLSCHAFT
UNIVERSIDAD NACIONAL DE COLOMBIA
UNIVERSIDAD DE ANTIOQUIA

The Max Planck Society (MPS), the Administrative Department of Science, Technology and Innovation (COLCIENCIAS), the Universidad Nacional de Colombia, Bogotá, and the Universidad de Antioquia, Medellín, intend to establish several independent

MAX PLANCK TANDEM GROUPS

- **in Infectious Diseases (hosts, pathogens, vectors), and**
- **in Biological Diversity and Chemical Approaches for Disease Intervention.**

We are seeking candidates for the position of the Principal investigator (PI), with the title of MAX PLANCK TANDEM GROUP LEADER (MPTGL). The candidate must be at the beginning of a successful scientific career with at least three years of postdoctoral experience, and be highly motivated to develop and carry out a competitive research program at the international level.

Other than the research activities, responsibilities include high-impact publications and the supervision of postdocs, students and technicians. Solid, sustainable ties of collaboration will be developed between the Tandem Groups within their host institution and other universities and research institutes in Colombia, and the Max Planck Institutes that are part of the Agreement.

The salary of the position is highly competitive according to local standards. Additional funds will be allocated for staff, supplies and research equipment. The successful candidate will be appointed initially for 5 years with the possibility of two year extension following an outstanding independent external evaluation.

Applications, including a curriculum vitae, list of publications, reprints of three selected papers, a two-page description of scientific achievements, a two-page research plan and two letters of recommendation should be sent electronically as one pdf file to: Ines Conde, Max Planck Liaison Office for Latin America, Buenos Aires, email: latam@gv.mpg.de

Deadline for registration is 15 June 2015. Short-listed candidates will be invited to a selection symposium in Bogotá, Colombia, from 25 to 28 August 2015, at which they will have the opportunity to present their research. For further information and detailed instructions, see **www.facebook.com/sociedadmaxplanck**

COLCIENCIAS
Ciencia, Tecnología e Innovación

Download Free
Career Advice Booklets!
ScienceCareers.org/booklets

Featured Topics:
- Networking
- Industry or Academia
- Job Searching
- Non-Bench Careers
- And More

ScienceCareers
FROM THE JOURNAL SCIENCE AAAS

FUNDING OPPORTUNITIES — U.S. Department of Defense

Defense Medical Research and Development Program

Peer Reviewed Medical Research Program

The Peer Reviewed Medical Research Program (PRMRP) funds exceptional research with the goal to improve the health and well-being of all military Service Members, Veterans, and their beneficiaries. The PRMRP received ***$247.5 million*** in fiscal year 2015 (FY15) and seeks grant applications in the following ***topic areas:***

Acupuncture
Acute lung injury
Advanced prosthetics
Arthritis
Burn pit exposure
Cardiovascular health
Chronic migraine and post-traumatic headache
Congenital heart disease
Dengue
Diabetes
DNA vaccine technology for post-exposure prophylaxis
Dystonia
Focal segmental glomerulosclerosis
Food allergies
Fragile X syndrome
Healthcare-acquired infection reduction
Hepatitis B
Hereditary angioedema
Hydrocephalus
Inflammatory bowel disease
Integrative medicine
Interstitial cystitis
Lupus
Malaria
Metals toxicology
Mitochondrial disease
Nanomaterials for bone regeneration
Osteoarthritis
Pancreatitis
Pathogen-inactivated dried plasma
Polycystic kidney disease
Post-traumatic osteoarthritis
Psychotropic medications
Pulmonary fibrosis
Respiratory health
Rheumatoid arthritis
Scleroderma
Sleep disorders
Tinnitus
Vascular malformations
Women's heart disease

Descriptions of the FY15 PRMRP Program Announcements and General Application Instructions are anticipated to be posted on Grants.gov by ***mid-April 2015:***

- Clinical Trial Award
- Discovery Award
- Focused Program Award
- Investigator-Initiated Research Award
- Technology/Therapeutic Development Award

All applications must conform to the Program Announcements and General Application Instructions that will be available for electronic downloading from the Grants.gov website (all viewable under CFDA number 12.420). Execution management support will be provided by the Congressionally Directed Medical Research Programs.

http://cdmrp.army.mil
http://cdmrp.army.mil/funding/prmrp.shtml

NAVAL RESEARCH LABORATORY
Superintendent, Chemistry Division

www.nrl.navy.mil

Senior Executive Service Career Opportunity
ES-0401/1310/1320: $121,956 to $183,300 per annum*
*Actual salary may vary depending on the scope and complexity of the position and the qualifications and current compensation of the selectee.

Become a member of an elite research and development community involved in basic and applied scientific research and advanced technological development for tomorrow's Navy and for the Nation.

- Manages, directs, and administers a recognized scientific work force conducting a broad spectrum research program in the various areas of chemistry including chemical physics, chemical engineering, surface chemistry, nanoscience and nanotechnology.
- Executive direction and technical visionary leadership in development of programs, policies, and objectives necessary in conducting a program of research, development, and evaluation leading to creation, adoption and application of improved and new concepts, principles, methods, and techniques applicable to understanding and observing in a chemical environment.
- Principal consultant to the Navy, other agencies and nations on the science and developing applications for the R&D programs under his/her cognizance.
- Applicants should be recognized as national/international authorities and should have planned and executed difficult programs of national significance or specialized programs that show outstanding attainment in their field of research.

For information regarding this vacancy and specific instructions on how to apply, go to www.usajobs.gov, log in and enter the following announcement number: **NW5XXXX-00-1354889K9071628S**. Please carefully read the announcement and follow instructions when applying. The announcement closes **May 31, 2015**. Please contact Annemarie Slattery at **annemarie.slattery@nrl.navy.mil** for more information. E-mailed resumes cannot be accepted.

NRL is an Equal Opportunity Employer.

NRL, 4555 Overlook Ave SW, Washington DC 20375

For Women in Science

CALL FOR NOMINATIONS

L'OREAL-UNESCO FOR WOMEN IN SCIENCE
INTERNATIONAL AWARDS
2016 EDITION, LIFE SCIENCES

Created in 1998, the L'Oréal-UNESCO For Women in Science International Awards identify and support eminent women in science throughout the world. Each year, five Laureates are recognized for their contributions to the advancement of science, in Life or Physical Sciences in alternating years.

The 2016 Awards will designate five outstanding researchers in the Life Sciences, working in one of each of the following regions:

Africa & the Arab States
Asia-Pacific
Europe
Latin America
North America

Each of the five Laureates will receive an award of €100,000

More information and the nomination forms are available on the website www.fwis.fr
Deadline to submit nominations: June 16th 2015

ScienceCareers online @sciencecareers.org

ScienceCareers online @sciencecareers.org

For recruitment in science, there's only one Science

What makes *Science* the best choice?

- Read and respected by 570,400 readers around the globe
- 78% of readers read *Science* more often than any other journal
- Your ad sits on specially labeled pages to draw attention to the ad
- Your ad dollars support AAAS and its programs, which strengthens the global scientific community.

Why choose this biotechnology section for your advertisement?

- Relevant ads lead off the career section with special Biotechnology banner
- Bonus distribution to:

  BIO International Convention
  June 15–18, 2015, Philadelphia, PA

  BIO Career Fair
  June 18, 2015, Philadelphia, PA.

Expand your exposure. Post your print ad online to benefit from:

- Link on the job board homepage directly to biotechnology jobs
- Dedicated landing page for jobs in biotechnology
- Additional marketing driving relevant job seekers to the job board.

* Ads accepted until June 8 on a first-come, first-served basis.

SCIENCECAREERS.ORG

ScienceCareers
FROM THE JOURNAL SCIENCE AAAS

To book your ad: **advertise@sciencecareers.org**

The Americas
202-326-6582

Europe/RoW
+44(0)1223-326500

Japan
+81-3-3219-5777

China/Korea/Singapore/Taiwan
+86-186-0082-9345

Cernet

ScienceCareers

“《科学》职业”已经与Cernet/赛尔互联开展合作。中国大陆的高校可以直接联系Cernet/赛尔互联进行国际人才招聘。

请访问
Sciencecareers.org/CER
点得联系信息。

中国大陆高校以外的 招聘广告，或者高校 的其它业务，请与国 际合作、出版副总监吴若蕾联系：
+86-186 0082 9345
rwu@aaas.org

Science

Co-Director, Institut Pasteur of Shanghai (IP-S)

Location: Shanghai
Term: Minimum 2 years
Hired: As soon as possible
Task: Co-Director of IP-S
Hierarchy: Director General/Board of Directors of IP-S

Institut Pasteur

Structure: The “Institut Pasteur Shanghai, Chinese Academy of science” is an independent, non-profit life sciences institute to address public health issues in China and the Asian region, created by an agreement signed on 30 August 2004, by the Chinese Academy of Sciences, the Municipality of Shanghai, and the Institut Pasteur. IPS creates synergies between the Institut Pasteur and CAS networks, leveraging all the assets of Shanghai as one of Asia’s leading business and technology hubs.
More information on: **english.shanghaipasteur.cas.cn**

Activities: Within the management team, the Co-Director plays a key role in science at IP-S. He/she is also responsible for international relations, including the promotion of interactions and collaborations with research institutions as the Institut Pasteur and its international Network.

Skills and qualification: The co-director is highly experienced research scientist with an excellent publication record and international reputation in bio-science including infection biology, immunology, microbiology (viruses, bacteria or parasites) and cell biology.

- Extensive leadership, team building and management skills.
- Successfully created new research groups, and assisted them to achieve excellence.
- An excellent track record in research funding through national and international research grants and management of research consortia.
- A thorough knowledge of the Institut Pasteur and its international Network.
- Experience in translating research discoveries into pharmaceutical developments, including patents and licenses.

The working language of the institute in English - Communicating in Chinese is an advantage.

How to hire:
Format: Motivation letter, curriculum vitae, titles and works, only one pdf file by e-mail
Deadline: Applications are accepted from April 13 to May 27, 2015

To whom: Please send your application by e-mail to:

1. **emploi.international@pasteur.fr**
2. **Prof Philippe Kourilsky, co-president of the selection committee: philippe.kourilsky@pasteur.fr**
3. **European candidates must imperatively submit their applications by following the online procedure from the link below: https://pastel.diplomatie.gouv.fr/transparenceext/statiques_transparence_dossier_candidature.php**

CHIEF, RNA BIOLOGY LABORATORY
CENTER FOR CANCER RESEARCH
NATIONAL CANCER INSTITUTE - FREDERICK, MARYLAND
NATIONAL INSTITUTES OF HEALTH
DEPARTMENT OF HEALTH AND HUMAN SERVICES

Application Deadline: June 15, 2015

CENTER FOR CANCER RESEARCH

NCI is seeking an outstanding, internationally recognized scientist to serve as Chief of the RNA Biology Laboratory (RBL) in the Center for Cancer Research (CCR). The position, which is the equivalent of an academic Department Chair, is the key component of a major initiative to expand CCR’s RNA Biology research at the NCI. The RBL Chief will play leading roles in developing an integrated program in RNA Biology and in the CCR RNA Initiative. In addition, the RBL Chief will direct an extensive individual research program at the Frederick campus which will complement and augment CCR expertise in chromosome biology, immunology, HIV/AIDS, cancer biology and molecular oncology, areas in which Centers of Excellence have been established. Supported with stable financial resources, the RBL will have access to a wide array of intellectual and technological assets, including high-quality technology cores dedicated to protein chemistry, natural products chemistry, biophysics, mass spectrometry, imaging, microscopy, proteomics and genomics, bioinformatics/bio-statistics, and flow cytometry, in addition to clinical support.

The National Cancer Institute (NCI) is part of the National Institutes of Health (NIH) in the Department of Health and Human Services (DHHS), a federal government agency. CCR is the largest component of the NCI Intramural Research Program, providing an environment conducive to advancing translational research and collaborative interactions through investigator-initiated and interdisciplinary team science. Additional information on CCR research priorities can be found at: http://ccr.cancer.gov.
In addition to a Ph.D., M.D./Ph.D., or equivalent doctoral degree in a relevant discipline, applicants should possess outstanding communication skills and documented leadership experience. Tenured faculty or industrial scientists of equivalent rank with a demonstrated commitment to RNA Biology should apply. Salary will be commensurate with experience and accomplishments. Applications should include a description of research interests and leadership philosophy, career synopsis, and current curriculum vitae with complete bibliography.

Review of applications will begin on or about **June 15, 2015** but applications will be accepted until the position is filled. Send applications to **Dr. Janelle Cortner, RNA Biology Laboratory Search Committee, National Cancer Institute Building 428/46, PO Box B, Frederick MD 21702**, or by email to **CCR_RNA_Biology@mail.nih.gov**

DHHS, NIH and NCI are Equal Opportunity Employers.

NATIONAL INSTITUTES OF HEALTH

NATIONAL CANCER INSTITUTE

By **Rachel Bernstein**

From war to science paradise

Waiting for the sun to rise over the mountains on the Big Island of Hawaii, botany graduate student Gerry Cobian readies for his day's work, collecting plant leaves. When he gets the samples back to the lab, at the University of Hawaii, Manoa, in Honolulu, he'll study the fungi that live inside those leaves, investigating their diversity and community dynamics. Now though, in the forest, he soaks in the peaceful beauty. "It's amazing," he says. "You couldn't ask for a better place to be alone."

Cobian hasn't always worked in such idyllic surroundings. He was a U.S. Marine from 2000 to 2004, a machine gunner in the force that invaded Iraq and marched on to Baghdad. He enlisted after finishing high school because at the time, he says, "I had no idea what to do with my life." During his childhood he moved around California—Los Angeles, Santa Ana, Chico—playing baseball and romping outside with friends. He spent summers on his grandparents' farm in rural Mexico, milking cows, planting corn, and playing soccer. He did well in school but was never excited about science, and his interest in schoolwork waned as he got older. "My main objective in high school was skateboarding," he says.

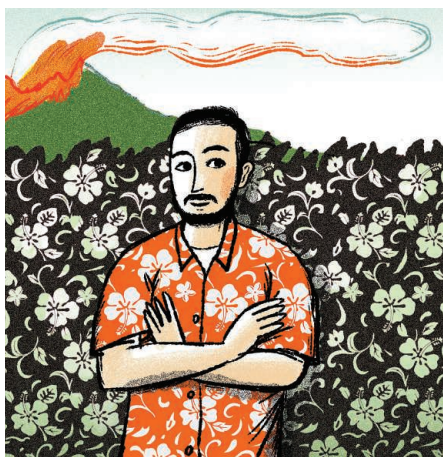

"You couldn't ask for a better place to be alone."

His father pushed him to go to college, but Cobian "didn't see it as that important at the time." Instead, he enlisted in the Marine Corps and did two Iraq tours. During his service, he decided he should continue his education when he went home, but "I was kind of scared when I first came out," he says. "I was 22, and I thought I was too old to go to school." Instead, he worked construction.

A few years later, he took his sister, 6 years his junior, to her college orientation. That trip convinced him to follow her. He started community college, studying economics. He transferred to the University of California (UC), Berkeley, took a biology class, and "just fell in love with how life works," he says. "The part that got me was the life cycles," particularly of plants and fungi, which are so diverse and different from those of animals.

He faced a difficult choice: Stick with economics or start college over. His family encouraged him to stay on the economics track because he had already invested so much work and time, but he followed his heart instead. He went back to community college for the biology prerequisites and completed his UC Berkeley degree in genetics and plant biology. His research on fungus ecology and evolution inspired him to go to graduate school. His goal: to become a professor and run his own lab.

He got married as he was finishing up at UC Berkeley. Now he has a 2-year-old daughter; another child is on the way. He works hard to balance work and family life, in part because of his own childhood experience. His parents split up before he was a year old, and he lived with his father for most of his childhood. They didn't see each other much, though, because his dad was always working: driving trucks, doing body work on cars, installing kitchens for restaurants. He appreciates the work ethic that his father instilled in him—he describes his family members as "probably the hardest working people I know"—but he wants his daughter's childhood to be different.

"I'm grateful for what my dad gave me, but I want to have a presence at home," he says—so he leaves the house before his family wakes so that he can be home before dinner. When he travels from Honolulu to the Big Island for fieldwork, his family usually goes along. The balance isn't always ideal—this semester, for example, he was studying for his comprehensive exams and couldn't spend as much time with his family as he wanted to—but he thinks he has much to look forward to. "It's a sacrifice for now, but if this is what I want to do, I have to make the sacrifice." It doesn't hurt that, for now at least, he gets to make it in Hawaii. ■

Rachel Bernstein is a staff writer for Science *Careers. For more on life and careers, visit www.sciencecareers.org. Send your story to SciCareerEditor@aaas.org.*

ILLUSTRATION: ROBERT NEUBECKER

Downloaded from www.sciencemag.org on April 30, 2015

Published by AAAS